

LOCKHEED MARTIN ENERGY RESEARCH LIBRARIES



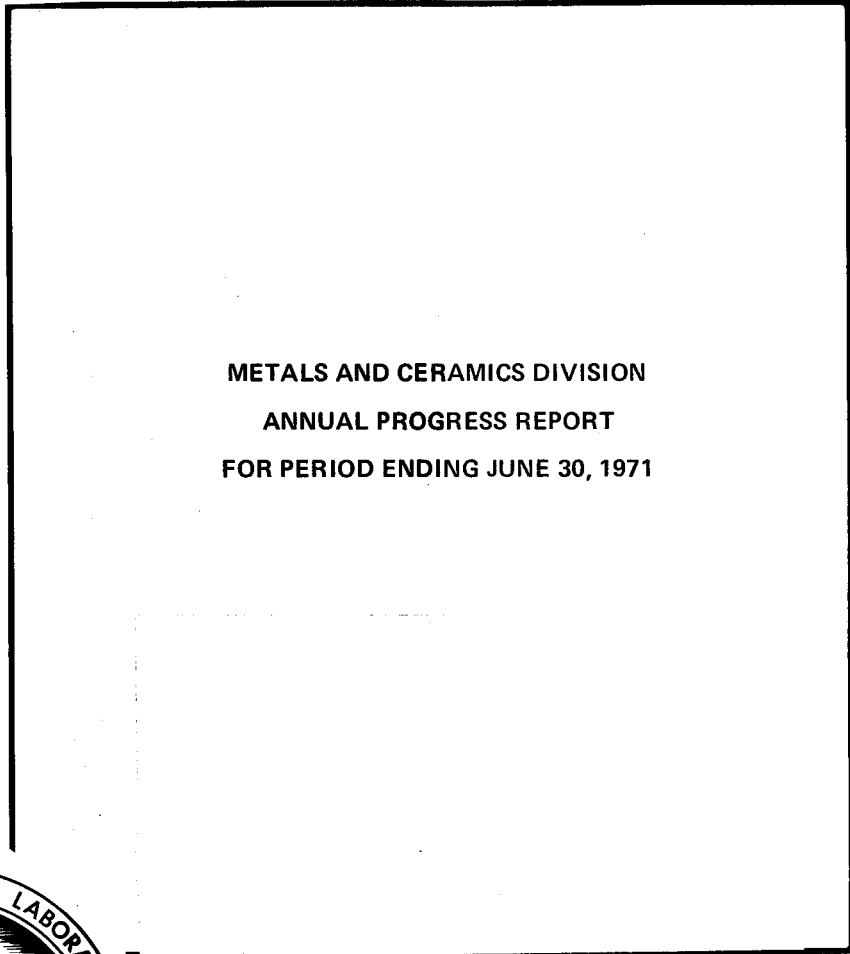
CENTRAL RESEARCH LIBRARY
DOCUMENT COLLECTION

3 4456 0515399 0

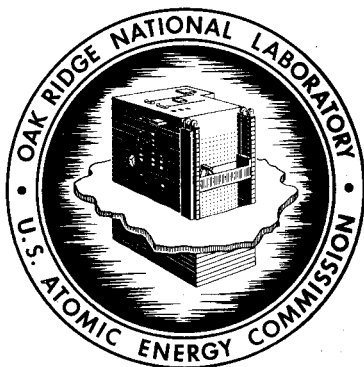
cy.1

ORNL-4770

UC-25 - Metals, Ceramics, and Materials



**METALS AND CERAMICS DIVISION
ANNUAL PROGRESS REPORT
FOR PERIOD ENDING JUNE 30, 1971**



OAK RIDGE NATIONAL LABORATORY

operated by

UNION CARBIDE CORPORATION

for the

U.S. ATOMIC ENERGY COMMISSION

Printed in the United States of America. Available from
National Technical Information Service
U.S. Department of Commerce
5285 Port Royal Road, Springfield, Virginia 22151
Price: Printed Copy \$3.00; Microfiche \$0.95

This report was prepared as an account of work sponsored by the United States Government. Neither the United States nor the United States Atomic Energy Commission, nor any of their employees, nor any of their contractors, subcontractors, or their employees, makes any warranty, express or implied, or assumes any legal liability or responsibility for the accuracy, completeness or usefulness of any information, apparatus, product or process disclosed, or represents that its use would not infringe privately owned rights.

Contract No. W-7405-eng-26

METALS AND CERAMICS DIVISION ANNUAL PROGRESS REPORT
for Period Ending June 30, 1971

J. H. Frye, Jr., Director
J. E. Cunningham, Associate Director

Section Heads

G. M. Adamson, Jr.
W. O. Harms
C. J. McHargue
P. Patriarca
J. R. Weir, Jr.

Compiled and Edited by Sigfred Peterson

SEPTEMBER 1971

OAK RIDGE NATIONAL LABORATORY
Oak Ridge, Tennessee
operated by
UNION CARBIDE CORPORATION
for the
U.S. ATOMIC ENERGY COMMISSION

LOCKHEED MARTIN ENERGY RESEARCH LIBRARIES



3 4456 0515399 0

Reports previously issued in this series are as follows:

ORNL-28	Period Ending March 1, 1948
ORNL-69	Period Ending May 31, 1948
ORNL-407	Period Ending July 31, 1949
ORNL-511	Period Ending October 31, 1949
ORNL-583	Period Ending January 31, 1950
ORNL-754	Period Ending April 30, 1950
ORNL-827	Period Ending July 31, 1950
ORNL-910	Period Ending October 31, 1950
ORNL-987	Period Ending January 31, 1951
ORNL-1033	Period Ending April 30, 1951
ORNL-1108	Period Ending July 31, 1951
ORNL-1161	Period Ending October 31, 1951
ORNL-1267	Period Ending January 31, 1952
ORNL-1302	Period Ending April 30, 1952
ORNL-1366	Period Ending July 31, 1952
ORNL-1437	Period Ending October 31, 1952
ORNL-1503	Period Ending January 31, 1953
ORNL-1551	Period Ending April 10, 1953
ORNL-1625	Period Ending October 10, 1953
ORNL-1727	Period Ending April 10, 1954
ORNL-1875	Period Ending October 10, 1954
ORNL-1911	Period Ending April 10, 1955
ORNL-1988	Period Ending October 10, 1955
ORNL-2080	Period Ending April 10, 1956
ORNL-2217	Period Ending October 10, 1956
ORNL-2422	Period Ending October 10, 1957
ORNL-2632	Period Ending October 10, 1958
ORNL-2839	Period Ending September 1, 1959
ORNL-2988	Period Ending July 1, 1960
ORNL-3160	Period Ending May 31, 1961
ORNL-3313	Period Ending May 31, 1962
ORNL-3470	Period Ending May 31, 1963
ORNL-3670	Period Ending June 30, 1964
ORNL-3870	Period Ending June 30, 1965
ORNL-3970	Period Ending June 30, 1966
ORNL-4170	Period Ending June 30, 1967
ORNL-4370	Period Ending June 30, 1968
ORNL-4470	Period Ending June 30, 1969
ORNL-4570	Period Ending June 30, 1970

Contents

SUMMARY	xv
PART I. FUNDAMENTAL PROGRAMS	
1. CRYSTAL PHYSICS	1
Internal Centrifugal Zone Growth	1
Directional Solidification in a Multicomponent Metal–Metal Oxide System	1
UO ₂ -MO _x Eutectics	1
Continued UO ₂ -W Eutectic Study	2
Other Metal–Metal Oxide Eutectics	2
High-Temperature Solution Growth of Single-Crystal Plutonium Dioxide	2
Czochralski Growth of Single-Crystal Mg ₂ SiO ₄ (Forsterite)	2
Czochralski Growth of Transuranic-Doped CaWO ₄ Single Crystals	2
Czochralski Growth of Doped KMgF ₃ Single Crystals	3
High-Temperature Solution Growth of Single-Crystal ThO ₂ Doped with About 0.1 at. % ²⁴¹ Pu	3
Electron Paramagnetic Resonance of Several Rare-Earth Impurities in the Cubic Perovskite KMgF ₃	3
ESR of Pb ³⁺ Centers in ThO ₂	3
Electron Paramagnetic Resonance Investigations of 5f ⁵ Configuration Ions in Cubic Single Crystals: Pu ³⁺ in ThO ₂ and SrCl ₂ , and Am ⁴⁺ in ThO ₂	3
Electron Paramagnetic Resonance Investigations of Divalent Americium and Trivalent Curium in Strontium Chloride	4
Characterization of RbOH-Grown Quartz by Infrared and Mass Spectroscopy	4
Lamellar Dendritic Growth in Lead Sulfide	4
Temperature-Gradient Zone Melting of Graphite	4
2. CRYSTAL SPECTROSCOPY	5
Construction on a High-Temperature Spectrometer	5
Construction on a Low-Temperature Spectrometer	5
The Raman Spectra of Molten Aluminum Trihalide–Alkali Halide Systems	5
Magnetic Moment of Ti(AlCl ₄) ₂	5
Coordination Chemistry of Nickel(II) in Liquid Mixtures of Cesium Chloride and Aluminum Chloride	5

3. DEFORMATION OF CRYSTALLINE SOLIDS	7
The Representation of Solid Solutions	7
Dissociation of Nonbasal Dislocations in Hexagonal Close-Packed Metals	7
Displacement Fields of Straight Dislocations in Anisotropic Crystals	7
Elastic Interaction of a Point Defect with a Prismatic Dislocation Loop in Hexagonal Crystals	8
Morphological Forms of the Alpha-Phase During Precipitation from a bcc Matrix in Nb-Hf Alloys	8
Strengthening Nb-Hf Alloys by Alpha Precipitation	8
Observations of $\text{Cu } K\alpha_{3,4}$ Reflections in X-Ray Diffraction Experiments	9
4. DIFFUSION IN SOLIDS	10
Tracer Self-Diffusion in Fe–17 wt % Cr–12 wt % Ni	10
Thermotransport of Cadmium in Sodium and Potassium Chlorides	10
Cation Self-Diffusion in Rutile (TiO_2)	11
Cation Self-Diffusion in Titanium Monoxide	11
Diffusion Under High Pressures	11
5. ELECTRON MICROSCOPY	12
Damage in Aluminum by 200-kV Electrons	12
The Effects of Electron Irradiation on Preexisting Defects in Aluminum	12
The Effects of Irradiation Temperature and Preinjected Gases on Voids in Aluminum	12
Radiation Voids in High-Purity Magnesium	13
Void Coarsening in High-Purity Aluminum During Postirradiation Annealing	13
The Effects of Different Microstructures on the Formation of Dislocation Loops in Aluminum During Electron Irradiation	13
Effects of Preinjected Hydrogen on the Electron Displacement Damage in 1100 Aluminum	14
Swelling of Carbonyl Nickel	14
Mechanisms of Void Formation in Solids Under Irradiation	14
Vacancies in Ternary Alloys	14
Defects in Boron Carbide Before and After Neutron Irradiation	14
Dislocation Nodes in the Boron Carbide Structure	15
Dislocations in Double Helices	15
Maps of Brillouin Zone Boundaries	15
Hardness–Flow Stress–Grain Size Relationships in Iron	15
Planar Interfaces and the Hardness of Polycrystalline α -Brass	15
An Analysis of Some Theories of Work Hardening in Terms of Stored Energy Data on fcc Single Crystals	16
The Energy Stored in Polycrystalline Cu_3Au : Effects of Long-Range Order	16
The Energy Stored in Polycrystalline Copper Deformed at Room Temperature	16
Comments on “Stored Energy and Work Hardening Theories”	17
Effects of Composition and Aging on the Microstructure of Hastelloy N Modified with Hafnium, Titanium, and Niobium	17

6. FUNDAMENTAL AND PHYSICAL CERAMICS RESEARCH	18
Deformation of Hyperstoichiometric UO_2 Single Crystals	18
Further Deformation Studies of Hyperstoichiometric UO_2	18
Deformation of Calcium Fluoride Single Crystals	18
TGA/Vapor Pressure Apparatus	19
7. FUNDAMENTAL PHYSICAL METALLURGY	20
Solid Solution Impurities and Grain Growth in Metals	20
The Specimen Thickness Effect in Grain Growth	20
Preferred Orientation in a U-7.5 wt % Nb-2.5 wt % Zr Alloy	20
Partial Correlation Functions for Vacancy Diffusion in Body-Centered Tetragonal Lattices	20
A Catalogue of Calculated Auger Transitions for the Elements	21
A Computer Program to Calculate Auger Transitions for a Surface Containing Several Kinds of Atoms	21
8. PHYSICAL PROPERTY RESEARCH	22
Apparatus Development	22
Thermal Conductivity Apparatus	22
Computerized Data Acquisition	22
Coefficient of Thermal Expansion Apparatus	23
Radial Heat Flow Apparatus	23
Heat Transport in Metals	23
Molybdenum	23
Tungsten	23
UN, ThN, and (Th,U)N Alloys	24
Lattice Heat Transport: Rubidium Halides	24
Heat Capacity of Metals: Ni_3Mn	25
9. SUPERCONDUCTING MATERIALS	26
Superconductivity in Mo-Re and Nb-Ir σ -Phases	26
The Influence of Surface Current on Bean Method Critical Current Density Measurements	26
The Influence of Grain Size and Dislocation Distribution on Superconducting Critical Current Density in a Nb-10 at. % Ti Alloy	26
The Influence of Metallurgical Variables on Superconductivity in Hf-Nb Alloys	27
Evidence to Support the Rigidly Pinned Vortex Model for the Peak Effect	27
Superconductivity in Technetium and Its Alloys	27
Anisotropy of the Upper Critical Field of Superconducting Technetium	27
10. SURFACE PHENOMENA	28
Oxidation of Uranium-Base Alloys	28
The Oxidation Properties of U-16.6 at. % Nb-5.6 at. % Zr and U-21 at. % Nb	28
Flexure Measurements on a U-Nb-Zr Alloy During Oxidation and Temperature Cycling	28
Refractory Metal Oxidation	29
Stress Measurements During the Oxidation of Refractory Metal Alloys	29
Impurity Distribution in Anodic Oxide Films	29

Diffusion Studies	29
The Structure and Properties of Thin Oxide Films	30
11. THEORETICAL RESEARCH	31
Densities of States in Cu-Rich Ni-Cu Alloys by the Coherent-Potential Approximation: Comparisons with Rigid-Band and Virtual-Crystal Approximation	31
The Densities of States of Cu-Ni Alloys	31
Electronic States in Disordered Alloys: Comparison of Methods	31
A Simple Method for Symmetrizing KKR Band Theory Calculations	32
Electronic States in Some Disordered Noble Metal–Transition Metal Alloys	32
Application of the Discrete Variational Method to the Electronic Structure of LiF	32
<i>Ab Initio</i> Calculation of the Electronic Structure and Optical Properties of Diamond Using the Discrete Variational Method	32
The Hartree-Fock-Slater Model for Molecules	32
Copper-Zinc Alloys as Treated by Virtual Crystal and Related Approximations	33
12. X-RAY DIFFRACTION	34
Routine Analyses	34
Thermal Expansion of Rare Earth Oxide–UO ₂ Solid Solutions	34
The Interpretation of Intensity Distributions from Disordered Binary Alloys	34
The Short-Range Structure of (CaF ₂) _{1-x} (YF ₃) _x	35
Measurement of Bremsstrahlung from Photoelectrons Produced by Absorption of Monochromatic Cu K α Radiation	35
Uranium-Niobium-Zirconium Alloys	36
Crystal Structures of Unirradiated and Neutron-Irradiated Boron Carbides	36
Small-Angle X-Ray Diffraction Studies of Radiation-Induced Voids in Aluminum	37
Some Properties of Octafluorocyclobutane (C ₄ F ₈) of Interest in X-Ray Absolute Intensity Experiments	37
A Comparison of Two Methods for Absolute Intensity Calibration	37
PART II. FAST REACTOR TECHNOLOGY	
13. FAST BREEDER REACTOR OXIDE FUELS	38
Development of Fabrication Processes	38
Sphere-Pac Development	38
Pellet Development and Fabrication	39
Stoichiometry Control	40
Fuel Pin Fabrication	40
Construction of Fuel Cycle Alpha Facility	40
Characterization of (U,Pu)O ₂ Fuels	41
Analytical Chemistry	42
Homogeneity of (U,Pu)O ₂	42
Microstructure of Sol-Gel (U,Pu)O ₂ Pellets	42
Fission Product Behavior in Oxide Fuels	42

Irradiation Behavior	45
Fast Flux Irradiation Tests	45
Transient Irradiation Tests	46
Uninstrumented Thermal Flux Irradiation Tests	47
ETR Instrumented Tests	50
ORR Instrumented Thermal Performance Tests	50
Fuel-Cladding Mechanical Interaction Tests	51
Analysis of Fuel Element Performance	52
Performance Model Development	52
Electron Microscopy of Irradiated (U,Pu)O ₂	52
(U,Pu)O ₂ Grain Growth	54
Actinide and Oxygen Redistribution in Irradiated (U,Pu)O ₂	54
Radial Porosity Distribution and Its Influence on the Fuel Temperature Profile	57
Fuel-Cladding Chemical Interaction	57
Discrete Element Analysis of Cladding Deformation	57
Mechanical Properties of Stainless Steel Tubing	57
14. ADVANCED FAST BREEDER REACTOR FUELS DEVELOPMENT	61
Irradiation Testing	61
Thermal Flux Tests	61
Fast Flux Tests	61
Fabrication of (U,Pu)N Fuel	62
Fuel for EBR-II Tests	62
Sintering Experiments on (U,Pu)N	62
Characterization of (U,Pu)N	63
Analytical Methods for Determining Nitrogen In Mononitride and Sesquinitride Phases	63
The Lattice Parameter of (U,Pu)N Solid Solutions	64
Mercury Pycnometer Facility	65
Compatibility of Cladding with Nitride Fuels	66
Phase Investigations in the Pu-Cr-N System	66
Review of the Cr-N System	66
Compatibility of (U,Pu)N with LMFBR Stainless Steel, a Literature Review	66
Thermodynamic Properties of Uranium Mononitride	67
Kinetic Studies of the Synthesis of Carbides, Carbonitrides, and Hypostoichiometric Oxides in the U-Pu-O-C-N System	67
Performance Capability of Advanced Fuels for Fast Breeder Reactors	68
15. CLADDING AND STRUCTURAL MATERIALS	69
Swelling of Austenitic Stainless Steels	69
Effect of Irradiation Temperature on Void Formation in Type 304 Stainless Steel	69
Comparison of Standard and Titanium-Modified Type 316 Stainless steel	70
Effects of Microstructure	70
Effect of a Thermal Neutron Environment	72
Mechanical Properties of Austenitic Stainless Steels	72
Type 304 Stainless Steel	72
Type 316 Stainless Steel	73
Other Austenitic Alloys	76
16. FABRICATION DEVELOPMENT OF FAST BREEDER REACTOR CLADDING	78
Evaluation of Planetary Swaging for Producing High-Quality Cladding	78

Ultrafine Grain Size Type 316 Stainless Steel Tubing	78
Elevated-Temperature Drawing	78
Generation and Evaluation of Artificial Defects	78
As-Machined Notch Studies	78
Altered Notch Studies	80
Study of Fabrication-Introduced Discontinuities	80
Creep Rupture of Type 316 Stainless Steel Tubing with Artificial Defects	81
17. WELDING DEVELOPMENT	82
Stainless Steel	82
Submerged-Arc Process	82
Shielded Metal-Arc Process	82
Heat Treatment Studies	84
Corrosion Studies	85
Irradiation Studies	85
Ferritic Steels	85
Stabilized Grades	85
Chromium-Molybdenum Low-Alloy Steel with Low Carbon Content	86
18. CORROSION OF ADVANCED STEAM GENERATOR ALLOYS	90
General Corrosion	90
Stress Corrosion Cracking	92
19. SODIUM CORROSION IN LMFBR SYSTEMS	95
Effect of Oxygen in Sodium on the Corrosion of Vanadium and Vanadium Alloys	95
Oxidation of Vanadium and Vanadium Alloys	95
20. SODIUM REMOVAL AND CAUSTIC EFFECTS	97
Examination of ALCO/BLH Steam Generator	97
Study of Methods for Cleaning Surfaces of Materials Exposed to Sodium	97
Corrosion Effects of Sodium Leaks or Spills in Gases Containing Oxygen	98
21. NONDESTRUCTIVE TESTING TECHNIQUES FOR LMFBR	100
Development of Advanced Nondestructive Testing	100
Eddy-Current Instrument	100
Ultrasonic Schlieren Techniques for Inspection of Welds	100
Measurement of Cold Work in Stainless Steel	100
22. FAST BREEDER NEUTRON ABSORBER MATERIALS	102
Indexing of X-Ray Diffraction Powder Patterns of Boron Carbide	102
X-Ray Diffraction from Irradiated Boron Carbide Powders and Crystals	102
Transmission Electron Microscopy of Irradiated Boron Carbide	103
Effect of Elemental Boron on Gas Release from Irradiated Boron Carbide Powders	103
In-Reactor Gas Pycnometer Feasibility Experiment	104
Fast Reactor Irradiation Testing of Absorber Materials	104

PART III. SPACE POWER TECHNOLOGY

23. MATERIALS DEVELOPMENT FOR ISOTOPIC POWER PROGRAMS	105
Cladding Materials Program	105
New Platinum-Rhodium-Tungsten Cladding Alloys for Space Isotopic Heat Sources	105
Atomic Ordering and Structural Transformation in the V-Co-Ni Ternary Alloy	106
Cermets Fuels	106
Evaluation of Fabrication Techniques for Cermet Isotope Fuel Simulants	106
Controlled Porosity Cermets for Application to Curium Fuel Forms	107
Compatibility	107
Plasma-Arc Welding of an Isotope Capsule	108
24. METALLURGY OF REFRACTORY ALLOYS	109
Basic Physical Metallurgy	109
Nitrogen Solubility in T-111	109
Creep of T-111 in Low-Pressure Nitrogen	109
Effects of Oxygen Contamination on the Tensile Properties of T-111	109
Simple Method of Determination of the Distribution and Solubility Limit of Interstitials in Substitutional Solid Solutions	111
Solid-Solution Theory and Spinodal Decomposition	111
Joining Studies	111
Refractory Alloy Welding Development	111
Brazing Alloy Remelt Studies	112
Thermal Conductivity of Refractory Alloys	112
Mechanical Properties of Commercial Refractory Alloys	113
Alkali-Metal Corrosion of Refractory Alloys	113
Forced Circulation Lithium Loop	113
Effect of Oxygen on the Compatibility of Refractory Metals with Alkali Metals	114
The Tantalum-Oxygen-Sodium System	114
25. TUNGSTEN METALLURGY	115
Extrusion of Tungsten Alloy Tubing	115
Chemical Vapor Deposition of Tungsten Alloys	115
Evaluation of Methods for Joining Tungsten and Its Alloys	117
Behavior of Tungsten Alloys Under Fast-Neutron Irradiation	118
Effect of Low-Pressure Gases on the Creep Properties of Tungsten Alloys	118
Formation of Creep Cavities in Powder-Metallurgy Tungsten	119
26. URANIUM NITRIDE FUELS	120
Fabrication of Uranium Mononitride	120
Irradiation Testing of Uranium Nitride	121
Examination of Capsule UN-3	121
Capsule Fabrication	121
Capsule Operation	123
Proposed UN Tests in EBR-II	123

PART IV. GENERAL FUELS AND MATERIALS RESEARCH

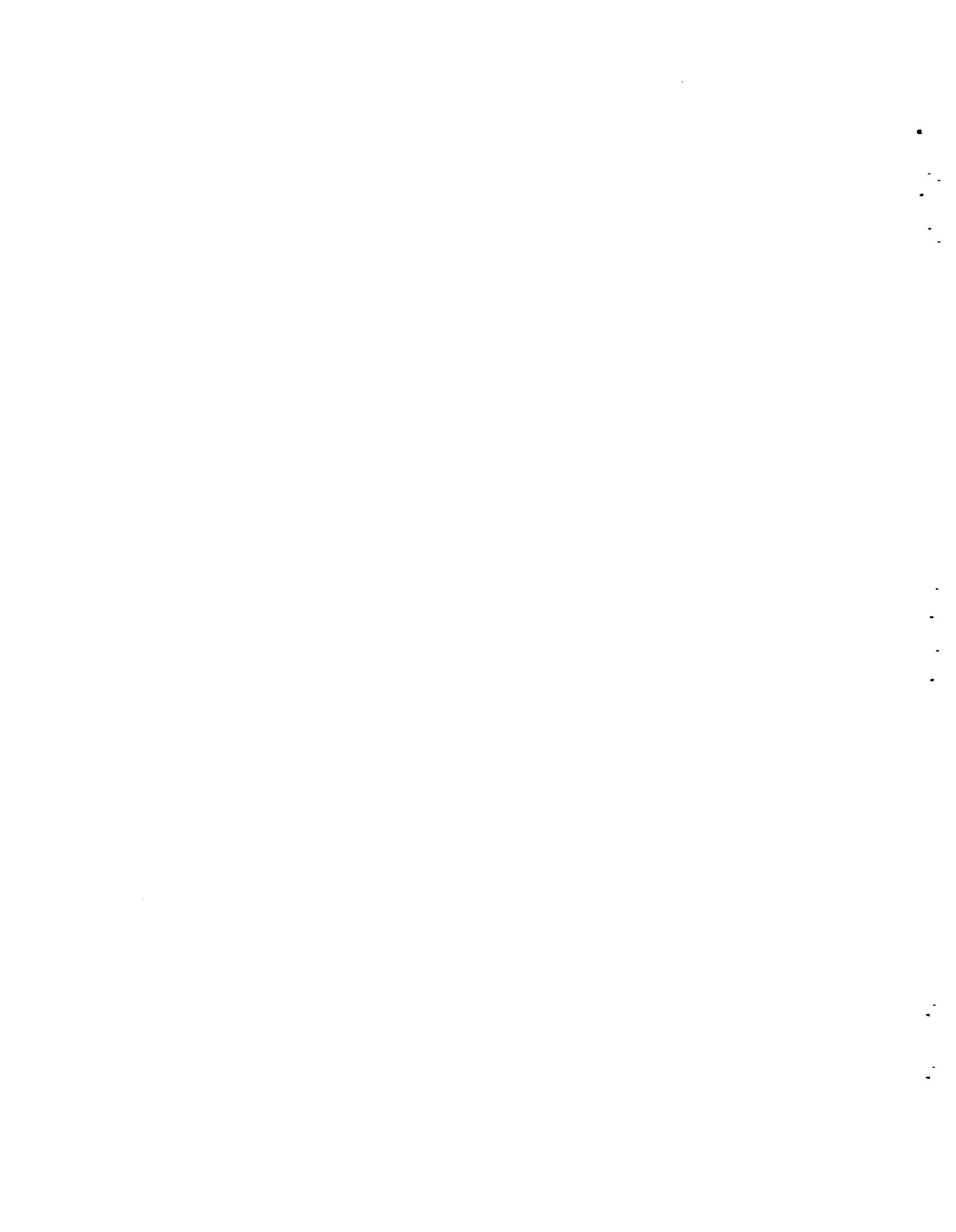
27. FUEL ELEMENT FABRICATION DEVELOPMENT	124
Irradiation Experiment on the Swelling Behavior of Aluminum-Base Dispersion Fuels	124
HFIR Fuel Element Support	124
HFIR Fuel Element Manufacture	124
Modifications and Improvement to HFIR Fuel Plates	125
Thermal Conductivity of U ₃ O ₈ -Aluminum Fuel Plate Cores	126
Establishment of X-Ray Attenuation Standards for Burned U ₃ O ₈ and High-Loaded, High-Fired U ₃ O ₈ Plates	126
Deformation Behavior of Fuel Cores During Rolling	127
Examination of a Failed ATR Fuel Plate	127
28. JOINING RESEARCH ON NUCLEAR MATERIALS	128
Ductility of Inconel 600 Base Metal at Intermediate Temperatures	128
Studies on Incoloy 800 Weld Metal	128
Weldability of Austenitic Stainless Steels	129
29. MECHANICAL PROPERTIES OF IRRADIATED METALS AND ALLOYS	131
Void Formation in Irradiated Nickel 270	131
Preparation of Transmission Electron Microscopy Specimens in a Hot Cell by Remote Techniques	132
Irradiation Damage to Body-Centered Cubic Metals	133
The Effect of Neutron Irradiation on the Strength Properties and Failure Mode of Molybdenum Alloys	133
Voids and the Microstructure of Neutron-Irradiated Niobium	133
The Effect of Alloying and Purity on the Formation and Ordering of Voids in BCC Metals	133
Effects of Irradiation on Aluminum Alloys	134
General Effects of Neutron Irradiation on Aluminum and Aluminum Alloys	134
Effects of Elevated-Temperature Irradiation on 8001 Aluminum Alloy	134
Irradiation Effects in 6061 Aluminum Alloy and Its Utility for In-Reactor Service	135
30. NONDESTRUCTIVE TEST DEVELOPMENT	136
Electromagnetic Inspection Methods (Eddy Currents)	136
Theoretical Analysis	136
Development of Computer Programs	136
Computer Studies of General Eddy-Current Problems	136
Computer Studies of Specific Eddy-Current Problems	137
Experimental Verification of Computer Calculations	137
Instrument Design and Construction	137
Ultrasonic Inspection Methods	138
Frequency Analysis	138
Optical Visualization of Ultrasound	138
Penetrating Radiation Inspection Methods	138
Radiation Scattering	138
Closed-Circuit Television for Radiographic Evaluation	138
Shield for ²⁵² Cf Neutron Source	139

PART V. REACTOR DEVELOPMENT SUPPORT

31. GAS-COOLED REACTOR PROGRAM	140
Coated Particles from Ion Exchange Resins	140
Coated-Particle Bonding Development for HTGR Fuels	143
Thermal Conductivity of Bonded-Bed Materials	144
Irradiation Testing of Prototype HTGR Fuel Elements	144
Blended Beds of Loose Coated Particles	144
Testing of Matrix and Filler Materials for Bonded Fuel Sticks	145
Irradiation Test of Bonded Coated-Particle Fuels in an Instrumented Capsule in HFIR	146
Effect of Density and Heat Treatment on the Rheology of Restrained Low-Temperature Isotropic Coatings	146
Gas-Cooled Fast Breeder Reactor Fuel Element Development	146
Thermal Reactor Experiments	147
Fast Reactor Tests	147
32. HEAVY SECTION STEEL TECHNOLOGY	149
Characterization of Heavy Section Steel Plate	149
Radiation Studies on HSST Plates and Welds	149
Simulated Service Test	150
Technique for Generating Sharp Cracks in Low-Alloy High-Strength Steels	150
The Determination of Retemper Temperature for the Intermediate Vessel Test Courses	150
33. MILITARY REACTOR FUEL ELEMENT PROCUREMENT ASSISTANCE	156
34. MOLTEN-SALT REACTOR PROGRAM	157
Examination of MSRE Components	157
Microstructural Studies of Modified Hastelloy N	158
Properties of Unirradiated Modified Hastelloy N	159
Postirradiation Properties of Modified Hastelloy N	160
Corrosion of Hastelloy N in Fluoride Salts	160
Corrosion of Hastelloy N in Steam	161
Construction of a Molybdenum Reductive-Extraction Test Stand	162
Fabrication Development of Molybdenum Components	162
Molybdenum Welding Development	162
Development of Bismuth-Resistant Filler Metals for Joining Molybdenum	163
Corrosion of Structural Materials in Bismuth	164
CVD Coatings for Corrosion Resistance	164
Coatings for Corrosion Resistance by Deposition from Molten Salts	165
Reduction of Graphite Permeability by Pyrolytic Carbon Sealing	165
The Irradiation Behavior of Graphite at 715°C	166
Procurement of and General Physical Property Measurements on New Grades of Graphite	168

Reduction of Gas Permeability of Graphite by Fluoride Salt Impregnation	169
Graphitization of a Lampblack-Pitch Carbon	169
Thermal Conductivity of Graphite	169
35. THORIUM UTILIZATION	171
Thorium-Uranium Recycle Facility	171
Refabrication Development	172
Coating	172
Stick Fabrication	172
Element Assembly	174
HTGR Recycle Fuels Irradiation	174
Capsule Irradiations	174
Large-Scale Irradiations	174
36. TRANSURANIUM PROGRAM	176
Target Fabrication	176
HFIR Target Performance	176
Status of the Targets Exposed in HFIR	176
Analysis of Target Performance	176
Thermal Conductivity Studies	177
Nondestructive Test Development	178
Aluminum Irradiation Damage	178
HFIR Target Performance Model	179
37. WATER REACTOR SAFETY	182
Program Coordination	182
Multirod Transient Burst Experiment	182
Embrittlement of Light-Water Reactor Fuel Cladding	184
Metallurgical Support	185
PART VI. OTHER PROGRAM ACTIVITIES	
38. METALLOGRAPHY	186
Electron Microprobe Analysis	186
Alpha Metallography Facility	189
Etching of Type 308 Stainless Steel Weld Metal	189
Beta Autoradiography	190
Quantitative Television Microscopy	190
Revealing Ferromagnetic Phases with Ferrofluids	191
Improved Metallograph Illumination System	192
Examination of the ALCO/BLH Steam Generator	192
Photography	192
Metallography	193
Optical Anisotropy Factor Studies	193

39. NERVA PROGRAM METALLURGICAL SUPPORT	195
Effects of Space Environment on NERVA Materials	195
Outgassing of NERVA Fuel Elements	195
Adhesion and Friction of NERVA Materials	196
Thermal Conductivity of P-03 Graphite	198
40. POWDER PROCESS DEVELOPMENT FOR LWBR	199
Precipitation	199
Centrifugation and Microwave Drying	199
Reduction and Stabilization	199
Production of Enriched Powder	200
41. REACTOR EVALUATION	201
Fuel Fabrication Cost Analysis	201
Fuel Recycle Task Force	201
HTGR Fuel Cost Analysis	201
Metals and Ceramics Division Information Activities	202
42. EXAMINATION OF NICKEL HEAT PIPES CONTAINING POTASSIUM	203
PRESENTATIONS AT TECHNICAL MEETINGS	204
PUBLICATIONS	212
AUTHOR INDEX	222
ORGANIZATION CHART	225



Summary

PART I. FUNDAMENTAL PROGRAMS

1. Crystal Physics

Steady-state solidification of the metal-metal oxide system (W-UO₂) was achieved below its binary eutectic temperature (2640 ± 20°C) by the addition of MgO. When our internal centrifugal zone growth technique was used, the lower melting liquid zone migrated directionally through the solid. Directional solidification in three oxide-oxide eutectic systems was also achieved: MgO rods in UO₂, UO₂ rods in Al₂O₃, and NiO plates in UO₂. The internal centrifugal zone growth system is now sufficiently controlled that we can plan experiments to compare metal-metal oxide and oxide-oxide systems with current theory. High-temperature solution growth gave single crystals of ²³⁹PuO₂ up to 2 × 2 × 3 mm. Single crystals of Mg₂SiO₄ up to 8 mm in diameter × 3 cm long were pulled from the melt in air at approximately 1900°C. Transuranic-doped CaWO₄ and KMgF₃ single crystals up to 5 mm in diameter × 6 cm long are being grown by the Czochralski method for future spectroscopic, laser, and EPR studies. The growth of single crystals doped with select isotopes and follow-on electron paramagnetic resonance studies continued. Quartz crystals grown in supercritical RbOH solutions were characterized by infrared and mass spectroscopy. Evidence of an unusual lamellar dendritic growth on lead sulfide grown supercritically in the system RbOH-PbS-H₂O is presented. Equipment for electron-beam or inductive heating of samples has been constructed for further study of the growth of graphite by the temperature-gradient zone melting technique.

2. Crystal Spectroscopy

Research on the chemistry and spectroscopy of molten salts was phased out and research was started on piezospectroscopy and high-temperature spectroscopy of crystals.

3. Deformation of Crystalline Solids

Anisotropic elasticity calculations were made for nonbasal dislocations in hexagonal metals, for dislocation displacements, and for the interaction of dislocations with point defects. Work on precipitation in the Nb-Hf system is continuing. We also have an interest in the simulation of solid solutions with respect to short-range order and displacement effects.

4. Diffusion in Solids

Volume self-diffusion coefficients have been determined for Fe-17 wt % Cr-12 wt % Ni by conventional and newly developed techniques to cover a very wide temperature range, including the relatively low temperatures of usual engineering applications. Thermotransport in sodium and potassium chlorides is being studied theoretically and experimentally as steps in our efforts to understand this phenomenon in ceramics. Radioactive ⁴⁴Ti is being used along with standard techniques to characterize diffusion rates and determine jump mechanisms in both rutile (TiO₂) and titanium monoxide (TiO_x) of varying stoichiometry. Research on atomic diffusion in refractory metals and alloys at high pressures and high temperatures is being initiated.

5. Electron Microscopy

Some effects of material and irradiation variables on the damage produced in metals by neutron and electron irradiation are described. Features of the annealing of voids in irradiated aluminum and the development of porosity in carbonyl nickel by heat treatment are reported. A program for evaluating the mechanisms involved in void formation during neutron irradiation is summarized, and a theoretical description of vacancies in ternary alloys is given. The defect structure of boron carbide is described, and a discussion of dislocations in the double helix structure is presented. Hardness-grain

size relationships in α -brass and iron are reported. Some recent measurements of the energy stored during plastic deformation are presented and related to current work hardening theories. The effects of composition on the aging characteristics of Hastelloy N are described.

6. Fundamental and Physical Ceramics Research

Deformation of hyperstoichiometric UO_2 single crystals was investigated. Deformation studies of $\text{Ca}_{1-x}\text{Y}_x\text{F}_{2+x}$ are in progress. A TGA/vapor pressure apparatus has been built for high-temperature nitride research.

7. Fundamental Physical Metallurgy

Hillert's theory of normal grain growth was extended to include solute impurity effects and the effect of specimen thickness. Rolling and recrystallization textures of a metastable bcc uranium alloy were determined. Partial correlation functions were derived for vacancy diffusion in body-centered tetragonal lattices. Auger electron spectra for each element have been calculated and catalogued.

8. Physical Property Research

Emphasis on measurement technique improvements yielded accurate thermal conductivity, electrical resistivity, and specific heat capacity data in the range 1.2 to 2500°K on Mo, W, (Th,U)N, Ni_3Mn , and three alkali halides. These data were analyzed in terms of their electronic and lattice components.

9. Superconducting Materials

The fundamental superconducting properties of Mo-Re and Nb-Ir σ -phases were studied by low-temperature specific heat capacity measurements. The results were correlated with work on other σ -phases. Our chief experimental technique for measuring superconducting critical current density was re-examined to take account of the influence of surface currents.

Flux-pinning (critical current density, J_c) due to crystal defects was studied in several systems. These included Nb-10 at.% Ti, where the influence on J_c of grain size and dislocation distribution was examined, and Nb-Hf, where the influence of a Hf-rich precipitate on J_c was studied.

Work on technetium and its alloys included studying superconductivity in Tc-Mo and Tc-Ti alloys and the preparation of high-purity technetium single crystals in cooperation with Argonne National Laboratory.

10. Surface Phenomena

We studied the oxidation properties of a series of uranium-base alloys containing Nb, Zr, Ti, and Mo. Special emphasis was placed on characterizing the complex morphology of the oxide films and on determining the origin of the enormous oxide film stresses. Ternary Ta-W-Hf alloys were also shown to be subject to large stresses during oxidation; these stresses are probably instrumental in producing a period of catastrophic oxidation for such alloys during which oxidation proceeds with explosive violence. The movement of fluorine- and phosphorous-rich marker layers during the growth of anodic oxide films on tantalum was studied in order to understand better the mechanism of anodization. An elastic stress (maximum 20,000 psi) had a small but detectable effect on the diffusion rate of ^{95}Nb in a tantalum-base alloy. The structure and properties of thin oxide films were reviewed with regard to the manner in which they influence the oxidation process for metals.

11. Theoretical Research

We applied the Kirkpatrick, Velický, and Ehrenreich form of the coherent potential approximation (CPA) to the problem of calculating the electronic states of disordered Cu-Ni alloys across the entire range of concentrations. This is the first such calculation to be successfully carried out, and the comparison of these theoretical predictions with the results of photo-emission experiments yields the most clear-cut proof to date that the CPA is capable of describing the electronic states of real alloys reliably. We also applied the CPA to other transition metal alloys.

We considered the theoretical background of the CPA and showed how it could be extended to treat liquid metals with and without short range order. We compared the CPA predictions for the integrated density of states of a one-dimensional model problem with exact calculations and investigated its range of validity.

One reason for our success with the alloy problem was our ability to carry out KKR band theory calculations on the pure constituent metals. We extended our KKR techniques by adding group theory and coupling it with an interpolation procedure. We also developed new techniques for obtaining reliable muffin-tin potentials to use in KKR calculations on real systems.

Because of the effective limitation of the KKR technique to the use of the muffin-tin approximation, which is good for metals but bad for ionic and covalent compounds, we have developed a new band-theory

technique called the discrete variational method (DVM), which doesn't have this limitation and also has other advantages for treating compounds. We have extended this technique by coupling it with a Fourier-type interpolation scheme and have also added a continuous \mathbf{k} representation that allows the band theory problem to be solved for many wave vectors, \mathbf{k} , with only a slight increase in time over that required for treating a few \mathbf{k} 's.

12. X-Ray Diffraction

We applied the technique developed to analyze diffuse x-ray scattering from imperfectly ordered binary alloys to data from Cu-16 at. % Al and Au-40 at. % Ni. An x-ray diffraction study of short-range structure in $(\text{CaF}_2)_{1-x}(\text{YF}_3)_x$ crystals should extend both our experimental methods and the power of our interpretive schemes.

Bremsstrahlung produced by photoelectrons generated in matter by absorption of monoenergetic x-ray beams has been observed and its general features measured. Important advances in x-ray fluorescence analysis will be developed from this experimental arrangement.

Additional x-ray diffraction observations of aging reactions in gamma-quenched uranium-base alloys provided clues to the "memory" effects shown by the material. We are attempting to illuminate some of the confusion surrounding the crystal structure of boron carbide and also gathering diffraction data on neutron-irradiated crystals of "B₄C."

Small-angle x-ray scattering studies of neutron-irradiated aluminum crystals have successfully shown effects due to radiation-induced voids. Progress in accurate absolute intensity calibrations for high- and low-angle x-ray scattering measurements follows from recent experimental correlation of two disparate techniques.

PART II. FAST REACTOR TECHNOLOGY

13. Fast Breeder Reactor Oxide Fuels

This program is being conducted to advance the technology of $(\text{U,Pu})\text{O}_2$ as a fuel for the Liquid-Metal Fast Breeder Reactor. The determination of the properties and performance of sol-gel-derived oxide fuels fabricated by Sphere-Pac and pelletizing techniques has been emphasized, but comparison with materials derived from other processes such as mechanical blending is a part of our objective.

The Sphere-Pac process was used to load a variety of fuel pins for irradiation in the ETR, EBR-II, and ORR. Smear densities in the range 81 to 84% of theoretical are typical. Sol-gel-derived pellets were fabricated with controlled densities from 84 to 97% of theoretical. An equation was developed to predict the time required to reduce mixed oxide fuels to any oxygen-to-metal ratio desired. The Pu/U ratio of sol-gel-derived $(\text{U,Pu})\text{O}_2$ fuels varied only slightly from batch to batch and not detectably from sphere to sphere within a batch. We characterized the microstructure of these fuels and assessed the effect of fission products on the structural state and therefore the properties.

The irradiation test program was continued to determine the in-reactor properties and performance of $(\text{U,Pu})\text{O}_2$ fuel pins as functions of fabrication form, porosity distribution, stoichiometry, and irradiation conditions. We include both fast and thermal neutron irradiations at steady-state, cyclic, and transient power conditions. In our fast flux tests in EBR-II, five fuel pins containing Sphere-Pac $(\text{U,Pu})\text{O}_2$ were irradiated to a calculated peak burnup of 6% FIMA. Two pins were removed for examination and three are being irradiated to 12% FIMA. No fuel-cladding mechanical interaction has occurred at 6% FIMA. The fission gas release rate of 80% agrees with other EBR-II-irradiated oxide fuels, and we detected no significant fuel-cladding chemical interaction, even at inner surface temperatures up to 570°C. This in contrast to the results with non-sol-gel-derived material. Microprobe analysis showed no fission products in the cladding grain boundaries. Six fuel pins containing unirradiated sol-gel $(\text{U,Pu})\text{O}_2$ subjected to transients in the TREAT facility were examined. Both pellet and sol-gel Sphere-Pac fuel behaved the same. One capsule containing Sphere-Pac mixed oxide was irradiated in the ETR to a calculated burnup of 10% FIMA but not yet examined. Other instrumented and uninstrumented irradiations are being continued in the ETR on mechanically blended pellets, sol-gel-derived pellets, and Sphere-Pac material. Instrumented tests in the ORR with fuel having a smear density of 82% indicate that fuel-to-cladding thermal conductance in a Sphere-Pac pin is more than twice that of a pellet fuel pin with a small initial fuel-cladding gap. In ORR instrumented capsules operated at low fuel burnup, very localized cladding attack was seen in the pellet fuel pin but none in the Sphere-Pac fuel.

We initiated a series of irradiation tests to measure in-reactor axial extension of the fuel column and cladding and the internal gas pressure developed during operation under carefully controlled prototypic LMFBR power and temperature conditions.

We are developing analytical models for predicting and evaluating the performance of LMFBR fuel pins and are performing detailed examinations of irradiated fuel pins for comparison. We modified the FMØDEL fuel performance code for steady-state, power cycling, and limited transient applications. It now includes a dynamic model for fuel restructuring based on a vapor-condensation mechanism of pore migration, sub-routines for grain growth and plutonium redistribution, a fuel cracking model, and an improved cladding mechanical model to include neutron-enhanced creep. The code has been used in a variety of applications and shown excellent correspondence between calculated and measured diametral expansions, restructuring, center-line temperatures, and porosity distribution. Our work in support of the integrated fuel performance modeling effort has included replica electron microscopy of irradiated (U,Pu)O₂ to improve our understanding of fuel restructuring, porosity distribution, fuel swelling, and fission gas release and has included an investigation of the kinetics of in-reactor and out-of-reactor (U,Pu)O₂ grain growth, actinide and oxygen redistribution in irradiated (U,Pu)O₂, and radial porosity distribution. In each case the physical observations have been used concurrently with development of mathematical description. Other activities include improvements and analysis for cladding deformation, a survey of fuel-cladding chemical interactions, and measurement of the properties of stainless steel tubing used for cladding.

14. Advanced Fast Breeder Reactor Fuels Development

Thermal flux irradiation of eight mixed nitride fuel pins is in progress in the ETR. The peak linear heat rate is 30 kW/ft with scheduled exposures of 30,000 and 60,000 MWd/metric ton. Seven fuel pins were fabricated for testing in the EBR-II.

We produced and characterized (U,Pu)N fuel and UN insulator fuel for eight EBR-II pins. The sintering of UN and U_{0.8}Pu_{0.2}N depends strongly upon the nitrogen pressure. The sintering of mechanically mixed (U,Pu)N is limited by low-density regions at the original sites of the PuN particles. The nitrogen in mononitride and sesquinitride phases can be accurately determined by the Dumas method; the Kjeldahl technique with phosphoric acid dissolution is satisfactory only for mononitride. The lattice parameter of (U,Pu)N does not obey Vegard's law.

15. Cladding and Structural Materials

Irradiation of austenitic stainless steels at temperatures between 350 and about 650°C to fast neutron fluences in excess of 1×10^{21} neutrons/cm² creates voids and dislocations. This damage increases volume and also degrades the mechanical properties, particularly the ductility. We are defining the irradiation-induced property changes in standard types 304 and 316 stainless steel (cladding and structural materials for FFTF and demonstration plants) as a function of temperature and neutron fluence and attempting to decrease the property changes through control of alloy composition and microstructure. The radiation-induced volume change in types 304, 316, and titanium-modified 316 stainless steel can be significantly reduced by cold working to introduce a high dislocation density before irradiation. Further, titanium-modified types 304 and 316 stainless steel, which were developed for resistance to radiation embrittlement above about 650°C, also exhibit higher postirradiation ductilities in the range 500 to 600°C. Thus, in the modified alloys cold work can be utilized to control the swelling without a drastic reduction in ductility.

16. Fabrication Development of Fast Breeder Reactor Cladding

We are studying various methods to produce a cheaper but higher quality of cladding. Two methods of tubing fabrication, planetary swaging and hot plug drawing, were investigated. The slow planetary swaging process does not appear economic compared to the more conventional processing procedures. Methods for hot plug drawing at temperatures up to 760°C were developed. The relationship between defects and mechanical properties at elevated temperatures is being examined. Cold worked tubing is more sensitive to surface defects than annealed tubing. At high stress and short creep-rupture lives, surface notches cause a reduced lifetime and lower ductility. A procedure was developed for producing, in material for mechanical testing, artificial defects that resemble the sharp surface defects found in some lots of tubing.

17. Welding Development

We are continuing a study of the behavior of weldments in austenitic stainless steel at 370 and 650°C as a function of both welding process and variables within a process for application to LMFBR vessels and components. Submerged-arc welds exhibited lower

creep-rupture strength and higher ductility in general than typical type 304 stainless steel base plate. Shielded metal-arc welds in general exhibited strength comparable with base plate. Weld-metal ductility decreased with increasing rupture life. From a study of the effect of certain minor elements including S, P, Si, B, and C, a "controlled residual element" filler metal possessing superior strength and ductility was developed for the FFTF vessel.

We have completed a state-of-the-art review of the weldability of stabilized low-alloy steels. Reports concerning the weldability of the stabilized steels have been contradictory. We identified at least one cause of the difference of opinion. Poor weldability can be attributed to hot cracking in the heat-affected zone due to the melting of a niobium-rich eutectic.

Low-carbon 2.25% Cr-1% Mo weld metal was responsive to thermal cycling due to multipass welding techniques. This is particularly true of the low-carbon heat-affected zones, where the hardness increased from 129 to over 160 DPH. As expected, the strength of these alloys depends on the carbon level; however, the difference in as-welded strength at 565°C is reduced from a factor of 2 to about 1.4 by a 700°C postweld heat treatment.

18. Corrosion of Advanced Steam Generator Alloys

Steam generator alloys with ground surfaces and with the effects of grinding removed by electropolishing were exposed in steam for up to 14,000 hr at 650 and 595°C (1200 and 1100°F). Electropolishing substantially increased the corrosion of Incoloy 800, moderately increased it for Inconel 600, but slightly decreased it for Inconel 625 and Hastelloy X. Although the amount of corrosion on electropolished Incoloy 800 was comparatively large, the projected total attack in 20 years was still impressively low because its second-stage corrosion rate decreases significantly with time.

Stress-corrosion tests on weldments using conventional U-bend specimens in superheated steam contaminated with NaCl and oxygen failed to produce cracks. Under conditions that incorporated cycling periodically to the steam saturation temperature and introducing 25 ppm NaCl and 50 ppm O₂, many weldments with ground surfaces failed. Inconel 625 weldments did not fail under any conditions of surface treatment.

19. Sodium Corrosion in LMFBR Systems

Several vanadium alloys were tested at 600°C in static capsules to determine the effect of alloying elements on the solubility and diffusivity of oxygen in vanadium. Chromium, molybdenum, and iron lower the oxygen solubility much more than tantalum and niobium. We derived equations to determine the effect of alloying components on the oxygen diffusion coefficient; experiments designed to test the equations showed in some instances that an essential boundary condition is not met experimentally.

20. Sodium Removal and Caustic Effects

We evaluated cleaning procedures for removing sodium from metallic surfaces with respect to their corrosion effects. An apparatus was constructed to determine the effect of sodium on the oxidation of stainless steel as a function of sodium leak rate and temperature. We dissected and examined the ALCO/BLH steam generator to learn the cause of cracking in the lower tube sheet.

21. Nondestructive Testing Techniques for LMFBR

We are developing new methods, techniques, and equipment for nondestructively inspecting LMFBR cladding and structural materials, with emphasis on measuring cold work in type 316 stainless steel tubing for FFTF fuel-pin cladding.

Theoretical equations, computer programs, and calibration equipment were developed leading to new eddy-current instrumentation to identify both the size of a flaw and its depth below the surface.

We are applying ultrasonic schlieren techniques to improve our understanding of weld inspection. A transducer with multiple sensors was developed. Delta and schlieren techniques are being correlated on a stainless steel sample that scatters ultrasonic energy excessively.

We are developing magnetic permeability measurement in both flat and tubular type 316 stainless steel to determine cold work. A low-frequency eddy-current bridge was designed, constructed, and used to inspect tubing and rod with good results. A new coil system was designed to improve the sensitivity to changes in permeability.

22. Fast Breeder Neutron Absorber Materials

Characterization of and the effect of irradiation damage on neutron absorber materials are being investigated. Improved methods for indexing the x-ray diffraction powder patterns of boron carbide were developed, and patterns of the irradiated powder were interpreted. The microstructure of irradiated boron carbide powders was investigated by transmission microscopy. Damage typical of displacement damage in metals was observed, but no evidence of helium bubbles or other evidence of reaction product agglomeration was found. Free boron as a contaminant in boron carbide was shown to greatly increase the helium release rate during irradiation.

PART III. SPACE POWER TECHNOLOGY

23. Materials Development for Isotopic Power Programs

A new alloy containing platinum, rhodium, and tungsten has been developed comparable to refractory alloys in strength properties but retaining the superior oxidation resistance of the noble alloys. This solid solution alloy, designated Pt-3010, is fabricable, is weldable, and melts above 2000°C. Methods for fabricating thoria-molybdenum cermets using molybdenum powders were investigated; the products were compared with cermets produced by chemical vapor deposition of the molybdenum. The cermets produced by hot pressing CVD-molybdenum-coated thoria were superior in thermal conductivity and strength. Techniques for fabricating molybdenum-thoria cermets as stand-ins for Mo-²⁴⁴Cm₂O₃ and noble metals-²⁴⁴Cm₂O₃ cermets are also being investigated. These cermets with controlled porosity have been fabricated to provide for helium release and at the same time maintain desirable strength. The compatibility of ²⁴⁴Cm and ⁹⁰Sr compounds with candidate container materials was ascertained for times to 10,000 hr.

Plasma-arc welding was successfully applied to Hastelloy C capsules fueled with ⁹⁰Sr titanate. This technique overcame many of the difficulties associated with remote gas-tungsten arc welding.

24. Metallurgy of Refractory Alloys

This base-technology program for high-temperature alloys is principally concerned with tantalum-, niobium-, and molybdenum-base alloys.

Alloy T-111 was more compatible than Ta with the nitrogen partial pressure over UN in the range 1200 to

1500°C, despite its hafnium content. This behavior has tentatively been attributed to the tungsten, which permits a greater equilibrium nitrogen pressure over T-111. A simple method for calculating the solubility limit of interstitial species in solid solutions from a single lattice parameter measurement was developed. The method is used to explain previously reported but apparently quite different solubility limits in two chemically similar alloys. Oxygen contents up to 3000 ppm had little effect on the tensile properties of T-111 if the doped specimens were heat treated before testing. However, as-doped specimens were completely brittle when contaminated to only 750 ppm. Apparently the form and distribution of the oxide precipitate has a greater effect than the oxygen content. Low nitrogen pressure moderately strengthened T-111 in creep at 1400°C but reduced the rupture strain. Several experimental observations of spinodal decomposition that cannot be explained satisfactorily by current theory were accounted for by taking into account free energy changes resulting from atomic clustering.

Hot cracking involved liquid films in Mo and TZM welds. Both oxygen and carbon were detected on the surfaces of the cracks. Grain boundary porosity in the fusion and heat-affected zones also contributed to cracking. We have fabricated T-111 and Mo thermal-convection loops. A crack in the Mo loop was successfully repaired by welding. The melting point of one brazing alloy was raised by volatilization of Cr and solution of Ta and that of another was slightly lowered by Be segregation.

High-temperature thermal conductivity of T-111 estimated from low-temperature values and high-temperature electrical resistivity data was within 3% of measured values. Electrical resistivity was also used to estimate the high-temperature thermal conductivity of ThO₂-Mo cermets.

Creep testing of tantalum alloys showed shorter rupture lives of welded than unwelded specimens at high stresses. Alloy SU-31 had the strongest stress-rupture properties of any Nb alloy yet tested.

We began to examine the T-111 forced convection loop that was operated with lithium for 3000 hr at a 1370°C heater exit temperature. In static tantalum capsules at 600°C, increasing the oxygen concentration of the sodium led to increased dissolution of the tantalum in the sodium. When the concentration of oxygen in tantalum exceeded a threshold level, the sodium penetrated the tantalum.

25. Tungsten Metallurgy

We extended our capability for extruding tungsten alloy tubing to include W-5% Re and W-2% ThO₂. Chemical vapor deposition of W-5% Re was optimized. We evaluated welding techniques, including gas tungsten arc and electron beam with and without filler metals, for joining tungsten and W-25% Re.

The creep strength of W-25% Re is significantly greater in low-pressure O₂ than in ultrahigh vacuum. A carbon-containing atmosphere lowers the creep strength of unalloyed tungsten. Preexisting gas bubbles in powder-metallurgy tungsten expand to form the creep cavities by the stress-directed diffusion of vacancies along the grain boundaries.

A high-temperature irradiation experiment for EBR-II was designed and constructed to find the effect of irradiation temperature and alloying on the void formation and electrical properties of tungsten.

26. Uranium Nitride Fuels

The performance of UN fuel at 1500°C was satisfactory for 5800 hr of irradiation at ~9 kW/ft. The T-111 cladding of two fuel pins developed voids and cracks, leading to failure of one fuel pin. The third fuel pin had W-25% Re cladding and performed satisfactorily. Three additional capsules were fabricated to irradiate nine fuel pins at 1000°C cladding temperature – six with UN in T-111, two with UO₂ in Nb-1% Zr, and one with UO₂ in T-111. The UO₂ fuel is for evaluation of the backup design.

PART IV. GENERAL FUELS AND MATERIALS RESEARCH

27. Fuel Element Fabrication Development

An irradiation experiment to determine the factors controlling the upper burnup limit of ATR and HFIR type fuels was completed. Manufacturing yields for the HFIR fuel element continued to increase, to a net of 97.8% for fuel plates fabricated in FY 1971. New x-ray attenuation standards for fuel homogeneity were based on more precise chemical sampling and analysis techniques. The deformation studies on dogboning were completed. Shaped cores are a solution if the cladding strength is at least half that of the core. Examination of a small failed section from an ATR fuel plate showed no evidence of foreign material within the core. Thermal conductivity of aluminum-U₃O₈ cermet was smaller for burned than high-fired U₃O₈ and consistent with expectations for aluminum containing dispersed insulator and void space.

28. Joining Research on Nuclear Materials

Experimental compositions of Inconel base metal lost ductility when tested above 500°C and did not recover it. These results corroborate those of a previous study on Incoloy 800, where ductility was not recovered for compositions that did not contain titanium.

Tensile tests at 650°C were completed on Incoloy 800 welds made with both experimental and commercially obtained filler metals. Two new alloys from International Nickel Company compared favorably with the recommended filler metal (Inconel 82).

We investigated a microfissured electron-beam weld that joined an Inconel 600 tube to an Inconel 82-clad carbon steel tube sheet. The microfissure occurred in the overlay (the heat-affected zone of the weldment) at a location in which weld bead geometry led to a stress concentration. The microfissure was attributed to liquation of a niobium-rich phase during welding.

The Schaeffler diagram, which is often employed for predicting the amount of ferrite in austenitic stainless steel welds, does not consider the large effect of heat input. Further, high manganese contents lead to erroneous ferrite predictions. Alloys with 5% Mn, which are predicted by the diagram to be fully austenitic, contained from 3 to 8% ferrite.

29. Mechanical Properties of Irradiated Metals and Alloys

Nickel 270 (99.98% nominal purity) was irradiated in EBR-II to fluences ranging from 1.0×10^{18} to 1.5×10^{22} neutrons/cm² over the range 375 to 525°C. Voids were formed over the entire range of conditions and were inhomogeneously distributed at the lower fluences. Samples of Mo, Mo-0.5% Ti, Mo-50% Re, Ta, Nb, V, and V-20% Ti were irradiated in EBR-II at various temperatures to fluences up to 3×10^{22} neutrons/cm². We characterized the microstructure using a newly developed remote thinning technique for the Ta. Tensile tests were run on the Mo-base alloys, and the DBTT was raised markedly.

The types of damage that occur in 1100, 8001, and 6061 aluminum-base alloys have been characterized. Alloy 6061 shows considerably less swelling than the other alloys. This is attributed to the fine Mg₂Si precipitate in the 6061 alloy, whereas the others are basically solid solution alloys.

30. Nondestructive Test Development

We continued analytical studies of eddy-current phenomena with emphasis on development and use of

computer programs to solve specific problems. Phase-sensitive eddy-current instrumentation was stabilized at high frequencies.

Improved models and experimental techniques for flaw characterization by ultrasonic frequency analysis were developed and confirmed on test specimens containing artificial flaws. The acousto-optic equipment was modified and stabilized to allow studies of schlieren, Bragg diffraction, and holographic techniques with less concern about loss of optical alignment.

Several combinations of cladding and base materials were studied by scattering and fluorescence generated by ^{147}Pm radiation. To increase accuracy and inspection speed, work was initiated with an x-ray unit and a mechanical scanner. Preliminary calibration curves and resolution studies show promise for using closed-circuit television for interpretation of radiographs. We completed a conceptual design for a laboratory facility for neutron attenuation studies using ^{252}Cf .

PART V. REACTOR DEVELOPMENT SUPPORT

31. Gas-Cooled Reactor Program

Particles of $(\text{Th,U})\text{O}_2$ or $(\text{Th,U})\text{C}_2$ coated with pyrolytic carbon and SiC offer considerable advantage as fission-product-retaining fuel for high-temperature gas-cooled reactors (HTGR's). Coating materials and simulated fuel elements are prepared, characterized, and irradiation tested to high fast fluence. Coated-particle beds bonded with coal-tar pitch containing high concentrations of a variety of carbonaceous filler materials survived full HTGR fast fluences without loss of integrity or coating failures. However, blended beds of loose particles suffered severe shrinkage and settling. We are also developing and testing techniques to fabricate less expensive or more stable fuel sticks.

An important recent contribution has been the development of coated particles derived from ion exchange resins. Certain resin spheres retain their shapes when carbonized slowly in a fluidized bed, and stable coatings may be applied to them. Sufficient uranium may be absorbed in such particles before carbonizing to make them an attractive alternate to the small fissile particles in the HTGR fuel cycle. Such particles have performed well to a burnup of 20 at. % heavy metal and full HTGR fast neutron fluence.

The Program also contributed to the development of fuel elements for a gas-cooled fast breeder reactor (GCFBR). We prepared the $(\text{U,Pu})\text{O}_2$ fuel and fuel pin for a test of a new manifolded-vented fuel element design. This instrumented fuel pin has performed

satisfactorily for about half of a planned irradiation to 75,000 MWd/ton. We are also participating in the testing of GCFBR fuel pins in EBR-II at temperatures ranging from 600 to 800°C.

32. Heavy Section Steel Technology

We substantiated the previous observation that the Charpy V-notch properties but not the tensile properties are affected by the anisotropy of 12-in.-thick plate. Electroslag weld metal was less sensitive to irradiation than submerged-arc welds in Charpy V-notch studies. This difference, however, is compensated for by the superior toughness of the submerged-arc weld in the unirradiated condition.

A technique was developed for generating sharp fatigue-like cracks for use in the intermediate test vessels and allied tests. Cracks are induced with hydrogen in a confined martensitic region with residual stresses.

The 6-in.-thick ASTM A508 class 2 steel shell sections of the 39-in.-diam intermediate test vessel were tempered at 1270°F following a water quench. The tensile properties of this material were excessive; means to reduce the strength were sought by heat treatment studies and metallography. We selected a 1320°F retemper to obtain mechanical properties within typical ranges for this grade of steel.

33. Military Reactor Fuel Element Procurement Assistance

Assistance in standardization of specifications, review of technical requirements, and participation in quality control audits were associated with the procurement of components for the Army's MH-1A reactor and the Navy's PM-3A reactor. Accomplishments included the following surveillances and inspections: (1) 31 MH-1A Type I fuel element assemblies for final delivery in March, (2) cleaning and packaging of PM type 4 Core -01 and repair of its previously rejected control rods for delivery in May, (3) initiation of procurement of 32 MH-1A Type II fuel element assemblies scheduled for delivery next fiscal year. The PM Type 4 Core Specification was upgraded and final draft issued.

34. Molten-Salt Reactor Program

Several components from the MSRE have been examined. The only problem noted was intergranular cracking of the Hastelloy N to a depth of about 0.005 in. Laboratory melts of modified Hastelloy N containing Ti, Nb, and Hf were prepared with acceptable

resistance to irradiation embrittlement. Small commercial melts with Ti additions had properties similar to those of the laboratory melts, but the alloys with Hf additions were not as good. Hastelloy N showed excellent resistance to corrosion by fluoride salts of the LiF–BeF₂ base. The material corrodes more rapidly in NaBF₄–8 mole % NaF, and the corrosion seems to be controlled by the presence of oxidizing impurities. Tests in steam show a very low corrosion rate for unstressed Hastelloy N.

Fabrication and joining techniques were developed for a molybdenum test stand for reductive-extraction chemical processing studies. Back-extrusion was developed for fabricating 3⁷/₈-in.-OD containers up to 4 in. long. Electron-beam and tungsten-arc welding parameters were determined for tube-to-tube, tube-to-header, and header-to-header joints. Iron-base brazing alloys were formulated and tested for wettability, flowability, strength, and compatibility with bismuth and molten salts.

Compatibility studies of molybdenum, TZM, tantalum, T-111, and graphite were continued at 650–700°C in pure bismuth and Bi-Li solutions; molybdenum, TZM, T-111, and graphite appear very promising. Studies of methods of putting adherent coatings of W and Mo on Ni- and Fe-base alloys were continued, and coatings were tested by exposure to bismuth.

35. Thorium Utilization

The objective of the Thorium Utilization Program is to demonstrate economic processes and techniques for the Th-²³³U fuel cycle for the High-Temperature Gas-Cooled Reactor. Fabrication processes and equipment are being developed to handle the highly radioactive recycle fuel, and the fuel designs of interest are being irradiation tested. The program is to demonstrate recycle capability starting in 1976. We continued maintenance and improvement of TURF and development of refabrication, with emphasis on engineering-scale deposition of pyrolytic carbon and bonding coated fuel particles with a carbonaceous matrix. We commenced irradiation of a number of recycle fuel particle types in the Peach Bottom Reactor and the Engineering Test Reactor. In addition, we were instrumental in developing a comprehensive program plan for the national demonstration of HTGR fuel recycle technology.

36. Transuranium Program

The Transuranium Project is producing heavier transuranium elements by successive neutron captures. Tar-

get elements are removed, reprocessed to obtain the product actinides, and recycled to the HFIR. Special target elements of the higher isotopes are fabricated and irradiated, and product actinides are encapsulated. We fabricate targets and rabbits for HFIR and special encapsulations for neutron and gamma sources, evaluate the performance of the target elements, and improve the processing equipment. We fabricated 17 target elements loaded with ²⁴⁴Cm, five hydraulic rabbits with ²⁴⁴Pu, ²⁵³Es, and ²⁵²Cf, 20 neutron sources of ²⁵²Cf, and two gamma sources. Only four targets failed out of 44; two failures were predicted by the performance model and the others were satisfactorily explained. The target performance model has been updated to include individual pellet analysis and is being extended to cover the targets loaded with americium-curium oxide. For nondestructively determining the thermal conductivity of individual pellets, the limits of the work have been outlined, desired results stated, and feasibility of a technique with the desired sensitivity has been established.

37. Water Reactor Safety

Efforts on consequences of fuel rod failure during a light-water reactor loss-of-coolant accident include coordination of nationwide research, measurement of channel blockage in multirod transient tube-burst tests, and experimental and mathematical analysis of high-temperature embrittlement of Zircaloy by steam.

PART VI. OTHER PROGRAM ACTIVITIES

38. Metallography

Our electron microprobes continue to be extremely useful. Demands on low detection limits have been met by long counting times (100 sec) and a stable electron beam. In one examination, two or three monolayers of La₂O₃ deposited on NaCl have been analyzed. Beam scanning capabilities for elemental characterization have proven to be a useful, informative, economical approach for analyses with the model 400S microprobe. The alpha metallography facility was moved from Building 3019 to 4508, and we made some minor improvements deemed necessary through operating experience. Efforts to better understand and identify the microconstituents of δ-ferrite, σ-phase, and carbide in welds by chemical etching, autoradiography, and magnetic etching have yielded fruitful results. Additional information was published on the proper use of xenon illumination systems on metallographs. A new recording approach was audio-video taping of the

extensive disassembly and investigation of a steam generator. We upgraded our Quantitative Image Analyzer, and are developing equipment for measuring anisotropy characteristics with polarized light.

39. NERVA Program Metallurgical Support

The outgassing characteristics of NERVA XE II fuel elements were determined in simulated space environments for temperatures between 50°C and 870°C. Elements were tested both as received and after firing above 2000°C in hydrogen. The results were used to predict the gaseous environment in the reactor core exit plenum chamber. The frictional behavior of NERVA graphite was shown to be very sensitive to both wear and surface contamination. Both uncontaminated surfaces and wear are required to cause the coefficient of friction to increase from the values in air (~0.25) to those observed under conditions of heavy loading in vacuum (>0.6).

We are providing baseline data for thermal conductivity, electrical resistivity, and thermopower of the NERVA materials for use in irradiation tests. The results of thermal conductivity measurements on P-03 graphite are reported from 300 to 1000°K.

40. Powder Process Development for LWBR

We are developing processes and specifications for producing $^{233}\text{UO}_2$ powder. Bettis Atomic Power Laboratory will blend this powder with ThO_2 for pelletization. In the UO_2 powder process ammonium diuranate is precipitated from the nitrate solution with gaseous ammonia, centrifuged from its supernate, dried

by microwave heat, and reduced by hydrogen at 600 to 700°C; the reduced powder is then stabilized. This process differs from usual UO_2 production processes in the centrifugation step and the use of microwave drying. Microwave drying appears to be attractive for commercial preparation of UO_2 , PuO_2 , and $(\text{U,Pu})\text{O}_2$ powders. Limited parametric studies were carried out in precipitation, centrifugation, drying, reduction, and stabilization. In addition to developing the $^{233}\text{UO}_2$ process specifications, we produced 18 kg of fully enriched UO_2 powder by the developed processes for evaluation by BAPL.

41. Reactor Evaluation

We assist the AEC in evaluating and optimizing reactor designs by analyzing the cost of fuel fabrication and evaluating nuclear fuel performance. We used previously developed cost analysis computer codes to prepare Geneva IV papers concerning the status of economics of the fuel cycle in the United States. We assisted the AEC in revising the report of the Fuel Recycle Task Force, and we commenced writing a new computer code for analysis of HTGR fuel fabrication and processing costs. Information indexing activities were continued.

42. Examination of Nickel Heat Pipes Containing Potassium

An examination of nickel heat pipes that contained potassium as the working fluid revealed corrosion effects symptomatic of localized segregation of oxygen in the evaporator region of the pipes.

Part I. Fundamental Programs

1. Crystal Physics

G. W. Clark

Our central concern is with the growth of crystals of high-melting refractory materials. Very specific crystals (composition, phase, purity, perfection, size, etc.) are often required to characterize physical properties uniquely or to operate technical devices. Frequently, it is difficult to obtain suitable crystals; hence, we are conducting a continuing program to provide crystals needed in research, to devise and improve methods of crystal growth, and to develop an increased understanding of crystal-growth processes and kinetics. Crystals are grown by several methods: by internal centrifugal zone growth, from molten-salt solvents, by temperature-gradient zone melting, from supercritical aqueous systems, and by the general Verneuil method. During this report period, our crystals were shared with at least 21 different researchers for such diverse investigations as: electron spin resonance; optical, defect, magnetic, and elastic properties; deformation; gas bubble migration; diffusion; field emission; and radiation damage. Also, we are investigating selected physical properties, both those related to the crystal growth process and those important for characterizing new compounds and eutectic structures.

INTERNAL CENTRIFUGAL ZONE GROWTH

Directional Solidification in a Multicomponent Metal-Metal Oxide System

G. W. Clark J. C. Wilson
B. F. Oliver¹ A. T. Chapman²

Steady-state eutectic solidification of the metal-metal oxide system W-UO₂ was achieved below its

binary eutectic temperature ($2640 \pm 20^\circ\text{C}$) by the addition of a third component, MgO. Magnesium oxide was selected because it exhibits binary eutectic behavior with both UO₂ and W, has reasonable liquid solubility of W, and yet has a moderately low solubility in the resulting solids, UO₂ and W. Both tungsten rods and lamellae were grown in a single-crystal UO₂ matrix. The procedure was somewhat analogous to the migration of a liquid zone through a solid, as described earlier by Tiller.³ A controlled molten zone was established within a pressed bar of blended powders by inductively coupling 4-MHz power to this preheated semiconductor. The molten zone was then caused to travel by moving the bar through a shaped radiofrequency field. About 30% less power was required to maintain a molten zone in the ternary system than in the W-UO₂ binary system. This is attributed to a lowering of the melt temperature and to an increase in the electrical conductivity of the ternary melt zone.

With Al₂O₃ as the third component, results similar to those with MgO were not observed.

UO₂-MO_x Eutectics

J. C. Wilson G. W. Clark

In the above work we directionally solidified UO₂-MgO eutectics in which the MgO appeared as rods in a UO₂ matrix. In the UO₂-Al₂O₃ system, the UO₂ appeared with rod morphology in an Al₂O₃ matrix. In preliminary experiments with the UO₂-NiO system (in cooperation with Carlos Bamberger of the Reactor Chemistry Division), NiO plates formed in a UO₂ matrix with contraction of the UO₂ lattice parameter; solution of NiO in solid UO₂ is therefore postulated.

1. Consultant from the University of Tennessee.

2. Consultant from the Georgia Institute of Technology.

3. W. A. Tiller, *J. Appl. Phys.* **34**, 2757 (1963).

Continued UO₂-W Eutectic Study

J. C. Wilson G. W. Clark

Using a new batch of UO₂ (atomic ratio 2.055), we experienced difficulty with both the sintering and swelling of the rod before crystal growth could begin. This difficulty was caused by oxidation of the tungsten powder to at least three distinguishable oxides. Apparently an oxygen-to-uranium ratio of 2.04 or less is required to prevent substantial oxidation of the tungsten. More recently the crystal growth system has been controlled sufficiently well to plan a series of experiments to compare the metal-metal oxide system to current theory. An electron-beam system is being assembled to investigate the directional solidification of a UO₂-W composite so as to produce radial tungsten rods in the UO₂ bar.

Other Metal-Metal Oxide Eutectics

B. F. Oliver¹ J. C. Wilson G. W. Clark

We searched for tungsten eutectics with TiO₂, NiO, V₂O₃, and Nb₂O₅ without success. A eutectic was sought but not found in the Pd-MgO system, in which Lugton and Warble⁴ reported a low-melting phase observed with an electron microscope.

HIGH-TEMPERATURE SOLUTION GROWTH OF SINGLE-CRYSTAL PLUTONIUM DIOXIDE

C. B. Finch G. W. Clark

Single crystals of ²³⁹PuO₂ up to 2 × 2 × 3 mm were grown from (1) PbF₂-2 wt % B₂O₃ and (2) Li₂O·2MoO₃ solvents at 1200 to 1300°C. The crystals (black polyhedra with well-developed faces) have a cubic {100} habit grown from (1) and octahedral {111} from (2). The parameters for good-quality PuO₂ growth approximate those previously reported for growth of the isostructural CeO₂, ThO₂, and NpO₂ (ref. 5) from similar solvents. Spectroscopic, x-ray diffraction, and oxygen analyses indicate that crystals are of good purity (>99.95%) and nearly stoichiometric (PuO_{1.97±0.03}).

4. F. D. Lugton and C. E. Warble, *J. Appl. Phys.* **41**, 1793 (1970).

5. C. B. Finch and G. W. Clark, *J. Crystal Growth* **6**, 245-48 (1970).

CZOCHELSKI GROWTH OF SINGLE-CRYSTAL Mg₂SiO₄ (FORSTERITE)⁶

C. B. Finch G. W. Clark

Single crystals of Mg₂SiO₄ up to 8 mm in diameter × 3 cm long were pulled from the melt in air at approximately 1900°C. A pull rate appropriate for good quality Mg₂SiO₄ growth is 1.2 cm/hr, with seed rotation at 10 to 25 rpm. Crystals were grown doped with less than 0.2 wt % of Mn²⁺, Cr³⁺, or Fe³⁺, with variable effects on color and quality.

CZOCHELSKI GROWTH OF TRANSURANIC-DOPED CaWO₄ SINGLE CRYSTALS

C. B. Finch G. W. Clark L. J. Nugent⁷

Previously we developed the skill of routinely growing optical-quality pure and Nd-doped CaWO₄ single crystals by the Czochralski (crystal pulling) technique in a radiation-protecting glove box.⁸ Cylindrical single crystals of CaWO₄ up to 4 mm in diameter × 6 cm and containing from 0.1 to 1.8 at. % ²⁴³Am³⁺ have since been grown to evaluate potential laser properties of transuranic ions.

The crystals appeared transparent straw yellow through the polished ends of a rod. Only Am³⁺ was responsible for the optical absorption; no Am⁴⁺ was detected. Because of radiation damage, the crystals become increasingly amber-colored with prolonged room-temperature storage in air. Although the crystals photoemit strongly at several frequencies in the visible when excited by radiation of a lower frequency, all room-temperature attempts to lase *c*- and *a*-axis CaWO₄:Am³⁺ rods of the above composition range have been unsuccessful.

To determine whether the above failure to lase is primarily the result of radiation damage, a CaWO₄-1 at. % Nd³⁺ crystal was grown containing an amount of radiation-producing dopant (~0.004 at. % ²⁴⁴Cm) equivalent to that in a CaWO₄-1.8 at. % ²⁴³Am³⁺ crystal. The ²⁴⁴Cm, which produced marked radiation damage with minimal chemical effect, caused only an approximate 10% reduction in laser threshold energy (relative to a CaWO₄-1 at. % Nd³⁺ boule not containing ²⁴⁴Cm).

6. Abstract of *J. Crystal Growth* **8**, 307-8 (1971).

7. Chemistry Division.

8. C. B. Finch and G. W. Clark, *Metals and Ceramics Div. Annu. Progr. Rept. June 30, 1970*, ORNL-4570, pp. 2-3.

A CaWO_4 boule (~ 5 mm diam \times 6 cm) was grown doped with about 0.3 at. % $^{239}\text{Pu}^{3+,4+}$. The boule is transparent green and will be subjected to future spectroscopic, laser, and EPR studies.

CZOCHELSKI GROWTH OF DOPED KMgF_3 SINGLE CRYSTALS

C. B. Finch M. M. Abraham⁹

The Czochralski method was successfully applied in pulling from the melt single crystals of the congruently melting perovskite, KMgF_3 (mp $\sim 1075^\circ\text{C}$). In separate runs, boules up to 8 mm in diameter \times 3 cm were doped with: (1) <1 at. % Ni^{2+} , (2) <0.1 at. % ^{207}Pb , and (3) <0.1 at. % ^{244}Cm . The crystals were pulled from inductively heated platinum crucibles under a protective blanket of flowing argon in a glove box providing radiation protection (needed only in the case of ^{244}Cm dopant). Good quality, optically transparent growth was achieved at pull rates less than 1 cm/hr ($\{100\}$ pull direction) with seed rotation at 25 rpm. The KMgF_3 : $^{244}\text{Cm}^{3+}$ crystals emit a vivid red thermoluminescence when heated from room temperature to about 300°C , and the capability for this is automatically rejuvenated by storage at lower temperatures. The resulting crystals will be subjected to spectroscopic and EPR studies.

HIGH-TEMPERATURE SOLUTION GROWTH OF SINGLE-CRYSTAL ThO_2 DOPED WITH ABOUT 0.1 at. % ^{241}Pu

C. B. Finch

The described thermal gradient method¹⁰ was used to grow octahedral single crystals of ThO_2 -0.1 at. % ^{241}Pu up to 3 mm on edge from $\text{Li}_2\text{O}\cdot 2\text{WO}_3$ -2 wt. % B_2O_3 solvent at 1250 to 1300°C . A nutrient-crystallization zone temperature differential of about 40°C produced good quality growth over a period of two weeks (platinum vessel, air atmosphere). The resulting crystals are being studied by EPR.

ELECTRON PARAMAGNETIC RESONANCE OF SEVERAL RARE-EARTH IMPURITIES IN THE CUBIC PEROVSKITE KMgF_3 (Ref. 11)

M. M. Abraham⁹ C. B. Finch
J. L. Kolopus⁹ J. T. Lewis¹²

The electron paramagnetic resonance spectra of doped KMgF_3 single crystals containing Yb^{3+} , Tm^{2+} , Er^{3+} , Dy^{3+} , and Gd^{3+} have been observed at 9 GHz.

Cubic symmetry sites have been identified for these ions, and the data indicate that the Yb^{3+} , Tm^{2+} , Er^{3+} , and Dy^{3+} substitute for the sixfold-coordinated Mg^{2+} ion, but the gadolinium probably substitutes for a 12-fold-coordinated K^+ ion. Noncubic symmetry sites were also observed for Yb^{3+} , Er^{3+} , and Gd^{3+} . Hyperfine structure for the isotopes ^{171}Yb , ^{173}Yb , ^{169}Tm , ^{167}Er , ^{161}Dy , and ^{163}Dy was identified, and in some cases superhyperfine interactions with the fluorine ligand ions were observed with good resolution.

ESR OF Pb^{3+} CENTERS IN ThO_2 (Ref. 13)

J. L. Kolopus⁹ M. M. Abraham⁹ C. B. Finch

Spectra of Pb^{3+} in sites having cubic and axial symmetry have been identified in ThO_2 crystals grown from a PbF_2 -based solvent and irradiated with electrons or gamma rays. That part of the spectra arising from the 20%-abundant ^{207}Pb isotope ($I = 1/2$) is characterized by a large zero-field hyperfine splitting. The Pb^{3+} center with $\langle 111 \rangle$ axial symmetry shows a superhyperfine interaction with a ^{19}F nucleus. Part of this spectrum has previously been attributed to the F center in ThO_2 . After exposure to ionizing radiation, no centers were detected in ThO_2 crystals grown from a $\text{Li}_2\text{O}\cdot 2\text{WO}_3$ -based flux. Neutron irradiation of all crystals produced another center with $\langle 100 \rangle$ axial symmetry.

ELECTRON PARAMAGNETIC RESONANCE INVESTIGATIONS OF $5f^5$ CONFIGURATION IONS IN CUBIC SINGLE CRYSTALS: Pu^{3+} IN ThO_2 AND SrCl_2 , AND Am^{4+} IN ThO_2 (Ref. 14)

M. M. Abraham⁹ L. A. Boatner¹⁵
C. B. Finch R. W. Reynolds¹⁵

Electron paramagnetic resonance spectra of the iso-electronic ions Pu^{3+} and Am^{4+} in cubic sites of fluorite-structure single crystals have been investigated at 1.5 and 4.2°K . The observed isotropic spectra and associated g values identify the ground states at Γ_7

9. Solid State Division.

10. C. B. Finch and G. W. Clark, *J. Appl. Phys.* 36, 2143-45 (1965).

11. Abstract of *Phys. Rev. B* 3, 2855-64 (1971).

12. Oak Ridge Graduate Fellow from the University of Tennessee under appointment from the Oak Ridge Associated Universities.

13. Abstract of *Phys. Rev. B* 2, 2040-45 (1970).

14. Abstract of *Phys. Rev. B* 3, 2864-68 (1970).

15. Advanced Technology Center, Inc. (formerly LTV Research Center), Dallas, Texas.

doublets. This ground state is produced by intermediate-coupling effects that are much larger for $5f^5$ configuration ions than for the analogous $4f^5$ ions. Spin-Hamiltonian parameters were determined to be: $g = 1.3124 \pm 0.0005$, $A = (65.4 \pm 0.2) \times 10^{-4}/\text{cm}$ for $^{239}\text{Pu}^{3+}$ in ThO_2 ; $g = 1.1208 \pm 0.0005$, $A = (127.9 \pm 0.4) \times 10^{-4}/\text{cm}$ for $^{239}\text{Pu}^{3+}$ in SrCl_2 ; and $g = 1.2862 \pm 0.0005$, $A = (45.7 \pm 0.1) \times 10^{-4}/\text{cm}$ for $^{241}\text{Am}^{4+}$ and $A = (45.3 \pm 0.1) \times 10^{-4}/\text{cm}$ for $^{243}\text{Am}^{4+}$ in ThO_2 . Spectra observed for both Pu^{3+} and Am^{4+} were characterized by very anisotropic line widths and by a dependence of line width on the nuclear-spin projection quantum number m_I .

ELECTRON PARAMAGNETIC RESONANCE INVESTIGATIONS OF DIVALENT AMERICIUM AND TRIVALENT CURIUM IN STRONTIUM CHLORIDE¹⁶

M. M. Abraham⁹ C. B. Finch
L. A. Boatner¹⁵ R. W. Reynolds¹⁵
H. Zeldes⁷

The cubic-site electron paramagnetic resonance spectra of divalent americium and trivalent curium ($5f^5$ configuration) in SrCl_2 were observed. The ground states are Γ_6 doublets, indicating that the fourth-order parameters c of the cubic crystal-field Hamiltonian are negative. Because of the relatively small cubic crystal-field interaction with the $^8S_{7/2}$ state, the Γ_6 ground-state transitions were anisotropic, permitting a determination of the zero-field splitting. Additionally, an excited state (Γ_7) resonance was detected for curium, and curium resonances were observed at temperatures as high as 200°K . The g_J value obtained was 1.9264 ± 0.0008 for Cm^{3+} and 1.9283 ± 0.0008 for Am^{2+} . Assuming that the sixth-order parameters are negligible, the values of c are $-1.83 \pm 0.02/\text{cm}$ for curium and $-1.92 \pm 0.16/\text{cm}$ for americium. The hyperfine structure constants for americium were 83.9 ± 0.1 G for ^{241}Am ($I = 5/2$) and 8.32 ± 0.1 G for ^{243}Am ($I = 5/2$). The previously unknown nuclear spin of ^{245}Cm was determined to be $7/2$ with an A value of 19.0 ± 0.2 G. By comparison with ^{241}Am and ^{243}Am , the magnetic moment $|\mu(^{245}\text{Cm})| = (0.5 \pm 0.1)\mu_N$ was estimated.

CHARACTERIZATION OF RbOH-GROWN QUARTZ BY INFRARED AND MASS SPECTROSCOPY¹⁷

O. C. Kopp¹ P. A. Staats¹⁸

Infrared frequencies of RbOH-grown quartz include ten bands in the region 3200 to 3600/cm. An unusual time- (or temperature-) related phenomenon increases the absorbance in the region 2900 to 3550/cm when

crystals are examined over intervals up to several hours in a liquid-nitrogen cell. The band at 3580/cm is not affected. A linear relationship, which is influenced by the temperature of the growth zone, exists between average growth rate and extinction coefficient ($\alpha_{3580/\text{cm}}$). Typically, the extinction coefficient decreases (and presumably the crystal quality improves) as the growth temperature increases for a given growth rate. Impurity ions such as Li^+ , Na^+ , and K^+ present in the RbOH solvent are taken preferentially into the quartz structure because of their smaller sizes. Aluminum and iron present are derived from the nutrient and vessel liner, respectively. The ratio of Fe^{3+} and Al^{3+} to total alkalis is close to but slightly greater than one.

LAMELLAR DENDRITIC GROWTH IN LEAD SULFIDE¹⁹

O. C. Kopp¹ G. W. Clark

Platelets of cubic lead sulfide, with the larger faces in the $\{111\}$ plane, were grown in the system RbOH-PbS- H_2O . One of these platelets shows evidence of an unusual form of growth, not noted by us previously. Growth appears to be taking place through the coalescing of dendrites whose growth directions are along the traces of the dodecahedral axes $[110]$ of the crystal in the $\{111\}$ plane. The crystal appears to be layered, and several of the layers show noticeable indentations, such as might develop through the incomplete coalescing of lamellar dendrites.

TEMPERATURE-GRADIENT ZONE MELTING OF GRAPHITE

J. C. Wilson G. W. Clark

Using nickel sheet to form a nickel-carbon eutectic ($T \gg 1300^\circ\text{C}$) molten zone between two carbon specimens, we grew single (or pseudo-single) crystals of graphite. Equipment for electron beam or inductively heating samples has been constructed, and better controlled experiments are in progress. With the electron beam heating, much steeper temperature gradients were produced than with the earlier induction heating. To date, instabilities at the growth interface have prevented any meaningful results.

16. Abstract of *Phys. Rev. B* 1, 3555-60 (1970).

17. Abstract from *J. Phys. Chem. Solids* 31, 2469-76 (1970).

18. Physics Division.

19. Abstracted from *J. Crystal Growth* 8, 135-36 (1971).

2. Crystal Spectroscopy

G. P. Smith

In preceding years, research by this group centered on applications of spectroscopy to chemistry in molten salts, with some supporting solid state work. During the current year, however, the liquid state research was phased out and the program was reoriented to center on applications of spectroscopy to chemistry in ionic crystals. The research summaries that follow cover preliminary phases of the new program and some phases of the old program that could be salvaged.

CONSTRUCTION ON A HIGH-TEMPERATURE SPECTROMETER

C. R. Boston

The purpose of this work is to study the behavior of dopant ions in crystals at very high temperatures. The only absorption spectra of crystals above 1000°C appear to be those reported by this group several years ago. These were measurements on a ruby crystal at 1450°C and a "dummy" sample at 2200°C. The experimental feasibility of spectral measurements at these temperatures was adequately demonstrated by these early studies. To further explore this field a 10-kW induction heating unit is being installed to heat crystals held in the sample compartment of the Cary 14H spectrophotometer to 2000°C and above.

CONSTRUCTION ON A LOW-TEMPERATURE SPECTROMETER

G. P. Smith

We are building an optical spectrometer designed to operate with the specimen at liquid helium temperatures under static uniaxial compression. Later we plan to modify the apparatus for modulated stress so that low stress levels can be studied. The purpose of this device is to probe the electronic and geometrical symmetries of impurity ion defects in host lattices and to measure electron-lattice coupling.

THE RAMAN SPECTRA OF MOLTEN ALUMINUM TRIHALIDE-ALKALI HALIDE SYSTEMS¹

G. M. Begun² G. Torsi³
C. R. Boston G. Mamantov⁴

Raman spectra were measured for $\text{AlBr}_3\text{-NaBr}$ and $\text{AlI}_3\text{-CsI}$ melts in the region 50 mole % to pure aluminum halide. The data were compared with previous data for the $\text{AlCl}_3\text{-NaCl}$ system. Raman frequencies were assigned for the AlBr_4^- , Al_2Br_7^- , AlI_4^- , and Al_2I_7^- ions. Valence force constants were calculated for the series of tetrahedral ions: AlCl_4^- , AlBr_4^- , AlI_4^- .

MAGNETIC MOMENT OF $\text{Ti}(\text{AlCl}_4)_2$

J. Brynestad A. S. Dworkin²

The magnetic susceptibility of the compound⁵ $\text{Ti}(\text{AlCl}_4)_2$ was measured by the Guoy method. The molar susceptibility was $(3.5 \pm 0.1) \times 10^{-3}$ cgs units at room temperature ($\sim 25^\circ\text{C}$). Using the Langevin expression, this gives a magnetic moment of 2.9 ± 0.1 Bohr magnetons, indicating two unpaired electrons per titanium atom (d^2). So far, $\text{Ti}(\text{AlCl}_4)_2$ is the only known compound of divalent titanium with this property.

COORDINATION CHEMISTRY OF NICKEL(II) IN LIQUID MIXTURES OF CESIUM CHLORIDE AND ALUMINUM CHLORIDE

J. Brynestad

The coordination chemistry of Ni(II) was studied in liquid CsAlCl_4 and in liquid mixtures of $\text{CsAlCl}_4\text{-CsCl}$

1. Abstract of paper submitted to *Inorganic Chemistry*.
2. Chemistry Division.
3. University of Bari, Bari, Italy.
4. University of Tennessee.
5. J. Brynestad, S. von Winbush, H. L. Yakel, and G. P. Smith, *Inorg. Nucl. Chem. Letters* 6, 889-93 (1970).

and $\text{CsAlCl}_4\text{-AlCl}_3$ by optical absorption spectroscopy. Evidence was obtained for the three-coordinate complex NiCl_3^- (ref. 6) and the complex $\text{NiCl}^+\cdot(\text{AlCl}_4^-)_x$

6. J. Brynestad and G. P. Smith, *J. Amer. Chem. Soc.* **92**, 3198-99 (1970).

with unknown coordination geometry. The following equilibrium data valid in the range 400 to 700°C were obtained: $\text{NiCl}_4^{2-} \rightleftharpoons \text{NiCl}_3^- + \text{Cl}^-$, $\Delta H^\circ = 13.3 \pm 0.2$ kcal, $\Delta S^\circ = 9.8 \pm 0.1$ cal/deg; $\text{CsNiCl}_3(\text{s}) \rightleftharpoons \text{NiCl}_3^- + \text{Cs}^+$, $\Delta H^\circ = 25.8$ kcal, $\Delta S^\circ \approx 23.5$ cal/deg; $\text{CsNiCl}_3(\text{s}) + \text{Cl}^- \rightleftharpoons \text{NiCl}_4^{2-} + \text{Cs}^+$, $\Delta H^\circ \approx 13.1$ kcal, $\Delta S^\circ \approx 14.6$ cal/deg.

3. Deformation of Crystalline Solids

R. O. Williams

We are primarily concerned with the internal structure of metals and alloys, specifically with features that determine the chemical and physical properties. Current work includes precipitation studies, simulation of solid solutions, and analysis of dislocation interactions.

THE REPRESENTATION OF SOLID SOLUTIONS

R. O. Williams

In solid solutions the atoms are normally not distributed randomly over the lattice sites nor do they sit precisely on the sites because of size effects. Diffuse x-ray measurements are the primary source of information on these effects. Our concern is learning how one describes the solid solutions in the most meaningful fashion.

The first problem is obtaining short-range order and strain parameters from the x-ray data. We have written a computer program that evaluates these parameters by a multiple regression analysis while introducing all known corrections. The advantages of this method over previous ones is that one has considerable liberty on how the data are taken, higher levels of corrections are used, and the errors in the parameters are calculated. Using a standard format for repeated runs saves considerable time.

A program to carry out a simulation of displacements in solid solutions was written, based on first-neighbor interactions. Tests will be started shortly to establish the degree to which this model can represent measured displacements.

All possible long-range-ordered structures for binary face-centered cubic lattices having nine or fewer sites per primitive cell have been determined. This information is important in establishing the degree of uniqueness in the simulation of short-range order in solid solutions.

DISSOCIATION OF NONBASAL DISLOCATIONS IN HEXAGONAL CLOSE-PACKED METALS¹

M. H. Yoo B. T. M. Loh

An analysis is given of the possible dissociations of dislocations with Burgers vectors $\langle \mathbf{a} \rangle$ and $\langle \mathbf{c} + \mathbf{a} \rangle$ on various nonbasal planes. Three partial displacement vectors of $\frac{1}{4}\langle 42\bar{6}3 \rangle$, $\frac{1}{6}\langle 10\bar{1}3 \rangle$, and $\frac{1}{6}\langle 20\bar{2}3 \rangle$ types are identified on the basis of three kinds of metastable positions (triangular, tetrahedral, and octahedral sites) revealed on various "atomically flat surfaces" of a hard-sphere model. The stabilities of the extended configurations of $\frac{1}{3}\langle 11\bar{2}0 \rangle$ dislocation in $(1\bar{1}00)$ and $(1\bar{1}01)$ planes and $\frac{1}{3}\langle 1\bar{1}23 \rangle$ dislocation in $(1\bar{1}00)$, $(2\bar{1}\bar{1}1)$, $(10\bar{1}1)$, and $(11\bar{2}2)$ planes are determined for 14 hexagonal metals by anisotropic elasticity theory. For those elastically stable dissociations, the widths of the extended dislocations are obtained as functions of the anisotropic parameters and the stacking fault energies.

DISPLACEMENT FIELDS OF STRAIGHT DISLOCATIONS IN ANISOTROPIC CRYSTALS²

M. H. Yoo B. T. M. Loh

We analyzed in detail the displacement fields of active slip dislocations in common crystal structures by taking full account of the elastic anisotropy. Each displacement component can be generally expressed in terms of 12 real coefficients. Interdependent relationships among these coefficients are discussed. For those cases

1. Abstract of paper presented at the 1970 Fall Meeting of the Metallurgical Society of AIME, Cleveland, Oct. 19-22, 1970.

2. Summary of paper presented at the 1971 Spring Meeting of the Metallurgical Society of AIME, Atlanta, May 17-20, 1971.

for which no analytically tractable solutions exist, we calculate the coefficients numerically using the computer program written for anisotropic elastic properties of a dislocation.³

Two notable areas of application requiring the exact solution of the displacement fields are the dislocation contrast analyses in transmission electron microscopy and the atomistic calculations of dislocation core structures. Since each displacement component obtained from the elastic solution is referred to an arbitrary origin, one needs to find the integration constant with respect to the crystal axis of dislocation, particularly for the latter application where the exact magnitude of the displacement is to be used as a boundary condition. The method of determining the integration constants in accordance with the crystal symmetry is presented.

ELASTIC INTERACTION OF A POINT DEFECT WITH A PRISMATIC DISLOCATION LOOP IN HEXAGONAL CRYSTALS⁴

M. H. Yoo S. M. Ohr⁵

Expressions for the strain components of a finite prismatic dislocation loop in a hexagonal crystal are obtained by taking into account elastic anisotropy. A point defect in a hexagonal crystal is simulated by three orthogonal sets of unequal double forces without moment. By making use of the elastic Green's function available for hexagonal crystals, we calculate the strengths of force dipoles in terms of volume change associated with the point defect. The elastic solutions thus obtained are used to calculate the interaction energy between the point defect and a prismatic dislocation loop. Hexagonal crystals exhibit qualitative differences from corresponding results for an isotropic medium.

MORPHOLOGICAL FORMS OF THE ALPHA PHASE DURING PRECIPITATION FROM A BCC MATRIX IN Nb-Hf ALLOYS²

R. W. Carpenter

The precipitation of the hcp alpha phase from supersaturated bcc Nb-Hf alloys begins with the forma-

tion of coherent zones, which coarsen into disk-shaped precipitate particles approximately parallel to $\beta\{100\}$ planes upon further aging. Diffraction shows the disk structure to be strained hcp with nearly the same lattice constants as equilibrium alpha; there is also diffuse intensity characteristic of "diffuse omega" present, but not omega spots. With further aging, the alpha morphology changes to rod type, and strain effects disappear from the diffraction pattern.⁶ The crystallographic relationship between alpha and beta is the Burgers type, $\langle 11\bar{2}0 \rangle \parallel \langle \bar{1}11 \rangle$, $(0001) \parallel (110)$. The long axis of an alpha rod is parallel to one of its $\langle 10\bar{1}0 \rangle$ poles, and this direction is nearly parallel to one of the $\langle 113 \rangle$ directions of the beta bcc matrix. This indicates that during isothermal precipitation two distinct morphological forms of the precipitate exist. The disk type alpha is termed⁷ "strained transition alpha." Other published data concerning titanium alloys show morphological forms during alpha precipitation similar to those reported here, so it appears that this precipitation sequence may be quite general for isothermal precipitation of an hcp phase from a bcc matrix.

STRENGTHENING Nb-Hf ALLOYS BY ALPHA PRECIPITATION⁸

R. W. Carpenter C. T. Liu

Niobium-hafnium alloys containing 38 and 54 at. % Hf were quenched from the single-phase bcc beta region and isothermally aged at temperatures within the alpha plus beta two-phase field. During aging at 600°C the hardness of both alloys reached a maximum at short times (~10 min) and then slowly decreased. When the alloys were aged at 1000°C an immediate hardness drop below the quenched value was observed; the hardness attained a steady state appreciably lower than the quenched value after aging for longer than about 100 min. Observations of the morphological changes occurring in the alloys during aging at 600°C showed that the hardness maximum observed at 600°C is caused by initial precipitation of the at least partially coherent transition alpha (α_t) morphology. The subsequent

3. M. H. Yoo and B. T. M. Loh, *Numerical Calculation of Elastic Properties for Straight Dislocations in Anisotropic Crystals*, ORNL-TM-3408 (June 1971).

4. Abstract of paper submitted for presentation at the 1971 Fall Meeting of the Metallurgical Society of AIME, Detroit, Oct. 18-22, 1971.

5. Solid State Division.

6. R. W. Carpenter, C. T. Liu, and P. G. Mardon, "Phase Relations in Concentrated Ta-Hf and Nb-Hf Alloys," *Met. Trans.* 2, 125-31 (1971).

7. R. W. Carpenter and C. T. Liu, "Transition Morphology During HCP Precipitation from Beta-Isomorphous Alloys," *Scripta Met.* 5, 255-57 (1971).

8. Abstracted from pp. 674-78 in *Second International Conference on the Strength of Metals and Alloys, Conf. Proc.*, vol. II, The American Society for Metals, Metals Park, Ohio, 1970.

decrease in hardness upon longer aging at 600°C in both alloys is attributed to coarsening of these particles. During aging at 1000°C the incoherent rod-type alpha appears after very short aging times. These particles are coarse and large and were not effective in strengthening either alloy.

OBSERVATIONS OF $\text{Cu K}\bar{\alpha}_{3,4}$ REFLECTIONS IN X-RAY DIFFRACTION EXPERIMENTS⁹

R. W. Carpenter H. L. Yakel

During an investigation of precipitation in certain niobium-hafnium alloys, which for thermodynamic reasons one expects to exhibit side bands at some stage

of the reaction, only a single diffuse maximum was observed on the low angle side of the matrix Bragg peaks. The maximum did not shift its position during the precipitation reaction in the manner expected from the theory of precipitation. Subsequent investigation showed the diffuse maximum to result from the relatively little known $\text{K}\bar{\alpha}_{3,4}$ weak maximum in the copper emission spectrum, located at a slightly higher energy than the $\text{K}\alpha_1$ peak. Thus the diffuse maximum observed, although in a position expected from a structural modulation of the crystal lattice, is a result of weak maximum in the copper emission spectrum. To ascribe weak diffraction effects observed to specific structural causes, the experimenter must have a detailed knowledge of the energy spectrum incident on the specimen. Otherwise weak scattering of the major spectral component (usually a $\text{K}\bar{\alpha}_{1,2}$ line characteristic of the x-ray tube target) can be easily confused with strong scattering of a minor spectral component.

9. Abstracted from *J. Appl. Phys.* 42, 887-88 (1971).

4. Diffusion in Solids

T. S. Lundy

Our interest includes the whole area of atomic diffusion in crystalline substances. Our research effort concentrates on the examination of diffusion rates under various conditions by the macroscopic redistribution of radioactive tracers in refractory metals and ceramics. This includes diffusion coefficient measurements under isothermal conditions at approximately atmospheric pressures as well as effects of temperature gradients and high pressures. We seek to relate experimentally determined diffusion parameters to theoretical models that consider the possible elementary atomic jumps in materials systems under consideration.

TRACER SELF-DIFFUSION IN Fe-17 wt % Cr-12 wt % Ni

Namik K. Tunali¹

Volume self-diffusion coefficients in the ternary alloy Fe-17 wt % Cr-12 wt % Ni for the radioactive tracers ⁵⁹Fe, ⁵¹Cr, and ⁶³Ni are being determined by conventional lathe and grinding techniques at high temperatures and by a newly developed radiofrequency sputtering technique² below about 700°C. The sputtering technique allows very thin sectioning (in the range of 100 Å), so that extremely small diffusion coefficients (of the order of 10⁻¹⁸ cm²/sec) can be measured directly. This new procedure permits diffusion coefficient measurements in a wide variety of materials in the usual temperature range of their engineering application and therefore represents a breakthrough in attempts to relate basic atomic transport properties to applied problems.

We found that ⁵¹Cr diffuses significantly faster than ⁵⁹Fe for the range up to 1300°C. Upward deviations from Arrhenius plots at low temperatures are due to

short-circuiting and the limited resolution of conventional sectioning techniques.

THERMOTRANSPORT OF CADMIUM IN SODIUM AND POTASSIUM CHLORIDES

P. T. Carlson L. C. Manley, Jr.
D. Heitkamp³ R. A. Padgett, Jr.

The thermal diffusion of ^{115m}Cd tracer in single crystals of sodium and potassium chlorides is under investigation with the intent to gain a better understanding of the heat of transport in ionic systems. An adequate understanding of this parameter permits quantitative predictions regarding the amount of segregation that occurs in a material under the influence of a temperature gradient. A theoretical treatment of the heat of transport, which considers the thermodynamics of irreversible processes, was developed. This treatment shows that the flow of heat associated with matter transport can be described in terms of changes in either Gibbs free energies or total enthalpies.

For the experimental determination of the heat of transport, disks of high-purity NaCl and KCl single crystals doped with cadmium tracer are annealed in a temperature gradient of 1000°C/cm for seven days under 2 atm Ar. Conventional sectioning and multi-channel counting techniques are employed to determine the concentration distribution of tracer in the diffused sample. The heat of transport of the tracer impurity, Q^{**} , is then calculated from the slope of a plot of $\ln c$ against $1/T$ with the aid of the expression

$$\frac{d \ln c}{d(1/T)} = \frac{Q^{**}}{R}, \quad (1)$$

1. On leave from Middle East Technical University, Ankara, Turkey.

2. D. M. Kroeger and E. W. Chandler, *Metals and Ceramics Div. Annu. Progr. Rept. June 30, 1971*, ORNL-4570, p. 14.

3. On leave from Institute of Physical Chemistry, Jülich, Germany.

where c is the mole fraction of impurity and T the absolute temperature. Preliminary results show that cadmium migrates toward the higher temperature, indicating a negative heat of transport for cadmium in single crystals of sodium chloride.

Ionic materials are convenient systems in which to study thermotransport because of the existence of adequate literature on interatomic potentials, lattice energies, and formation energies of lattice defects. Furthermore, the extension of the treatment for ionic systems to that for ceramic systems is direct, since ionic forces contribute significantly to the interatomic forces present in ceramic materials.

CATION SELF-DIFFUSION IN RUTILE (TiO₂)

T. S. Lundy R. A. Padgett, Jr. L. C. Manley, Jr.

The titanium sublattice of rutile (TiO₂) is body-centered tetragonal and therefore requires determination of two coefficients, $D_{\parallel c}$ and $D_{\perp c}$, at each temperature to completely define the lattice diffusion process. We have used oriented single crystals from two sources with ⁴⁴Ti tracer and standard serial sectioning techniques to find both coefficients in the range 1200 to 1550°C. At each temperature $D_{\perp c}$ is larger than $D_{\parallel c}$, and the ratio varies from about 2.6 to 1.3 as the temperature increases. The results cannot be explained solely in terms of the diagonal jump but require significant contributions from the c -direction atomic jump. Coghlin (Chap. 7 of this report) has calculated partial correlation functions for diffusion by a vacancy mechanism in this system, and we are using his results to assist in identification of elementary atomic jumps.

CATION SELF-DIFFUSION IN TITANIUM MONOXIDE

T. S. Lundy R. A. Padgett, Jr. M. D. Banus⁴

The high-temperature phase of titanium monoxide has a wide range of stoichiometry and very large vacancy concentrations.⁵ We are initiating a joint program on diffusion in TiO _{x} , $0.8 \leq x \leq 1.3$, to determine the atomic migration properties relative to other well-known characteristics of such systems. Diffusion coefficients of ⁴⁴Ti will be measured by standard grinding techniques as functions of temperature, stoichiometry, and possibly pressure, with the goal of understanding operative mechanisms of atomic migration.

DIFFUSION UNDER HIGH PRESSURES

T. S. Lundy

Our experiments involving measurements of diffusion coefficients at very high pressures are awaiting fabrication and installation of equipment designed for operation up to 14 kbar and 1500°C. Initial research will concentrate on diffusion in the refractory metals Nb, Ta, and W, for which the very sensitive anodizing-and-stripping technique will allow measurements of pressure effects on lattice as well as short-circuiting diffusion. The resulting data will yield activation volumes and other information on atomic migration in these body-centered cubic systems.

4. MIT Lincoln Laboratory.

5. See for example, M. D. Banus and T. B. Reed, "Structural, Electrical and Magnetic Properties of Vacancy Stabilized Cubic 'TiO' and 'VO,'" pp. 488-520 in *The Chemistry of Extended Defects in Non-Metallic Solids*, ed. by L. Eyring and M. O'Keefe, North-Holland, Amsterdam and London, 1970.

5. Electron Microscopy

J. O. Stiegler

The activities of the Electron Microscopy Group stress the relationship between the microstructures of materials and their mechanical and physical properties. A large share of the group's effort is devoted to studies of the radiation damage introduced into materials by bombardment with fast neutrons in reactors or with electrons in the electron microscope. Interest is also focused on naturally occurring defects in materials. In the area of room-temperature plastic deformation, attention is directed to the role of grain boundaries as strengthening agents and to the energy stored during plastic deformation. In the area of elevated-temperature deformation the development of creep cavities in powder-metallurgy tungsten is being pursued. Finally, the effects of composition and heat treatment on the microstructure of Hastelloy N and type 316 stainless steel are being studied.

In this chapter we report results of work funded by the AEC Division of Research and some studies that are primarily microstructural in nature. Additional work in support of other programs in the Division appears in Chaps. 3, 15, 22, 24, 25, 29, and 34 of this report.

DAMAGE IN ALUMINUM BY 200-kV ELECTRONS¹

A. Wolfenden

Defect clusters formed in aluminum during examination in a 200-kV electron microscope. Experimental and theoretical considerations indicate that the damage was due to the direct displacement of atoms by the electron beam. The damage results in the random nucleation of point defect clusters, which grow to form loops observed throughout most of the thickness of the specimen foil. A Burgers vector analysis of these loops was attempted, but difficulties due to the cube texture of the aluminum foils were encountered. The observation that vacancy loops (formed by previously quenching some foils from about 650°C into room

temperature water) are "eaten away" by these point defects suggests that some of the latter are interstitials. These experiments and their future potential are discussed in terms of the general field of radiation damage.

THE EFFECTS OF ELECTRON IRRADIATION ON PREEXISTING DEFECTS IN ALUMINUM²

A. Wolfenden

Electron displacement damage is produced in high-purity (99.999+%) aluminum foils in an electron microscope operating at accelerating voltages as low as 200 kV. These displacement defects interact with preexisting defects such as dislocations, Frank sessile vacancy loops, and voids. In less pure aluminum (99%), no displacement damage due to the electron beam is seen, but if the specimens are first neutron irradiated, subsequent bombardment in the electron microscope causes the further development of visible dislocation loops. These loops form preferentially at grain boundaries, precipitate particles, and grown-in dislocations and may denote the positions of preexisting defects that were too small to be resolved in the electron microscope. The future potential of such experiments will be discussed.

THE EFFECTS OF IRRADIATION TEMPERATURE AND PREINJECTED GASES ON VOIDS IN ALUMINUM³

K. Farrell A. Wolfenden R. T. King

Voids in high-purity aluminum irradiated to a fast (>1 MeV) fluence of 4×10^{20} neutrons/cm² at 125 and 150°C (0.43 and 0.45 T_m - absolute melting point) are fewer but very much larger than those in material

1. Summary of *J. Nucl. Mater.* 38, 114-15 (1971).

2. Abstract of a paper prepared for the Second International Conference on High Voltage Electron Microscopy, April 14-16, 1971, Stockholm, Sweden (to be published in the proceedings).

3. Abstract of a paper to be published in *Radiation Effects*.

irradiated at 55°C ($0.35T_m$). Additionally, at 125 and 150°C the voids adopt a variety of shapes including plates, ribbons, cylinders, and more equiaxed polyhedra and are frequently associated with particles of transmutation-produced silicon. At the higher temperatures voids are larger near grain boundaries than in grain interiors. Injection of hydrogen or helium before irradiation causes an increase in the number and a corresponding decrease in size of voids in specimens irradiated at 150°C; 3 at. ppm He is more effective than either 3 or 9 at. ppm H. The gases do not appear to influence swelling.

A commercially pure (99%) aluminum subjected to the same irradiation treatments did not develop voids whether preinjected with gases or not; the visible radiation damage consisted solely of small loops on or near grown-in dislocations.

RADIATION VOIDS IN HIGH-PURITY MAGNESIUM³

A. Jostsons⁴ K. Farrell

Zone-refined magnesium was irradiated to 2×10^{21} neutrons/cm² (>0.1 MeV) at a temperature between 55 and 100°C. It swelled by 1.9%. Transmission electron microscopy revealed many voids arranged in layers parallel to the basal planes. The general shape of the voids was that of a hexagonal prism squashed in $\langle 0001 \rangle$ so that its largest faces were the basal planes. Their sizes ranged up to 2000 Å measured along the long axis. Between the voids, and also on the basal planes, were large numbers of stacking faults. Voids and stacking faults were eliminated by a 1-hr anneal at 300°C.

VOID COARSENING IN HIGH-PURITY ALUMINUM DURING POSTIRRADIATION ANNEALING⁵

J. T. Houston K. Farrell

The annealing response of voids was compared in 500- μ m-thick disks of high-purity aluminum cut from 3.18-mm-diam rods irradiated in HFIR at 55°C to fluences (>0.1 MeV) of 1.6×10^{21} and 1.6×10^{22} neutrons/cm². These irradiations caused about 1 and

7.5% swelling, respectively. The lower fluence specimen had 3.8×10^{14} voids/cm³ with a maximum size of 700 Å. No significant void annealing occurred up to 200°C. Between 250 and 275°C the smaller voids disappeared, and at 300°C all voids were dissolved. No void growth was observed. The higher fluence specimen had 6.4×10^{14} voids/cm³ with a maximum diameter of 1100 Å. Little or no effect of annealing was noted until 300°C, where the small voids disappeared and some voids grew appreciably. These growing voids were often elongated in a $\langle 110 \rangle$ direction and were invariably associated with transmutation-produced silicon particles. At 350 and 400°C many large (up to 1.5 μ m) voids grew by depleting their surroundings of smaller voids. All voids disappeared at 500°C. These observations are explained in terms of an Ostwald-type ripening process.

THE EFFECTS OF DIFFERENT MICROSTRUCTURES ON THE FORMATION OF DISLOCATION LOOPS IN ALUMINUM DURING ELECTRON IRRADIATION⁶

A. Wolfenden

Exposure to the beam in a 200-kV electron microscope caused defect clusters to form in high-purity aluminum foils. The damage was due to the direct displacement of atoms by electrons. The point defect clusters nucleated randomly and grew to form dislocation loops. Contrast analysis showed that the loops had Burgers vectors in either $\{111\}$ or $\{110\}$ planes. The microstructure of the aluminum was varied by quenching or alloying. In high-purity foils containing previously quenched-in Frank sessile vacancy loops, the subsequent electron irradiation-induced defects interacted with the preexisting defects. In 99% aluminum and in alloy 2024 (4.5% Cu, 1.5% Mg, 0.6% Mn, balance Al) no electron-induced damage was seen. However, when the 99% aluminum specimens were first neutron irradiated, subsequent bombardment by electrons caused the development of visible dislocation loops. These formed preferentially near grain boundaries, precipitate particles, and grown-in dislocations. No electron damage was observed in the 2024 alloy specimens even after neutron irradiation. The important conclusion is that the presence and distribution of electron irradiation damage in aluminum is extremely sensitive to microstructure.

4. On attachment from Australian Atomic Energy Commission Research Establishment.

5. Abstract of a paper to be published in *Journal of Nuclear Materials*.

6. Abstract of a paper submitted to *Micron*.

EFFECTS OF PREINJECTED HYDROGEN ON THE ELECTRON DISPLACEMENT DAMAGE IN 1100 ALUMINUM⁵

A. Wolfenden

When a metal foil is electron irradiated in an electron microscope operating at voltages higher than a critical voltage, point defects are created by displacement damage. These defects may agglomerate to form visible dislocation loops. The study here is concerned with the electron bombardment of 1100 aluminum (99 wt % pure aluminum). Specimens were investigated in two conditions: some were annealed; others were annealed, preinjected with protons in a cyclotron (9 at. ppm H), and then reannealed. Subsequent electron irradiation in the microscope produced visible dislocation loops in only the latter group of specimens. These loops formed preferentially near grain boundaries. This observation shows that the agglomeration of point defects resulting from electron bombardment damage is stimulated by preinjected hydrogen. Impurities present at the part-per-million level can thus affect the formation and distribution of electron irradiation-produced dislocation loops in 1100 aluminum.

SWELLING OF CARBONYL NICKEL⁷

J. T. Houston K. Farrell

Nickel slabs deposited by thermal decomposition of nickel carbonyl vapor are relatively hard and contain grown-in microscopic porosity associated with dislocations and grain boundaries. On annealing in vacuum at up to 500°C the shapes of the pores are altered and the slabs soften and shrink more than 1/2%. Annealing above 500°C develops large grain-boundary porosity that causes 2% swelling during a 1000°C anneal. These observations are consistent with a model involving entrapment of gases during deposition of the nickel.

MECHANISMS OF VOID FORMATION IN SOLIDS UNDER IRRADIATION

B. T. M. Loh

We are attempting to model quantitatively by computer simulation void formation processes in solids under irradiation. Preliminary results show that the classical nucleation theory cannot be applied directly because of the coexistence of the excess vacancies and

interstitials that are created simultaneously in the solid by the high-energy radiation. Therefore, we are developing and testing theories that include not only the effects of the excess interstitials but also the effects of the helium atoms generated during irradiation. To determine the void growth mechanisms, we are using the experimental void formation data in type 304 stainless steel (i.e., an empirical nucleation rate) in the simulation program to compare the calculated void size distributions with the experimental histograms.

VACANCIES IN TERNARY ALLOYS⁸

B. T. M. Loh C. T. Liu

The thermodynamics of vacancies in substitutional ternary alloys has been treated using the model of nearest-neighbor pair approximation. One modification incorporated in the model is the consideration of not only the bond energies between atoms, but also the apparent binding energies of vacancy-vacancy and vacancy-atom pairs. An expression for the equilibrium concentration of divacancies is obtained, and it differs from the previous expression by a factor that depends on the vacancy concentration. The equilibrium concentration of vacancies is obtained for dilute solutions and compared with the previous results for binary alloys. The introduction of the apparent binding energies facilitates the interpretation of results. It is particularly true in the case that the interactions between solute atoms and vacancies are the main concern.

DEFECTS IN BORON CARBIDE BEFORE AND AFTER NEUTRON IRRADIATION⁸

K. H. G. Ashbee⁹

Many crystalline compounds contain regular geometrical arrangements of atoms that are so stable that the presence and motion of defects such as dislocations are expected to leave these units more or less intact. In boron and most of its compounds, the stable units are icosahedral groups of 12 boron atoms. In boron carbide, which is rhombohedral with rhombohedral angle 65°36', the B₁₂ icosahedra are arranged in an array that is almost a face-centered cubic lattice. As a result of this, fault surfaces analogous to stacking faults in close-packed metals are observed. The small departure from cubic symmetry is, however, sufficient to

8. Abstract of a paper to be published in *Acta Metallurgica*.

9. On leave of absence from the H. H. Wills Physics Laboratory, University of Bristol, England.

7. Abstract of *Metallography* 4, 157-64 (1971).

impose a distinction between rhombohedral planes, which are hosts for translation twin boundaries created by the dissociation of glide dislocations, and the basal plane, which is believed to contain Frank partial dislocation loops resulting from the agglomeration of point defects introduced during neutron irradiation. Another important consequence of the rhombohedral distortion is that the atomic displacements produced by the leading and trailing partials in an extended dislocation are different. In physical terms, both refinements of the close-packed cubic case arise from the presence of the carbon atoms. The analogy to close-packed metals is carried over to the relationship between translation twins and orientation twins. The dissociation of a glide dislocation in boron carbide is accompanied by rotation of the C_3 chains that thread the slip plane, and this rotation both may and may not be sufficient to render the translation twin boundary region identical to a thin orientation twin.

DISLOCATION NODES IN THE BORON CARBIDE STRUCTURE¹⁰

K. H. G. Ashbee⁹ C. K. H. DuBose

Dislocations in the boron carbide structure can be described in terms of dislocations in the arrangement of B_{12} icosahedra, the normal lattice of which is close to a face-centered cubic (fcc) array. Perfect dislocations dissociate on rhombohedral planes but, due to a structural peculiarity, not on the basal plane. Consequently, extended threefold nodes are seen only on rhombohedral planes. Threefold nodes involving basal dislocations do exist and take the form of mixed perfect and imperfect dislocation configurations. The specific translation twin energy has been estimated from the geometry of both types of nodes at about 75 ergs/cm². Many dislocation nodes constitute sites for the nucleation and growth of voids during crystal growth.

DISLOCATIONS IN DOUBLE HELICES¹¹

K. H. G. Ashbee⁹

The stability of the SiO_4 tetrahedron suggests that dislocations in α - and β -quartz should be regarded as dislocations in the helical arrangements of SiO_4 tetrahedra, whose axes are coaxial with the observed

Burgers vectors. Some of these arrangements are double helices, and the resulting core distortions represent defects that suggest novel imperfections for other double helix structures, such as that of the polynucleotide chains that form the backbone of the DNA structure.

MAPS OF BRILLOUIN ZONE BOUNDARIES

K. H. G. Ashbee⁹ B. T. M. Loh

We are using a computer plotting method to construct stereographic projections of Brillouin zone boundaries for primitive space lattices from each of the seven crystal systems. The computer program is written in such a way that it can generate a map for any given solid angle in reciprocal space.

We have used maps for boron carbide (trigonal) to index Kikuchi patterns obtained at 200 and 650 kV, maps for rock salt (fcc) to index extinction contours obtained at 80 kV, and maps for tungsten (bcc) to simulate field ion micrographs. By increasing the wavelength to the x-ray range, we have also plotted maps suitable for interpreting Kossel line patterns.

HARDNESS—FLOW STRESS—GRAIN SIZE RELATIONSHIPS IN IRON¹²

K. Farrell B. T. M. Loh

Hardness, H , and tensile flow stresses, σ_f , were measured as functions of grain size, d , in recrystallized Armco iron and followed the equations $H = H_0 + k_H d^{-n}$ and $\sigma_f = \sigma_{0,f} + k_f d^{-n}$, where $n = 1/2$ or 1. The ratios of the hardness and flow stress parameters are shown to be $(H_0/\sigma_{0,f}) = (k_H/k_f) = 3.3$ for flow stresses measured at 7.5% elongation. Hardness is not a simple function of grain size at large grain sizes.

PLANAR INTERFACES AND THE HARDNESS OF POLYCRYSTALLINE α -BRASS¹³

K. Farrell J. T. Houston

In α -brass the annealing twin interfaces are generally believed to supplement the grain boundaries in resisting the transmission of slip. The effects of these twins should therefore be considered when the grain size dependence of mechanical properties is measured. We found that the interfacial spacing, S , between the

10. Abstract of a paper submitted to the *Journal of the American Chemical Society*.

11. Abstract of a paper submitted to *Science*.

12. Abstract of a paper submitted to *Journal of the Iron and Steel Institute*.

13. Abstract of *Scripta Met.* 5, 463–66 (1971).

combined twin and grain boundary interfaces in recrystallized α -brass varies with grain diameter, d , as $S = 0.4 d^{0.945}$. Also, the indentational hardness, H , $= H_0 + k_H d^{-1/2}$ or $H_0 + k_H S^{-1/2}$. Exclusion of the twins increases the slope, k_H , from 3.25 to 4.5 kg/mm^{3/2}, but H_0 remains almost unaltered at 38 kg/mm². Plots of $d^{-1/3}$ and $S^{-1/3}$ against hardness are also linear, but plots of d^{-1} and S^{-1} are not. Comparing these data with published tensile flow stress measurements confirms that $(H_0/\sigma_{0,f}) = (k_H/k_f) \cong 3$ when the flow stresses correspond to about 4% strain. Some discrepancies in the literature can be explained in terms of omission of twin interfaces.

AN ANALYSIS OF SOME THEORIES OF WORK HARDENING IN TERMS OF STORED ENERGY DATA ON FCC SINGLE CRYSTALS¹⁴

A. Wolfenden

The accumulated results of several stored and dissipated energy investigations on silver, copper, and aluminum single crystals deformed in tension at two temperatures (ambient and 78°K) are used to analyze some modern theories of work hardening. Attention is first concentrated on those theories whose parameters will permit estimates of the ratio of stored to expended energy (E_s/E_w) during single-crystal deformation. Allowances are made for the fact that both dislocations and point defects contribute to energy storage and hence to the ratio E_s/E_w , whereas the theories of work hardening concern themselves with dislocations only. The comparison of the theoretical estimates for E_s/E_w with the experimental data leads to some important conclusions about the work hardening theories.

Although the orientation dependence of work hardening has been widely investigated, the dependence of energy storage on crystal orientation needs more detailed study. Single crystals with initial tensile axes oriented towards the [001]-[111] symmetry line generally store the most energy. More recently, the orientation dependence of the energy terms E_w and E_d (dissipated energy) was investigated for the case of aluminum single crystals deformed at room temperature. Their orientation dependence as a function of strain was best demonstrated by plotting energy values as functions of $\lambda_0 - \lambda_c$, using the notation of Mitchell,

Foxall, and Hirsch.¹⁵ (Effectively, the angle $\lambda_0 - \lambda_c$ is a measure of the angle between the initial specimen orientation and the symmetry line.) However, what is needed for an elucidation of the theories is a method of relating the orientation dependence of energy storage to the work hardening parameters. Some progress in studying such dependence of these energy terms has been made with an analysis of Hirsch's theory of work hardening and is discussed.

THE ENERGY STORED IN POLYCRYSTALLINE Cu₃Au: EFFECTS OF LONG-RANGE ORDER¹⁶

A. Wolfenden

The energy stored during the room-temperature tensile deformation of polycrystalline Cu₃Au has been measured as a function of long-range order. Specimens with long-range order parameters (S values) of approximately 0, 0.5, 0.8, and 1 were pulled in a single-step deformation calorimeter. The specimens with S values of 1 and 0.8 stored about 35 cal/g-atom at 0.3 true strain, this energy was about twice that stored in the disordered specimen ($S \approx 0$). Most of the incremental values of the ratio of stored to expended energy ($\Delta E_s/\Delta E_w$) fell in the range 0.10 to 0.25. The stored energy was proportional to the square of the flow stress. The data are compared with those of Cohen and Bever¹⁷ on rolled and wire-drawn specimens ($S = 0, 1$), and are discussed in terms of the mechanical behavior of the specimens.

THE ENERGY STORED IN POLYCRYSTALLINE COPPER DEFORMED AT ROOM TEMPERATURE¹⁸

A. Wolfenden

The results of the calorimetric determination of the stored energy for polycrystalline copper deformed in tension at room temperature are reported. They are in good agreement with those of Williams¹⁹ obtained for like specimens and test conditions. Differences between the new stored energy data and those of other authors can be rationalized in terms of calorimetric technique.

14. Abstracted from pp. 489-93 in *Second International Conference on the Strength of Metals and Alloys, Conf. Proc.*, vol. II, The American Society for Metals, Metals Park, Ohio, 1970.

15. T. E. Mitchell, R. A. Foxall, and P. B. Hirsch, *Phil. Mag.* **8**, 1895-1920 (1963).

16. Abstract of *Scripta Met.* **5**, 371-78 (1971).

17. J. B. Cohen and M. B. Bever, *Trans. Met. Soc. AIME* **218**, 155-65 (1960).

18. Abstract of a paper submitted to *Acta Metallurgica*.

19. R. O. Williams, *Acta Met.* **13**, 163-68 (1965).

**COMMENTS ON "STORED ENERGY AND WORK
HARDENING THEORIES"²⁰**

A. Wolfenden

Kuhlmann-Wilsdorf has attempted to rationalize the experimental values of stored energy in terms of work hardening theories for face-centered cubic single crystals. Some of the criticisms and comments made by Kuhlmann-Wilsdorf about the author's work are well made and well taken. Others deserve the further comments presented.

**EFFECTS OF COMPOSITION AND AGING ON THE
MICROSTRUCTURE OF HASTELLOY N MODIFIED
WITH HAFNIUM, TITANIUM, AND NIOBIUM²¹**

R. E. Gehlbach S. W. Cook H. E. McCoy, Jr.

Various types, distributions, and morphologies of carbides precipitate in modifications of the nickel-base

20. Abstract of *Scripta Met.* 4, 899-904 (1970).

21. Summary of a paper presented at the 1971 Spring Meeting of the Metallurgical Society of AIME, Atlanta, May 17-20, 1971.

alloy, Hastelloy N (Ni-12% Mo-7% Cr-4% Fe-0.2% Mn-0.05% C), when small additions of various alloying elements are made. We have studied the effects of variations in the carbon and silicon concentrations on the microstructures produced at 650 and 760°C in Hastelloy N modified with 0.5% Hf, 0.5% Ti, and 0.6% Nb. The small hafnium addition is responsible for precipitation of small particles and platelets (0.1 to 0.5 μm) of MC carbide in the grain boundaries and matrix. The size and density of carbides are quite dependent on the aging temperature but not on the aging time.

Increasing the carbon concentration over the range 0.008 to 0.05% results in more and larger MC carbide particles at both aging temperatures. High carbon levels (0.08 to 0.14%) result in coarse primary M_2C carbide at the expense of much of the age-induced MC precipitation. Additions of silicon (to 0.5%) result in the precipitation of coarse silicon-rich M_6C , again at the expense of MC. At 0.5% Si, all matrix MC precipitation is suppressed at 760°C, although a considerable amount of this carbide does form at 650°C.

6. Fundamental and Physical Ceramics Research

J. Brynestad

As a consequence of the restructuring of this group, parts of the former research programs have been abandoned, and other programs are being started. Emphasis is placed on the study of extended defects in refractory ceramic materials and their relations to chemical and physical properties. The study of the effects of stoichiometry on the deformation mechanism of UO_2 has been continued.

DEFORMATION OF HYPERSTOICHIOMETRIC UO_2 SINGLE CRYSTALS¹

C. S. Yust C. J. McHargue

Hyperstoichiometric uranium dioxide single crystals having oxygen-to-metal ratios in the range 2.06 to 2.10 were deformed in compression. The active slip plane for deformation as found from slip traces has an orientation between $\{112\}$ and $\{111\}$. The critical resolved shear stress values for hyperstoichiometric specimens are approximately the same as those measured for stoichiometric specimens. However, the dislocation structures, as revealed by transmission electron microscopy, are very different and suggest more rapid motion or climb of dislocations in the hyperstoichiometric material. The response to strain rate changes during deformation also reflects the differences in deformation behavior of the two types of crystal.

FURTHER DEFORMATION STUDIES OF HYPERSTOICHIOMETRIC UO_2

C. S. Yust

Additional testing of hyperstoichiometric UO_2 single crystals has confirmed previous observations of the modification of the active slip system and the dislocation substructure when excess oxygen is introduced into the lattice. The slip system change has also been

observed in crystals oriented for maximum shear stress on $\{110\}\langle 110\rangle$. In the range 600 to 1000°C, the hyperstoichiometric crystals slip on a plane that is found by two-surface slip-trace analysis to be nearly a $\{111\}$ plane. Above 1000°C the slip plane returns to that observed in stoichiometric crystals.

Internal friction studies on UO_2 single crystals² have suggested that the oxygen interstitials reorder in hyperstoichiometric UO_2 under the application of stress. A preferential alignment of the oxygen lattice defect configuration in the fluorite lattice may influence the choice of slip plane, but as the temperature is increased, thermal effects allow a return to the normal slip plane.

Varying the strain rate from 6×10^{-4} to 6×10^{-1} /min did not alter the modification of the slip system in the hyperstoichiometric specimens.

Transmission electron microscopy revealed significant differences between the dislocation structures produced in deformed stoichiometric crystals and hyperstoichiometric crystals. The typical stoichiometric structure is shown in Fig. 6.1; the dislocations are distributed on the slip plane in loops, dipoles, and tangles. The typical hyperstoichiometric structure is seen in Fig. 6.2, where the dislocations are largely in a network arrangement.

DEFORMATION OF CALCIUM FLUORIDE SINGLE CRYSTALS

C. S. Yust J. Brynestad

Calcium fluoride is being used as a comparison test material for UO_2 since it has the same crystal structure. The comparison can be extended to hyperstoichiometric UO_2 by using calcium fluoride containing yttrium fluoride, $\text{Ca}_{1-x}\text{Y}_x\text{F}_{2+x}$. The additional fluoride ions produce anion lattice defects of the same type

1. Abstract of paper submitted to *Journal of the American Ceramic Society*.

2. G. Socino, R. De Batist, and R. Gevers, "Relaxation Processes in Single-Crystal UO_2 ," *Proc. Brit. Ceram. Soc.*, No. 9, *Point Defects*, July 1967, p. 73.

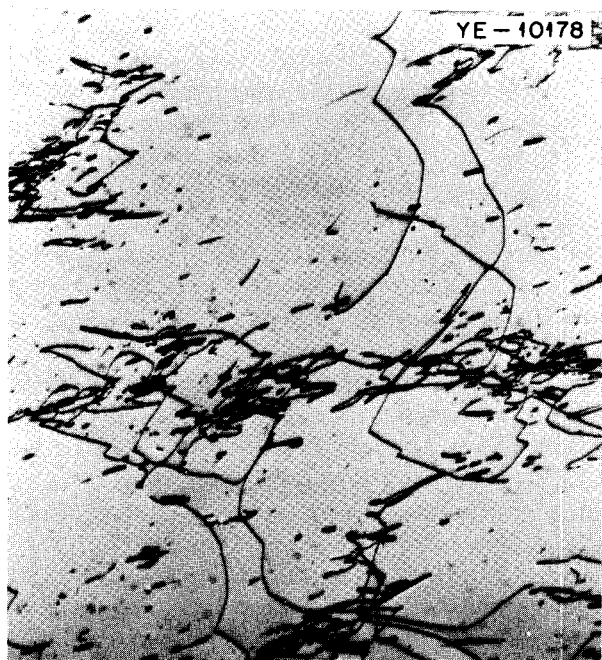


Fig. 6.1. Stoichiometric UO_2 , deformed at 800°C , 7×10^{-3} /min. Dislocations on the slip plane. 13000 \times .



Fig. 6.2. Hyperstoichiometric UO_2 , deformed at 800°C , 7×10^{-3} /min. Specimen sectioned on slip plane, showing extensive network formation. Dark regions are precipitated U_4O_9 , some of which is seen adjacent to dislocations. 13000 \times .

as those produced in UO_2 by excess oxygen.³ Deformation experiments were performed on CaF_2 single crystals, and glide occurred on the expected $\{001\}\langle 110 \rangle$ slip system. Similar experiments on yttrium-doped CaF_2 specimens are planned to aid in the interpretation of the behavior of hyperstoichiometric UO_2 .

3. B. T. M. Willis, "The Study of Extended Defects by X-ray and Neutron Diffraction," pp. 272-93 in *The Chemistry of Extended Defects in Non-Metallic Solids*, ed. by L. Eyring and M. O'Keefe, North-Holland, Amsterdam, 1970.

TGA/VAPOR PRESSURE APPARATUS

J. P. DeLuca J. M. Leitnaker J. Brynestad

As part of our program to investigate thermodynamic properties of nonstoichiometric refractory materials, we have built a combination TGA and vapor pressure apparatus. The system consists of a recording microbalance, a residual gas analyzer, and a split tungsten-mesh heater, all in a high-vacuum enclosure. An inert-atmosphere glove box is installed around the furnace part to allow the handling of easily oxidized materials. The system is being calibrated and tested and will be used mainly in the study of nitrides at high temperatures.

7. Fundamental Physical Metallurgy

R. A. Vandermeer

Our program, which is characteristic of today's outlook and approach to metallurgy and materials science, is an effort to discover interrelationships between a material's properties and its structure. Structure, however, is a mixture combining perfection and imperfection. We seek to blend the extrapolation of simple, idealistic models with experience in an effort to extract knowledge applicable to practical situations.

SOLID SOLUTION IMPURITIES AND GRAIN GROWTH IN METALS¹

R. A. Vandermeer

Hillert's theory² of normal grain growth was modified to include solute impurity effects, utilizing Cahn's theory³ of the impurity drag. In the limiting case, distinguished by the condition that the average drift velocity of a solute atom *across* a grain boundary is greater than the product of the average driving force and the mobility of a pure grain boundary, grain growth remains normal. The relative spatial grain size distribution, if initially unimodal, will remain unchanged, and the average grain size will increase, proportionately to the square root of time at constant temperature. Compositional variation of the apparent activation energy for grain growth predicted by our modified theory agrees to within about $\pm 10\%$ of the experimental observations of Holmes and Winegard⁴ on tin containing solute additions of lead.

THE SPECIMEN THICKNESS EFFECT IN GRAIN GROWTH

R. A. Vandermeer

Grain growth equations including the effect of specimen thickness were derived by extending Hillert's theory² of normal grain growth. Analysis of data by Drolet and Galibois⁵ using these equations confirmed that the unusual grain growth kinetics they observed

was not an artifact due to specimen thickness, as suggested by Feltham.⁶

PREFERRED ORIENTATION IN A U-7.5 wt % Nb-2.5 wt % Zr ALLOY¹

J. C. Ogle

Rolling and recrystallization textures of metastable bcc U-7.5 wt % Nb-2.5 wt % Zr were studied by x-ray diffraction. At low to moderate rolling reductions, unlike for other bcc materials, the texture could be described ideally in terms of a $\{113\}$ in the rolling plane and a $\langle 112 \rangle$ in the *transverse* direction. At higher reductions this texture gradually changed to a bcc texture similar to that described previously⁷ for niobium. A $\langle 110 \rangle 30^\circ$ from the normal direction toward the rolling direction served as the rotation axis for the progression of texture development. A recrystallization heat treatment of 1 hr at 800°C after 90% deformation resulted in a near-cube — that is, $(001)[140]$ — texture.

PARTIAL CORRELATION FUNCTIONS FOR VACANCY DIFFUSION IN BODY-CENTERED TETRAGONAL LATTICES⁸

W. A. Coghlan

In complicated systems involving vacancy diffusion with different atomic jumps having different jump

1. Abstract of paper presented at the 1970 Fall Meeting of the Metallurgical Society of AIME, Cleveland, Oct. 19-22, 1970.
2. M. Hillert, *Acta Met.* **13**, 227 (1965).
3. J. W. Cahn, *Acta Met.* **10**, 789 (1962).
4. E. L. Holmes and W. C. Winegard, *Trans. Met. Soc. AIME* **224**, 945 (1962).
5. J. P. Drolet and A. Galibois, *Acta Met.* **16**, 1387 (1968).
6. P. Feltham, *Scripta Met.* **3**, 853 (1969).
7. R. A. Vandermeer and J. C. Ogle, *Trans. Met. Soc. AIME* **242**, 1317-26 (1968).
8. Abstract of paper presented at the 1971 Spring Meeting of the Metallurgical Society of AIME, Atlanta, May 17-20, 1971.

frequencies, correlation factors become correlation functions dependent upon these frequencies. Using a method described by Mullen in 1961, we calculated four partial correlation functions for vacancy diffusion in body-centered tetragonal lattices, allowing three possible atomic jumps, each having a variable jump frequency. Previously, Mullen calculated three of these functions, allowing atoms to jump in the basal plane or diagonally to the body-centered position. The current work extends these calculations to include vacancy jumps perpendicular to the basal plane. The addition of the third jump makes it possible to explain experimental observations where $D_{xx}c^2/D_{zz}a^2 < 1$. One example illustrating the possible application of these calculations is in the diffusion of titanium in TiO_2 where Lundy, Padgett, and Manley (Chap. 4 of this report) report values near 0.5 for the above ratio.

A CATALOGUE OF CALCULATED AUGER TRANSITIONS FOR THE ELEMENTS⁹

W. A. Coghlan R. E. Clausing

The possible Auger transitions between 10 and 3000 eV for the elements from atomic number 3 through 92 were calculated for 6000-eV incident electrons. The spectra were calculated from the empirical expression

9. Abstract of report in preparation.

$E_{\text{Auger}} = E_v - E_{x'} - E_{y'}$, where E_v is the binding energy of the initial electron vacancy, $E_{x'} = [E_{x(z)} + E_{x(z+1)}]/2$, and $E_{y'} = [E_{y(z)} + E_{y(z+1)}]/2$. The atomic binding energies $E_{x(z)}$ and $E_{x(z+1)}$ are for the x electron in atoms having atomic numbers z and $z + 1$, respectively; $E_{y(z)}$ and $E_{y(z+1)}$ are the same for the y electron. The spectra are listed in order of increasing atomic number, with the transitions for each element identified and listed in order of increasing energy.

A COMPUTER PROGRAM TO CALCULATE AUGER TRANSITIONS FOR A SURFACE CONTAINING SEVERAL KINDS OF ATOMS⁹

W. A. Coghlan

A computer program was written to calculate the energy of Auger electrons emitted from a surface containing several kinds of atoms. The transitions are listed in order of increasing energy and are plotted with the line printer and also with a Calcomp plotter if desired. One can find all the possible transitions or, alternatively, only those represented by 69 energy level combinations that are thought to be the most probable. The spectra have been calculated from the empirical expression $E_{\text{Auger}} = E_v - E_{x'} - E_{y'}$, where the symbols are defined in the previous section of this chapter. An example of the output for all the spectra and for the strong lines is given for a stainless steel surface containing C, O, S, Cr, Fe, and Ni.

8. Physical Property Research

D. L. McElroy

We are seeking an improved theoretical and practical understanding of the physical properties of solids. This work emphasizes accurate property measurements from 1.2 to 2500°K on a spectrum of solids selected to test theories, to seek periodic trends, and to provide a basis for improved property estimations where data are difficult to obtain. Multiple analysis of such interrelated properties as thermal conductivity, λ , electrical resistivity, ρ , thermopower, S , and specific heat capacity, C_p , has improved our understanding of physical properties, stimulated theoretical work, improved property estimations, suggested means to control properties, and led to better measurements. A significant by-product of this work is heat and electrical transport information useful to other projects, as presented in other chapters of this report.

APPARATUS DEVELOPMENT

Accurate physical property measurements over a broad temperature range are prerequisites to this research. Consequently, measurement technique improvement is emphasized through critical analysis of experimental equipment and close cross-checking of results from different techniques and laboratories.¹

Thermal Conductivity Apparatus

A guarded-longitudinal-heat-flow technique² for measuring λ , ρ , and S on small (1×7 cm) rods from 300 to 1000°K was tested with an Armco iron standard. An error analysis indicates a most probable determinate uncertainty in λ of $\pm 1.6\%$. The λ results on the standard agree with the assumed values to this uncertainty, except at 970°K where a 1 or 3%

difference is noted, depending on the method of calculation.³ Chapter 34 of this report contains λ results on two graphites using this apparatus.

Further improvement in the accuracy of our low temperature absolute linear heat flow apparatus is being sought in a modification designed to yield λ to $\pm 0.5\%$ and ρ to $\pm 0.1\%$ from 80 to 400°K. Features of this modification include: in-situ calibrations of the measuring thermocouples against a platinum resistance thermometer, extended periods of temperature control to 0.001°K, and dc voltage measurements using a turns-ratio nanovolt potentiometer.

Computerized Data Acquisition

An ORNL-designed computer-operated data-acquisition system (CODAS) has been employed to measure accurately the specific heat ($\pm 1\%$) and electrical resistivity ($\pm 0.5\%$) of a solid as a function of temperature. The acquisition sequence from the six input data channels is programmable and can be executed on a real-time base. Normal computer capabilities are available, and computer-activated relays and contact sensors allow experiment control and synchronization.

The accuracy of absolute and differential voltage measurements for the system was established by a determinate error analysis and by comparison with a potentiometer.⁴ The system has an accuracy of at least ($\pm 0.013\%$, $\pm 0.4 \mu\text{V}$) for absolute measurement and ($\pm 0.06\%$, $\pm 0.13 \mu\text{V}$) for differential measurements.

The applicability of CODAS to control and monitor experimental equipment was increased by doubling the core memory to 8000 words, by increasing disk storage

1. M. J. Laubitz and D. L. McElroy, "Precise Measurement of Thermal Conductivity at High Temperatures (100–1200 K)," *Metrologia* 7, 1–15 (1971).

2. J. P. Moore and D. L. McElroy, *Metals and Ceramics Div. Annu. Progr. Rept. June 30, 1970*, ORNL-4570, pp. 185–86.

3. J. P. Moore and D. L. McElroy, paper to be presented at the XI Thermal Conductivity Conference, Albuquerque, N.M., Sept. 28–Oct. 1, 1971.

4. T. G. Kollie, D. L. McElroy, R. K. Adams, and J. M. Jansen, "Measurement Accuracy of a Computer-Operated Data-Acquisition System," 5th Symposium on Temperature, NBS, Washington, D.C., June 21–24, 1971.

50% to 96,000 words, and by adding several hardware pieces. The improved system currently yields on-line and instantaneous computation of several thermo-physical properties.

Room temperature ρ values on 120 graphite samples were obtained by CODAS and combined with λ measurements on representative samples to establish a λ : ρ correlation to predict room-temperature λ values to about $\pm 8\%$. Data collected by CODAS on ρ as functions of temperature and time at temperature allowed the phase transformations of a steel (ASTM-508 Class II) to be studied. The latter data distinctly separated the proeutectoid ferrite and pearlite transformations.

The phase transformations of a uranium-based alloy (U-7.5% Nb-2.5% Zr) are complicated, but ρ and C_p measurements between 4 and 1350°K using CODAS have aided our understanding of this alloy. Isothermal studies of ρ as a function of time revealed that above 700°K the transformations in the alloy are diffusion-controlled and similar to those in steel. Specimens quenched from 1100°K exhibit both isothermal and athermal transformations below 700°K. The isothermal transformations involve short-range, excess-vacancy-assisted diffusion of solute atoms to form clusters. The athermal transformations are diffusionless-shear or martensitic transformations, and ρ measurements between 4 and 700°K show the transformation to be continuously reversible.

Coefficient of Thermal Expansion Apparatus

Machining is being completed on a quartz dilatometer to measure the temperature dependence of the temperature coefficient of thermal expansion of solids from 77 to 1200°K. This apparatus will be interfaced to CODAS to control the experiment and to obtain the length, temperature, and electrical resistivity of the specimen.

Radial Heat Flow Apparatus

Installation of this apparatus in a glove box will allow λ measurements on packed beds of ThO₂, UO₂, and (U,Pu)O₂ microspheres to 1300°K and to 10 atm. A controlled atmosphere will maintain stoichiometry of the specimens. A glass-oxide mixture for waste storage containment was tested from 300 to 850°K with λ results lower than expected.⁵

5. Work by R. J. Dippenaar, visiting scientist, South African Atomic Energy Board.

HEAT TRANSPORT IN METALS

Molybdenum

J. P. Moore

Previous work indicated the lattice thermal conductivity, λ_p , of molybdenum to be smaller than that of either tungsten or chromium.⁶ Current λ results are significantly smoother than our prior measurements on this sample (resistance ratio $\approx 5 \times 10^3$). Deviations from an arbitrary equation are shown in Fig. 8.1. These measurements will be extended to existing, well-characterized Mo-Zr and Mo-Nb alloys to obtain data for the alloy separation method of studying λ_p and the electronic Lorenz function of molybdenum.

Tungsten

R. K. Williams J. P. Moore

The electrical resistivity of a zone-refined tungsten sample ($R_{273}/R_{4.3} = 9.6 \times 10^3$) was determined between 1100 and 2500°K. The measurements were conducted in vacuum at indicated pressures that varied from 4×10^{-12} torr at 1100°K to 1×10^{-8} torr at 2500°K. The sample temperature was usually held constant to better than 0.1°K during a measurement, and the maximum temperature gradient along the sample was about 2.2°C/cm. The scatter of the 48 data points appears to be about $\pm 0.05\%$, and the results are about 0.4% lower than our previous data⁷ in the range (1100–1700°K) where the two studies overlap.

Temperature measurement uncertainty is the principal source of error in the high-temperature measurements. Uninsulated W-3% Re vs W-25% Re thermocouples were used for the primary temperature sensors, and these thermocouples were calibrated in situ against an automatically balancing optical pyrometer. With this arrangement, the sample temperature is obtained from NBS calibrated strip lamps by transferring the strip lamp calibration to the optical pyrometer and then to

6. R. K. Williams and W. Fulkerson, "Separation of the Electronic and Lattice Contributions to the Thermal Conductivity of Metals and Alloys," pp. 389–456 in *Thermal Conductivity, Proc. 8th Conf.*, ed. by C. Y. Ho and R. E. Taylor, Plenum Press, New York, 1969.

7. J. P. Moore, R. S. Graves, W. Fulkerson, and D. L. McElroy, "The Physical Properties of Tungsten," pp. V-G-1–V-G-35 in *The 5th Conference on Thermal Conductivity, Held at Denver, Colorado, October 20, 21, and 22, 1965*, Denver University, Department of Metallurgy, College of Engineering, Denver, Colorado, 1967. Volume 1 Sessions I, II, III; Volume 2 Sessions IV, V, VI.

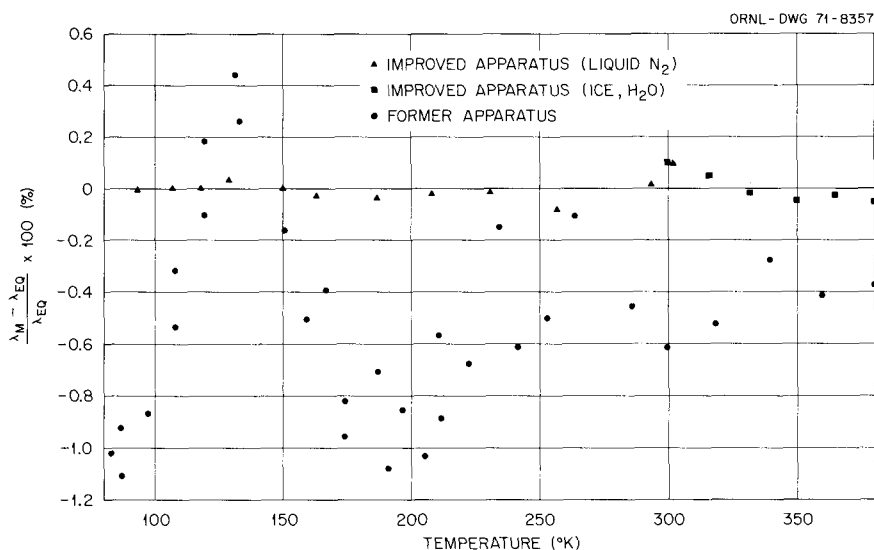


Fig. 8.1. Deviation of measured thermal conductivity values for molybdenum (resistance ratio $\approx 5 \times 10^3$) from $\lambda_{EQ} = 1.435477 - 0.467489 \times 10^{-3} T + 0.667656 \times 10^2 T^{-1} - 0.122172 \times 10^5 T^{-2} + 0.949105 \times 10^6 T^{-3}$.

the thermocouples. Final calculation of the sample temperatures is in progress, and the preliminary checks are encouraging. The manufacturer's thermocouple calibration and our tentative pyrometer calibration differed by a maximum of $+7^\circ\text{K}$ at 1700°K and -25°K at 2500°K , and no thermocouple drifts ($<2^\circ\text{K}$) could be detected.

Thermionic emission effects are important for some high-temperature physical properties studies. Seebeck coefficient data for the tungsten sample were in excellent agreement with our previous data⁷ at 1700°K but showed obvious errors at 2100°K . Also, the output of the thermocouples could be altered by grounding the resistance furnace, the shifts amounting to as much as an indicated temperature change of -25°K at 2500°K . The electrical resistance measurements do not appear to be affected by thermionic emission, but further experimental verification of this observation is being sought.

The λ , ρ , and S of zone-refined tungsten, W-2.8% Re, and W-5.4% Re were redetermined in a modified version of the existing low-temperature, absolute-linear heat flow apparatus. Several small data inconsistencies near 400°K were found for the W-5.4% Re alloy.

UN, ThN, and (Th,U)N Alloys⁸

S. C. Weaver⁹ T. G. Kollie

A UN specimen successively treated at 1800°C in 1100, 0.01, and 1100 torr of N_2 yielded resistance ratios of 150, 25, and 150; and Néel temperatures T_N of 55, 52, and 55°K , respectively, as reversible effects. Three CODAS-generated resistance-temperature curves

showed similarities near T_N but were not completely reversible. These effects may be due to changes in UN stoichiometry, grain size, and density.

We prepared ThN, UN, and (Th,U)N alloys directly from metal or alloy rods by zone melting in nitrogen. This process is about 100 times faster than current processes for making UN samples and yields dense, large-grain samples with less than 1% free metal, which can be removed by heat treatment. Measurements from 80 to 400°K of λ , ρ , and S were completed on zone-prepared samples of ThN, (Th-2% U)N, and (Th-5% U)N. Alloy separation analysis indicates that ThN behaves similar to a metal; that is, L approaches the Sommerfeld limit near 400°K , and $1/\lambda_p$ is linear in T from 80 to 400°K with a slope about twice the Leibfried-Schlomann predicted value. Extrapolated λ values are about 20 times that of UO_2 and 4 times that of (U,Pu)N fuels at reactor operating temperatures, and other reactor qualities involving ThN are equally impressive.

LATTICE HEAT TRANSPORT: RUBIDIUM HALIDES

J. P. Moore

Theoretical treatments of heat conduction by phonons in the range $0.5\theta_D$ to $4\theta_D$ (where θ_D is the

8. To be presented at the University of Tennessee by S. C. Weaver as part of a dissertation for the doctorate degree.

9. Present address: U.S. Nuclear Corporation, Oak Ridge, Tenn.

Debye characteristic temperature) indicate that $1/\lambda_p$ should be linear in T . Our studies on silicon¹⁰ and thoria¹¹ show $1/\lambda_p$ to be linear from $\theta_D/2$ to θ_D , to have a slope change near θ_D , and to be linear again up to at least $2\theta_D$. To further evaluate this and to assist electronic heat transport analysis, λ was measured on a selected series of electrically insulating alkali halides, RbBr, RbCl, and RbI. These have cubic structures, low θ_D (110–130°K), large band gaps, melting points that allow measurements to at least $3\theta_D$, and different mass ratios. This combination of properties should yield information on the effects of acoustic and optic mode interactions on heat transport. The results from 80 to 400°K indicate that $1/\lambda_p$ of each is linear from $0.6\theta_D$ to θ_D , where a positive slope change occurs. Above θ_D , $1/\lambda_p$ of RbBr, with a mass ratio near unity, is linear to $3\theta_D$; and for RbI (ratio 1.49) and RbCl (2.41) $1/\lambda_p$ is linear only to $2\theta_D$, where a negative slope change

occurs. Thus, these results confirm aspects of our earlier observations and suggest an area for theoretical studies. Repeat measurements are planned on purer RbI and RbBr samples, since these contained about 2% Cs.

HEAT CAPACITY OF METALS: Ni₃Mn

T. G. Kollie J. O. Scarbrough

Measurements of C_p between 1.2 and 4.4°K were completed on disordered Ni₃Mn in magnetic fields of 0, 15, and 35 kG. The C_p decreased with increasing field because of a decrease in the spin-wave contribution and a decrease in the nuclear contribution, which was attributed to a decrease in the hyperfine magnetic field at the manganese nucleus. Because configurational ordering in the Ni₃Fe is known¹² to decrease C_p , measurements of C_p of the ordered state of Ni₃Mn are planned.

10. W. Fulkerson, J. P. Moore, R. K. Williams, R. S. Graves, and D. L. McElroy, *Phys. Rev.* **167**, 765–82 (1968).

11. J. P. Moore and D. L. McElroy, *J. Amer. Ceram. Soc.* **54**, 40–46 (1971).

12. T. G. Kollie, J. O. Scarbrough, and D. L. McElroy, *Phys. Rev. B* **2**, 2831–39 (1970).

9. Superconducting Materials

C. C. Koch

We are studying the effects of metallurgical variables on the properties of superconducting materials. The most highly structure-sensitive superconducting property appears to be current-carrying capacity in an applied magnetic field; it is sensitive to mechanical strain, preferred orientation, fabrication and heat-treatment procedures, grain size, and the morphology, composition, and volume fraction of second-phase particles. Meaningful correlation of structure and properties requires detailed knowledge of both. Consequently, much of our effort is devoted to obtaining basic metallurgical information on phase diagrams, transformation kinetics and products, and the microstructures that result from them in systems based upon superconducting materials. The alloy systems of primary interest are those based on niobium and technetium.

SUPERCONDUCTIVITY IN Mo-Re AND Nb-Ir σ -PHASES¹

C. C. Koch J. O. Scarbrough

Superconducting transition temperatures and low-temperature specific heat capacities were measured for well-characterized Nb-Ir and Mo-Re σ -phase alloys. The transition temperatures, T_c , and the electronic specific-heat-capacity coefficients, γ , varied only slowly with composition in these alloys. By considering data from the literature on other σ -phase alloys as well as our own data, we concluded that no clear correlation could be made between T_c and γ (and therefore the electronic density of states at the Fermi level). Good correlation was obtained, however, between McMillan's electron-phonon coupling constant, λ , and T_c . This suggests that the phonon spectrum may be more important than the electronic density of states at the Fermi level in controlling T_c for σ -phases. The high value of T_c (9.8°K) reported by others for the Nb-40 at. % Ir

σ -phase is believed to be due to small quantities of a second superconducting phase.

THE INFLUENCE OF SURFACE CURRENT ON BEAN METHOD CRITICAL CURRENT DENSITY MEASUREMENTS²

D. M. Kroeger C. C. Koch

The Bean ac susceptibility method for measuring J_c in cylindrical superconducting specimens is very useful for metallurgical studies of superconductors. However, as first discussed by Ullmaier, the Bean analysis does not take account of surface currents, which shield the specimen interior from field changes less than some value, ΔH . To determine the importance of this effect for Bean-type J_c measurements, we used equations developed by Ullmaier to recalculate the Fourier amplitudes, first obtained by Bean, for the voltage induced in a coil on the surface of a cylinder in a dc magnetic field with a superimposed ac field. The results indicate that under proper conditions only a small correction to the original Bean formula for J_c is required. This calculation also gives the phase relationships between the odd harmonics and the fundamental. Measurement of these phase relationships constitute a check on the validity of the surface current model.

THE INFLUENCE OF GRAIN SIZE AND DISLOCATION DISTRIBUTION ON SUPERCONDUCTING CRITICAL CURRENT DENSITY IN A Nb-10 at. % Ti ALLOY³

C. C. Koch D. M. Kroeger

In recent years a number of experiments have been carried out to test models of flux pinning in type II superconductors. The crystal dislocation has been a

1. Abstracted from *Phys. Rev. B* 3, 742-48 (1971).

2. Abstracted from paper presented at American Physical Society 1971 Meeting, Cleveland, Mar. 29-Apr. 1, 1971.

3. Abstracted from paper presented at the Spring Meeting of the Metallurgical Society of AIME, Atlanta, May 17-20, 1971.

avored defect for both theoretical calculations and experiments on defect-fluxoid interactions. High-angle grain boundaries are also apparently effective flux pinners. We are studying the relative importance of high-angle grain boundaries and dislocation distribution in a single alloy, Nb-10 at. % Ti. Grain size is varied by heat treatment, and dislocation distribution is changed by varying the temperature of tensile deformation. Critical current measurements are correlated with observations by optical and electron microscopy.

THE INFLUENCE OF METALLURGICAL VARIABLES ON SUPERCONDUCTIVITY IN Hf-Nb ALLOYS⁴

C. C. Koch R. W. Carpenter

Certain Hf-Nb alloys (Hf-35% Nb to Hf-50% Nb) are promising high-field superconductors, with upper critical fields (H_{c2}) of approximately 80 kG at 4.2°K. These alloys also exhibit wide variations in critical current density (J_c) with microstructure. Transmission electron microscopy and x-ray diffraction studies have been carried out to clarify the Hf-Nb phase diagram and to understand the kinetics and morphology of the $\beta \rightarrow \beta + \alpha$ phase transformation. We correlate the results of that metallurgical study with the superconducting parameters of the respective Hf-Nb alloys, with emphasis on the early stages of the precipitation reaction. Precipitation from the body-centered cubic solid solution appears to be the most effective method for enhancing the critical current density in these alloys. Coherent hafnium-rich precipitate particles formed by isothermal aging at 600 to 850°C are believed to be the effective flux pinning sites.

EVIDENCE TO SUPPORT THE RIGIDLY PINNED VORTEX MODEL FOR THE PEAK EFFECT⁵

M. S. Lubell⁶ D. M. Kroeger

Data are presented on the peak effect of a niobium-titanium alloy. The temperature dependence of the

critical current at a field equal to or higher than the peak field is shown to agree with a model of a rigidly pinned vortex lattice.

SUPERCONDUCTIVITY IN TECHNETIUM AND ITS ALLOYS

C. C. Koch Z. R. McNutt

Technetium, which has the second highest superconducting transition temperature for an element, is the base for promising superconducting alloys. Our research on technetium this year involved studying superconductivity in Tc-Mo and Tc-Ti alloys and a cooperative effort with G. Kostorz, Argonne National Laboratory, in the preparation of high-purity technetium single crystals. Results of initial work on the technetium single crystals are presented below.

ANISOTROPY OF THE UPPER CRITICAL FIELD OF SUPERCONDUCTING TECHNETIUM⁷

G. Kostorz⁸ R. L. Panosh⁸
L. L. Isaacs⁸ C. C. Koch

The anisotropy of the upper critical field H_{c2} of a noncubic superconductor was studied for the first time. A torque magnetometer was used to detect H_{c2} between 2 and 7°K as a function of orientation in a small single crystal of technetium. The relative anisotropy of H_{c2} consists of a large temperature-independent and possibly a small temperature-dependent part. The temperature-independent contribution can be attributed to the anisotropy of the effective mass.

4. Abstracted from paper presented at the Fall Meeting of the Metallurgical Society of AIME, Cleveland, Oct. 19-22, 1970.

5. Abstracted from paper to be published in *Physica*.

6. Thermonuclear Division.

7. Abstracted from paper submitted to *Physical Review Letters*.

8. Materials Science Division, Argonne National Laboratory.

10. Surface Phenomena

J. V. Cathcart

Our research is concerned with investigations of basic oxidation processes for metals and alloys. Areas of study include stress generation during oxidation, oxide morphology, oxygen solution effects, internal oxidation, the influence of the mechanical properties of oxide and metal on the oxidation process, anodic oxidation, and, in cooperation with the Diffusion in Solids Group, diffusion in metals.

Specific projects include studies of the oxidation properties of uranium-base alloys, the high-temperature oxidation of certain tantalum-base alloys, and crystallization processes in anodic films on refractory metal alloys. The distribution of impurities in anodic films was also investigated as was the effect of elastic stress on diffusion rates in a metal.

OXIDATION OF URANIUM-BASE ALLOYS

J. V. Cathcart R. E. Pawel G. F. Petersen

Uranium alloys exhibit oxidation behavior that reflects, many times in dramatic fashion, a number of factors important in the oxidation of alloys generally. We are studying the oxidation properties of a series of uranium alloys in the belief that patterns will emerge that will lead to an understanding of the oxidation process not only for the uranium alloys themselves but for other alloys as well. Systems currently under investigation include a ternary U-Nb-Zr alloy plus binary combinations of U with Nb, Zr, Mo, and Ti. For the sake of completeness a Zr-Nb binary is also included. The completed portions of this work are summarized below.

The Oxidation Properties of U-16.6 at. % Nb-5.6 at. % Zr and U-21 at. % Nb (Ref. 1)

J. V. Cathcart R. E. Pawel G. F. Petersen

The fundamental oxidation characteristics of two uranium-base alloys, U-16.6 at. % Nb-5.6 at. % Zr and U-21 at. % Nb, in the range 500 to 1000°C are

described. Both alloys undergo large dimensional changes during oxidation above 650°C because of stresses generated in the oxide. Oxidation rate curves for both alloys were determined at 100° intervals between 500 and 1000°C; the activation energy for the process was small. The morphology of the oxide scale formed on the two alloys is complex and is described in detail. Stresses estimated at 10⁶ psi are shown to develop in oxidizing specimens, and a mechanism for the generation of these stresses is proposed.

Flexure Measurements on a U-Nb-Zr Alloy During Oxidation and Temperature Cycling²

R. E. Pawel J. V. Cathcart

As part of a general program to study the fundamental oxidation characteristics of a U-16.6 at. % Nb-5.6 at. % Zr alloy, measurements of the flexure of thin specimens reacting on one side were used to assess the extent of stress generation during oxidation. During the early stages of reaction at 700°C, rapid flexing of the specimen was observed. Because the depth or thickness of the layer involved in this reaction was quite small, the stress within this zone must have been large to account for the observed bending stresses. A model relating flexure to a uniform stress in the growing oxide film led to film stress values of the order of 10⁶ psi. The rapid dissipation of this stress when the oxidation rate decreased was analyzed in terms of a balance between stress generation and relief in both oxide and metal.

Flexure measurements during thermal cycling were also used to study the kinetics of some of the structural transformations exhibited by this alloy. An elastic stress gradient was necessary to promote significant flexure during the transformation period in these specimens,

1. Abstract of paper submitted to *Oxidation of Metals*.
2. Abstract of paper submitted to *Journal of the Electrochemical Society*.

suggesting that shear forces play an important role in the transformations, particularly those involving the α'' structure.

REFRACTORY METAL OXIDATION

R. E. Pawel

We are continuing our studies of the oxidation of several tantalum-base refractory-metal alloys. Two commercial alloys, T-111 and T-222, are of particular interest. These alloys, whose nominal compositions are Ta-8 wt % W-2 wt % Hf and Ta-10 wt % W-2 wt % Hf, respectively, not only are subject to large stresses during oxidation, but also oxidize catastrophically and with explosive violence during prolonged exposure to oxygen at 800°C. To study the stability of refractory-metal alloy oxide films, we are investigating the phase relationships in crystallizing anodic oxide films formed on T-111, T-222, Ta-25% W, and Ta-50% W. The distribution of impurities during the formation of anodic films on tantalum is also of interest.

Stress Measurements During the Oxidation of Refractory-Metal Alloys³

R. E. Pawel

The general features of the early stages of oxidation of two commercial refractory-metal alloys, T-111 and T-222, were studied over the range 500 to 800°C in dry oxygen at atmospheric pressure. Under these conditions the process for both alloys was characterized by a period of protective oxidation in which oxygen dissolved in the base metal and an adherent oxide film formed. The average rate of oxidation then accelerated because of the formation of regions of porous, non-protective oxide on the specimens. The stresses induced by oxidation were measured by the flexure technique. During the protective period, a linear increase of the total strain energy of the specimen with time was observed at each temperature. Maximum bending stresses in the metal of approximately 20,000 psi were regularly observed.

Impurity Distribution in Anodic Oxide Films⁴

R. E. Pawel J. P. Pemsler⁵

Anodization of tantalum in electrolytes containing phosphorous or fluorine ions resulted in the incorporation of a quantity of these elements in the anodic film. We determined the distribution of foreign ions injected

into these anodic films during sequential anodization in different electrolytes. The concentration profiles obtained in this work were determined with an ion microprobe mass spectrometer, a continuously measuring spectrometer used in conjunction with a sensitive ion-beam sectioning device. The behavior of thin fluorine- and phosphorous-rich marker layers during a variety of anodization schedules was studied. These impurities are of particular interest because we previously observed that each leads to a pronounced effect on certain characteristics of the anodic films. Our data clarify the nature of these effects and lead to a better understanding of the atomic movements that occur during anodization.

DIFFUSION STUDIES

R. E. Pawel

Our previous research has revealed many obvious examples of dramatic, often catastrophic, responses of an oxidizing metal to the system of stresses accompanying oxidation. Until now, however, the effect of a biaxial elastic stress on diffusion rates has never been directly assessed. In cooperation with the Diffusion in Solids Group, we measured simultaneously the diffusion rates on each side of a thin specimen in which an elastic stress gradient was maintained by flexing the specimen about its long axis; thus, on one side diffusion occurred under the influence of compressive stress, while on the other the surface layers of the specimen were in tension.

Experiments on flexed specimens, using T-111 alloy as the host material and ^{95}Nb as the diffusing species, are in progress. Specimens were sectioned by the anodic-film stripping technique, and the data were treated by computer to minimize unintentional bias. Preliminary results for ^{95}Nb diffusion at 1225°C indicate that the diffusivity is about 10% higher on the convex (tension) side of the specimen than on the concave (compression) side. Maximum bending stresses of about 20,000 psi were involved. Corresponding experiments with unflexed specimens yielded variations of less than 2% in diffusion rates on the two sides.

3. Abstract of paper to be presented at the Gordon Conference on Corrosion, New London, N.H., July 26-30, 1971.

4. Abstract of paper to be presented at the Symposium on Anodic Films, Electrochemical Society, Cleveland, Oct. 3-8, 1971.

5. Ledgemont Laboratory, Kennecott Copper Corp.

The Structure and Properties of Thin Oxide Films⁶

J. V. Cathcart

This paper reviews the structure and properties of thin oxide films formed on metals. Consideration is

6. Abstracted from proceedings, ASM Precongress Seminar on Oxidation of Metals and Alloys, Cleveland, 1970, ed. by D. L. Douglass, in press.

restricted to films up to a few thousand angstroms thick, and film properties that influence the oxidation process are emphasized. Specific film properties discussed include epitaxy, film topography, mosaic structure, and stress and strain distributions in films. The final section of the paper illustrates the role of oxide film structure in the development of the marked oxidation rate anisotropy exhibited by such metals as copper and nickel.

11. Theoretical Research

J. S. Faulkner

The purpose of our research is to contribute to those aspects of theoretical solid state physics that are most useful within a materials science context. We contributed to the recent development of the Korringa-Kohn-Rostoker method for band theory calculations of electronic states in metals and ordered alloys, and we are continuing to exploit this technique for such systems. We are developing a powerful new technique called the discrete variational method for band theory calculations on ionic and covalent compounds, and a recent breakthrough in this area promises interesting results. The newly developed coherent potential approximation is the first promising technique for calculating the electronic states of disordered systems, such as random alloys and liquid metals. We are calculating the properties of these technologically interesting materials and also extending this new approach. The most direct contact between solid state theory and other fields of materials science is in the area of total energy calculations. We are preparing to move into that area.

DENSITIES OF STATES IN Cu-RICH Ni-Cu ALLOYS BY THE COHERENT POTENTIAL APPROXIMATION: COMPARISONS WITH RIGID-BAND AND VIRTUAL-CRYSTAL APPROXIMATION¹

G. M. Stocks R. W. Williams² J. S. Faulkner

It is shown that the coherent potential approximation is capable of explaining the densities of states of Cu-rich Ni-Cu alloys as obtained from recent photoemission experiments. The coherent potential approximation predicts the formation of a separate nickel *d*-band for these alloys, which is consistent with the qualitative picture of Friedel-Anderson virtual bound states. This picture cannot be obtained from either the rigid-band model or the virtual-crystal approximation.

1. Abstracted from *Phys. Rev. Letters* **26**, 253–56 (1971).

2. Now at the University of Vermont, Burlington, Vt. 05401.

THE DENSITIES OF STATES OF Cu-Ni ALLOYS³

G. M. Stocks R. W. Williams² J. S. Faulkner

The densities of states of the near ideally substitutional random alloy system Cu-Ni are calculated by the coherent potential approximation for a range of concentrations of the constituents across the complete alloy diagram. We show that previous model calculations for nickel-rich Cu-Ni alloys using the coherent potential approximation can be extended to alloys of arbitrary concentration if appropriate Cu and Ni potential functions are used. The results obtained are consistent with experimental photoemission and soft x-ray emission profiles in so far as comparisons can be effected. The results indicate the limits of this simple nonmagnetic random alloy theory for discussing the conventional low-temperature specific heat data of these alloys. For copper-rich alloys the results correspond to a split band regime, whereas for nickel-rich alloys the *d*-bands associated with Cu and with Ni sites in the alloy overlap to a considerable extent. For all Ni-Cu alloys the rigid-band model and the virtual-crystal approximation are quite inappropriate.

ELECTRONIC STATES IN DISORDERED ALLOYS: COMPARISON OF METHODS⁴

J. S. Faulkner

The history of the development of techniques for calculating the electronic states of disordered systems is reviewed and illustrated with the help of model calculations. The position of the coherent potential approximation in this development is pointed out.

3. Abstract of an article submitted for publication in the *Physical Review*.

4. Abstract of an article to be published in the proceedings of the Sanibel Symposium, *International Journal of Quantum Chemistry*.

A SIMPLE METHOD FOR SYMMETRIZING KKR BAND THEORY CALCULATIONS⁵

J. S. Faulkner

In KKR band theory calculations for cubic crystals the matrix $D(\mathbf{k}, E)$ that determines $E(\mathbf{k})$ through $\det D(\mathbf{k}, E) = 0$ is calculated using real spherical harmonics $Y_{l,m}(\theta, \phi)$. In the original formulations, it was pointed out that for special \mathbf{k} the matrix $D(\mathbf{k}, E)$ can be replaced with smaller matrices $d^\alpha(\mathbf{k}, E)$ by using lattice harmonics instead of spherical harmonics, and the eigenvalues $E^\alpha(\mathbf{k})$ corresponding to a particular irreducible representation of the group of the \mathbf{k} -vector can then be obtained from $\det d^\alpha(\mathbf{k}, E) = 0$. It is also true that for such a \mathbf{k} a matrix S can be found such that $D(\mathbf{k}, E)$ calculated with spherical harmonics can be brought into block diagonal form by $S^{-1}D(\mathbf{k}, E)S$, the submatrix blocks being the $d^\alpha(\mathbf{k}, E)$. We feel that in practice it is often more convenient to use this second method for symmetrizing the calculation. A single subroutine that can be used to find the $E^\alpha(\mathbf{k})$ for \mathbf{k} 's corresponding to the point Γ and the lines Δ , Σ , and Λ in any cubic Brillouin zone as well as the points, K , X , L , and W in the fcc zone will be described.

ELECTRONIC STATES IN SOME DISORDERED NOBLE METAL-TRANSITION METAL ALLOYS⁴

G. M. Stocks

It is shown that the coherent potential approximation is capable of explaining the densities of states functions as observed in the photoemission experiment for alloys of Cu-Pd, Cu-Ni, and Ag-Pd rich in the noble metal. The analysis reveals the importance of the separation in energy between the d -scattering resonances associated with each of the constituent atomic species in these alloys. In all of these alloys the separation between the d -scattering resonances is sufficient to render both the rigid-band model and the virtual-crystal approximations incapable of explaining the observed photoemission data.

APPLICATION OF THE DISCRETE VARIATIONAL METHOD TO THE ELECTRONIC STRUCTURE OF LiF (Ref. 4)

G. S. Painter

The discrete variational method, which has been successfully applied previously to several covalent

crystals, was used to calculate the energy bands and charge density of the ionic crystal LiF, using various crystal potential models. The great sensitivity of the energy bands to the atomic configuration used to construct the potential and to the scaling of the statistical exchange is explained in terms of differences in the spatial properties of the crystal wave functions. The excited bands are found to be characterized by diffuse orbitals, and these are converged by use of a mixed basis of Bloch atomic-like functions and symmetrized plane waves. Basis convergence problems posed by ionic systems for linear variational techniques are discussed in the conclusion.

AB INITIO CALCULATION OF THE ELECTRONIC STRUCTURE AND OPTICAL PROPERTIES OF DIAMOND USING THE DISCRETE VARIATIONAL METHOD³

G. S. Painter D. E. Ellis⁶ A. R. Lubinsky⁶

The electronic band structure, charge density, and optical properties of diamond were calculated by the discrete variational method in an ab initio approach with an LCAO Bloch basis set. This technique, described in a previous article, avoids most of the difficulties encountered with evaluation of the matrix elements of the Hamiltonian and allows inclusion of the nonspherical terms in the potential. A comparative study of the relative effects of muffin-tin averaging and scaling the $\rho^{1/3}$ statistical exchange indicates that the former is about five times more influential on the energy gaps in diamond, demonstrating the inadequacy of the muffin-tin approximation for quantitative calculations. A comparison of the energy and location in the Brillouin zone of the indirect transition threshold indicates excellent agreement with experiment for an exchange scaling close to that determined by the X_α method. The conventional energy level ordering is found, as opposed to that obtained in recent pseudo-potential calculations. An analysis of the interband density of states reveals that this approach gives very good agreement with the optical properties of diamond.

THE HARTREE-FOCK-SLATER MODEL FOR MOLECULES³

D. E. Ellis⁶ T. Parameswaran⁶ G. S. Painter

A discrete variational method, based on the Slater statistical exchange approximation widely used in

5. Abstract of a paper presented at the March meeting of the American Physical Society, Cleveland, Mar. 29-Apr. 1, 1971.

6. Physics Department, Northwestern University, Evanston, Ill. 60201.

atomic and solid state theory, is developed and applied to the calculation of the electronic structure of molecules. Accurate one-electron eigenfunctions of the Hartree-Fock-Slater effective Hamiltonian are obtained using a linear-combination-of-atomic-orbitals basis; in contrast to previous work, the full molecular potential is treated without recourse to muffin-tin spherical approximations. Results are presented for the carbon atom and for methane and benzene molecules, which demonstrate the accuracy and rate of convergence of the method. The use of Hartree-Fock-Slater eigenfunctions in studying excited states and optical spectra of molecular systems and the results of self-consistent calculations are discussed.

COPPER-ZINC ALLOYS AS TREATED BY VIRTUAL CRYSTAL AND RELATED APPROXIMATIONS⁷

N. H. March⁸ J. S. Faulkner
G. M. Stocks P. Gibbs⁸

Results are presented for the virtual crystal model of a Cu-Zn alloy in the range of concentrations from 0 to

20 at. % Zn. These were obtained by the Korringa-Kohn-Rostoker method, and at each concentration the measured x-ray lattice parameter in the alloy was used. The potentials V_{Cu} and V_{Zn} were generated following the proposals of Mattheiss, the pure Cu potential, in essence, being that employed by O'Sullivan, Switendick, and Schirber. Crystal eigenvalues were calculated at symmetry points Γ , X , L , K , and W ; about 20 eigenvalues are presented for pure Cu and for 1, 10, and 20% Zn alloys. Densities of states are also presented.

To test the usefulness of such a model, we compared our results with the de Haas-van Alphen measurements of Chollet and Templeton of Cu-Zn alloys for concentrations up to 0.1% Zn, with optical absorption experiments, and with measurements of the electronic specific heat.

7. Abstract of an invited paper to be presented at the international meeting on Perspectives for Computation of Electronic Structure in Ordered and Disordered States to be held at Menton, France, Sept. 20, 1971.

8. Department of Physics, The University, Sheffield, England.

12. X-Ray Diffraction

H. L. Yakel Bernard Borie

Our laboratory continues to carry out its dual function of applying x-ray diffraction methods to problems encountered by other investigators and to problems of fundamental interest in which diffraction techniques play a primary part. In the latter area, we briefly describe work dealing with short-range structures, processes of x-ray absorption, aging of gamma-quenched uranium alloys, the structure of boron carbide, small-angle scattering from voids in irradiated aluminum, and two topics of special interest to the calibration of absolute intensities in x-ray scattering experiments.

ROUTINE ANALYSES

L. A. Harris R. M. Steele H. L. Yakel

We performed routine diffraction analyses on over 560 samples during the reporting period. Significant results for materials originating within the Metals and Ceramics Division may be found in reports of the initiating groups and will not be repeated here.

A saving in the time and labor required to measure photographically recorded x-ray diffraction data should follow acquisition of a stepping microdensitometer that records the optical density found at each step on magnetic tape.

THERMAL EXPANSION OF RARE EARTH OXIDE-UO₂ SOLID SOLUTIONS

L. A. Harris

A high-temperature x-ray diffraction study was carried out on a series of solid solutions of UO₂ containing 0, 10, 15, 20, 30, and 40 mole % EuO_{1.5}. The lattice parameters were obtained as a function of temperature and oxygen pressure to permit extrapolation to general fission product behavior in oxide fuels.

Samples were physically mixed with equal weights of thorium oxide, which was used as an internal diffrac-

tion standard. The mixtures were slurried by wetting with alcohol and then deposited on the platinum sample holder-heating element of a high-temperature diffractometer attachment. Oxygen pressures were controlled by passing fixed mixtures of CO₂ and CO through the heated chamber. Temperatures were measured with a Pt vs Pt-10% Rh thermocouple, which was spot welded to the bottom of the sample holder.

Each polymorph of EuC₂ (fcc and bct CaC₂ type) was observed. Their synthesis evidently occurred via a carburization reaction catalyzed by trace amounts of iron and nickel carbonyls in the carbon monoxide gas. The source of these carbonyls was the carbon monoxide gas cylinder itself; corrosion and consequent explosive failure of steel cylinders holding carbon monoxide at high (>1500 psi) pressure for extended (>1 year) time periods have been noted previously¹ but are frequently ignored by manufacturers and users. Beside the significant risk of explosion, the possibility of spurious chemical effects due to the carbonyls in the gas stream should be emphasized.

THE INTERPRETATION OF INTENSITY DISTRIBUTIONS FROM DISORDERED BINARY ALLOYS

Cullie J. Sparks, Jr. Bernard Borie

A general method for treating diffuse x-ray scattering from imperfectly ordered binary alloys, yielding independently the Warren order parameters, linear displacement parameters, and quadratic displacement parameters, has been developed and described elsewhere.² Current research concerns applying the method to

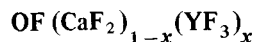
1. J. Sendroy, Jr., H. A. Collison, and H. J. Mark, *Anal. Chem.* **27**, 1641-45 (1955).

2. B. Borie and C. J. Sparks, Jr., accepted for publication in *Acta Crystallographica*.

specific alloy systems, Cu—16 at. % Al and Au—40 at. % Ni, both of which have the face-centered cubic structure. The diffuse intensity distributions under study in each case are confined to the h_1h_20 plane of reciprocal space.

The separation method was applied to reduce the intensity to four periodic functions. In the case of the gold-nickel alloy, that part of the intensity related to short-range order would have been completely obscured by the displacement contributions without the use of our method. Any attempt to recover order parameters from the raw data would have been fruitless. Although both alloys are face-centered cubic, they clearly have distinctly different short-range structures. We are attempting to formulate quantitative models for the short-range structure for each alloy from which each of the four functions can be computed and compared with experiment.

THE SHORT-RANGE STRUCTURE



Bernard Borie

A logical escalation of complexity from our diffraction studies of imperfectly ordered metallic alloys is the short-range structure of mixed ceramic crystals. We have chosen to measure the changes in the diffuse scattering from CaF_2 caused by a small amount of YF_3 in solid solution. The structure of this material should be related to that of UO_{2+x} , but the relative magnitudes of the x-ray scattering factors of the components should cause the short-range structure to manifest itself much more clearly in the diffraction pattern than would be the case for analogous heavy-metal ceramic compounds. This research is being undertaken with the cooperation of the Fundamental and Physical Ceramics Group.

We obtained a large single crystal of the solid solution, and it shows sharp Laue spots and is quite homogeneous. From its composition ($x = 0.08$), density, and lattice constant, we find that the average cubic unit cell contains 3.68 calcium atoms, 0.32 yttrium, and 8.33 fluorines. It thus seems likely that the primary imperfection is interstitial fluorine, with the usual cation sites of CaF_2 occupied by an as yet undetermined distribution of Ca and Y.

We expect our diffuse intensity measurements to cast light on the details of the distribution of the cations, its relation to the distribution of interstitial fluorine, and the static atomic displacements resulting from the structural imperfections.

MEASUREMENT OF BREMSSTRAHLUNG FROM PHOTOELECTRONS PRODUCED BY ABSORPTION OF MONOCHROMATIC Cu $K\alpha$ RADIATION

Cullie J. Sparks, Jr.

The total cross section for absorption of photons in the energy region from 1 to 20 keV is about 95% photoelectric and the remainder Compton and coherent scattering. Each photon absorbed releases an electron with kinetic energy $E_e = h\nu - E_B$, where $h\nu$ is the energy of the incident photon and E_B is the binding energy of the electron. As the electrons slow down in the material, they give rise to "braking" radiation, or bremsstrahlung.

We have measured the intensity of the bremsstrahlung created by ejection of photoelectrons by 8.04-keV x rays (Cu $K\alpha$) in various elements from carbon through gold. Our observations follow.

1. The intensity distribution of the bremsstrahlung is isotropic.
2. The plot of intensity against energy has structure reminiscent of that for photoelectric absorption in the material. A sharp intensity increase occurs at the energy of the incident photon minus the binding energy of the most tightly bound electrons that can be ejected by the incident radiation.

Our measurements are the first quantitative clearly defined determinations of bremsstrahlung for thick targets in this energy range. The contribution of this radiation to the diffuse x-ray scattering from alloys is large enough to explain a well known intensity discrepancy found in these experiments³

Similar experiments are reported⁴⁻¹⁰ for targets of $Z < 7$, although one author⁴ reported observations to $Z =$

3. C. J. Sparks and B. Borie, "Methods of Analysis for Diffuse X-Ray Scattering Modulated by Local Order and Atomic Displacements," chap. 1, pp. 5-50 in *Local Atomic Arrangements Studied by X-Ray Diffraction* (Proceedings of a Symposium sponsored by the Physics and Chemistry of Metals Committee of the Institute of Metals Division, the Metallurgical Society, American Institute of Mining, Metallurgical, and Petroleum Engineers, Chicago, Illinois, February, 1965) ed. by J. B. Cohen and J. E. Hilliard, Gordon and Breach Science Publishers, New York, 1966. See discussion on p. 47.

4. K. Das Gupta, *Phys. Rev. Letters* **3**, 38 (1959).

5. M. Copper and J. A. Leake, *Phil. Mag.* **13**, 603 (1966).

6. T. Suzuki, *J. Phys. Soc. Japan* **21**, 2087 (1966).

7. N. G. Alexandropoulos and G. G. Cohen, *Phys. Rev.* **187**, 455 (1969).

8. T. Suzuki, *J. Phys. Soc. Japan* **22**, 1139 (1967).

9. T. Suzuki et al., *J. Phys. Soc. Japan* **29**, 730 (1970).

10. C. J. Sparks, Jr., *Metals and Ceramics Div. Annu. Progr. Rept. June 30, 1966*, ORNL-3970, pp. 57-58; *ibid.*, June 30, 1967, ORNL-4170, p. 59.

29. In all cases the results are interpreted in terms of Raman or Raman-Compton interactions (inelastic scattering from bound electrons). Because our measurements show an isotropic distribution, we believe their interpretation of the observed x-ray intensity to be incorrect.

Because of the high intensity of incident monochromatic radiation obtained by use of a doubly bent graphite monochromator¹⁰ for this experiment, it was feasible to extend x-ray fluorescence spectroscopy as an analytical tool to determine trace amounts (parts per billion) for total elemental analysis. The choice of monochromatic radiation just beyond the absorption edge for excitation of the element of interest will give at least a 100-fold increase in sensitivity over "white" tungsten radiation.

In contrast with ESCA,¹¹ by which electrons that interact with the surface are studied, this research shows that one may study the interaction of electrons with matter deep inside the material. The experimental information is in the form of x rays that do not undergo energy changes but only intensity reduction.

URANIUM-NIOBIUM-ZIRCONIUM ALLOYS

H. L. Yakel

Beginning with alloys of known chemical composition, I have confirmed the sensitivity of the as-gamma-quenched structure to small (<1 at. %) changes in niobium and zirconium content. Variations within a given homogenized grain may give rise to the γ° -condition (long-range displacement order) in one region and to the γ^s -condition (short-range displacement order) in another.

Aging studies in a salt bath in our laboratory suggest that the reversion reaction reported previously¹² was an error, and that aging at 550°C of a crystal previously aged below 400°C ($\gamma^{\circ} \rightarrow \alpha''$) merely produces the reaction ($\alpha'' \rightarrow \alpha' + \gamma_{\text{Nb-rich}}$), which is a hypothetical part of the ($\gamma^{\circ} \rightarrow \alpha' + \gamma_{\text{Nb-rich}}$) reaction observed on direct aging at 550°C.

Orientations of the alpha-like phases formed on aging the as-quenched γ^s or γ° structures were sensitive to the original orientations of the tetragonal c axes, that is, to the directions of long-range ordered atom displacements.

The preferred orientations of monoclinic α'' or orthorhombic α' axes were readily understood in view of the further atom movements required to complete the $\gamma^{\circ} \rightarrow \alpha''$ or $\gamma^{\circ} \rightarrow \alpha'$ transitions. This observation may aid in interpreting the "memory" effects shown by the alloys.

CRYSTAL STRUCTURES OF UNIRRADIATED AND NEUTRON-IRRADIATED BORON CARBIDES

L. A. Harris H. L. Yakel

We successfully unraveled the high-angle x-ray diffraction patterns of a well-crystallized boron carbide, with composition approximating B_4C , exposed to several x radiations (Cr $K\alpha$, Fe $K\alpha$, Co $K\alpha$, Ni $K\alpha$, and Cu $K\alpha$). Lattice parameters of this material could be estimated to better than 0.002% (hexagonal a) and 0.003% (hexagonal c). Patterns of boron carbides with carbon contents varying from 10 to 20 at. % C, prepared by solid-state reaction of boron and graphite at 1800°C, were more difficult to interpret, since some reflections were diffuse. Nevertheless, the unit cell parameters of none of these materials agreed with those measured from " B_4C " prepared from the melt.

Selected crystals of well-crystallized " B_4C " were irradiated in the ORR at about 500°C to 2×10^{20} neutrons/cm² (>0.1 MeV). Postirradiation x-ray diffraction studies of these crystals generally confirmed earlier results of Tucker and Senio,¹³ but interesting exceptions were noted. Among the most significant of these was the recognition of sharp and diffuse maxima near each reciprocal lattice point. Sharp components were affected by a large Debye-Waller factor (probably due to static displacements) that was anisotropic, producing its greatest intensity reductions for reflections with $l^2 \gg h^2 + k^2 + hk$ (Hexagonal indices). Diffuse components lay directly under sharp components for $h^2 + k^2 + hk \gg l^2$ but were displaced to higher scattering angles as l became larger relative to h and k . The hexagonal cell corresponding to the sharp reflections was expanded in both a and c compared with parameters of unirradiated material; that corresponding to the diffuse maxima was expanded in a but contracted in c .

We have recently completed irradiations of selected crystals of " B_4C " in the hydraulic tube of the High Flux Isotope Reactor. Burnups of 3, 28, and 96% ^{10}B were achieved at fluences of 1.7×10^{18} , 1.7×10^{19} , and 1.7×10^{20} neutrons/cm² (>1 MeV), respectively.

11. K. Siegbahn, C. Nordling, and A. Fahlman, *Electron Spectroscopy for Chemical Analysis*, AFML-TR-68-189 (AD-844315) (October 1968); *ESCA. Atomic, Molecular, and Solid State Structure by Means of Electron Spectroscopy*, Alquist and Wilksells, Uppsala, 1967.

12. H. L. Yakel and L. A. Harris, *Metals and Ceramics Div. Annu. Progr. Rept. June 30, 1970*, ORNL-4570, p. 45.

13. C. W. Tucker, Jr., and P. Senio, *Acta Cryst.* 8, 371 (1955).

The irradiation temperature was $65 \pm 10^\circ\text{C}$. Results are currently being evaluated.

SMALL-ANGLE X-RAY DIFFRACTION STUDIES OF RADIATION-INDUCED VOIDS IN ALUMINUM

J. E. Epperson R. W. Hendricks

High-purity (99.9999%) aluminum single crystals ($10 \times 30 \times 1$ mm) with several orientations were grown by the Bridgeman method and irradiated at 55°C to fluences up to 5×10^{21} neutrons/cm² in the hydraulic tube of the High Flux Isotope Reactor. With a modified Kratky small-angle diffractometer we examined small-angle x-ray scattering by the crystals before and after irradiation. After we developed a technique for removing the oxide scale that forms while the crystals are in contact with the reactor cooling water, we detected small-angle scattering from the irradiated crystals. We attribute this scattering to radiation-induced voids. The scattering decreases if the irradiated crystals are isochronally heat treated at increasing temperatures and reaches a background value after 1 hr at 400°C . We are now analyzing the data to determine the number density and size distribution of voids as a function of neutron fluence and postirradiation heat treatment.

SOME PROPERTIES OF OCTAFLUOROCYCLOBUTANE (C_4F_8) OF INTEREST IN X-RAY ABSOLUTE INTENSITY EXPERIMENTS^{1,4}

R. W. Hendricks L. B. Shaffer^{1,5}

The number density, isothermal compressibility, and linear absorption coefficient (Cu $K\alpha$ radiation) of octafluorocyclobutane are tabulated as functions of temperature and pressure.

A COMPARISON OF TWO METHODS FOR ABSOLUTE INTENSITY CALIBRATION^{1,6}

L. B. Shaffer^{1,5} R. W. Hendricks

The power in the incident beam of an x-ray diffractometer has been determined by measuring (1) the small-angle scattering from octafluorocyclobutane and (2) the high-angle scattering from polystyrene. After the necessary corrections appropriate to each sample, the results agreed to better than $\pm 1\%$.

14. Abstract of ORNL-TM-3407 (July 1971).

15. Oak Ridge Associated University Research Participant, Summer 1970 and 1971, on leave from Anderson College, Anderson, Indiana.

16. Abstract of a paper submitted to the *Journal of Applied Crystallography*.

Part II. Fast Reactor Technology

13. Fast Breeder Reactor Oxide Fuels

A. L. Lotts C. M. Cox

This program is being conducted to advance the technology of (U,Pu)O₂ as an LMFBR fuel. Determination of the properties and performance of sol-gel-derived oxide fuels fabricated by Sphere-Pac and pelletizing techniques is emphasized, but these fuels are also compared with other fuels, such as pellets from mechanically blended or coprecipitated oxide. The main objectives of our program are:

1. to establish the performance characteristics and limitations of (U,Pu)O₂ fuels fabricated by different processes,
2. to obtain a fundamental understanding of the mechanisms involved in the irradiation behavior of fuel elements incorporating these fuels,
3. to develop fabrication techniques that provide both economy and a product with optimized performance, and
4. to develop analytical models sufficiently accurate to optimize experimental design and to predict fuel element response to LMFBR conditions.

These objectives are being met through a program that includes fabrication of fuel with different structures, characterization of these by out-of-reactor methods, and irradiation under a variety of conditions. The emphasis is on irradiation testing, postirradiation examination of the various fuel structures, and evaluation in terms of performance models. We are utilizing such facilities as the Oak Ridge Research Reactor, the Transient Reactor Test Facility, the Experimental Breeder Reactor II, and the Engineering Test Reactor. The program includes instrumented and noninstrumented tests under steady-state, power cycling, and transient conditions. The interpretation of the results depends heavily upon the preirradiation character-

ization and quality assurance program on the fuels and upon correlations with the theoretical fuel modeling work.

This program also provides technology that applies to the Gas-Cooled Breeder Reactor, development for which is reported in Chap. 31. This is a joint program with the Chemical Technology Division, which prepares the sol-gel-derived fuel, and the Reactor Division, which conducts the irradiation tests in the ORR.

DEVELOPMENT OF FABRICATION PROCESSES

J. D. Sease

The objective of our (U,Pu)O₂ fabrication program is to develop processes by which mixed oxide fuel of controlled density and stoichiometry can be fabricated for irradiation tests. A large portion of this program has been the development of Sphere-Pac and sol-gel pellet fabrication techniques. The Sphere-Pac process was used to load approximately 175 in. of fuel for irradiation tests. Sol-gel-derived pellets with controlled densities from 84 to 97% of theoretical were fabricated for irradiation tests in EBR-II.

Sphere-Pac Development

R. A. Bradley W. J. Lackey J. D. Sease

The Sphere-Pac process uses low-energy vibration to infiltrate a close-packed bed of coarse microspheres (420–600 μm) with fine microspheres (<44 μm) to achieve packed bed densities 85% of theoretical.¹

1. R. B. Fitts, A. R. Olsen, and J. Komatsu, "Sphere-Pac Fabrication of Sol-Gel Nuclear Fuels," *Amer. Ceram. Soc. Bull.* 47(9), 844 (1968).

The density of fuel pins loaded by the Sphere-Pac process is a linear function of the coarse bed density,² which varies as much as 5% between pins.³ We conducted a statistically designed experiment to determine the source and magnitude of the variation in coarse bed densities.² The experiment covered a coarse bed density range from 57.6 to 61.3% of theoretical. An analysis of variance on the data led to the following conclusions:

1. we were more than 99% sure that there was a variation between batches,
2. there was not sufficient evidence to indicate a difference between operators nor between two samples from a particular batch, and
3. the standard deviation describing a single operator's ability to reproduce his work with the same sample of microspheres was 0.40.

We believe that most of the observed variation in coarse bed densities was caused by differences in the densities of the microspheres in different batches. This experiment showed that the density of the coarse bed from a given batch of microspheres can be reproduced within 1% if the loading conditions are properly controlled. Later we found that the feed rate and the time and amplitude of vibration had no significant effect on the density of the coarse bed.

Since the density of the microspheres has the greatest effect on the density of the coarse bed and thus on the final smear density, we conclude that altering the density of the microspheres is the most practical way of controlling the density of Sphere-Pac fuel pins. This conclusion was substantiated when we loaded 13 Sphere-Pac pins for the EBR-II, Series II irradiation

2. R. A. Bradley and W. J. Lackey, *Fuels and Materials Development Program Quart. Progr. Rept. June 30, 1970*, ORNL-4600, pp. 5-7.

3. R. A. Bradley, *Fuels and Materials Development Program Quart. Progr. Rept. March 31, 1970*, ORNL-4560, pp. 6-7.

experiment. Even though we attempted to vary the smear density from 80 to 85% of theoretical, all 13 fuel pins had smear densities between 81.6 and 83.8% of theoretical.⁴

An alternate Sphere-Pac method, which incorporates all of the plutonium in the coarse fraction, has been proposed.^{5,6} This process offers several significant advantages over the conventional Sphere-Pac process, including a reduction in the number of steps required to load a fuel rod and decreased alpha contamination.

Pellet Development and Fabrication

R. A. Bradley

The objectives of this work are to develop methods of fabricating sol-gel (U,Pu)O₂ pellets and to produce pellets of controlled density and stoichiometry for irradiation tests. In addition to fabricating sol-gel (U,Pu)O₂ pellets we have procured mechanically mixed (U,Pu)O₂ pellets from WADCO and heat treated them to reduce sorbed gas to the specified limit.

The sol-gel process for making (U,Pu)O₂ pellets and methods of density control have been described.⁷ This process was used for fabricating 84 to 97%-dense pellets for the EBR-II, Series II irradiation experiment and 88 to 92%-dense pellets for the GCBR F-1 irradiation experiment replacement pins. The pellets fabricated during the past year are summarized in Table 13.1.

4. R. A. Bradley, W. J. Leonard, T. B. Lindemer, and W. H. Pechin, *Fuels and Materials Development Program Quart. Progr. Rept. Sept. 30, 1970*, ORNL-4630, pp. 13-15.

5. J. D. Sease, R. A. Bradley, C. R. Reese, W. H. Pechin, and A. L. Lotts, "Sphere-Pac and Pelletization of (U,Pu)O₂," pp. 323-41 in *Symposium on Sol-Gel Processes and Reactor Fuel Cycles, Gatlinburg, Tennessee, May 4-7, 1970*, CONF-700502.

6. J. D. Sease and F. E. Harrington, "U-Fines - A New Concept in Microsphere Fuels," *Amer. Ceram. Soc. Bull.* **50**, 423 (1971).

7. R. A. Bradley, *Metals and Ceramics Div. Annu. Progr. Rept. June 30, 1970*, ORNL-4570, pp. 48-49.

Table 13.1. (U,Pu)O₂ pellets fabricated for irradiation experiments

Irradiation experiment	Pellet configuration	Density (% of theoretical)	Oxygen-to-metal ratio
EBR-II, series II	Solid	84	1.96
	Solid	89.5	1.955, 1.98
	Solid	97	1.97
GCBR F-1 replacement pins	Annular ^a	92.3	1.94
	Annular ^a	92.3	1.98
	Solid ^a	88.6	1.98

^aDished end.

Stoichiometry Control

R. A. Bradley T. B. Lindemer

Uranium-plutonium dioxide fuel for LMFBR applications is required to have an oxygen-to-metal ratio near 1.97. For some of our irradiation experiments ratios as low as 1.94 are required. It is not always easy to achieve these oxygen-to-metal ratios; therefore, we investigated the reduction of mixed oxide to the hypostoichiometric state.

We theoretically analyzed the reduction of $(U,Pu)O_2$ in flowing hydrogen. The reduction process is kinetically controlled and limited by the rate at which water vapor can be removed from the furnace. Using Markin's⁸ thermodynamic data, the following equation was developed to predict the time required for reduction to any oxygen-to-metal ratio.

$$t = \frac{11.208Nx}{f} \int_4^{V_{Pu}} H dV_{Pu},$$

where

t = time required to reduce $U_{1-x}Pu_xO_2$ to desired V_{Pu} ,

V_{Pu} = valence of plutonium,

N = moles of mixed oxide,

f = flow rate of H_2 in liters per unit time at STP, and

H = the average H_2/H_2O during an increment of reduction.

The integral $\int_4^{V_{Pu}} H dV_{Pu}$ has been evaluated as a function of V_{Pu} and reduction temperature and is given in Fig. 2 of ref. 9. The details of the kinetic analysis are described elsewhere.^{9,10} Using the knowledge gained in this study we have consistently obtained the oxygen-to-metal ratio required for various irradiation experiments.

We also investigated the reduction of $(U,Pu)O_2$ by the C-CO-CO₂ system. In this system it is important that the carbon be in close proximity to the mixed oxides; for example, less than 0.025 in. The reduction is then controlled by the rate of the reaction $C + CO_2 \rightleftharpoons 2 CO$.

The kinetic analysis and experimental data show that reduction by the C-CO-CO₂ system is much quicker than by flowing hydrogen.^{9,10} Also, much lower oxygen-to-metal ratios can be achieved than is practical by hydrogen reduction.

Fuel Pin Fabrication

R. A. Bradley J. H. Erwin
W. J. Leonard M. K. Preston¹¹

Fuel pins for irradiation testing in the ORR, ETR, and EBR-II were fabricated this year. We completed 19 unencapsulated fuel pins for a 37-pin EBR-II sub-assembly shared with Babcock and Wilcox Company.¹² We fabricated 12 fuel pins for irradiation in the ETR to provide fuel for the Chemical Technology Division's fuel reprocessing studies.¹³ We also loaded one fuel pin for irradiation in the ORR to study mechanical interaction between fuel and cladding during power cycling.¹⁴

Construction of Fuel Cycle Alpha Facility

R. A. Bradley

Our capability for working with plutonium and other alpha emitting materials was significantly improved by the construction of the Fuel Cycle Alpha Facility (FCAF). The FCAF, which replaces the Building 3019 Interim Alpha Facility, consists of two 24 X 48 ft and one 24 X 24 ft laboratories in Building 4508, Room 265. The FCAF is equipped with its own room ventilation and exhaust system and a separate glove box exhaust system which permits operation of glove boxes in a once-through purge mode or in conjunction with a gas purifier and recirculating system. A layout of the FCAF, showing the location of presently installed glove boxes, is shown in Fig. 13.1.

A 5-in. prototype coater for pyrolytic carbon coating microspheres for HTGR recycle is in laboratory 1. Operations there will not involve highly alpha-active materials. Principal operations in the two alpha laboratories will be:

Laboratory 2

1. preparation of uranium-plutonium oxide powder,

8. T. L. Markin, *Chem. Eng. Progr. Symp. Ser.* 80, 43 (1967).

9. T. B. Lindemer and R. A. Bradley, *Kinetic Models for the Synthesis of $(U,Pu)O_{2-y}$ by Hydrogen-Reduction and Carbothermic Techniques*, ORNL-TM-3358 (April 1971).

10. T. B. Lindemer and R. A. Bradley, "Kinetic Models for the Synthesis of $(U,Pu)O_{2-y}$ by Hydrogen-Reduction and Carbothermic Techniques," accepted for publication in *Journal of Nuclear Materials*.

11. On loan from General Engineering Division.

12. R. A. Bradley, W. J. Leonard, and M. K. Preston, *Fuels and Materials Development Program Quart. Progr. Rept. Dec. 31, 1970*, ORNL-TM-3300, pp. 3-4.

13. R. A. Bradley, *ibid.*, pp. 4-6.

14. R. B. Fitts, R. L. Senn, and R. A. Bradley, *Fuels and Materials Development Program Quart. Progr. Rept. March 31, 1971*, ORNL-TM-3416, pp. 25-26.

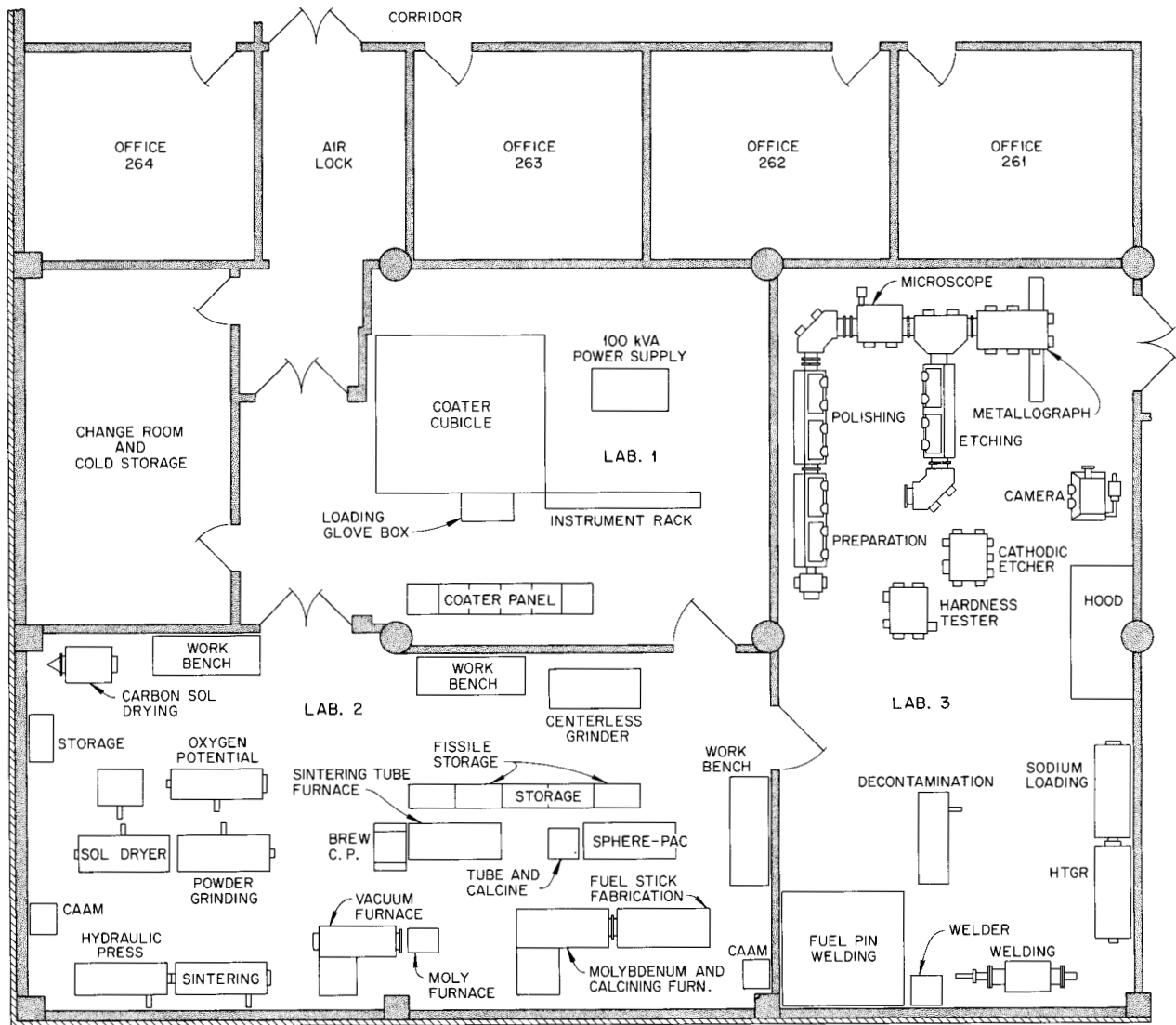


Fig. 13.1. Fuel cycle alpha facility.

2. fabrication of uranium-plutonium oxide pellets,
3. heat treatment of plutonium-bearing oxide, carbides, or nitrides,
4. centerless grinding of ceramic fuel bodies,
5. loading of fuel rods,
6. fabrication of carbon-bonded HTGR fuel rods,
7. storage of fissile material.
4. sodium and NaK bonding of fuels,
5. storage of fissile materials.

CHARACTERIZATION OF (U,Pu) O_2 FUELS

J. D. Sease J. M. Leitnaker

Laboratory 3

1. metallography of alpha-active materials,
2. welding of fuel rods,
3. decontamination of fuel rods,

The preirradiation characterization of a fuel material is necessary for understanding the fabrication processes and for interpreting irradiation test results. Characterization includes both the examination of the fuel material as produced and the determination of basic properties of the fuel.

Analytical Chemistry

W. H. Pechin R. A. Bradley W. J. Lackey

The analytical techniques for determining water content and metallic impurities in (U,Pu)O₂ have been given considerable attention because of the highly variable results that have been obtained.

The specifications for (U,Pu)O₂ fuel require that the average moisture content be less than 30 ppm. It is determined by passing dry nitrogen over the specimen as it is heated to 900°C and measuring the amount of water released with a P₂O₅ electrolytic cell.

Moisture contents ranging from 7 to 60 ppm have been obtained for a single batch of mixed oxide. To determine the source of this variation, a statistically designed experiment was performed.¹⁵ We concluded that most of the variability was due to moisture-laden air introduced into the apparatus as the sample was loaded. The addition of an air lock for loading samples without introducing air into the analyzer reduced the variability to acceptable values.¹⁶

Metallic impurities in (U,Pu)O₂ have been determined by emission spectroscopy, spark source mass spectroscopy, and wet chemical analysis. The results have been highly variable, particularly for Fe, Cr, and Ni. Metallographic examination of the mixed oxide revealed metallic inclusions scattered throughout the samples. We believe that analysis of very small samples (<0.050 g) of the material containing impurities as a second phase leads to variable results. We now analyze for impurities using solutions obtained by dissolving an entire pellet; the results are considerably more reproducible.

Homogeneity of (U,Pu)O₂

R. A. Bradley W. J. Lackey W. H. Pechin

We reported previously the use of gamma-ray spectroscopy to determine quantitatively the ratio of plutonium to uranium in a batch of microspheres that had been found to be inhomogeneous by alpha autoradiography.¹⁷ We used gamma spectroscopy to analyze 11 additional batches that appeared by alpha

15. R. A. Bradley and W. H. Pechin, *Fuels and Materials Development Program Quart. Progr. Rept. Dec. 31, 1970*, ORNL-TM-3300, pp. 8-10.

16. R. A. Bradley and W. H. Pechin, *Fuels and Materials Development Program Quart. Progr. Rept. March 31, 1971*, ORNL-TM-3416, pp. 3-5.

17. W. J. Lackey, R. A. Bradley, and W. H. Pechin, *Metals and Ceramics Div. Annu. Progr. Rept. June 30, 1970*, ORNL-4570, pp. 50-51.

autoradiography to be uniform. These analyses showed that there was a slight variation in ratio from batch to batch, but within the limits of detection (about 0.5%), there was no variation from sphere to sphere within a batch.¹⁸

Microstructure of Sol-Gel (U,Pu)O₂ Pellets

R. A. Bradley W. J. Lackey

The microstructure of the 84, 89, and 97%-dense sol-gel (U,Pu)O₂ pellets prepared¹⁹ for the EBR-II, Series II fuel pins is shown in Fig. 13.2. The microstructure of the 84%-dense pellets consisted of a very porous matrix with open, surface-connected porosity, regions of almost theoretically dense material dispersed throughout the matrix, and regions with an intermediate amount of closed porosity. This structure is typical of low-density pellets produced from sol-gel (U,Pu)O₂. The average grain size of these pellets was about 3 μm.

The 89 and 97%-dense pellets, which were made from powder whose properties had been altered by an oxidation-reduction treatment, contained a more uniform distribution of porosity. The 89%-dense pellets contained considerable closed porosity trapped inside grains in addition to porosity on the grain boundaries. The trapped porosity was a result of rapid grain growth during sintering in an oxidizing atmosphere. The 97%-dense pellets, which were made from the same powder as the 89%-dense ones but sintered in a reducing atmosphere, had very fine porosity on the grain boundaries and a relatively small number of larger pores scattered uniformly throughout the pellet. The small grain size, about 4 μm, and lack of trapped porosity are attributed to the reducing atmosphere.

Fission Product Behavior in Oxide Fuels

J. M. Leitnaker L. A. Harris J. P. DeLuca

Fission products in mixed oxides may cause several important effects. One of these is that they may interact directly with the cladding material. A second effect is that these fission products will affect the oxygen potential of the fuel, and, as a secondary result, the oxygen may react with the cladding material. A third effect is that the fission products differ in volume

18. R. A. Bradley, W. J. Lackey, and W. H. Pechin, *Fuels and Materials Development Program Quart. Progr. Rept. June 30, 1970*, ORNL-4600, pp. 11-12.

19. R. A. Bradley, *Metals and Ceramics Div. Annu. Progr. Rept. June 30, 1970*, ORNL-4570, p. 48.

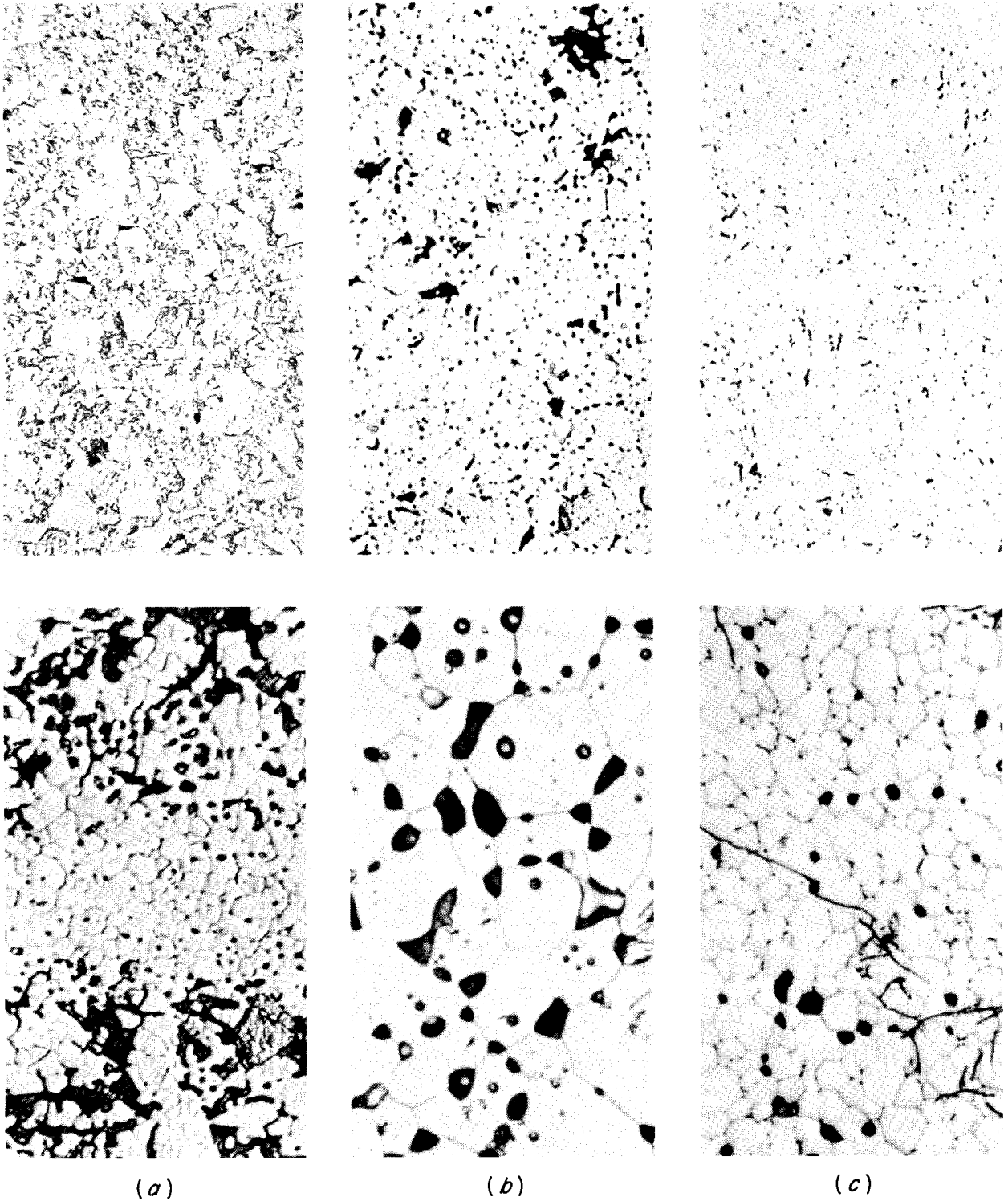


Fig. 13.2. Microstructure of sol-gel $(U,Pu)O_2$ pellets for EBR-II series II irradiation experiment. (a) 84% dense, calcined in argon and sintered in Ar-4% H_2 , 3 μm grain size. (b) 89.5% dense, calcined by oxidation-reduction and sintered in Ar-10% CO_2 , 16 μm grain size. (c) 97% dense, calcined by oxidation-reduction, sintered in Ar-4% H_2 , 4 μm grain size. Upper photos 200X, lower 1000X.

from the parent fuel. This change in volume may cause increased fuel-cladding interaction. Our goal has been to define or measure these effects as accurately as possible.

Dissolution of rare-earth oxides in oxide fuels. Rare earths and yttrium use up to 60% of the oxygen released when mixed oxide fuel undergoes fissioning. The bound state of the oxygen is uncertain. For example, Johnson et al.²⁰ assumed that the rare earths dissolve largely as the sesquioxide. We have shown by two methods that $\text{EuO}_{1.5}$, which may be considered typical of the trivalent rare earths, dissolves in the fluorite lattice with consequent oxidation of the solid solution.

The first method used was direct measurement of sample weight gain. UO_2 and Eu_2O_3 , equilibrated at an oxygen potential defined by a CO-to- CO_2 ratio of 10 at 1000°C , were subsequently mixed, pressed into pellets, and reequilibrated in the same atmosphere. Substantial weight gains indicated that solution was accompanied by oxidation, approaching a composition $(\text{U,Eu})\text{O}_{2.00}$.

The second method was less direct but equally conclusive. We measured x-ray lattice parameters of coprecipitated urania-europia samples that varied in europium-to-uranium ratio and had been equilibrated at a CO-to- CO_2 ratio of 10. The parameters deviated from the line predicted²¹ for solution of Eu_2O_3 in fluorite lattices but agreed with the line predicted for $(\text{U,Eu})\text{O}_{2.00}$.

We constructed an apparatus to measure the weight change of $(\text{U,Eu})\text{O}_{2\pm x}$ samples in controlled gas atmospheres. Preliminary measurements indicate variations in oxygen-to-metal ratios of less than 0.04 over oxygen pressure from 10^{-22} to 10^{-7} atm at 1000°C . Improvement of the apparatus has made it possible to define the composition to ± 0.002 in oxygen-to-metal ratio and extend the temperature range of measurements to 1300°C . Calibration is currently under way.

Thermal expansion of $(\text{U,Eu})\text{O}_2$ – implication to $(\text{U,Pu})\text{O}_2$. Thermal expansion measurements of $(\text{U,Ce})\text{O}_{2.00}$ by Markin et al.²² showed a remarkable nonlinearity over a range of cerium-to-uranium ratios. Using techniques described in Chap. 12, we found this same nonlinearity by high-temperature x-ray diffraction for $(\text{U,Eu})\text{O}_2$ solid solutions at oxygen potentials

20. C. E. Johnson, I. Johnson, and C. E. Crouthamel, "Fuel-Clad Chemical Interactions in Mixed Oxide UO_2 -20 w/o PuO_2 Stainless steel Clad Fast Reactor Fuel," paper presented at American Nuclear Society New Orleans Meeting, April 1971.

21. G. Brauer and H. Gradinger, *Z. Anorg. Allgem. Chem.* **276**, 209–26 (1954).

22. T. L. Markin, R. S. Street, and E. C. Crouch, *J. Inorg. Nucl. Chem.* **32**, 59–75 (1970).

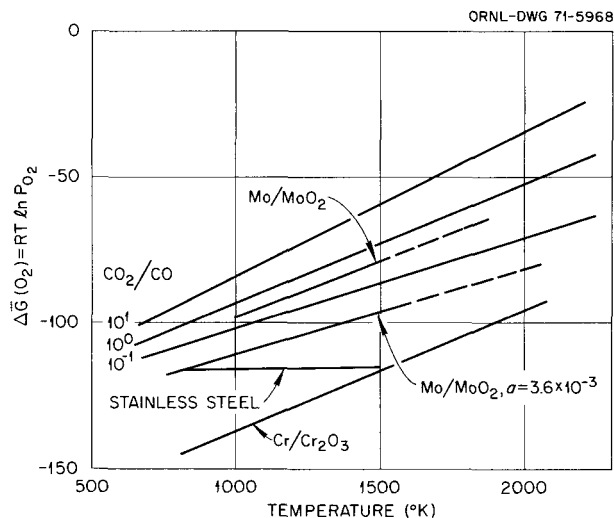


Fig. 13.3. Oxygen potentials of systems of interest in oxide fuel pins.

defined by CO_2 -to-CO ratios of 100 and 10. At the lower oxygen potentials the lattice size varied linearly with temperature.

The similarity between $(\text{U,Ce})\text{O}_2$ solid solutions and $(\text{U,Pu})\text{O}_2$ solid solutions²³ leads to questions about the thermal expansion of the fuel itself. Previous measurements on $(\text{U,Pu})\text{O}_2$ were made on samples prepared in hydrogen-nitrogen mixtures,²⁴ and thus undoubtedly substantial nitrogen was combined in the lattice.²⁵

The $(\text{U,Eu})\text{O}_2$ measurements thus assume a much larger importance in indicating a differing behavior of the metal ions at different oxygen potentials. The $(\text{U,Eu})\text{O}_2$ measurements also suggest that the fuel $(\text{U,Pu})\text{O}_2$ will have a linear rather than nonlinear expansion as suggested by the $(\text{U,Ce})\text{O}_2$ measurements.

Oxygen potentials determined by molybdenum in $(\text{U,Pu})\text{O}_2$ fuels. Fission product molybdenum, seen in metallic inclusions in irradiated fuel, can indicate the oxygen potential under reactor operating conditions. The oxygen potential is indicated by the extent of the reaction $\text{Mo}(\text{S, in inclusion}) + 2 [\text{O}] (\text{in fuel}) \rightleftharpoons \text{MoO}_2 (\text{S, in fuel})$. Figure 13.3 illustrates the relationship between oxygen potentials fixed by various CO-to- CO_2 ratios to that by the Mo/MoO₂ couple with molybdenum at unit activity and with MoO₂ at unity activity and at an activity of 3.4×10^{-3} . The variation of

23. T. L. Markin and E. C. Crouch, *ibid.*, 77–82.

24. T. B. Lindemer and R. A. Bradley, Oak Ridge National Laboratory, unpublished work.

25. J. Roth et al., *Trans. Amer. Nucl. Soc.* **10**, 457–58 (1967).

activity of molybdenum is reflected by variation of the molybdenum-to-ruthenium ratio in the fission product inclusions. Published results^{26,27} show this ratio to vary with location in the fuel pin and even more with different fuel samples, presumably because of their different initial oxygen potential. We have calculated the ratio for different fuel compositions and irradiation histories given by Olsen, Fitts, and Cox²⁸ and found wide variations. The calculation illustrates that shifts in fission product yields can affect the calculated oxygen potential dramatically. We conclude from these calculations that molybdenum can be used as a marker to measure the fuel's oxygen potential and that careful calculation of the fission product composition using the actual fuel pin history is necessary.

IRRADIATION BEHAVIOR

C. M. Cox T. N. Washburn

We are determining the in-reactor properties and performance of (U,Pu)O₂ fuel pins as functions of fabrication form, porosity distribution, stoichiometry, and irradiation conditions. This program includes both fast and thermal flux irradiations and steady-state, cyclic, and transient power conditions. To obtain a fundamental understanding of the irradiation behavior of these fuels, we concentrate on well-characterized operating conditions, detailed postirradiation examinations, and analysis in terms of fuel performance models.

Fast Flux Irradiation Tests

A. R. Olsen

The ORNL oxide fuels irradiations in the EBR-II currently involve two series of tests. All five pins in the encapsulated Series I group containing Sphere-Pac (²³⁵U-20% Pu)O₂ were irradiated initially to a calculated peak burnup of 6% FIMA. Two pins were examined, and the other three are being irradiated toward a target peak burnup level of 11.8% FIMA. A revised safety analysis for this extended testing has been issued.²⁹ Unencapsulated pins are being irradiated in

the Series II tests.³⁰ We fabricated 19 of the pins in the 37-pin subassembly, while the other 18 were fabricated by the Babcock & Wilcox Company (B&W). During the past year we assumed responsibility for the irradiation test and postirradiation examination of the entire series. Details of the testing program and the individual pin operating conditions are reported in the data package for these tests. All fuels are (²³⁵U-20% Pu)O₂. The ORNL pins contain sol-gel-derived fuel, while the B&W pellets and Vi-Pac shards were processed from coprecipitated powder. The tests have been coordinated to provide data for:

1. the evaluation of particulate fuels (Sphere-Pac and Vi-Pac) for LMFBR use, and
2. the comparison of performance characteristics of pellets fabricated from coprecipitated or sol-gel-derived powders.

The emphasis in these tests is on the effects of fuel form and void distribution on the release of fission gas, fission product redistribution, and mechanical and chemical interactions of fuel and cladding. A linear heat rate of 14 kW/ft, cladding temperatures of 550 to 650°C, and burnup levels to 100,000 MWd/metric ton are planned.

The postirradiation examination is continuing for the two Series I pins that have completed their scheduled irradiation. The details of the examination are reported as they are obtained.³¹⁻³³ The operating conditions and available performance data are summarized in Table 13.2. The significant results to date follow.

1. We found no fuel-cladding mechanical interaction, since the diametral changes are essentially those predicted³⁴ for fast-flux-induced void swelling in the stainless steel cladding. The annealed type 304 cladding swelled almost twice as much as the annealed type 316 cladding.

2. The fission gas release rate of 80% agrees with other EBR-II oxide fuel tests but is higher than that

30. A. R. Olsen et al., *Preirradiation Data for ORNL Series II and B & W Oxide Fuel Tests in EBR-II*, ORNL-TM-3446, in preparation.

31. A. R. Olsen, *Fuels and Materials Development Program Quart. Progr. Rept. Sept. 30, 1970*, ORNL-4630, pp. 27-29.

32. A. R. Olsen, *Fuels and Materials Development Program Quart. Progr. Rept. Dec. 31, 1970*, ORNL-TM-3300, pp. 15-19.

33. A. R. Olsen, J. L. Miller, and D. R. Cuneo, "Fast Flux Irradiation Tests," *Fuels and Materials Development Program Quart. Progr. Rept. March 31, 1971*, ORNL-TM-3416, pp. 15-20.

34. T. T. Claudson, R. W. Barker, and R. L. Fish, *Nucl. Appl. Technol.* 9, 10-23 (1970).

26. D. R. O'Boyle, F. L. Brown, and J. E. Sanecki, *J. Nucl. Mater.* 29, 27-42 (1969).

27. J. I. Bramman et al., *J. Nucl. Mater.* 25, 201-15 (1968).

28. A. R. Olsen, R. B. Fitts, and C. M. Cox, *Analysis of the Validity of Fast Reactor Fuel Tests in Existing Test Reactors*, ORNL-TM-2716 (October 1969).

29. A. R. Olsen and F. J. Homan, *Experiment Description and Hazards Evaluation for the Series I ORNL Oxide Fuels Irradiation in EBR-II*, ORNL-TM-2635 supplement (June 1970).

Table 13.2. Fabrication and operating data for pins with irradiation completed in EBR-II series I oxide fuel tests

Conditions and results	Pin S-1-A	Pin S-1-E
Cladding, type of stainless steel	304	316
Fuel smear density, % of theoretical	83	82
Linear heat rate, kW/ft at 193 MeV/fission		
Peak	13.7	13.5
Average	12.2	12.0
End-of-life peak	12.7	12.5
Peak cladding temperatures, °C		
Inner surface	570	570
Outer surface	540	540
Equivalent days at full power	234.1	234.1
Peak cladding fluence, neutrons/cm ²		
Total	4.2×10^{22}	4.2×10^{22}
>0.1 MeV	3.6×10^{22}	3.6×10^{22}
Fuel burnup, % FIMA by ¹⁴⁸ Nd analysis		
Peak	5.87 ^a	5.74
Average	5.24 ^a	5.12
Fission gas release, %		80
Peak cladding diametral change, %	0.71 ± 0.16	0.40 ± 0.08
Peak capsule diametral change, %	0.29	0.32

^aPredicted from EBR-II fission rates, analysis not yet available.

found for similar fuel irradiated in a thermal flux.³⁵ This difference was expected since a higher percentage of the fuel in the fast flux tests operated above 1700°C, where essentially all of the gas is released, and self-shielding causes more fissions in the cooler regions in the thermal flux tests.

3. There was no evidence of significant fuel-cladding chemical interaction even at cladding inner surface temperatures up to 570°C. Figure 13.4 shows typical transverse cross sections from the peak heat rate region in both pins, together with higher magnification views of the interfaces. We have seen only minor uniform reactions and no intergranular penetration of the cladding in these tests or in thermal flux tests with Sphere-Pac fuels. This lack of penetration has been confirmed by microprobe analysis, which shows no fission products in the cladding grain boundaries. This result is compared with those of other irradiation tests in "Fuel-Cladding Chemical Interaction" later in this chapter.

35. A. R. Olsen, *Trans. Amer. Nucl. Soc.* **13**, 32–33 (1970).

Transient Irradiation Tests

C. M. Cox D. R. Cuneo³⁶ E. J. Manthos

Destructive examinations and final evaluations were completed for the transient irradiation tests previously reported.³⁷ Six fuel pins containing unirradiated sol-gel (U,Pu)O₂ were subjected to power transients, as described in Fig. 13.5, at the Transient Reactor Test Facility (TREAT). No failure occurred, even though 50 vol % of the fuel melted in the peak power regions of two Sphere-Pac pins. Figure 13.6 shows the as-polished microstructures at the fuel column midplanes after the tests. The large circular voids are believed to be bubbles formed by coalescence of adsorbed gases present from fabrication. While appreciable restructuring in four pins is evident, examination of etched microstructures indicated that fuel melted only in pins TR-2A and TR-2B. Flux peaking caused localized melting at the ends of the fuel columns of pins TR-1A and Tr-1B.

Operating and examination data are summarized in Table 13.3. Note that appreciable grain growth was observed in all pins except TR-1C. Although the fuel pins showed no significant dimensional changes, neutron radiographic and destructive examinations showed extensive fuel relocation within the cladding. This included fuel column separations, densification during cooling from the molten state, axial migration, and the previously noted large bubbles.

A gap formed between the Sphere-Pac fuel and cladding by a combination of sintering and shrinkage during cooling from the melt. The influence of fuel column separations on length changes tended to be offset by sintering and shrinkage. Pellet fuel pins showed occasional separations at pellet interfaces, apparently due to ratcheting. The melt volume corresponds to a fuel-to-cladding heat transfer coefficient of 3.4 W cm⁻² °C⁻¹ or greater for the Sphere-Pac fuel pins, at least double the steady-state value reported by Fitts in a later section of this chapter.

Comparison with data reported by other investigators indicates that for the types of transients considered in this work, Sphere-Pac fuel of the same smear density and sol-gel and coprecipitated pellets behave equivalently.³⁸

36. On loan from the Reactor Chemistry Division.

37. C. M. Cox, D. R. Cuneo, E. J. Manthos, and R. E. Adams, *Metals and Ceramics Div. Annu. Progr. Rept. June 30, 1970*, ORNL-4570, pp. 58–59.

38. C. M. Cox, D. R. Cuneo, and E. J. Manthos, *Performance of Sphere-Pac and Pelletized (U,Pu)O₂ During Severe Overpower Transients*, ORNL-TM-3384 (July 1971).

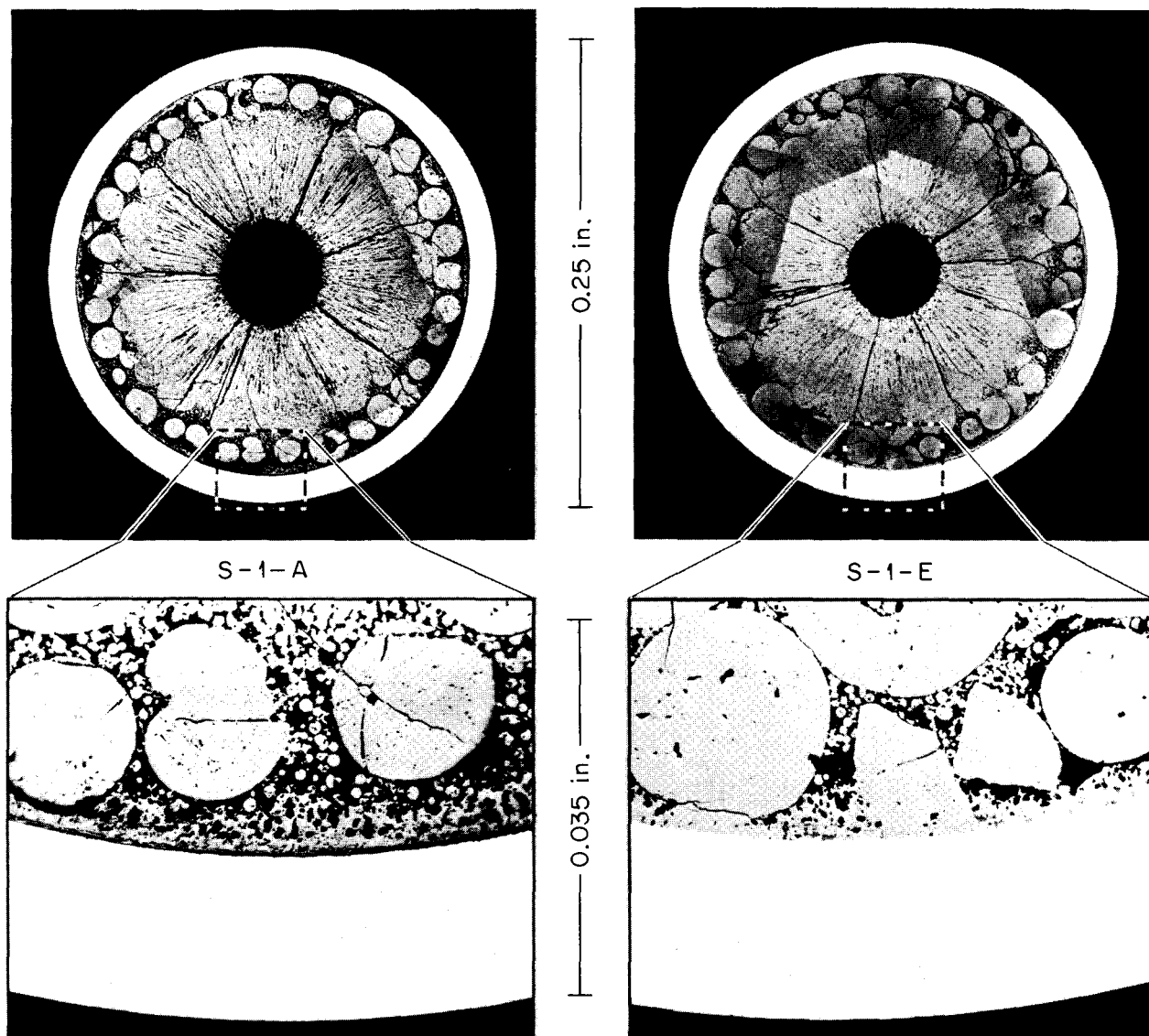


Fig. 13.4. Transverse metallographic sections from the peak heat rate section of EBR-II series I pins containing (^{235}U -20% Pu) O_2 fuel.

Uninstrumented Thermal Flux Irradiation Tests

A. R. Olsen D. R. Cuneo³⁶

The purpose, scope, conditions, and some results have been given³⁹ with detailed descriptions of the 11 numbered capsules of this series. The results of the tests irradiated to low and intermediate burnup levels have been presented.^{40,41}

Capsule 43-113 was removed from the reactor at a calculated burnup of 10% FIMA and awaits examination.

Capsules 43-117, 43-118, and 43-119 are the first capsules that we have irradiated with mechanically mixed (U,Pu) O_2 pellet fuel. Although the tests are primarily for head-end chemical processing studies, we removed one metallographic section each from three of the four pins in capsule 43-117. This capsule was

39. A. R. Olsen and D. R. Cuneo, *Metals and Ceramics Div. Annu. Progr. Rept. June 30, 1970*, ORNL-4570, pp. 53-55.

40. A. R. Olsen, C. M. Cox, and R. B. Fitts, *Trans. Amer. Nucl. Soc.* **12**, 605-6 (1969).

41. A. R. Olsen, *Trans. Amer. Nucl. Soc.* **13**, 32-33 (1970).

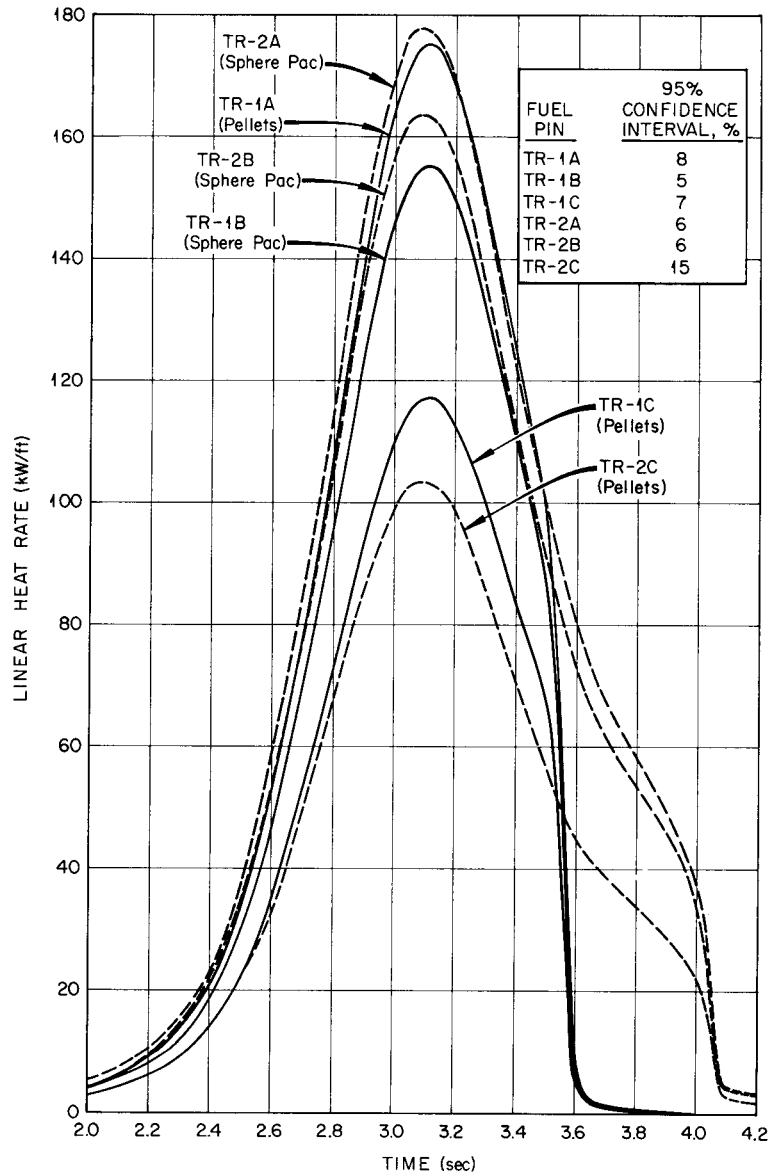


Fig. 13.5. Time variation of heat rate at fuel column midplane in transient experiments.

irradiated at a peak linear heat rate of 13 kW/ft to calculated burnup of 1.3% FIMA. Neutron radiographs of these pins showed: (1) interrupted central void formation in the top and bottom pins, which operated at linear heat rates of 8 to 10 kW/ft; (2) evidence that the "central" void is wandering off the fuel axis; and (3) a separation between the $^{238}\text{UO}_2$ insulator pellet and the top fuel pellet in the cooler outer regions of the pellet. This separation is not evident near the central

void. The metallographic examination is scheduled for next year.

We have continued the examination of all tests in this series, with emphasis on electron microscopy and microprobe analysis. The data have been used to improve our understanding of in-reactor fuel performance and to develop mathematical models to predict such performance. This is discussed in subsequent sections.

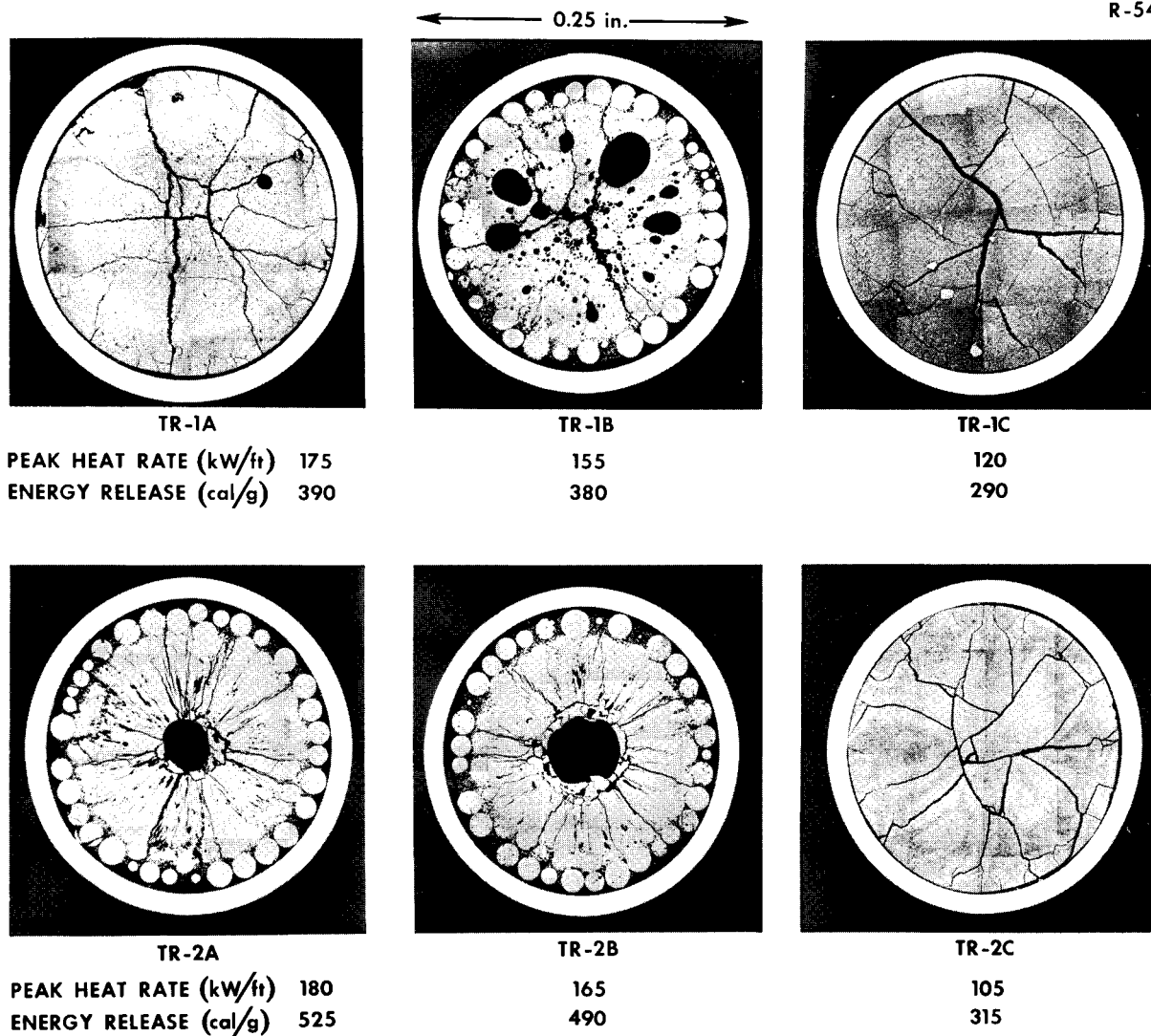


Fig. 13.6. Transverse sections taken from the midlengths of fuel pins irradiated in TREAT.

Table 13.3. Summary of operating and examination data for ORNL TREAT capsules^a

Fuel pin	TR-1A	TR-1B	TR-1C	TR-2A	TR-2B	TR-2C
Operating data ^b						
Fuel pin temperature before transient, °C	410	449	414	400	436	410
Peak instantaneous linear power, kW/ft	175	155	118	178	164	103
Energy release, cal/g	390	380	292	525	491	313
Postirradiation examination						
Overall fuel column length change, ^c mils	90	-20	-30	-60	-30	40
Radius of fuel central void, ^b mils	0	0	0	17	28	0
Volume of fuel melting, ^b %	0	0	0	50 ^{±2}	51 ^{±2}	0
Radius of equiaxed grain growth, ^b mils	94	111	0	111	111	78
Fuel-cladding radial gap, ^b mils	2.4 ^{±1.2}	3 ^{±3}	1.5 ^{±1}	4.4 ^{±2.6}	3.7 ^{±3}	1.2 ^{±1.2}

^aFabrication data and preliminary results are given in Table 15.7, p. 58, ORNL-4570.^bAt fuel column midplane.^cBased on neutron radiographs; estimated accuracy, ±20 mils.

ETR Instrumented Tests

T. N. Washburn R. A. Buhl

The ETR instrumented tests are designed to determine the performance of mixed oxide fuel under simulated LMFBR design operating conditions. The first two capsules (43-120 and 43-121) are being irradiated to investigate fuel swelling and fuel-cladding chemical interactions of Sphere-Pac and pellet (U,Pu)O₂ fuels. These capsules have been irradiated to a peak burnup of approximately 4.4% FIMA (as of May 9, 1971). Each capsule contains four fuel pins, with two thermocouples at the axial midplane of each pin. The peak cladding inside surface temperature is 540°C with the reactor at 175 MW. All thermocouples appear to be operating satisfactorily.

The second set of tests in this series consists of three instrumented capsules, each designed to measure fission gas pressure during testing and each containing one fuel pin with a 20-in.-long column of fuel. One capsule contains FTR-type pellets of the highest permissible density (94% of theoretical), the second contains FTR pellets of the lowest permissible density (88% of theoretical), and the third contains a packed bed of Sphere-Pac U-fines fuel. In the latter fuel, all the plutonium is contained in the coarse fraction (approx 400 μm diam), and a fine fraction (<44 μm diam) of depleted UO₂ is infiltrated into the coarse bed.

Hardware for the three capsules has been machined, inspected, and cleaned. The FTR pellets have been received from WADCO and will be completely characterized.

ORR Instrumented Thermal Performance Tests

R. B. Fitts

The ORR instrumented tests are designed⁴² to monitor the thermal performance of fuel pins as they operate in the Oak Ridge Research Reactor Poolside Facility.⁴³ The temperatures of the cladding and fuel center line and the rates of heat generation are continuously monitored and recorded. The general results from the first three capsules were reported last

42. R. B. Fitts and V. A. DeCarlo, *Metals and Ceramics Div. Annu. Progr. Rept. June 30, 1968*, ORNL-4370, pp. 145-49.

43. D. B. Trauger, *Some Major Fuel Irradiation Test Facilities of the Oak Ridge National Laboratory*, ORNL-3574 (April 1964).

year.⁴⁴ They showed that within ±8% the central temperature developed in pellet and Sphere-Pac fuels is the same at identical operating conditions.

The fuel microstructures developed in the pellet and Sphere-Pac fuel pins from capsule SG-3 have been analyzed in detail.^{45,46} A typical cross-section from each fuel pin is shown in Fig. 13.7 with the calculated⁴⁶ temperature profiles superimposed on the fuel structures. The first discernible outlining of the grain boundaries in both fuels occurs at 1300°C, and complete restructuring takes place above 1700°C.

This analysis has also led to a preliminary conclusion that the fuel-to-cladding thermal conductance in a Sphere-Pac pin (1.93 W cm⁻² °C⁻¹) is higher than that in a pellet fuel pin (0.73 W cm⁻² °C⁻¹) with a small (0.0015 in. radial) initial fuel-cladding gap. This conclusion is based upon small differences in the measured heat generation rates and temperatures for the two fuel pins, and, although we believe these differences to be real, we have begun to statistically analyze the data to assess the significance of these measured differences.

The chemical compatibility of stainless steel cladding with the (U,Pu)O₂ fuels was better for Sphere-Pac than pellet fuel.⁴⁷ This observation was supported by the results from the pellet and Sphere-Pac fuels tested in the SG-3 capsule. Although the test times and fuel burnup were low in this test, the pellet fuel pin contained several areas of very localized cladding attack,⁴⁶ whereas the Sphere-Pac fuel pin contained no such areas.

The performance of the tungsten-rhenium thermocouples used in these tests was generally good, although at 2000°C some chemical attack was observed on the wires and sheaths. This attack appears to be a result of the vaporization of oxides of tungsten and rhenium.⁴⁸

44. R. B. Fitts, V. A. DeCarlo, and D. R. Cuneo, *Metals and Ceramics Div. Annu. Progr. Rept. June 30, 1970*, ORNL-4570, pp. 56-57.

45. R. B. Fitts, V. A. DeCarlo, and D. R. Cuneo, *Fuels and Materials Development Program Quart. Progr. Rept. Sept. 30, 1970*, ORNL-4630, pp. 35-36.

46. R. B. Fitts, E. L. Long, Jr., and J. L. Miller, Jr., *Fuels and Materials Development Program Quart. Progr. Rept. Dec. 30, 1970*, ORNL-TM-3300, pp. 23-29.

47. C. M. Cox, R. B. Fitts, A. R. Olsen, and E. L. Long, Jr., *Trans. Amer. Nucl. Soc.* **14**, 173-75 (1971).

48. R. B. Fitts, J. L. Miller, Jr., and E. L. Long, Jr., "Observations on Tungsten-Rhenium Thermocouples used In-Reactor in (U,Pu)O₂ Fuel Pins," to be published in the Transactions of the 5th Symposium on Temperature, its Measurement and Control in Science and Industry, held in Washington, D.C., June 21-24, 1971.

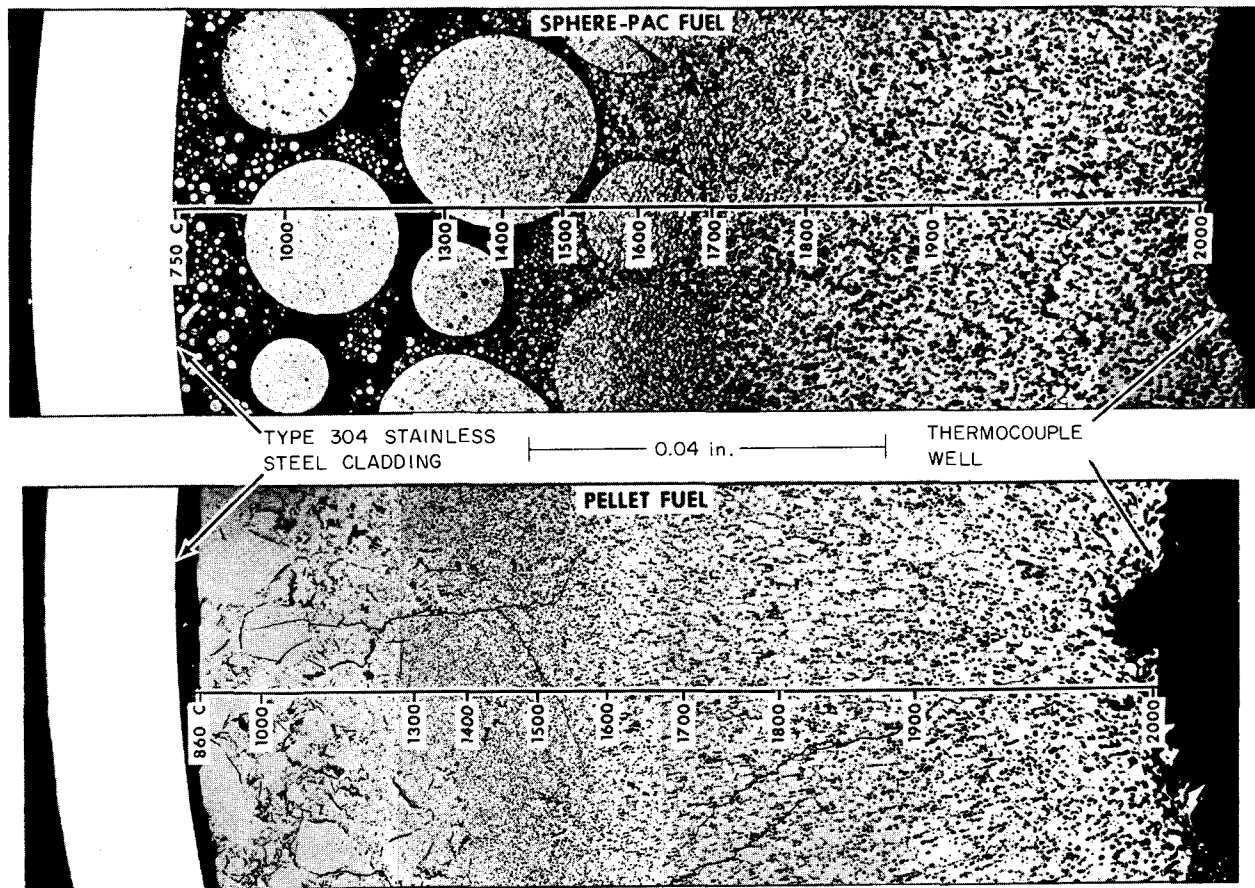


Fig. 13.7. Fuel restructuring in ORR instrumented tests of $U_{0.8}Pu_{0.2}O_{1.99}$. The structure of Sphere-Pac and pellet fuel is compared with calculated temperature profiles from the type 304 stainless steel cladding to the inner surface of the annular fuel.

Fuel-Cladding Mechanical Interaction Tests

R. B. Fitts B. Fleischer R. L. Senn⁴⁹

This series of irradiation tests⁵⁰ is intended to measure in-reactor the axial extension of the fuel column and cladding and the internal gas pressure developed in LMFBR-type fuel pins during operation under carefully controlled prototypic LMFBR power and temperature conditions. The tests, lasting for 1 to 2 years and producing burnups in the $(U,Pu)O_2$ fuels of 5 to 9%, will include programmed power cycles and occasional overpower cycles. The measurements will provide information on the frequency and mode of fuel-cladding mechanical interaction and the buildup of fuel pin internal gas pressure during irradiation. This

information is important to the economics and safety of the LMFBR.

The design^{51,52} and fabrication^{53,54} of the first capsule, which contains a prototypic Fast Test Reactor fuel pin (except for fuel length), is nearly complete. This capsule will begin operation in the ORR poolside facility in June 1971.

49. Reactor Division.

50. R. B. Fitts, J. D. Jenkins, J. G. Morgan, and R. L. Senn, *Metals and Ceramics Div. Annu. Progr. Rept. June 30, 1970*, ORNL-4570, p. 60.

51. R. B. Fitts, R. L. Senn, J. G. Morgan, and J. D. Jenkins, *Fuels and Materials Development Program Quart. Progr. Rept. June 30, 1970*, ORNL-4600, pp. 58-63.

52. R. B. Fitts and R. L. Senn, *Fuels and Materials Development Program Quart. Progr. Rept. Sept. 30, 1970*, ORNL-4630, pp. 36-38.

53. R. B. Fitts and R. L. Senn, *Fuels and Materials Development Program Quart. Progr. Rept. Dec. 31, 1970*, ORNL-TM-3300, pp. 29-33.

54. R. B. Fitts, R. L. Senn, and R. A. Bradley, *Fuels and Materials Development Program Quart. Progr. Rept. March 1971*, ORNL-TM-3416, pp. 25-26.

ANALYSIS OF FUEL ELEMENT PERFORMANCE

C. M. Cox

We are developing analytical models for predicting and evaluating the performance of LMFBR fuel pins and are examining irradiated fuel pins in detail. The models have emphasized the thermal, chemical, and mechanical performance of the fuel elements, particularly during startups, power cycles, and transients. This work includes direct support of the irradiation testing program in terms of optimizing experimental designs, interpreting results, and extrapolating these results to LMFBR conditions. Irradiated fuels are characterized in terms of redistribution of fuel components, porosity, and fission products and the quantitative identification of chemical interactions of fuel and cladding. This involves electron microscopy, electron microprobe analysis, and quantitative metallography.

Performance Model Development

F. J. Homan

The FMØDEL code described last year⁵⁵ was essentially a steady-state performance model, which we had begun to modify for power cycling calculations. This modification is now complete, and the code is suitable for steady-state, power cycling, and limited transient applications. Rapid cooldowns and other off-normal operating conditions can also be evaluated. In addition, the reactor power history can now be followed in detail. The empirical fuel restructuring model used previously⁵⁶ has been discarded in favor of a dynamic model based on a vaporization-condensation mechanism of pore migration.⁵⁷ Other additions to FMØDEL during the past year include Lackey's treatment of grain growth⁵⁸ and plutonium redistribution,⁵⁹ a fuel crack-

ing model,⁶⁰ and improvement of the cladding mechanical model to include flux enhanced creep.⁶¹

FMØDEL has been used recently in a variety of applications. First was the modeling round robin exercise,⁶² where the performance characteristics of a number of pins were predicted by several AEC contractors, and the results were compared. Then a summary of comparisons between predicted and measured fuel pin behavior was presented at the American Nuclear Society topical meeting on Fast Reactor Fuels.^{63,64} Included in the comparisons were fuel pin diametral expansions, restructuring, center-line temperatures, and porosity distributions. Figure 13.8 compares measured and predicted diametral expansions, and Fig. 13.9 measured and predicted fuel restructuring for a series of fuel pins irradiated by the General Electric Company⁶⁵ in EBR-II. These fuel pins had fuel densities ranging from 84 to 98% of theoretical and operated with peak heat rates of 10 to 17 kW/ft to burnups of about 50,000 MWd/metric ton. Most recently, FMØDEL was used to predict the results of the PNL-19 heat rate to melting experiment.⁶⁶

FMØDEL currently exists as two versions. A single-node version is used in the detailed analysis of one axial section of fuel. A multinode version calculates performance at several axial positions. The multinode version also has the capabilities of the single-node version, but computer running times may be excessive for a very complex case involving fuel-cladding mechanical interaction and perhaps a detailed following of the reactor history. For this reason the multinode version will be most useful in broader, less detailed analyses.

Electron Microscopy of Irradiated (U,Pu)O₂

W. J. Lackey

Replica electron microscopy of irradiated (U,Pu)O₂ is being conducted to improve our understanding of

55. F. J. Homan, *Metals and Ceramics Div. Annu. Progr. Rept. June 30, 1970*, ORNL-4570, p. 68.

56. C. M. Cox and F. J. Homan, *PRØFIL - A One-Dimensional FØRTRAN IV Program for Computing Steady-State Temperature Distributions in Cylindrical Ceramic Fuels*, ORNL-TM-2443 (March 1969); Addendum (August 1969).

57. F. J. Homan, *LMFBR Fuel Cycle Studies Progress Report for December 1970*, No. 22, ORNL-TM-3281, pp. 56-62.

58. J. L. Miller, Jr., and W. J. Lackey, *LMFBR Fuel Cycle Studies Progress Report for January 1971*, No. 23, ORNL-TM-3312, pp. 101-3.

59. W. J. Lackey, *LMFBR Fuel Cycle Studies Progress Report for July 1970*, No. 17, ORNL-TM-3095, pp. 61-65.

60. F. J. Homan, *LMFBR Fuel Cycle Studies Progress Report for September 1970*, No. 19, ORNL-TM-3180, pp. 72-73.

61. F. J. Homan, *LMFBR Fuel Cycle Studies Progress Report for March 1971*, No. 25, ORNL-TM-3375, pp. 65-71.

62. F. J. Homan, *Oak Ridge National Laboratory Solutions to a Modeling Round-Robin Exercise*, ORNL-TM-3360 (in press).

63. F. J. Homan, W. J. Lackey, and C. M. Cox, *Comparison Between Predicted and Measured Fuel Pin Performance*, ORNL-TM-3386 (May 1971).

64. F. J. Homan, W. H. Bridges, W. J. Lackey, and C. M. Cox, *Trans. Amer. Nucl. Soc.* **14** (suppl 1), 8-10 (April 1971).

65. R. C. Nelson et al., *Performance of Plutonium-Uranium Mixed-Oxide Fuel Pins Irradiated in a Fast Reactor (EBR-II) to 50,000 MWd/Te*, GEAP-13549 (August 1969).

66. F. J. Homan et al., "Heat Rate to Melting Predictions," *LMFBR Fuel Cycle Studies Progr. Rept. June 1971*, No. 28, ORNL-TM-3487 (in press).

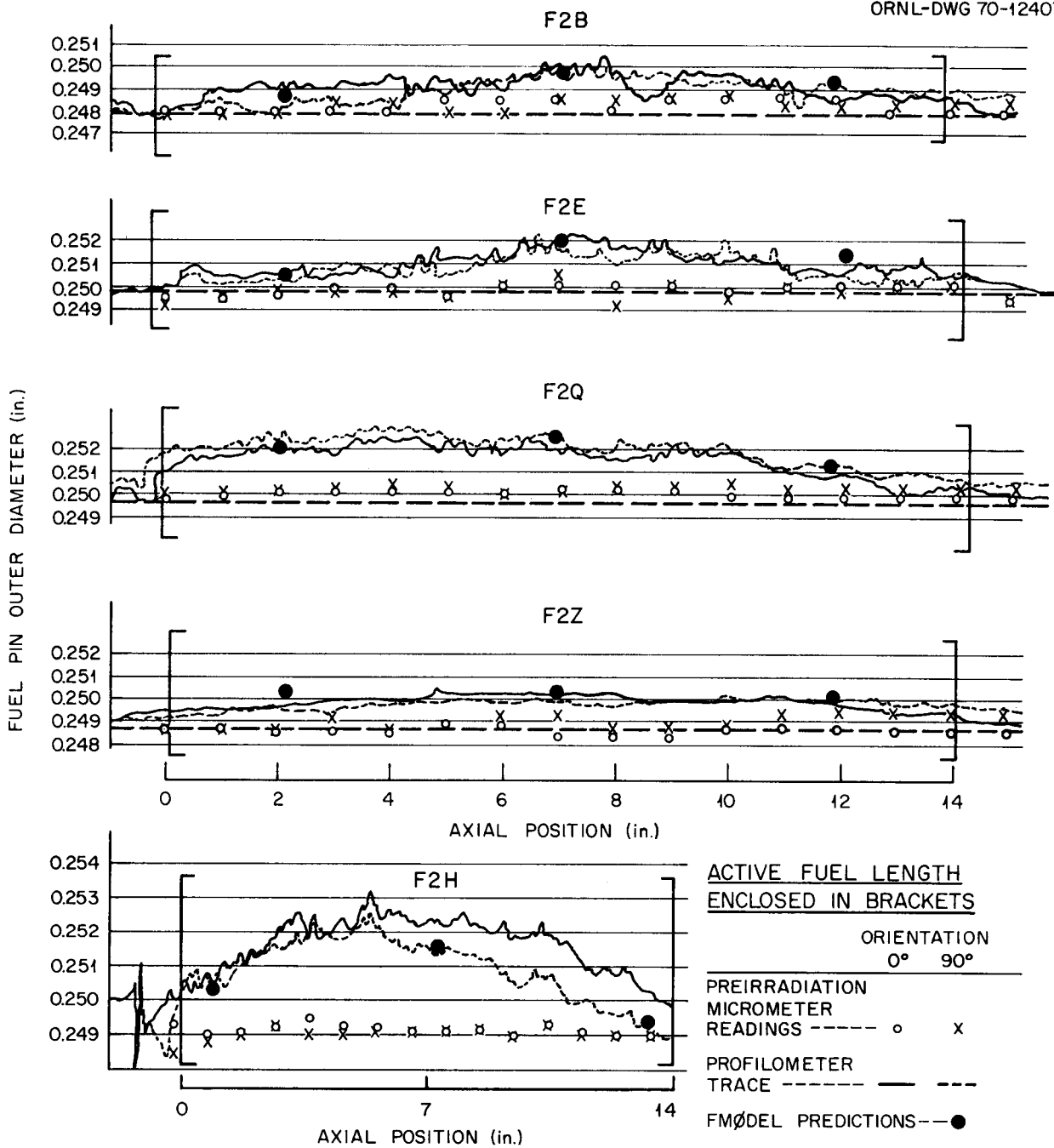


Fig. 13.8. Postirradiation profilometer traces and ORNL-predicted expansions for five fuel pins from General Electric F-2 series.

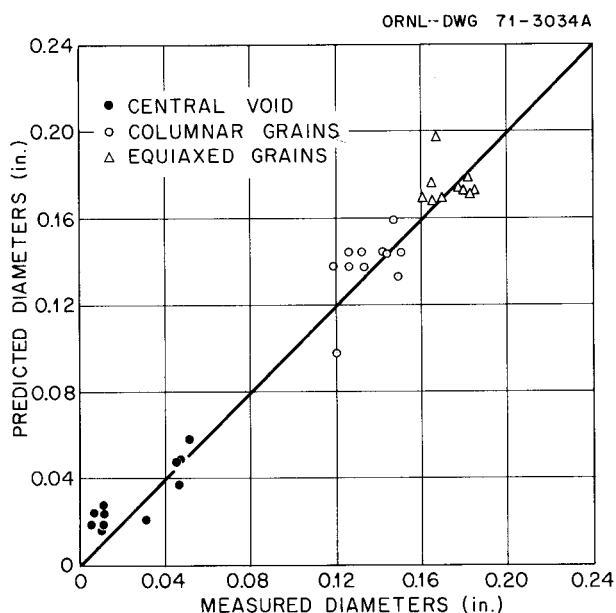


Fig. 13.9. Summary of comparisons between predicted diameters for central void, columnar, and equiaxed grain regions.

restructuring, fuel swelling, and fission gas release. Previously we reported⁶⁷ the examination of fuel irradiated to a burnup of 0.7% FIMA. Similar fuel after irradiation in the ETR with a cladding inner surface temperature of about 370°C at a time-averaged linear heat rate of 14 kW/ft to a burnup of 4.2% FIMA is shown in Fig. 13.10. The microstructure of the fuel immediately adjacent to the cladding appears to be unchanged from that of the unirradiated material. This is strong evidence that intergranular pores as large as 0.2 μm in diameter do not disappear during irradiation.⁶⁸ This is not to say that a large number of considerably smaller fission gas bubbles do not disappear as a result of resolution processes. There were indications that fission gas bubble migration and coalescence were influenced by movement of columnar grain boundaries perpendicular to the thermal gradient as well as by the presence of subgrains 1 to 3 μm across within the equiaxed grain region.^{68,69}

(U,Pu)O₂ Grain Growth

W. J. Lackey R. A. Bradley

Because of the influence that grain size is expected to have on release of fission gas, fuel swelling, and Nabarro-Herring creep of (U,Pu)O₂, we investigated the

67. W. J. Lackey, *Metals and Ceramics Div. Annu. Progr. Rept. June 30, 1970*, ORNL-4570, pp. 68-69.

68. W. J. Lackey, *LMFBR Fuel Cycle Studies Progr. Rept. April 1971, No. 26*, ORNL-TM-3412, pp. 79-83.

kinetics of in-reactor and out-of-reactor grain growth.^{69,70} The size of the equiaxed grains was determined as a function of radial position for three Sphere-Pac U_{0.85}Pu_{0.15}O_{2.00} fuel pins after irradiation in the ETR. The initial grain size of the fuel was 1.2 μm . Data for two low-burnup pins were combined and analyzed as shown in Fig. 13.11. The least-squares equations given in the figure relate the observed grain size in microns (D) to the initial grain size (D_0), the irradiation time in hours (t), and the irradiation temperature in degrees centigrade (T). In the higher temperature region, solid fission products or gas bubbles apparently retard the rate of grain growth. The low activation energies indicate that in-reactor grain growth is not nearly as temperature dependent as out-of-reactor grain growth of UO₂ and ThO₂. Comparisons of the grain size after a burnup of 4.2% FIMA with the grain size of the two low burnup pins showed that grain growth was not complete at the conclusion of the low burnup irradiations.

Out-of-reactor isothermal annealing of archive fuel resulted in extensive agglomeration of porosity in conjunction with grain growth. In addition, annealing at 1550°C apparently caused the fuel density to actually decrease. Such a decrease in density is unusual, but it has been observed for ThO₂ isothermally annealed out-of-reactor.⁷¹ Thus, this mechanism of swelling may be a contributing factor to fuel swelling in the equiaxed grain region of oxide fuel pins.

Actinide and Oxygen Redistribution in Irradiated (U,Pu)O₂

W. J. Lackey D. K. Bates⁷²
J. L. Miller, Jr. A. R. Olsen

Because of the anticipated influence of component redistribution on the thermal and compatibility behavior of fast reactor fuel pins, we have measured^{73,74}

69. W. J. Lackey, *Fuels and Materials Development Program Quart. Progr. Rept. March 31, 1971*, ORNL-TM-3416, pp. 33-38.

70. W. J. Lackey, *Fuels and Materials Development Program Quart. Progr. Rept. Sept. 30, 1970*, ORNL-4630, pp. 47-54.

71. K. H. McCorkle and C. S. Morgan, *Metals and Ceramics Div. Annu. Progr. Rept. June 30, 1970*, ORNL-4570, p. 26.

72. Summer employee sponsored by Oak Ridge Associated Universities.

73. J. L. Miller, Jr., and W. J. Lackey, *Fuels and Materials Development Program Quart. Progr. Rept. March 31, 1971*, ORNL-TM-3416, pp. 39-44.

74. W. J. Lackey, A. R. Olsen, and J. L. Miller, Jr., "Actinide Redistribution in Irradiated (U,Pu)O₂," *LMFBR Fuel Cycle Studies Progr. Rept. May 1971, No. 27*, ORNL-TM-3456, in press.

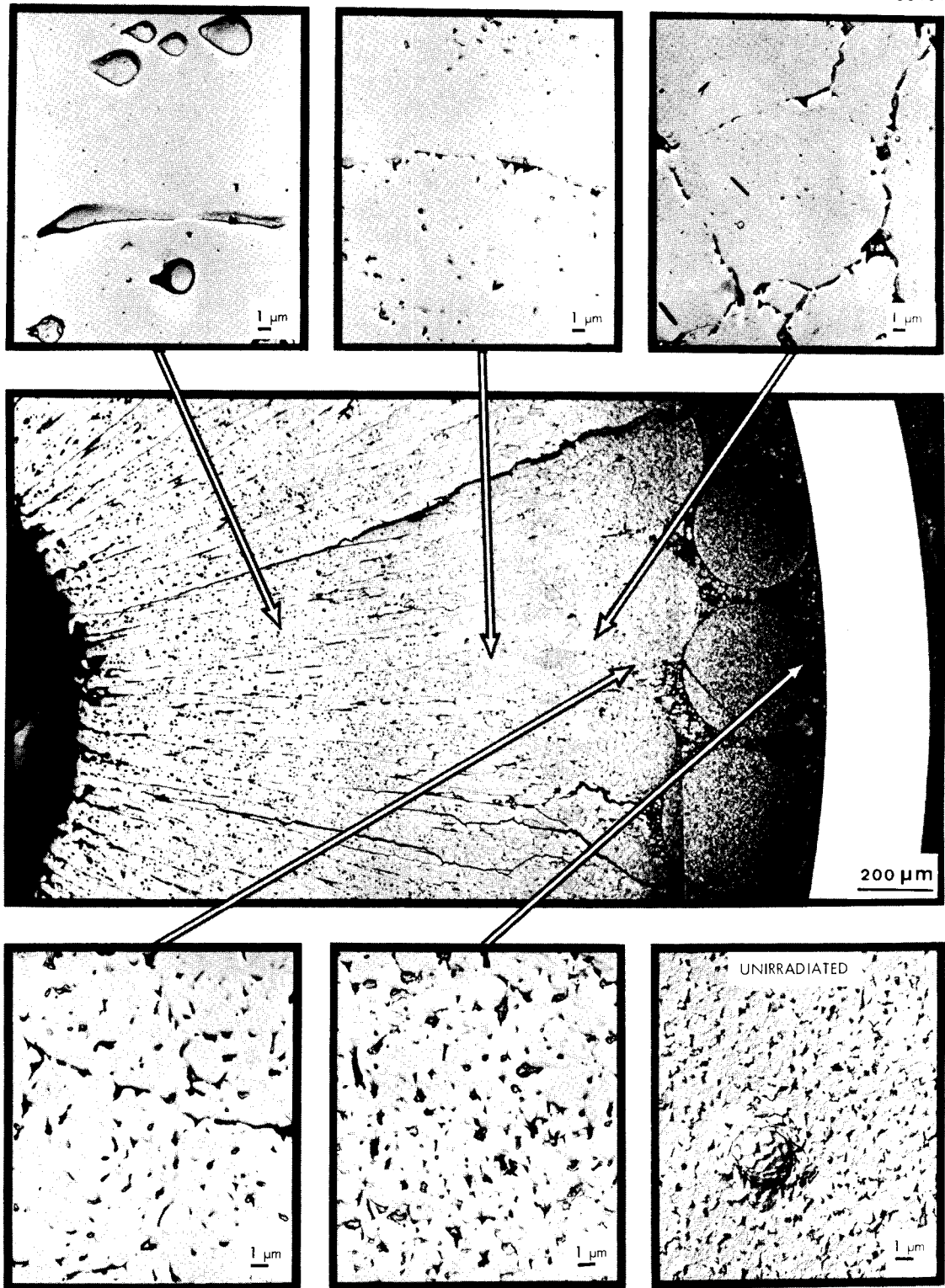


Fig. 13.10. Selected-area replica electron micrographs of irradiated $U_{0.85}Pu_{0.15}O_{2.00}$.

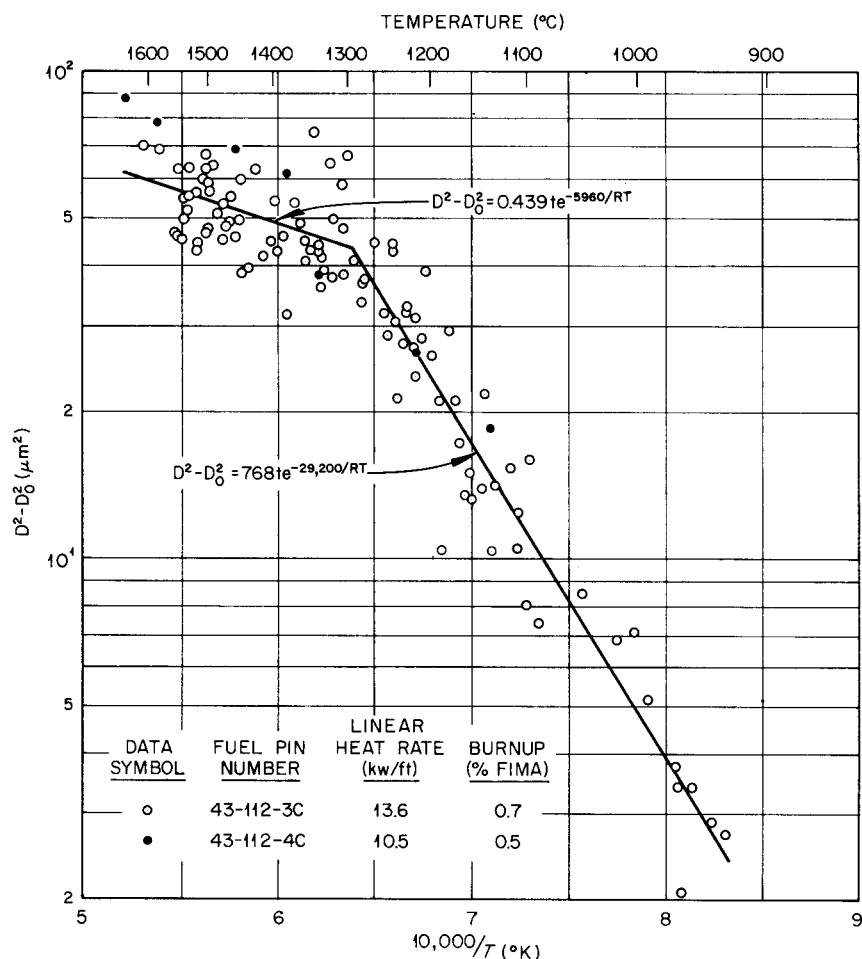


Fig. 13.11. Grain growth of $U_{0.85}Pu_{0.15}O_2$ in-reactor.

the radial distribution of uranium and plutonium as well as analytically modeled⁷⁵⁻⁷⁷ actinide and oxygen redistribution that occurs during irradiation of $(U,Pu)O_2$. Both electron microprobe⁷³ and alpha autoradiography^{75,76} studies showed that fuel that deposited from vapor in the region of transition from columnar to equiaxed grains was rich in uranium. This is strong evidence, at least for stoichiometric fuel, that

75. A. R. Olsen, R. B. Fitts, and W. J. Lackey, "In-Reactor Restructuring Temperatures and Kinetics for $(U,Pu)O_2$," paper presented at the Conference on Fast Reactor Fuel Element Technology, New Orleans, April 13-15, 1971, American Nuclear Society.

76. W. J. Lackey, A. R. Olsen, J. L. Miller, Jr., and D. K. Bates, *Trans. Amer. Nucl. Soc.* **14**, 180-82 (1971).

77. W. J. Lackey, "Actinide Redistribution in Irradiated $(U,Pu)O_2$," *LMFBR Fuel Cycle Studies Progr. Rept. June 1971*, No. 28, ORNL-TM-3487, in press.

actinide redistribution occurs by an evaporation-condensation mechanism.

The analytical model is kinetic. The commonly observed depletion in uranium near the central void is accounted for by the formation and subsequent transport down the temperature gradient of a vapor rich in uranium compared to the initial solid. The actinide composition of each of a set of radial increments is calculated as a function of time from a series of calculations of the quantity and plutonium-to-uranium ratio of the material that condenses into and evaporates from the increment during a short time period. Contrary to what occurs for slightly substoichiometric and hyperstoichiometric fuel, the model predicts preferential evaporation of plutonium and thus concentration of uranium at the central void for appreciably hypo-stoichiometric material.

Radial Porosity Distribution and Its Influence on the Fuel Temperature Profile

W. J. Lackey F. J. Homan T. M. Kegley, Jr.

Knowledge of the radial porosity distribution of the fuel as a function of time is necessary to accurately calculate fuel temperatures, creep rate, and other structure-sensitive properties. We measured⁷⁸ the radial porosity profile for an irradiated (U,Pu)O₂ fuel pin and developed a computer model that calculates⁷⁹ the porosity profile based on the evaporation-condensation mode of material transport down a temperature gradient. Additionally, we determined the influence of the porosity profile on fuel temperatures.⁸⁰

The measured and predicted porosity profiles are shown to compare favorably in Fig. 13.12. The columnar grain region is shown to be considerably more porous than previously generally believed. The calculated fuel center temperature was 200°C higher when based on the observed porosity distribution rather than the previously generally assumed three-zone porosity distribution model.

Fuel-Cladding Chemical Interaction

R. B. Fitts A. R. Olsen
C. M. Cox E. L. Long, Jr.

Chemical interactions between mixed oxide fuel, fission products, and cladding materials may be a major factor limiting the life of fuel rods in oxide fueled fast breeder reactors. We have examined in- and out-of-reactor tests at ORNL and the available literature for evidence of such chemical interactions and have summarized our findings.^{81,82} An overall summary of this information is given in Fig. 13.13. The ORNL Sphere-Pac data, represented by the diamond symbols, are obviously well below the data from other sites for pellet

78. W. J. Lackey and T. M. Kegley, Jr., *Fuels and Materials Development Program Quart. Progr. Rept. Dec. 31, 1970*, ORNL-TM-3300, pp. 40-43.

79. F. J. Homan, *Fuels and Materials Development Program Quart. Progr. Rept. Dec. 31, 1970*, ORNL-TM-3300, pp. 33-39.

80. W. J. Lackey and F. J. Homan, *Fuels and Materials Development Program Quart. Progr. Rept. March 31, 1971*, ORNL-TM-3416, pp. 31-34.

81. R. B. Fitts, E. L. Long, Jr., and J. M. Leitnaker, "Observations of Fuel-Cladding Chemical Interactions as Applied to GCBR Fuel Rods," presented at ANS Conference on Fast Reactor Fuel Element Technology, April 1970, New Orleans; ORNL-TM-3385 (July 1971).

82. C. M. Cox, R. B. Fitts, A. R. Olsen, and E. L. Long, Jr., *Trans. Amer. Nucl. Soc.* 14, 173-75 (1971).

and Vi-Pac fuels. The principal conclusions from this work follow.

1. Stainless-steel-clad mixed-oxide fuel pins fabricated with Sphere-Pac fuel have shown no fuel-cladding chemical interaction, in marked contrast to some fuel pins made with pellet fuels and operated under the same conditions.
2. Fuel-cladding chemical interaction is primarily due to oxidation of the cladding material.
3. Hastelloy X appears to be able to operate at 50 to 100°C higher temperature than stainless steel without excessive fuel-cladding chemical interaction.

Discrete Element Analysis of Cladding Deformation

B. R. Dewey⁸³

As a specialized form of finite element stress analysis, the discrete element method was developed and programmed⁸⁴ for hollow cylindrical solids subjected to pressure and thermal loading. The solution allows arbitrary radial variation of mechanical properties and temperature, computes elastic and inelastic stresses and displacements, and predicts time-dependent deformation based on empirical creep laws. This work was undertaken to extend the method to axial as well as radial variation of temperature, loading, and material properties. The two-dimensional loading is of particular interest at fuel element spacers, where it cannot be analyzed with the finite difference method used in the FMØDEL code.

Mechanical Properties of Stainless Steel Tubing

R. W. Swindeman R. D. Waddell, Jr.

Exploratory tests were performed on annealed and cold-worked type 316 stainless steel tubing in support of the fuel element modeling activity. The purpose was to gain some insight regarding the response of 316 stainless steel under conditions that are not being investigated elsewhere but are anticipated during start-up of a fast breeder reactor. Into this category fall: (1) low-strain-rate tensile conditions, which may result from fuel thermal expansion straining the cladding; (2) relaxation of thermally induced stresses; and (3) creep at high stresses under changing thermal and load conditions. For a "low-strength" heat of type 316

83. Consultant from the University of Tennessee.

84. B. R. Dewey, *Discrete Element Analysis of the Creep of Stainless Steel Tubing for LMFBR Application*, ORNL-TM-3294 (March 1971).

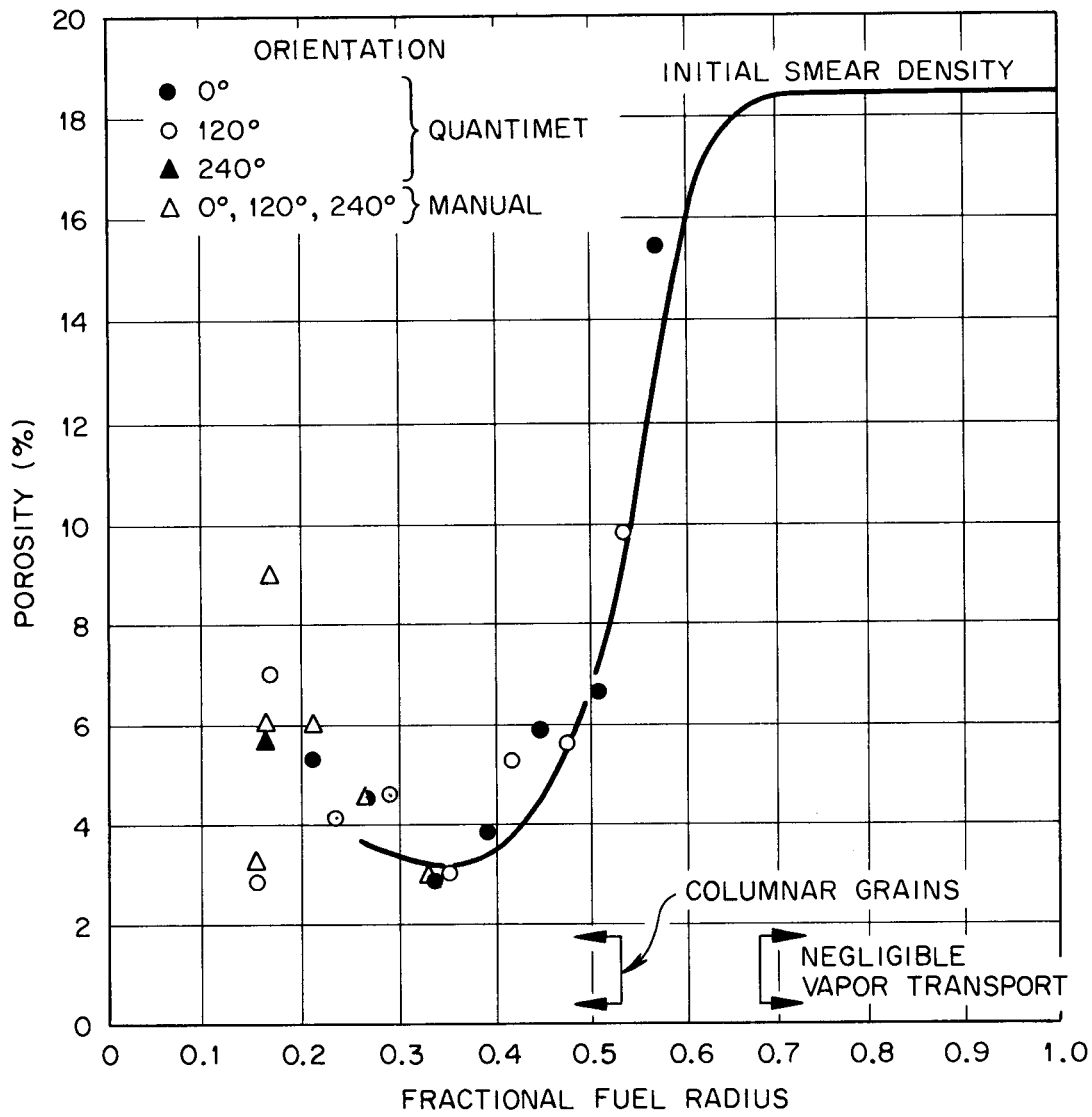
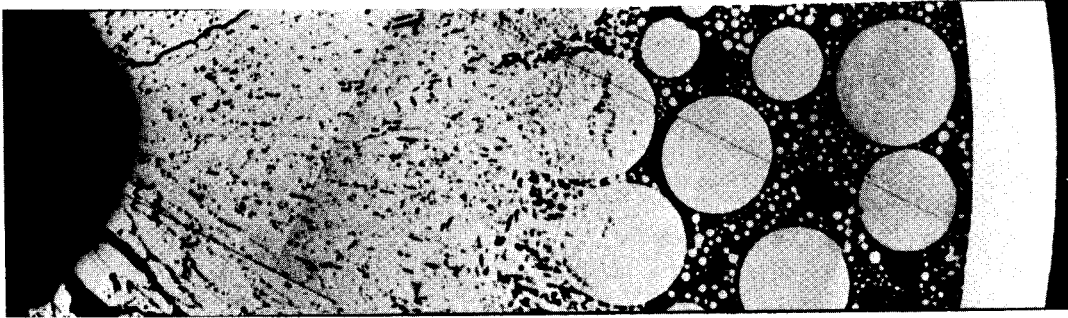


Fig. 13.12. Comparison of calculated and measured radial porosity distribution for $U_{0.85}Pu_{0.15}O_2$ irradiated at 13.6 kW/ft to 0.7% FIMA.

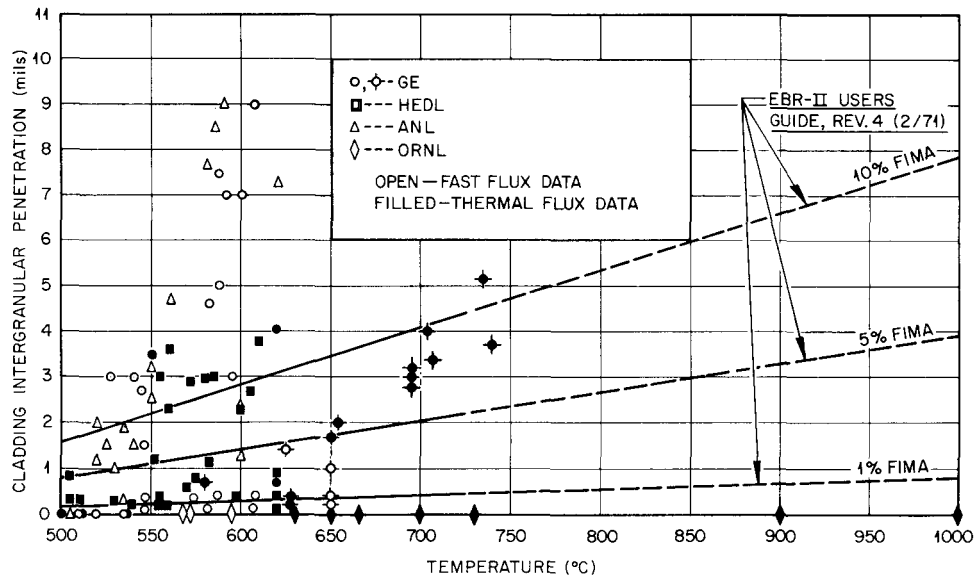


Fig. 13.13. Summary of fuel-cladding interaction data from stainless-steel-clad fuel pins.

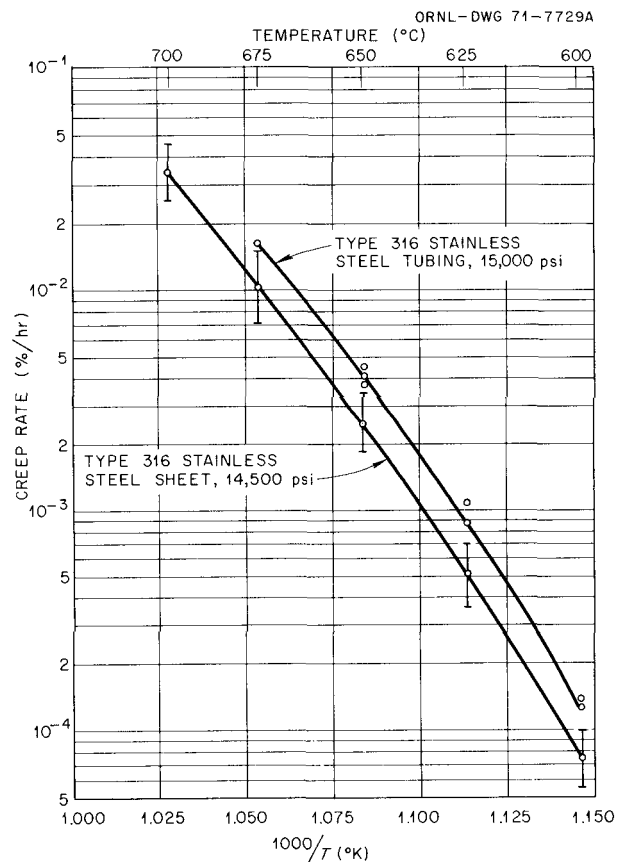
Fig. 13.14. Creep rate of type 316 stainless steel tubing under thermal cycling conditions.

stainless steel sheet, we found⁸⁵ little or no short-term influence of thermal and load cycling on the creep rate. We have extended testing to include $\frac{1}{4}$ -in.-diam \times 0.015-in.-wall tubing. The creep rates obtained from thermal cycling are compared for the two materials in Fig. 13.14. The thermal dependence of creep around 15,000 psi appears quite similar for these two materials. Strain or time has some effect on creep rate, but the time duration is of questionable significance since irradiation effects will probably dominate not long after startup of a reactor. Low-strain-rate tensile testing of annealed tubing has shown very little strain rate sensitivity.⁸⁶ However, we found significant relaxation in annealed tubing at 1100 and 1200°F. Curves are shown in Fig. 13.15. In contrast to annealed tubing, we found a significant strain rate effect on the tensile yield of cold-worked tubing.⁸⁷ Relaxation tests on this material are being planned.

85. R. W. Swindeman, *Metals and Ceramics Div. Annu. Progr. Rept. June 30, 1970*, ORNL-4570, pp. 71-73.

86. R. W. Swindeman, *Fuels and Materials Development Program Quart. Progr. Rept. March 31, 1970*, ORNL-4560, pp. 81-84.

87. R. W. Swindeman, *ibid.*, pp. 83-85.



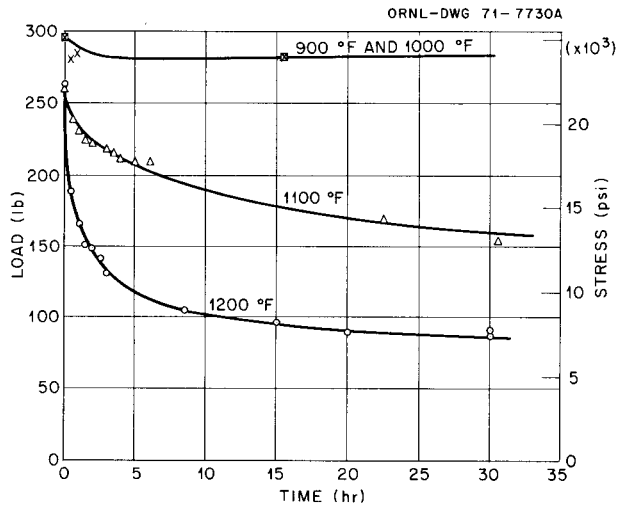


Fig. 13.15. Relaxation curves for annealed type 316 stainless steel tubing starting from 0.2% total strain.

14. Advanced Fast Breeder Reactor Fuels Development

J. L. Scott P. Patriarca

The goals of this program are to investigate the properties and behavior of those uranium- and plutonium-base ceramic fuels that we term conductors — such as the mononitrides, carbonitrides, and monocarbides — and to compare their potential as liquid-metal fast breeder reactor (LMFBR) fuel with that of (U,Pu)O₂, which by comparison is an insulator. Since the thermal conductivity of the ceramic conductors is about ten times that of (U,Pu)O₂, one could theoretically operate a conductor at ten times the power density with the same central temperature. In practice, heat transfer limitations, thermal stresses in the cladding, and high rates of swelling at high temperatures limit the power density to about two or three times that of (U,Pu)O₂ — still a challenging improvement. Additionally, the margins for transient overpower are much higher in the ceramic conductors than in (U,Pu)O₂.

To evaluate the true potential of these fuels, we need to define the structures, composition, and quality control required to achieve 150,000 MWd/metric ton at peak linear heat ratings of 30 to 50 kW/ft. We must also demonstrate the possibility of a low-cost fuel cycle for manufacturing fuel with the needed properties. Our work is oriented primarily toward demonstrating the irradiation performance of (U,Pu)N at high burnups and high heat ratings. Therefore, much of our effort is devoted to fabricating and characterizing fuel for irradiation testing.

Other work on nitride fuels is reported in Chaps. 6, 8, and 26.

IRRADIATION TESTING

T. N. Washburn

Thermal Flux Tests

The initial series of irradiation tests are two noninstrumented capsules of four pins each in the ETR. These “screening” tests are to determine the performance of nitride fuel synthesized from metal. The peak

linear heat rating is 30 kW/ft to burnups of 30,000 and 60,000 MWd/metric ton. The fuel is cold-pressed pellets with densities from 86 to 91% of theoretical, and the fuel pins have a 0.010-in. radial gap between the fuel pellet and cladding, filled with NaK-19 to enhance heat transfer.

Capsules 43-N1 and 43-N2 were neutron radiographed at TREAT before insertion into the ETR. The reactor went to full power on December 9, 1970; as of May 9, 1971, the capsules have operated for 102 effective full-power days to a burnup of approximately 2% FIMA.

Fast Flux Tests

E. J. Manthos M. K. Preston J. H. Erwin

Seven unencapsulated fuel pins, five for testing in the EBR-II and two spares, are being fabricated. The 19-pin subassembly will be shared with Battelle Memorial Institute, Columbus Laboratories. The ORNL fuel pins are described in Table 14.1.

Table 14.1. Characteristics of unencapsulated Fuel Pins for testing in EBR-II

Fuel	
Composition	(U-18% Pu)N
Enrichment, % ²³⁵ U	93
Pellet diameter, in.	0.260
Pellet density, % of theoretical	90
Cladding	
Material	Type 316 stainless steel
Outer diameter, in.	0.310
Wall thickness, in.	0.015
Cold work, %	20
Fuel Pin	
Smear density, % of theoretical	78
Sodium bond thickness, in.	0.010
Fuel column length, in.	13.5
Overall length, in.	40
Operating Conditions	
Linear heat rating, kW/ft	30
Specific power, W/g	220
Peak cladding temperature, °C	650
Fuel center-line temperature, °C	1050

FABRICATION OF (U,Pu)N FUEL

Fuel for EBR-II Tests

E. S. Bomar V. J. Tennery

We completed a campaign to synthesize and fabricate mixed nitride fuel for loading eight pins for irradiation in the EBR-II. This material consisted of 117 in. of fuel, 0.26 in. in diameter, weighing 1.36 kg, and fabricated into 413 pellets. Additional nitride fuel was produced for characterization and archives. The quantitative chemical and x-ray characterization data are given in Table 14.2. The microstructure showed a single mononitride phase. The fuel pellets were centerless ground in an inert atmosphere glove box to diameters of 0.260 ± 0.001 in. Also, 20 in. of high-purity UN was produced and machined for use as insulator material in the ends of the EBR-II irradiation pins.

Sintering Experiments on (U,Pu)N

V. J. Tennery E. S. Bomar

We confirmed the role of the nitrogen pressure in the sintering of compacts of (U,Pu)N by experiments with powders derived from uranium-plutonium alloy as well as those produced by mechanically blending UN and PuN powders. For the alloy-source nitride powders, sintering conditions corresponding to points A, B, C, and A', B', and C' shown on the phase diagram in Fig. 14.1 were selected. The samples were heated to the temperatures indicated, while the nitrogen pressure was maintained at the value shown. The $U_{0.81}Pu_{0.19}N$ samples were maintained at temperature for 300 min, then cooled to 1400°C , and the furnace was evacuated before further cooling to room temperature. The densities of the specimens after sintering are shown in

Fig. 14.2, and the sintering enhancement due to the reduced nitrogen pressure is clearly indicated.

Similarly, compacts made from mechanically mixed UN and PuN powders were sintered under conditions shown in Fig. 14.3, with the low P_{N_2} runs corresponding roughly to line "Y" and the higher pressure sintering runs corresponding to the line designated as "X." Two different UN powders were used to determine if variations in the sinterability of the UN powder significantly affected the densification of the UN-PuN blend.

The data for the densification of these mechanical mixtures are shown in Fig. 14.4. For the blend of UN

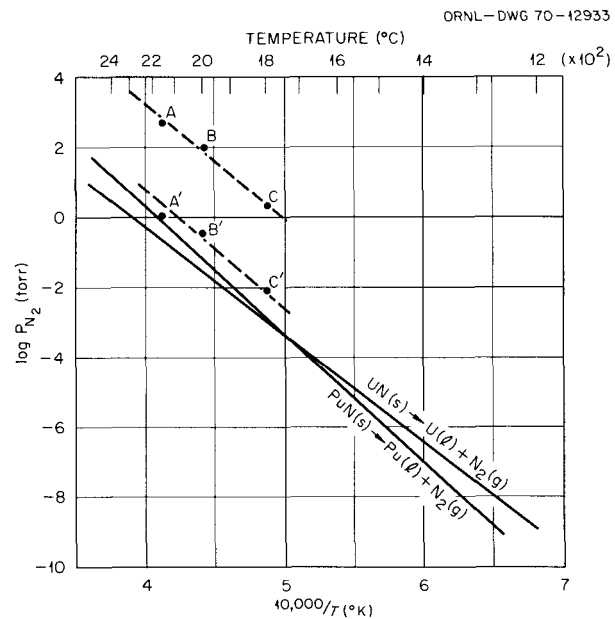


Fig. 14.1. Temperature-pressure conditions used for sintering $U_{0.81}Pu_{0.19}N$ specimens derived from alloy powders.

Table 14.2. Analytical chemistry and x-ray data for (U,Pu)N fuel for EBR-II irradiation study

Sample	Content (wt %)					Mass balance (%)	Lattice parameter (Å)
	U	Pu	N	O	C		
510	79.26	15.24	5.42	0.043	0.034	99.997	4.8905
570	79.23	15.30	5.40	0.040	0.043	100.014	4.8907
630	79.24	15.32	5.40	0.044	0.055	100.06	4.8911
690	79.49	15.20	5.42	0.040	0.030	100.18	4.8907
750	79.49	15.30	5.44	0.040	0.030	100.30	4.8905
809	79.49	15.34	5.46	0.050	0.020	100.36	4.8905
869	79.39	15.32	5.47	0.030	0.020	100.23	4.8906
926	79.39	15.16	5.44	0.020	0.020	100.03	4.8906
981	79.19	15.25	5.44	0.030	0.020	99.93	4.8908
1011	79.39	15.07	5.48	0.020	0.020	99.98	4.8907

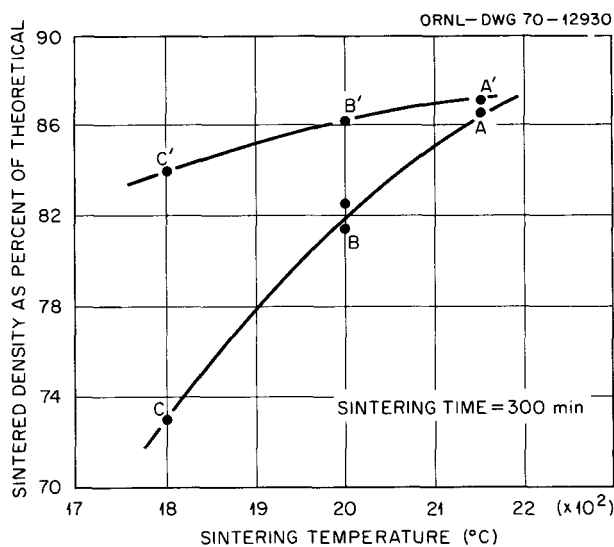


Fig. 14.2. Sintered densities of $U_{0.81}Pu_{0.19}N$ specimens sintered under conditions of Fig. 14.1.

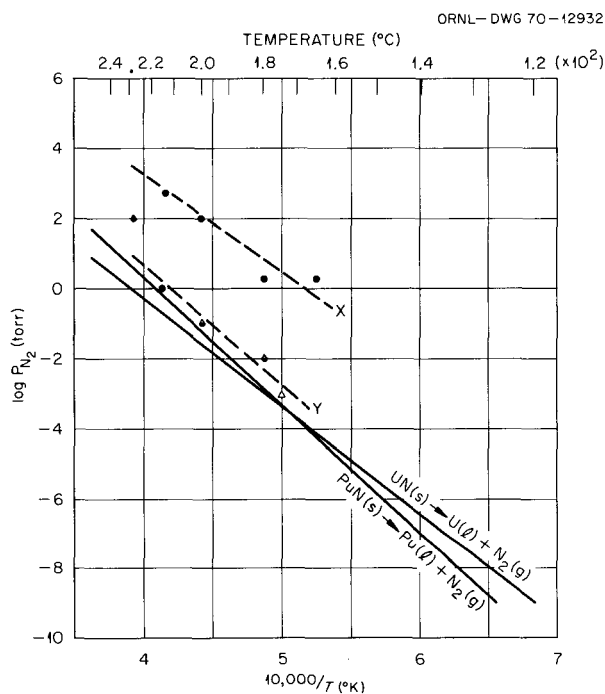


Fig. 14.3. Temperature-pressure conditions used for sintering $U_{0.80}Pu_{0.20}N$ specimens derived from mechanical mixtures of UN and PuN.

(4 + 5) and PuN (4) sintered along lines "X" or "Y," the sintered density was essentially a linear function of the sintering temperature. Again, sintering under lower nitrogen pressures improved the densification. In the case of the mechanical mixture of UN (3S-3) and PuN (4), the densification was a nonlinear function of the

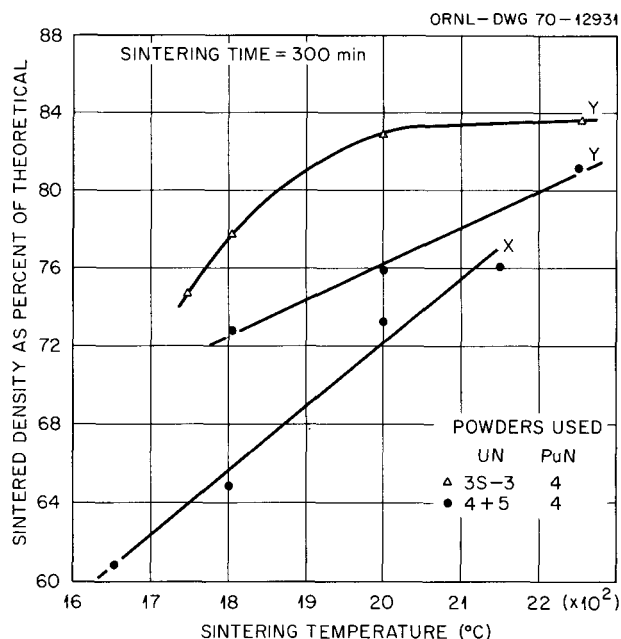


Fig. 14.4. Sintered densities of $U_{0.8}Pu_{0.2}N$ from mechanical mixtures of UN and PuN powders. Powder 3S-3 was finer than 4 + 5. Letters X and Y refer to sintering conditions in Fig. 14.3.

sintering temperature and achieved a limit about 84% of theoretical. In fact, all the mechanical mixtures approached a density about 84% of theoretical at the highest practical sintering temperature ($\leq 2300^{\circ}C$). The reason for these relatively low densities is evident in the microstructure of a sintered mechanically blended sample. Numerous large voids exist in the microstructure and are apparently at sites of the original PuN particles, and the presence of these low-density regions effectively limits the ultimate density that can be achieved in the sintered compacts.

CHARACTERIZATION OF (U,Pu)N

Analytical Methods for Determining Nitrogen in Mononitride and Sesquinitride Phases

V. J. Tennery J. L. Botts¹

The Kjeldahl method is the standard technique used in the FFTF program for nitrogen analysis of the oxide and nitride fuels. However, this technique characteristically gives significantly lower results when sesquinitride phases are present. Lindemer and Bradley² have shown that the use of nitrogen-hydrogen mixtures for reducing mixed oxides can result in the solution of

1. Analytical Chemistry Division.
2. T. B. Lindemer and R. A. Bradley, private communication.

nitrogen into the fluorite lattice and the subsequent precipitation of an M_2N_3 -type phase. Consequently, the dissolution step in the Kjeldahl analysis may result in low nitrogen values since the M_2N_3 phase is very difficult to dissolve in acids. When a mononitride phase is present the dissolution procedure used is of utmost importance if nitrogen losses are to be avoided before the distillation and titration steps of the Kjeldahl analysis.

We have compared the nitrogen values determined for a sample of $U_{0.8}Pu_{0.2}N$ using $HCl + HF$ and H_3PO_4 . The use of copper selenate in the dissolution was also investigated. The results obtained for a number of nitrogen determinations of (U,Pu)N are given in Table 14.3. The use of H_3PO_4 is superior. Copper selenate was unsatisfactory.

The Dumas method for nitrogen determinations has been found to be satisfactory for both mononitride and sesquinitride phases. Because the Kjeldahl method is unsatisfactory for samples containing the M_2N_3 phase, we assembled a Dumas facility and tested it by analyzing several uranium nitride samples, including UN and U_2N_3 . The sample is oxidized to release nitrogen gas, which is quantitatively collected and measured. This method is capable of analyzing the nitrogen in U_2N_3 phases as easily as mononitride phases since it does not depend upon dissolution. Typical results for

nitrogen as well as the other major elements are given in Table 14.4 for three samples. Obviously, sesquinitride phases can be analyzed readily for nitrogen by the Dumas technique.

The Lattice Parameter of (U,Pu)N Solid Solutions³

V. J. Tennery E. S. Bomar

Anselin⁴ reported that UN and PuN form a continuous solid solution of the NaCl structure and that the lattice parameter obeys a Vegard relationship.^{4,5} Considerable work has been reported⁴⁻¹⁰ on the lattice parameters of UN and PuN.

We measured the lattice parameters of the cubic solid solutions from the system $U_{1-x}Pu_xN$ at 25°C in samples in which the oxygen contents were measured at the time the x-ray specimens were prepared. The lattice constants and the analyzed chemical contents of the samples are given in Table 14.5. The composition dependence is shown in Fig. 14.5.

Table 14.3. Comparison of dissolution methods for $U_{0.8}Pu_{0.2}N$

Dissolution acid	Analyzed nitrogen ^a content (wt %)	Total nonmetal ^b content (wt %)
H_3PO_4	5.44, 5.45, 5.46	5.53
$HCl + HF$	5.14, 5.15, 5.01	5.24

^aTriplicate aliquots were analyzed as shown.

^bOxygen plus carbon content of sample was 0.093 wt %.

3. Paper presented at the Annual Meeting of the American Ceramic Society, Chicago, April 24-29, 1971. Published in *J. Amer. Ceram. Soc.* 54, 247-49 (1971).

4. F. Anselin, *J. Nucl. Mater.* 10, 301-20 (1963).

5. F. Anselin, *Preparation and Study of the Nitrides and Mixed Carbides Nitrides of Uranium and of Plutonium*, CEA-R-2988 (June 1966); ORNL-tr-1722.

6. J. M. Leitnaker, R. A. Potter, K. E. Spear, and W. R. Laing, *High Temp. Sci.* 1, 389-400 (1969).

7. P. E. Evans and T. J. Davies, *J. Nucl. Mater.* 10, 43-55 (1963).

8. R. Lorenzelli, *Contribution to the Study of the System (U,Pu)C,N*, CEA-R-3536 (May 1968); ORNL-tr-3019.

9. W. M. Pardue, V. W. Storhok, and R. A. Smith, pp. 721-38 in *Plutonium 1965*, ed. by A. E. Kay and M. B. Waldron, Chapman and Hall, London, 1967.

10. M. W. Shupe, R. L. Nance, and D. Kelley, *Nitrides, Advanced Plutonium Fuels Program*, LA-4284-MS (June 1969).

Table 14.4. Chemical analysis results for UN and UN_x phases

Sample	Dumas			Kjeldahl ^b			Content (wt %)			Percent mass balance ^d	Mole ratio ^d N + O + C/U
	Determinations	% N	% S ^a	Determinations	% N	% S ^a	U ^c	O	C		
Sintered UN	36	5.47	0.35	19	5.49	0.90	94.48	0.029	0.04	100.02	0.997
UN powder	17	5.46	0.34				94.44	0.049	0.04	99.99	0.000
UN_x	17	8.40	0.32				91.55	0.028	0.03	100.01	1.571

^a% S = relative standard deviation; % S = $100s/\bar{x}$, where s = standard deviation of a set and \bar{x} = mean of the set.

^bPhosphoric acid dissolution was used.

^cUranium was determined gravimetrically.

^dThe Dumas nitrogen results were used for this calculation.

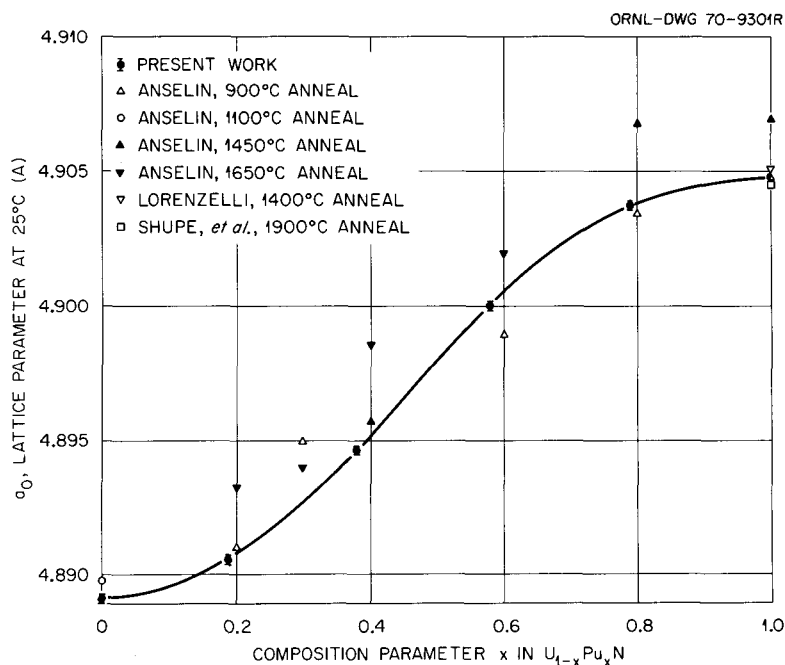


Fig. 14.5. Dependence of the lattice parameter of (U,Pu)N composition.

Table 14.5. Lattice parameters and chemical compositions of $U_{1-x}Pu_xN$ solid solutions

Composition ^a x	Lattice parameter ^b (a_0 at 25°C) (Å)	Element (wt %)					(N + C + O)/(U + Pu) ^f (mole ratio)
		Uranium ^c	Plutonium ^c	Nitrogen ^d	Oxygen ^e	Carbon ^e	
0.00	4.88920 ± 0.00017	94.45	0	5.41	0.09	0.030	0.998
0.19	4.89060 ± 0.00022	77.00	17.40	5.47	0.08	0.026	1.004
0.38	4.89470 ± 0.00015	58.60	35.90	5.45	0.05	0.020	0.999
0.58	4.90020 ± 0.00025	40.20	54.80	5.45	0.04	0.030	0.993
0.79	4.90380 ± 0.00013	21.35	73.10	5.30	0.04	0.020	0.968
1.00	4.90480 ± 0.00008	0	94.39	5.40	0.10	0.020	0.9972

^aUncertainty in x as a result of uncertainties in element determinations.

^bThe error is the standard deviation as computed by the machine.

^cUncertainty is ±0.3%.

^dUncertainty is ±5%.

^eUncertainty is ±10%.

^fAccumulated uncertainty in (N + C + O)/(U + Pu) is ±0.02.

Mercury Pycnometer Facility

J. P. DeLuca

The ability to determine the bulk density is of great importance and practical use in developing and characterizing a sintered ceramic nuclear fuel body. For this purpose we installed a mercury pycnometer in an inert atmosphere in a glove box to determine the bulk density of sintered pellets of (U,Pu)N and other plutonium-bearing ceramics.

The pycnometer is an improved version of an earlier design¹¹ and employs a precision hydraulic cylinder

and piston. The movement of the piston is measured by a micrometer, and the mercury pressure is shown on a digital display.

The sample chamber is approximately 1 cm in diameter × 1 cm high. The ultraprecision syringe can displace 2.5 cm³ of Hg, and the mercury pressure can be read to 1400 torr by a stainless steel diaphragm transducer. The electronic readout and control system

11. S. E. Dismuke, "Vacuum Pycnometer Using Mercury with Plunger Displacement for Hot Cell Use," pp. 37-39 in *Proc. 17th Conf. on Remote Systems Technol., 1969*, American Nuclear Society, Hinsdale, Illinois.

consists of the vacuum readout of the sample chamber, the mercury pressure readout, and the remote drive for the syringe. The system also includes a mercury vapor detector and filter to continuously monitor mercury vapor in the off-gas stream and remove it.

An analytical balance in the same glove box permits a complete density determination within the one box. The pycnometer was calibrated against steel balls of known volumes over a range typical of fuel pellets. The precision of the volume determination is $\pm 0.001 \text{ cm}^3$.

COMPATIBILITY OF CLADDING WITH NITRIDE FUELS

J. P. DeLuca J. M. Leitnaker

The compatibility of nitride fuels with candidate cladding alloys must be thoroughly investigated and understood if these fuel materials are to be considered seriously for use in LMFBR systems. The problem is complicated because of the several multicomponent cladding alloys under consideration and the important effects of burnup on the composition, constitution, and nitrogen activity of the fuel. Our approach is to investigate systematically the thermodynamics and kinetics of those interactions that are pertinent to the compatibility problem. Such interactions involve components of the fuel and cladding.

Phase Investigations in the Pu-Cr-N System

J. P. DeLuca J. M. Leitnaker

The solid-state phase behavior of the Pu-Cr-N system was investigated from 790 to 1700°C and over a hydrogen pressure range from 2.6×10^{-10} to 1 atm. A partial phase diagram of the system at 1 atm total pressure and 1700°C is shown in Fig. 14.6; Cr, Cr₂N, and CrN all form a two-phase region with PuN under the conditions investigated. No ternary compound was found as reported by Spear and Leitnaker¹² for the U-Cr-N system.

The heat treatments were carried out in an induction furnace that was installed in an alpha glove box. The samples were analyzed metallographically and with x rays.

Review of the Chromium-Nitrogen System

J. P. DeLuca J. M. Leitnaker

The known thermodynamic data in the chromium-nitrogen system were analyzed. The high-temperature

12. K. E. Spear and J. M. Leitnaker, "Phase Investigations in the U-Cr-N System," to be published.

ORNL-DWG 71-467R

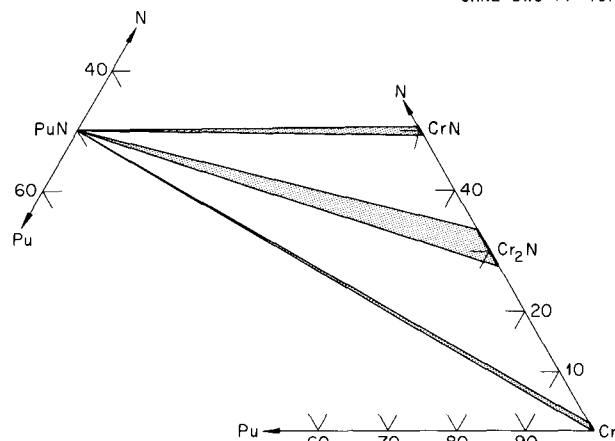


Fig. 14.6. Partial ternary phase diagram of the Pu-Cr-N system.

heat content measurements of Satoh¹³ were reevaluated, and the molar heat of Cr₂N was determined to be $15.05 + 6.58 \times 10^{-3} T$ (°K); that for CrN was $11.10 + 1.58 \times 10^{-3} T$ cal mole⁻¹ °C⁻¹. Using these heat capacities and an estimated $\Delta S_{298,f}^{\circ} = 20 \pm 1$ cal/°C per gram atom N for the formation of the two nitrides, second- and third-law calculations were made for all available vapor pressure data. Excellent agreement between the two calculations was found for Mills¹⁴ data. The third law ΔH_{298}° for the formation of Cr₂N from metal and nitrogen was -32.18 ± 0.05 kcal/mole Cr₂N, and the second-law calculation gave -31.51 ± 0.56 kcal/mole. For the formation of CrN from Cr₂N and nitrogen, the third law gave $\Delta H_{298}^{\circ} = -24.91 \pm 0.03$ kcal/mole of CrN, and the second-law calculation gave $\Delta H_{298}^{\circ} = -24.87 \pm 0.74$ kcal/mole. Because of this good internal consistency, Mills' data was taken to be the most reliable. A partial phase diagram of the chromium-nitrogen system was also prepared from all available data.

Compatibility of (U,Pu)N with LMFBR Stainless Steels, a Literature Review

J. P. DeLuca

We compiled the available data on compatibility experiments to determine whether compatibility problems exist between the nitrides and candidate claddings. Considerable work has been done on compatibility, both in and out of reactor.

13. S. Satoh, "The Heat of Formation and Specific Heat of Chromium Nitride," *Sci. Papers, Inst. Phys. Chem. Res. (Tokyo)* 34, 819, 1001 (1938).

14. T. Mills, *J. Less Common Metals* 22, 373 (1970).

Two major conclusions were drawn from the review. The first is that mixed nitrides and stainless steel can and do react at reactor temperatures. One needs to understand what controls the elemental activities to be able to prevent or limit nitriding of stainless steel in a reactor.

The second conclusion is that if nitride fuels are to be made on a large scale and if they are to be clad in commercial-grade stainless steel, a minimal oxygen contamination will have to be accepted, and an understanding of the quantitative effects of oxygen on the compatibility of mixed nitrides with stainless steel is important. Reports that conclude that the pure, stoichiometric, mixed nitrides are compatible out-of-reactor with low-oxygen-content stainless steel have taken only the first step. The second step should be the acquisition of enough information to allow one to determine and control what effect the associated impurities (C and O) will have on the compatibility of mixed nitrides with LMFBR claddings.

Thermodynamic Properties of Uranium Mononitride¹⁵

F. L. Oetting¹⁶ J. M. Leitnaker

The high-temperature enthalpy, $H_T^\circ - H_{298}^\circ$, of uranium mononitride has been determined from 298 to 1700°K by a copper block drop calorimeter of the isoperibol type. The experimental data may be expressed by the following equation:

$$H_T^\circ - H_{298}^\circ = 11.681T + 1.3291 \\ \times 10^{-3}T^2 + 9.812 \times 10^4/T - 3.930 \times 10^3$$

The heat capacity of uranium mononitride is expressed as

$$C_p^\circ = 11.681 + 2.6582 \times 10^{-3}T - 9.812 \times 10^4 T^{-2}$$

in the same temperature range. Combination with data at 298°K available from the literature made it possible to construct a table of thermodynamic functions for uranium mononitride. An evaluation of the published vaporization data on uranium mononitride combined with the present enthalpy data indicates that the $\Delta H_{f,298}^\circ$ of uranium mononitride is -70.6 ± 1.0 kcal/mole and the heat of vaporization of uranium metal is 128 ± 2 kcal/mole.

15. Submitted to *Journal of Chemical Thermodynamics*.

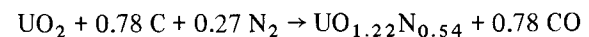
16. Dow Chemical Co., Rocky Flats, Colo.

Kinetic Studies of the Synthesis of Carbides, Carbonitrides, and Hypostoichiometric Oxides in the U-Pu-O-C-N System

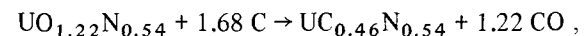
T. B. Lindemer

An attractive process for producing carbides, nitrides, and carbonitrides in the uranium-plutonium system is the carbothermic conversion of oxide-carbon mixtures produced by the sol-gel process. Consequently, the kinetics of the reactions are being studied to ascertain the mechanisms controlling the conversion; this information is then applied to the design parameters of specific conversion equipment. Particular kinetic studies reported¹⁷⁻¹⁹ during the last year include UC with N₂, UC₂ with N₂, and UO₂ with C, and the information was used to analyze the fluidized-bed conversion of oxide-carbon mixtures to fuel compounds in the U-Pu-C-N system.²⁰ The latter analysis was tested by converting 250 g of sol-gel U_{0.8}Pu_{0.2}O₂-C shards to (U,Pu)(C,N) in a fluidized-bed reactor. These shards were pressed and sintered into 89% dense, 0.63-cm-OD × 0.535-cm-long pellets that contained no second-phase compounds.²¹

A current kinetic study involves the simultaneous reaction of UO₂, C, and N₂ to produce U(C,N). This is being accomplished with oxide pellets, so that quantitative weight change and metallographic techniques can be used to follow the progress of the reaction. At 1700°C, with $P_{CO} = 10$ torr and $P_{N_2} = 380$ torr, the conversion is accomplished by two successive chemical reactions:



and



in which the UO_{1.22}N_{0.54} is a composition in a

17. J. M. Leitnaker, T. B. Lindemer, and C. M. Fitzpatrick, "Reaction of UC with Nitrogen from 1475° to 1700°C," *J. Amer. Ceram. Soc.* 53, 479-81 (1970).

18. T. B. Lindemer, J. M. Leitnaker, and M. D. Allen, "Kinetics of the Reaction of UC₂ and Nitrogen from 1500° to 1700°C," *J. Amer. Ceram. Soc.* 53, 451-56 (1970).

19. T. B. Lindemer, M. D. Allen, and J. M. Leitnaker, "Reply to 'Discussion of Kinetics of the Graphite-Uranium Dioxide Reaction from 1400° to 1765°C,'" *J. Amer. Ceram. Soc.* 53, 581 (1970).

20. T. B. Lindemer, "Rate Controlling Factors in the Carbothermic Synthesis of Advanced Fuels," *Nucl. Appl. Technol.* 9, 711-15 (1970).

21. T. B. Lindemer, *LMFBR Fuel Cycle Studies Progress Report for October 1970, No. 20*, ORNL-TM-3217, pp. 43-46.

solid-solution field that includes²²⁻²³ UO_2 . This sequence of reactions in the synthesis of U(C,N) has apparently never been reported. It is significant to note that UO_2 is converted to $\text{UO}_{1.22}\text{N}_{0.54}$ by the approximate replacement of each three atoms of oxygen by two of nitrogen and that the nitrogen present in the final U(C,N) appears to be incorporated in the system by the initial reaction.

PERFORMANCE CAPABILITY OF ADVANCED FUELS FOR FAST BREEDER REACTORS

T. N. Washburn J. L. Scott

We studied²⁴ the practical performance limits of $(\text{U,Pu})\text{C}$ and $(\text{U,Pu})\text{N}$ relative to that of $(\text{U,Pu})\text{O}_2$ for use in an LMFBR. The boundary limits of fuel performance are best shown on plots of specific power (W/g) against linear power (kW/ft). For $(\text{U,Pu})\text{O}_2$ fuels, as shown in Fig. 14.7, these boundaries form a triangle with borders of about 100 W/g minimum specific power, about 0.200 in. minimum fuel diameter, and a maximum linear power of about 12 kW/ft for the core

average or about 19 kW/ft for the highest rated fuel pin in which the fuel temperature would be near melting at the fuel center line. For $(\text{U,Pu})\text{C}$ and $(\text{U,Pu})\text{N}$ fuels, the minimum specific power and minimum fuel diameter are the same as for the oxides. However, the higher thermal conductivity of these advanced fuels permits linear powers to about 30 kW/ft core average and about 45 kW/ft for the highest rated pin, as shown in Fig. 14.8, when a sodium bond is used between the fuel and cladding to prevent excessive fuel temperatures and to provide space to accommodate fuel swelling. Also included are comparisons of the fuel performances specified in the LMFBR in follow-on studies²⁵⁻²⁹ to our more generalized study. There is substantial economic advantage in operating fuel at highly rated conditions, but a large amount of development work and irradiation testing must be performed with both the carbides and nitrides to permit an absolute comparison of their worth relative to oxides.

22. J. M. Martin, *J. Nucl. Mater.* 34, 81-85 (1970).
 23. R. Benz, G. Balog, and B. H. Baca, *High Temp. Sci.* 2, 221-51 (1970).
 24. T. N. Washburn and J. L. Scott, *Performance Capability of Advanced Fuels for Fast Breeder Reactors*, ORNL-TM-3388 (May 1971).

25. General Electric Company, *1000 Mw(e) Liquid Metals Fast Breeder Reactor Follow-On Study*, GEAP-5710, vol. 1.
 26. Atomics International, *1000 Mw(e) Liquid Metals Fast Breeder Reactor Follow-On Study*, AE-AEC-12792, vol. 1.
 27. Babcock and Wilcox Company, *1000 Mw(e) Liquid Metals Fast Breeder Reactor Follow-On Study*, BAW-1328, vol. 1.
 28. Combustion Engineering, *1000 Mw(e) Liquid Metals Fast Breeder Reactor Follow-On Study*, CEND-337, vol. 1.
 29. Westinghouse Electric Corporation, *1000 Mw(e) Liquid Metals Fast Breeder Reactor Follow-On Study*, WARD-2000-97.

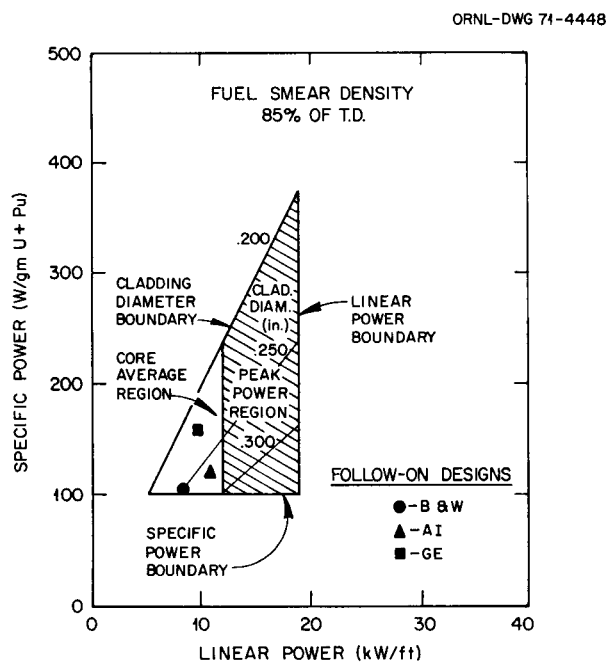


Fig. 14.7. Performance boundaries of stainless-steel-clad, helium-bonded $(\text{U,Pu})\text{O}_2$ fuel pins in an LMFBR.

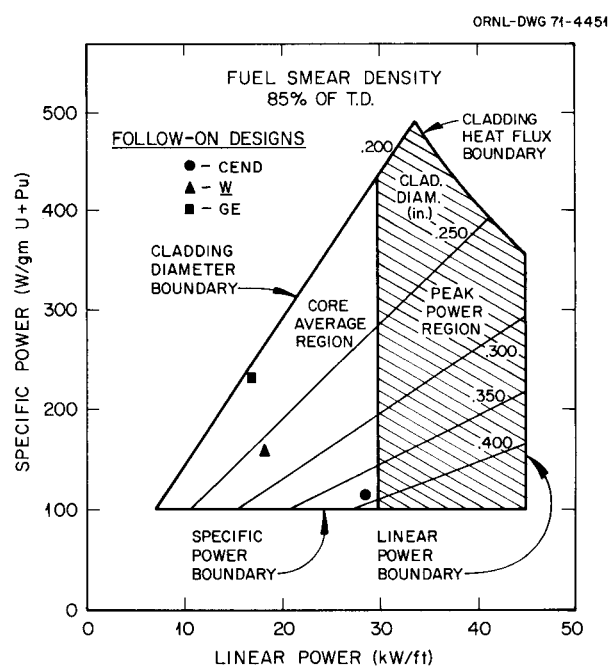


Fig. 14.8. Performance boundaries of stainless-steel-clad, sodium-bonded $(\text{U,Pu})\text{C}$ or $(\text{U,Pu})\text{N}$ fuel pins in an LMFBR.

15. Cladding and Structural Materials

J. R. Weir, Jr. H. E. McCoy, Jr.

This work is concerned with the development of suitable fuel cladding materials for LMFBR's. The cladding material chosen for the FFTF is 20%-cold-worked type 316 stainless steel. However, most of the data for material exposed to high fluences of fast neutrons has been for type 304 stainless steel, since it is used as a structural material in EBR-II. These data, although not directly applicable to FFTF, do contribute to the general understanding of austenitic stainless steels. A cladding material with better resistance to irradiation damage is needed. We have developed and are studying modified compositions of types 304 and 316 stainless steel with small additions of titanium.

High fluences of fast neutrons can cause two property changes of concern. The numerous atomic displacements can result in void formation and a density decrease. The dislocations and other defects produced by the displacements and the helium produced by transmutations can cause significant changes in the mechanical properties, a decrease in the fracture strain being of major concern.

SWELLING OF AUSTENITIC STAINLESS STEELS

E. E. Bloom J. O. Stiegler

The swelling that occurs in stainless steels during neutron irradiation has been shown to be a sensitive function of the irradiation conditions and of the microstructure and composition of the steel.¹ We are evaluating the effects of these variables by the use of quantitative transmission electron microscopy and immersion density measurements on a variety of materials irradiated in EBR-II and HFIR. Significant findings of

1. E. E. Bloom, *An Investigation of Fast Neutron Radiation Damage in an Austenitic Stainless Steel*, ORNL-4580 (August 1970).

work completed during the past year are described below.

Effect of Irradiation Temperature on Void Formation in Type 304 Stainless Steel

Previous work¹ has shown that in the range between about 370 and 500°C void concentration increases with increasing fluence, at least up to 7×10^{22} neutrons/cm². The mean void size increases with increasing irradiation temperature but is relatively insensitive to fluence, increasing as about the 0.15 power² of fluence. Maximum void sizes increase with increasing temperature, but not with fluence above about 5×10^{21} neutrons/cm² (ref. 1).

During the past year we found essentially opposite behavior in material irradiated at 590°C. Void concentrations saturated and void sizes increased with no evidence of the limiting void size found at lower irradiation temperatures. Void concentration measurements at 375, 465 and 590°C are shown in Fig. 15.1, and void size distributions for specimens irradiated to three different fluences at 590°C are given in Fig. 15.2. The latter figure shows that the void concentration increases very little on increasing the fluence from 2.25 to 3.5×10^{22} neutrons/cm² but that the distribution shifts to larger void sizes. The absence of voids smaller than 180 Å in diameter supports the contention that nucleation has ceased. Over the fluence range covered in Fig. 15.2 both maximum and mean diameters increased as the 0.5 power of fluence. This value is considerably higher than that observed at lower temperatures or in high purity aluminum.³ It is, however, in agreement with the model of diffusion-controlled growth of the

2. H. R. Brager et al., "Irradiation Produced Defects in Austenitic Stainless Steel," *Metallurgical Transactions* (to be published).

3. N. H. Packan, "Fluence and Flux Dependence of Void Formation in Pure Aluminum," *Journal of Nuclear Materials* (to be published).

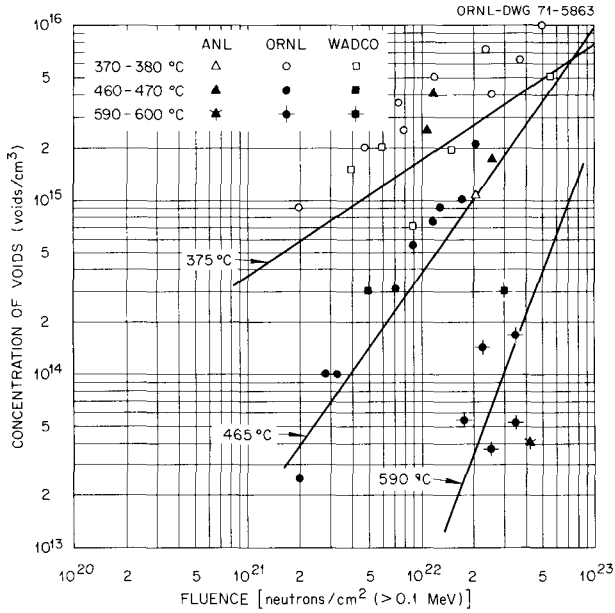


Fig. 15.1. Void concentration as a function of neutron fluence for annealed type 304 stainless steel irradiated at three temperatures. The solid lines represent the empirical equation developed by Brager et al.²

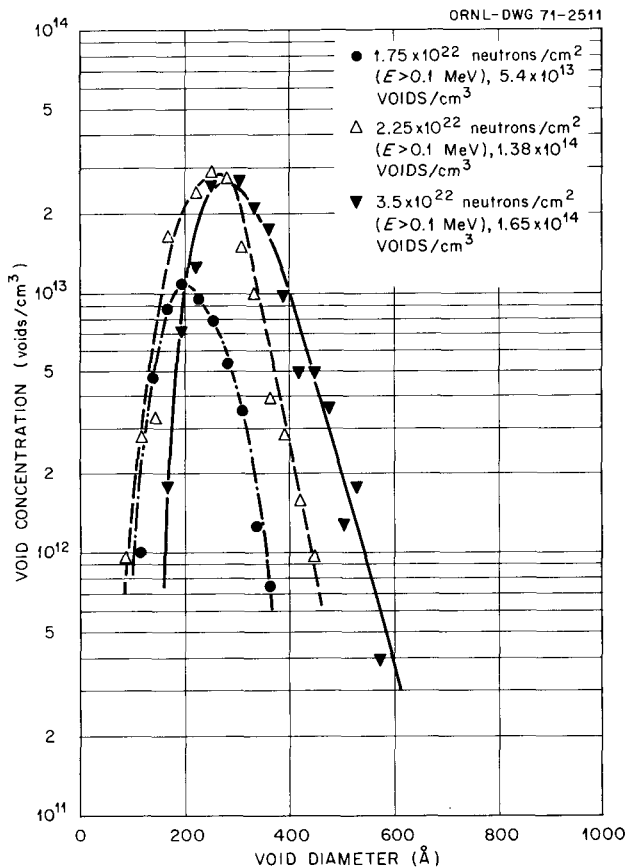


Fig. 15.2. Effect of fast neutron fluence on the void size distribution in annealed type 304 stainless steel irradiated at 590°C.

voids under conditions of constant vacancy supersaturation.⁴

On the logarithmic plot in Fig. 15.1 the slopes of the straight lines that can be drawn through the data points increase with irradiation temperature, from 0.66 at 375°C to about 5 at 590°C. The data may alternately be plotted on a linear scale. Then the slope decreases with increasing temperature, but the fluence intercept (threshold below which voids are not found) increases with increasing temperature. Threshold fluences for void formation are about 1×10^{20} neutrons/cm² at 375°C, 1.2×10^{21} neutrons/cm² at 465°C and 1.5×10^{22} neutrons/cm² at 590°C. Other observations indicate that the threshold may be composition sensitive.

Comparison of Standard and Titanium-Modified Type 316 Stainless Steel

Preliminary examination of specimens of annealed standard and modified (0.23% Ti) type 316 stainless steel have shown that the modified alloy swells significantly less than the standard material. Electron microscopy of specimens irradiated at 580°C indicate that the reason for the reduced swelling in the modified alloy is a large reduction in the concentration of voids. The concentration of voids in the standard steel is about 1×10^{13} , and all voids are associated with precipitate particles. The distribution of void sizes is bimodal, with large voids located on the large, blocky precipitate particles and smaller ones associated with the needle-like precipitate. No precipitate particles were found in the modified alloy, and the concentration of voids was less than 10^{12} /cm³. By comparison, the void concentration in standard type 304 stainless steel irradiated under these conditions would be about 1.8×10^{14} voids/cm³ (ref. 2), which further illustrates the strong dependence of the damage state on composition.

Dislocation structures also depend on composition. The standard steel contained Frank loops and a loose dislocation structure probably formed by glide and climb of loops that had unfaulted. Only a few faulted loops were found in the modified alloy. Small loops were observed in association with the dislocation structure.

Effects of Microstructure

We have already pointed out that at the higher irradiation temperatures voids were often associated

4. T. T. Claudson et al., "Fast-Reactor Radiation-Induced Changes in Cladding and Structural Materials," vol. 2, p. 165 in *Radiation Damage in Reactor Materials, proceedings of a Symposium, Vienna, June 2-6, 1969*, International Atomic Energy Agency, Vienna, 1969.

with precipitate particles and that specimens that contained fewer particles also contained fewer voids. In many of these cases the voids and precipitate particles both formed during the irradiation, and it is not clear which came first. We have found one clear example in which the voids nucleated on precipitate particles. For specimens of titanium-modified type 304 stainless steel, annealing 1 hr at 952°C following cold working produced a high density of coherent precipitate particles aligned in rows, as shown in Fig. 15.3(a). The microstructures after irradiation to fluences of 2.0 and 3.0×10^{22} neutrons/cm² at 590°C are displayed in Figs. 15.3(b) and 15.3(c). There is an obvious association of voids with the aligned noncoherent precipitate particles. Areas having high precipitate concentrations also have high void concentrations, and larger particles have larger voids attached to them. Apparently the voids nucleated at the sites of the original precipitate, although it is not clear whether this happened when they were coherent or noncoherent. The correlation between precipitate and void size indicates that the voids and precipitate grew simultaneously, suggesting that one or more of the elements present in the precipitate have been bound strongly to the vacancies and dragged to the void-precipitate complexes.

Swelling is also modified by the presence of a dislocation structure, but in a complex way. Cold worked materials show small but consistent increases in density during irradiation. Electron microscopy indi-

cates the presence of voids, which should contribute to a density decrease. The overall increase is evidently due to the overriding effect of densification as a result of precipitation reactions.

The swelling of heavily cold worked materials from void formation was appreciably less than that of annealed materials because of a large reduction in the concentration of voids; sizes were only slightly decreased. Different behavior was found in lightly deformed or recovered materials containing moderate dislocation densities, about 10^{10} /cm². Void concentrations were not affected, but void sizes were increased resulting in a greater overall swelling. This apparent anomaly can be rationalized by considering the roles of both the vacancies and the interstitials generated by the irradiation. Void formation is believed to occur because dislocations have a greater attraction for interstitials than vacancies and thus preferentially remove them from the system, leaving a net excess of vacancies available for void formation. Dislocation densities increase excessively in the annealed, recovered, and cold worked materials. In the cold worked material, dislocation densities are high enough that both vacancy and interstitial concentrations are depressed. In recovered materials the dislocations are far enough apart that they reduce interstitial concentrations but only slightly perturb the vacancy population. In annealed materials the grown-in dislocations are so far apart that they have little effect on the interstitial concentrations.

PHOTO 1087-71

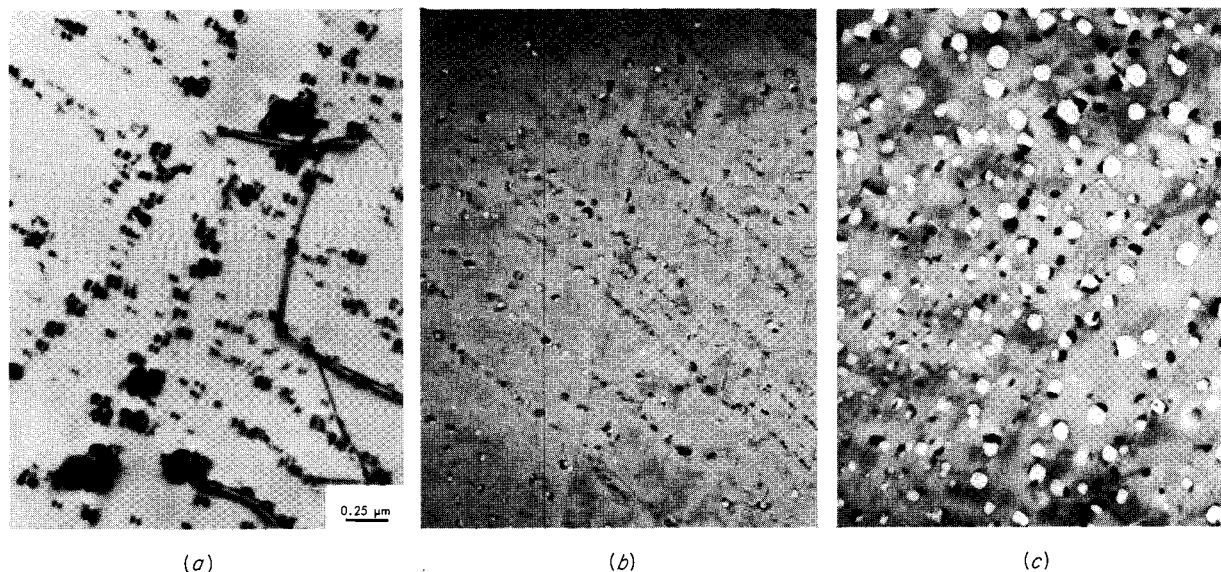


Fig. 15.3. Effect of irradiation at 590°C on the microstructure of titanium-modified (0.2% Ti) type 304 stainless steel. (a) Annealed at 925°C. (b) Irradiated at 590°C to 2.0×10^{22} neutrons/cm². (c) Irradiated at 590°C to 3.0×10^{22} neutrons/cm².

In the latter two cases the major interstitial sink is probably the radiation-produced dislocation structure. This interstitial sink is augmented enough in the recovered material to increase the net vacancy concentration, and it swells more than an annealed structure. It is not clear whether the reduced void concentrations in cold worked materials are due to the reduced vacancy concentration or to trapping of helium atoms on the dislocations and thus inhibiting void nucleation.

Effect of a Thermal Neutron Environment

Significant differences have been found in swelling between specimens irradiated in a fast reactor (EBR-II) and those irradiated in a thermal reactor (HFIR). For example, specimens of standard type 316 stainless steel irradiated in HFIR to a fluence of 2.9×10^{22} neutrons/cm² at 575°C swelled 3.9%, as measured by immersion density and confirmed by electron microscopy. In comparison, irradiation in EBR-II to a fluence of 2.7×10^{22} neutrons/cm² at 575°C resulted in a volume change of only 0.68%. Most, if not all, of this difference can be attributed to increased helium production in HFIR. Weitman, Däverhög, and Farvolden⁵ recently pointed out an anomalously high production rate of helium in nickel irradiated in a mixed fast-thermal spectrum. They suggested that a fast-neutron reaction produced an intermediate, short lived product that had a very high thermal neutron (n, α) cross section. This was verified in this experiment, in which 1800 at. ppm He was found in the sample irradiated in HFIR, compared with an expected 2 ppm for a comparable EBR-II irradiation. In the specimen irradiated in HFIR many of the cavities were found on grain boundaries, suggesting that they were helium bubbles rather than voids.

Composition also affected swelling in specimens irradiated in HFIR. The addition of 0.33% Ti to type 316 stainless steel reduced the swelling from 3.9 to 0.9%. A further increase of titanium content to 0.46% reduced the density decrease to 0.8%.

MECHANICAL PROPERTIES OF AUSTENITIC STAINLESS STEELS

E. E. Bloom	R. E. Gehlbach
J. O. Stiegler	D. Fahr

As discussed previously, the microstructural damage that is produced as a result of a given irradiation is a

function of the irradiation temperature and fast neutron fluence. Below about 350°C small defect clusters, a few tens of angstroms in diameter, are formed. Irradiation at 350 to 650°C produces voids and dislocations, and above 650°C the only visible damage is helium bubbles formed by the precipitation of (n, α)-produced helium. Precipitation of carbides and various intermetallic phases as well as recovery of dislocation structures, such as those introduced by cold work, occur as a result of aging at elevated temperatures. These processes may be accelerated and modified during neutron irradiation. The effects of irradiation on mechanical properties are thus sensitive to alloy composition, initial microstructure, irradiation temperature, fast neutron fluence, and irradiation time.

Type 304 Stainless Steel

The effect of irradiation on the yield strength and uniform elongation of annealed type 304 stainless steel is shown in Fig. 15.4.⁶ The specimens were irradiated and tested at approximately the same temperatures. The yield strength was increased by irradiation for temperatures up to about 650°C. The magnitude of the change is strongly sensitive to the irradiation temperature. Uniform strain was reduced over the entire temperature range. At 450°C the reduced uniform strain was primarily a result of the reduced ability of the material to strain harden, leading to plastic instability early in the deformation. At 750°C the stress-strain behavior of the material was unaffected, but the ductility was reduced by premature grain boundary fracture. These observations are in agreement with the microstructural observations. At 450°C a high density of irradiation-produced voids and dislocations caused a large change in stress-strain behavior (increased yield stress and reduced work hardening) and thus reduced uniform strain. As the irradiation temperature was increased the void and dislocation concentrations decreased and the changes in yield strength became less. At 750°C no displacement damage was observed, but helium bubbles were present in the matrix and at grain boundaries. For this condition the stress-strain behavior was essentially unaffected by irradiation. However, the ductility was reduced by premature grain boundary fracture, indicating grain boundary embrittlement due to transmutation-produced helium.

5. H. Weitman, N. Däverhög, and S. Farvolden, *Trans. Amer. Nucl. Soc.* 13, 577 (1970).

6. E. E. Bloom and J. O. Stiegler, "Effects of Fast Neutron Irradiation of the Tensile Properties of Austenitic Stainless Steels," pp. 768-72 in *Second International Conference on the Strength of Metals and Alloys, Conf. Proc.* vol. II, The American Society for Metals, Metals Park, Ohio, 1970.

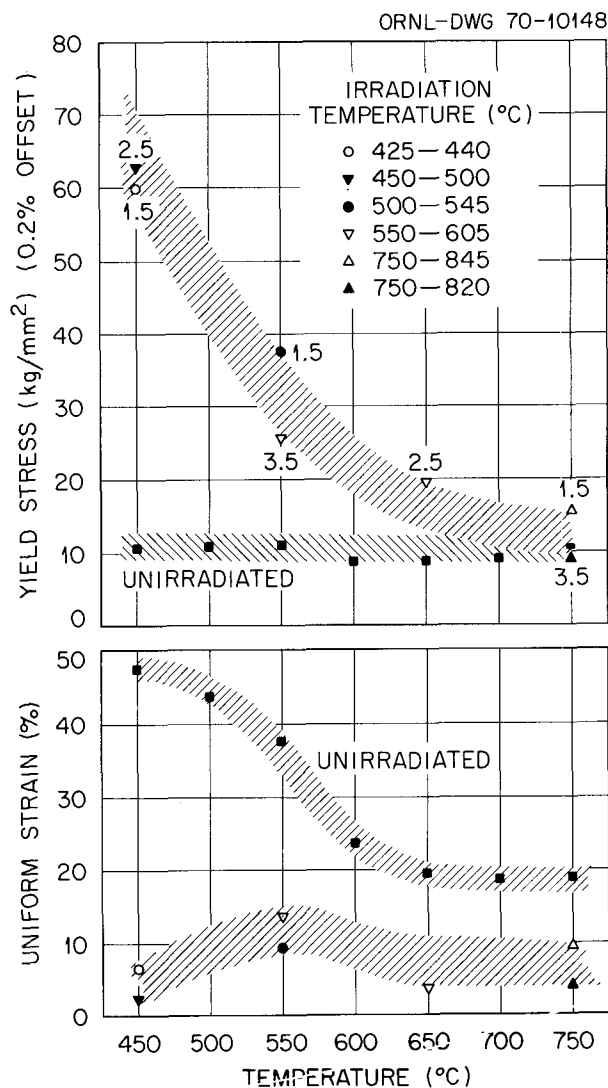


Fig. 15.4. Effect of fast neutron irradiation on the tensile properties of type 304 stainless steel when irradiated and tested at approximately the same temperature. The numbers by the points indicate the fast fluence in units of 10^{22} neutrons/cm².

The effects of irradiation on creep properties are of concern over the entire temperature range in the LMFBR. Below about 500°C the major process is radiation-enhanced creep. This phenomenon must of course be investigated during irradiation. Above about 500°C thermal creep processes are expected to dominate. Thus above 500°C postirradiation tests on samples irradiated at the test temperature can be used to estimate the in-reactor behavior of the material at the particular fluence in question. The effects of irradiation on the creep-rupture properties of annealed type 304 stainless steel irradiated to 1.5 to 3.5×10^{22} neutrons/cm² (>0.1 MeV) are shown in Fig. 15.5. At 550 and 600°C, irradiation to these fluences produced no

major change in the rupture life. Creep rates of the irradiated samples tended to be slightly lower than those of the unirradiated samples, with the effect being more pronounced at 550°C than at 600°C. The ductility, as measured by total elongation, was significantly reduced. At 704°C an increase in minimum creep rate was observed. This effect might result from the precipitation of carbon from solution during irradiation. The combination of increased creep rate and reduced ductility at high temperatures leads to a rather large reduction in rupture life.

Studies⁷ on material irradiated at 370 to 470°C to a range of fluences and then tested at 550 and 600°C have shown that for irradiation temperatures at which voids and dislocations are formed, the reductions in rupture life and ductility become more severe with increasing fluence. Scanning electron microscopy and optical metallography have shown that for these conditions the fractures are intergranular and that essentially no grain boundary cracks are formed along the gage section. It thus appears that a crack once initiated propagates rapidly to cause failure.

Type 316 Stainless Steel

Type 316 stainless steel is being investigated over a wider range of experimental variables than type 304 stainless steel because it is the cladding alloy for the FFTF. As already discussed, a high dislocation density such as that produced by cold working appears to reduce the swelling. Cold working also produces significant changes in the mechanical properties and in the phase transformation and precipitation reactions that occur in both unirradiated and irradiated material.

We identified the phases formed in both solution-treated (1 hr at 1050°C) and 20%-cold-worked samples during aging 4000 hr at 350, 450, 550, and 650°C. Very little precipitation is present after aging at the two lower temperatures and significantly greater amounts at 550 and 650°C. The $M_{23}C_6$ carbide and intermetallic compounds are formed in solution-treated material during aging at 550°C or above. Cold work before aging has a marked effect on precipitation. In 20%-cold-worked material the formation of the $M_{23}C_6$ carbide is drastically suppressed and sigma and laves phase are formed, particularly at 650°C.

7. E. E. Bloom and J. O. Stiegler, "Effect of Fast Neutron Irradiation on the Creep Rupture Properties of Type 304 Stainless Steel at 600 C," pp. 451-67 in *Irradiation Effects on Structural Alloys for Nuclear Reactor Applications, Spec. Tech. Publ. 484*, American Society for Testing and Materials, Philadelphia, March 1971.

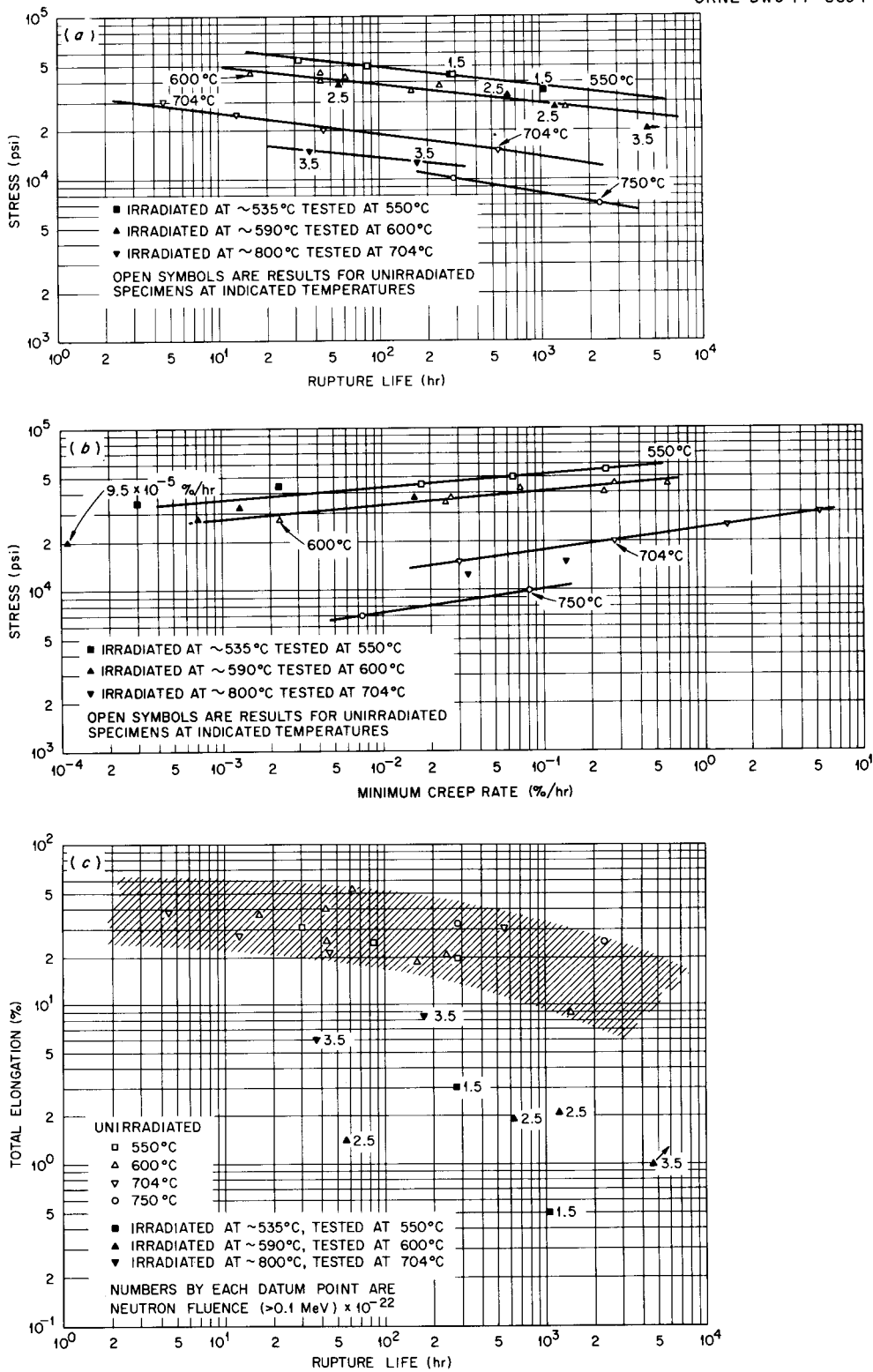


Fig. 15.5. Effect of fast neutron irradiation on the creep-rupture properties of type 304 stainless steel. (a) Rupture life, (b) minimum creep rate, (c) ductility.

When type 316 stainless steel is irradiated in the annealed condition the changes in tensile properties are similar to those discussed for annealed type 304 stainless steel. When the material is cold worked 20% the yield stress is increased and the elongation decreased over the range 350 to about 750°C, as

illustrated in Fig. 15.6. Aging 20%-cold-worked material for 4000 hr at 450, 550, or 650°C or irradiation in the range 450 to 750°C caused a reduction in yield stress, which became more pronounced with increasing temperature. The effects of irradiation on the ductility of 20%-cold-worked material are complex. At 450 to

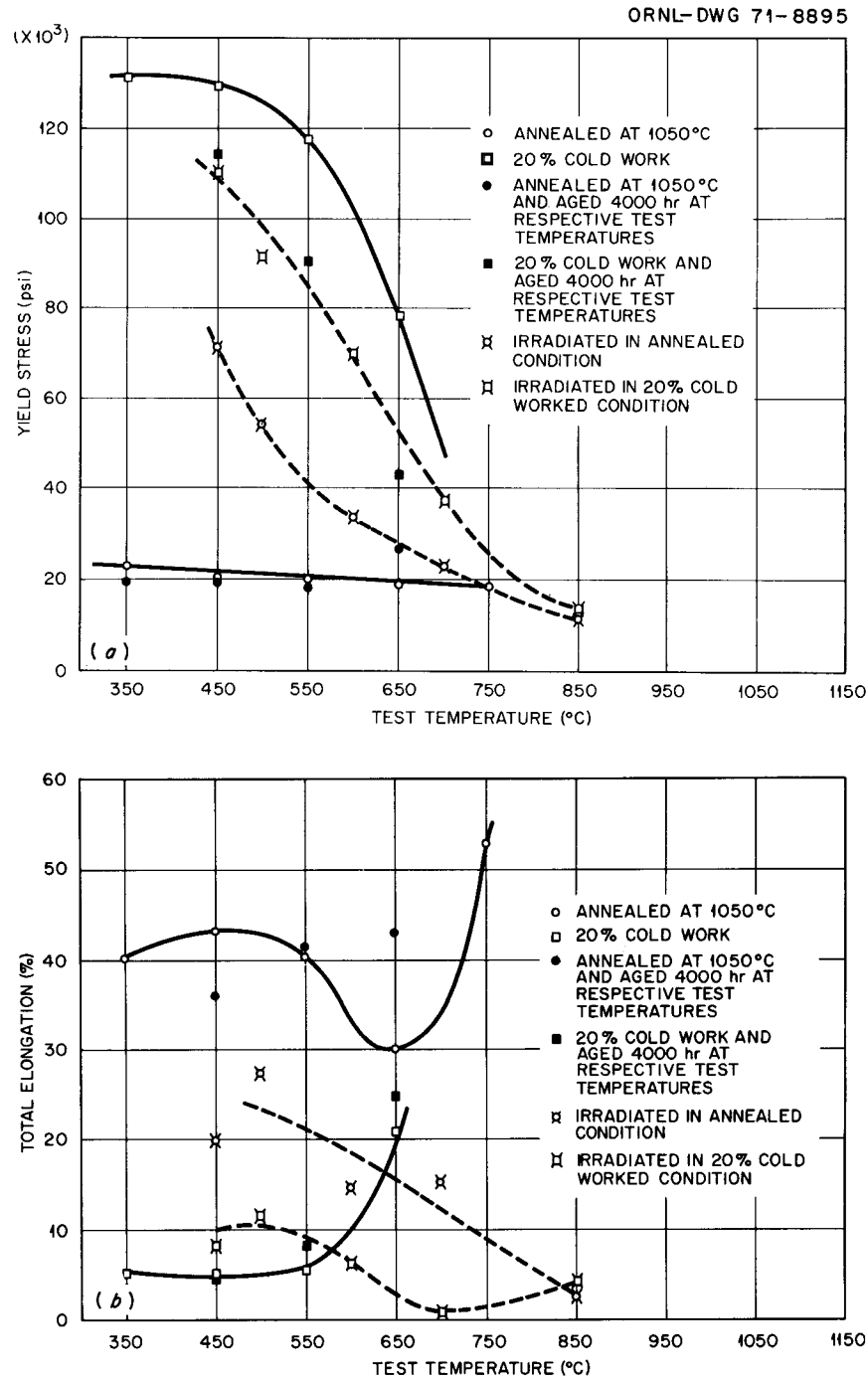


Fig. 15.6. Effect of thermal aging and irradiation on the tensile properties of annealed and 20%-cold-worked type 316 stainless steel. (a) Yield stress, (b) total elongation.

550°C and fluences of 1.5 to 2.3×10^{22} neutrons/cm² (>0.1 MeV) the postirradiation tensile ductility was actually higher than in the as cold worked condition, presumably because of recovery during irradiation. In the range 600 to 800°C the ductility was low and exhibited a minimum. Over this temperature range significant microstructural changes occurred. Some void and dislocation formation was observed in the range 600 to 650 or 700°C, significant recovery of the cold worked structure occurred at all temperatures, and above about 700°C some recrystallization occurred. Carbide precipitation and σ -phase formation occurred over the entire temperature range. These complex microstructural changes, acting in combination with the transmutation-produced helium, give the resultant properties.

The effects of irradiation on creep-rupture properties of annealed and cold worked type 316 stainless steel are being investigated. Initial results indicate that irradiation to a fluence of 2 to 3×10^{22} neutrons/cm² (>0.1 MeV) significantly reduces the ductility, with the most pronounced effects occurring in the range 550 to 650°C, where total elongations are generally in the range 1 to 5%.

Other Austenitic Alloys

Investigation of the effects of fast neutron irradiation on the properties of alloys that show promise as cladding and structural materials in LMFBR's has continued. Alloys included are titanium-modified types 304 and 316 stainless steel, type 318 stainless steel, SANDVIK 1272HV, and 19-9-DL.

The tensile properties of titanium-modified type 304 stainless steel after irradiation were measured. The strength properties do not differ significantly from those of standard type 304 stainless steel irradiated and tested under similar conditions.⁶ Ductility, as measured by uniform strain, total elongation, or reduction in area, is higher for irradiation and test temperatures above about 450°C. Figure 15.7 compares the total elongation of standard and titanium-modified type 304 stainless steel after irradiation in the EBR-II. The modified alloy had much greater elongation at test temperatures above 450°C.

The creep-rupture properties after irradiation have been measured. At 600°C, the rupture life of modified type 304 stainless steel was one-tenth that of the standard type 304 stainless steel irradiated at the same temperatures; its minimum creep rate was about ten times higher. These differences in strength properties were a result of the finer grain in the titanium-modified type 304 stainless steel (annealed 1 hr at 925°C before

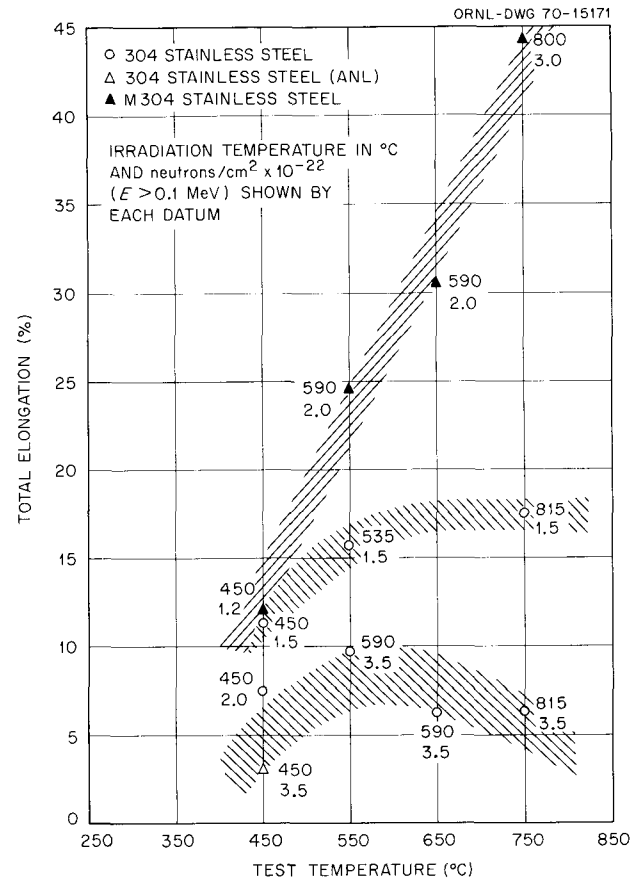


Fig. 15.7. Tensile ductility of standard and titanium-modified type 304 stainless steel after irradiation in EBR-II.

irradiation) as compared to the standard type 304 stainless steel (annealed 1 hr at 1050°C before irradiation). The ductility of the modified alloy after irradiation, in terms of elongation at the end of second-stage creep, total elongation, or reduction in area, was significantly higher than that of the standard type 304 stainless steel.

Metallographic examination of titanium-modified type 304 stainless steel, annealed 1 hr at 925°C, irradiated at about 590°C to 3.0×10^{22} neutrons/cm² (>0.1 MeV), and then tested at 600°C and 27,500 psi stress, was completed. The material strained about 11% before going into third-stage creep. Transmission electron microscopy of specimens removed from the stressed gage section revealed that a dislocation cell structure had formed, with the voids and precipitate particles acting as pinning points. Most significant was the observation by scanning electron microscopy that the specimen had failed in a very ductile, predominantly transgranular mode. This was compared to the brittle intergranular fracture of standard type 304 stainless steel. Irradiated titanium-modified type 304

stainless steel is significantly more ductile at temperatures where helium embrittlement predominates. The present results demonstrated that the improved ductility was retained under irradiation and test condition where both displacement damage (voids and dislocation structure) and helium affect mechanical properties, particularly ductility.

Similar differences in properties occur between standard and titanium-modified type 316 stainless steel. For all conditions where comparative data were available,

the titanium-modified alloy had significantly higher total elongation. At lower temperatures the modified alloy was also stronger. As the irradiation and test temperatures were increased, the differences in strength properties diminished. After holding for long periods of time at 600°C or higher the modified alloy may be somewhat weaker than the standard alloy because of a finer grain size and the precipitation of carbon from solution. Improved strength can be obtained if necessary by using a higher annealing temperature.

16. Fabrication Development of Fast Breeder Reactor Cladding

W. R. Martin

High-quality but economical tubing is required to meet the performance requirements for liquid-metal fast breeder reactors. Our goal is to develop methods of fabrication that meet the needs of the FBR. This program is currently concentrating on type 316 stainless steel.

EVALUATION OF PLANETARY SWAGING FOR PRODUCING HIGH-QUALITY CLADDING

G. A. Reimann

We have evaluated the planetary swaging process. Although it affords a unique method for producing tubing, certain characteristics of the technique restrict its application as a production tool for fabricating the quantity of high-quality cladding envisioned for the Fast Breeder Reactor.

Planetary swaging was most effective when limited to several light ironing passes to produce tubing of finished size. Dimensional control was precise and surface finish was superior. But the inherent slowness of the process at rates of 4 ft/min cannot compete with the higher rates obtained in conventional drawing. Planetary swaging frequently produces a surface with hardness values that correspond to 50% cold work while reducing the cross-sectional area of the tube only 20%.

Attempts to swage at higher speeds and heavier reductions to improve the economics produced surface defects in the tubing. The principal cause for such defects was the formation of a pronounced circumferential ridge just ahead of where the swaging balls first contacted the tube surface. The development of this ridge, shown in Fig. 16.1, was a major factor limiting the reduction obtainable from a single pass.

ULTRAFINE GRAIN SIZE TYPE 316 STAINLESS STEEL TUBING

G. A. Reimann A. C. Schaffhauser

Using the successful procedures developed previously¹ to obtain a fine grain size (ASTM 14) as a base,

we have attempted to refine that grain size to ASTM 20. A powder metallurgy approach using small-diameter atomized type 316 stainless steel powder was not successful. Temperatures required to sinter the product increased the grain size of the starting product. Oxide particulates from the surface of the atomized powders did not restrict grain growth. Additionally, the presence of some large particles caused microcracking in the alloy at high levels of cold work.

ELEVATED-TEMPERATURE DRAWING

G. A. Reimann

Type 316 stainless steel was successfully drawn at temperatures within the range 200 to 760°C with carbide plugs and dies. Deformations equal to a 40% reduction in cross-sectional area were completed without intermediate heat treating. Surfaces of the tubing produced would require chemical or mechanical treatment to meet the quality level now specified for reactor tubing. This method of drawing develops, particularly at 760°C, a fine cellular dislocation structure that may result in improved properties.

GENERATION AND EVALUATION OF ARTIFICIAL DEFECTS

W. R. Martin

As-Machined Notch Studies

K. V. Cook R. W. McClung

The purpose of the as-machined notch study is to produce flaws of various sizes by electro-discharge machining in type 316 stainless steel tubular specimens for mechanical property testing. Notches such as these are normally used to establish test sensitivity for both ultrasonic and eddy-current tests and are as narrow as we can machine them at the present time (0.0023 in.).

1. G. A. Reimann, *Metals and Ceramics Div. Annu. Progr. Rept. June 30, 1970*, ORNL-4570, p. 86.

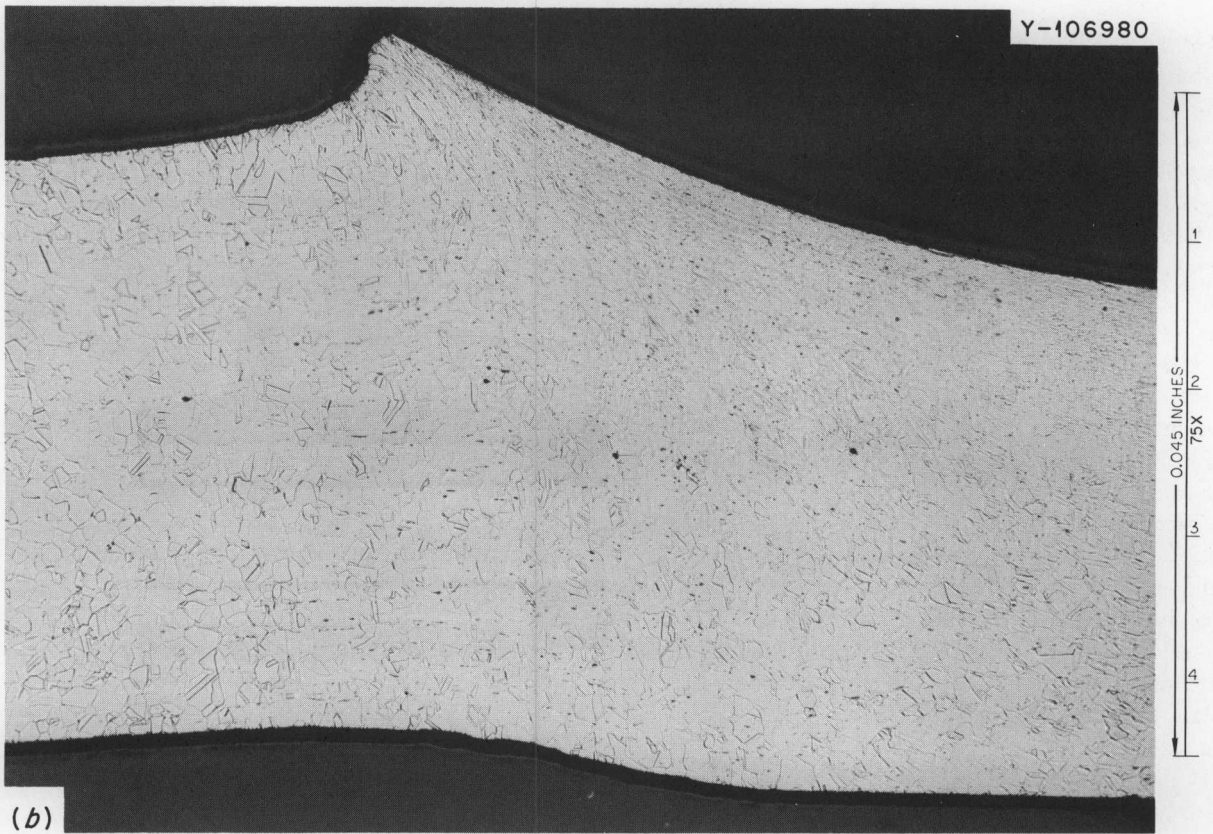
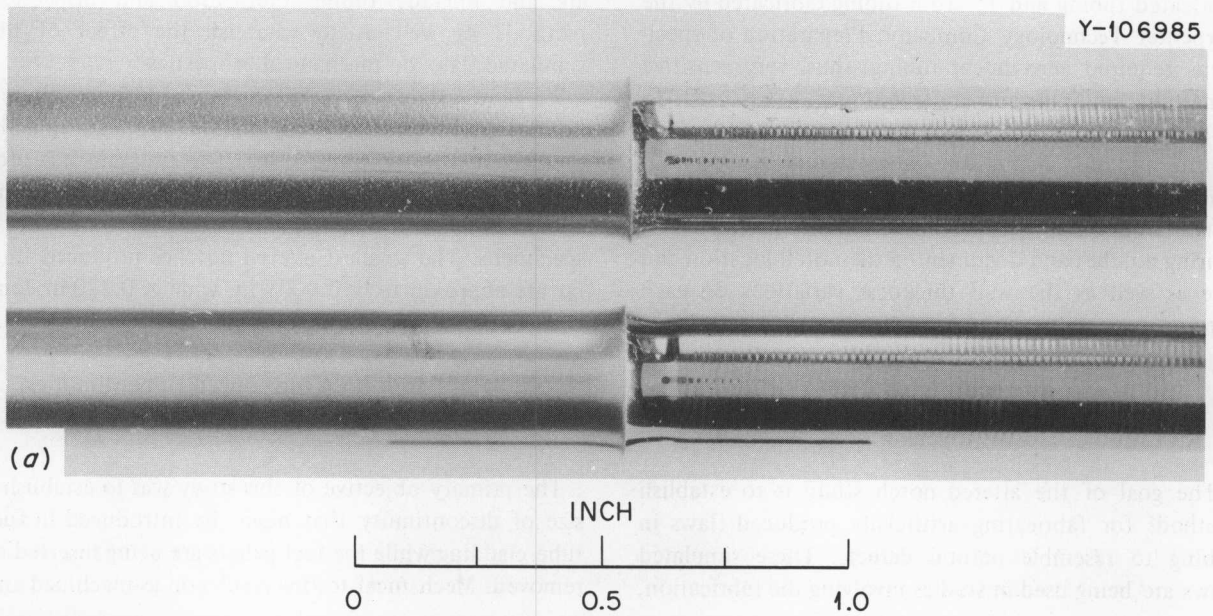


Fig. 16.1. Circumferential ridge formed by subjecting tubing to "heavy" reductions by planetary swaging. (a) Partially planetary swaged tubes. (b) Cross section at the ridge. 75X. Etch: HCl, HNO₃, H₂O.

We prepared approximately 120 samples from ORNL-fabricated tubing and 15 from tubing fabricated by the Carpenter Technology Company. Preparation of specimens required zero-defect tubing; thus, very sensitive penetrant and ultrasonic techniques were used to inspect the material. Following the nondestructive testing and documentation, we selected, labeled, and marked the 4-in.-long sections for the burst specimens. After sectioning, we machined those specimens requiring notches and documented the notch location and size as well as the wall thickness variations on each specimen.

Altered Notch Studies

K. V. Cook G. A. Reimann R. W. McClung

The goal of the altered notch study is to establish methods for fabricating artificially produced flaws in tubing to resemble natural defects. These simulated flaws are being used in studies involving the fabrication,

inspection, and mechanical properties groups to evaluate and upgrade tubing fabrication and inspection methods as well as to establish the effect of the simulated flaws on mechanical properties.

We have established procedures to produce altered notches in drawn or sunk tubing and can reliably predict final notch dimensions. The program has produced enough ORNL-fabricated tubing, containing altered notches, to supply approximately 30 tube burst specimens. The smallest altered notches produced thus far are approximately 0.0001 in. wide \times 0.270 in. long \times 0.0018 in. deep, as shown in Fig. 16.2.

Study of Fabrication-Introduced Discontinuities

K. V. Cook

The primary objective of this study was to establish a size of discontinuity that might be introduced in fuel tube cladding while the fuel pellets are being inserted or removed. Mechanical testing results on as-machined and

ORNL-DWG 70-13052

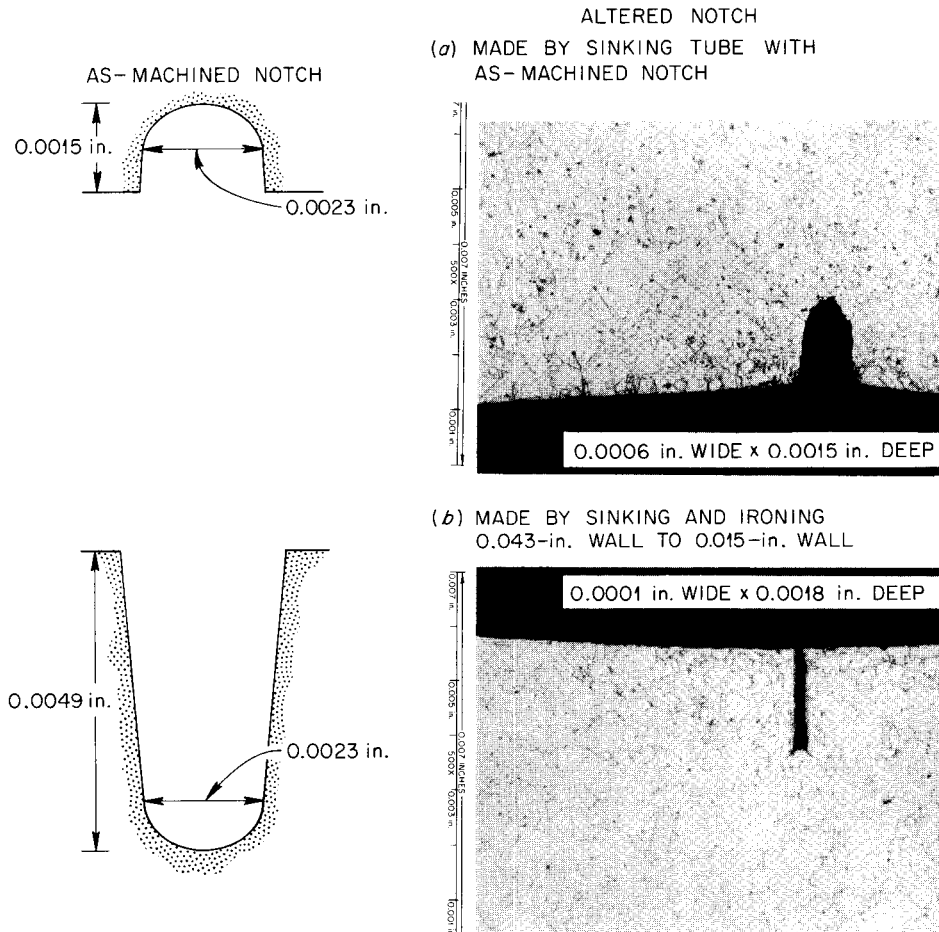


Fig. 16.2. Representation of as-machined notch and the altered notch in type 316 stainless steel.

altered EDM notches should establish the importance of such discontinuities induced during loading of the fuel.

A 0.230-in.-OD \times 0.015-in.-wall type 316 stainless steel tube fabricated by the Carpenter Technology Company was selected for this study. The tube had been purchased in accordance with FFTF specifications, which required ultrasonic inspection using a 0.001 in. deep \times 0.030 in. long EDM reference notch. We ultrasonically tested the tube using such a notch to confirm the integrity before fuel loading. After fueling and introducing scratches, the tube was rechecked in the ultrasonic inspection setup. The deepest scratch detected was 0.0002 to 0.0003 in. A metallographic cross section of this scratch confirmed the depth measurement and established that the defect was about 0.002 in. wide.

CREEP RUPTURE OF TYPE 316 STAINLESS STEEL TUBING WITH ARTIFICIAL DEFECTS

R. T. King G. A. Reimann K. V. Cook

Previous investigators^{2,3} have recommended that the maximum defect depth allowed in stainless steel nuclear-grade tubing be 10% of the tube wall thickness, basing their conclusion on short-term tests of tubes containing artificial or natural defects. We are attempting to learn whether these conclusions are applicable to 0.23-in.-diam \times 0.016-in.-wall-thickness type 316 stainless steel tubing, which is the proposed fuel cladding for liquid-metal fast breeder reactors.

Tubing fabricated from one heat of type 316 stainless steel was ultrasonically inspected to guarantee that no natural flaws existed in 4-in. specimen lengths of 20% cold-worked material. Longitudinal notches 0.0025 in. wide were then electro-discharge machined into either the inner or outer surfaces of some of these tubes; the notch depths were about 10, 33, and 66% of the tube wall thickness, and the notches were machined to 0.030- or 0.250-in. lengths. The notches were machined on the thin side of the tube wall, whenever thickness variations were found. Some of the tubes were then annealed at 925°C for 1 hr in hydrogen, while others were left in the cold-worked condition. Creep-rupture tests were performed in He-1% O₂ at 650°C at stresses that caused rupture after a few tenths of an hour to several hundred hours. The results for 20% cold-worked

2. R. F. Kirby, *Evaluation of 300 Series Stainless Steel Tubing for Fuel Cladding*, GEAP-4095 (October 1962).

3. T. Lauritzen, A. Montes, and A. Conti, *The Influence of Surface Defects on the Short-Term Mechanical Properties of Austenitic Stainless Steel Tubing*, GEAP-13550 (December 1969).

tubing containing notches may be summarized as follows.

1. Notches accelerate the intergranular fracture process in the metal beneath the notch, reducing the rupture lifetime of the tubing (see Fig. 16.3) and the amount of circumferential strain that occurs before failure.
2. Within the limits of experimental error, the detectable effects of notches on the inner and outer wall are the same.
3. As notch length increases, the notches become more detrimental to properties, because the constraint provided by the rest of the tube decreases with increasing notch length.
4. Both rupture time and strain decrease with increasing notch depth.

The results for annealed tubing presently available indicate the following.

1. Notches of depth equal to about 10% of the wall thickness of annealed tubing cause less reduction in the rupture time or circumferential fracture strain than in cold-worked tubing.
2. Notches of depth equal to about 33 and 66% of the wall thickness seriously reduce both the rupture time and circumferential fracture strain of annealed tubing.

These significant differences in the behavior of annealed and cold-worked tubing are compelling reasons for reexamining the inspection standards of stainless steel fuel cladding materials. Other factors that may be important but which have not yet been investigated include the test environment, the test temperature, the notch geometry or origin, and the combination of irradiation and defect effects on cladding properties.

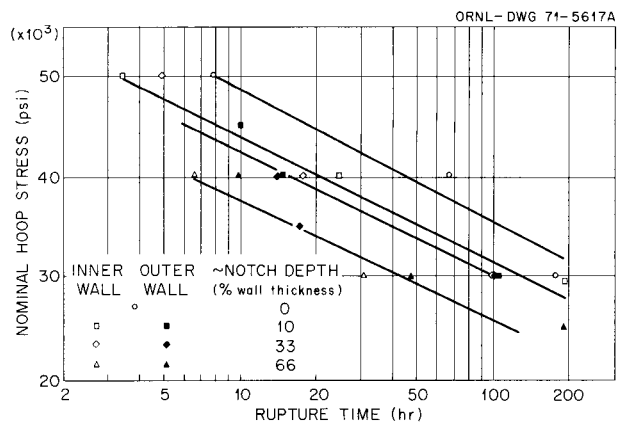


Fig. 16.3. Effect of notches on the rupture times of cold-worked type 316 stainless steel tubing tested at 650°C in He-1% O₂.

17. Welding Development

G. M. Slaughter

The LMFBR welding development program is concentrated on two types of materials, austenitic stainless steels and ferritic steels.

STAINLESS STEEL

G. M. Goodwin N. C. Binkley
N. C. Cole R. G. Berggren

We are studying the effect of both welding process and variables within a process on the behavior of weldments in austenitic stainless steels at 370 to 650°C for application to LMFBR vessels and components. The solidification substructure (the structure in its finest microscopically resolvable detail) markedly influences the mechanical properties of a weldment at elevated temperatures. Since the size and type of substructure in a weldment are significantly influenced by factors that the welding operator can control, we determine the effects of composition, individual welding process, and the welding variables (current, voltage, travel speed, etc.) on the observed microstructure and, subsequently, on elevated-temperature mechanical properties. In all instances, highly pedigreed materials are used, and all of the variations in composition are within allowable specifications. The effects of postweld heat treatment and neutron irradiation are also investigated.

We reviewed the published data concerning the elevated-temperature mechanical properties of austenitic stainless steel weldments. Little information was available, and it showed a high degree of scatter, particularly in ductility.¹ For type 347 stainless steel weld metal, for example, the total elongation values from stress-rupture tests at 650°C, plotted as a function of rupture life, show an essentially random pattern. Most of the total elongation values are less than 10%, and many are 1% or less. Thus, our welding programs were undertaken to augment the meager literature data and to determine the individual effects of some of the variables that we feel are responsible for the above

situation, such as changes in welding input parameters and minor composition variations. The information generated in these programs was influential in the selection of a "controlled residual element" filler metal for the Fast Flux Test Facility (FFTF) vessel, and characterization studies indicate that this filler metal possesses superior strength and ductility.

Submerged-Arc Process

We are investigating the effects of variations in welding parameters and minor compositional changes due to flux composition variations for the submerged-arc process. Eleven different weldments are included in the study, each having an intentional variation in either welding parameters or flux composition. Figure 17.1 shows stress plotted against rupture life for submerged-arc weldments at 650°C. The upper scatter band represents literature data for type 304 stainless steel base material. Note that the weld metal is generally weaker than base metal, with only a few weld metal data points falling within the base metal scatter band. Figure 17.2 shows total elongation plotted against rupture life for the same tests shown in Fig. 17.1. Note the relatively high degree of scatter, but the total elongation values are generally greater than 10% and there is only a moderate trend toward decreasing ductility with increasing rupture life. These results will be compared in the next section with those for the shielded metal-arc process.

Shielded Metal-Arc Process

Our objective is to determine the effects of electrode coating variables on the shielded metal-arc (stick electrode) welding process. We are comparing the substructures and elevated-temperature mechanical properties of 23 shielded metal-arc weldments made with type 308 stainless steel electrodes.² Included are the three most

1. G. M. Goodwin, *Fuels and Materials Development Program Quart. Progr. Rept. Sept. 30, 1969*, ORNL-4480, pp. 105-8.

2. N. C. Binkley, G. M. Goodwin, and D. G. Harman, *Fuels and Materials Development Program Quart. Progr. Rept. Dec. 31, 1969*, ORNL-4520, pp. 165-72.

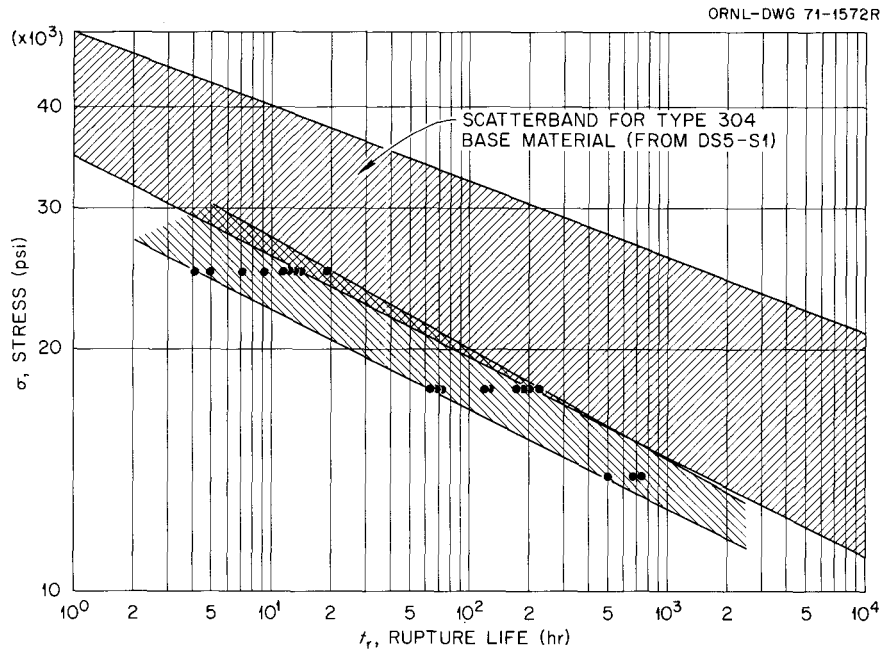


Fig. 17.1. Stress plotted against rupture life for type 308 stainless steel submerged-arc welds at 650°C.

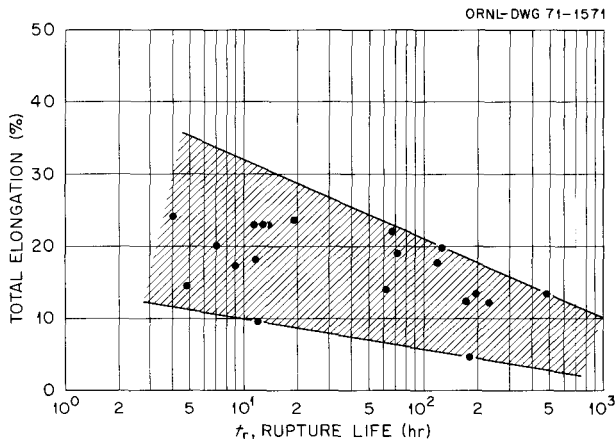


Fig. 17.2. Elongation in stress-rupture tests of type 308 stainless steel submerged-arc welds at 650°C.

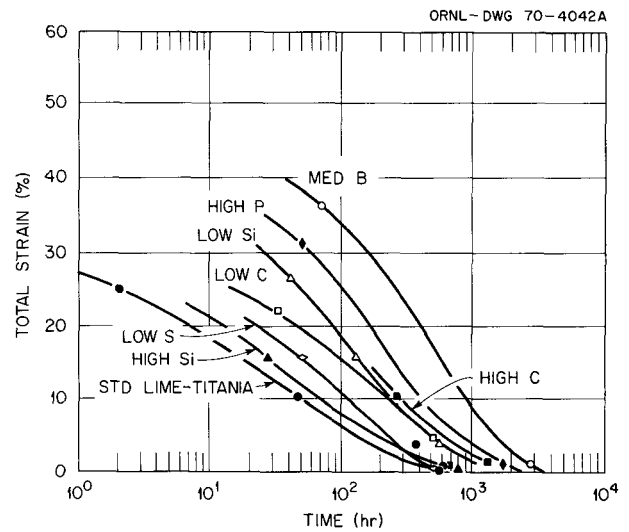


Fig. 17.3. Effect of composition on the creep ductility of shielded metal-arc welds at 650°C.

popular electrode coatings produced by a commercial supplier: lime, titania, and lime-titania. The last mentioned is the most widely used, and we are studying the effects of minor changes in C, Si, P, S, and B contents of the electrode coating and subsequent deposited weld metal (deposit composition is within the allowable type 308 composition limits in all cases). Significant variations in creep strength and ductility were observed. Figure 17.3 shows total elongation plotted against rupture life for a series of weld metals. Note that what

appears to be a broad scatter band of ductility values can now be resolved into a family of curves for the individual weldments. Although some of the individual weldments show decidedly superior ductility, all show markedly decreasing ductility with increasing rupture life at 650°C.

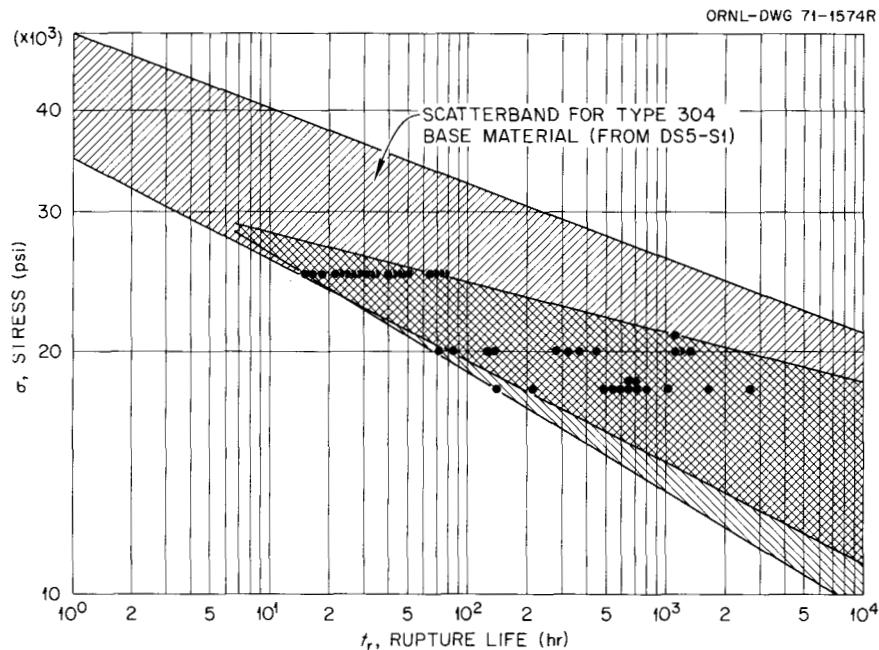


Fig. 17.4. Stress plotted against rupture life for type 308 stainless steel shielded metal-arc welds at 650°C.

Based on these initial test results, several heats of "second-generation" weld metal were produced containing controlled amounts of certain beneficial residual elements — namely, boron and phosphorus. Additional testing showed these filler metals to have superior strength and ductility and led to the selection of an optimized "controlled residual element" filler metal for the FFTF vessel.

Figure 17.4 summarizes the stress vs rupture life data for shielded metal-arc welds at 650°C. Note, in contrast to the results for the submerged-arc welds, that the stress-rupture properties fall within the scatter band for type 304 base material. The total elongation values for these same tests are shown vs rupture life in Fig. 17.5. In this figure, test results from 20 standard type 308 weldments are shown as solid symbols, enclosed by a scatter band; the open symbols represent data from the two second-generation filler metals and the actual FFTF filler metal. Note the significant improvement in ductility with no significant sacrifice in strength. A more detailed analysis shows the FFTF filler metal to be superior to both of the second-generation filler metals, with respect to both strength (rupture life) and ductility (total elongation).

Heat Treatment Studies

A comprehensive study of heat treatments was initiated to determine the effects of time and tempera-

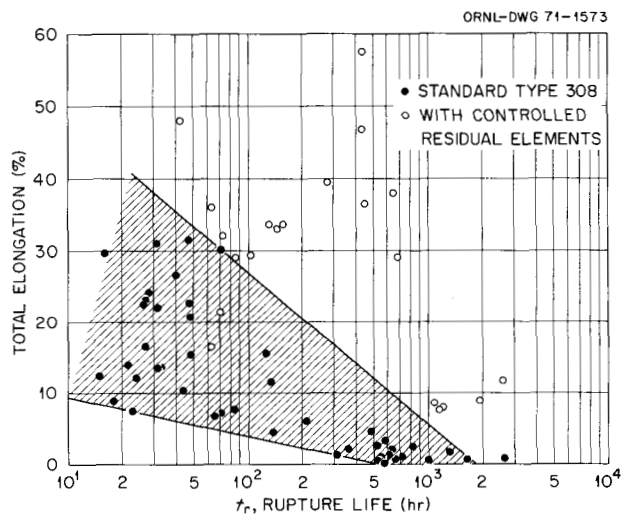


Fig. 17.5. Elongation in stress-rupture tests of type 308 stainless steel shielded metal-arc welds at 650°C.

ture exposure upon the microstructure and properties of welds in austenitic stainless steels. Three general types of heat treatments are being investigated: (1) solution annealing, (2) solution annealing followed by an intermediate-temperature carbide agglomeration treatment, and (3) long-term aging.

As would be anticipated, each of the different weld metals, having a slightly different composition and microstructure, responds differently to heat treatment.

In general, solution treating dissolves and agglomerates the δ -ferrite phase to a degree dependent upon the amount and distribution of ferrite in the as-welded structure, solution-treating temperature, and time at temperature. This, in turn, affects the response of the material to carbide agglomeration treatments. The finer ferrite phase in the shielded metal-arc weld dissolves more readily, allowing extensive grain-boundary migration and, subsequently, extensive carbide precipitation at lower temperatures. The submerged-arc weld, on the other hand, is more resistant to ferrite dissolution and agglomeration and shows carbide precipitation predominantly at remaining austenite-ferrite boundaries.

Long-term aging studies have shown that the rate of formation of σ -phase and rate of carbide precipitation depend in a complex fashion upon starting microstructure (as welded or as heat treated), composition, aging temperature, and time at aging temperature. In general, σ -phase formation is accelerated by a coarser ferrite distribution.

Metallographic techniques were developed for the selective identification of ferrite, σ -phase, and precipitated carbides.

Corrosion Studies

The relative corrosion resistance of stainless steel weldments, both as welded and in various heat-treated conditions, is of interest for the fabrication, shipment, installation, and service of a stainless steel reactor vessel. We have performed Strauss tests on 56 composite wafers representing five different weld-metal compositions, four base-metal compositions, and nine heat-treatment conditions.

All specimens in the as-welded condition passed the Strauss test. Heat treatments typical of those being considered for the FFTF vessel³ caused all base metals (except low-carbon ones) to fail the Strauss test. This indicates that it is highly likely that any reasonable heat treatment that may be applied to the FFTF vessel (0.05–0.07% C) would cause it to fail the Strauss test.

Irradiation Studies

We prepared 226 composite weldment specimens for irradiation in the Experimental Breeder Reactor II. Of these specimens, 168 make up a statistically designed experiment that involves eight weld-metal compositions, five specimen locations, and three heat-treatment

conditions. The remaining 58 specimens represent additional welds, heat-treatment conditions, and specimen locations that could not be included in the main experiment because of the number of variables involved. The irradiation exposure will be completed in FY 1973, and postirradiation testing will include tensile and creep-rupture tests.

FERRITIC STEELS

D. A. Canonico N. C. Binkley

The successful operation of a steam generator depends upon the mechanical properties, corrosion resistance, and weldability of the materials from which it is fabricated. Currently, a number of commercial steam generator designs are being considered. This program is concerned with several types of ferritic steels that are candidates for use in their construction. The low-carbon grades of low-alloy steels and the stabilized low-alloy steels are emphasized in our study because little basic information is known about them and because they eliminate the carbon transport problem, which is one of the primary concerns in steam generators heated by liquid sodium.

The purpose of the program is to determine the weldabilities of the various steels and determine the advantages and limitations of each. The assessment of weldability includes microstructural studies as well as mechanical property measurements. Determination of susceptibility to cracking as a consequence of welding and the effects of welding on the mechanical properties is of prime importance.

Stabilized Grades

Carbon in the low-alloy steels has been stabilized with a number of carbide-forming elements; however, the use of all except niobium has been abandoned. A state-of-the-art review of the weldability of the stabilized low-alloy steels has been completed.⁴ An abstract of the report follows.

Stabilized 2 $\frac{1}{4}$ % Cr–1% Mo low-alloy steels have been proposed as materials for the construction of sodium-to-water steam generators for LMFBR applications. Stabilizing elements such as Ti, Nb, V, and Ta have been used by various manufacturers to "tie up" the carbon (about 0.10% C) and thereby prevent its loss to the flowing sodium. For various reasons, such as poor impact properties, most stabilized versions have been abandoned; the primary exception is the alloy with 0.5% Ni added to improve impact strength. This alloy is

3. G. M. Goodwin and N. C. Cole, *Fuels and Materials Development Program Quart. Progr. Rept. March 31, 1971*, ORNL-TM-3416, pp. 137–42.

4. N. C. Binkley, *State-of-the-Art Review – Weldability of Stabilized 2 $\frac{1}{4}$ Cr–1 Mo Steel*, ORNL-TM-3490 (in press).

available commercially as Sandvik HT8X6 and carries the German designation of 10CrMoNiNb910.

While this HT8X6 alloy shows considerable promise in regard to impact properties and resistance to loss of carbon, there is some doubt about its general weldability and fabricability. Problems in welding could arise primarily from weld-associated cracking due to the formation of a eutectic composition between iron and niobium. In general, the European sources have produced the bulk of literature on this alloy, and they seem to be quite optimistic about its use. They believe that cracking as a result of welding will not occur. On the other hand, some sources in the United States seem to think that this material has poor weldability from the standpoint of U.S. codes and specifications. However, since little actual experience with this alloy exists in the United States, a thorough weldability study is warranted.

The recommended heat treatment for tubing manufactured from this steel is to austenitize at 1050°C for 20 min, cool in air to 500°C, and then temper at 750°C for 1 hr. The resulting microstructure is similar to that of unstabilized 2.25% Cr–1% Mo tubing (ASTM A213-T-22) except for the occurrence of angular precipitate particles. Hardenability studies employing the Jominy end quench test showed that these steels respond to a heat treatment similarly to the 2.25% Cr–1% Mo alloy (ASTM A387, grade D) plate except that the overall hardness is lowered. Electron-beam microprobe studies of the base metal show the niobium to be associated with the precipitate, thereby explaining the lower hardness values. This association (which appears to satisfy the NbC stoichiometry) results in a material whose mechanical properties should be similar to those of a low-carbon 2.25% Cr–1% Mo steel.

Initially we used the TIGAMAJIG weldability testing device on 1/4-in.-thick commercial plate. Both high- and low-heat-input welds were made, and a metallographic investigation revealed cracks in the specimens. These cracks were partially filled with a lower melting phase, as shown in Fig. 17.6. Further, in the low-heat-input welds the grain boundaries in the heat-affected zone appeared to have been melted during welding. Also, a eutectic microstructure was associated with the niobium-rich precipitate in the region close to the fusion line. The presence of a constituent that melts below the melting temperature of the bulk steel could easily account for the reported weldability problems cited in the state-of-the-art review.

An electron-beam microprobe analysis of these liquated phases showed them to be rich in niobium. Figure 17.7 shows the results of the microprobe study of the cracks. A semiquantitative analysis of the back-filled structure corresponded to the Fe₂Nb- α eutectic. The

eutectic temperature, 1370°C, is in good agreement with the temperature of observed melting in a hot-ductility study. The hot ductility study showed excellent on-heating ductility for this steel. Further, the recovery of ductility after heating to the zero-ductility temperature, 1330°C, was excellent.

Chromium-Molybdenum Low-Alloy Steel with Low Carbon Content

Another alternative to the elimination of the carbon migration problem in ferritic steels lies in decreasing the carbon levels to near the solid solubility limit. An investigation of the weldability and mechanical properties of weldments of this grade of material is also under way. Carbon contents of 0.003, 0.045, and 0.11% in a nominal 2.25% Cr–1% Mo low-alloy steel are included in the study. (The 0.11% C is typical for a 2.25% Cr–1% Mo steel, ASTM A213-T-22 and ASTM A387, grade D.)

Fully restrained gas tungsten-arc welds made with filler metal from each carbon level show a factor of 2 difference between the tensile strength of the 0.003% C and 0.11% C at 565°C. Postweld heat treating at 700°C for 1 hr had essentially no effect on the low-carbon welds but appreciably lowered the strength of the high-carbon steel. Table 17.1 contains tensile results at room temperature and 565°C for the weld metal. These data indicate that the medium- and high-carbon steels may suffer from a decrease in strain rate. The reduction-in-area values, in particular, dropped precipitously.

Microhardness traverses were made across weldments made with these filler metals, and Table 17.2 contains the results. We studied areas from both the last and early passes (weld metal that had been exposed to thermal excursions due to the multipass weld technique employed). The strengthening effect of the multipass weld technique on the heat-affected zone (HAZ) of the low-carbon welds is noteworthy. The last pass has a diamond pyramid hardness (DPH) number of 129, whereas the reheated HAZ is strengthened considerably (DPH of about 165). Further, the weld metal of the high (0.11%) carbon is softened by the multipass technique.

The use of the low-carbon 2.25% Cr–1% Mo steel may require that a cosmetic pass (or passes) be employed to avoid what may be a metallurgical notch due to the low strength in the HAZ. These passes could be subsequently removed by grinding.

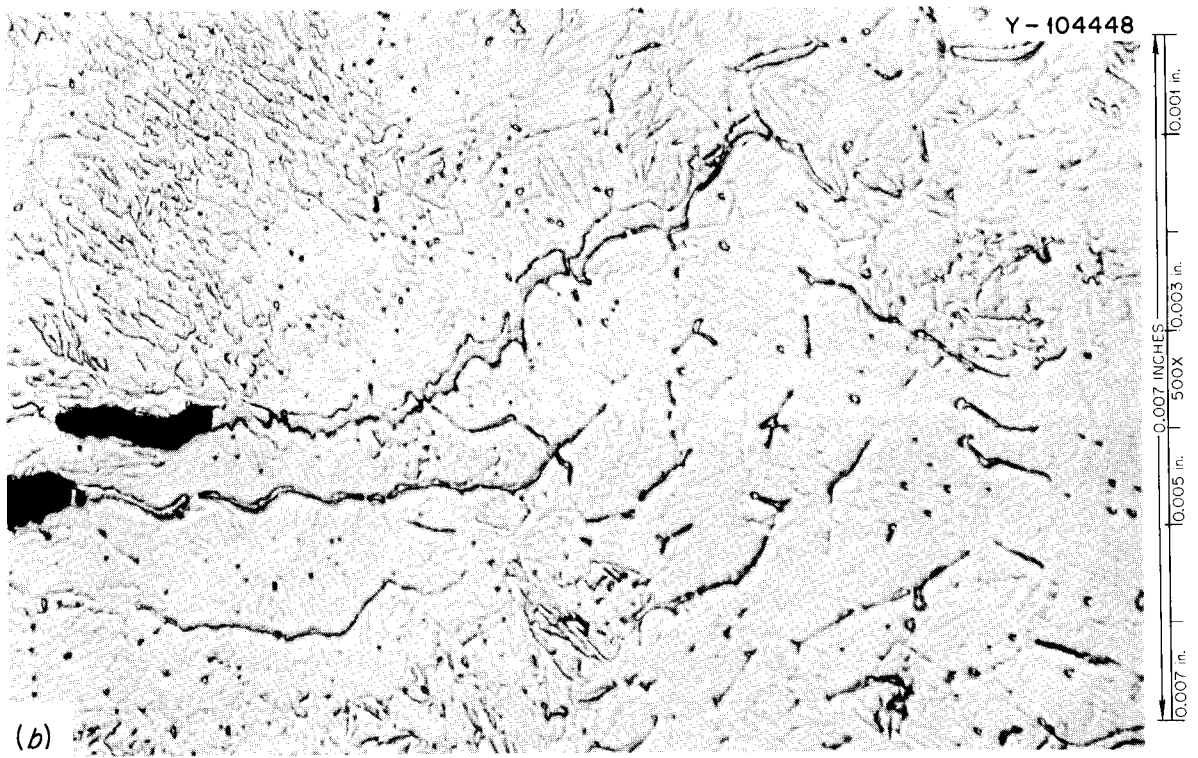
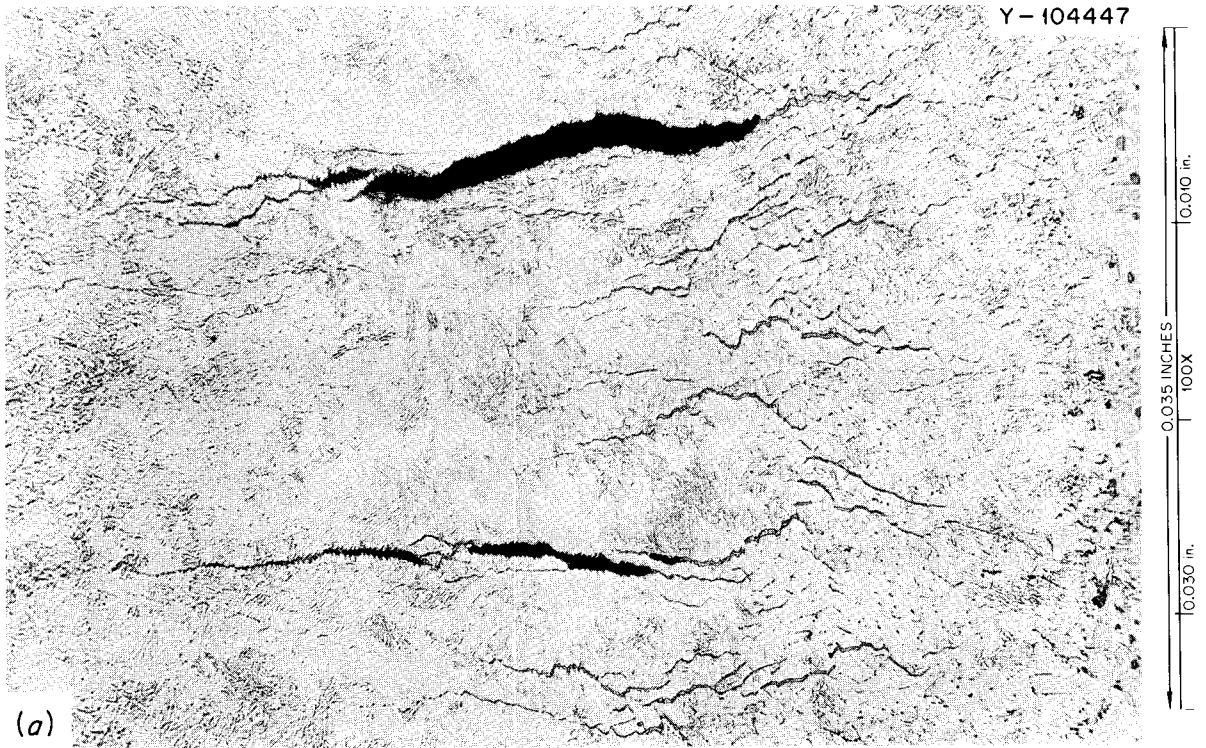


Fig. 17.6. Cracks in welds in niobium-stabilized low-alloy steel. (a) Backfilling of cracks. (b) Crack tips and backfilled phase at higher magnification.

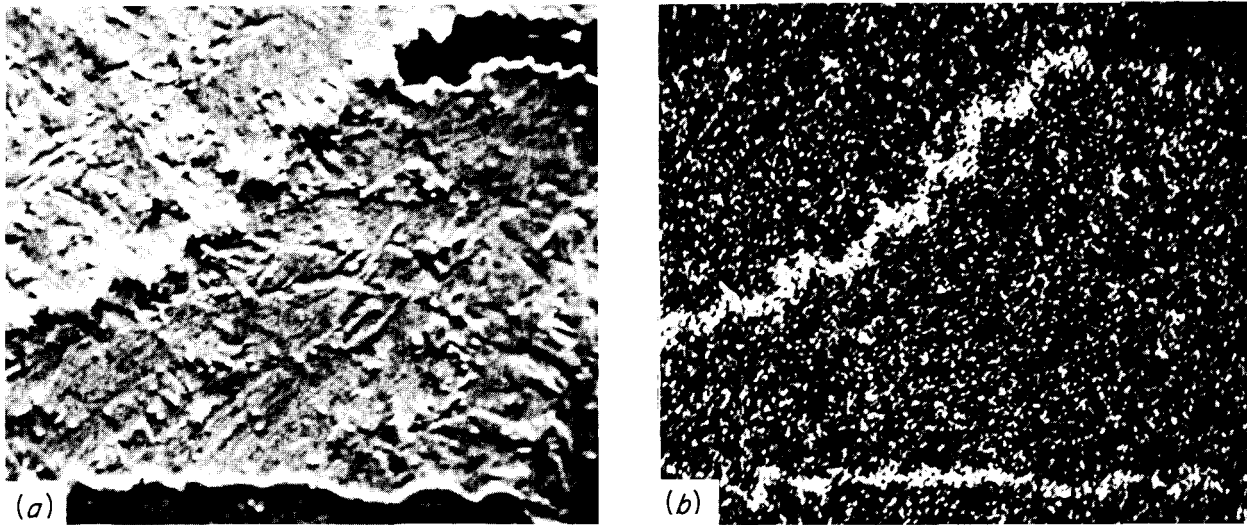


Fig. 17.7. Results of electron-beam microprobe analysis of liquated phase in heat-affected zone of a niobium-stabilized low-alloy steel weld. Note enrichment of niobium in backfilled portion of cracks. (a) Image shown by secondary electrons. (b) Display of Nb $L\alpha$ x rays from same area.

Table 17.1. Results of all-weld-metal tensile tests on low-carbon low-alloy steel welds

Specimen designation ^a	Test temperature (°C)	Stress (psi)		Ductility (%)	
		Yield	Ultimate	Total strain	Reduction in area
		$\times 10^3$	$\times 10^3$		
1A1-1	room	88.5	101.4	14.35	79.5
1A1-2	565	53.8	56.7	12.05	80.5
1A1-3 ^b	565	57.8	61.0	8.75	69.4
1A4-1A ^c	room	60.2	74.0	20.1	88.7
1A4-2A ^c	565	46.3	50.1	15.9	86.3
1B-1	room	82.0	104.5	15.65	80.4
1B1-2	565	68.8	92.4	17.8	69.7
1B1-3 ^b	565	74.6	90.7	12.55	52.5
1B6-1A ^c	room	72.2	86.1	18.6	81.2
1B-2A ^c	565	55.0	57.5	13.1	87.5
1C1-1	room	135.2	157.6	14.5	72.0
1C1-2	565	102.5	118.4	13.1	60.8
1C1-3 ^b	565	101.5	116.9	7.7	13.1
1C7-1A ^c	room	90.7	101.6	15.65	84.0
1C7-2A ^c	565	66.0	68.6	13.85	85.0

^aThe A, B, C middle letter designation refers to 0.003%, 0.035%, and 0.11% C, respectively.

^bTests conducted at head speed of 0.002 in./min. All others at 0.05 in./min.

^cDesignation describes a postweld heat treatment of 700°C for 1 hr.

Table 17.2. Hardness measurements in low-carbon low-alloy steel welds

Weld designation	Carbon (%)	Hardness (DPH)			
		Heat-affected zone		Weld metal	
		Last pass	Early pass	Last pass	Early pass
1A	0.003	129	161–171	224–257	162–210
1B	0.03	182	193	251–297	219–263
1C	0.11	245	251	339–401	276–305

18. Corrosion of Advanced Steam Generator Alloys

J. P. Hammond

The program on corrosion behavior of steam generator alloy weldments was expanded to give greater emphasis to materials being considered for LMFBR use and stress corrosion as the mode of failure.

The program currently includes two areas of investigation: (1) general corrosion (uniform scaling, including pitting and knife-edge attack at fusion lines) at 595 and 650°C (1100 and 1200°F); and (2) stress corrosion cracking (induced by chloride or caustic as contaminants) at 480°C (900°F) and higher.

GENERAL CORROSION

The general corrosion specimens of the similar- and dissimilar-alloy weldments in Table 18.1 recently accumulated a total exposure of 16,000 hr (about two years) in superheated steam at 595 and 650°C. Details of the preparation of specimens, whose surface finish was belt-ground, were given previously.¹ The various corrosion data were interpreted, and 20-year base-metal penetrations were calculated for the similar-metal weldments from weight gain as had been done after one year of exposure.²

Table 18.1. General corrosion specimens

Base metal	Base metal	Filler metal
Inconel 625	Inconel 625	Inconel 625
Inconel 625	Incoloy 800	Inconel 625
Inconel 625	Incoloy 800	Inconel 82
IN 102	IN 102	IN 102
IN 102	Incoloy 800	IN 102
IN 102	Incoloy 800	Inconel 82
Hastelloy X	Hastelloy X	Hastelloy X
Hastelloy X	Incoloy 800	Hastelloy X
Hastelloy X	Incoloy 800	Hastelloy W
Hastelloy X	Incoloy 800	Inconel 82
Incoloy 800	Incoloy 800	Inconel 82
Inconel 600	Inconel 600	Inconel 82
Type 304 stainless steel	Type 304 stainless steel	Type 308 stainless steel

The penetrations calculated for 20 years from the 16,000-hr exposure data were generally somewhat less than those from 8000 hr, reflecting shallower curve slopes (second-stage corrosion) for the former. Except for the stainless steel samples, specimens of the respective weldments showed no physical evidence of scale flaking. Therefore, we view the trend toward shallower slopes as favorable. The penetrations calculated³ for 20 years for the Inconel 625, Hastelloy X, IN 102, and Incoloy 800 similar-metal weldments at 595 and 650°C did not exceed 0.0005 in. Inconel 600 welded to itself with Inconel 82 was penetrated about 0.0015 in. at 595°C and 0.002 in. at 650°C. Penetrations were not determined on the stainless steel weldments since they flaked badly.

The structural characteristics of the scales that formed on the various base metals and weld deposits did not appear to have changed significantly as a result of the longer exposure.³ Neither were any indications of aggravated attack noted at fusion lines.

A comparison of our corrosion results on weldments with those of the General Electric Company (Vallecitos Laboratory) on wrought alloys showed that our materials corroded only one-third to one-half as much as theirs.² Since a difference in surface treatment of the specimens could have been a factor in this discrepancy, we assessed the importance of surface finish as a corrosion variable.

1. J. P. Hammond, *GCR Program Semiannu. Progr. Rept. Mar. 31, 1969*, ORNL-4424, pp. 63-72.

2. J. P. Hammond et al., "Corrosion of Advanced Steam Generator Alloy Weldments in 1100 and 1200°F (595 and 650°C) Steam," paper 46 presented at the National Association of Corrosion Engineers 26th National Conference, March 2-6, 1970, Philadelphia; to be published in the proceedings.

3. J. P. Hammond et al., "Corrosion of Nickel Base Alloy Weldments in Steam at 1100 and 1200°F (595 and 650°C)," paper presented at American Welding Society 52nd Annual Meeting, San Francisco, Calif., April 26-30, 1971 (submitted for publication).

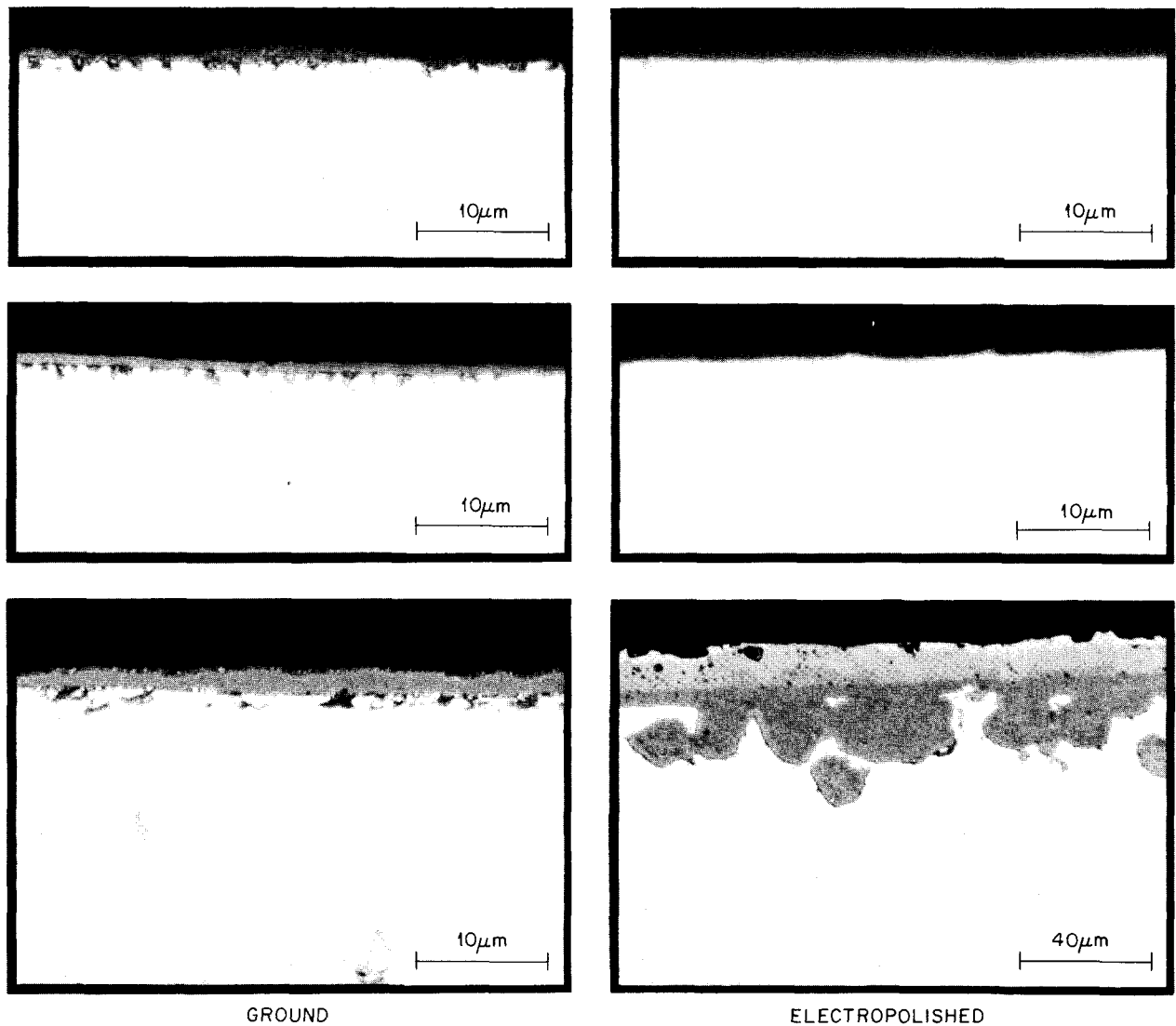


Fig. 18.1. Typical scales formed on a dissimilar-metal weldment after 8000 hr exposure at 650°C (1200°F). Top-to-bottom are plate (Inconel 625), filler metal (Inconel 625), and plate (Incoloy 800). Microspecimens unetched.

Identical studies were made with specimens ground on a 100-mesh-grit belt and with ones electropolished to remove the effects of surface grinding (0.002 in. removed). The electropolishing slightly improved the corrosion resistance of some base metals but greatly increased the corrosion of others. Figure 18.1 illustrates the effects of these surface finishes for one of the dissimilar-metal weldments (Inconel 625 welded to Incoloy 800 with Inconel 625 filler metal) after 8000 hr exposure at 650°C. The extent of scaling of the Inconel 625 both as base and filler metal is diminished by electropolishing, whereas that of Incoloy 800 is greatly increased.

To better analyze the effects of these finishes, specimens of the individual base metals were exposed in

duplicate for periods up to 14,000 hr. The weight-gain results for electropolished specimens exposed at 650°C are compared with belt-ground specimens in Fig. 18.2. Figure 18.3 gives the same results on an expanded scale and includes curves for Incoloy 800 at 595°C as well. The corrosion resistance of Hastelloy X as well as Inconel 625 apparently is somewhat improved with electropolishing, whereas that of Incoloy 800 and Inconel 600 is substantially reduced. The corrosion resistance of type 304 stainless steel also was vastly decreased by electropolishing, but results for it are not included in the graphs because of spallation.

A mathematical analysis of the individual alloy specimens represented in Fig. 18.3 indicates that the corrosion of electropolished Incoloy 800 is of a

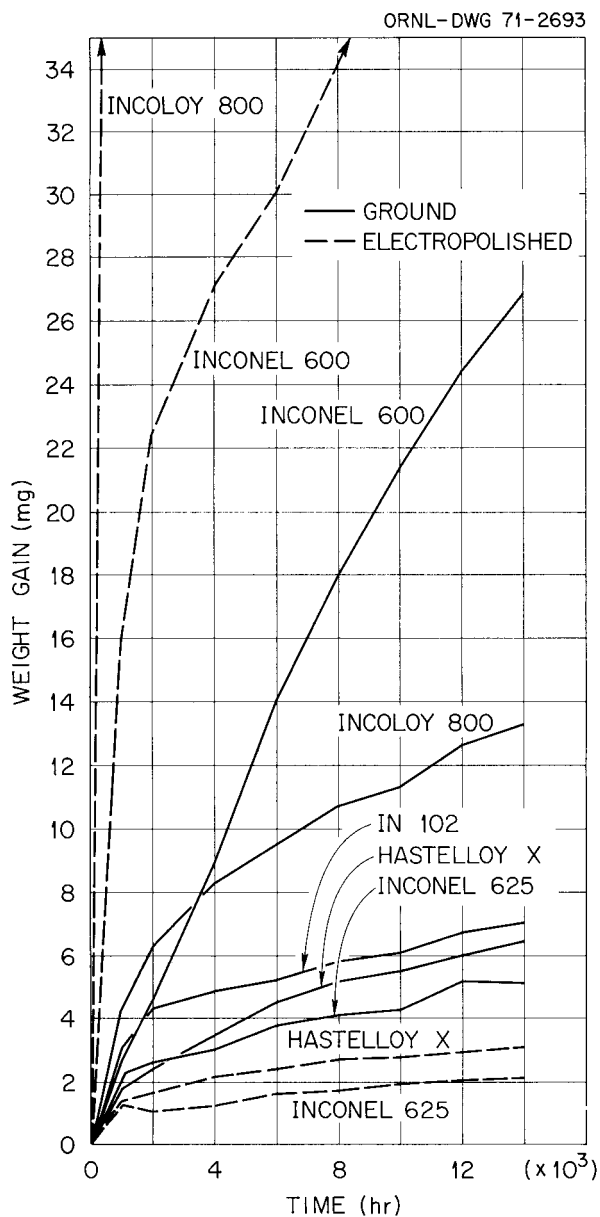


Fig. 18.2. Corrosion of base metal alloys at 650°C, as-ground and electropolished. Specimen area is 20 cm².

different form than that generally depicted for intermediate- and high-nickel alloys of this general class.³ Instead of its second-stage corrosion conforming to the usual linear equation, the data best fitted an equation of the form

$$Y = A + (1/B + CT)T,$$

where Y is the weight gained, T is time, and A , B , and C are constants. Features prominent in the corrosion of electropolished Incoloy 800 thus are unusually large first-stage corrosion, followed by slowly diminishing corrosion rates during the second stage. The calculated

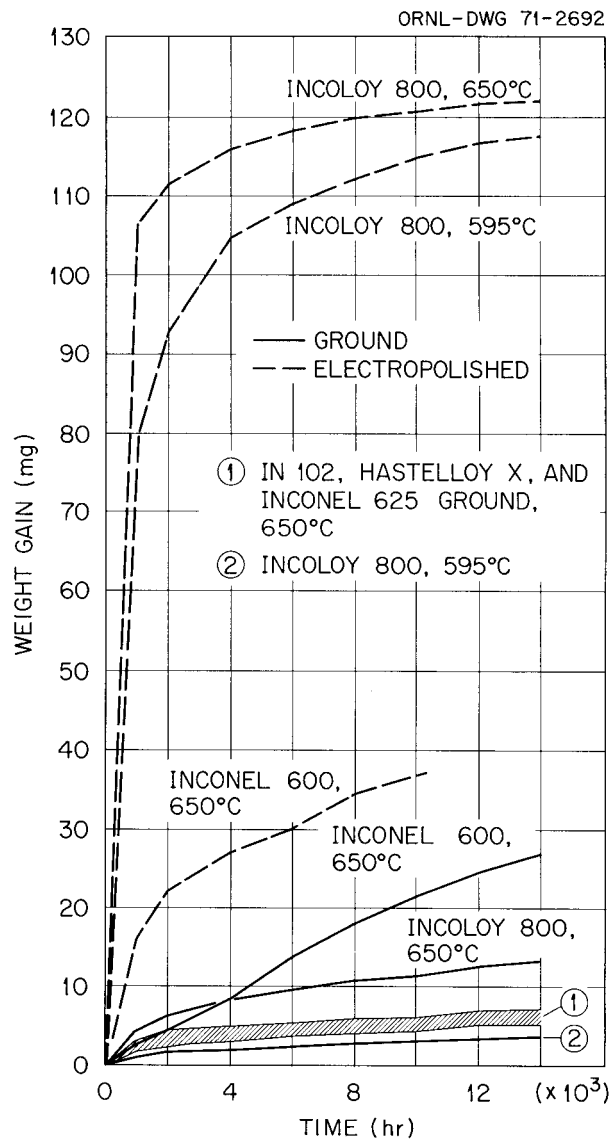


Fig. 18.3. Corrosion of Incoloy 800 as-ground and electropolished in comparison with other base metals.

20-year corrosion of electropolished Incoloy 800 at 595 and 650°C was comparable with that of the ground alloy. This finding, coupled with the fact that scale-retention tests showed electropolished Incoloy 800 to have extremely high resistance to flaking and spallation,³ reflects encouragingly on Incoloy 800 for high-temperature steam applications.

STRESS CORROSION CRACKING

Five test runs were conducted⁴ in the loop developed for the investigation of stress corrosion of weldments in

4. J. P. Hammond, *Fuels and Materials Development Program Quart. Progr. Rept. Sept. 30, 1970*, ORNL-4630, pp. 281-86.

steam contaminated with NaCl and oxygen. The materials tested, except for several stainless steels and chromium-containing ferritic materials, were much the same as those previously examined for general corrosion.³ The test specimens included welded and non-welded samples $3\frac{1}{4} \times \frac{1}{2} \times \frac{1}{16}$ in., and were statically stressed as U-bends by bending to a $\frac{1}{2}$ -in. radius. They were tested as ground, ground and annealed, and ground, annealed, and pickled.

Table 18.2 summarizes these tests. The first two tests, which were conducted to determine whether cracking occurs under superheated steam conditions, failed to produce cracks. A third run, identical to the first except

Table 18.2. Stress corrosion tests in steam with NaCl and oxygen as contaminants

Run	Conditions of test		Contaminants (ppm)		Results
	Time (weeks)	Temperature (°C)	NaCl	O ₂	
1	5	540	$\frac{1}{4}$	20	No cracks
2	5	315	$\frac{1}{4}$	20	No cracks
3	5	540-280 (2 hr at 280, 5 times per week)	$\frac{1}{4}^a$	20	No cracks
4	5	480-280 (2 hr at 280, 5 times per week)	$1\frac{1}{2}^a$	20	No cracks
5	7	480-280 (24 hr at 280, 3 times per week)	25^a	50	Some cracks

^aContamination level at 280°C only.

that the loop was cycled to the steam saturation temperature (280°C) periodically to introduce entrained moisture, also failed to produce cracks. The chloride level in these runs was held at 0.25 ppm, which is believed to be its saturation concentration in superheated steam at the test pressure (900 psi). In the fourth run, the chloride level was increased to 1.5 ppm, but still no failures occurred.

Finally, a substantially more severe test produced a large number of specimen failures. In this run, the NaCl and oxygen levels were 25 and 50 ppm, respectively, and the time at the steam saturation temperature was increased. Table 18.3 summarizes the information on the steam generator alloy weldments that cracked.

It should be noted that, whereas a considerable number of different alloy weldments with ground surfaces failed, cracks were not generally found in the same alloys when ground and annealed or ground, annealed, and pickled. Weldments of Inconel 625 welded with itself did not fail in any condition.

Figure 18.4 illustrates the failed Hastelloy X U-bend specimens and the microstructural characteristics of the stress-corrosion crack. The cracks in the various alloys were generally intergranular and usually initiated alongside the root pass in the heat-affected zone. Occasionally cracks propagated into the weld deposits.

Our test results on weldments generally confirm findings of other investigators working with wrought materials — namely, that some high-nickel alloys do fail by stress corrosion under adverse conditions in steam containing high concentrations of NaCl and oxygen.

Table 18.3. Steam generator alloy weldment specimens cracked by stress corrosion in steam containing 25 ppm NaCl and 50 ppm O

Base metal	Filler metal	Surface conditions	Crack time (weeks)	Number of failures	Crack length (in.)	Location ^a
Type 304 stainless steel	Type 308 stainless steel	Ground	2	3 of 3	1/2	B and W
18-18-2-stainless steel	18-18-2-stainless steel	Ground	2	2 of 3	1/2	W
Hastelloy X	Hastelloy X	Ground	2	3 of 3	3/32-1/2	B through W
Hastelloy N	Hastelloy N	Ground	1	4 of 4	1/2	W
Incoloy 800	Inconel 82	Ground	2-7	3 of 3	1/8-1/4	B
IN 102	IN 102	Ground	5	1 of 3	1/8-1/4	B
Inconel 600	Inconel 82	Ground ^b	7	3 of 3	1/8-1/4	B through W

^aB = base metal; W = weld metal.

^bSpecimens had a prior steam exposure as U-bend specimens without cracking. They were retightened and then tested.

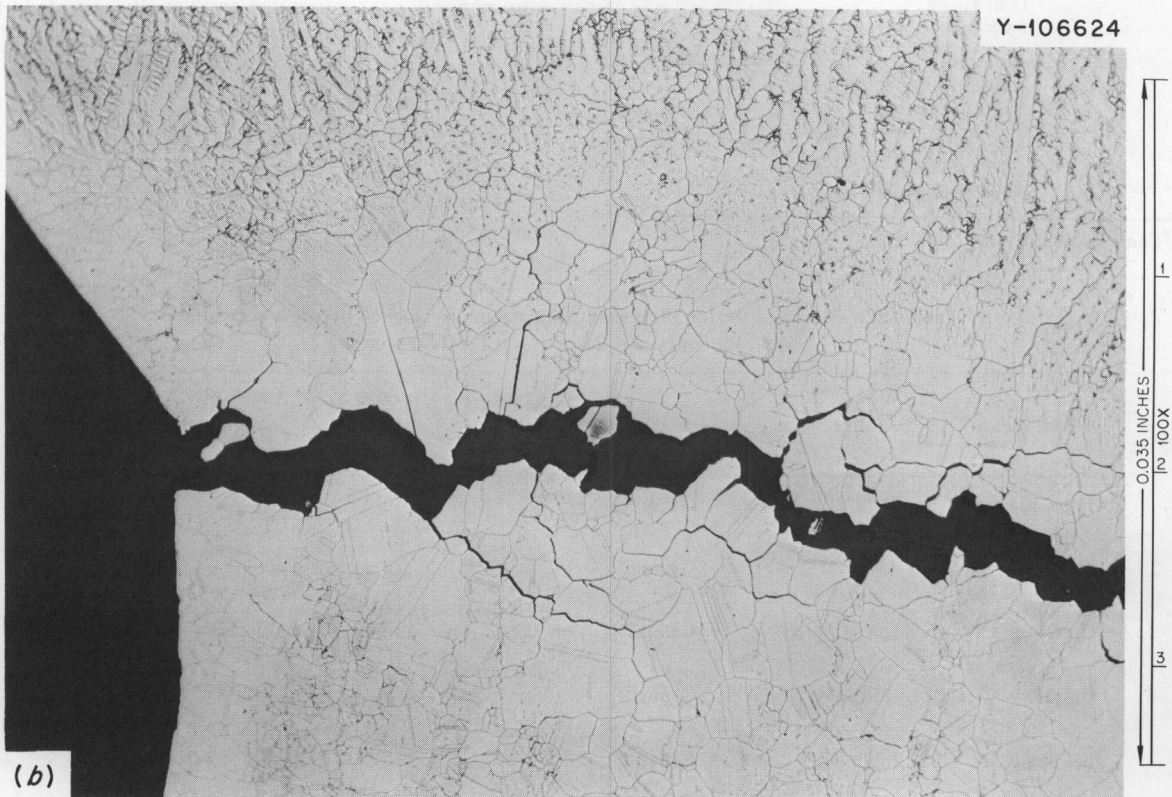
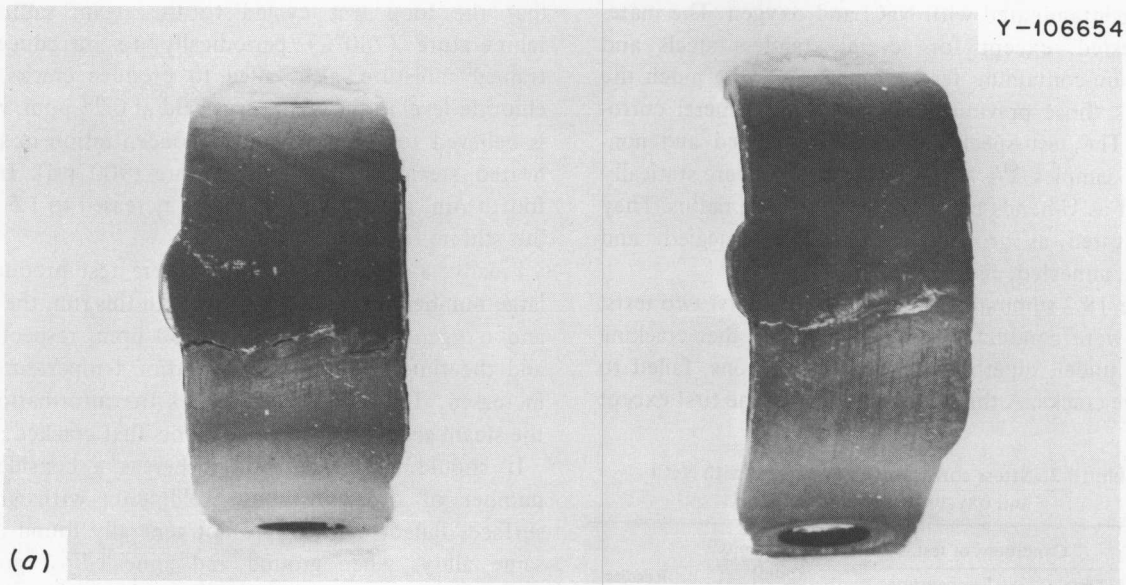


Fig. 18.4. Characteristics of chloride stress corrosion in Hastelloy X weldment. (a) U-bend specimens after failure. (b) Microstructural features of the crack. Etched with mixture of H_2O_2 and HCl. 100X.

19. Sodium Corrosion in LMFBR Systems

J. H. DeVan W. O. Harms

The purpose of this program is to determine the corrosion properties of fuel cladding and structural materials for liquid-metal fast breeder reactor (LMFBR) systems. Our studies are concerned with the effects of interstitial impurities in sodium on the corrosion properties of vanadium alloys.

EFFECT OF OXYGEN IN SODIUM ON THE CORROSION OF VANADIUM AND VANADIUM ALLOYS

R. L. Klueh

We continued our studies¹ to determine the effect of alloying elements on the solubility of oxygen in vanadium. We concluded that Cr, Mo, Fe, Ta, and Nb — none of which form internal oxides — lower the solubility of oxygen in vanadium — chromium, molybdenum, and iron much more than tantalum and niobium. By varying the chromium content, we determined the thermodynamic interaction parameter: $\epsilon_0^{(Cr)} \cong 7.5$.

We derived equations to determine the effect of alloying components in vanadium on the oxygen diffusion coefficient. We tested these equations using data from studies of the redistribution of oxygen between vanadium and vanadium alloy specimens that had been doped to various oxygen levels. The diffusion equations were derived under the assumption that the diffusion of oxygen was the rate controlling step in the oxygen transfer. However, our experiments showed that a surface reaction may control the transfer in some instances.

OXIDATION OF VANADIUM AND VANADIUM ALLOYS

R. L. Klueh

Studies of the effect of sodium on vanadium and vanadium alloys clearly demonstrate that corrosion is

directly related to the oxygen concentration of the sodium, and that oxidation studies can be used to augment sodium studies.² We therefore studied the oxidation kinetics of vanadium and V-20% Ti at 600 and 1000°C under reduced oxygen pressures (from 8×10^{-6} to 8×10^{-4} torr).

Under all conditions tested, oxidation occurred in two stages: an initial linear stage and a subsequent stage in which the rate decreased with time (parabolic-like). The initial state is symptomatic of a reaction rate determined by the rate of oxygen adsorption on the specimen surface. During the second stage a surface scale forms, and the reaction is probably controlled by diffusion through the scale. However, oxygen continues to dissolve in the metal matrix, so this stage is not completely parabolic. At 600°C, where the oxidation rate is significantly lower than at 1000°C, the length of the first stage is substantially reduced because of the lower oxygen diffusion coefficient at 600°C.

Simple microstructural studies on V-20% Ti have demonstrated the utility of oxidation studies for sodium applications. Studies of V-20% Ti in sodium reveal what investigators have described as a "hardened zone" immediately below the external surface. We showed² that the kinetics of penetration of the "hardened zone" follow that predicted for internal oxidation and concluded that a precipitate was not observed metallographically because the temperature of oxidation was too low (about 650°C) for appreciable titanium diffusion. Thus, oxidation and precipitation occurred in place, with little or no agglomeration.

To verify this, we oxidized V-20% Ti specimens for various times at 1000°C at an oxygen pressure of 5×10^{-5} torr and followed the progress of the internal oxidation zone into the specimen interior. For oxidation times longer than 2 hr, the initial precipitation zone was accompanied by the formation of a zone of different etching characteristics that started at the specimen surface and also moved inward with time,

1. R. L. Klueh, *Metals and Ceramics Div. Annu. Progr. Rept. June 30, 1970*, ORNL-4570, p. 92.

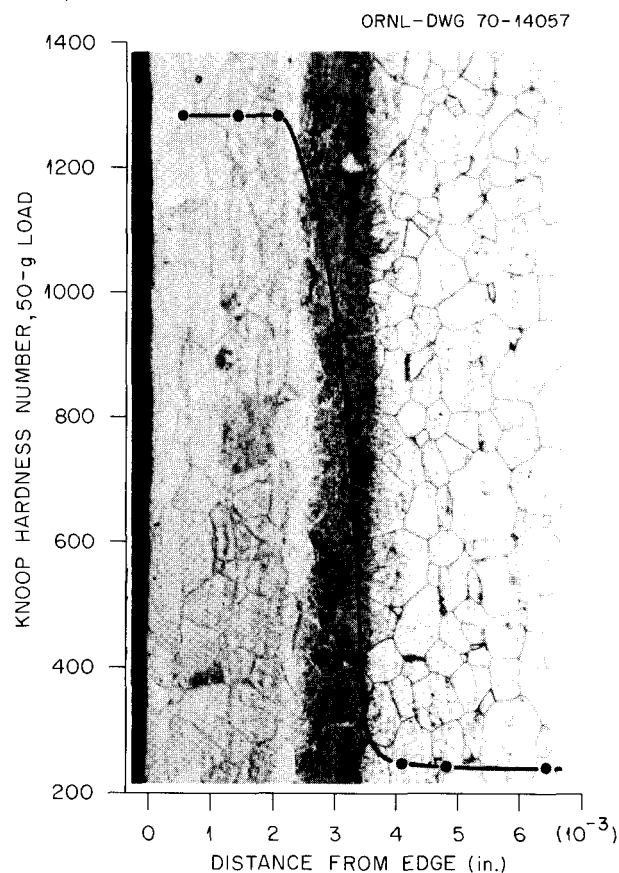
2. R. L. Klueh and J. H. DeVan, *J. Less-Common Metals* 22, 389-98 (1970).

consuming the internal oxidation zone. A similar microstructure was observed at 600°C, a temperature similar to that in sodium studies, and is shown in Fig. 19.1. This microstructure is identical to that observed by Levin and Greenberg³ on V-10% Ti exposed to zirconium-gettered sodium at 650°C. Knoop microhardness measurements reveal a constant hardness of 1290 through the light-etching region followed by a rapid decrease through the dark zone (apparently a zone of fine precipitate particles) and then a constant hardness of about 250 in the oxygen unaffected zone.

The darker zone apparently is formed as oxygen diffuses into the alloy and reacts with the titanium to precipitate titanium oxide. As this zone moves into the specimen interior, a concentration gradient develops between the specimen surface (oxygen concentration determined by the oxygen partial pressure) and the precipitation front (oxygen concentration near zero). Eventually, the concentration of oxygen near the surface increases enough to induce the α (bcc, solid solution) \rightarrow β (bct, solid solution) phase transformation.⁴ Evidently the extreme hardness of the β phase makes it impossible to resolve the precipitate. This conclusion is supported by the hardness measurements, which are consistent with measurements made at Ames Laboratory on α and β solid solutions. Since the phase transformation has not been observed on similarly oxidized vanadium (in a sodium or gaseous environment), it appears that the oxygen concentration for the transformation is lower in the vanadium-titanium system, perhaps as a result of the internal stresses generated by the oxide precipitate.

3. H. A. Levin and S. Greenberg, *An Exploratory Study of the Behavior of Niobium- and Vanadium-Base Alloys in Oxygen-Contaminated Sodium*, ANL-6982 (January 1968).

4. J. L. Henry et al., *J. Less-Common Metals* 21, 115-35 (1970).



20. Sodium Removal and Caustic Effects

W. O. Harms J. H. DeVan

The purpose of this program is to evaluate the corrosion of structural components caused by the products of sodium oxidation or hydrolysis. The program deals with oxidation problems arising from sodium-water reactions and from the leakage or spillage of sodium on metal surfaces that are in contact with mixtures of nitrogen and air. It is also concerned with corrosion effects that result from the cleaning and storage of materials after exposure to sodium.

EXAMINATION OF ALCO/BLH STEAM GENERATOR

G. M. Slaughter R. H. Jones¹
J. H. DeVan P. Patriarca

We are examining the ALCO/BLH steam generator,^{2,3} which failed while under test at the Liquid Metal Engineering Center (LMEC). After installation at the Sodium Components Test Installation of the LMEC in 1965, the steam generator operated intermittently with sodium for 7600 hr and with steam for 4100 hr. A water leak on the feedwater chest was found in May 1970, and was traced to an area of extensive cracking in the lower tube sheet. In view of the vital role of steam generators in the LMFBR demonstration-plant program and the well-documented fabrication and operational history of this unit, it is being examined to determine the mechanism of failure and to study other metallurgical features of interest.

The steam generator arrived at ORNL on December 7, 1970, and was placed in the Experimental Gas Cooled Reactor turbine building for examination. All tube-to-tube-sheet welds were dye-checked and found to be free of cracks. Flow tests on open tubes (those not previously welded shut with plugs) revealed them to be

essentially unblocked. However, leaks were found in two tubes that had been in service at the time of test termination. We observed a massive collection of reaction products in the argon cover gas space above the sodium level. These deposits covered the underside of the tube sheet, tube interstices, thermocouples, and the inner surface of the shell. Surfaces underlying these deposits showed corrosion effects typical of those caused by fused sodium hydroxide.

A detailed analysis of the 6 $\frac{3}{8}$ -in.-thick lower tube sheet, both nondestructive and metallographic, is currently under way. We found an extensive system of cracks in this region (Fig. 20.1), and a step-by-step procedure is being followed to determine the mechanism.

STUDY OF METHODS FOR CLEANING SURFACES OF MATERIALS EXPOSED TO SODIUM^{4,5}

J. H. DeVan D. H. Jansen

The effectiveness of various sodium removal techniques was tested by exposing several potential LMFBR structural alloys in static sodium for short periods of time, stripping the specimens of residual sodium, and re-exposing in sodium. Alloys chosen for investigation were types 304L and 321 stainless steel, 2.25% Cr-1% Mo steel, Incoloy 800, Inconel 625, and IN 102. These alloys were tested in one of two geometries: either as tubes fillet-welded into a small block or as side-by-side sheets welded on two opposite edges. Both designs provided built-in crevices typical of those existing in sodium heat exchangers. Sodium was removed from the specimens by hydroxide-forming solvents (steam, water, and alcohol), anhydrous ammonia, and vacuum distillation. An additional set of specimens was simply drained

1. Plant and Equipment Division.

2. J. H. DeVan and G. M. Slaughter, *Fuels and Materials Development Program Quart. Progr. Rept. Dec. 31, 1970*, ORNL-TM-3300, pp. 182-84.

3. J. H. DeVan, G. M. Slaughter, and R. H. Jones, *Fuels and Materials Development Program Quart. Progr. Rept. March 31, 1971*, ORNL-TM-3416, pp. 155-61.

4. J. H. DeVan, *Fuels and Materials Development Program Quart. Progr. Rept. Dec. 31, 1970*, ORNL-TM-3300, pp. 185-87.

5. J. H. DeVan, *Fuels and Materials Development Program Quart. Progr. Rept. March 31, 1971*, ORNL-TM-3416, pp. 161-65.

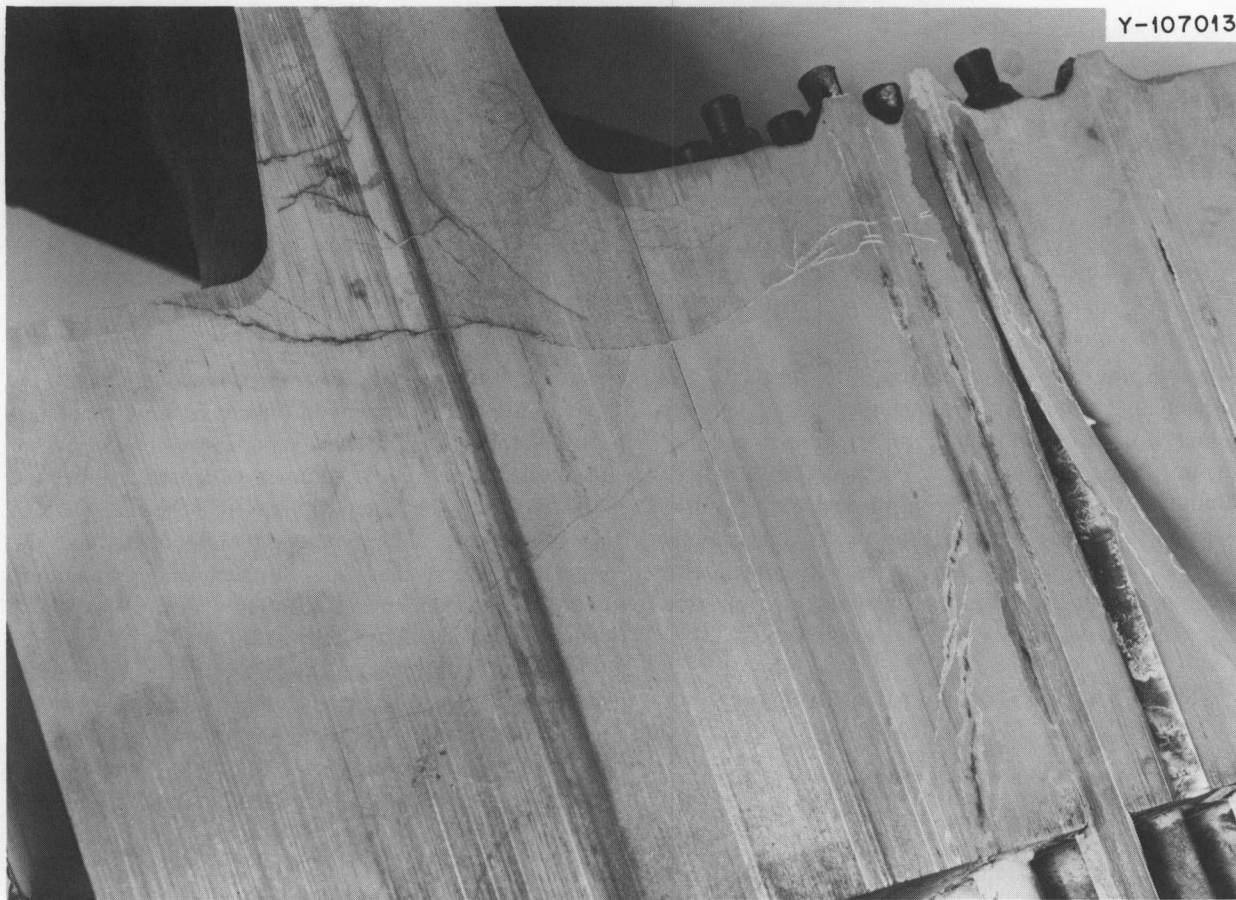


Fig. 20.1. Gross cracking in segment of lower tube sheet of ALCO/BLH steam generator. Tube sheet was $6\frac{5}{8}$ in. thick.

and exposed to air, with no attempt made to remove the residual sodium before the final sodium test. Two heating schedules were selected for the final sodium tests: (1) 100 hr at 700°F plus 900 hr at 1100°F and (2) 1000 hr at 1100°F.

Metallographic examinations of the specimens following these exposures showed significant corrosion of all specimens except those cleaned by water or steam. Corrosion was the result of a coating of Na_2O that remained on the specimen surface following cleaning, and corrosion was no heavier in the built-in crevices than on other surfaces. There were no indications in these studies of caustic attack occurring during sodium removal, even in the crevices.

The stainless steels and nickel-base alloys exhibited equivalent attack, and the 2 $\frac{1}{4}$ % Cr-1% Mo steel was attacked more than the other alloys. We saw no differences in attack as a function of the initial oxygen concentration of the sodium (up to 100 ppm), which

confirms that the attack was due to a locally high concentration of caustic at the specimen surface. Also, the extent of attack was the same for both of the final heating schedules cited above.

CORROSION EFFECTS OF SODIUM LEAKS OR SPILLS IN GASES CONTAINING OXYGEN^{4,5}

J. H. DeVan

Sodium in both the liquid and solid states oxidizes rapidly when exposed to atmospheres that contain O_2 , CO_2 , or H_2O . The resultant oxidation products are potentially damaging to structural components used in LMFBR systems. At 500°C or higher, damage accrues from the fluxing effects of sodium oxides on otherwise protective base-metal oxides. At lower temperatures, damage can result from dissolution and stress-corrosion effects of hydrated caustic residues.

Accordingly, we began a series of tests to evaluate the debilitating effects of sodium (or sodium compounds) on stainless steel in mixtures of nitrogen and air. Since the tests were aimed specifically at the problem of a leak or spill in the annulus between the containment vessel and the outer guard vessel of the FFTF reactor, we constructed a test apparatus that would maintain a controlled flow of sodium through a simulated defect in

a type 304 stainless steel specimen and into an atmosphere representative of that surrounding the exterior of the FFTF vessel. The test system was designed to provide a leakage rate of sodium through the specimen in the range 1 to 200 g/hr. In four test runs we verified the adequacy of the specimen design and the analytical capability of the gas analysis system. Work on this task was then discontinued.

21. Nondestructive Testing Techniques for LMFBR

W. O. Harms R. W. McClung

We are developing new methods, techniques, and equipment for nondestructively inspecting materials and components for the Liquid-Metal Fast Breeder Reactor (LMFBR) program. Among the methods studied are electromagnetic induction, ultrasonics, and penetrating radiation. Special emphasis is being given to developing techniques for measuring the degree of cold work in small-diameter type 316 stainless steel tubing.

DEVELOPMENT OF ADVANCED NONDESTRUCTIVE TESTING

Eddy-Current Instrument

C. V. Dodd

We derived the theoretical equations and wrote computer programs for determining both the depth and size of defects in cylindrical conductors. We also constructed a phase-shifting network to calibrate the modular phase-sensitive eddy-current instrument within 0.02° for the experimental verification.

Dual-frequency modules were designed, constructed, and tested for use with the modular instrument. With these modules, two parameters (e.g., conductivity and thickness) can be measured simultaneously.

Ultrasonic Schlieren Technique for Inspection of Welds

H. L. Whaley K. V. Cook

We continued our study of the response of ultrasound to various types of defects in stainless steel welds. A new type of transducer unit using multiple receiving elements was constructed and tested. With an increase of the signal-to-noise ratio, this device should be practical in situations where there is less dependence on exact flaw orientation. The weld samples were examined radiographically and then ultrasonically by the

Delta technique.¹ Results with the Delta technique were poor, apparently due to excessive scatter caused by the large grains of the welds. The optical system has been enlarged and improved so that placement of the heavy weld samples in the test tank no longer disarranges the optics. Examination of the stainless steel samples by the schlieren technique is under way. Visual observation of the interaction of ultrasonic pulses with the sample should give improved insight into the optimum test conditions for inspection of such samples.

MEASUREMENT OF COLD WORK IN STAINLESS STEEL

C. V. Dodd W. A. Simpson, Jr.

We are investigating methods for nondestructively measuring the degree of cold work in small-diameter stainless steel tubing for application to inspection of FFTF fuel-pin cladding. We emphasize the use of electromagnetic induction for detecting the changes in magnetic permeability produced by cold work.

We have designed, constructed, and tested a low-frequency eddy-current bridge system to measure the cold work in type 316 stainless steel tubing² at an inspection speed of 200 ft/min. Computer calculations indicated that we could measure cold work of 0.250-in.-diam tubing within 3.75% for the worst combination of variables, and experimental measurements gave results within 1.5%.

Our bridge system was used to test a set of 0.300-in.-OD type 316 stainless steel rods fabricated at Argonne National Laboratory to contain a range of cold

1. H. L. Whaley and K. V. Cook, *Fuels and Materials Development Program Quart. Progr. Rept. June 30, 1970*, ORNL-4600, pp. 153-55.

2. C. V. Dodd and W. A. Simpson, Jr., "Measurements of Small Magnetic Permeability Changes by Eddy-Current Techniques," paper presented at the 30th National Fall Conference for Nondestructive Testing in Cleveland, and to be published in *Materials Evaluation*.

work. A smooth curve of magnetic permeability vs cold work was obtained, although the change in permeability for a given difference in cold work was smaller for the rods than for the tubes.

A computer analysis was made on a new type of coil system for measuring cold work in tubing. The new system consists of two driving coils and two receiving coils. It had a calculated error of 2.4% for the worst combination of variables for measuring 0.230-in.-diam

tubing. The coils have been constructed and are being tested.

A computer study is being made on the use of reflection coils (such as those used with the phase-sensitive eddy-current instrument) to measure permeability changes on flat stainless steel specimens, such as the faces of the FFTF fuel subassembly shroud. Preliminary studies indicate high sensitivity with only small error due to variations in lift-off.

22. Fast Breeder Neutron Absorber Materials

W. R. Martin

Boron carbide has been used extensively as a neutron absorber in thermal reactors. For the fast breeder test and demonstration reactors, boron carbide and tantalum are presently the prime candidate materials. However, little is known about the performance of these or other absorber materials at the temperature and fluence expected in fast breeder reactors. The purpose of our current program has been to characterize boron carbide, investigate its basic irradiation behavior, and use this information to optimize its performance in fast reactor service. The key points are to identify the important materials variables and to determine what effect these have on performance in a fast reactor.

INDEXING OF X-RAY DIFFRACTION POWDER PATTERNS OF BORON CARBIDE

H. L. Yakel

We have completely indexed the Cu K α x-ray diffraction powder patterns of boron carbide.¹ Some of the previously unidentified lines were due to impurities. Due to the complexity of the Cu K α patterns of the boron carbide in the high-angle regions that are required for accurate lattice parameter measurements, we indexed patterns using the K α x rays from Cr, Fe, Co, and Ni. These longer wavelength x rays simplify the pattern in the high angle regions and thus simplify the measurement of lattice parameters with no loss of accuracy.

X-ray diffraction of boron carbide is also described in Chap. 12 of this report.

X-RAY DIFFRACTION FROM IRRADIATED BORON CARBIDE POWDERS AND CRYSTALS

G. L. Copeland V. J. Tennery H. L. Yakel

Lattice parameters calculated from Debye-Scherrer x-ray powder patterns of boron carbide powders irradiated at 350 to 500°C in the ORR to burnups of about 8% of ¹⁰B (1.6×10^{21} atoms/cm³) reveal a large

amount of strain in the lattice. In one case, the *a* parameter increased significantly and the *c* parameter decreased slightly. (*a* and *c* are the hexagonal indices corresponding to the rhombohedral boron carbide structure.) In another case, the *a* parameter decreased slightly and the *c* parameter increased. In both cases the volume of the unit cell increased 0.5%.

Single crystals of boron carbide have been irradiated to fluences of 1.8×10^{20} neutrons/cm² (thermal) in the ORR at 350 and 550°C. Results to date show a significant variation from those reported in 1955 by Tucker and Senio² for boron carbide crystals irradiated to 3×10^{20} neutrons/cm² at an unspecified temperature. Like the earlier data, our patterns are a composite of sharp Bragg maxima (unbroadened relative to the unirradiated crystal reflections) and diffuse reflections located at or near these sharp maxima. Again like the earlier data, a highly anisotropic Debye-Waller factor diminishes the intensities of reflections with *l* large compared to *h* and *k* (hexagonal indices). But whereas Tucker and Senio reported an anisotropic lattice expansion (*a* increases, *c* decreases on irradiation), we noted that both *a* and *c* increase over their unirradiated values if the sharp maxima alone are considered. The lattice parameters estimated from the positions of the *diffuse* reflections correspond to an increase in *a* and a decrease in *c*.

We suggest a tentative model of a damaged structure that might produce these observed x-ray diffraction effects. It imagines the crystal to be a composite of regions in which individual defects (displaced atoms, vacant icosohedral or chain sites) are located and regions containing extended planar collections of defects. The former give rise to the sharp Bragg maxima; the latter produce the diffuse peaks.

1. H. L. Yakel, *Fuels and Materials Development Program Quart. Progr. Rept. Dec. 31, 1970*, ORNL-TM-3300, pp. 188-91.

2. C. W. Tucker, Jr., and P. Senio, *Acta Cryst.* 8, 371 (1955).

TRANSMISSION ELECTRON MICROSCOPY OF IRRADIATED BORON CARBIDE

G. L. Copeland C. K. H. Dubose D. N. Braski³

We have produced thin films of irradiated boron carbide for transmission electron microscopy by two techniques.⁴ One consisted of preparing thin foils (0.003 in. thick) from a high-density pellet, irradiating the foils in a capsule, and then loading them directly into the ion-bombardment micromilling machine for further thinning. The second method was to irradiate boron carbide particles in a capsule, disperse the particles in an aluminum matrix, and then thin the composite. The ion milling machine attacks the aluminum and boron carbide at the same rate, so that uniform thin films may be obtained.

The microstructures are the same in each case for the ranges investigated. The burnups were about 8% of the ^{10}B (1.6×10^{21} atoms/cm³) at irradiation temperatures of 350 to 400°C. Figure 22.1 shows a grain boundary in a particle. The high density of black spots indicative of a large amount of lattice strain is uniform over the entire field, but the spots are out of contrast in one grain. The foil sample showed a large amount of microcracking and was extremely brittle. The high irradiation damage density was uniform throughout all the samples, with no observable differences near grain boundaries, twin boundaries, intragranular voids, or particle edges. No helium bubbles or other evidence of reaction product agglomeration was observed. Electron microscopy of boron carbide is also discussed in Chap. 5 of this report.

EFFECT OF ELEMENTAL BORON ON GAS RELEASE FROM IRRADIATED BORON CARBIDE POWDERS

G. L. Copeland

Irradiation of boron carbide powders containing different levels of elemental boron resulted in additional gas release over that expected from powders in which all the boron was combined with carbon. Elemental boron powder was blended with boron carbide powder and annealed at temperatures of 1000 to 2000°C. This treatment resulted in boron carbide containing free boron ranging from 0.6 to 11.6 wt %. Irradiation of the powders containing 11.6 wt % free boron in the ORR at 300 to 550°C resulted in helium

3. Isotopes Division.

4. C. K. H. Dubose, D. N. Braski, and G. L. Copeland, *Fuels and Materials Development Program Quart. Progr. Rept. Dec. 31, 1970*, ORNL-TM-3300, pp. 202-8.

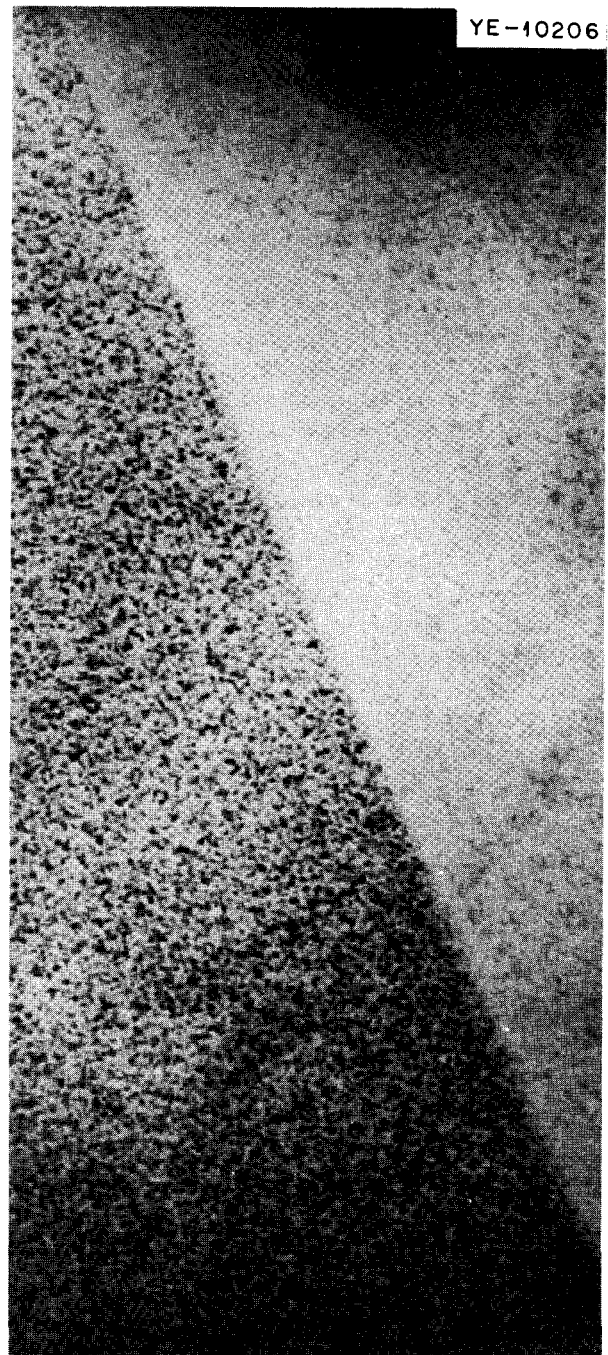


Fig. 22.1. Transmission electron micrograph of irradiated boron carbide particle, showing uniform damage up to grain boundary. 90,000 \times .

release up to 30% of that generated. Boron carbide powders with no free boron have exhibited helium release of about 5% under the same irradiation conditions. These results show that uncombined boron is an undesirable constituent for any nonvented fast reactor control rod.

IN-REACTOR GAS PYCNOMETER FEASIBILITY EXPERIMENT

G. W. Keilholtz⁵ R. E. Moore⁵ D. A. Dyslin⁶

A gas pycnometer that can measure the swelling of boron carbide specimens during irradiation is being tested. The measurement is based upon the ideal gas laws with a system containing helium. A specimen chamber in the reactor core will be connected by a capillary tube to a bellows volume changer and accurate pressure gage located outside the reactor. The specimen would operate at elevated temperatures, for example 700°C, and the capillary tube and bellows will be near room temperature. It is desirable to detect specimen swelling of 5% during a three-month irradiation.

A preliminary error analysis of the system has shown that the volume of a 1-in.³ specimen could be determined within ±0.6%. This predicted error is due to inaccuracies in pressure and temperature measurements as well as the initial volume of the system.

A gas pycnometer bench test with the entire system at room temperature has been run. The system pressure stabilized within 2 to 5 min after the system volume was changed, and the volume of a 1-in.³ specimen can be determined within ±0.3%. Additional tests will be required to establish the accuracy of the method at

elevated temperatures, since temperature changes between pressure readings are a major factor in this experiment.

FAST REACTOR IRRADIATION TESTING OF ABSORBER MATERIALS

G. L. Copeland R. E. Moore⁵
G. W. Keilholtz⁵ D. A. Dyslin⁶
R. G. Donnelly

An irradiation experiment described previously⁷ was built, was inserted in the EBR-II, and is proceeding on schedule.

A second test of seven capsules and a third test of four capsules are being prepared for insertion in the EBR-II. These tests are designed to determine: (1) the effects of neutron capture rate on solid swelling and gas release of boron carbide, (2) comparative irradiation performance of TaB₂ and Ta₂B, (3) effect of sodium bonding on the irradiation performance of boron carbide, (4) comparison of cold-pressed boron carbide pellets, and (5) effect of neutron irradiation on the physical and mechanical properties of tantalum and its alloys.

5. Reactor Chemistry Division.

6. General Engineering Division.

7. G. L. Copeland and G. W. Keilholtz, *Metals and Ceramics Div. Annu. Progr. Rept. June 30, 1970*, ORNL-4570, p. 102.

Part III. Space Power Technology

23. Materials Development for Isotopic Power Programs

R. G. Donnelly

Materials studies on isotopic power programs have been primarily in support of space activities, with only strontium compound compatibility and plasma-arc welding studies in support of terrestrial isotopic power. The development of new cladding alloys is aimed specifically at ^{238}Pu -fueled heat sources but could apply to ^{244}Cm when missions arise requiring this isotope.

Our cermet fuels studies have centered on determining fabricating methods to optimize specific properties. In these activities we have confined our efforts to molybdenum cermets containing ThO_2 as a stand-in for $^{238}\text{PuO}_2$ and $^{244}\text{Cm}_2\text{O}_3$. The lessons learned with these cheaper, more easily handled materials will be applied next year to fueled cermets and cermets containing noble metals.

In addition to the subjects reported here we also provided materials consultation on the Isotope Kilowatt Program.

CLADDING MATERIALS PROGRAM

New Platinum-Rhodium-Tungsten Cladding Alloys for Space Isotopic Heat Sources¹

C. T. Liu H. Inouye R. G. Donnelly

The radioisotopic fuel used for space power systems must be clad in a highly reliable material, not only to contain the fuel for normal operation of several years, but to survive launch abort situations, severe aerodynamic heating on re-entry, high-velocity impact, and postimpact environment. Because no single alloy of

current manufacture can meet the severe service and safety requirements, multiple layers of refractory alloys clad with a platinum-rhodium alloy, so that one alloy compensates for the shortcomings of another, are now being considered. However, recent studies indicate that the performance of refractory alloy components in such capsule assemblies is not as reliable as desired from the standpoint of oxidation resistance and compatibility. Moreover, the available platinum-base alloys (Pt-20% Rh and Pt-30% Rh) possess adequate oxidation resistance and fabricability but lack the desired mechanical strength and high melting point. Our program objective has been to develop fabricable alloys with better strength, excellent oxidation resistance, improved compatibility, and a high melting point. This paper summarizes the above properties in terms of the effect of tungsten content on the platinum-rhodium base.

Ingots of the platinum-base alloy designated as Pt-3010, containing 26 to 30% Rh and 6 to 10% W (wt %), are readily fabricable to sheet material by hot forging in air followed by cold rolling. Figure 23.1 shows the tensile properties as a function of testing temperature. The Pt-26% Rh-8% W alloy has about 15% elongation at room temperature, and this increases to 47% at 1316°C. This alloy is substantially stronger than Pt-30% Rh at all temperatures, stronger than T-111 and TZM to 1093°C, and equivalent to TZM at 1316°C.

Alloying with up to 10% W did not significantly impair the excellent oxidation resistance of the platinum-rhodium base. For example, the Pt-30% Rh-10% W alloy oxidized in air at an average rate of 7.5, 2.2, and 0.26×10^{-6} g cm⁻² hr⁻¹ at 1200, 1000, and 760°C, respectively. These rates are four orders of magnitude lower than those for molybdenum- and tantalum-base alloys and only 6 times those for

1. Abstracted from paper submitted for the 1971 Winter American Nuclear Society Meeting, Miami Beach, Oct. 17-21, 1971.

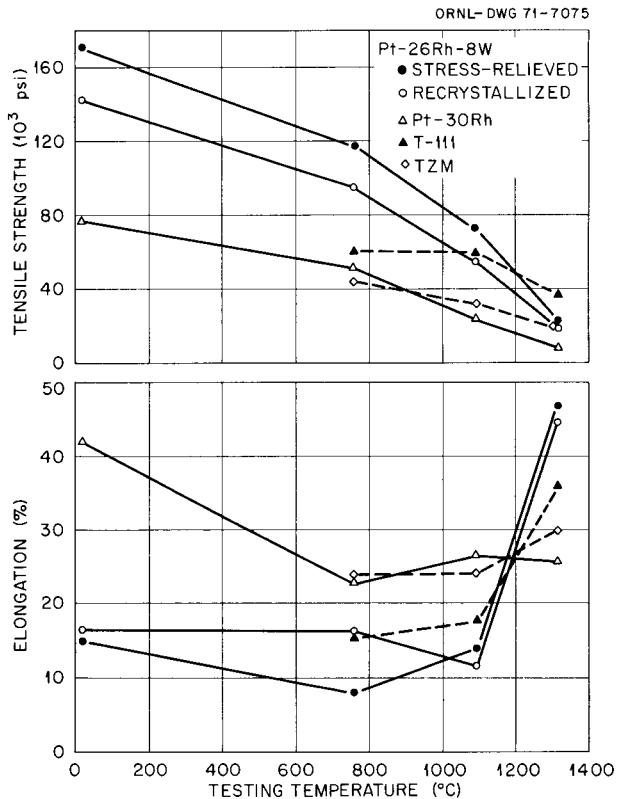


Fig. 23.1. Comparison of the tensile properties of Pt-26% Rh-8% W alloy with Pt-30% Rh, T-111, and TZM. Data for T-111 and TZM are from General Electric Company, *Multi-Hundred Watt, Radioisotope Thermoelectric Generator Program*, GESP-7034 (March 1970).

platinum. Furthermore, metallographic examination of the specimens oxidized at 1000°C showed no grain boundary oxidation.

In the binary alloy systems platinum-tungsten and rhodium-tungsten, an increase in the tungsten content increases the melting point. We found that Pt-3010 has a melting point above 2000°C, which fulfills the current requirement for space cladding material. The alloys have good weldability. Metallographic examination of TIG welds on sheet material showed no cracking as welded or after bending 90°. Also, Pt-3010 alloys are more compatible than the Pt-30% Rh alloy with T-111, tungsten, and molybdenum from 900 to 1700°C.

Atomic Ordering and Structural Transformation in the V-Co-Ni Ternary Alloys²

C. T. Liu

The transition behavior of the close-packed ordered nine-layered structure (K phase) existing in the V-Co-Ni

ternary alloys was investigated. Both neutron and x-ray diffraction indicate that atomic ordering and structural transformation take place separately. The first step of transition is to form the AuCu₃-type ordered structure (α' phase), and the apparent activation energy for atomic ordering is estimated to be 76 kcal/mole. The α' to K transition proceeds by nucleation and growth; however, both mode and morphology of transition vary with reaction temperature. These observations have been discussed in terms of temperature dependence of nucleation and growth processes. The structural transformation produces massive substructures, which harden the alloy substantially.

CERMET FUELS

Evaluation of Fabrication Techniques for Cermet Isotope Fuel Simulants¹

L. E. Poteat R. W. Knight
R. G. Donnelly J. I. Federer

The heat source used in the thermoelectric generator for the Pioneer and Transit programs contains ²³⁸Pu in the form of a plutonium oxide-molybdenum cermet (PMC). The molybdenum matrix improves the mechanical properties and increases the thermal conductivity. The heat source consists of a stack of 22 cermet disks, each about 2 in. in diameter × 0.25 in. thick. Because of the limited quantities of plutonium available and because of the safety hazard involved in handling this highly radioactive material, thoria-molybdenum cermet disks are being used to simulate the plutonia-molybdenum cermet during capsule qualification and generator testing.

Three different techniques for fabricating thoria-molybdenum cermets were investigated. The first was hot pressing of thoria powders coated with molybdenum by chemical vapor deposition, as used in the fabrication of PMC. For comparison, two less expensive alternate techniques, (1) cold pressing and sintering of blended molybdenum and thoria powders and (2) hot pressing of blended powders, were also investigated.

The microstructure of the hot pressed coated thoria particles shows low porosity and an almost continuous molybdenum phase. In this technique the 105- to 177- μ m thoria powder is coated with molybdenum by chemical vapor deposition in a fluidized bed. A 3- μ m coating is produced by the reduction of MoF₆ with hydrogen at 625°C and 1 atm to give 17.5% Mo. When hot pressed at 1800°C and 6600 psi for 1 hr, a 98%-dense cermet disk is produced.

The most economical alternate method of producing the cermet is blending the two powders followed by

2. Abstract of paper submitted for publication.

cold pressing and sintering. To develop high strength and high thermal conductivity, a continuous metal phase is desirable. To obtain the most continuous phase with a fixed amount of metal (17.5%), large grains (105 to 177 μm) of thoria were blended with fine (0.565 μm average) molybdenum powder. An 85%-dense cermet was produced by pressing at 63,000 psi and sintering in vacuum at 2200°C for 4 hr. The addition of 0.5% CaO to the thoria to increase its sinterability led to 90%-dense disks. The microstructure shows excessive porosity, and the molybdenum does not appear to be continuous.

To reduce the porosity, blended fine molybdenum powder and coarse thoria powder were hot pressed at various temperatures and pressures. Hot pressing at 1800°C and 6600 psi for 1 hr produced 99%-dense disks. The microstructure shows very little porosity and a more continuous metal phase.

Electrical resistivity was measured on structures produced by the three different techniques. The resistivity was about the same for the hot-pressed blended powder disks and the cold-pressed-and-sintered disks and was almost 50% greater than that of the hot-pressed CVD-coated particles. This would indicate that the thermal conductivity of the disks from the CVD-coated particles is greater than that of disks produced by the other two techniques. The mechanical strength of the cermets was determined by three-point bend tests. The disks produced from the CVD coated particles were 25% stronger than the others.

Of the three techniques investigated, the disks produced by hot pressing the CVD-molybdenum-coated thoria powders appear to have superior strength and conductivity. These superior properties are a result of the thoria grains being essentially encapsulated in a continuous matrix of molybdenum.

Controlled Porosity Cermets for Application to Curium Fuel Forms¹

M. M. Martin R. G. Donnelly

Because $^{244}\text{Cm}_2\text{O}_3$ has about 5 times the power density of $^{238}\text{PuO}_2$, it permits greater flexibility in the fuel form design. For instance, either a $^{244}\text{Cm}_2\text{O}_3$ cermet can have 5 times the power density of a $^{238}\text{PuO}_2$ cermet with an equivalent metal content, or additional metal can be used to improve the impact resistance and postimpact fuel containment and still allow a significant power density advantage. We have investigated ranges of fabrication conditions for molybdenum-ThO₂ as a stand-in for molybdenum- $^{244}\text{Cm}_2\text{O}_3$ and noble metal- $^{244}\text{Cm}_2\text{O}_3$ cermets. Our aim has

been to develop fuel forms with the most desirable combination of properties and to reduce the in-cell development requiring curium. We have specifically attempted to structure the cermet to provide for release of helium so that the fuel form should not swell and thereby be physically degraded.

Two fabrication approaches have been pursued: hot pressing, and cold pressing and sintering. Small cylindrical pellets of molybdenum with 0, 20, 40, 60, and 80 vol % ThO₂ powder were compacted and tested under varying conditions for porosity, helium permeability, compressive yield strength, and microstructure. Cold pressing and sintering parameters studied were pressure (25,000, 50,000, 100,000 psi), temperature (1400, 1600, 1800, 2000°C), and duration at temperature (60, 120, 240 min). Hot pressing parameters were temperature (100, 1300, 1600°C) and duration of 6000-psi applied load (15, 30, 60 min) at temperature.

The density of cold-pressed-and-sintered molybdenum-ThO₂ pellets depended primarily upon the pressing pressure and to a lesser extent upon the ThO₂ concentration. The pressing temperature established the degree of consolidation for the hot-pressed cermets, and pressing time produced little, if any, effect. Similar appearing microstructures produced by the two techniques also correspond to equivalent compressive yield strengths at 5% offset strain. During the 400°C compressive test, most specimens exhibited sufficient ductility to minimize the release of activity on testing. However, pellets hot pressed at 1000°C and cold-pressed-and-sintered cermets containing 40 vol % ThO₂ crumbled at low stress and strain. We can control the void content of both types of cermets over a rather wide range. More importantly, most of the voids are interconnected, resulting in a structure permeable to helium.

Both techniques have some drawbacks. The cold-pressed-and-sintered molybdenum-ThO₂ pellets contain numerous matrix fissures, which are perpendicular to the pressing direction. These flaws can be minimized by compacting at reduced pressure, but this maximizes void content.

Data on strength, permeability, and microstructures as a function of fabrication parameters are presented.

COMPATIBILITY

J. R. DiStefano

We have conducted experiments over the past several years to determine the compatibility of potential container materials with $^{244}\text{Cm}_2\text{O}_3$ at temperatures from 750 to 1850°C. For thermionic applications

(>1500°C) W-26% Re, TZM, and Mo appear to be satisfactory container materials.^{3,4} After 10,000 hr at 1250°C, Nb, Nb-1% Zr, Ta, Ta-10% W, Mo, and V appearing promising, but pure zirconium reacted extensively with ²⁴⁴Cm₂O₃.

Two strontium compounds, SrTiO₃ and Sr₂TiO₄, seem to be very compatible with Haynes alloy No. 25, Hastelloy C, and type 316 stainless steel,⁵ even after 10,000 hr at 1100°C. Strontium oxide reacts with these alloys but significantly less at 900°C than at 1100°C. In Hastelloy C the reaction is perhaps related to the presence of one or more intermetallic phases and appears to cease⁶ after 5000 hr. In laboratory heats containing very low silicon and relatively high carbon or in alloys containing very high silicon, these phases do not form, and no attack was observed. Potassium in SrO also decreased its compatibility with Hastelloy C.

PLASMA-ARC WELDING OF AN ISOTOPE CAPSULE¹

G. M. Goodwin B. F. Early⁷

A certain thermoelectric generator uses a ⁹⁰Sr titanate fuel form contained in a heavy-walled capsule of Hastelloy C, a nickel-base alloy with excellent strength, oxidation, and corrosion properties. The capsule design uses a threaded end cap, with a closure weld to ensure containment. Based upon a maximum anticipated seawater corrosion rate, a minimum weld penetration of 0.055 in. is required.

Autogeneous gas-tungsten arc (GTA) welding has been used to produce the closure; however, for certain weldment designs and materials, the attainment of the required penetration by GTA welding presents problems. Sample welds made before and after the fueled capsule weld are used to indicate the penetration of the actual capsule seal weld. The weld penetration by the GTA process is sensitive to electrode separation from work, alignment, variation of alloy composition, and welding parameters. We found that the plasma-arc process produces the required penetration with minimum sensitivity to these variables.

3. J. R. DiStefano, *Metals and Ceramics Div. Annu. Progr. Rept. June 30, 1970*, ORNL-4570, pp. 107-108.

4. J. R. DiStefano, "Compatibility of ²⁴⁴Cm₂O₃ with Refractory Metals at Thermionic Temperatures," pp. 26-33 in *IEEE Conference Record of 1970 Thermionic Conversion Specialist Conference, October 26-29, 1970*, The Institute of Electrical and Electronics Engineers, New York, 1970.

5. J. R. DiStefano, *Metals and Ceramics Div. Annu. Progr. Rept. June 30, 1970*, ORNL-4570, p. 111.

6. J. R. DiStefano and R. E. McHenry, *Compatibility of Strontium Alloys with Superalloys at 900 and 1000°C*, ORNL-4625 (to be published).

7. Isotopes Division.

A plasma-arc welding procedure was developed and successfully applied to four of these capsules, achieving an average penetration of at least twice the minimum requirement. The plasma-arc welding process is relatively new and is normally used in the "keyholing" mode, a technique involving a full-penetration weld in sheet or thin plate. This is, to our knowledge, the first application of the plasma process to a "blind" (non-full-penetration) weld.

The plasma-arc welding process provides increased penetration over that obtainable with the gas-tungsten-arc process through a constricted, highly ionized plasma — in this case, of argon gas. Careful control of the welding variables is required, however, since the plasma produces a depression in the molten weld puddle, which, under certain undesirable conditions, results in voids and cold shuts in the weld metal. The development effort therefore concentrated on selection of parameters to give adequate penetration with a minimum probability of entrapped voids.

Bead-on-plate test welds were produced with intentional variations in speed of travel (10 and 15 in./min), welding current (140, 155, 170 A), orifice size ($\frac{1}{8}$ and $\frac{3}{32}$ in.), and plasma gas flow (2.4 and 3.2 ft³/hr). Each of these conditions yielded a depth of penetration greater than 0.100 in., and entrapped voids occurred only with the more severe conditions — that is, high-travel speed, high current, small orifice, or high plasma gas flow.

Based upon these tests, three actual test pieces were welded with 10-in./min travel speed, 140-A welding current, $\frac{1}{8}$ -in. orifice, and 2.4-ft³/hr plasma gas flow. Depth of penetration achieved exceeded 0.100 in. No entrapped voids were observed upon sectioning.

We welded the four fueled capsules in-cell with the above conditions, using a programmable power supply that permitted entirely automated operation. No significant difficulties were encountered.

The advantages of the plasma welding process for this application include (1) ease of alignment — a low-current pilot arc can be used to align the torch with the weld joint before welding; (2) freedom from stubout and possible tungsten inclusions — the plasma process does not use an exposed tungsten electrode as does the GTA process; (3) freedom from arc-length considerations — torch-to-work distance can vary from approximately $\frac{1}{8}$ to $\frac{1}{2}$ in. without appreciable effect; and, most important, (4) increased penetration — because of the inherent characteristics of the plasma-arc welding process, sufficient penetration could easily be achieved to provide a factor of safety over the minimum penetration requirement.

24. Metallurgy of Refractory Alloys

R. G. Donnelly P. Patriarca

The purpose of this program is to provide a broad, base-technology evaluation of high-temperature alloys for use in high-performance nuclear reactors and isotopic heat sources for advanced space, terrestrial, and civilian power applications. Principal emphasis is placed on tantalum-, niobium-, and molybdenum-base alloys. Our work on tungsten and its alloys is reported in Chap. 25.

BASIC PHYSICAL METALLURGY

H. Inouye

Nitrogen Solubility in T-111

H. Inouye

The purpose of this study is to determine the feasibility of using T-111 (nominal composition Ta-8% W-2% Hf) as the cladding for UN fuel in a Rankine-cycle space reactor. The equilibrium nitrogen pressures over T-111 as a function of the nitrogen content were measured with a calibrated mass spectrometer. The nitrogen pressure over T-111 in the range 1200 to 1500°C is higher than that over tantalum¹ by up to two orders of magnitude. In terms of the nitrogen uptake, T-111 appears to be more compatible than tantalum with UN. Because Hf lowers the nitrogen pressure over Nb-rich Nb-Hf alloys by several orders in magnitude,² similar effects were also expected for T-111 since it contains about 2% Hf. These unexpected results are tentatively attributed to the tungsten in T-111.

Creep of T-111 in Low-Pressure Nitrogen

H. Inouye

Creep of T-111 is being measured in low-pressure nitrogen to determine if ultrahigh-vacuum creep data

1. R. Griffith and J. A. Pryde, *Trans. Faraday Soc.* **63**, 2599-2604 (1967).

2. A. Taylor and N. J. Doyle, *J. Less-Common Metals* **13**, 413-30 (1967).

apply to performance as cladding for UN. Testing at 1200 and 1400°C in vacuum and in low-pressure nitrogen showed moderate strengthening of T-111 by nitrogen at 1400°C. According to solubility studies (this chapter) the maximum nitrogen content at 4.7×10^{-6} torr and 1400°C is about 300 ppm.

The nitrogen environment also strengthens T-111 at 1200°C; however, the improvement was greater at 4.4×10^{-6} torr nitrogen than at 9.6×10^{-6} torr nitrogen. A rupture strain of only 2.2% for the specimen tested at the higher nitrogen pressure indicates that nitrogen embrittles the alloy.

Effects of Oxygen Contamination on the Tensile Properties of T-111

C. T. Liu

The objective of this study is to provide the necessary information for the use of T-111 in isotopic heat sources for space power. The T-111 alloy containing 7.98% W, 2.02% Hf, and 26 ppm O was doped with controlled amounts of oxygen in a dynamic system at oxygen pressures of 1 to 2×10^{-5} torr at 1000°C. The contaminated specimens were then tested in tension at two different conditions: annealed 15 min at 1700°C to simulate re-entry heating or as doped. The results for the annealed specimens are shown in Fig. 24.1. An initial reduction of ductility and increase in strength were observed at all temperatures. Calculations based on the lattice-parameter measurement indicate that the solubility of oxygen in T-111 is around 100 ppm at 1700°C. Beyond the 100 ppm level, surprisingly enough, both the strength and ductility were almost independent of oxygen level. The data in Fig. 24.1 indicate that annealed T-111 can tolerate oxygen contamination to 3000 ppm but loses its ductility completely at 4300 ppm.

In contrast the as-doped T-111 exhibits a much lower tolerance for oxygen contamination. Figure 24.2 shows the initial increase in strength and continuous decrease in ductility with oxygen level. At above 750 ppm O,

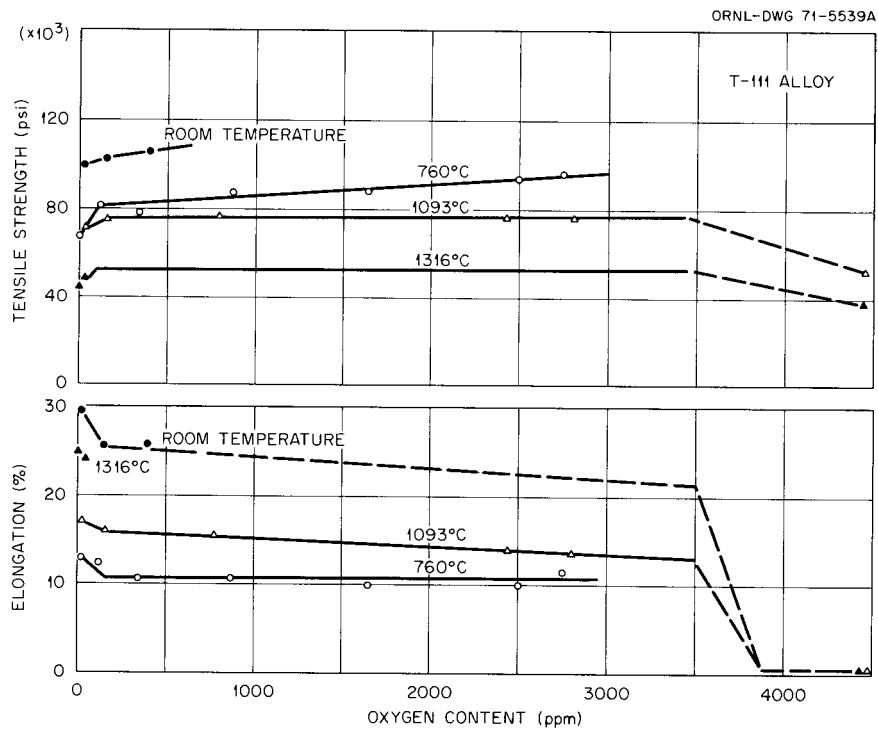


Fig. 24.1. Tensile properties of T-111 annealed 15 min at 1700°C after doping with various levels of oxygen at 1000°C.

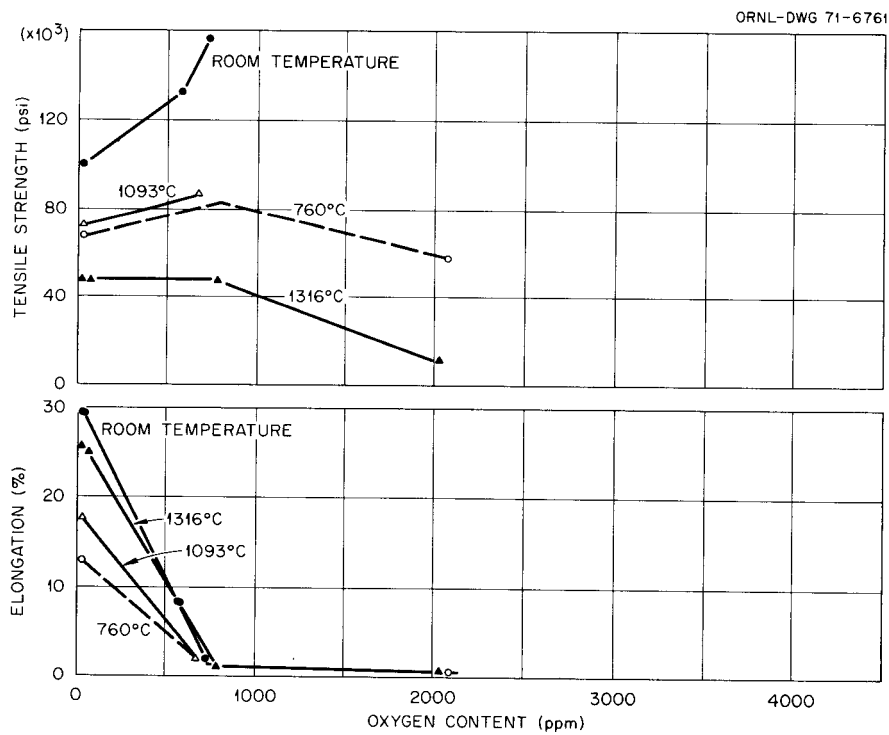


Fig. 24.2. Tensile properties of T-111 as doped with various levels of oxygen at 1000°C.

T-111 fractured in an extremely brittle manner; that is, within the elastic limit at temperatures as high as 1316°C. The contaminated specimens were also examined metallographically. All the results lead to the conclusions that the thermal history, by altering the form and distribution of the oxide precipitate, has a greater effect than the oxygen content on the mechanical properties of T-111.

Simple Method of Determination of the Distribution and Solubility Limit of Interstitials in Substitutional Solid Solutions³

C. T. Liu H. Inouye R. W. Carpenter

A simple method for calculation of the solubility limit of certain interstitial species in solid solutions from a single lattice parameter measurement is described. The calculation is based on thermodynamic considerations, and the result allows qualitative conclusions to be made about the randomness of the solute distribution. The method is used to calculate oxygen solubility limits in Nb-Zr and Nb-Hf alloys and to explain previously reported but apparently quite different solubility limits in the two chemically similar alloys.

Solid-Solution Theory and Spinodal Decomposition⁴

C. T. Liu B. T. M. Loh

The free energy of solid solution varies with the atomic arrangement or degree of mixing in solution. The change of free energy with solution state in an alloy system with a miscibility gap was examined step by step from the random state toward the equilibrium state by a series of approximations provided by the cluster-variation method. As equilibrium is approached, the gap corresponding to the nonequilibrium state gradually shrinks to the equilibrium gap, while the chemical spinodal region expands and eventually approaches the solubility limits. The effects of these features on the spinodal decomposition are discussed. Several experimental observations of spinodal decomposition that cannot be explained satisfactorily by previous theory can be accounted for when the free energy is considered to vary with the state of solution.

3. Abstract of paper accepted for publication in *Journal of the Less-Common Metals*.

4. Abstract of paper accepted for publication in *Philosophical Magazine*.

JOINING STUDIES

G. M. Slaughter

Refractory Alloy Welding Development

A. J. Moorhead C. D. Lundin⁵

Hot-cracking. As part of our program to determine the mechanisms and tendency of hot-cracking in refractory alloys, we have been examining the fracture surfaces of cracks in various refractory metals. We examined cracks that occurred during gas tungsten-arc welding of molybdenum alloy TZM test coupons in a glove box and during orbiting-arc welding of molybdenum tubing outside the box. Examination was by optical microscopy, scanning electron microscopy, and electron microprobe analysis. The results showed that (1) hot cracking that involves a liquid phase (illustrated in Fig. 24.3) can occur in both TZM and Mo, (2) hot cracking can and does influence subsequent cracking at temperatures well below the solidus, and (3) porosity at grain boundaries in the fusion zone and heat-affected zone of Mo welds leads to weld cracking.

The grain-boundary porosity is believed to result from lack of complete exclusion of air from the weld area during arc welding. The porosity observed in several welds tended to link in wormhole fashion (as shown in Fig. 24.4) to produce fissures in both the fusion and heat-affected zones. This, coupled with the large grain

5. Consultant from the University of Tennessee, Knoxville.

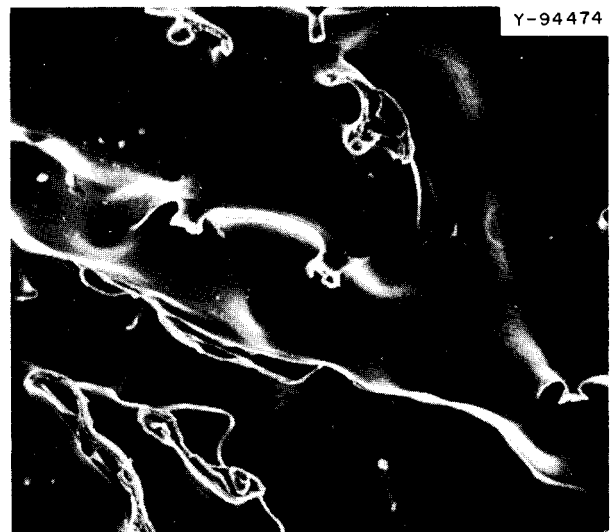


Fig. 24.3. Scanning electron micrograph of a portion of the fracture surface of a hot crack in a TZM weld. Note the protuberances, which solidified from liquid necks formed during cracking. 1000 \times . Reduced 23%.

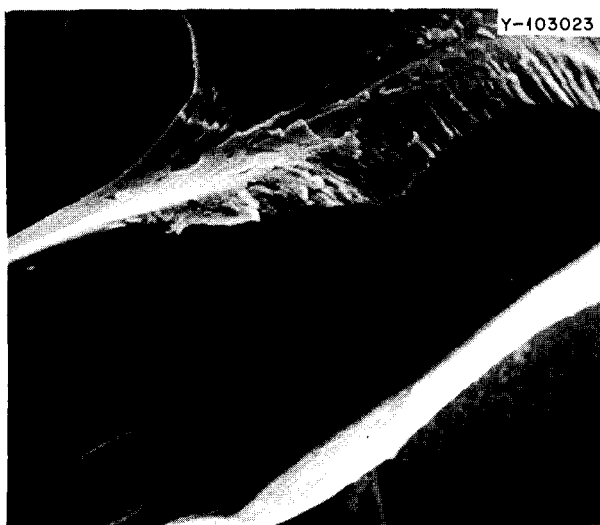


Fig. 24.4. Scanning electron micrograph showing porosity in a portion of the fracture surface of a crack in an orbiting-arc weld on a molybdenum tube. 1000X. Reduced 23%.

size inherent in the weld area, makes the welds exceedingly brittle.

The fracture surfaces of the TZM welds (which have both hot and cold cracks) were carefully examined with a scanning electron microprobe analyzer. Modest amounts of oxygen were in the hot-cracked areas, especially in the protuberances formed by liquid-metal necks during cracking. No significant oxygen concentrations were found in the cold-cracked areas of the weld. Carbon was also detected in small particles on the hot-cracked surfaces and in areas that produced a dark structure in the scanning micrographs.

Component fabrication. Molybdenum and T-111 thermal-convection loops were fabricated by welding. Both are of the same design, but the tubing of the T-111 loop is $\frac{7}{8}$ in. OD \times 0.050 in. wall. Both loops were welded in a vacuum-purged, argon-filled glove box by the manual gas tungsten-arc process using similar filler metal wire. Both were constructed with stringent cleaning, handling, and welding procedures; and the T-111 loop passed the radiographic inspection and was helium leaktight after welding. However, during leak checking of the molybdenum loop, a 1.5-in.-long crack was found in the upper crossover arm. This defect was apparently a previous flaw in the base metal that was propagated by the thermal stresses developed during welding. The crack was machined out and manually rewelded, resulting in a leaktight system. Although this type of defect is undesirable, the result was beneficial in that it demonstrated our ability to repair very large defects in molybdenum structures by welding.

Brazing Alloy Remelt Studies

D. A. Canonico

The use of filler metals for joining refractory metals quite often requires that the brazement function at or near its melting point. This requirement raises the question of remelt temperature. Ideally, two components would be brazed at a low temperature and then the brazement would be capable of withstanding temperatures considerably above the brazing temperature. We have attempted to determine the mechanisms by which the melting point is changed on a number of alloys developed at ORNL⁶ covering a broad range of temperatures.

The program was initiated on the premise that the melting point of the filler metal can be increased primarily by volatilization of an element and solution of a refractory element. Our initial studies centered on three alloys: (1) Ti-48% Zr-4% Be, (2) Ti-46% Zr-8% Ge, and (3) Ti-25% Cr-21% V. All three possess excellent wettability and flowability on refractory metals. Alloy 3 is excellent for the direct brazing of ceramics and graphite; alloy 2 is recommended for joining graphite. Miller-Peaslee shear specimens with a 3-mil joint opening were prepared for tantalum and brazed in a resistance furnace in a vacuum of 10^{-6} torr. After brazing, the specimens were returned to the furnace, stressed, and reheated until failure was observed.

For Ti-48% Zr-4% Be the brazing cycle lowered the melting point from 1800°F to about 1680°F. Electron-beam microprobe analysis showed areas enriched in Zr and, therefore, probably in the melting-point depressant Be as well. The Ti-46% Zr-8% Ge remelt temperature (about 2485°F) was only slightly different from the original melting point (2420°F). This observation is supported by the electron-beam microprobe analysis, which showed very little segregation. However, the melting point of the Ti-25% Cr-21% V alloy increased from 2460 to 2700°F. This increase is attributed to both the solution of Ta into the filler metal and the loss of Cr by volatilization; this was verified by the electron-beam microprobe.

THERMAL CONDUCTIVITY OF REFRACTORY ALLOYS

R. K. Williams J. P. Moore

Combining high temperature electrical resistivity data with low-temperature thermal conductivity data can

6. D. A. Canonico, N. C. Cole, and G. M. Slaughter, "Direct Brazing of Ceramics, Graphite, and Refractory Metals," to be published in *Metals Progress*.

provide good high-temperature thermal conductivity estimates for metals and alloys. Above 1300°K our conductivity estimates for pure tungsten⁷ and tantalum,⁸ which are based on experimentally determined phonon conductivity and Lorenz function values, are probably more reliable than available measurements. The tantalum analysis was extended to include T-111. Estimated values of thermal conductivity to 1000°C were about 3% higher than those measured.

The accuracy of our low-temperature absolute linear heat flow apparatus was improved to permit determinations of phonon conductivity and Lorenz function values for molybdenum. Accuracies in thermal conductivity of $\pm 0.5\%$ and electrical resistivity of $\pm 0.1\%$ from 80 to 400°K are anticipated (see Chap. 8 of this report). Dilute Mo-Zr and Mo-Nb alloys were obtained and characterized for this study.

Room temperature resistivity measurements were used to evaluate ThO₂-17.5% Mo cermets produced by two processes. The high-temperature thermal conductivity was estimated from our previous measurements on molybdenum⁹ and thoria.¹⁰

MECHANICAL PROPERTIES OF COMMERCIAL REFRACTORY ALLOYS

R. L. Stephenson

Since most practical devices require joining, we consider the creep properties of welds to be of critical importance in evaluating materials for use at high temperatures. Stress-rupture data on transverse welds in Ta-10% W, T-111, and T-222 have been reported previously.¹¹⁻¹³ In all cases, the rupture times of the

welds were equal to those of controls at low stresses but much shorter at high stresses.

We have begun testing longitudinal welds in Ta-10% W. At high stresses, these welds fail at times shorter than those of unwelded control specimens, but at low stresses rupture times for welds are at least as long as those of control specimens.

We have creep tested specimens of SU-31 (Nb-17% W-3.5% Hf-0.12% C-0.03% Si) at 980, 1095, 1205, and 1425°C. This particular heat of material has the strongest stress-rupture properties¹⁴ of any niobium-base alloy we have tested to date.

ALKALI-METAL CORROSION OF REFRACTORY ALLOYS

J. H. DeVan

Forced Circulation Lithium Loop

R. L. Klueh

We are examining an engineering-scale, forced-circulation loop constructed of the tantalum-base alloy T-111 (Ta-8% W-2% Hf) that was operated for 3000 hr with lithium.¹⁵ The loop ran at a maximum temperature of 1370°C, a minimum temperature of 1200°C, and a flow rate of approximately 6 gal/min (maximum velocity at heater outlet: 20 fps). Specimens of the T-111 alloy were placed in the heater-economizer section and the pump inlet and outlet lines to measure the effects of mass transfer, including effects on the mechanical properties.

The specimens have been removed from the loop, visually examined, and weighed. Specimens that gained weight had a beige to gold surface coating; specimens that lost weight appeared highly polished, with grains sometimes clearly outlined.

From the weight change data, deposition apparently began somewhere in the radiator, continued through the pump, the pump outlet tube, and about the first 24 in. into the economizer. The specimens in the 1200°C pump inlet and outlet lines showed essentially constant weight gains of 0.6 to 0.7 mg/cm². The only other specimens to show weight gains were those just inside the economizer, where the weight gains decreased from about 0.7 mg/cm² at 1200°C to essentially zero at 1225°C. A maximum weight loss of about 0.9 mg/cm² was found at 1305°C; it did not occur in the maximum

7. R. K. Williams, J. P. Moore, W. P. Murray, and D. L. McElroy, *Metals and Ceramics Div. Annu. Progr. Rept. June 30, 1969*, ORNL-4470, pp. 61-62.

8. R. K. Williams, J. P. Moore, and D. L. McElroy, *Metals and Ceramics Div. Annu. Progr. Rept. June 30, 1970*, ORNL-4570, p. 115.

9. R. K. Williams, J. P. Moore, and D. L. McElroy, *Metals and Ceramics Div. Annu. Progr. Rept. June 30, 1968*, ORNL-4370, pp. 66-67.

10. J. P. Moore, R. S. Graves, and D. L. McElroy, *ibid.* p. 37.

11. R. L. Stephenson, *Fuels and Materials Development Program Quart. Progr. Rept. Sept. 30, 1970*, ORNL-4630, pp. 193-94.

12. R. L. Stephenson, *Fuels and Materials Development Program Quart. Progr. Rept. March 31, 1970*, ORNL-4560, pp. 181-82.

13. R. L. Stephenson, *Fuels and Materials Development Program Quart. Progr. Rept. Dec. 31, 1970*, ORNL-TM-3300, pp. 234-35.

14. R. L. Stephenson, *Fuels and Materials Development Program Quart. Progr. Rept. March 31, 1971*, ORNL-TM-3416, pp. 197-200.

15. B. Fleischer, *Metals and Ceramics Div. Annu. Progr. Rept. June 30, 1970*, ORNL-4570, pp. 103-4.

temperature zone because of the lower liquid velocity there.

Effect of Oxygen on the Compatibility of Refractory Metals with Alkali Metals

R. L. Klueh

We concluded our study of the effect of oxygen on the compatibility of tantalum with the alkali metals potassium, sodium, and lithium.¹⁶ Reactions with oxygen in these systems depend upon whether the oxygen is present in the refractory metal or the alkali metal. Oxygen added to the alkali metal promotes dissolution of the refractory metal. Oxygen added to the refractory metal above a threshold concentration renders the metal subject to penetration by the alkali metal.

The Tantalum-Oxygen-Sodium System¹⁷

The effect of oxygen, both in the sodium and in the tantalum, on the compatibility of tantalum and sodium was investigated at 600°C by static capsule tests.

16. R. L. Klueh, *Metals and Ceramics Div. Annu. Progr. Rept. June 30, 1970*, ORNL-4570, pp. 104-5.

17. Abstract of paper presented at the 1970 Fall Meeting of the Metallurgical Society of AIME, Cleveland, Oct. 19-22, 1970.

Increasing the oxygen concentration of the sodium led to increased dissolution of the tantalum in the sodium. Oxygen migrated from the sodium to the tantalum, and with increasing oxygen concentrations in the sodium, the specimens first gained and then lost weight. Most of the oxygen acquired by the tantalum was in a surface scale. The addition of oxygen to sodium produced a loosely adhering ternary oxide scale on the surface of the tantalum specimen. In high-oxygen sodium, the ternary oxide also formed along grain boundaries.

When the concentration of oxygen in tantalum before test exceeded a "threshold" level, the tantalum was penetrated by sodium. The threshold level was found to be about 200 ppm O. Penetration, as in other refractory metal-oxygen-alkali metal systems previously investigated, proceeds with the formation of a ternary oxide by a wedging mechanism. At low oxygen concentrations, attack proceeds along grain boundaries; as the oxygen concentration of the tantalum is increased, the number of grain boundaries attacked and the depth of attack increases. Still higher oxygen concentrations induce transgranular attack. The penetrated specimens were quite brittle and were easily fractured. Figure 24.5 shows a scanning electron micrograph of a freshly fractured tantalum specimen that contained 2000 ppm O before exposure to sodium and shows the voluminous amounts of corrosion products that form on grain boundaries.

Y-103067

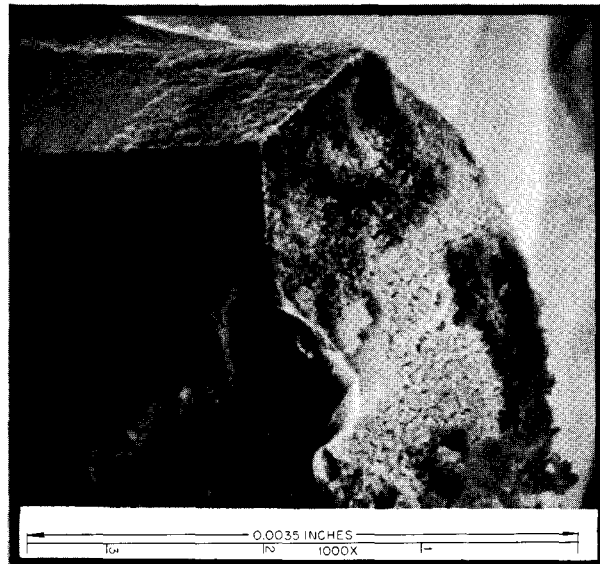


Fig. 24.5. Scanning electron micrograph of a freshly fractured surface of a tantalum specimen that contained 2000 ppm O before exposure to sodium at 600°C.

25. Tungsten Metallurgy

P. Patriarca A. C. Schaffhauser

The objective of this program is to provide the base technology on tungsten alloys for advanced space-power and general reactor technology applications. We are developing fabrication processes for tungsten alloys based on modification of conventional extrusion, chemical vapor deposition, and welding techniques. Since the primary criterion for the use of tungsten alloys for these applications is based on the creep properties, we are conducting extensive long-time tests at the temperatures of interest. We are also determining the mechanisms that control the creep behavior and the effect of interactions with the vapor species from an isotope or reactor fuel. The behavior of tungsten alloys under fast-neutron irradiation is also being evaluated.

EXTRUSION OF TUNGSTEN ALLOY TUBING

R. E. McDonald A. C. Schaffhauser

We continued development of the floating-mandrel technique for the extrusion of tubing of advanced tungsten alloys. Previously we extruded $\frac{3}{4}$ - to 2-in. OD tubing with wall thicknesses between 0.06 and 0.3 in. of tungsten and W-25% Re from powder-metallurgy and arc-cast billets.¹ Recently we expanded our capability to arc-cast W-5% Re and powder-metallurgy W-2% ThO₂. The W-5% Re tubing $\frac{7}{8}$ in. OD \times $\frac{1}{16}$ in. wall thickness was successfully extruded in a molybdenum alloy billet at 1700°C. Tubing of W-2% ThO₂ was successfully extruded to 1 in. OD \times $\frac{1}{8}$ in. wall thickness in a molybdenum alloy billet and to $1\frac{1}{2}$ in. OD \times $\frac{1}{4}$ in. wall thickness directly from a 3-in.-diam billet at 1750°C.

CHEMICAL VAPOR DEPOSITION OF TUNGSTEN ALLOYS

J. I. Federer

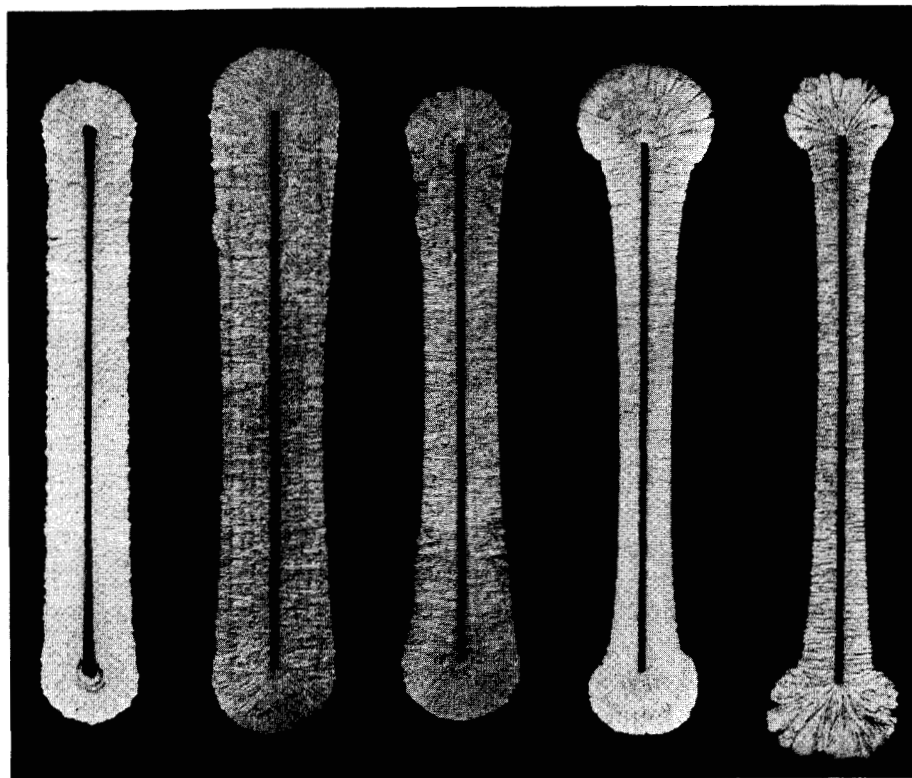
The optimum conditions for chemical vapor deposition of W-5% Re sheet by H₂ reduction of WF₆ and ReF₆ were determined. These conditions minimize nodules and associated porosity in the microstructure.

Previous attempts to minimize nodules by interrupting the deposition process were not successful.² Since a minimum temperature of 700°C is necessary for compositional uniformity, and since pressures in excess of 10 torr suppressed rhenium deposition, the effect of gas mixture was investigated.³ Small deposits (4 in.²) were prepared with gas mixtures having H₂/MF₆ ratios ranging from 1 to 20. The stoichiometric ratio is 3. The other conditions were temperature 750°C, pressure 5 torr, and flow rates of 95 and 5 cm³/min of WF₆ and ReF₆, respectively. The macrostructure of these deposits with the substrate still in place is shown in Fig. 25.1. Gas flow was perpendicular to the view shown. The rhenium content increased from 4 to 7% as the H₂/MF₆ ratio increased from 1 to 20. The uniformity of thickness around the substrate is clearly dependent upon H₂/MF₆ ratio. As the H₂ content of the gas mixture increased, the surface texture of the deposits changed from grainy (like fine sandpaper) to smooth, but the smoother deposits contained many more nodular growths. The edges of the deposit (Fig. 25.1) prepared with the largest amount of hydrogen illustrate nodular growths, which occurred with increasing frequency throughout the deposits with increasing hydrogen content in the gas mixture. Figure 25.1 also shows that the metal recovery, or deposition efficiency, and the deposition rate were maximum for the deposit prepared with a stoichiometric gas mixture. Another series of small deposits prepared with a stoichiometric mixture of gases showed that the deposition rate

1. R. E. McDonald and G. A. Reimann, *Floating-Mandrel Extrusion of Tungsten and Tungsten-Alloy Tubing*, ORNL-4210 (February 1968).

2. J. I. Federer, *Metals and Ceramics Div. Annu. Progr. Rept. June 30, 1970*, ORNL-4570, pp. 118-19.

3. J. I. Federer and A. C. Schaffhauser, "Chemical Vapor Deposition and Characterization of Tungsten-Rhenium Alloys," pp. 74-81 in *IEEE Conference Record of 1970 Thermionic Conversion Specialist Conference, October 26-29, 1970*, The Institute of Electrical and Electronics Engineers, New York, 1970.



H ₂ , cc/min	100	300	500	1000	2000
(WF ₆ + ReF ₆), cc/min	100	100	100	100	100
Recovery, %	15	29	26	23	19
Deposition Rate at Midsection, mil/hr	4.6	8.0	7.2	4.8	4.0

Fig. 25.1. Morphology of nominal W-5% Re deposits produced at 750°C and 5 torr.

continuously increased with increasing total gas flow rate at least up to 1400 cm³/min.

On the basis of information derived from the small deposits, larger sheet-type deposits of nominal W-5% Re alloy having about 55 in.² of surface area were successfully prepared. The material deposited on 2-in.-wide × 16-in.-long resistance-heated molybdenum substrates contained within a water-cooled chamber. The direction of gas flow through the chamber was periodically reversed to minimize the effect of gas depletion and improve thickness uniformity. Deposits having thickness up to 0.090 in. have been prepared with a variation of only about 0.010 in. over 90% of the length. The microstructure was fine grained and contained only a few nodules.

We can now give the optimum conditions for depositing nominal W-5% Re alloys on stationary sheet substrates: temperature 700 to 750°C, pressure 5 to 10 torr, and H₂/(WF₆ + ReF₆) ratio of 3. We obtained a deposition rate of about 0.006 in./hr at an efficiency of about 60% with flow rates of 600, 190, and 10 cm³/min of H₂, WF₆, and ReF₆, respectively.

The effect of gas mixture on the morphology and grain structure of nominal W-25% Re deposits was also studied. As in the above study, the H₂/MF₆ ratio was varied from 1 to 20 while other factors were held constant in the preparation of small deposits. The deposit prepared with a H₂/MF₆ ratio of 1 contained 51% Re, an unexpected result. The rhenium content of the other deposits was in the range 19 to 24%. The

morphology and grain structure were greatly affected by the H_2/MF_6 ratio. The smoothest deposits were obtained at ratios of 3 and 5; at ratios of 1, 10, and 20 the deposits had numerous nodules on the surfaces and rough nodular edges. The microstructure ranged from columnar grains with a small amount of porosity to noncoherent structures with increasing H_2/MF_6 ratio. The results suggested that deposits of best quality would be obtained with a near-stoichiometric gas mixture. This was found to be true in the coating of 0.040-in.-diam wires with a nominal W-25% Re alloy deposit. Coatings prepared with a mixture having a H_2/MF_6 ratio of 3 were mostly smooth, with only a few nodules, whereas coatings prepared with gas mixtures having a ratio of 15 were completely nodular and very porous. In the latter state the coatings have practically no mechanical strength.

EVALUATION OF METHODS FOR JOINING TUNGSTEN AND ITS ALLOYS

N. C. Cole G. M. Slaughter

We have welded tungsten and its alloys using many different methods. Previously, we had gas-tungsten-arc (GTA) welded unalloyed tungsten with and without the addition of filler metals.^{4,5} We have also GTA welded tungsten alloys (W-25% Re, W-25% Re-30% Mo, and W-5% Mo) without the addition of filler metals.⁶ Now we have electron-beam (EB) welded (without adding filler metal) sheets of arc-cast and CVD unalloyed tungsten. We have also GTA welded W-25% Re, adding either Mo-50% Re or W-25% Re-30% Mo filler metals.

Arc-cast and CVD unalloyed tungsten sheets were EB welded with varying degrees of success. Transverse cracks were plentiful in EB welds made without a regulated preheat in arc-cast 0.060-in.-thick tungsten. We preheated the workpiece as much as practicable with the torch, but this type of preheat was not sufficient to prevent cracking. However, this same material was GTA welded crack-free by preheating to 175°C with a heating fixture. In some cases, two welding passes were made with no cracking.

The EB welds in CVD 0.075-in.-thick tungsten were free of cracks even when welded without a preheat. The base material contained only 5 ppm F. In the past, we

4. N. C. Cole and G. M. Slaughter, *Metals and Ceramics Div. Annu. Progr. Rept. June 30, 1968*, ORNL-4370, pp. 73-75.

5. N. C. Cole and G. M. Slaughter, *Metals and Ceramics Div. Annu. Progr. Rept. June 30, 1970*, ORNL-4570, p. 120.

6. N. C. Cole, R. G. Gilliland, and G. M. Slaughter, "Welding of Tungsten," to be published in *The Welding Journal*.

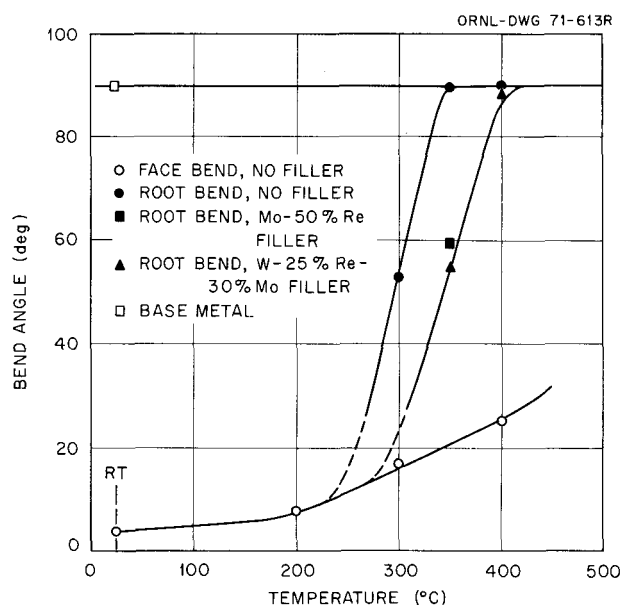


Fig. 25.2. Ductile-to-brittle transition curves of welded W-25% Re sheet.

found that 10 ppm F in the base metal caused bubble coalescence in the heat-affected zone, resulting in grain-boundary cracking.⁷ Even after welding, the CVD tungsten with 5 ppm F contained no grain-boundary bubble formation detectable by the optical microscope.

Welding W-25% Re with Mo-50% Re and W-25% Re-30% Mo filler metals was generally successful. However, we had cracking problems when welding with the Mo-50% Re filler wire. The Mo-50% Re filler wire appeared to be slightly contaminated, which affected the quality of the welds. However, the welds did not contain porosity because the filler wires and base metals were arc-cast.

The ductile-to-brittle transition temperature (DBTT) curves of these welds are compared in Fig. 25.2 with curves for GTA manually welded W-25% Re in which filler metal was added. The arc-cast W-25% Re sheet base metal tested in the stress-relieved condition was ductile at room temperature. The DBTT of welds in W-25% Re was considerably higher than room temperature. The addition of Mo-50% Re or W-25% Re-30% Mo filler metal to the welds caused the DBTT to be even higher. The welds with no filler metal were tested with either the face or root of the weld in tension. The bends with the root in tension were more ductile. We achieved a 90° root bend at 350°C but only a 25° face bend at 400°C. Probably the slight notch on

7. N. C. Cole, *Fuels and Materials Development Program Quart. Progr. Rept. June 30, 1968*, ORNL-4330, pp. 295-301.

the face of the weld (due to the weight of the molten metal) contributed to the loss of ductility. Root bends in welds made with either W-25% Re-30% Mo or Mo-50% Re achieved only 60° at 350°C.

BEHAVIOR OF TUNGSTEN ALLOYS UNDER FAST-NEUTRON IRRADIATION

F. W. Wiffin R. K. Williams
D. A. Dyslin⁸ D. L. McElroy
H. E. McCoy, Jr.

Data from the fast-neutron irradiation damage of other refractory metals, which are reported in Chap. 29 of this report, suggest that voids will form in tungsten for irradiation temperatures between 830 and 1570°C, 0.3 and 0.5 times the absolute melting temperature. Void densities may be as high as 10^{17} voids/cm³, and the accompanying swelling may exceed 1%. Limited data on powder-metallurgy tungsten show high densities of small voids after irradiation to 1.5×10^{20} neutrons/cm² (>1.0 MeV) at 1000 and 1300°C. These effects in tungsten could be detrimental to the performance of thermionic diodes for space power applications and high-temperature thermocouples for fuel center-line temperature measurement in LMFBR experiments. As the void density increases, the intervoid spacing will approach the mean free path of conduction electrons, and a significant increase in resistivity is expected. This behavior could affect the high-current performance of thermionic diodes and produce changes in the thermoelectric power and shunting of thermocouples.

We have designed and constructed a one-pin experiment for EBR-II to test the effect of irradiation temperatures between 1000 and 1500°C on the behavior of tungsten and tungsten alloys at a maximum fluence of 2.8×10^{21} neutrons/cm² (>0.1 MeV). We are irradiating 0.10-in.-diam rod specimens of tungsten

and tungsten-rhenium alloys produced by powder-metallurgy, arc-melting, and CVD techniques. Determination of the high-temperature electrical resistivity of control specimens for this experiment is under way. The data and techniques used for these measurements are presented in Chap. 8 of this report. Laser welding appears to be an excellent method for attaching the necessary instrumentation leads to the irradiated tungsten resistivity specimens. Wires of Pt and Pt-10% Rh laser welded to tungsten rods sustained thermal cycles to 1400°C and static load tests.

EFFECT OF LOW-PRESSURE GASES ON THE CREEP PROPERTIES OF TUNGSTEN ALLOYS

H. Inouye

The creep properties of W-25% Re were measured in low-pressure oxygen to simulate interaction with oxygen derived from the decomposition of oxides at high temperatures. The results are compared with the creep properties of the alloy in a vacuum of 10^{-7} torr. Between 1650 and 2000°C and stresses of 1000 and 2000 psi, the creep rates were as much as 250 times lower in 10^{-5} torr O₂ than in vacuum; however, rupture strains were only 2 to 7% in the O₂ environment. At 1800°C the creep strength in 10^{-5} torr O₂ was twice that in vacuum. Specimens exposed to oxygen before creep testing in vacuum were also stronger than specimens tested in vacuum. The oxygen content was generally lower in specimens tested in oxygen than in the as-received material. The lower creep rates of W-25% Re in oxygen are attributed to a surface layer of σ -phase resulting from selective volatilization of tungsten oxides.

We are also measuring the creep properties of 0.040-in.-diam tungsten wire in low-pressure CH₄ to simulate the effect of carburization by uranium carbide at thermionic temperatures. Table 25.1 compares the

8. General Engineering Division.

Table 25.1. Comparison of creep properties of tungsten at 1800°C and 2000 psi in vacuum and in CH₄

Pressure of environment (torr)	Time (hr) for strain of			Rupture results		Creep rate (hr ⁻¹)
	0.5%	1%	2%	Life (hr)	Elongation (%)	
1.8×10^{-7} (vacuum)	23	53	117	327	7.0	1.5×10^{-4}
2.6×10^{-6} (CH ₄)	16	30	62	278	6.5	2.0×10^{-4}
5.2×10^{-6} (CH ₄)	22	42	77	163	4.9	3rd stage only
2.6×10^{-5} (CH ₄)	16	36	71	113	3.9	3rd stage only

creep behavior in vacuum and in CH_4 at 1800°C and a stress of 2000 psi; carburization lowers the creep strength. A progressive decrease in the rupture life and ductility with an increase in CH_4 pressure is also noted. Temperature measurements during the test show an increase in the $0.665\ \mu\text{m}$ spectral emissivity of tungsten from 0.43 to about 0.6 after about a 30-hr exposure to CH_4 . This increase is attributed to the formation of W_2C at the surface. After test the specimen showed a silvery metallic surface and no change in weight.

FORMATION OF CREEP CAVITIES IN POWDER-METALLURGY TUNGSTEN

J. O. Stiegler

At elevated temperatures metals lose ductility because grain-boundary cracks form. Details of the nucleation and growth of these cracks in powder-metallurgy tungsten were studied by electron fractography. Creep tests were interrupted, and the specimens were fractured at room temperature to expose any cavities or cracks formed at high temperatures.

After annealing 1 hr at 1600°C the grain boundaries of the tungsten were populated by about 10^7 gas bubbles per square centimeter, averaging approximately $0.2\ \mu\text{m}$ in diameter. The bubbles were distributed nonrandomly and showed large variations in size and distribution. Different grades of tungsten showed different grain-boundary structures.

Under stress at 1600°C these bubbles expanded. At low stresses they grew slowly and maintained equiaxed, crystallographic shapes. At high stresses they grew rapidly in the plane of the grain boundary and formed irregular, flat cavities about $1\ \mu\text{m}$ thick. These cavities grew rapidly in certain directions but always kept blunt ends. No evidence of cavities nucleated by deformation

was obtained, but a few rare cases of possible triple-grain junction cracks were found. Only a slight tendency for rounding of the flat cavities was noted for annealing times as long as 100 hr at 1600°C .

The model most in agreement with these observations is one in which the gas bubbles expand to form the cavities by the stress-directed diffusion of vacancies along the grain boundaries. At low stresses this occurs slowly enough that the cavities can maintain equiaxed shapes by surface diffusion. When the growth rate exceeds some critical value, surface diffusion becomes too slow, and the cavities grow in the plane of the boundary. Their irregular shapes suggest that the average stress does not direct their growth but that local variations in stress, possibly resulting from grain-boundary sliding or deformation within the grains, are responsible. The wedgelike cracks observed with the optical microscope arise when the flat cavities reach a triple-grain junction and are opened into a wedge by sliding on the adjacent grain boundaries. This model reconciles the conflicts in some of the previous models for crack formation.

Since the specimen elongates as the cavities expand, their growth constitutes a creep mechanism. The creep rate from the diffusion-controlled growth of equiaxed cavities is in order-of-magnitude agreement with measured creep rates for materials containing cavities. The creep rate from growth of cavities at the concentrations present in the powder-metallurgy material is about two orders of magnitude faster than Nabarro-Herring diffusional creep in the same material. Some unusual observations made on a powder-metallurgy W-25% Re alloy, which deformed at a faster rate at 1650°C than at 2200°C at a stress of 500 psi, were explained semi-quantitatively by this model of creep due to cavity growth and the observed microstructural features.

26. Uranium Nitride Fuels

J. L. Scott P. Patriarca

Uranium mononitride is of interest as a fuel material for space-nuclear reactors because of its high thermal conductivity, high melting point of 2800°C , and good irradiation stability. Because space reactors reject heat by radiation, fuel pin cladding temperatures of interest are 1000°C or greater. The objective of our program is to establish the rate of swelling and fission-gas release of UN irradiated in refractory metal cladding at surface temperatures above 1000°C . The program also includes development of fabrication of very high-purity UN, because impurities such as carbon or oxygen may adversely affect performance.

Development of nitride fuels for fast breeders is reported in Chap. 16 of this report, and fundamental studies of nitrides are in Chap. 6 and others.

FABRICATION OF URANIUM MONONITRIDE

V. J. Tennery R. A. Potter T. G. Godfrey

We developed the techniques required to isostatically press large annular cylinders of UN so as to produce sintered parts having dimensions within 0.015 in. of nominal. During this process, oxygen contamination of the UN is prevented. The cylinders have the nominal dimensions: OD = 0.63 in., ID = 0.20 in., length = 1.6 in., and the mass ≈ 110 g. The isostatic pressing form is loaded in an inert atmosphere glove box sealed off from the atmosphere, removed from the box, isopressed at 60×10^3 psi, then returned to the box and unloaded. Machining techniques using diamond grinding tools were developed and the cylinders were machined to within ± 0.0005 in. on the diameters and lengths, with a TIR below 0.001 in. A group of the sintered and machined cylinders are shown in Fig. 26.1. Approximately 130 of these cylinders were produced for an irradiation study of UN. The oxygen content of the UN in all this material was below 400 ppm. Techniques were also developed for producing some very small cylinders of UN, which were fully enriched in ^{235}U . The specimens were used in fission gas release studies and were required to be 0.050 in. OD \times 0.030 in. ID \times

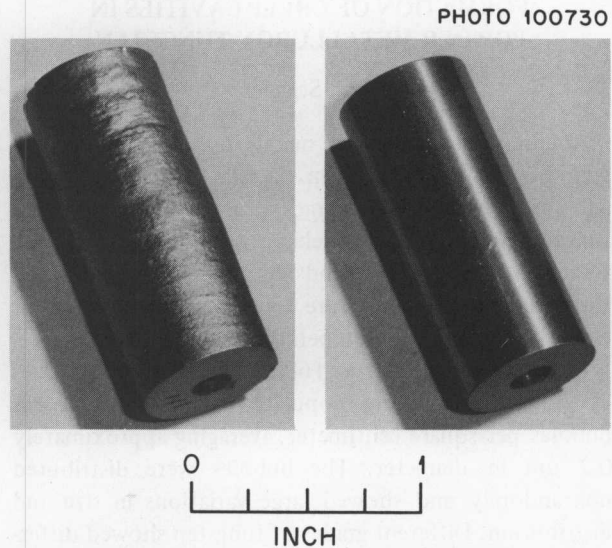


Fig. 26.1. Sintered and machined annular cylinders of uranium mononitride.

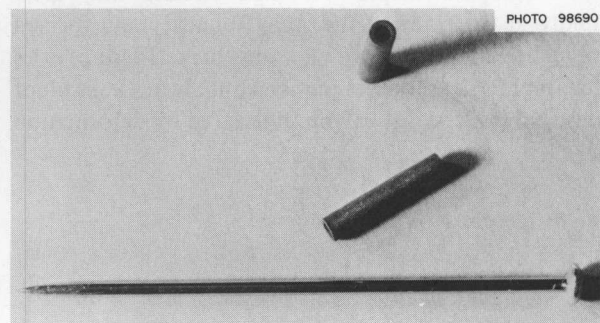


Fig. 26.2. Fission gas release specimens of uranium mononitride. Straight pin length = 1.11 in.

0.26 in. long. The insides of these cylinders were successfully machined by electrostatic discharge methods. Approximately 50 of these specimens were produced. Two of the cylinders are shown beside a straight pin in Fig. 26.2.

IRRADIATION TESTING OF URANIUM NITRIDE

T. N. Washburn

The objective of the ORNL program for irradiation testing of uranium mononitride (UN) is to obtain basic information on fuel swelling, fission-gas release, and compatibility with cladding materials at fuel temperatures from 1000 to 1500°C, cladding outside surface temperatures of 900 to 1400°C, and linear heat ratings of 5 to 10 kW/ft. Detailed descriptions of our capsule design¹ and previous test results²⁻⁴ have been reported.

Examination of Capsule UN-3

D. R. Cuneo⁵

Examination of capsule UN-3 was completed. Partial results of the postirradiation examination have been given previously.⁶ This capsule contained 3-in.-long UN-fueled pins. The top pin cladding was W-25% Re, and the middle and bottom pin cladding was T-111 (Ta-8% W-2% Hf) with a tungsten barrier between the cladding and the UN fuel. The top fuel pin exposure was 1.4 at. % burnup, and the other two pins reached estimated burnups of 1.75 at. %.

Briefly, the findings since last year are summarized below. Details are reported elsewhere.^{7,8}

Electron microprobe analysis of the cladding of the failed middle fuel pin revealed no indications of uranium contamination from the fuel, or of any diffusion from the tungsten liner into the T-111 cladding. However, large concentrations of hafnium

were noted at cracks and voids, both in the T-111 cladding and in the CVD tungsten liner. The mechanism for this concentration of hafnium is not known. Grain size in the failed portion of the cladding was six times that in the unfailed region. A scanning electron micrograph of the failed region of the cladding is shown in Fig. 26.3.

Similarities in dimensional and microstructural changes for the bottom fuel pin showed that with additional time or higher temperature operation, this pin would have failed in a similar mode. These fuel pins were identical in cladding material and uranium enrichment (T-111 with 3-mil tungsten liner, and 12% ²³⁵U). Typical metallographic observations from a transverse section of the bottom fuel pin are seen in Fig. 26.4. The accumulation of fission gas at grain boundaries in the fuel is seen at the higher magnification. Self-shielding in a thermal-neutron flux caused a much higher fission rate near the periphery of the fuel, and accumulation of fission gas at the grain boundaries is sufficient to cause grain pullout in this region during specimen preparation.

The top fuel pin, which operated at 1350°C fuel center temperature and 1300°C cladding outside surface temperature, was clad with W-25% Re and fueled with 20%-enriched UN. Metallographic examination showed no evidence of any general chemical incompatibility between the UN fuel and the cladding. An apparent general intergranular penetration of the cladding by the fuel reached a maximum depth of only 20 μm. Examination of the interface between fuel and cladding also showed that the fuel was in intimate contact with the cladding during irradiation. In several regions grains of fuel separated from the periphery of the fuel pellet during cooling and remained attached to the cladding. No deleterious effects were noted.

Capsule Fabrication

E. J. Manthos

Three new irradiation test capsules were fabricated: one (UN-5) sponsored by the AEC and two (UN-4 and UN-6) by NASA. Capsules UN-4 and UN-5 contain two types of UN pellets — solid 85%-dense cylinders and annular 95%-dense cylinders. The inner diameter of the annular pellets was sized such that both types of pellets gave the same fuel smear density. The six fuel pins in these two capsules have T-111 (Ta-8% W-2% Hf) cladding. Capsule UN-6 contains UO₂ pellets with T-111 cladding on one fuel pin and Nb-1% Zr on two. Capsule UN-6 serves to investigate the backup or derated design being considered for advanced space reactors. The control cladding temperature of each

1. V. A. DeCarlo, F. R. McQuilkin, R. L. Senn, K. R. Thoms, and S. C. Weaver, *Design of a Capsule for Irradiation Testing of Uranium Nitride Fuel*, ORNL-TM-2363 (February 1969).

2. T. N. Washburn, D. R. Cuneo, and E. L. Long, Jr., "Irradiation Performance of Uranium Nitride at 1500°C," *Amer. Ceram. Soc. Bull.* **50**, 427 (1971).

3. T. N. Washburn, K. R. Thoms, S. C. Weaver, D. R. Cuneo, and E. L. Long, Jr., "Examination of UN-Fueled Pins Irradiated at 1400°C Cladding Temperature," *Trans. Amer. Nucl. Soc.* **13**, 101 (1970).

4. S. C. Weaver, K. R. Thoms, and V. A. DeCarlo, "Irradiation Testing of UN in ORR," *Trans. Amer. Nucl. Soc.* **12**, 547 (1969).

5. On loan from the Reactor Chemistry Division.

6. T. N. Washburn, S. C. Weaver, K. R. Thoms, D. R. Cuneo, and E. L. Long, Jr., *Metals and Ceramics Div. Annu. Progr. Rept. June 30, 1970*, ORNL-4570, pp. 116-117.

7. D. R. Cuneo and E. L. Long, Jr., *Fuels and Materials Development Program Quart. Progr. Rept. June 30, 1970*, ORNL-4600, pp. 177-80.

8. D. R. Cuneo and E. L. Long, Jr., *Fuels and Materials Development Program Quart. Progr. Rept. Sept. 30, 1970*, ORNL-4630, pp. 180-85.

R-54109

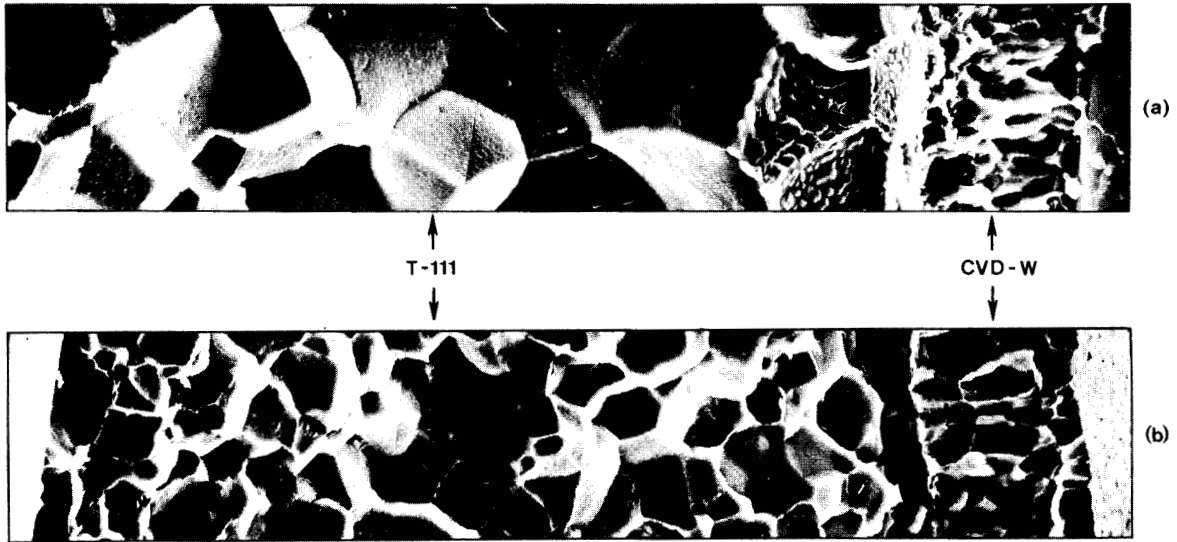


Fig. 26.3. Scanning electron micrograph of T-111 cladding of the failed middle fuel pin of capsule UN-3. (a) Grain size in region near failure is about 6 times that of other sections. (b) Smaller grain size of region away from failure.

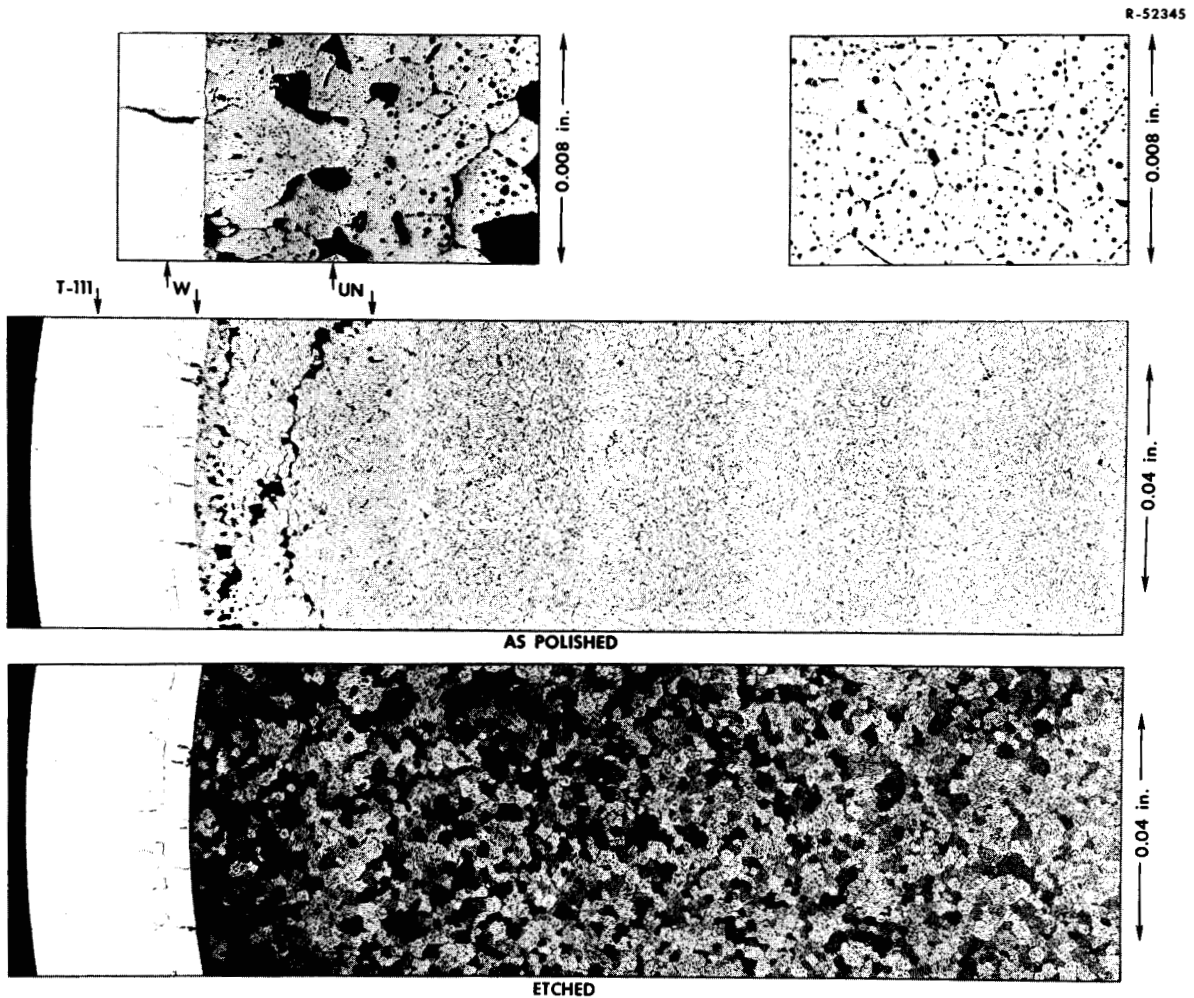


Fig. 26.4. Transverse section of bottom fuel pin of capsule UN-3.

capsule test is 1000°C, with the UO₂ fuel central temperature restricted to 1550°C. Thus, the UO₂ fuel will operate at 6.5 kW/ft maximum, while the UN will operate at 9 to 10 kW/ft.

Capsule Operation

B. Fleischer K. R. Thoms⁹

Capsule UN-4 and UN-5 have operated satisfactorily since their insertion in the ORR; their thermal history has been presented graphically.¹⁰ A detailed thermal analysis has been made using the calorimeter and the cladding thermocouples. We have detected and rationalized temperature penetrations and have a reasonable explanation for our operation at higher heat ratings than anticipated for maintenance of 1000°C cladding temperature. The need for a higher heat rating is apparently caused by reduced thermal resistance between the fuel elements and the ORR coolant. The low thermal resistance is a result of the NaK capsule being slightly off center with respect to the primary container. This condition requires UN-4 and UN-5 to operate at 15% higher heat ratings than anticipated.

The thermal perturbations are also related to the position of the NaK capsule with respect to the primary container. Sporadic thermal cycles as great as 80°C and lasting about 12 sec are apparently caused by shifting of

the NaK capsule with respect to the container. Calculations show that as little as 0.001 in. movement would cause a 40°C change in temperature at design power level. As a result of these findings we have reduced the dimensional tolerances for UN-6 to reduce the perturbations and achieve the desired cladding temperature at the designed power level.

Proposed UN Tests in EBR-II

B. Fleischer M. K. Preston¹¹

A proposal for testing of UN—refractory metal fuel elements in EBR-II was prepared and submitted to the AEC. The proposal, described in more detail in the periodic reports,^{12,13} provides for testing of Nb—1% Zr, T-111, and W—25% Re cladding at 1000°C using 95%-dense annular fuel pellets. These materials would be tested over a range of burnup from 0.75 to 5.5% FIMA and heat ratings from 4 to 11.5 kW/ft. Data from these tests are considered essential for future engineering development of fuel elements for space nuclear systems.

9. Reactor Division.

10. B. Fleischer and K. R. Thoms, *Fuels and Materials Development Program Quart. Progr. Rept. March 31, 1971*, ORNL-TM-3416, pp. 176–80.

11. On loan from General Engineering Division.

12. B. Fleischer, T. N. Washburn, and M. K. Preston, *Fuels and Materials Development Program Quart. Progr. Rept. Dec. 31, 1970*, ORNL-TM-3300, pp. 220–22.

13. B. Fleischer, T. N. Washburn, and M. K. Preston, *Fuels and Materials Development Program Quart. Progr. Rept. March 31, 1971*, ORNL-TM-3416, pp. 179–81.

Part IV. General Fuels and Materials Research

27. Fuel Element Fabrication Development

G. M. Adamson, Jr. W. R. Martin

The objective of this program is twofold, to improve fuel element fabrication technology for research and test reactors, and to advance the knowledge concerning those factors that limit irradiation performance of HFIR and ATR fuel elements. Two recent reports describe postirradiation examination¹ and manufacturing development² of HFIR fuel plates.

IRRADIATION EXPERIMENT ON THE SWELLING BEHAVIOR OF ALUMINUM-BASE DISPERSION FUELS

M. M. Martin

The goal of this experiment is to determine factors that may influence the performance of aluminum-clad UAl_x and U_3O_8 dispersions in the ATR and HFIR at fission densities up to 2.5×10^{21} fissions/cm³. Material variables included are (1) initial void content of the fuel dispersions (i.e., type of fuel dispersoid, dispersoid concentration, and fabrication procedure); (2) void stability in the absence of significant burnup; (3) fuel dispersoid particle size; and (4) dimensional stability of aluminum-clad Al-24 wt % α - Al_2O_3 dispersion, which may be substituted for the aluminum in the filler section of HFIR inner and outer annulus fuel plates. Two grades of U_3O_8 , burned and high-fired, and arc-cast UAl_x were used at dispersoid concentrations that correspond to current HFIR and ATR loadings and 25% increases in these loadings. Table 27.1 lists the

pertinent attributes of the unirradiated plates and their exposure in HFIR.

All components for the capsule were fabricated with strict quality assurance. Final assembly, testing, and installation in HFIR were accomplished without difficulty. It was irradiated in the beryllium reflector from January 11, 1971, to May 13, 1971. Our miniature fuel elements were free of obstruction and appeared to be in good physical condition with no evidence of failure. Detailed examination is under way.

HFIR FUEL ELEMENT SUPPORT

W. R. Martin G. M. Adamson, Jr.

HFIR Fuel Element Manufacture

R. W. Knight

Assistance to Texas Instruments, Inc. has continued throughout the past year. To date, 107 fuel assemblies have been delivered. None has met all the specifications, but all have been accepted on waiver and will be operated at full power. The most troublesome factor for all assemblies was welding. The welding machine had two malfunctions, which caused burnthrough that had to be repaired by broaching. One lot of No. 3 sideplate stock (13 pieces) was sent to salvage because internal stresses in it created excessive out-of-roundness in the outer assembly. The fuel plate yields for plates in groups are presented in Table 27.2. The major cause of fuel plate rejection is bond defects. These FY 1971 results show a 2.5% improvement in yield over the FY 1970 total. The net yield of plates for FY 1971 was 97.8%.

During the year, 29 approval requests were submitted and processed: Of these, seven were for waivers on 165

1. A. E. Richt, R. W. Knight, and G. M. Adamson, Jr., *Postirradiation Examination and Evaluation of the Performance of HFIR Fuel Plates*, ORNL-4714 (in press).

2. R. W. Knight and T. L. Sherman, *Development of Manufacturing Procedures for HFIR Fuel Plates to ORNL Specifications*, ORNL-4713 (in press).

Table 27.1. Miniature test fuel plates irradiated in HFIR for 11,613 MWd

Reference plate number	Core composition ^a (wt %)	²³⁵ U Loading		Fuel particle size distribution		Irradiation conditions		
		Enrichment in fuel particle (wt %)	Volumetric core composition (g/cm ³)	Upper range (μm)	<44 μm (wt %)	Center-line temperature (°C)		Peak ²³⁵ U Burnup (fissions/cm ³)
						Maximum	End of life	
								× 10 ²¹
11 ^b	53 arc-cast UAl _x	0.2	0.00	44–149	21	49	49	0.0
21	54 arc-cast UAl _x	0.2	0.00	44–149	21	49	49	0.0
31 ^c	55 arc-cast UAl _x	0.2	0.00	44–149	21	49	49	0.0
12	47 high-fired U ₃ O ₈	93.2	1.41	44–88	10	89	71	2.5
22	50 burned U ₃ O ₈	93.2	1.43	44–88	11	85	68	2.5
32 ^{b,d}	51 arc cast UAl _x	93.1	1.31	44–149	24	80	63	2.2
01–02 ^e	47 high-fired U ₃ O ₈	93.2	1.40	44–88	10	89,93	72,74	2.2–2.6
13	40 high-fired U ₃ O ₈	93.2	1.14	44–88	10	84	63	2.2
23	42 burned U ₃ O ₈	93.2	1.15	44–88	11	83	62	2.2
33	54 arc-cast UAl _x	0.2	0.00	None	100	51	49	0.0
14	53 arc-cast UAl _x	93.1	1.32	44–149	24	92	69	2.6
24 ^b	52 arc-cast UAl _x	93.1	1.31	44–149	24	90	68	2.5
34	53 arc-cast UAl _x	93.2	1.32	44–53	97	88	67	2.5
03–04 ^e	44 high-fired U ₃ O ₈	93.2	1.29	44–88	10	94,94	71,72	2.5–2.6
15	63 arc-cast UAl _x	93.1	1.67	44–149	24	98	78	3.0
25	64 arc-cast UAl _x	93.1	1.69	44–149	24	96	76	3.0
35	63 arc-cast UAl _x	93.2	1.66	44–53	97	94	74	2.9
16	40 high-fired U ₃ O ₈	0.2	0.00	44–105	9	58	51	0.0
26	40 high-fired U ₃ O ₈	0.2	0.00	44–88	39	57	51	0.0
36	24 α-Al ₂ O ₃			44–88	55	54	51	0.0
05–06 ^e	51 high-fired U ₃ O ₈	93.2	1.58	44–88	10	101,99	80,78	2.6–3.0

^aCladding and matrix materials are aluminum alloys 6061 and 101, respectively.

^bPlates hot rolled to final gage to lower fabrication void content.

^cPlates cold rolled an additional 20% in thickness to increase fabrication void content.

^dPlate hot pressed after hot rolling operation to decrease fabrication void content.

^eInstrumented plates. Temperatures at other plates are calculated.

fuel plates; 110 were approved. The other 22 requests submitted and approved dealt with revisions to manufacturing practices, procurement and disposal of materials and equipment, and occasional special and experimental manufacturing tasks.

Modifications and Improvement to HFIR Fuel Plates

R. W. Knight

The reduced incidence of nonbonds in fuel plates shown in Table 27.2 can be attributed to the switch from commercial to reagent grade nitric acid, since no other production change directly affected fuel plate assembly. The cost of the higher priced acid was offset by less consumption and improved yields.

Six inner and six outer annulus fuel plates containing the cheaper burned grade of U₃O₈ were used in the HFIR in fuel element assembly 100. This fuel assembly operated normally in the reactor. Assessment of the fuel plates in the hot cell will start in January 1972. The void volume of the fuel section of the core in the as-rolled plate increased an average of 3.9 and 2.6% for the outer and inner fuel plates, respectively.

Work is continuing to increase the void volume of the fuel core filler section with the addition of Al₂O₃. One miniature plate has been irradiated in HFIR. Void volume produced by this method was stable during irradiation. Dummy fuel plates are being made at Texas Instruments, Inc. to establish manufacturing parameters and assess nonbond results. Data for homogeneity

Table 27.2. HFIR fuel plates rejected during manufacture^a

Reasons for rejections	FY 1971		FY 1970		All production to date	
	Number rejected	Percent	Number rejected	Percent	Number rejected	Percent
Compacts	6	0.06	2	0.02	287	0.42
Surface	21	0.23	27	0.30	2009	2.93
Bond defects	134	1.45	354	3.96	3581	5.22
Core location	31	0.33	57	0.64	628	0.91
Homogeneity	122	1.32	84	0.94	1399	2.04
Dimensions	0	0.00	48	0.54	142	0.21
Form	0	0.00	1	0.01	36	0.05
Miscellaneous	0	0.00	6	0.07	236	0.34
Total	314	3.39	579	6.48	8318	12.12
Accepted on waiver	110	1.19	159	1.78	2626	3.83
Net rejected	204	2.20	420	4.70	5692	8.29

^aNumber manufactured: 9264 in FY 1971, 8934 in FY 1970, 68,638 total.

standards have been evaluated and are reported in a later section of this chapter.

Thermal Conductivity of U₃O₈-Aluminum Fuel Plate Cores

R. S. Graves

The thermal conductivity and electrical resistivity of U₃O₈-Al cermet were measured from 7 to 127°C in a guarded longitudinal heat flow apparatus for the HFIR project. Four samples were machined from fuel plate material fabricated by the picture-frame technique using two forms of U₃O₈. Oxide volume fractions of 0.12 and 0.18 were obtained using 13.5 and 19.5% burned U₃O₈ (density 7.6 g/cm³) and 12.5 and 18.1% high-fired U₃O₈ (density 8.2 g/cm³). The resistivity values, which reflect the volume fraction of electrically nonconducting material (oxide and voids), indicate larger void volume fractions for the burned U₃O₈ samples. For this temperature range the thermal conductivity values for a given cermet are independent of temperature to within 2%, as expected from previous results on 101 aluminum.³ The thermal conductivity values decrease with increasing volume fraction of electrically nonconducting material and fall within 3.5% of the values expected for aluminum containing voids. The thermal conductivity of the burned U₃O₈ sample was less than that of the high-fired by 2.5% at 0.12

volume fraction and 7.5% at 0.18 volume fraction. Both results are consistent with the higher void volume of the burned U₃O₈ samples.

Establishment of X-Ray Attenuation Standards for Burned U₃O₈ and High-Loaded, High-Fired U₃O₈ Plates

B. E. Foster S. D. Snyder

One inner- and one outer-annulus plate containing high-fired U₃O₈ at the standard HFIR fuel loading, one inner plate with 1.35 times that loading, one outer plate with 1.25 times that loading, and four similar plates loaded with burned U₃O₈ were fabricated by the Texas Instruments, Inc. We made x-ray attenuation scans of these plates, and the appropriate places were analyzed for uranium content. We plotted the weight of uranium in 0.078-in.-diam right-circular cylinders through the fuel plate as a function of x-ray attenuation at the normal energy conditions of 50 kVcp, 2.5 mA. As with past data we observed a bias for the inner-annulus plate containing high-fired U₃O₈ at the standard HFIR loading when compared with our original calibration data. However, a considerable reduction in point scatter allowed us to see that the bias was very uniform. The reduction in point scatter is attributed to the use of improved control of sample machining and location and more precise chemical analysis obtained from more stable transistorized coulometers.

We used a least-squares polynomial fit of the uranium content as a function of attenuation in computer programs to derive in tabular form our calibrations for

3. D. L. McElroy, R. S. Graves, and J. P. Moore, *Metals and Ceramics Div. Annu. Progr. Rept. June 30, 1970*, ORNL-4570, pp. 134-35.

both the inner- and outer-annulus high-fired U_3O_8 and burned U_3O_8 plates. Contrary to past practice, we find that each type plate has its own calibration; a continuous calibration cannot cover both the inner and outer annulus for a particular type of oxide. We tested the high-fired U_3O_8 calibrations by determining from attenuation scan data the content of uranium in one inner and one outer plate fabricated with production techniques and containing a standard loading. Agreement with the quoted uranium content of these plates is within 0.5%.

After establishing and confirming the proper x-ray energy and calibration curve, we determined equivalent thicknesses of aluminum for the fabrication of contoured attenuation standards for fuel plates containing the standard loading of burned oxide as well as increased loadings for both high-fired and burned oxide fuels.

DEFORMATION BEHAVIOR OF FUEL CORES DURING ROLLING

J. H. Erwin R. G. Donnelly

In our effort to eliminate nonuniform deformation (dogboning) from fuel cores roll bonded within cladding materials somewhat weaker than the fuel core, we fabricated a limited number of simulated plates. These plates represent the completion of this effort to solve the dogboning problem. Before the billets were assembled, each end of the cores was relieved at midthickness by milling a 60 or 90° included angle the full width of the core. For the 60° relief, cores were machined to depths of 0.114, 0.146, and 0.200 in., the equivalent of 3, 5, and 10% of the longitudinal area of the 0.272-in.-thick \times 1.800-in.-long cores. For the 90° relief, cores were machined to depths of 0.087, 0.110, and 0.130 in., the equivalent of 3, 5, and 7.5% of the longitudinal area. The simulated cores were aluminum alloys, either 6061 or 2219, and the cladding was alloy 8001. We rolled the billets at 490°C, one group at reductions according to HFIR schedule on a 12-in.-diam mill and another group at reductions 1.5 times the HFIR schedule on a 20-in.-diam mill. We removed billets from the rolling schedule at thicknesses of about 0.200, 0.100, 0.063, and 0.050 in. to observe the cross section.

Visual examination of these simulated cores revealed the following.

1. For the range of variables examined, we found no influence of size of rolling mill or reduction rate.
2. Shaping of the core with radii within the range from 0 to 1 in. reduced the dogboning significantly when the ratio of fuel core to cladding strength was 2.0. But at strength ratios of near 3, the core shaping was ineffective in reducing dogboning.
3. A V-shape core was effective in reducing the dogboning of plates containing the very strong cores, but extensive fishtails were produced that would be objectionable.

EXAMINATION OF A FAILED ATR FUEL PLATE

A. E. Richt J. L. Miller, Jr.

A substantial effort was made to assist the AEC and Idaho Nuclear Corporation (INC) in analyzing the localized failures in a few ATR fuel elements. A number of fuel plates in the ATR had released small amounts of fission products to the reactor coolant. The failures were small protuberances that looked like pimples on the surfaces of the fuel plates. The pimples are generally located near the corners of the fuel core and are open to the coolant water.

We examined one metallographic sample, which contained a single, longitudinal cross section through a pimple near the upper (i.e., coolant inlet) end of a fuel plate. The microstructure of that cross section was studied, and it was chemically analyzed with the electron microprobe.

Since the failures might have been caused by the accidental contamination of the fuel cores with some foreign material, we analyzed the material within the cavity with the electron microprobe. A spectral scan of this material revealed significant amounts of only Al and U; however, since we cannot presently detect the elements with lower atomic numbers, this material may also have contained O, H, N, and C. Scans across this material, however, revealed that the Al and U concentrations varied inversely in a rather periodic manner. We interpreted this as an indication that the material within the cavity consisted of oxidized or hydrolyzed fuel material (i.e., corrosion products of the $Al-UAl_x$ fuel dispersion) and that no organic foreign materials were present to account for the failure.

Metallographic examination of the specimen also indicated that the failures might have been a result of corrosion. Many small pits were in the cladding near the blistered area. A deeper pit was found a short distance away from the blistered area. This pit completely penetrated the 6061 alloy cladding, which is nominally 0.015 in. thick.

28. Joining Research on Nuclear Materials

G. M. Slaughter

The purpose of this program is to gain needed fundamental and practical information on the welding of structural materials used to manufacture critical components for the nuclear industry. The quality of the welds can be affected by chemical composition, melting practice used in making the base metal or filler wire, and welding techniques. Research is centered on the weldability of alloys that are candidate materials for the construction of vessels, intermediate heat exchangers, steam generators, and core components for liquid-metal fast breeder reactor plants. Stainless steels and Incoloy 800 are emphasized because of their immediate applicability.

DUCTILITY OF INCONEL 600 BASE METAL AT INTERMEDIATE TEMPERATURES

W. J. Werner D. A. Canonico

Tensile studies were conducted on specially melted Inconel 600 alloys at intermediate temperatures (400 to 1000°C) in an argon atmosphere at a strain rate of 0.002/min. The investigation was similar to that conducted previously¹ in Incoloy 800. The compositions of the alloys ranged from a pure ternary Ni-Cr-Fe alloy to an alloy that contained nominal amounts of C, Si, and Cu and larger amounts of P, S, and Mn. Compositions containing these elements individually were also investigated.

In all instances, the alloys lost ductility above 500°C. The ductility is shown as a function of test temperature in Fig. 28.1. Since recovery was not observed, these alloys behaved like the Incoloy 800 compositions without titanium.

Figure 28.1 also shows the dependence of the yield and ultimate strengths on temperature. The results fell within the indicated ranges, and, as expected, the more complicated alloys generally were stronger.

1. W. J. Werner, *An Investigation of the Effect of Certain Minor Elements on the Elevated Temperature Ductility of Incoloy 800* (thesis, ORNL-4504 (March 1970).

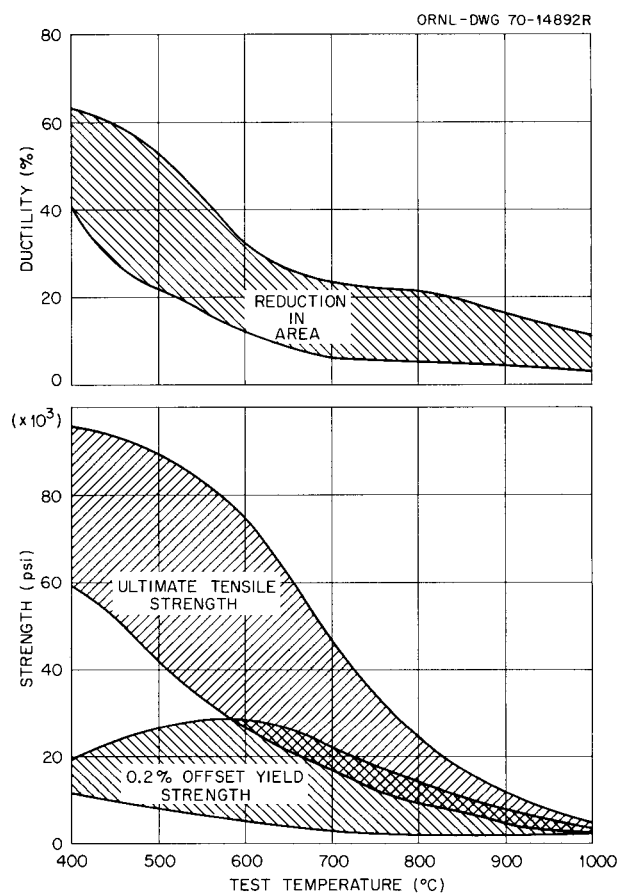


Fig. 28.1. The effect of test temperature on the strength and ductility of experimental Incoloy 600 alloys.

STUDIES ON INCOLOY 800 WELD METAL

D. A. Canonico

Experimental alloys of basic Incoloy 800 composition (Fe-31.5% Ni-21.5% Cr) were drawn to wire and used as filler metals for welding commercial Incoloy 800 sheet and plate. Included in this series of weldments were (I) the commercial Inconel filler metal (82T) that is recommended for joining Incoloy 800 and dissimilar

Table 28.1. Chemical composition of commercially obtained filler metals

Filler metal designation	Form	Chemical composition (wt %)									
		C	Mn	Fe	S	Si	Cu	Ni	Cr	Mo	Others
82T	Wire	0.02	3.00	1.00	0.007	0.20	0.04	Bal	20		Ti-0.55
Y32A1	Flux-coated	0.10	5.65	Bal	0.007	0.47	0.26	40.26	21.16	2.67	
5409	Wire	0.09	4.78	Bal	0.005	0.68	0.32	41.29	20.76	2.62	

materials, (2) two new commercially developed filler metals approaching the Incoloy 800 composition, (3) a filler metal that had been prepared from electroslog remelted Incoloy 800, and (4) 21 experimental filler metals from heats previously studied in our hot ductility tests. These welds were made on fully restrained, 1/2-in.-thick commercial Incoloy 800 plates with the gas tungsten-arc process.

The strongest and most ductile welds were those made with the commercial Inconel and modified Incoloy filler metals. However, a number of the experimental Incoloy 800 alloys were nearly of the same high quality. The ORNL alloy with a medium carbon content (nominally 0.04%) was the strongest and most ductile. The high-sulfur and low-carbon alloys cracked during welding. Filler metals with equally high sulfur and titanium did not crack. This is further evidence of the beneficial effect of titanium. The analyses of the Inconel 82T and the new Incoloy 800-type commercial filler metals are given in Table 28.1.

The commercial filler metal, 82T, although recommended for joining Incoloy 800, has reported sensitivity toward hot cracking. We obtained some fissured Inconel 600 welds from industry and have performed electron-beam microprobe analyses on them. The fissures appear to be enriched in niobium. These results, as well as those obtained in our hot ductility study, have given us reason to question the generally recognized effects of various elements on the weldability of nickel-rich materials. For instance, niobium is reputed to be beneficial, titanium variable, phosphorus detrimental, and manganese of no consequence. This study has shown that niobium may be detrimental, titanium is beneficial (because it counteracts the effects of sulfur), manganese can be detrimental for a given sulfur level, and phosphorus at low levels may be beneficial.

WELDABILITY OF AUSTENITIC STAINLESS STEELS

A. J. Moorhead D. A. Canonico

Our studies have continued to center on the effect of chemical composition on the amount and morphology

of the ferritic phases usually present in stainless steel weld metal. Additional investigations on stainless steel welds are presented in Chap. 17. We have concentrated on the prediction of the amount of ferrite present and its measurement. The amount of ferrite was determined with both the Magne-Gage and the Quantitative Television Microscope (QTM). The ferrite content is normally predicted from the Schaeffler diagram.² In general, the amount of ferrite measured by the two techniques correlated well. However, these measurements agreed rather poorly with predictions by the Schaeffler diagram. Although the diagram was developed for as-deposited weld metal and not for cast or homogenized ingots, better correlation for ingots was expected, since the quenching rate for these drop-cast ingots is not greatly different than that for high-heat-input welds. The ferrite content of the as-cast bars was about 1.5 to 3 times that predicted from the Schaeffler diagram.

We measured the ferrite content of autogeneous welds made on coupons from drop castings of experimental compositions. The procedures used in making these welds, by both the gas tungsten-arc and electron-beam processes, were described earlier.³ After etching cross sections with boiling Murakami's reagent, a series of measurements of ferrite content were taken along the weld center line, using the QTM. The averages of these readings on four compositions, along with the ferrite content predicted from the Schaeffler diagram for stainless steel weld metal, are given in Table 28.2. Two important observations can be made from this table. First, although the Schaeffler diagram predicts that the manganese-bearing heat (No. 5409) should be strongly austenitic, weld metal of this composition had from 3% (electron-beam weld) to 8.5% (tungsten-arc weld) ferrite. This anomaly was further substantiated by a Magne-Gage measurement of over 9% ferrite in the drop-cast ingot. Another manganese-bearing heat of similar composition had about 7% ferrite in the as-cast

2. A. L. Schaeffler, *Welding J.* 26, 601-s-20-s (1947).

3. A. J. Moorhead and D. A. Canonico, *Fuels and Materials Development Program Quart. Progr. Rept. Dec. 31, 1970*, ORNL-TM-3300, pp. 297-303.

Table 28.2. Ferrite content (measured with the QTM) of autogeneous welds in experimental stainless steel alloys

Heat	Composition (wt %)			Ferrite content (%)		
	(bal Fe)			Schaeffler diagram	EB weld	GTA weld
	Cr	Ni	Mn			
5409	18.3	11.9	4.8	0	2.9	8.5
5410	18.3	9.8		7	0.25	3.3
5416	22.2	13.5		7	1.5	7.0
5422	24.1	18.8		0	0	0

ingot. It is also interesting to note that a ternary alloy having the same Fe, Cr, and Ni contents of heat 5409 (i.e., Fe–18.3% Cr–11.9% Ni) would be expected to contain about 2% ferrite in the weld metal. This

indicates that, although manganese in small amounts may act as an austenitizer, in greater amounts it may have no effect or, in fact, become a ferrite former.

The second noteworthy feature of Table 28.2 is the effect of weld energy input on the ferrite content of the weld metal. The energy input of the electron-beam weld was 1700 J/in. and of the GTA weld 4500 J/in. By comparing the ferrite content of the welds made on a single heat, the large effect of energy input can be seen. For example, welds having the composition of heat 5410 (which has Ni and Cr equivalents on the Schaeffler diagram comparable to those of type 304) may or may not contain enough ferrite to prevent hot cracking, depending on the process used. This effect is illustrated dramatically in Fig. 28.2.

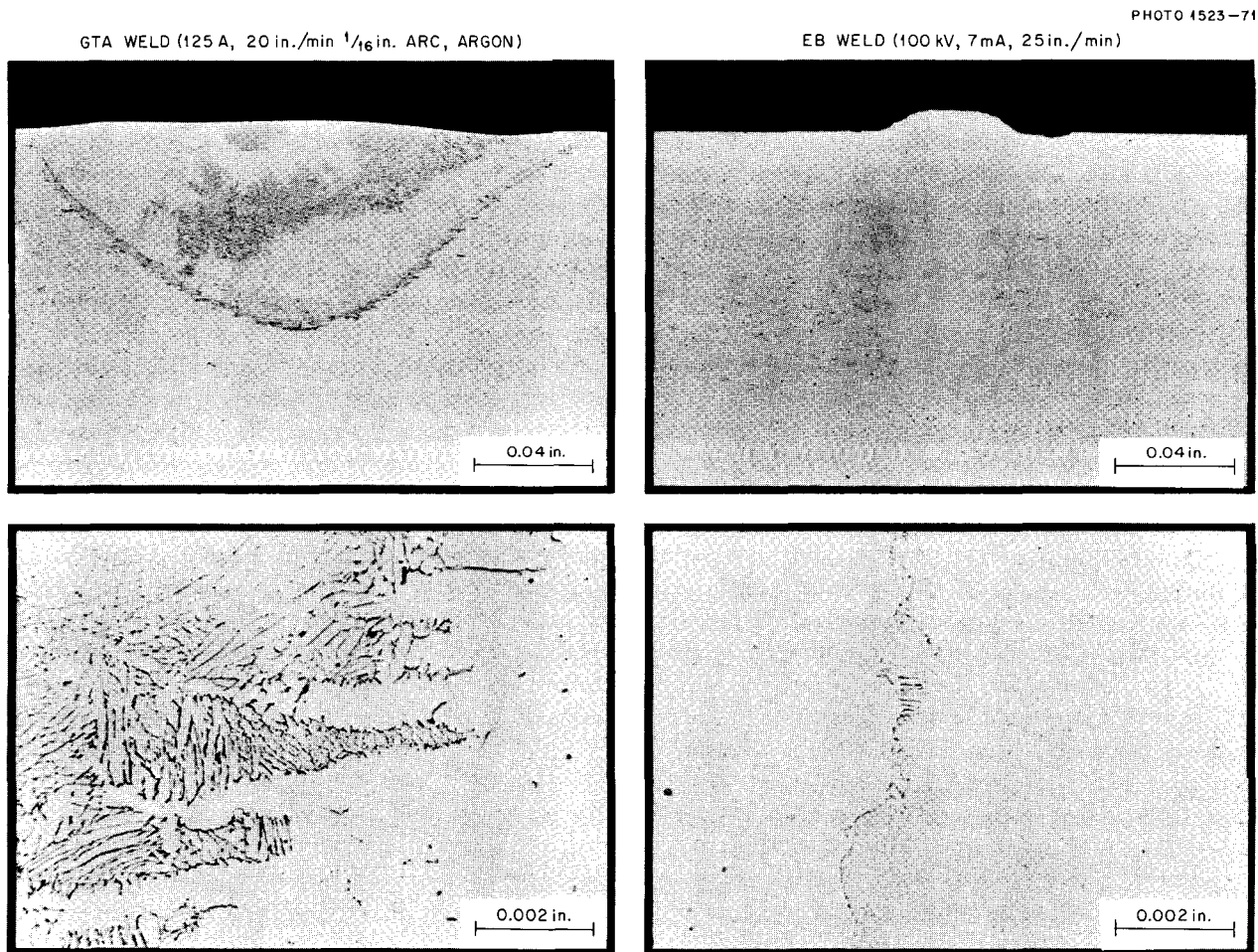


Fig. 28.2. Gas tungsten-arc (left) and electron-beam (right) welds on heat 5410 (Fe–18.3% Cr–9.8% Ni) etched with Murakami's reagent to reveal ferrite. The bottom photomicrographs show the fusion lines of the welds.

29. Mechanical Properties of Irradiated Metals and Alloys

J. R. Weir, Jr. H. E. McCoy, Jr.

Neutron irradiation alters the properties of metals by atomic displacements and by transmutation. Atomic displacements can cause the formation of various defects including dislocations and voids. These can cause marked changes in the mechanical properties as well as swelling. Various transmutation products can be formed in structural alloys, but helium and hydrogen are the most common. In aluminum-base alloys the production of silicon is important. These transmutation products not only directly change the mechanical properties but can have second-order effects by their effect on the defect structure.

The materials problems associated with different reactor concepts due to neutron irradiation vary widely, depending on the neutron spectrum and the structural materials. The LMFBR has a high fast flux in the core, and the stainless steel cladding will experience property changes due to atomic displacements and due to helium produced by transmutations. This work was discussed in Chap. 15, but further work in this chapter is related to LMFBR systems. Some work has been done on pure nickel in an effort to better understand the mechanisms of void formation. Work has also been done on molybdenum and vanadium alloys as potential cladding materials and tantalum for control applications in LMFBR's. This required that we develop the capability of remotely thinning samples for transmission electron microscopy. Niobium and molybdenum are candidate structural materials for controlled thermonuclear reactor applications that involve large fast-neutron fluxes.

Aluminum alloys are in use in numerous reactors, but the HFIR probably exposes them to the most severe conditions of temperature and thermal and fast neutron fluxes. The failure of parts of HFIR has raised the general question of the behavior of aluminum alloys under such service conditions.

The molten-salt reactor exposes Hastelloy N (Ni-base alloy) to high thermal neutron fluxes, and the main effect of irradiation remains the production of helium. This problem will be discussed in Chap. 34.

VOID FORMATION IN IRRADIATED NICKEL 270 (Ref. 1)

J. O. Stiegler E. E. Bloom

To supplement our work on radiation damage in stainless steels we are conducting additional experiments on a relatively pure face-centered cubic metal, nickel. Specimens of Nickel 270 (99.98% nominal purity) were irradiated in EBR-II to fluences ranging from 1×10^{18} to 1.5×10^{22} neutrons/cm² (>0.1 MeV) at temperatures between 375 and 525°C. Voids were observed in all specimens in concentrations of 1 to 3×10^{14} /cm³, independent of irradiation temperature and fluence. At low fluences the voids existed in clusters, and the reported concentration is an average value over a volume encompassing several clusters. At higher fluences the voids appeared to be distributed homogeneously, but the average concentration did not increase. We contend that the concentration did not increase because the voids that were nucleated in the regions between the clusters were compensated for by merger of closely spaced voids within the clusters. At an irradiation temperature of 470°C and a fluence of 1.5×10^{22} neutrons/cm² no voids smaller than 250 Å in diameter were found, suggesting that at this point nucleation had truly ceased. In this specimen voids as large as 1300 Å in diameter were found, in contrast to the apparent maximum limiting size of less than 300 Å for stainless steel irradiated at the same temperature.²

Although void concentrations did not decrease with increasing irradiation temperature, void shapes were strongly influenced by temperature. At 385°C the voids were cubic, at 470°C they appeared to be truncated octahedra, and at 525°C about one-third of them were elongated along <110> directions. In the latter case the

1. Summary of a paper to be published in *Radiation Effects*.
2. E. E. Bloom, *An Investigation of Fast Neutron Radiation Damage in an Austenitic Stainless Steel*, ORNL-4580 (August 1970).

maximum length-to-width ratio was about 5. No measurable changes in total void volume were detected over this temperature range at a fluence of 1.4×10^{20} neutrons/cm².

In addition to the voids the specimens contained complex dislocation structures. At low fluences patches of perfect dislocation loops were observed. As the fluence increased these apparently evolved into a loose dislocation structure, with small loops located adjacent to the dislocation lines. This structure coarsened with increasing irradiation temperature. At very high fluences only a system of dislocation lines was observed, many of which appeared to thread the voids.

The heterogeneous void distributions observed at low fluences and the lack of dependence of void concentration on irradiation temperature suggest that many of the voids were nucleated on sites existing in the material before irradiation. Gas bubbles have been observed to form in this material by high temperature annealing treatments alone, and finely dispersed bubbles were suggested as the preexisting nuclei. The eventual formation of voids in the regions between clusters indicates an additional nucleation mechanism that is initiated or augmented by the irradiation.

The sizes and concentrations of voids found were compared with results of two other investigations. A difference of nearly two orders of magnitude in void concentration was found for irradiation at 475 to 500°C at a fluence of about 10^{20} neutrons/cm². It was suggested that impurities were responsible for these differences, although spectral effects may be important.³

PREPARATION OF TRANSMISSION ELECTRON MICROSCOPY SPECIMENS IN A HOT CELL BY REMOTE TECHNIQUES⁴

C. K. H. DuBose T. L. Chandler⁵

With a semiautomatic technique developed at Oak Ridge National Laboratory,⁶⁻⁸ specimens for transmission electron microscopy have been prepared routinely from $\frac{1}{8} \times \frac{1}{8} \times 0.020$ in. pieces reading up to 10 R/hr. The specimen is first dimpled with an electrolytic jet and then polished uniformly in a standard electrolytic cell until a hole forms in the dimpled region. The region adjacent to the hole is usually sufficiently transparent to electrons to provide a usable specimen. Better specimens are produced near smaller holes, and a light beam and photocell detector halt the polishing automatically as soon as a hole forms.

Tantalum from all irradiations and some stainless steels irradiated in HFIR have activities over an order of

magnitude higher than the limit cited above for preparation of specimens in the laboratory. The need to examine such materials has led to the development of techniques for the complete preparation of specimens for transmission electron microscopy in a hot cell. While the ORNL technique does produce excellent specimens, it is a two-step process that requires complicated handling and precise manipulation and alignment of specimens. In the interest of simplicity, speed, and economy, we modified the commercial electropolishing unit for hot-cell operation. This provides a one-step process in which the specimen is mounted in a special holder and immersed in an electrolyte that is agitated by a pair of submerged jets. The light source, electronic system, photo detector, and power supply from the ORNL system were substituted for those supplied with the commercial unit.

A jig was designed to support the specimen holder during loading and unloading. A light was built into the jig to allow confirmation that a hole had formed and to locate its position. The jig also allows different specimen holders to be aligned with the retaining ring that locates their position in the polishing unit.

The specimens are loaded into specimen holders in the hot cell and are transferred to the electron microscope in a shielded container. They are removed from the container and inserted in the microscope with special tongs that keep the operator at least 3 ft from the specimen. Once the specimen is in the microscope stage, the microscope itself provides shielding for the operator. Slight contamination of the microscope-specimen exchange mechanism has occurred, but the specimen stage and microscope column have been clean.

Specimens of tantalum and stainless steel reading up to 100 R/hr at 5 in. have been successfully prepared and examined by this technique. Specimen quality is appreciably lower than in specimens prepared in the

3. J. O. Stiegler, "Void Formation in Neutron Irradiated Metals," paper presented at the International Conference on Radiation-Induced Voids in Metals, Albany, N.Y., June 9-11, 1971; to be published in the proceedings.

4. Summary of a paper to be submitted for publication.

5. Operations Division.

6. C. K. H. DuBose and J. O. Stiegler, *Semiautomatic Preparation of Specimens for Transmission Electron Microscopy*, ORNL-4066 (February 1967).

7. C. K. H. DuBose and C. Jones, *Techniques for the Preparation of Transmission Electron Microscopy Specimens from Tubing*, ORNL-TM-2408 (January 1969).

8. C. K. H. DuBose and C. Jones, "The Preparation of Transmission Electron Microscopy Specimens from Tubing," *Metallography* 2, 31-39 (1969).

laboratory. Usable areas are obtained in about 50% of the specimens, and about 25% of the specimens are judged good. The low yield may occur because the technique is not well suited to the relatively thick starting material used in these studies. The speed and simplicity of the technique make this sacrifice worthwhile.

IRRADIATION DAMAGE TO BODY-CENTERED CUBIC METALS

F. W. Wiffen

The Effect of Neutron Irradiation on the Strength Properties and Failure Mode of Molybdenum Alloys⁹

Recrystallized samples of arc-cast Mo and Mo-0.5% Ti and powder-metallurgy Mo-50% Re irradiated near 425°C to fluences between 1.5 and 3.5×10^{22} neutrons/cm² (>0.1 MeV) in EBR-II were tensile tested at a variety of strain rates and temperatures. Irradiation increased the yield and ultimate tensile strengths and reduced the work-hardening ability and ductility. In all three materials and for all available test conditions, the ultimate tensile strength occurred within 0.2% plastic elongation. The Mo and the Mo-0.5% Ti behaved similarly, with both showing a strain-rate-dependent ductile-brittle transition temperature (DBTT) of 400 to 550°C, compared with less than 20°C for unirradiated controls. Tests of the irradiated Mo and Mo-0.5% Ti above the DBTT showed elongation limited by the inability to work harden. Elongations less than 10% accumulated in the neck region before specimen failure. The Mo-50% Re was brittle to the highest temperature tested, 800°C, for a strain rate of 0.02/min. Transmission electron microscopy of the as-irradiated Mo showed a very high density of small dislocation loops, more than 10^{17} loops/cm³, with most of the loops arranged in linear arrays. Scanning electron microscopy of fracture surfaces showed failures below the DBTT to be predominantly cleavage with only a small component of grain-boundary separation. Failures above the DBTT showed the dimples characteristic of ductile fracture and were no different than fractures in unirradiated control specimens.

Voids and the Microstructure of Neutron-Irradiated Niobium⁹

Specimens of niobium irradiated in EBR-II at 425, 600, and 800°C to a fluence of 2.5×10^{22} neu-

trons/cm² (>0.1 MeV) were examined by transmission electron microscopy. Irradiation-produced voids were present for all three irradiation temperatures. The void populations were quite similar for the two lower irradiation temperatures, with densities near 2×10^{17} voids/cm³ and average and maximum void diameters of 70 and 130 Å, respectively. The associated volume increases were between 3 and 5%. The void formation at 425°C is very significant because this temperature is only 0.26 of the melting temperature, T_m , and is a clear violation of the common assumption that voids do not form at irradiation temperatures below about $0.30T_m$. At 800°C the void density was 2.4×10^{15} /cm³, the average diameter 185 Å, and the maximum 275 Å. The associated swelling is about 0.9%. The void distribution in the specimen irradiated at 800°C shows a strong ordering tendency, with the voids clearly showing a preference to be arranged on {110} planes. Tilting experiments establish that the ordered arrangement is three dimensional, with the voids on the points of an irregular bcc superlattice that is parallel with the metal lattice and has a lattice parameter of about 670 Å. The ordering is locally incomplete and is also broken by areas of random void arrangement. The defect structure seen in diffraction contrast consists of loops and dislocation segments in all specimens. The density of these defects decreases with increasing irradiation temperature.

The Effect of Alloying and Purity on the Formation and Ordering of Voids in BCC Metals¹⁰

The void populations in Mo, Nb, V, and one alloy of each of these were compared by electron microscopy. All three of the systems responded differently to the alloying. The void concentrations and sizes in the Mo and Mo-0.5% Ti irradiated at 790°C were identical within the measurement limits. After irradiation at 585°C the Mo-0.5% Ti contained more voids, but the sizes were nearly identical. Alloying niobium with 1% Zr reduced the void concentration after irradiation at 790°C by more than an order of magnitude, but this was compensated by an increase in void size. High void concentrations were observed in vanadium irradiated at 385 to 600°C, but samples of V-20% Ti irradiated in the range 475 to 600°C had no detectable voids. They contained high densities of irradiation-produced dislocations in networks and tangles. Voids in Mo, Mo-0.5% Ti, Nb, and Ta were ordered on a bcc

9. Summary of paper presented at the 1971 Spring Meeting of the Metallurgical Society of AIME, Atlanta, May 17-20, 1971.

10. Abstract of paper presented at the 1971 International Conference on Radiation-Induced Voids in Metals, Albany, N.Y., June 9-11; to be published in the proceedings.

superlattice parallel to the metal bcc lattice. Void ordering was not observable in the Nb-1% Zr or in vanadium.

EFFECTS OF IRRADIATION ON ALUMINUM ALLOYS

R. T. King K. Farrell A. Jostsons^{1 1}

General Effects of Neutron Irradiation on Aluminum and Aluminum Alloys

Because of concern over the safety of critical components of water-cooled test and isotope-production reactors, which are made of aluminum alloys, neutron damage to these materials is under study. The types of irradiation damage found are:

1. The formation of voids and dislocation loops, which condense from vacancies and interstitial atoms produced by atomic displacements. The distribution and extent of this damage has been shown to be very sensitive to irradiation temperature,^{12,13} neutron fluence,¹⁴ the presence of hydrogen and helium,^{12,15} and gross chemical composition and microstructure.^{15,16} We recently obtained evidence that some precipitates may retard void formation to very high fluences.^{16,17} Voids and dislocations are sources of irradiation strengthening.

2. The formation of silicon precipitate particles. Silicon is generated by the thermal-neutron-induced

$^{27}\text{Al}(n,\gamma)^{28}\text{Al}$ reaction followed by a β^- decay to silicon;¹⁸ the size range and distribution of the silicon particles are strongly temperature sensitive. Irradiation-induced strengthening of alloys at temperatures above the range for void formation can be explained on the basis of the dispersed silicon phase. Increases in both the yield strength and resistance to creep deformation are observed.

3. The formation of helium by $^{27}\text{Al}(n,\alpha)$ reactions and other (n,α) reactions. Most of the helium present after irradiation to high neutron fluences comes from the former source, although there are small contributions from certain alloying elements. Thermal neutron reactions with lithium and boron, which are usually present as tramp impurities, probably produce a heterogeneous helium distribution. Helium reduces the tensile ductility of solid-solution aluminum alloys above about 200°C, and probably plays a role in premature intergranular failure at lower temperatures and slow strain rates.¹⁹

4. The formation of hydrogen by $^{27}\text{Al}(n,p)$ reactions. The amount of hydrogen gas produced that remains in aluminum during irradiation is uncertain, and its effects on mechanical properties are not known. Satisfactory chemical analyses for hydrogen in irradiated aluminum have not been achieved, and it is not known whether some hydrogen from the coolant enters the aluminum. Hydrogen and/or helium may play some role in determining the eventual forms assumed by displacement damage.^{12,20}

11. On attachment from Australian Atomic Energy Commission Research Establishment.

12. K. Farrell, A. Wolfenden, and R. T. King, "The Effects of Irradiation Temperature and Preinjected Gases on Voids in Aluminum," *Radiation Effects* 8, 107-14 (1971).

13. R. T. King, A. Jostsons, and K. Farrell, "Effects of Elevated-Temperature Neutron Irradiation on Aluminum," presented at the American Nuclear Society Spring Meeting, Boston, Mass. (June 1971).

14. N. H. Packan, *Voids in Neutron Irradiated Aluminum*, ORNL-TM-3019 (January 1971).

15. K. Farrell, J. T. Houston, A. Wolfenden, R. T. King, and A. Jostsons, "Effects of Structural Imperfections on Voids in Aluminum," paper presented at the International Conference on Radiation-Induced Voids in Metals, Albany, N.Y., June 9-11, 1971; to be published in the proceedings.

16. J. O. Stiegler, K. Farrell, C. K. H. DuBose, and R. T. King, "High-Fluence Neutron-Irradiation Damage in Aluminum," pp. 215-32 in *Radiation Damage in Reactor Materials Vol. II* (Proceedings of a Symposium, Vienna, 2-6 June 1969), International Atomic Energy Agency, Vienna, 1969.

17. R. T. King, K. Farrell, and A. Jostsons, "The Effect of High Fast Neutron Fluence on the 6061 Aluminum Alloy," presented at the 1971 Spring Meeting of the Metallurgical Society of AIME, Atlanta; to be published.

Effects of Elevated-Temperature Irradiation on 8001 Aluminum Alloy

Irradiation effects are being studied in 8001 aluminum alloy because it is the target cladding material that failed in service in the High Flux Isotope Reactor. Metallographic investigation of the failed tube showed radial cracking that occurred after no measurable circumferential strain. Portions of a failed target rod irradiated to over 1×10^{22} neutrons/cm² (>0.8 MeV) were found, by transmission electron microscopy, to contain many heterogeneously distributed transmutation-induced silicon particles and voids. The voids

18. K. Farrell, J. O. Stiegler, and R. E. Gehlbach, "Transmutation-Produced Silicon Precipitates in Irradiated Aluminum," *Metallography* 3, 275-84 (1970).

19. R. T. King, *Cyclotron Simulation of Neutron-Transmutation Produced Gases in Reactor Cladding and Structural Materials*, ORNL-TM-3299 (April 1971).

20. A. Wolfenden, "Effects of Preinjected Hydrogen on the Electron Displacement Damage in 1100 Aluminum," Chap. 5, this report.

tended to form at two preferred sites, alongside stringers of inclusions and near some grain boundaries. Work is now under way to establish whether these voids are involved in the failure of the target rods. Postirradiation tensile tests on 1100 aluminum specimens containing walls of voids near grain boundaries have shown that the voids probably play an important role in premature intergranular failure. Creep tests have been made on 8001 alloy specimens that had been irradiated between 125 and 175°C to a fluence of 1.6×10^{22} neutrons/cm² (>0.8 MeV). These specimens did not contain voids but were hardened by the silicon particles. The specimens all deformed several percent before failing, but changes of about 30°C in the irradiation temperature had a greater effect on strength than doubling the neutron fluence, other conditions being constant.

We feel that voids were not observed in the 8001 alloy creep specimens either because the specimens had been irradiated at a higher temperature than the cladding or because the hoop stresses present in the cladding may have affected void formation. The role of stress during irradiation is not yet known.

Irradiation Effects in 6061 Aluminum Alloy and Its Utility for In-Reactor Service

Because of its high strength, the Mg₂Si precipitation-hardened 6061 aluminum alloy has been selected for numerous reactor components. It has now been examined after irradiation. One component, the High Flux Isotope Reactor target basket, was examined and found not to contain voids at fluences below about $3 \times$

10^{22} neutrons/cm² after irradiation at 60°C; above this fluence voids formed. Only 1.1% swelling was measured after irradiation to 5.4×10^{22} neutrons/cm² (>0.8 MeV). This is very much less than the swelling in 1100 aluminum or alloy 8001 at similar fluences. Of this 1.1% swelling, about half was attributable to void formation and half to precipitation of transmutation-produced silicon.

When voids do form in the slightly overaged 6061 alloy, they usually develop around the coarser Mg₂Si particles and around large inclusions. These features are believed to be incoherent with the matrix and are surrounded by regions that are free of smaller Mg₂Si particles of unproven coherency. Such observations suggest that the optimum structure for minimization of void formation is one containing a finely divided, coherent Mg₂Si precipitate. This structure must be stable during irradiation. In this respect, we found that the original structure in age-hardened 6061 alloy is intact even after irradiation at 150°C to high fast neutron fluences.

Irradiation at temperatures and fluences that did not cause void formation slightly increased the creep strength of the 6061 alloy while decreasing its ductility to the 2 to 5% range. The transmutation-induced silicon probably increased the strength of the alloy.

The resistance of the 6061 alloy to void formation, its high strength, and its stability under irradiation make it preferable to the solid solution alloys for most high neutron fluence applications. Although the postirradiation ductilities of the latter alloys are the greater, the 6061 alloy probably has sufficient ductility for most reactor applications, but more work is needed to study the influence of transmutation-produced gases on ductility at higher neutron fluences.

30. Nondestructive Test Development

W. O. Harms R. W. McClung

This program is designed to develop new and improved methods of examining reactor materials and components. To achieve this we study the pertinent physical phenomena, develop instrumentation and other equipment, devise application techniques, and design and fabricate reference standards. Among the subjects being actively pursued are electromagnetics (with major emphasis on eddy currents), ultrasonics, and penetrating radiation.

ELECTROMAGNETIC INSPECTION METHODS (EDDY CURRENTS)

C. V. Dodd C. C. Lu¹
W. A. Simpson, Jr. W. E. Deeds²
C. C. Cheng³

Our broad program on research and development of electromagnetic inspection methods includes (1) theoretical analysis of basic eddy-current problems, (2) programming the analytical equations for numerical solutions on a digital computer, (3) application of the computer programs to general eddy-current problems, (4) application of the computer programs to specific eddy-current inspection problems, (5) experimental verification of solutions to these problems, and (6) instrument design and construction.

Theoretical Analysis

We developed solutions for multiple planar conductors as described in the following abstract:⁴

A general theory is presented for the axially symmetric, time-harmonic eddy currents produced by a probe coil of rectangular cross section in linear, isotropic, homogeneous, conducting media bounded by an arbitrary number of parallel

plane boundaries. First, the Green's function in each medium is calculated by a matrix method, which greatly simplifies the procedure. Then the vector potential and other quantities of interest are calculated from the Green's functions. The general results are specified to three cases: a probe coil above an arbitrary number of parallel-plane conductors, a probe coil between two three-layer conductors, and a probe coil above a three-layer conductor. We have written computer programs that numerically calculate electromagnetic properties if one specifies the location and physical properties of the coil and conductors.

We have extended the above solutions for multiple planar conductors to the cases of a coil coaxial to and encircling or encircled by cylindrical conductors.

Development of Computer Programs

We published many of our new programs in a report with the following abstract:⁵

This report contains computer programs for solving some eddy-current problems frequently encountered in nondestructive testing. Operating instructions and examples are given for each program. These programs are written in BASIC language and may be used on a time-sharing computer. Various eddy-current tests can be quickly and accurately designed by utilizing these programs.

We wrote additional programs to calculate the impedance of a probe-type coil near multiple planar conductors and to calculate the magnitude and phase of a reflection-type coil above multiple conductors. We also wrote a program to calculate the conductivity and lift-off for a given coil above a conductor if the normalized impedance of the coil is given. We improved our relaxation calculations to include the effect of velocity of the conductor past the coil.

Computer Studies of General Eddy-Current Problems

We are using our computer calculations to determine the optimum parameters for measuring specimen thickness, cladding thickness, and electrical conductivity and

1. Mathematics Division.
2. Consultant, University of Tennessee, Knoxville.
3. Consultant, Northwestern College, Orange City, Iowa.
4. C. C. Cheng, C. V. Dodd, and W. E. Deeds, "General Analysis of Probe Coils Near Stratified Conductors," to be published in *International Journal of Nondestructive Testing*.

5. W. A. Simpson, C. V. Dodd, J. W. Luquire, and W. G. Spoeri, *Computer Programs for Some Eddy-Current Problems - 1970*, ORNL-TM-3295 (June 1971).

for detecting defects.⁶ A number of curves were prepared that show that the eddy-current signal produced by a defect varies as a function of test parameters for various arrangements of the coil and conductor, with special emphasis on differential encircling coils. From these curves the optimum parameters can be selected for a particular test. We determined that there is an optimum value of $\omega\mu\sigma\bar{r}^2$ (Fig. 30.1) to produce maximum sensitivity (phase shift) for measuring the thickness of one conductor clad on another. The figure shows the variation with coil radius of the optimum value of $\omega\mu\sigma\bar{r}^2$ for maximum sensitivity and the phase shift for a 10% change in cladding thickness at that optimum value. This graph demonstrates the optimum value for maximum phase shift. Figure 30.2 shows both the optimum coil radius and the phase shift at the 10% variation in cladding thickness at this optimum plotted against the ratio of conductivities of the base and cladding materials. From this graph we can select the optimum coil size for a given conductivity ratio and cladding thickness and then determine the sensitivity at this optimum. Similarly, we determined the optimum parameters for conductivity measurements.

Computer Studies of Specific Eddy-Current Problems

We applied our computer programs to design specific eddy-current tests. These studies include the design of systems to (1) detect sodium voids in irradiation capsules, (2) detect small surface cracks in aluminum-clad control rods, (3) measure the electrical conductivity of pellets of actinide oxide in an aluminum matrix, (4) measure the level of a liquid metal in a processing system, and (5) measure rapid temperature changes by detecting changes in the permeability of iron caused by the changes in temperature.

Experimental Verification of Computer Calculation

We confirmed some of our computer calculations experimentally. These include the measurement of normalized coil impedance of encircling coils as a function of cladding thickness,⁷ the variation in coil impedance with defects for encircling coils, and phase shift vs thickness for reflection coils.

6. C. V. Dodd, W. E. Deeds, and W. G. Spoeri, "Optimizing Defect Detection in Eddy-Current Testing," *Mater. Evaluation* 29, 59-63 (1971).

7. F. D. Mundt, *Eddy-Current Measurements with a Coil Encircling a Two-Conductor Rod*, MS Thesis and Y-1787 (April 1971).

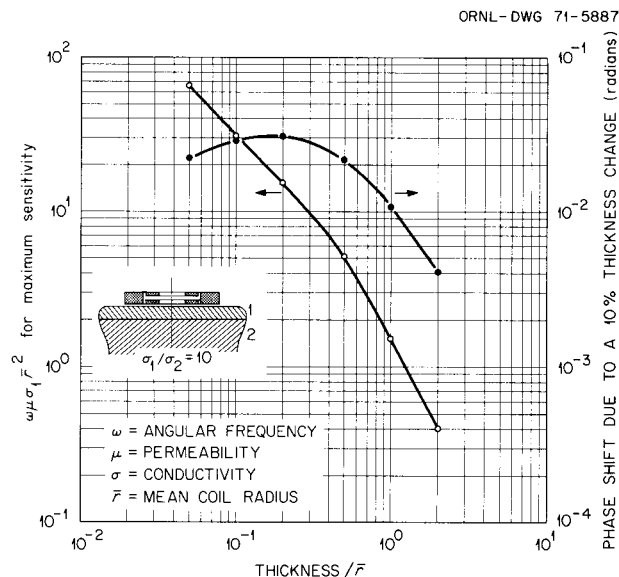


Fig. 30.1. Optimum $\omega\mu\sigma_1\bar{r}^2$ for maximum sensitivity and phase shift due to a 10% cladding thickness change plotted against normalized cladding thickness (divided by coil mean radius).

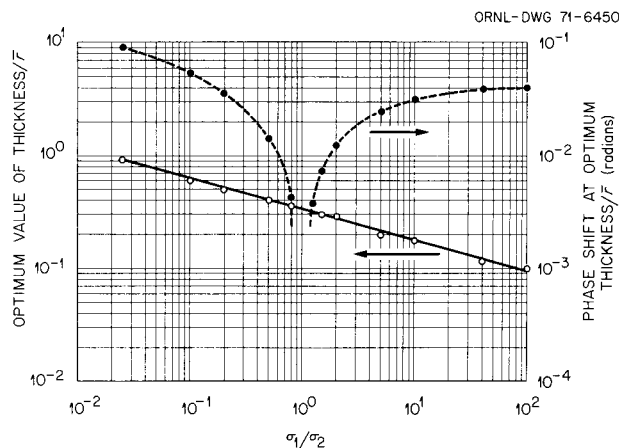


Fig. 30.2. Optimum value of cladding thickness divided by coil mean radius and phase shift for a 10% change in cladding thickness as functions of the ratio of conductivities of the cladding and base materials.

Instrument Design and Construction

The stability of the modular phase-sensitive eddy-current instrument has been improved at the higher frequencies. The instrument drifts typically $0.03^\circ/24$ hr at 1 MHz. Tuned frequency amplifiers have been constructed for frequencies from 1 kHz to 2 MHz in a 1, 2, 5 sequence.

ULTRASONIC INSPECTION METHODS

H. L. Whaley K. V. Cook Laszlo Adler²

Frequency Analysis

We improved our theoretical models⁸ and experimental techniques for characterization of flaws by ultrasonic frequency analysis. The basis of our approach is extraction and evaluation of data from the spectral analysis of a broadbanded ultrasonic pulse that has interacted with a discontinuity. The conceptual procedure reported previously,⁹ outlining the steps necessary to characterize a randomly oriented natural flaw in a material, was tested in practice.¹⁰ The sample was a thick block of steel in which flat-bottomed holes of various sizes were drilled at different angles with respect to the surface. Size determination by spectral analysis was demonstrated to be far superior to that by the conventional amplitude technique. To determine both size and orientation, a computer program was devised to solve the transcendental equations involved. Progress was also made in the very difficult problem of characterization of irregularly shaped reflectors (discontinuities) with random orientation. Two separate electronic gates were used simultaneously, allowing any two selected portions of the reflected pulse to be fed to the spectrum analyzer. We determined that thin foils of brass may be used to easily make reflectors of any desired shape, size, and surface contour, thus greatly expanding the availability of samples. A two-transducer method for reflector characterization was also developed. The basic equations are similar to those developed for the one-transducer case. This approach appears to offer a number of important practical advantages and may simplify mechanical motions necessary to obtain the spectral information.

Optical Visualization of Ultrasound

The equipment for acousto-optic imaging has been relocated in a new laboratory space. The design of the optical layout was improved to provide for an imaging system of more general capabilities including, in addition to schlieren, Bragg diffraction and volume holo-

graphy. The working area in which the ultrasonic tank containing the specimen is located is now completely disconnected from the optics so that large samples can be moved in and out without loss of optical alignment. Also, all the optical components and supporting structures have been firmly secured so that the system as a whole remains in excellent alignment under normal use. The sensitivity of the new system was maximized by using two light sources and a variety of samples interacting with the propagation of the ultrasound. A new optical table was constructed employing simplified and inexpensive optical benches and component carriers. This table will be employed to set up prototype optical systems for evaluating ideas that cannot conveniently be tested with the large permanent system.

PENETRATING RADIATION INSPECTION METHODS

B. E. Foster S. D. Snyder

Radiation Scattering

Studies were continued on the use of scattered and fluorescent radiation for measuring the thickness of coatings or claddings on reactor components. In addition to the previously reported measurements of the thickness of Al clad to U, we examined several other combinations of materials such as W on Mo, Mo on type 304L stainless steel, and W on type 304L stainless steel.¹¹

With the ¹⁴⁷Pm isotopic radiation source presently being used, the monitoring time required to accumulate a sufficient number of counts for a valid measurement is about 25 min. This lengthy counting time is tolerable during the initial development work, but for most practical applications the technique should be capable of scanning a specimen with a short dwell time on any given area. Toward this end we have begun studies using one of our mechanical scanning systems that incorporates a commercial x-ray unit as the radiation source.¹²

Closed-Circuit Television for Radiographic Evaluation

We are investigating the use of a closed-circuit television system as a rapid densitometer for reading

8. Laszlo Adler and H. L. Whaley, "Interface Effects in a Multifrequency Ultrasonic Pulse Echo and Its Application to Flaw Characterization," to be published in *Journal of the Acoustical Society of America*.

9. K. V. Cook, H. L. Whaley, Jr., and L. Adler, *Metals and Ceramics Div. Annu. Progr. Rept. June 30, 1970*, pp. 150-51.

10. H. L. Whaley, K. V. Cook, and L. Adler, *Fuels and Materials Development Program Quart. Progr. Rept. Dec. 31, 1970*, ORNL-TM-3300, pp. 306-10.

11. B. E. Foster and S. D. Snyder, *Fuels and Materials Development Program Quart. Progr. Rept. Sept. 30, 1970*, ORNL-4630, pp. 275-77.

12. B. E. Foster and S. D. Snyder, *Fuels and Materials Development Program Quart. Progr. Rept. March 31, 1971*, ORNL-TM-3416, p. 236.

radiographs. The preliminary equipment consists of a film viewer as a source of illumination, an RCA 525-line closed-circuit television system with a scan rate of 9623 in./sec, and an oscilloscope to delay and display any one of the 525 active lines of video. The radiograph is viewed by a zoom lens with a 20- to 80-mm focal length or a microscope lens with magnification of up to 20X.

A calibration curve was made for a range of film densities from 0.4 to 3.4 density units without changing the intensity of film illumination. The sensitivity to a given change in density is about 0.005 density unit. This system is capable of double-pulse operation, which allows selection and magnification of specific areas of interest.¹³

We still have problems with noise and jitter,¹⁴ with most of the noise problems related to repetition rate. The sampling oscilloscopes are excellent for fast pulses of 1 GHz but have excessive noise or jitter at 60 Hz, which is the framing rate of the TV system.

13. B. E. Foster and S. D. Snyder, *Fuels and Materials Development Program Quart. Progr. Rept. Sept. 30, 1970*, ORNL-4630, pp. 277-78.

14. B. E. Foster and S. D. Snyder, *Fuels and Materials Development Program Quart. Progr. Rept. Dec. 31, 1970*, ORNL-TM-3300, pp. 311-12.

Preliminary evaluation of a newly procured sampling unit with low-impedance cables and probe shows good system stability. The new sampling unit reduces but does not eliminate the jitter. With this system we have been able to measure the wire diameter or spacing on a radiograph of a 400-mesh screen with an accuracy better than 3 μm . The wire spacing was 33 μm and wire diameter 29 μm . The total magnification (optical and electronic) achieved for this measurement was slightly greater than 2600X, yielding an x-y recorder readout of 3 $\frac{1}{2}$ in. for the 33- μm spacing between the wires.

Shield for ²⁵²Cf Neutron Source

We completed the conceptual design of a facility to use 10 mg of ²⁵²Cf as a neutron source for both attenuation studies and radiography.¹⁵ The facility was designed to be located and operated within the Nondestructive Testing Laboratory without radiation hazard to personnel.

15. B. E. Foster and S. D. Snyder, *Fuels and Materials Development Program Quart. Progr. Rept. March 31, 1971*, ORNL-TM-3416, p. 237.

Part V. Reactor Development Support

31. Gas-Cooled Reactor Program

J. H. Coobs

Our materials effort in support of the Gas-Cooled Reactor Program is directed primarily toward the development of unclad ceramic fuel elements for high-temperature gas-cooled converter reactors (HTGR's), such as the Fort St. Vrain Reactor, which is nearing completion by Gulf General Atomic for Public Services Corporation of Colorado. The reference fuel elements consist of hexagonal graphite blocks containing coated (Th,U)O₂ or (Th,U)C₂ microspheres and are designed to retain most of the fission-product activity within the fuel element to simplify maintenance.

Our program has consisted principally of developing techniques for bonding coated particles into fuel elements and preparing, characterizing, and irradiation testing pyrolytic carbon coatings, coated particles, and simulated bonded fuel elements. After the successful demonstration of bonded fuel stick performance in several experiments, the emphasis in the program shifted to the preparation and testing of coated fuel particles derived from ion exchange resin particles. Irradiation testing is now done principally in HFIR target and reflector positions, but a few tests have been run in the Dounreay Fast Reactor (DFR). Bonded-bed specimens and resin-derived particles have been irradiated to fast-neutron exposures approaching the peak HTGR fluence of 8×10^{21} neutrons/cm² (>0.18 MeV) and to burnups of about 20 at. % heavy metal. Temperatures have spanned the range experienced in an HTGR, 600 to 1250°C.

A significant part of our program now involves participation with Gulf General Atomic in a cooperative effort to develop fuel elements for a Gas-Cooled Fast Breeder Reactor (GCFBR). We are conducting an experiment in the ORR to test a vented fuel pin, which was adopted as the reference GCFBR design. Eight fuel pins that simulate the vented design were also constructed and are being tested in EBR-II.

COATED PARTICLES FROM ION EXCHANGE RESINS

C. B. Pollock J. L. Scott
W. P. Eatherly

We continued development of fuel particles made from ion-exchange resins.¹ These low-density particles have a number of processing and performance advantages over dense fuel kernels with thick, porous buffer layers and are now being considered seriously as HTGR fissile particles. Conventional cation exchange resins are contacted with uranyl or plutonyl nitrate until all active sites are filled. The microspheres are then dried, carbonized in argon in a fluidized bed to 1000°C, and coated by conventional techniques without the porous buffer layer. The overall process utilizes inexpensive raw materials and involves fewer processing steps than other methods for making fissile particles. Particles made this way are more resistant to amoeba migration than dense UC₂ or UO₂ and show excellent irradiation stability.

Resin selection. Ion exchange resins may be either thermosetting or thermoplastic. We use the thermosetting because thermoplastic resins melt during carbonization. Many commercial resins are thermosetting, and this property is enhanced by increased cross linking and the presence of actinide ions.

The fuel density after carbonization depends strongly on the resin selected. We first studied styrene-divinyl benzene (DVB) resins. The styrene supplies the spine structure, and DVB is the cross-linking agent. Since the styrene molecule contains eight carbon atoms per active sulfonic (SO₃H) group, the carbon-to-uranium ratio is high in the final carbonized state. We have now

1. J. L. Scott, J. M. Leitnaker, and C. B. Pollock, *Metals and Ceramics Div. Annu. Progr. Rept. June 30, 1970*, ORNL-4570, pp. 161-62.

evaluated methyl acrylic acid–DVB resins and acrylic acid–DVB resins. These acids contain respectively four and three carbon atoms per active carboxylic site and when fully loaded carbonize to much lower carbon-to-uranium ratios than the sulfonic resins. Furthermore, they produce a sulfur-free product. Sulfur would be a corrosive contaminant if it escaped to the helium coolant.

Fuel loading. To seek maximum and reproducible loading of metal in various copolymers, we have systematically studied the loading kinetics of uranium onto the reference strong-acid resins and are able to control the uranium loading in this system. One exploratory experiment demonstrated that fissile particles containing plutonium can be fabricated.

We developed a column loading technique that monitors the exchange reaction with pH, and systematically studied the loading kinetics of the reference strong-acid resins. We also loaded a number of weak-acid resins with uranium and found that the most important variables are pH and the form of the resin. These resins are stable in the pH range of 4 to 10, but uranyl nitrate solution becomes unstable above pH 4. A weak-acid resin in the sodium form can be loaded at much lower pH and with better control. The strong-acid resin loads best in the acid form and behaves quite well at very low pH.

Other important practical considerations in loading a resin are solution flow rate and bed volume. The time required for the exchange reaction is controlled by these factors, with a minor influence by particle size. For example, 10 to 12 bed volumes of solution are required to completely load a strong acid resin. Table 31.1 gives the composition of recently fabricated fuel particles from both resins after carbonizing to 1000°C.

Table 31.1. Composition of typical resin-derived fuel particles carbonized to 1000°C in argon

Starting material	Content (wt %)			
	Uranium	Carbon	Oxygen	Sulfur
Dowex 50WX8 ^a	46.71	36.85	7.03	10.57
Dowex 50WX8	47.02	37.14	5.33	11.24
	48.68	35.62	4.89	10.54
	48.74	33.99	6.42	9.95
	46.60	35.60	8.12	10.26
Amberlite IRC 50 ^b	44.41	47.84	7.40	0
Amberlite IRC 50	65.62	22.07	12.0	0
	69.29	18.04	12.0	0

^aStyrene-DVB sulfonic resin from Dow Chemical Company.

^bCarboxylic resin from Rohm and Haas.

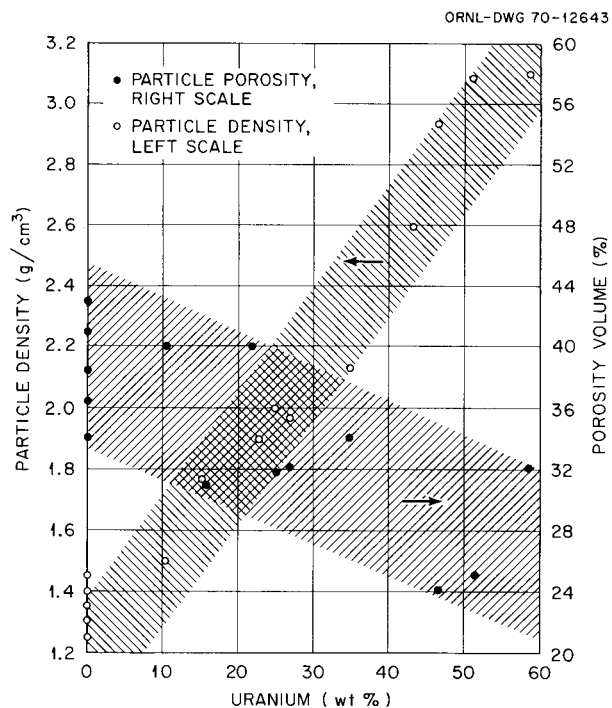


Fig. 31.1. Effect of uranium loading on porosity and density of carbonized fuel-loaded ion exchange resin particles.

The density of carbonized fuel kernels depends on uranium content, and Fig. 31.1 relates particle loading to density.

Carbonization and thermal stability. The quality of carbonized fuel particles is very dependent upon the drying and heating rates. Therefore, we studied the carbonization cycle up to 1000°C with the aid of DTA and TGA. The fuel form at 1000°C is UOS in strong-acid resins and UO₂ in weak-acid resins, both of which are finely dispersed in porous glassy carbon.

Pyrolytic-carbon-coated fuel particles fabricated from strong-acid resins resisted fuel migration in a temperature gradient (amoeba effect). Particles have been tested in a temperature gradient of 0.7°C/μm, with a center-line temperature of 1800°C for a time of 31 hr. Resin-derived particles survived this treatment, while fully dense carbides failed.

Particle design studies. The STRETCH code by Scott and Prados,² which was developed to predict the irradiation performance of coated fuel particles, was recently used to calculate stresses in BISO³ coatings on

2. J. W. Prados and J. L. Scott, "The Influence of Pyrolytic-Carbon Creep on Coated Particle Fuel Performance," *Nucl. Appl.* 3, 488–94 (1967).

3. A BISO coating comprises two layers of pyrolytic carbon, a porous inner layer and a dense outer layer. A TRISO coating also includes a silicon carbide layer.

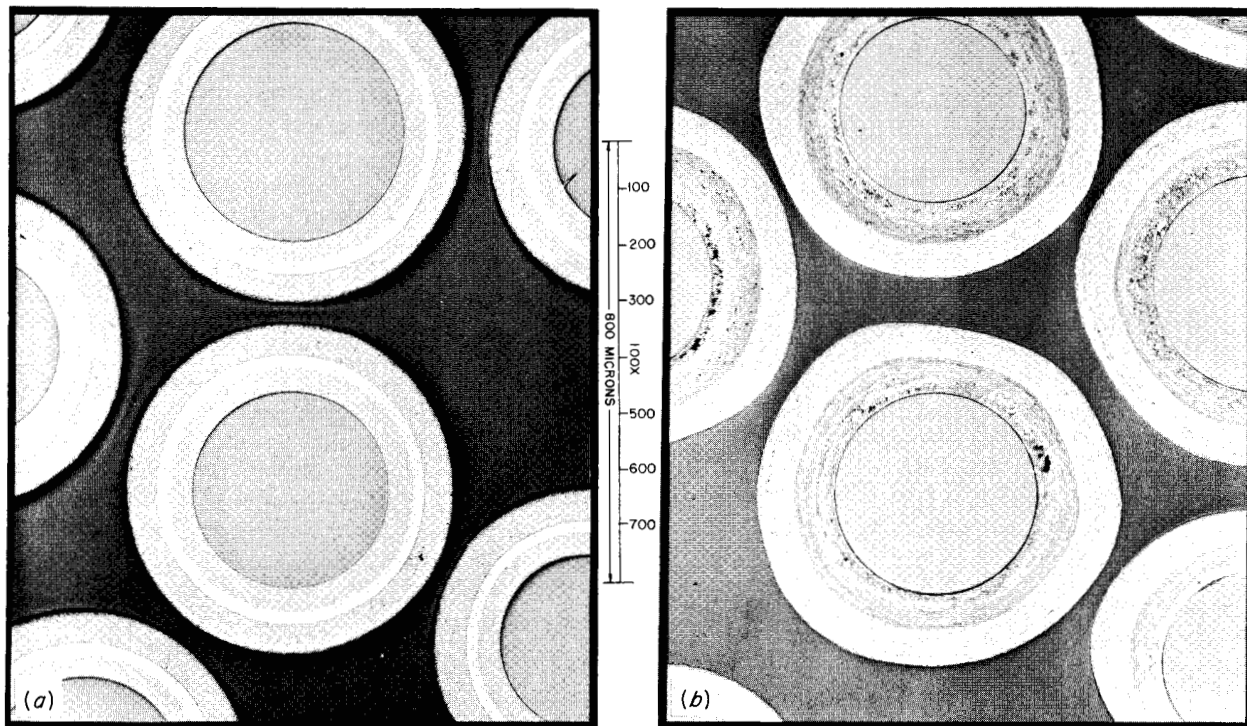


Fig. 31.2. Coatings proposed for advanced HTGR fuel particles. (a) Resin-derived fissile particle. (b) Sol-gel ThO_2 fertile particle.

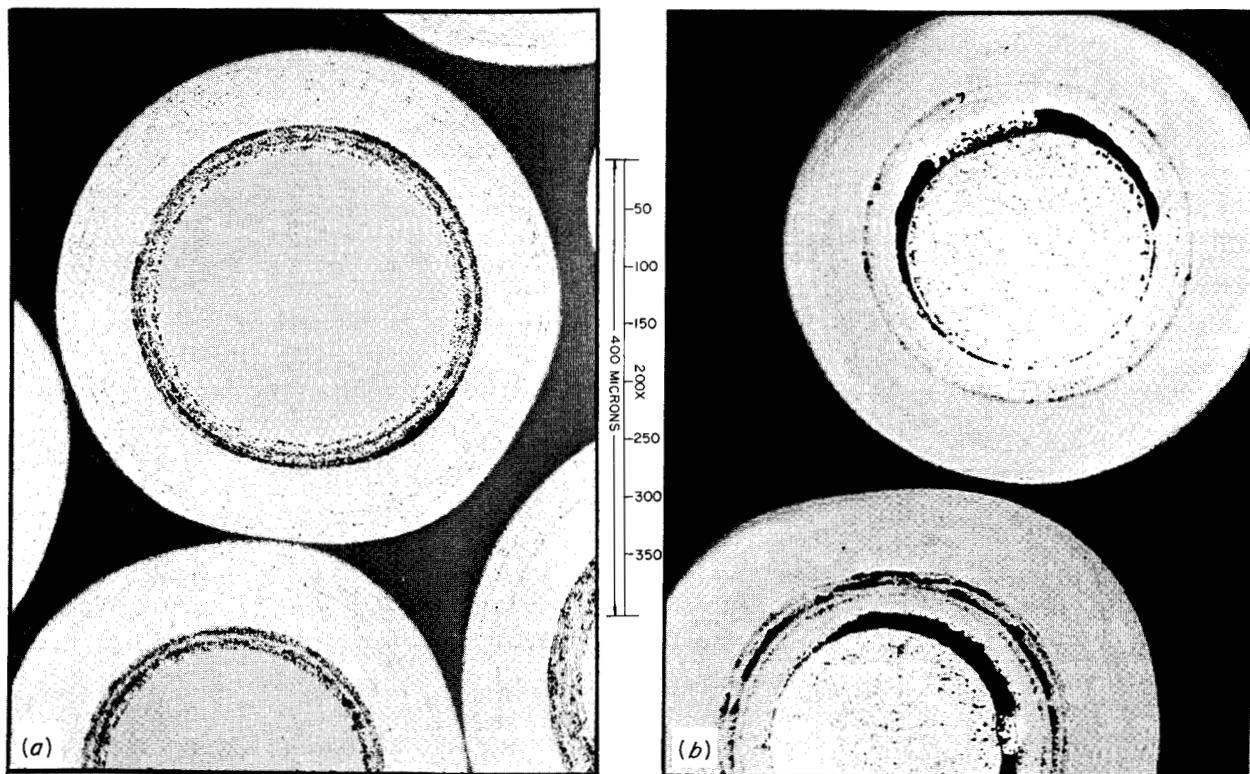


Fig. 31.3. Coated fuel particles derived from ion exchange resins. (a) As coated. (b) Irradiated at 1050°C to a burnup of 18.5% heavy metal and a fast-neutron fluence of 7.2×10^{21} neutrons/cm² (>0.18 MeV).

fuel particles derived from strong-acid resins. The code predicts that the particles will survive HTGR conditions of temperature, fluence, and burnup without a buffer coat. Therefore our experimental effort has been to develop new coating designs that do not require a buffer layer. Because this layer is the most difficult to control, such a design change can simplify existing coating processes. Figure 31.2 compares resin particles enclosed in a type of TRISO³ coating prepared for resin fuels and conventional BISO-coated ThO₂ particles. Fuel elements containing this combination of particles would be desirable because the coatings are simple and easy to apply and such a combination would be thermally very stable.

Irradiation testing. We have now exposed resin-derived particles up to a fast fluence of 7.2×10^{21} neutrons/cm² (>0.18 MeV) at 1080°C to a maximum burnup of 18.5% FIMA. Figure 31.3 shows such a particle before and after the test. The kernel diameter has decreased, buffer layer density has increased, and porosity is now visible in the kernel. Outer coatings of particles tested in this experiment were unaffected.

COATED-PARTICLE BONDING DEVELOPMENT FOR HTGR FUELS

J M Robbins R. L. Hamner
W. P. Eatherly

Our program for the development of bonded coated-particle beds for high-temperature gas-cooled converter

reactors consists principally of (1) investigating experimental matrices, (2) investigating alternate fuel rod fabrication techniques, (3) studying carbonizing, and (4) preparing selected types of specimens for irradiation testing.

Our objectives in the investigation of experimental matrices are to select optimum combinations of binder and filler materials based on cost and availability, ease of fabrication, irradiation stability, and high matrix densities for good thermal conductivity. The filler materials studied are listed in Table 31.2 and represent a broad spectrum of properties: graphitic and non-graphitic, isotropic and anisotropic. The filler contents noted represent the maximum that could be used in 15V pitch without making the mix too viscous to inject into the fuel bed. The spherical or isotropic fillers were much more amenable to fabrication than the anisotropic fillers, probably because of a more favorable morphology. The carbonized matrices were less dense than desired for relatively good thermal conductivity but did lend adequate strength to the bonded sticks.

The carbonization step still presents problems. The fuel rods require support during carbonization because the binder is thermoplastic. Hence, they were carbonized either in a packed bed of graphite powder or in graphite tubes. The latter resulted in higher matrix densities (increases of 9 to 30%) but generally caused fracture of some coatings. On the other hand, few if any broken coatings were observed in specimens carbonized in a graphite bed. The interaction of particle

Table 31.2. Experimental Filler Materials for Bonded Beds^a

Filler	Description	Filler content (wt %)	Maximum particle size (μm)	Carbonized matrix density (g/cm ³)
Thermal	Spherical carbon black, nongraphitic	50	<1	0.90
Poco AXZ	Isotropic, graphitic	35	40	0.65
Poco FXA	Isotropic, graphitic	40	40	0.70
JOZ	Anisotropic, graphitic	35	40	0.67
H378	Anisotropic, graphitic, from reimpregnated JOZ graphite	35	27	0.70
Asbury-325 ^b	Anisotropic, graphitic natural flake	35	40	0.74
Asbury 6353 ^c	Anisotropic, graphitic, natural flake	27	40	0.64
Santa Maria	Isotropic, graphitic	40	40	0.73
Robinson	Isotropic, graphitic, from airblown coke	40	27	0.72
No. 2 coke	Anisotropic, graphitic	35	40	0.73

^aAll used in preparing bonded-bed specimens with 15V coal tar pitch.

^bAn old Asbury -325-mesh sample.

^cReference filler for Core A of the Ft. St. Vrain Reactor.

coatings and bonding matrices apparently contributes to coating breakage, but the mechanism has not been defined. Carbonization in graphite boats contoured to fit the fuel rods produced distorted rods that stuck to the boats. We are now investigating combinations of thermosetting and thermoplastic binders that can be both cured (hardened) and graphitized.

New techniques in fabrication of conventional and advanced bonded-bed fuel rods were investigated. With the present end-injection technique, the length of fuel rods is limited to about 2 in. because the fuel bed filters the filler material. We successfully fabricated 6-in.-long rods by annular injection, in which the bonding matrix need be forced only through small segments of the fuel bed. This suggests that even longer fuel rods can be made in this manner. Another optional procedure for fabricating fuel rods consists of slurry blending the fuel particles and matrix and then warm molding them into fuel rods at 1000 to 2000 psi. Such a fuel rod has a continuous, relatively dense matrix for improved thermal conductivity but contains only about 50 vol % particles. We have calculated that by using 400- μm -diam fissile kernels instead of the 175- to 300- μm -diam particles now specified, we could maintain the fuel loading of the present reference element with the reduced particle volume fraction. In preliminary work, fuel rods with 48% particle volume loadings and matrix densities of 1.4 g/cm³ were successfully fabricated by this technique. We anticipate that extrusion of fuel rods will follow if this type of element performs well under irradiation.

THERMAL CONDUCTIVITY OF BONDED-BED MATERIALS

R. S. Graves W. M. Ewing

A guarded axial heat flow technique⁴ yielded thermal conductivity, λ , ($\pm 3\%$) and electrical resistivity, ρ , ($\pm 0.4\%$) from 80 to 400°K on two bonded-bed samples. These samples were fabricated with 65 vol % inert particles in a matrix of Poco AXZ graphite and 15V pitch and treated in argon at 1250 and 1800°K. These two samples represent the outer limits of a set of eight samples with bulk densities of 1.28 and 1.30 g/cm³ and ρ 's of 8180 and 7600 $\mu\Omega\text{-cm}$ at room temperature.

Table 31.3 lists smoothed λ , ρ , and $\lambda\rho/T$ values for these samples. From 80 to 400°K, λ increases, ρ decreases, and $\lambda\rho/T$ peaks near 170°K. The latter is a useful property estimation parameter for graphites.

4. J. P. Moore, D. L. McElroy and R. S. Graves, *Can. J. Phys.* 45, 3849-65 (1967).

Table 31.3. Thermal conductivity and electrical resistivity of two bonded-bed materials

Temperature (°K)	Sample JG 25-1			Sample JG 25-8		
	ρ^a	λ^b	$\lambda\rho/T^c$	ρ^a	λ^b	$\lambda\rho/T^c$
			$\times 10^6$			$\times 10^6$
100	9132	0.0136	1.237	8478	0.0142	1.200
200	8622	0.0306	1.321	7999	0.0334	1.334
300	8159	0.0428	1.164	7593	0.0464	1.173
400	7815	0.0478	0.933	7247	0.0542	0.983

^aElectrical resistivity in $\mu\Omega\text{-cm}$.

^bThermal conductivity in $\text{W cm}^{-1} (\text{°K})^{-1}$.

^cIn $\text{V}^2 (\text{°K})^{-2}$.

These data suggest that one means to increase λ is to reduce ρ , which is a structure-sensitive property for these materials.

IRRADIATION TESTING OF PROTOTYPE HTGR FUEL ELEMENTS

J. L. Scott D. M. Hewette II

J. H. Coobs J. A. Conlin⁵

B. H. Montgomery⁵

Blended Beds of Loose Coated Particles

Just before the successful demonstration that bonded beds of HTGR fuels could survive design fast-neutron (>0.18 MeV) fluences ($\sim 8 \times 10^{21}$ neutrons/cm²), interest was renewed in the use of loose beds of particles in HTGR fuel elements. Such fuel elements would require that two or more types of particles be blended in each fuel hole and form a stable bed that would not segregate or settle severely during transport and irradiation.

Several experiments were performed to study the behavior of loose beds of particles in graphite tubes and showed that a bed will "lock" in place when force is applied from the bottom of the column, provided the length of the column is at least 7 times the diameter. This behavior indicated that a critical feature of such a loose bed would be interaction with the graphite tube or fuel element during irradiation. In an HTGR environment the graphite will shrink in the axial (extrusion) direction throughout life and will shrink initially and then expand in the perpendicular direction. The net volume change expected in an element operating at 1020°C is greater than 4%. On the other hand, a bed of

5. Reactor Division.

coated particles will shrink initially as the outer isotropic coating densifies under irradiation and will assume a stable volume at an exposure between one-half and two-thirds of the design fluence.

To study these effects, an irradiation experiment was designed to test the behavior of loose beds contained in needle-coke graphite tubes. Two loose blended beds that had length-to-diameter ratios greater than 11 were prepared; one consisted of large (~600- μm -diam) particles with high-temperature isotropic carbon coatings and smaller (~400- μm -diam) particles with low-temperature isotropic coatings; the other bed consisted of particles with low-temperature isotropic coatings on both large and small particles. The two types of particles were loaded into the tube by coincident feeding from vibrating-trough feeders, and the two beds were vibrated to a stable volume and finally topped with compressed plugs of graphite felt to hold them in place.

The two blended beds were assembled into HFIR target capsule HT-5 and were irradiated for 69 days to a peak fast-neutron exposure of about 7.2×10^{21} neutrons/cm² (>0.18 MeV) at 890 to 1020°C. Upon completion of the irradiation, the capsule was transferred to the ORR pool for neutron radiography and then to the hot cell for gamma scanning before disassembly. These transfers were made without disturbing the test beds (i.e., the capsule was maintained upright and handled carefully). Comparison of the neutron radiographs and gamma scan with a preirradiation x-radiograph showed that the beds shrank 18.1 and 18.5% in length. Visual examination and metallography of particles from the blended beds did not reveal fractured coatings. Thus the settling and bed shrinkage must have been caused primarily by densification and shrinkage of the coatings. The needle-coke graphite container was bowed somewhat by the flux gradient in the experiment but did not show other damage. Clearly such settling and shifting of fuel cannot be tolerated in a reactor loading, even if no damage to the fuel element is associated with it. Therefore, consideration of loose beds in HTGR's was discontinued.

Testing of Matrix and Filler Materials for Bonded Fuel Sticks

Recent improvements in the structure and stability of bonded fuel sticks led to the development of satisfactory although not optimum binders. These improvements were brought about by increasing the matrix density and filler content of intrusion-bonded particle beds. Matrix densities as high as 1.25 g/cm³ were

Table 31.4. Dimensional changes of bonded beds irradiated in capsule HT-6

Matrix filler		Dimensional change during irradiation (%)			
Material	Content (wt %)	at 1070°C 7.2×10^{21} neutrons/cm ²		at 800°C 5×10^{21} neutrons/cm ²	
		Length	Diameter	Length	Diameter
Thermax	50	-5.2	-4.6	-3.6	-3.8
Santa Maria	40	-5.0	-5.0	-3.5	-3.2
Asbury 6353	27	-5.8	-5.8	-3.9	-4.1
JOZ	40			-3.5	-3.3
H-378	35	-4.8	-5.6		
Robinson ^a	40	-6.5	-6.7	-4.5	-4.7
Poco FXA ^a	40	-7.5	-6.9	-4.8	-5.0

^aCoated inert particles only; other specimens contain mixture of coated ThO₂ and coated inert particles.

achieved by adding large amounts of stable filler material (<40- μm -diam Poco graphite flour or Thermax carbon black) to pitch or furfuryl alcohol. A HFIR test of coated inert particles bonded with these materials was the first demonstration that such beds could survive full HTGR fast-neutron fluences.^{6,7}

Since the isotropic filler material (Poco graphite powder) used in the successfully irradiated specimens is not available in large quantities at low prices, fabrication experiments were conducted on bonding of fuel sticks with matrices consisting of a variety of readily available or inexpensive filler materials in 15V pitch. Bonded specimens consisting of BISO-coated fissile and inert particles bonded with the series of experimental matrices shown in Table 31.4 were exposed to fast-neutron fluences up to 7.2×10^{21} neutrons/cm² at 1070 and 800°C in capsule HT-6. All bonded specimens were intact and shrank as much as 6% in linear dimensions. The shrinkage was greater at the higher exposures and temperatures and seemed to be controlled by the properties of the two-layer carbon coatings on the two kinds of particles. The controlling

6. J. L. Scott, J. H. Coobs, J. M. Robbins, D. M. Hewette II, J. A. Conlin, and R. L. Senn, "Development of Bonded Coated-Particle Beds for HTGR Fuel Elements," pp. 456-73 in *Proceedings of Gas-Cooled Reactor Information Meeting at the Oak Ridge National Laboratory, April 27-30, 1970*, CONF-700401.

7. J. L. Scott, J. A. Conlin, J. H. Coobs, D. M. Hewette II, J. M. Robbins, and R. L. Senn, "Development of Bonded Beds of Coated Particles for HTGR Fuel Elements," (Summary) *Trans. Amer. Nucl. Soc.* 13, 134-35 (June 1970).

feature seemed to be the densification of the coatings during irradiation, which as calculated was consistent with the actual shrinkages of 3 to 6%.

Metallographic examination of bonded fuel sticks from this experiment indicated that all particle coatings were intact and that the matrix structure was not seriously affected. These results indicate that successful performance of bonded fuel sticks to full HTGR fast-neutron fluences ($>7 \times 10^{21}$ neutrons/cm²) can be achieved by injection bonding with pitch containing a wide variety of carbonaceous filler materials.

Irradiation Test of Bonded HTGR Coated Particle Fuels in an Instrumented Capsule in HFIR⁸

J. L. Scott D. M. Hewett II
 J. A. Conlin⁵ J M Robbins
 J. H. Coobs R. L. Senn⁵
 B. H. Montgomery⁵

We designed and conducted an experiment to study the interaction of the particle coatings, bonding matrix, and graphite block during irradiation. The instrumented and swept capsule contained a graphite sleeve that supported specimens of coated particles bonded with both low- and high-density matrices. The capsule was irradiated in the removable beryllium facility of HFIR for 186 days at fuel temperatures of 1000 to 1250°C. The peak burnup was 22 at. % in coated UO₂ particles, and the maximum fast fluence was 5.8×10^{21} neutrons/cm² (>0.18 MeV). The fission-gas release rates were moderate and increased slightly after about 120 days. After irradiation, the specimens bonded with phenolic resin (low-density matrix) debonded and crumbled easily, while samples that were bonded with high-density matrices were intact. The fracture of some outer carbon coatings on TRISO-coated fuel particles was attributed to densification and interaction of the coating layers. No fuel particles with completely failed coatings were found. These results indicate the need for certain changes in coating design and binder designations and suggest that fuel sticks bonded with high-density matrices can be expected to retain integrity after full HTGR exposure of about 8×10^{21} neutrons/cm² (>0.18 MeV).

Effect of Density and Heat Treatment on the Rheology of Restrained Low-Temperature Isotropic Coatings

A series of irradiation experiments now in progress is designed to study the effects of density and heat

8. Abstract of a topical report in preparation.

treatment on the dimensional stability and performance of low-temperature isotropic (LTI) pyrolytic-carbon coatings. Test specimens comprise coated particles with inert carbon kernels and coatings containing SiC barrier layers. Neutron-induced distortions in the outer coatings will be restrained by the SiC layer. The as-deposited densities of the LTI coatings range from 1.7 to 2.0 g/cm³, and specimens heat treated to 1900°C have slightly higher densities (up to 2.04 g/cm³) and larger crystallite sizes. All of the LTI coatings are isotropic or nearly so, as measured optically. We will measure the changes in density, dimensions, and preferred orientation as a function of neutron fluence on loose particles after exposures of 5, 10, and 15×10^{21} neutrons/cm² (>0.18 MeV) at about 1100°C. Similar samples were bonded into fuel sticks and are being irradiated to 7.5×10^{21} neutrons/cm² to study the interactions of the outer LTI coatings with the matrix. Results from these experiments will help to define the physical property specifications, especially density, of LTI coatings for high-performance coated particle fuels.

The first of these experiments is being examined after irradiation to a peak fluence of 10×10^{21} neutrons/cm² (>0.18 MeV). Coatings with intermediate and highest densities performed without failure, but lower density coatings showed 4% failure. Preliminary dimensional change data indicate that the stability of the higher density coatings (~ 1.90 g/cm³) is greater, as would be predicted by previous data from unrestrained specimens of coating materials.⁹ Conclusive results must await data from examination of samples irradiated to lower and higher exposures.

GAS-COOLED FAST REACTOR FUEL ELEMENT DEVELOPMENT

R. B. Fitts T. N. Washburn
 A. W. Longest⁵ J. A. Conlin⁵

Most of the effort to develop a fast breeder reactor is being applied to the sodium-cooled LMFBR. There is, however, much interest in the development of the gas-cooled fast breeder reactor¹⁰ (GCFBR) as an alternate. It has the potential of lower cost power production and would avoid the sodium void coeffi-

9. D. M. Hewette II, *Metals and Ceramics Div. Annu. Progr. Rept. June 30, 1970*, ORNL-4570, pp. 162-63.

10. P. Fortescue and W. I. Thompson, "The GCFR Demonstration Plant Design," pp. 795-811 in *Proceedings of Gas-Cooled Reactor Information Meeting at the Oak Ridge National Laboratory, April 27-30, 1970*, CONF-700401.

cient problem and maintenance difficulties that are peculiar to the liquid-metal-cooled systems.¹¹

An irradiation testing program is being conducted, in cooperation with Gulf General Atomic, to evaluate the adequacy of various fuel pin designs for use at GCFBR operating conditions. These tests are being conducted in a thermal flux environment in the Oak Ridge Research Reactor (ORR) and in a fast flux in the EBR-II. Two basic design approaches have been employed: (1) a sealed fuel pin, and (2) a vented fuel pin. The results from the tests of the first 19 fuel pins, all of the sealed pin type, were recently summarized.¹² At present one vented pin is operating in the ORR, a second has been designed for the ORR, and seven sealed pins designed to simulate the vented type are operating in the EBR-II.

Thermal Reactor Experiments

The vented design fuel pin was chosen¹⁰ as the reference design for the GCFBR because of its potential for successful and safer operation at higher cladding temperatures than the sealed fuel pin. The first irradiation test of an instrumented, stainless-steel-clad (U,Pu)O₂ fuel pin of the GCFBR vented design (test GB-9) has been operating in the ORR poolside facility¹³ since April 1970. This test has achieved (as of May 27, 1971) about half the planned burnup of 75,000 MWd/ton. During most of this period¹⁴⁻¹⁸ the fuel pin was operated at its normal operating conditions: 16 kW/ft and 685 ± 15°C peak cladding outer surface temperature, the internal charcoal fission product trap at 300°C, 1000 psig internal pressure and 975 psig external pressure on the cladding. Two modes

of sweep gas flow were employed – one with the sweep flowing across the top of the fuel pin above the charcoal trap, and one with the sweep gas flowing in at the bottom of the trap and out through the trap. The gamma activity of the sweep gas line leaving the trap was continuously monitored, and samples of the sweep gas were taken periodically and analyzed for fission product isotope content.

Detailed analyses^{19,20} of the data obtained from this experiment have shown that the charcoal trap is very effective in reducing the release of short-lived isotopes during steady-state operation (e.g., ¹³⁸Xe, 17-min half-life, $R \approx 0.04$)²¹ and less effective for longer lived isotopes (e.g., ¹³³Xe, 5.27-day half-life, $R \approx 0.9$). Typical release-to-birth rate ratios for various fission product gases under these flow conditions are shown in Fig. 31.4. Also, the activity in the sweep gas exit line is quite sensitive to pressure fluctuations, which momentarily alter the transport of gaseous fission products through the trap from diffusional transport to bulk flow. In addition, the sweep gas activity is sensitive to small changes (~15°C) in the average fuel pin cladding temperature, and the activity undergoes a steady buildup to an equilibrium level over an 8- to 10-hr period after return to full power operation following low- or zero-power operation.

The next test in this series will be similar but will contain solid rather than annular (U,Pu)O_{1.98} pellet fuel. This test will provide for sweeping gases directly from the fuel and the UO₂ blanket regions in addition to the trap region. This capsule has been designed.

Fast Reactor Tests

Eight fuel pins and capsules have been fabricated for irradiation in the EBR-II to test GCFBR fuel pins with internal charcoal traps under fast reactor operating conditions. The type 316 stainless-steel-clad U_{0.85}Pu_{0.15}O_{1.98} fuel pins will operate at approximately 15 kW/ft with cladding temperatures between 590 and 790°C to burnups between 25,000 and 100,000 MWd/ton. The specific cladding temperatures and burnups for each capsule and the design and

11. *An Evaluation of Alternate Coolant Fast Breeder Reactors*, WASH-1090 (April 1969).

12. T. N. Washburn, R. B. Fitts, and J. A. Conlin, *Fuel Element Development for the Gas-Cooled Fast Breeder, Part I, Sealed Fuel Rod Design*, ORNL-TM-3427 (June 1971).

13. D. B. Trauger, *Some Major Fuel Irradiation Test Facilities of the Oak Ridge National Laboratory*, ORNL-3574 (April 1964).

14. R. B. Fitts, E. L. Long, Jr., and A. W. Longest, *Metals and Ceramics Div. Annu. Progr. Rept. June 30, 1970*, ORNL-4570, pp. 167–69.

15. A. W. Longest et al., *GCR Program Semiann. Progr. Rept. Sept. 30, 1969*, ORNL-4508, pp. 87–97.

16. J. R. Lindgren et al., *Planned Thermal Irradiation of Manifolder-Vented (U,Pu)O₂-Fueled Rod in ORR Capsule P-9*, GA-9896, (Mar. 15, 1970).

17. A. W. Longest et al., *GCR Program Semiann. Progr. Rept. Mar. 31, 1970*, ORNL-4589, pp. 91–96.

18. A. W. Longest, J. A. Conlin, K. R. Thoms, and E. D. Clemmer, *GCR and Thorium Utilization Programs Semiann. Progr. Rept. Sept. 30, 1970*, ORNL-4637, pp. 40–47.

19. A. W. Longest, N. Baldwin, J. A. Conlin, R. B. Fitts, and J. R. Lindgren, "Fission Gas Release Measurements from Fast Breeder (U,Pu)O₂ Fuel," *Trans. Amer. Nucl. Soc.* **13**, 604 (1970).

20. R. J. Campana, J. R. Lindgren, and N. L. Baldwin, *Fuel Element Development for the Gas-Cooled Fast Breeder Reactor: Part II, Vented Fuel Rod Design*, GA-10657 (in publication).

21. R = ratio of fission gas release rate with sweep flow across top of trap to that with sweep flow through trap.

fabrication details have been reported previously.^{12,22,23}

Seven capsules were inserted in the EBR-II in November 1970. The eighth was stored to replace the first

22. T. N. Washburn, *GCR and Thorium Utilization Programs Semiann. Progr. Rept. for Sept. 30, 1970*, ORNL-4637, pp. 47-50.

23. P. W. Flynn et al., *High-Temperature Fast-Flux Irradiation Experiment for Mixed-Oxide Fuel Rods*, GA-10264 (Oct. 15, 1970).

capsule, which will be removed after reaching a burnup of 25,000 MWd/ton at a cladding midwall temperature of 700°C. It will be examined to determine fuel pin swelling, fission-gas release, chemical and mechanical interaction between fuel and cladding, and the effects of this irradiation on the sorption properties of the charcoal fission product traps. The designs have been completed for five additional capsules to replace others as they are removed for examination.

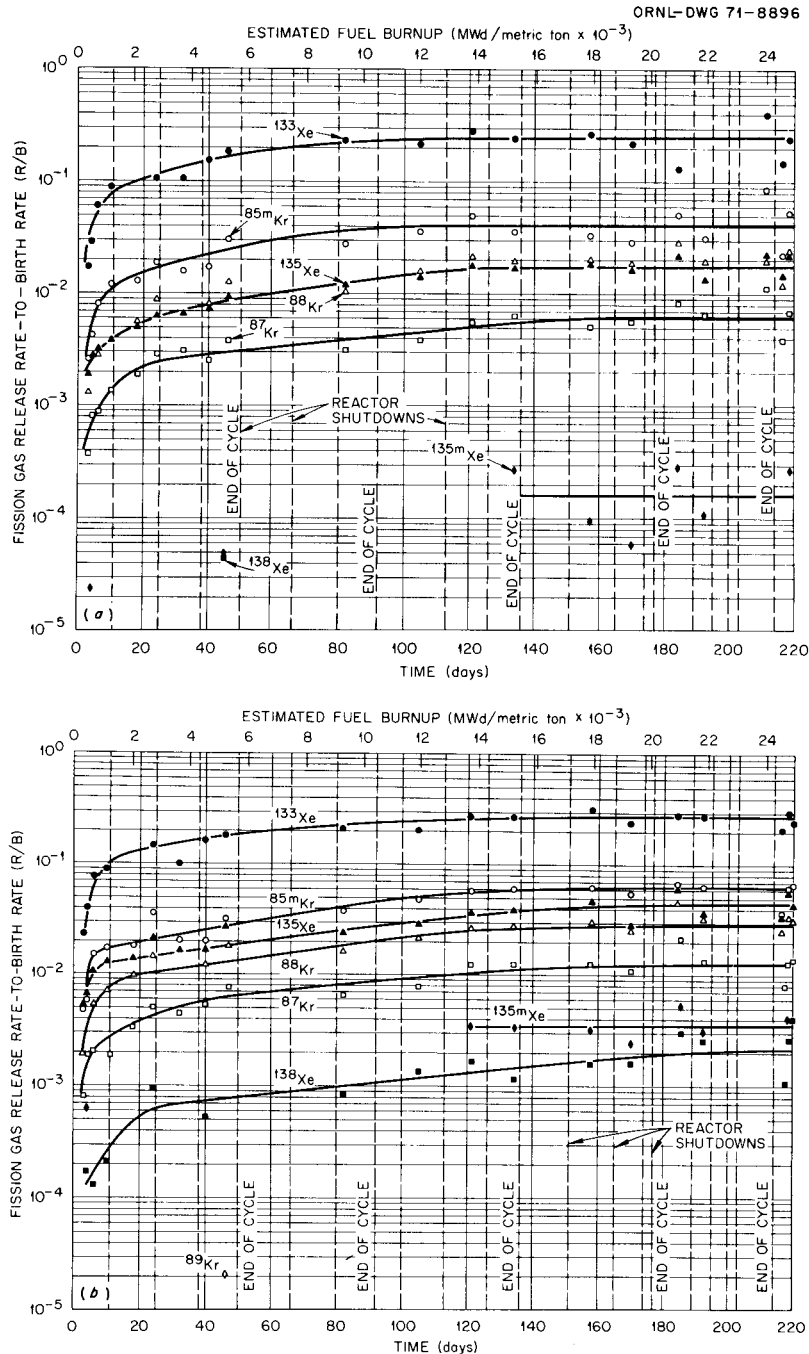


Fig. 31.4. Steady-state fission gas release from vented capsule at full power for two different sweep gas modes. (a) Flow across top of charcoal trap. (b) Flow through charcoal trap.

32. Heavy Section Steel Technology

D. A. Canonico

The Heavy Section Steel Technology Program is an engineering effort to determine the structural behavior of the thick plates and pressure vessels needed for large light water nuclear reactors. The overall program emphasizes the effects of flaws, discontinuities, and inhomogeneities on the integrity of the reactor vessel during both shutdown and operation. Extensive testing programs are being conducted on weldments and plates. These include the determination of strength and classical fracture toughness properties as well as the development and application of fracture mechanics for those steels currently being used in the fabrication of light-water nuclear pressure vessels.

We participate as both consultants and experimentalists. First, we serve on the staff of the Program Office as metallurgical consultants and are expected to contribute to decisions that require metallurgical knowledge. In addition, we are involved experimentally in those tasks that require the facilities and expertise available within the Division.

CHARACTERIZATION OF HEAVY SECTION STEEL PLATE

W. J. Stelzman R. G. Berggren

An additional region of HSST plate 01 was investigated by use of standard 0.505-in. and the 0.178-in. gage diameter tensile specimens and the standard Charpy V-notch impact specimens. The plate section investigated (01C1) was from near one of the upper corners of the plate associated with the top ingot end. Yield data¹ showed the same insensitivity to specimen orientation in the longitudinal (R) and transverse (W) directions² as in previous plate locations. The 01C1

region exhibited lower yield strengths than the nearby top center and the midplate regions at all locations except the midlevel, where the yield strengths were equal. In contrast, the 01C1 yield strengths were equivalent to the lower center region yield strength except at the midthickness location, where they were higher.

The Charpy V-notch impact data indicate a lower transition temperature at a 30 ft-lb correlation energy and higher shelf energy from longitudinal (RW) than from transverse (WR) oriented² test specimens. This appears to be consistent with results from other portions of the plate. The impact results at all levels were in good agreement with results for other regions of the plate.

RADIATION STUDIES ON HSST PLATES AND WELDS

W. J. Stelzman R. G. Berggren

Impact and tensile data were obtained from specimens of HSST submerged-arc and electroslag weldments irradiated at 150, 450, and 550°F to fluences of 6 to 12×10^{18} neutrons/cm² (>1 MeV). The tensile properties of the irradiated submerged-arc weldment using miniature (0.178-in. gage diameter and 1.250-in. gage length) tensile specimens show greater sensitivity to radiation damage than those of either the base plate at 150, 450, or 550°F or the electroslag weldment at 150 or 550°F.

The impact data for the irradiated electroslag and submerged-arc weldments using standard Charpy V-notch specimens indicated that the submerged-arc weld is tougher than the electroslag weld metal and base plate in the unirradiated condition but is more sensitive to irradiation damage than the electroslag weld metal at 130 and 560°F. The electroslag weld metal has a better transition temperature but a poorer shelf energy than the base plate in the unirradiated condition, but it is less sensitive to irradiation damage at 130 and 560°F.

1. R. G. Berggren and W. J. Stelzman, "Characterization of Heavy Section Steel Plate," *HSST Program Semiann. Progr. Rept. Feb. 28, 1971*, ORNL report in preparation.

2. Symbols for specimen orientations are defined by R. G. Berggren and W. J. Stelzman, *HSST Program Semiann. Progr. Rept. Feb. 28, 1969*, ORNL-4463, pp. 20-21.

A summary of radiation-induced changes in the mechanical properties of the ASTM A-533, grade B, class 1 plate and welds used in the HSST Program was compiled and will be published.³ An abstract follows.

Fast neutron induced changes in mechanical properties of a 12-in.-thick manganese-molybdenum-nickel steel plate and matching submerged arc and electroslag weldments are presented. The increases of strength and notch-impact transition temperature and decreases in ductility are given for several temperatures of irradiation. Some observations using an instrumented Charpy testing machine are also presented.

SIMULATED SERVICE TEST

D. A. Canonico

The simulated service test task of the program has as its objective the demonstration of a capability for predicting safe behavior of a full-size pressure vessel. The culmination of this task is the testing of a full-size pressure vessel built to nuclear standards. In pursuing this goal, the influence and interaction of factors that specifically affect the fracture load of thick pressure vessels must be established. We must demonstrate the capability of predicting the "vessel transition temperature" for a selected crack configuration. Further, we must predict those combinations of crack configuration, load, and temperature that will not cause failure and, finally, the combination that will cause failure in both the tough and frangible conditions.

The successful culmination of this test requires that a method for generating sharp cracks in thick steel sections be developed. Usually, the generation of cracks in fracture mechanics tests depends upon fatiguing the specimen. In large specimens or small irregularly shaped specimens, this may be impossible. After a cracking technique is satisfactorily developed, a series of tests involving large tensile specimens and intermediate vessel tests must be conducted.

During the past year we assisted in the procurement of the intermediate test vessels. These are 39-in.-OD vessels, about 78 in. long with 6-in.-thick walls. In addition, we were given the task of developing a technique for producing sharp "fatigue-like" cracks in ferritic materials. This work is discussed below.

Technique for Generating Sharp Cracks in Low-Alloy High-Strength Steels

D. A. Canonico J. D. Hudson

The production of cracks in low-alloy high-strength steel was premised on the role of hydrogen in the

3. R. G. Berggren and W. J. Stelzman, "Radiation Strengthening and Embrittlement in Heavy Section Plate and Welds," *Nuclear Engineering and Design*, in press.

formation of cracks in ferritic materials. It is well established that hydrogen is responsible for underbead cracking in the heat-affected zone of ferritic weldments. Further, the cracking is associated with stresses and microstructure. Our technique is based on producing a suitable microstructure (martensite) in these steels by rapidly cooling them from the austenitic temperature range. This is easily accomplished by an autogeneous weld on the surface. The second requirement is stress, and the use of an electron-beam welder concentrates the heat in a small region, thereby assuring that residual stresses of yield-point magnitude are located in a very narrow band. The third requirement for cracking is the presence of hydrogen, which can be "pumped" electrically into the weld metal. The test specimen except for the weld is masked and placed in a 10% H₂SO₄ electrolyte. A lead bar is immersed in the bath, and the system is wired so that the specimen is at the lower potential. A current density of about 0.5 A/in.² of unmasked area causes cracking in less than 2 hr. Figure 32.1 schematically illustrates the process.

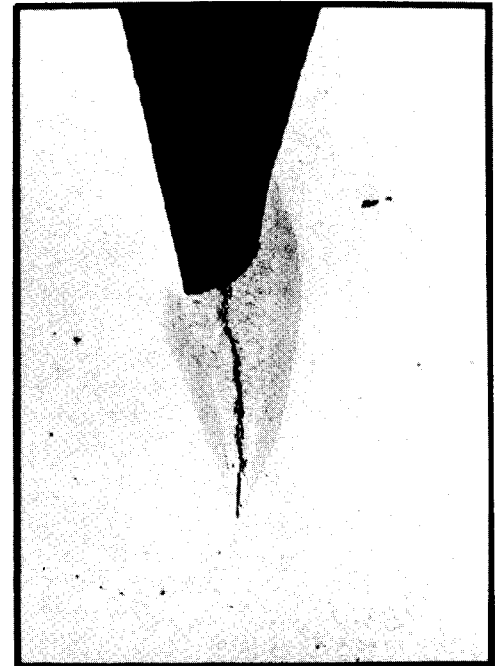
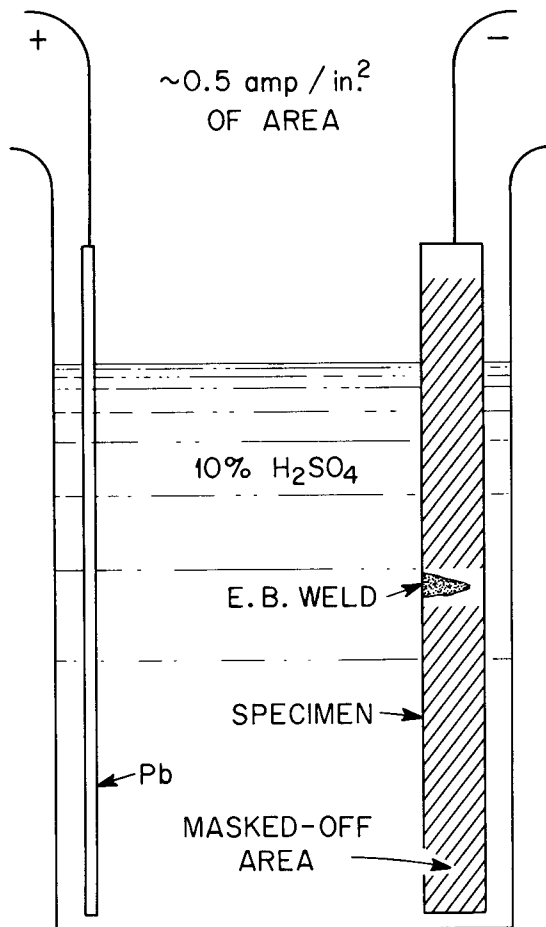
We have successfully cracked ASTM A533, grade B steel in thicknesses from 1/2 to 4 in. The thicker materials are more easily cracked because they provide a better heat sink and, consequently, the optimum microstructure and residual stress pattern. The cracks are quite similar to fatigue cracks. They propagate through the weld metal and heat-affected zone and culminate at the end of the weldment. Figure 32.1 contains some typical cracks. We have successfully formed cracks ranging from 0.075 in. to over 1.5 in. in depth. The technique has a number of attractive features. Among these is the possibility of cracking a specimen during testing, thereby simulating a pop-in condition and permitting dynamic fracture toughness measurements.

This procedure has been used in a study of scaled-down intermediate-test-vessel requirements. The cracks were placed in 3-in.- and 6-in.-diam vessels with excellent control of crack depth.

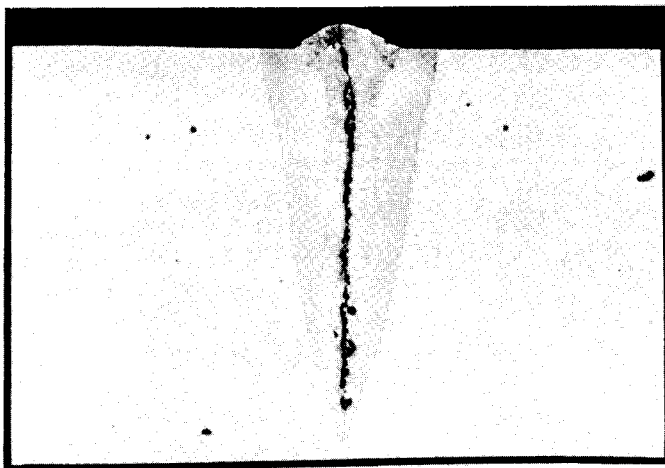
The Determination of Retemper Temperature for the Intermediate Vessel Test Courses

D. A. Canonico W. J. Stelzman R. G. Berggren

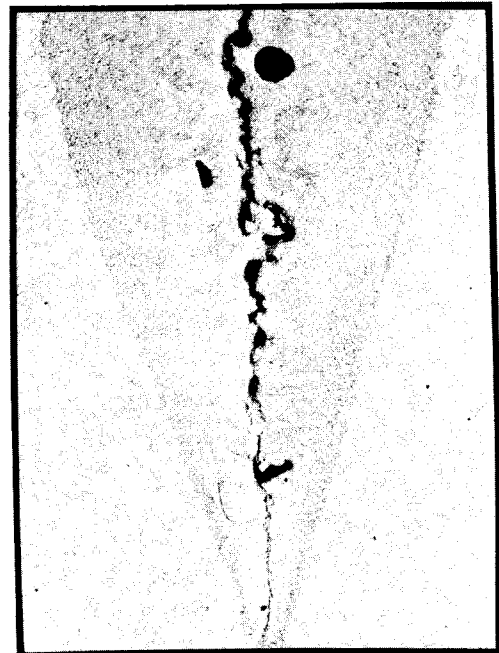
The design and test parameters for the cylindrical body forging that are to be used in the fabrication of the Intermediate Test Vessels (ITV) were based on the mechanical properties typical for ASTM A508 class 2 steel. This specification requires that the minimum yield strength and ultimate tensile strengths be 50,000 and 80,000 psi, respectively. In addition, a toughness



22 X



22 X



100 X

Fig. 32.1. Schematic presentation of the hydrogen embrittlement technique for producing sharp cracks in ferritic materials. Hydrogen is generated at the cathode (welded sample) of an electrolytic cell. Typical cracks are shown.

requirement of an average of 30 ft-lb at +10°F was imposed. The original cylindrical body forgings supplied for the vessels had yield and ultimate tensile strengths in excess of 82,000 and 102,750 psi. Moreover, the nil-ductility temperature of the steel, as determined by the drop-weight test, was below -20°F. The properties of the steel are acceptable as far as the ASTM A508 class 2 specification is concerned. However, the high tensile values are cause for concern because the ultimate tensile strength of typical submerged-arc welds may be equal to or below the yield strength of the cylindrical body forging.

From a review of the ITV study program, we concluded that the cylindrical body forgings should possess mechanical properties within the following ranges.

Ultimate tensile strength	80,000 to 95,000 psi
0.2% offset yield strength	50,000 to 75,000 psi
Elongation in 2 in. (min %)	18%
Reduction in area (min %)	38%
Charpy impact energy (at 40° F)	
Average of set of 3 specimens	30 ft-lb
Minimum value of 1 specimen	25 ft-lb

We were assigned the task of selecting reheat-treatment methods to provide the cylindrical body forgings with mechanical properties within these values.

General metallurgy. First we verified the reported heat treatments, as reported below. Chemical analyses conducted by the Oak Ridge National Laboratory and a large steel company were in agreement with the analysis reported by the vendor for all elements except carbon. ORNL found from 0.29 to 0.30% C; the steel company and the vendor reported 0.27%.

The original heat treatment of the forgings was as follows:

Normalize	6 hr	1700° F
Austenitize	7 hr	1580° F
Quench in water		
Temper	6 hr	1270° F

Thermocouples imbedded in the cylindrical shell forgings during heat treating showed the cooling rate to half-temperature at the quarter-thickness to be about 2.5°F/sec. Our initial response was to reduce this rate by re quenching the steel in a less severe medium. We heated a 3/4-in.-square × 6-in.-long piece of steel to 1600°F, held it at temperature for 1 hr, and furnace cooled it at 0.07°F/sec, which is 1/36 the rate for the forgings. The hardness value was 16 R_c, compared to 20 R_c for the quenched-and-tempered forging. The change in cooling rate did not appear to provide an easy means for reducing the strength. This supposition was sup-

ported by the Data-Trak studies wherein the cooling rate was 20°F/hr. Further, the microstructure of extremely slowly cooled (about 0.006°F/sec) steel is even more atypical of ASTM A508 class 2 than the higher tensile properties of the forgings.

We then sought to lower the strength by retempering. A heat-treatment study was undertaken, and changes in hardness values were used to measure effectiveness. A through-the-thickness hardness survey was made on the as-received steel. The R_c values ranged from 23 on the surface to 19 at a depth of 4 3/8 in.

We retempered at 1220 and 1280°F and saw no apparent change in hardness. At 1300°F, there was a small drop, about 2 in R_c, within the steel, but the surfaces were essentially unchanged. Retempering at 1325°F increased hardness. We assume that the steel began to transform to austenite, and upon air cooling the 3/4-in. section hardened.

Concurrently with the hardness, electrical resistivity was studied to determine the eutectoid temperature. The transformation occurred between 1315 and 1346°F (713 and 730°C), in good agreement with the change in hardness observed after the 1325°F retemper treatment.

We also studied the hardenability of the body forging steel, using the Jominy End Quench Test (JEQT). This test allows us to assess the effect of cooling rate on the hardness of a steel. The results are shown in Fig. 32.2. Austenitizing temperature had no effect over the 200°F range employed. The JEQT results are typical for this grade of steel with 0.25 to 0.30% C.

The effect of tempering temperature was investigated by conducting a conventional JEQT on steel that had been austenitized at 1600°F and then tempered at 1280, 1310, and 1340°F. These results are also shown in Fig. 32.2. The 1340° temper resulted in a hardness of about R_c 20. This hardness is equal to or higher than what can be expected in the 6 7/8-in.-thick forging because the slowest cooling rate possible in the JEQT is faster than that of the 1/4 T location in the forging. This study does indicate, however, that heating the steel above the eutectoid temperature did not dramatically change hardness.

Mechanical properties. Tensile and Charpy V-notch impact tests⁴ were performed upon specimens from an end portion of one of the heat-treated vessel shells. The original temper was 6 hr at 1270°F, with estimated heating and cooling rates of 200°F/hr. Retempering was

4. R. G. Berggren and W. J. Stelzman, "Retempering Study of HSST Intermediate Test Vessels," *HSST Program Semiann. Progr. Rept. Feb. 28, 1971*, ORNL report in preparation.

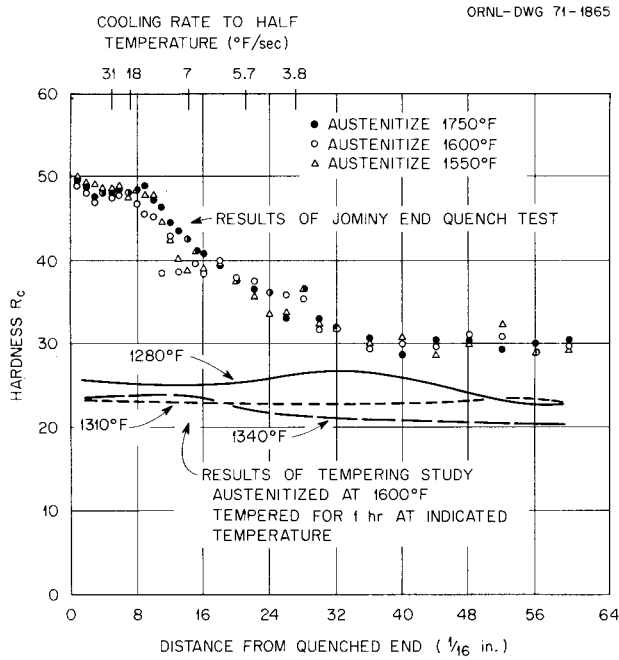


Fig. 32.2. Effect of cooling rate and tempering temperature on hardness of ASTM A508 class 2 steel.

performed in the Research Inc. thermal cycle simulator or Data-Trak system at prescribed heating and cooling rates, with a hold or soak period of 6 hr at the retemper temperature. The effect of cooling rate and retemper temperature were investigated on the standard 0.505-in.-gage-diam tensile specimen and compared with the tensile properties of a specimen that had been held at 1596°F for 6 hr and cooled very slowly (20°F/hr) so as to provide minimal strength properties. Results of the tensile tests after heating and cooling at 200°F/hr are presented in Table 32.1 and indicate a 20% drop in yield and ultimate stresses between the vendor's 1270°F original temper and the 1310°F retemper, with a more gradual reduction in strength to the 1345°F limit of the study. Extrapolation to the 1596°F treatment indicated that most of the reduction in strength had occurred before the 1345°F limit of the study. We found very little change in total elongation and a steady decrease in reduction of area as the retemper temperature was increased, especially for the axially oriented specimens.

Fracture properties were investigated for retemper at 1315 and 1340°F, with 200°F/hr heating and cooling

Table 32.1. Effect of retempering on the tensile properties of intermediate vessel course No. 5 material (ASTM A-508, class 2)

Depth in vessel wall	Specimen orientation	Retemper treatment ^a			Tensile properties ^b				
		Heating rate (°F/hr)	Hold period		Cooling rate (°F/hr)	Yield stress (psi)	Ultimate stress (psi)	Total elongation (%)	Reduction of area (%)
			Time (hr)	Temperature (°F)					
					× 10 ³	× 10 ³			
			Vendor data						
	Axial		6 ^c	1270 ^c		86.5	107.0	22.5	66.3
	Axial		6 ^c	1270 ^c		87.0	107.5	22.5	67.0
			ORNL data						
1/4 T	Tangential		6 ^c	1270 ^c		92.2	109.0	19.4	52.2
3/4 T	Tangential		6 ^c	1270 ^c		91.1	108.9	18.1	38.6
1/4 T	Tangential	<i>d</i>	1	1300	<i>d</i>	83.9	102.3	22.2	56.8
3/4 T	Tangential	200	6	1312	200	73.7	92.9	22.5	57.4
1/4 T	Axial	200	6	1596	20	60.0	89.4	24.4	46.2
1/4 T	Axial	200	6	1303	200	78.7	96.3	25.0	70.0
1/4 T	Axial	200	6	1331	200	69.2	95.8	26.0	66.9
1/4 T	Axial	200	6	1300	200	75.6	96.1	25.0	69.7
1/3 T	Axial	200	6	1346	200	65.3	96.0	22.5	66.5
1/3 T	Axial	200	6	1338	200	66.7	95.1	26.5	65.3

^aRetemper was performed with a Research Inc. thermal cycle simulator.

^b0.505-in.-gage-diam specimens.

^cOriginal temper; specimens not retempered.

^dAmbient specimen was inserted into a large furnace at 1300°F, held for 1 hr, removed, and allowed to cool on firebrick in still air.

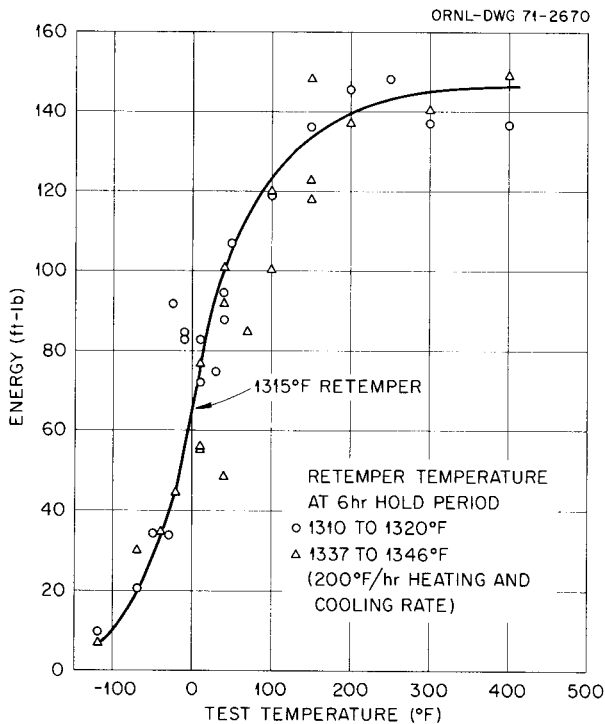


Fig. 32.3. Effect of retempering on Charpy V-notch impact properties of HSST intermediate test vessel No. 5.

rates and a 6-hr hold at temperature. The test specimens were standard Charpy V-notch impact bars of axial orientation and notched perpendicular to the vessel surface to provide circumferential crack propagation. Analysis of the fracture energy, fracture appearance, and lateral expansion data indicate a loss in impact properties or toughness. The fracture energy data are presented in Fig. 32.3; however, the scatter of the data obscures the small shift. Therefore, the three toughness parameters were investigated at fixed test temperatures (10, 40, and 150°F) for samples retempered at 1290 to 1345°F. The toughness parameters generally decreased

as the retemper temperature increased. This also indicates a shift of toughness at a given energy level to higher temperatures.

From the tensile and Charpy test results, we conclude that retempering at $1325 \pm 15^\circ\text{F}$ can reduce the ultimate stress from 107,000 to 87,000 psi and the yield stress from 95,000 to 70,000 psi. These values are compatible with those of other vessel components and are obtained without a significant loss in ductility or toughness. Retempering at as high as 1340°F results in properties that still appear to be acceptable for the ITV study.

Metallography. The microstructures of the as-received specimens and those retempered in the Data-Trak at 1298, 1311, and 1318°F are quite similar. The retemper at 1343°F resulted in a structure in which the amount of carbide appears to be reduced. This difference, however, is nowhere near that exhibited by the surface and $1/4 T$ locations of the forging. The $1/4 T$ and surface microstructures are dramatically different and yet represent a hardness variation of only about 3 R_c numbers.

This similarity in microstructures, combined with the results of the reheat treatment studies, resulted in our suggestion that the desired mechanical properties could be obtained by retempering the forgings at about 1320°F . The vendor felt that his furnaces were controllable within $\pm 15^\circ\text{F}$ in the temperature range of interest. Our data indicated that a retemper at $1320^\circ\text{F} \pm 25^\circ\text{F}$ would provide acceptable mechanical properties. The cylindrical shell forging was reheated at 1320°F . The heat treatment was monitored by a number of thermocouples and was observed by an ORNL representative. The result of heat treatment on the microstructure of the forging is shown in Fig. 32.4. The microstructure from the original 1270°F temper is included for comparison. There is little difference in the two microstructures.

Y-106176

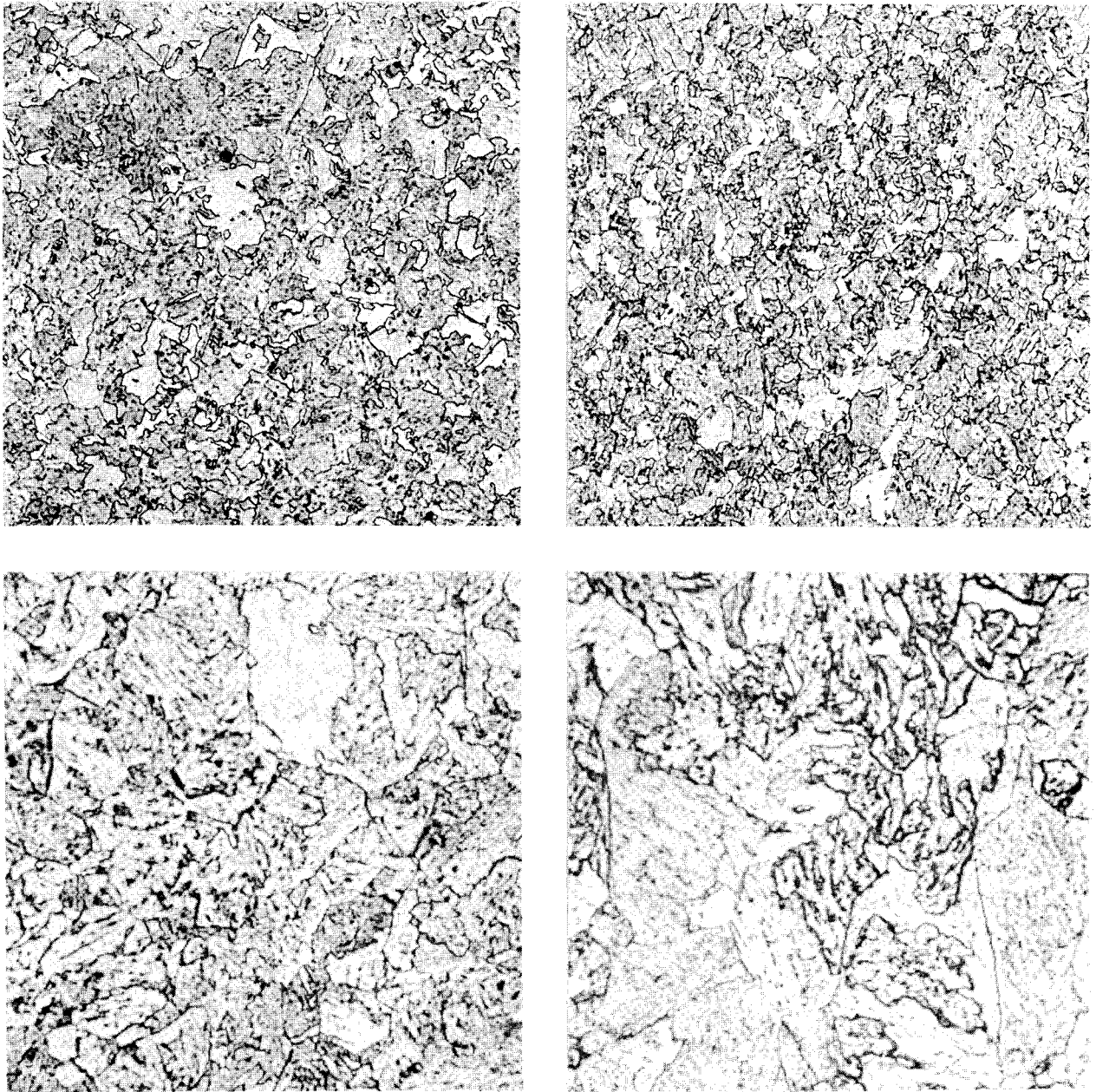


Fig. 32.4. Comparison of microstructures from forgings of intermediate test vessels. Material is ASTM A508 class 2, quenched and tempered at 1270°F (left) and 1320°F (right). The upper photomicrographs are 250X; the lower are 1000X.

33. Military Reactor Fuel Element Procurement Assistance

R. J. Beaver

This task provides technical assistance to the AEC and military services in procurement of reactor components. Included are such items as standardization of specifications, review of technical requirements for procurement packages, and participation in fuel procurement as well as quality control audits of fuel fabricators.

Thirty-one MH-1A Type I stainless steel fuel element assemblies were procured for the U.S. Army's power reactor on the U.S.S. Sturgis, Gatun Lake, Panama Canal Zone. Each assembly contained 104 fuel rods, each consisting of a 36-in.-long stack of 0.451-in.-diam. low-enriched UO_2 pellets in a 0.023-in.-thick type 348 stainless steel cladding. Final delivery by the Kerr-McGee Corporation, contractor to the New York Operations Office, was made in the spring of 1970.

The NYO 10748 specification for the longer-life MH-1A Type II fuel element assemblies was completed and procurement initiated under the auspices of the New York Operations Office. Kerr-McGee was the successful bidder for 32 fuel element assemblies. These assemblies are similar in design to the Type I assemblies except for the change to higher enrichment in the ^{235}U isotope and the substitution of several burnable-poison rods, consisting of pellets containing approximately 3.5 vol % B_4C in Zircaloy 2. Final delivery is anticipated in April 1972.

A program to upgrade the specifications for the U.S. Navy's PM Type 4 Core was initiated and included integration of RDT reference standards. Review of the last draft was completed in June 1971. The specification will be published early in FY 1972.

The PM Type 4 control rod assemblies, which were found defective by the ORNL inspection representative for the New York Operations Office, were repaired and accepted after close surveillance by ORNL representatives. Discovery of water at the bottom of the shipping container in which Core 01 was packaged was one of the factors that prompted return of this core from the Antarctica site. The contamination occurred after the zero power experiment conducted at Westinghouse, but the source was not identified. The core was not protected by the polyethylene cover, and evidence indicated that its components had become contaminated by droplets of water containing approximately 30 ppm chloride. Efforts to rinse the core of this contamination are believed to have been successful. This core was cleaned at NUMEC under close surveillance of ORNL representatives. The repaired control rod assemblies were fitted into this core, and the core was packaged for shipment under the close surveillance of ORNL representatives. Shipment was authorized by the New York Operations Office early in June 1971.

34. Molten-Salt Reactor Program

J. R. Weir, Jr. H. E. McCoy, Jr. W. P. Eatherly

This program has involved us with the operation of an 8-MW (thermal) experimental reactor (Molten-Salt Reactor Experiment, MSRE) and with the materials problems associated with the future construction of a molten-salt breeder reactor. Operation of the MSRE was terminated on December 12, 1969, after it successfully completed its mission. We have examined graphite and Hastelloy N specimens from the Reactor. The work in support of an advanced reactor involves (1) development of modified Hastelloy N with improved resistance to irradiation damage,^{1,2} (2) development of a graphite with improved dimensional stability under irradiation,² (3) development of a method for reducing the surface permeability of graphite to gaseous fission products,² (4) determination of the corrosion rate of Hastelloy N in a new coolant salt, sodium fluoroborate,² and (5) development of a technology for fabricating small processing plants for removing fission products by contacting the fertile-fissile salt with bismuth.

EXAMINATION OF MSRE COMPONENTS

B. McNabb, Jr. H. E. McCoy, Jr.

Selected components of the MSRE were examined to gather further information after the successful operation of the MSRE was completed. We examined a graphite moderator core block, a Hastelloy N control rod thimble, Hastelloy N shell and some tubes from the primary heat exchanger, a freeze valve that failed during final shutdown, a copper sampler tube that was lost in the pump bowl, the Hastelloy N sampler assembly from the pump bowl, and some parts from the radiator.

The graphite core block had machining marks still plainly visible in the fuel channels exposed to flowing fuel salt, indicating very little if any erosion or corrosion. Figure 34.1 shows the bottom of the graphite moderator assembly before operation, including the Hastelloy N grid support and the bottom of core block 1184-C 19 in position, and the inset shows the same core block after operation. The two cracks and

small chip on the right and the numbers appear unchanged by being at temperature for 26,000 hr. There were no measurable differences in the initial and final dimensions.

The Hastelloy N control rod thimble was cut up for mechanical property, metallography, and electrolytic dissolution specimens. Tensile tests showed little change in yield stress and ultimate stress, but the reduction in area at 825°C was reduced from 45% for unirradiated material to 28% for the thimble and that at 650°C from 20.6 to 9.7%. Similar changes were noted for the properties of surveillance samples reported previously.³

The primary heat exchanger shell and one of the tubes were examined metallographically. We saw little corrosion, but the grain boundaries in the tubing were cracked to a depth of about 5 mils and opened up more under stress in a tensile test. The yield and ultimate stresses were reduced about 10% and the ductility about 27% from the as-received tubing used in the heat exchanger.

The failure of the freeze valve on termination of operation of the MSRE was due to thermal fatigue caused by a field modification of the original design. The air cooling shroud was made rigid by the modification, so the different heating and cooling rates of the shroud and the salt-filled pipe during operation of the valve imposed stresses in the pipe and led to development of a fatigue crack.

The Hastelloy N sampler assembly had a thick deposit on the lower regions of the sampler cage rods and mist shield, which had been in the liquid region of the pump bowl. A thin, sooty deposit on these components in the

1. H. E. McCoy, "The INOR-8 Story," *ORNL Review* 3(2) 35-49 (Fall 1969).

2. H. E. McCoy, Jr., R. L. Beatty, W. H. Cook, R. E. Gehlbach, C. R. Kennedy, J. W. Koger, A. P. Litman, C. E. Sessions, and J. R. Weir, "New Developments in Materials for Molten-Salt Reactors," *Nucl. Appl. Technol.* 8, 156-69 (1970).

3. H. E. McCoy, *An Evaluation of the Molten-Salt Reactor Experiment Hastelloy N Surveillance Specimens - Fourth Group*, ORNL-TM-3063 (March 1971).

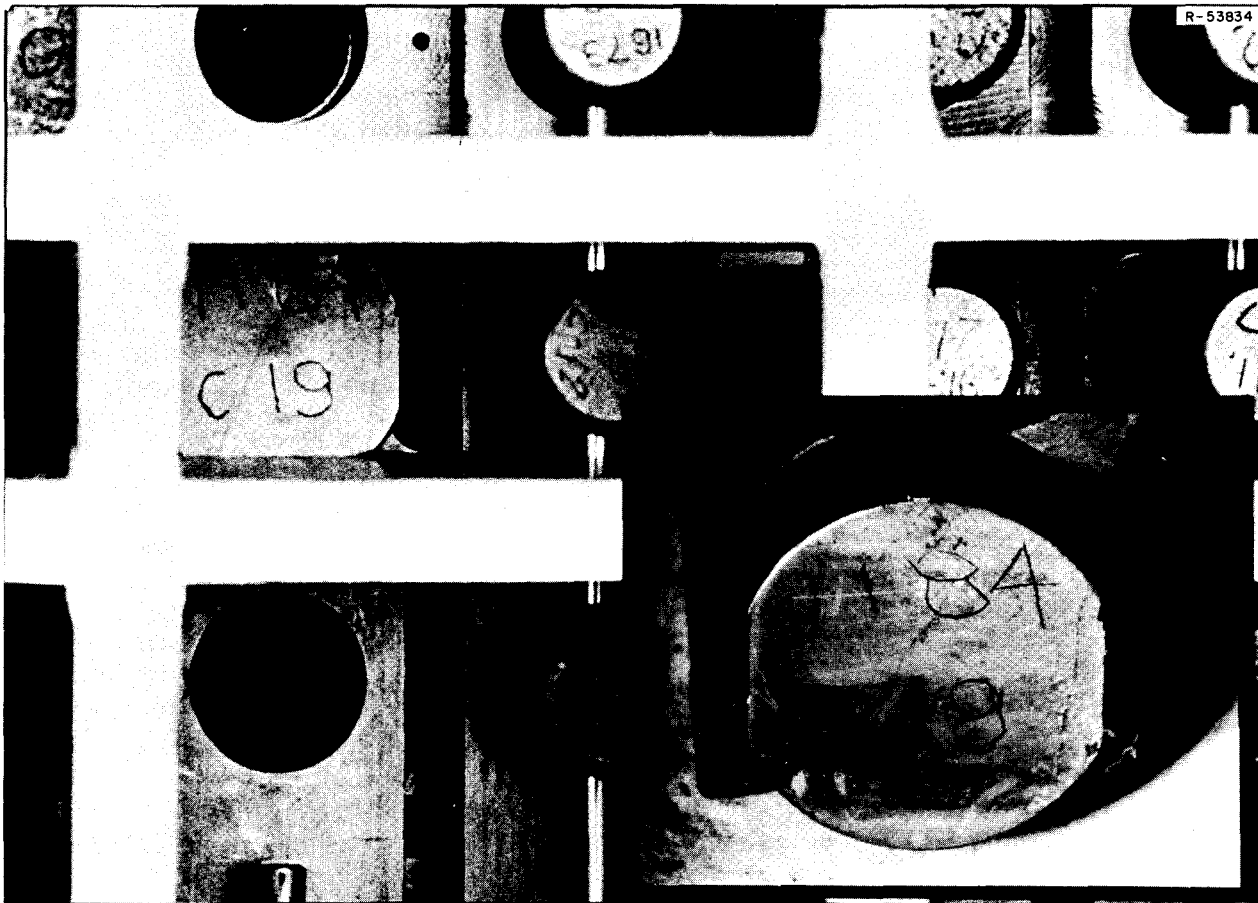


Fig. 34.1. Comparison of the bottom positioning stud on the graphite moderator element when initially installed (large picture) in the MSRE and after operation (lower right inset). The inset was made in the hot cells after the element had been at temperature for over three years.

vapor region was probably caused by oil leakage. Little, if any, corrosion of the cage rods in either the liquid or vapor region was found metallographically.

The copper sample capsule removed from the pump bowl had deposits on both surfaces. Microprobe analysis revealed them to be mostly copper and nickel, with some areas containing high concentrations of chromium and molybdenum. Spectrographic analysis detected fuel salt in the porous deposited material.

Two thermocouple wells and some of the radiator tubing from the coolant circuit were examined. There was no evidence of corrosion. The mechanical properties of the tubing had been modified slightly, but we attribute this to the carbide that precipitated during the 26,000 hr at temperature.

MICROSTRUCTURAL STUDIES OF MODIFIED HASTELLOY N

R. E. Gehlbach S. W. Cook

Our major efforts have involved microstructural characterization of laboratory and commercial heats of

modified Hastelloy N. Our work has been directed toward understanding the effects of small additions of Ti, Hf, and Nb on the microstructures generated by exposure in the range 650 to 760°C. The goal is to produce a microstructure that resists irradiation damage and is stable over a long period of time at the design temperature of 700°C. The types of microstructures produced by alloying and the responsiveness of the microstructures to variations in heat treatment vary markedly for the laboratory and the commercial melts.

Laboratory heats. Our studies of many laboratory heats modified with Ti, Hf, and Nb, either singly or in combination, show that small additions of hafnium are quite important in controlling the microstructure generated on aging. A fine dispersion of MC carbide is precipitated in the matrix and grain boundaries.⁴ The carbide particles are much finer and more numerous at 650°C than at 760°C. Very little effect is observed for aging times up to 1000 hr.

4. R. E. Gehlbach and S. W. Cook, *Metals and Ceramics Div. Annu. Progr. Rept. June 30, 1970*, ORNL-4570, pp. 136-37.

The effect of carbon concentration and silicon on the microstructures generated in Hf-Ti-Nb alloys has been studied and is summarized in Chap. 5 of this report.

Commercial alloys. We have examined the microstructure of nearly every commercial alloy received during the past three years for our scale-up program. Our studies included specimens aged at 650, 700, and 760°C for times up to 1000 hr. The alloys with 0.3 to 0.5% Si contain large amounts of M_6C , similar to that precipitated in standard Hastelloy N, and lesser quantities of MC carbide due to the addition of Hf, Ti, and Nb. Two commercial heats containing 1.1 and 2.1% Ti as the sole modifying addition have microstructures quite similar to their laboratory heat counterparts; that is, rough grain boundaries containing large amounts of MC with much acicular MC extending into the matrix 1 to 3 μm from the boundaries. The grain interiors are quite free of precipitate. Unlike the laboratory heats, the commercial alloys modified with both hafnium and titanium do not develop the "hafnium-type" fine carbide precipitate in the matrix and grain boundaries. Instead, the microstructures are not distinguishable from those of the titanium-modified alloys and do not appear to be at all sensitive to aging time or temperature over the range studied.

The commercial alloys containing hafnium as the sole modifying element behave somewhat differently from those containing titanium in that grain boundary precipitation is somewhat finer, and less carbide is present adjacent to the boundaries. The fine carbide dispersion always present in the laboratory heats after aging is virtually absent in the commercial alloys, although relatively coarse MC is present in the matrix.

Material from the two commercial heats modified only with hafnium was remelted and fabricated at ORNL by the procedures employed for our laboratory melts. These remelts are similar to each other after aging but differ from both the parent commercial alloys and laboratory equivalents. After aging at 760°C, grain boundaries in the remelted alloys strongly resemble hafnium-modified laboratory heats with fine carbide in the boundaries and no acicular precipitate in the matrix adjacent to the boundaries. However, a very small amount of carbide is present in the matrix. At 650°C the microstructures of both remelts are virtually free of any precipitation at all. We have no explanation at the present time for this recent observation.

High titanium alloys. Although additions of hafnium appear promising for producing a microstructure with resistance to irradiation-induced embrittlement, the zirconium present in the hafnium poses a potential welding problem.⁵ Thus far, alloys containing relatively

high concentrations of titanium appear to offer a reasonable alternative. We are investigating a series of laboratory alloys to define the level at which the Ni_3Ti intermetallic (eta phase, similar to gamma prime) forms. We want to keep the titanium concentration sufficiently low to avoid Ni_3Ti , which would seriously embrittle the alloy. Thus far we have observed copious quantities of eta in an alloy containing 2.9% Ti but smaller quantities, heterogeneously distributed, at 2.4% Ti. A 2% Ti level appears to be free of eta, at least for times up to 10,000 hr at 700°C.

PROPERTIES OF UNIRRADIATED MODIFIED HASTELLOY N

B. McNabb, Jr. H. E. McCoy, Jr.

In scaling up from laboratory heats of modified Hastelloy N to small commercial melts of from 50 to 100 lb, about 25 heats have been studied for mechanical properties and weldability, as reported previously.⁶ These alloys contain additions of up to 2% Ti, 1% Hf, and 2% Nb. Most of these alloys are stronger than standard Hastelloy N, and heat 69-648 (0.92% Ti, 1.95% Nb, 0.043% C) is the strongest.⁷ In creep at 650°C this alloy has an allowable stress about double that of standard Hastelloy N, but at 760°C the modified alloy is only 20% stronger. These property variations are attributed to different carbide distributions obtained when these various alloys are solution annealed at 1177°C and subsequently tested at 650 to 760°C. We know that zirconium is detrimental to the weldability,⁵ so we do not know whether the poor weldability was due to the zirconium or the combination of both elements. The cracks were confined to the weld metal, and two of these heats were rewelded with a heat of standard Hastelloy N filler metal. Four alloys that contained greater than 0.7% Hf and 0.04% Zr cracked during welding. Side bend specimens of these welded heats could be bent without cracking, demonstrating that the weld metal cracking problem could be remedied by adjusting the composition of the filler metal.

5. H. E. McCoy and R. E. Gehlbach, *Nucl. Technol.* **11**, 45-60 (1971).

6. B. McNabb and H. E. McCoy, *MSR Program Semiannual Progr. Rept. Aug. 31, 1970*, ORNL-4622, pp. 160-61; H. E. McCoy and B. McNabb, *ibid.*, pp. 161-64.

7. H. E. McCoy, R. E. Gehlbach, and B. McNabb, "Development of New Nickel-Base Alloys for High Temperature Service," to be published in the proceedings of Meeting of the Society of Aerospace Material and Process Engineers, Huntsville, Ala., Oct. 5-7, 1971.

POSTIRRADIATION PROPERTIES OF MODIFIED HASTELLOY N

H. E. McCoy, Jr.

Laboratory melts containing Ti, Hf, and Nb have been creep tested^{8,9} at 650°C after irradiation at 650, 700, and 760°C. Alloys containing from 1.5 to about 2.0% Ti have minimum fracture strains of about 4%. Alloys with above 0.5% Hf have fracture strains above 10%. Niobium by itself does not result in good properties, but niobium seems to improve the ductility when added in combination with titanium or hafnium.

The most recent work has concentrated on the evaluation of several small commercial melts containing additions of Ti, Nb, and Hf. The alloys all had about the same microstructure, which was characterized by a grain boundary precipitate and very little matrix precipitation. The single alloy that contained 0.79% Hf, based on our experience with laboratory melts, should have had large amounts of matrix precipitate, but it contained mainly coarse grain boundary precipitate. The microstructures seem quite insensitive to aging temperature over the range 650 to 760°C. Samples of most alloys have been irradiated at 760°C and tested at 650°C. Their properties are fair to poor, with rupture lives greater than those of standard Hastelloy N and fracture strains only slightly greater than those of standard Hastelloy N. Studies are in progress to determine the effects of different melting practices.

CORROSION OF HASTELLOY N IN FLUORIDE SALTS

J. W. Koger

Temperature, the impurity content of the salt, and flow rate are principal variables that can affect corrosion by molten fluoride salts. We are studying the effect of these variables on corrosion and mass transfer in experimental systems (capsules, thermal convection loops, and pumped loops) that are based on design parameters for conceptual molten salt reactors. The alloys under investigation are Hastelloy N, Hastelloy N modified for improved radiation properties, and type 304L stainless steel. Salt mixtures of interest include the proposed MSBR coolant salt, a eutectic mixture of NaBF₄-8 mole % NaF, and various compositions of the

LiF-BeF₂ system. Within the latter group are fuel salts (UF₄ added), blanket salts (ThF₄ added), and fertile-fissile salts (both UF₄ and ThF₄ added). The following significant observations were made this year.

Fuel, blanket, and fertile-fissile salts.

1. A thermal convection loop of Hastelloy N with standard and modified Hastelloy N specimens has circulated a simulated MSRE fuel salt with 1 mole % ThF₄ for 9.1 years at a maximum temperature of 705°C with no evidence of plugging.^{10,11}
2. A type 304L stainless steel thermal convection loop with the same salt has operated for 7.8 years at a maximum temperature of 688°C. The removable specimen at the highest temperature lost 60.0 mg/cm² in 23,800 hr, equivalent to about 1.1 mils/year uniform corrosion. Although this weight loss is relatively large, there have been no changes in the flow conditions of the loop.^{10,12}
3. Removable specimens in Hastelloy N thermal convection loops containing fuel, blanket, and fertile-fissile salts operating at a maximum temperature of 700°C have lost no more than 2.1 mg/cm² in the hot leg nor gained more than 1.6 mg/cm² in the cold leg in 24,000 hr; this is equivalent to 0.04 mil/year uniform corrosion. Modified Hastelloy N alloys, which contain 0.2 to 2.5% Ti and no iron, have generally shown better corrosion resistance than the unmodified Hastelloy N. The corrosion reactions in the fertile-fissile systems involve primarily the oxidation of chromium by both FeF₂ and UF₄. The overall corrosion process is controlled by solid-state diffusion of chromium in the alloy. No differences in mass transfer have been seen in a Hastelloy N system in which the salt contacts liquid bismuth and in a system that contains no bismuth.^{10,12}
4. We studied the compatibility of TZM (Mo-0.5% Ti-0.1% Zr) with the fertile-fissile salt at 1100°C. Corrosion was limited to a superficial removal of zirconium and titanium from the alloy.¹³

10. J. W. Koger, *MSR Program Semiannu. Progr. Rept. Aug. 31, 1970*, ORNL-4622, pp. 165-78 and 189-91.

11. J. W. Koger, *MSR Program Semiannu. Progr. Rept. Feb. 28, 1971*, ORNL-4676, pp. 192-201.

12. J. W. Koger and J. H. DeVan, "Selective Attack of Alloys by Molten Fluoride Salts," presented at National Association of Corrosion Engineers Annual Meeting in Chicago, March 22, 1971.

13. J. W. Koger, "Compatibility of Molybdenum-Base Alloy TZM with the Molten-Salt LiF-BeF₂-Th₄-UF₄ (68-20-11.7-0.3 mole %)," presented at Spring Meeting of the Metallurgical Society of AIME, Atlanta, May 20, 1971.

8. C. E. Sessions and H. E. McCoy, Jr., *Metals and Ceramics Div. Annu. Progr. Rept. June 30, 1970*, ORNL-4570, pp. 140-42.

9. M. W. Rosenthal et al., "Recent Progress in Molten-Salt Reactor Development," *Atomic Energy Review* (in press).

Coolant salt.

1. Corrosion of Hastelloy N in the NaBF_4 -8 mole % NaF coolant salt depends largely on the amount of moisture that contacts the salt. The inadvertent leakage of air into a Hastelloy N thermal convection loop caused an abrupt increase in the corrosion rate of removable test specimens and an immediate change in salt composition. The rates returned to a relatively low value once the leaks were corrected. At the maximum temperature position (605°C), the corrosion rate over 20,000 hr, including the time of air inleakage, averaged^{10,11} 0.6 mil/year. By comparison, a Hastelloy N loop with high-purity fluoroborate salt (<500 ppm oxide) has experienced^{10,11} a weight loss equivalent to 0.19 mil/year over a 12,000-hr period at a maximum temperature of 687°C . Capsule tests of Hastelloy N have shown negligible corrosion in the pure fluoroborate salt.¹⁴
2. Steam was injected into a Hastelloy N thermal convection loop system containing sodium fluoroborate and resulted in 0.5 mil attack in the first 200 hr at 607°C . However, the overall corrosion rate has decreased to approximately 3.0 mils/year in 3000 hr. About 2 mils of deposited material was found on specimens in the cold leg, but the loop has continued to operate without a significant change in flow rate.^{10,11}
3. A Hastelloy N pumped loop containing NaBF_4 -8 mole % NaF completed 11,000 hr of operation at a maximum salt temperature of 587°C . At that point the hot leg of the loop was damaged by an inadvertent power surge. The average weight loss at 587°C for 9500 hr was 24.0 mg/cm^2 (equivalent to 0.9 mil/year uniform loss). The corrosion rate for this loop was higher than that in a thermal convection loop with salt of a similar impurity content at comparable temperatures. This suggests that the impurity-controlled corrosion reactions are controlled by rate of solution and are dependent on velocity.^{10,11} This loop is being repaired for further operation.
4. A second Hastelloy N pumped loop has been constructed and will soon begin operation. This loop is unique in that the corrosion specimens can be removed without dumping the salt or cutting open the loop. The salt velocity in this loop will nearly duplicate that planned for the MSBR.^{10,11}

5. Because of interest in the disposition of tritium in a MSBR, we determined the extent to which tritium (as a gas) would be retained in a fluoroborate salt mixture circulating in a thermal convection loop. Little, if any, tritium exchanged with hydrogenous material in the salt.¹¹

Status of fluoride salt corrosion. The above results support our previous findings that the temperature-gradient mass-transfer corrosion mechanism in fluoride salt with a low fluoride ion potential involves the formation of the most stable structural metal fluoride (usually chromium) in a hot section, followed by deposition as reduced metal in a cool region. The presence of impurities in the salt may cause oxidation of still other constituents of the container alloy.

The corrosion rates for Hastelloy N in fuel, blanket, and fertile-fissile salts have been extremely low and acceptable for indefinite operation. Higher corrosion rates have been encountered with the sodium fluoroborate salt mixtures and traced to the reaction of the fluoroborate with water to form highly corrosive HF. The high corrosion rates in all cases are accompanied by increases in the oxide concentration in the salt.

CORROSION OF HASTELLOY N IN STEAM

B. McNabb, Jr. H. E. McCoy, Jr.

Hastelloy N continues to show good resistance to general corrosion in steam at 538 and 593°C . The same trends reported previously¹⁵ are being followed at both temperatures. The weight change continues to be linear after the initial stages, and the air-melted heat, which had an initially higher rate at 593°C , is converging with the vacuum-melted heat at 13,200 hr and a weight increase of 3.2 mg/cm^2 . Both air-melted and vacuum-melted heats of standard Hastelloy N and several heats of modified Hastelloy N at 538°C are continuing to follow the same low rates and are now at 6000 hr and a weight increase of 0.3 mg/cm^2 .

The facility at Bull Run Steam Plant has been modified to include stressed specimens. The modifications have been completed and the facility is back in service with four tube burst specimens being stressed at 77,000, 56,000, 42,000, and 28,000 psi, using the 3500 psi steam pressure available at the facility and machining specimens with the necessary wall thicknesses to give the desired stress. The specimens are double-walled

14. J. W. Koger and A. P. Litman, *Compatibility of Fused Sodium Fluoroborates and BF_3 Gas with Hastelloy N Alloys*, ORNL-TM-2978 (June 1970).

15. B. McNabb and H. E. McCoy, Jr., *Metals and Ceramics Div. Annu. Progr. Rept. June 30, 1970*, ORNL-4570, pp. 178-79.

tubes with an annulus into which the thin wall inner tube will burst. A capillary tube runs from the annulus into the condenser and will be used to detect rupture. By having this ability to maintain stress on the specimens we can determine if there is a stress corrosion problem in the steam environment.

CONSTRUCTION OF A MOLYBDENUM REDUCTIVE-EXTRACTION TEST STAND

J. R. DiStefano

We are fabricating a loop¹⁶ for the Chemical Technology Division to obtain engineering data on a reductive-extraction method of Molten-Salt Breeder Reactor fuel processing. Both bismuth and salt will countercurrently circulate through a 1 $\frac{1}{8}$ -in.-OD \times 5-ft-long Rachig-ring-packed column. Flow rate of each fluid is controlled by flow metering orifices in 3 $\frac{7}{8}$ -in.-OD \times 8-in.-long head pots. Bismuth and salt will be separated in 3 $\frac{7}{8}$ -in.-OD \times 16-in. and 21-in.-long containers located immediately above and below the column, respectively. The loop will be interconnected by four different sizes of tubing.

We have developed a back-extrusion technique for fabricating the closed-end containers with integral bosses for joining. Electron beam, tungsten-arc, and orbiting-arc welding techniques have been developed for joining the containers to each other and to the connecting lines. We also developed a mechanical (roll bonding) technique to join tubing to the bosses of the head pots and disengaging containers. An iron-base braze alloy that is compatible with bismuth was developed and will be used to reinforce the welded and mechanical joints. The following sections describe the fabrication and joining studies relating to the construction of this test stand.

FABRICATION DEVELOPMENT OF MOLYBDENUM COMPONENTS

R. E. McDonald A. C. Schaffhauser

We are continuing fabrication development on molybdenum components for a chemical processing test loop. This task includes consulting on the design of loop components, coordination of machining and procurement of components from a subcontractor,¹⁷ and fabrication of critical components.

Our major effort is on the development of a back-extrusion process for fabrication of the feed pots and disengaging sections of the extraction column.¹⁸ These components are about 4 in. in diameter \times 8 to 21 in. long, with end bosses for support of welded or

roll-bonded inlet and exit tubes. We have fabricated 14 prototype back extrusions having different boss geometries for welding and brazing development. We investigated extrusion temperatures between 1300 and 1600°C and loads from 700 to 1000 tons. The back-extrusion tooling was recently modified so all surfaces in contact with the hot molybdenum part during extrusion are coated with plasma-sprayed ZrO₂. This coating eliminates chemical interaction of the molybdenum and tool steel at the higher temperatures and reduces friction. Thus, we obtain longer back-extruded parts with excellent surface finishes.

MOLYBDENUM WELDING DEVELOPMENT

A. J. Moorhead

To fabricate the molybdenum test stand, various sizes of tubing must be joined to back-extruded dished heads, to themselves, and to various fittings, and two dished heads must be joined with a girth weld to form each of the four pots. Welding procedures have been developed for three basic types of joint: tube-to-tube, tube-to-header, and header-to-header.

Procedures were developed for making tube-to-tube welds in four sizes of the tubing. Short lengths were joined in a glove box by the manual GTA process, using low-carbon molybdenum filler wire drawn from arc-cast stock. The smaller sizes of tubing had a square butt weld joint, but the 1 $\frac{1}{8}$ -in.-diam tube had a 90° V-groove joint with a 0.015 in. root face. None of these welds showed defects with fluorescent penetrant. In addition, the smaller tubes were radiographed, and the welds were sound, with full penetration and little or no porosity. Seven of the eight welds had helium leak rates less than 1×10^{-9} atm cm³ sec⁻¹.

Procedures have also been developed for making tube-to-tube welds outside the glove box using a commercial semiautomatic orbiting-arc weld head, modified with small rubber boots to contain a localized high-purity inert environment. Helium leaktight and defect-free joints were welded in three sizes of molybdenum tubing by use of a semiconsumable insert. The weld bead is slightly convex and not as highly stressed as the concave bead produced with no insert. The

16. W. F. Schaffer, E. L. Nicholson, and J. Roth, *MSR Program Semiannu. Progr. Rept. Aug. 31, 1970*, ORNL-4622, pp. 212-13.

17. Thermo-Electron Corporation, Metals Division, Woburn, Mass.

18. R. E. McDonald and A. C. Schaffhauser, *Metals and Ceramics Div. Annu. Progr. Rept. June 30, 1970*, ORNL-4570, pp. 188-89.

complex welding procedure included a chemical cleaning technique, a preweld stress-relief heat treatment, and a programmed weld cycle with preheat and postheat.

The tube-to-header joints are all electron-beam welded, using a trepan inside the dished head. This groove permits an edge-weld joint geometry in which both parts have the same thickness. We have been very successful in welding all five tubing sizes; almost all have been helium leaktight, and penetration is at least one tube-wall thickness. We have successfully welded tubes into mockup parts.

We are developing header-to-header girth welding procedures using both the gas tungsten-arc and electron-beam processes. Two back-extruded heads were joined to form a full-size feed pot by the manual tungsten-arc process in an argon-filled glove box. Two weld passes were required to fill the 90° V-groove in the 1/8-in.-thick pot wall. No preheating other than with the welding arc was required. The weld was defect-free when inspected with fluorescent penetrant.

A procedure for electron-beam welding the girth joint is being developed, using a step joint in which complete weld penetration is not required. This eliminates the rough root area, which is typical of full-penetration, electron-beam welds. We had to preheat the dished heads with the defocused beam to minimize welding stresses and avoid cracking. We successfully welded a ring machined from bar stock to a back-extruded header, but a weld joining two complete headers had two areas containing cracks. We are rewelding to repair these cracked areas.

DEVELOPMENT OF BISMUTH-RESISTANT FILLER METALS FOR JOINING MOLYBDENUM

N. C. Cole J. W. Koger

In building complex structures of molybdenum, brazing can be useful as either the primary joining technique or as a backup to welding (as in back brazing). However, no commercial brazing alloys were known to have a satisfactory melting temperature and

be corrosion resistant to both molten bismuth and fluoride salts. Therefore, we are developing brazing filler metals for this MSBR application.

Since recrystallization and grain growth adversely affect the ductility of molybdenum, we want to braze at or below the recrystallization temperature of the base metal. Heat treatments of molybdenum sheet at 1180°C for 40 min and 1300°C for 3 min did not impair its ability to achieve a 90° bend. However, 10 min at 1200°C caused cracking after a 50° bend. Iron-base brazing alloys appeared promising because of their melting temperature and relatively low solubility in bismuth. Therefore, we formulated several iron-base molybdenum alloys containing other elements to depress the melting temperature. These alloys have shown excellent wettability and flowability on molybdenum at and below 1150°C.

To test the mechanical properties of brazed molybdenum joints, we shear tested two of the most promising iron-base alloys, 42M and 35M. Average results of samples pulled at room temperature and 650°C at a strain rate of 0.016/min are shown in Table 34.1. Room-temperature shear strengths were excellent for both brazes, and at 650°C the shear strength was very good for 42M and acceptable for 35M. Elongation for both brazes was acceptable at room temperature and excellent at 650°C.

For the molybdenum loop, we have determined suitable conditions for back-brazing welded tube-to-tube-sheet joints in a vacuum furnace and for field brazing split sleeves to welded tubing. An induction heater was used with an envelope of inert gas surrounding the braze area to protect molybdenum from the air.

Several molybdenum joints brazed with the experimental iron-base filler metals were tested in static bismuth, and filler metals 42M and 35M appeared to be the most corrosion resistant.^{19,20} Joints survived ex-

19. N. C. Cole, J. W. Koger, and R. W. Gunkel, *MSR Program Semiannu. Progr. Rept. Feb. 28, 1970*, ORNL-4548, pp. 255-56.

20. N. C. Cole and J. W. Koger, *MSR Program Semiannu. Progr. Rept. Aug. 31, 1970*, ORNL-4622, pp. 189-91.

Table 34.1. Mechanical properties of brazed molybdenum joints

Alloy	Composition (wt %)	Shear strength (psi)		Elongation (%)	
		Room temperature	650°C	Room temperature	650°C
42M	Fe-15 Mo-5 Ge-4 C-1 B	30,000	29,000	10	50
35M	Fe-15 Mo-4 C-1 B	31,000	18,000	11	42

tremely well at 700°C in a quartz thermal convection loop, operated as described below.

Molybdenum joints brazed with alloys 35M, 42M, and 16M (Fe-4% C-1% B) were exposed to a fuel salt for 1032 hr at about 670°C. Each gained about 1 mg/cm², but we saw no attack, visually or metallographically.

CORROSION OF STRUCTURAL MATERIALS IN BISMUTH

O. B. Cavin L. R. Trotter

The continuous processing of fuel salt in an MSBR to remove fission products necessitates the use of bismuth and in some stages up to 50 at. % Li in bismuth. Therefore, we have continued to study the compatibility of potential structural materials and braze alloys with bismuth and bismuth-lithium alloys in thermal convection loops and static capsules operated at 600 to 700°C.

Specimens of molybdenum and TZM (Mo-0.5% Ti-1.0% Zr) alloy were tested in quartz thermal convection loops containing bismuth or Bi-100 ppm Li and operated at a maximum temperature of 700°C with a temperature difference of $95 \pm 5^\circ\text{C}$. Neither material showed significant corrosion after exposures up to 3000 hr. Iron-base alloys developed for brazing molybdenum appeared to resist bismuth dissolution in static capsule tests.²¹ Molybdenum samples brazed with these alloys were then tested in quartz thermal convection loops. There was no visual deterioration of the brazes after 2100 hr, but microprobe analysis of the braze cross sections indicated that bismuth penetrated the entire fillet.²² Likewise, an Fe-5% Mo alloy that was not attacked by bismuth in a capsule test²³ at 600°C for 600 hr was severely attacked within 216 hr in a quartz loop test. Tantalum and T-111 alloy (Ta-8% W-2% Hf) showed negligible weight change or surface attack when tested in a loop; however, the ductility of the T-111 was drastically reduced.²⁴ Bismuth did not attack graphite when tested in a loop for 3000 hr, but the liquid metal did penetrate the open porosity. Chemical analyses of the graphite samples indicated an

uptake of 2 to 500 ppm Bi; the larger amount was found in graphite with greater pore entrance diameter. No increase in carbon concentration in the bismuth could be detected.

Thermal convection loops have been constructed of T-111 and molybdenum and will be tested with Bi-2.5 wt % (43.6 at. %) Li. Each loop contains, in each of the high- and low-temperature regions, metal tensile samples having the same composition as the container material. The molybdenum loop will be used later to test graphite, both as machined and with a pyrolytically sealed surface.

CVD COATINGS FOR CORROSION RESISTANCE

J. I. Federer L. E. Potat

A possible way to prevent corrosion by bismuth in MSBR reprocessing equipment constructed of iron- and nickel-base alloys is a corrosion-resistant coating, such as tungsten or molybdenum. Both can be coated on various substrates by chemical vapor deposition using hydrogen reduction of WF₆ and MoF₆. The coatings adhere to nickel and nickel-base alloys, such as Inconel and Hastelloys, and to steel and stainless steels if the latter are first plated with nickel. Tungsten deposition is well characterized, having been studied extensively in recent years. During the past year application of tungsten coatings to substrates of various sizes and shapes has been emphasized, and deposition conditions for molybdenum were optimized.

We found that the optimum gas mixture has a H₂/MoF₆ ratio of 3 to 6. Below 3 the MoF₆ reacts with the substrate, whereas above 6 the coatings are rough and nonuniform in thickness. Deposition rate or efficiency decreases rapidly below 800°C, and the coating usually contains some MoF₃. The effect of pressure was not studied, but as in the case of tungsten and other metals, low pressures (5 to 10 torr) are required for uniformly coating extended surfaces, and higher pressures are useful for causing deeper penetration into crevices.

A variety of objects have been coated with tungsten or molybdenum to demonstrate the applicability of the process and as a service to other studies. Stainless steel vessels measuring 1³/₈ in. ID. were coated inside with tungsten and molybdenum for corrosion testing in static bismuth at 600°C. Neither coating was attacked, but after 667 hr, some attack of the substrate occurred through several cracks in the tungsten coating. A Monel vessel measuring 4³/₈ in. ID × 36 in. long was coated inside with tungsten. No spalling or cracking of the coating was observed when a section of the vessel was

21. N. C. Cole, J. W. Koger, and R. W. Gunkel, *Metals and Ceramics Div. Annu. Progr. Rept. June 30, 1970*, ORNL-4570, pp. 189-90.

22. O. B. Cavin and L. R. Trotter, *MSR Program Semiannu. Progr. Rept. Feb. 28, 1971*, ORNL-4676, pp. 225-31.

23. O. B. Cavin, J. W. Koger, and L. R. Trotter, *Metals and Ceramics Div. Annu. Progr. Rept. June 30, 1970*, ORNL-4570, p. 187.

24. O. B. Cavin and L. R. Trotter, *MSR Program Semiannu. Progr. Rept. Aug. 31, 1970*, ORNL-4622, pp. 189-95.

thermally cycled 25 times between 25 and 600°C. A nickel-plated carbon steel vessel measuring 3 in. ID X 21 in. long was coated inside with tungsten over a length of about 10 in. The coating was required to protect the vessel from attack by liquid bismuth during metal transport experiments.

Stainless steel tubing was coated inside with tungsten for lengths of 4 to 5 ft by a moving hot zone technique, which could be used to coat much longer lengths. A 5/8-in.-OD nickel-plated stainless steel tube was coated outside with tungsten to serve as a liquid bismuth level probe indicator.

Mechanical joints made by roll bonding 1/2-in.-OD molybdenum tubing to heavier molybdenum sections were made helium leaktight by coating with tungsten and molybdenum. A Hastelloy N corrosion loop fabricated of 0.65-in.-OD tubing and measuring about 33 X 18 in. was coated inside with tungsten. We found small cracks in the coating at sharp corners where sections of tubing were welded together. This problem could probably be eliminated by modification of the joint design.

The coating studies performed over the past two years may be summarized as follows. Tungsten and molybdenum coatings can be applied to nickel, nickel-base alloys, and nickel-plated stainless steel by hydrogen reduction of WF_6 and MoF_6 . The nickel plate on stainless steels is necessary to prevent nonadherence due to reactions between iron and chromium in the steels with WF_6 and MoF_6 . The coatings resisted thermal cycling between 25 and 600°C and bending to a radius less than 1 in., and had bond strengths up to 35,000 psi.

Bismuth-resistant coatings have been applied to cylindrical shapes with a wide range of sizes. The principal difficulty in the use of tungsten and molybdenum coatings is the tendency to crack under stress at low temperatures, particularly at points of stress concentration, such as sharp corners.

COATINGS FOR CORROSION RESISTANCE BY DEPOSITION FROM MOLTEN SALTS

J. W. Koger

We are conducting experiments to plate molybdenum on a metal surface by reducing MoF_6 dissolved in a molten fluoride salt. A controlled corrosion reaction at the salt-metal interface oxidizes chromium, iron, and nickel from the alloy.^{25,26} We have obtained an

25. J. W. Koger, *MSR Program Semiannu. Progr. Rept. Aug. 31, 1970*, ORNL-4622, pp. 197-98.

26. J. W. Koger, *MSR Program Semiannu. Progr. Rept. Feb. 29, 1971*, ORNL-4676, pp. 232-33.

adherent coating in which molybdenum was deposited at the sample surface and penetrated grain boundaries to at least 350 μm . We are now determining the effect of concentration of MoF_6 on the process.

REDUCTION OF GRAPHITE PERMEABILITY BY PYROLYTIC CARBON SEALING

C. B. Pollock W. P. Eatherly

Graphite in the core of a MSBR must exclude fluoride salts and gaseous fission products. We have been studying techniques to seal the surface of the graphite with pyrolytic carbon. Two techniques have been used: a vacuum-pulse impregnation technique in which surface pores of the graphite are plugged with pyrolytic carbon and a procedure in which a continuous surface coating of impermeable pyrolytic carbon is deposited on the graphite. Both techniques have been successful in sealing commercially available graphite suitable for use in the core of a MSBR.

In conjunction with the fabrication program, graphite samples sealed with pyrolytic carbon are subjected to MSBR conditions of neutron fluence and temperature. A HFIR irradiation experiment containing 10 coated and 12 impregnated samples was recently completed.

Four of the coated samples have been cycled twice through HFIR and now have a total dose of 2.4×10^{22} neutrons/cm² (>50 MeV) at 700°C. Three samples appeared to be intact except for some small cracks on their ends, but independent of this the helium permeabilities went from less than 10^{-8} cm²/sec to greater than 10^{-2} cm²/sec. The remaining sample was extensively cracked. A second set of coated samples has been irradiated once to doses up to 1.3×10^{22} neutrons/cm² (>50 MeV) at 700°C. Five cracked badly and had helium permeabilities greater than 10^{-2} cm²/sec. However, one sample appeared to be unaffected.

The only significant difference between these two sets of coated samples is the coating thickness. The first group had coating thicknesses from 4 to 6 mils; the second set from 2 to 3 mils. The surviving coating of the second set was 3 mils thick. We infer that coating thickness and microstructure are the significant variables, but further work will be required to determine if satisfactory coatings can be devised.

The results on the 12 pyrolytically impregnated samples are given in Table 34.2. Six have been recycled in HFIR to fluences of up to 3.7×10^{22} ; six have received only their first irradiation up to 1.2×10^{22} . The new samples appear to be significantly better than previous samples irradiated to similar fluences. The pore size distribution of these samples will be examined by

Table 34.2. Irradiation results on impregnated graphite

Sample	Permeability (cm ² /sec He stp)		Fluence (neutrons/cm ²)	$\Delta L/L^a$ (%)
	Before	After		
			$\times 10^{22}$	
I231	2.3×10^{-9}	5.1×10^{-9}	1.2	
I208	1.3×10^{-9}	2.2×10^{-6}	0.9	
I236	2.2×10^{-9}	1.0×10^{-6}	0.8	
I211	1.5×10^{-9}	6.2×10^{-7}	1.2	
HR20	1×10^{-9}	2.3×10^{-8}	0.6	
HR12	1×10^{-8}	6.5×10^{-6}	1.1	
I205	4.4×10^{-10}	7.2×10^{-5}	1.7	0.7
I216	5.9×10^{-10}	9.8×10^{-5}	2.1	2.2
HL32	1.6×10^{-8}	9.1×10^{-5}	2.1	0.8
I182	1.7×10^{-8}	1.5×10^{-2}	3.1	6.0
I181	5.1×10^{-9}	9.0×10^{-2}	3.7	11.0
I163	7.0×10^{-9}	2.9×10^{-4}	2.6	2.0

^aLinear expansion.

mercury porosimetry. The amount of pyrolytic carbon required for sealing can be controlled by varying process parameters. Helium permeabilities less than 10^{-8} cm²/sec have been obtained in graphite samples whose weight increase was less than 4% with a processing time of only 2 hr at 750°C. Graphite samples sealed in this manner should behave more like unimpregnated base-stock graphite. A number of samples containing the minimum carbon needed for sealing has been prepared for the next experiment in an attempt to control the neutron-induced expansion of the graphite.

As noted in Table 34.2, one of the samples has increased its length by 11%, or substantially more than would be expected from the unimpregnated base-stock graphite at similar fluences.

THE IRRADIATION BEHAVIOR OF GRAPHITE AT 715°C

C. R. Kennedy W. P. Eatherly

We have extensively studied the neutron irradiation behavior of graphite at 715°C, primarily to determine the incremental or decremental changes in life expectancy resulting from a wide variety of starting materials and fabrication methods. Over 40 experimental and commercial grades of graphite were irradiated in the HFIR to fluence levels up to 4×10^{22} neutrons/cm² (>50 keV), invariably producing significant volume expansions. The changes in linear dimensions and bulk density were the prime measures in evaluating the materials.

The irradiation behavior of the graphites demonstrated that all of the various grades could be separated into four basic types of materials:

1. Conventional graphites. These graphites all consist of materials made from calcined coke or graphite flour as filler, bonded with either thermoplastic or thermosetting hydrocarbons. The general irradiation behavior is characterized by an immediate densification followed by a parabolic expansion, as shown in Fig. 34.2. The isotropic materials have a lower tendency for densification than the anisotropic graphites made with acicular cokes, and both demonstrate that the maximum densification varies inversely with the original density. A considerable degree of anisotropy in the densification process appears to depend on both the method of fabrication and the crystalline structure of the filler particles, which usually is reflected in their morphology. The more isotropic graphites always densified more in the extrusion direction for extruded grades and normal to the forming force for the molded grades.

The linear dimensional changes depended upon the anisotropy of the graphite, the crystallite size, and the density changes. The growth rates at fluences where the density change was constant agreed with the Reuss

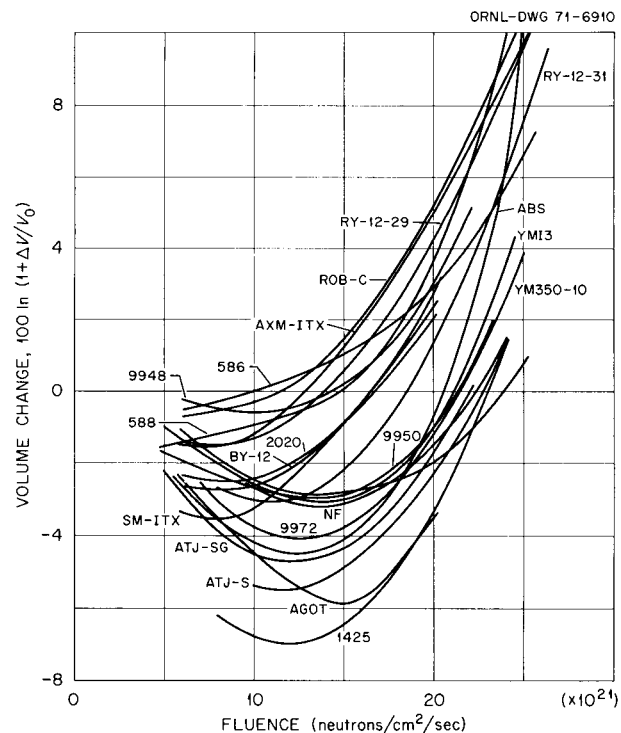


Fig. 34.2. Volume changes of conventional graphites irradiated at 715°C.

one-dimensional constant stress model.²⁷ The effect of crystallite size on the growth rate was in excellent agreement with that found by Bokros.²⁸

Conventional graphites all have virtually the same lifetime expectancy with no apparent effect of molding, extrusion, type of filler, Thermax additions, type of binder, or the type of impregnant. The choice of graphites within this category would depend upon the necessity of isotropy and other properties, such as thermal conductivity, mechanical properties, and coefficient of thermal expansion.

2. Apparently binderless graphites. The raw materials and the fabrication procedures for most of these graphites are proprietary. They are characterized by an apparently binderless single-phase microstructure with a fairly fine optical domain size. These graphites are all very isotropic, have a high coefficient of thermal expansion, and generally have a lower crystallite size than the conventional materials.

Their irradiation behavior, shown in Fig. 34.3, is characterized by a delay or an elimination of the densification process, yielding a more dimensionally stable graphite with about twice the lifetime of the conventional graphites. The linear dimensional changes are isotropic, reflecting only the bulk density changes. Thus, the individual crystallite growth rates cannot be calculated directly from extrapolated orientation dependence.

3. Hot-worked and meso-phase graphites. These graphites by virtue of hot working are highly anisotropic. Although the original densities may not be very high, the void structure for densification has apparently been eliminated by the hot working. None of these materials densified under irradiation, as shown in Fig. 34.4. The volume remained constant for a short period and then began to expand parabolically with fluence. The life expectancy of these grades is similar to that of the conventional grades; however, the linear dimensional changes are quite large due to the anisotropy and would not be acceptable for most designs. The linear dimensional behavior, excluding density changes, can be represented by the Reuss model.

4. Carbon black grades. These are grades in which all the filler is a carbon black. They are characterized by a structure of randomly oriented, ultrafine optical domains with no anisotropy and a fairly small crystallite size. The coefficient of thermal expansion is generally large, the thermal conductivity is low, and the mechani-

cal properties are fairly good for the generally low bulk density. The densification due to irradiation is quite rapid, as shown in Fig. 34.5, possibly reflecting high crystalline growth rates. The expansion after densifica-

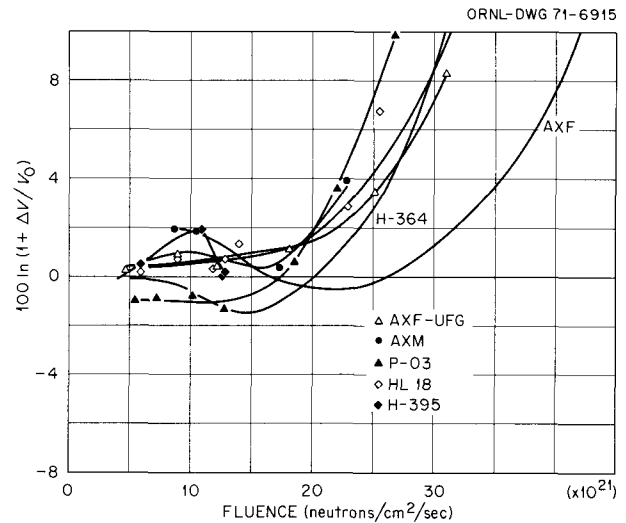


Fig. 34.3. Volume changes of apparently binderless graphites.

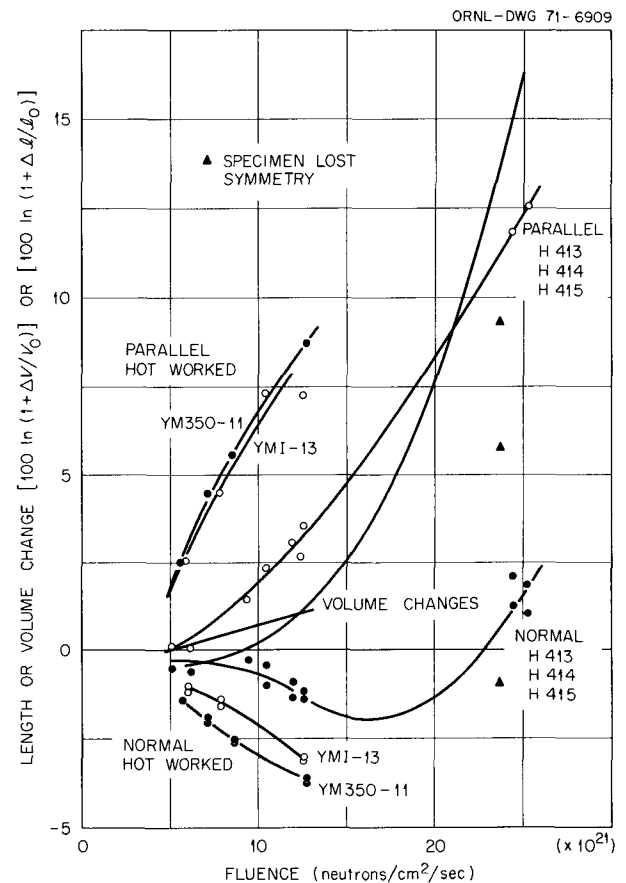


Fig. 34.4. Dimensional behavior of hot worked and meso-phase graphites irradiated at 715°C.

27. A. Reuss, *Z. Angew. Math. Mech.* 9, 49 (1929).

28. J. C. Bokros, G. L. Guthrie, and A. S. Schwartz, *Carbon* 6, 55 (1968).

tion, unlike for all other materials, is linear with fluence and seems to be independent of grade and heat treatment. The initial increase in density, however, depends upon final heat treatment temperature, as shown in Fig. 34.6, and there is some evidence that the densification is binder dependent as well. These materials are all isotropic, and the linear dimensional changes are again a result only of bulk density changes. The lifetime expectancy of these materials is equal to or greater than that of the apparently binderless grades.

Therefore, improved graphites for MSBR application will probably be developed from either the apparently binderless grades or the carbon black grades. Both types are commercially available in size of interest to MSBR. The thermal properties of the apparently binderless grades are more favorable.

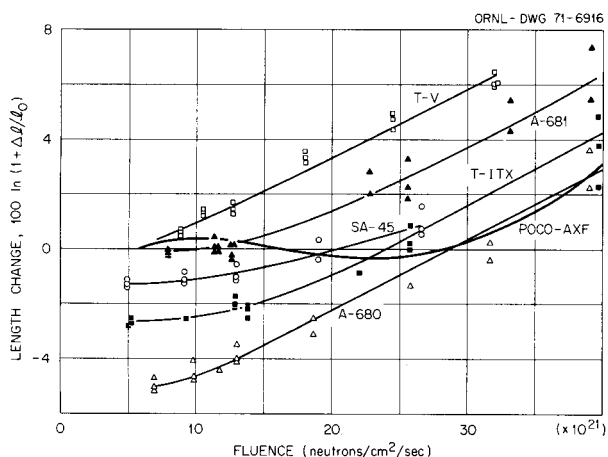


Fig. 34.5. The effect of irradiation on various carbon black graphites irradiated at 715°C.

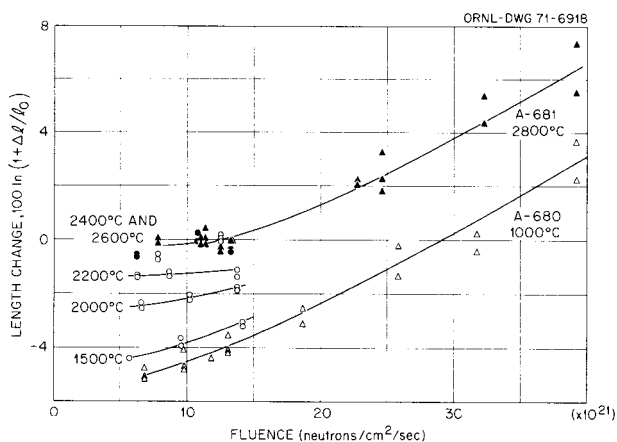


Fig. 34.6. The effect of final heat treatment on the dimensional stability of a carbon black grade irradiated at 715°C.

Both types of raw material systems are currently being investigated in our own fabrication program, and samples are being prepared for irradiation in HFIR.

PROCUREMENT AND GENERAL PHYSICAL PROPERTY MEASUREMENTS ON NEW GRADES OF GRAPHITE

W. H. Cook

Our procurement and evaluation of grades of graphite has changed to include well characterized raw materials for fabrication as well as experimental bodies that are fabricated by us and external vendors. Our routine evaluations of typical nuclear graphites produced during the past decade has been essentially completed. Almost all of these samples were obtained from external graphite producers. Our irradiation program is now directed toward obtaining a better understanding of fast neutron damage to graphite from 500 to 1100°C. Therefore, it is concentrated on the investigation of experimental grades of graphite that have the desired structural variations. In support of this, our fabrication effort has expanded and is reported separately. Commercial vendors are cooperating with us on the raw materials and in supplying samples of their experimental grades.

Our raw materials stocks include the isotropic commercially available filler materials,²⁹ Robinson (Air-Blown) raw coke and graphitized flour, Santa Maria coke, JOZ, PXE-5Q1S, and PXA-5Q1S.

We have acquired 20 different experimental grades of graphite from commercial vendors. In keeping with the goals of our irradiation program, these have been isotropic or nearly so and are generally fine-grained materials. These involve a variety of base materials from pitch coke, gilsonite coke, mesophase graphite, and proprietary and carbon blacks. The carbon-black-based materials represent a special and somewhat different approach.

Bulk densities for all grades are between 1.45 and 1.95 g/cm³. Since all are experimental and for neutron damage studies, none has been optimized for and none meets the requirements for an MSBR grade of graphite. Some of the evaluation data have been reported,³⁰ and other data are being determined.

29. W. H. Cook, *MSR Program Semiannu. Progr. Rept. Aug. 31, 1970*, ORNL-4622, pp. 134-35.

30. W. H. Cook, *ibid.*, pp. 135-36.

REDUCTION OF GAS PERMEABILITY OF GRAPHITE BY FLUORIDE SALT IMPREGNATION

W. H. Cook

It has been proposed that impregnating the accessible pores of graphite with unfueled fluoride salt may be a practical way of reducing its gas permeability. In preliminary tests with analog impregnation with bismuth and a direct test with unfueled salt, helium permeabilities of four different graphites were reduced to about 10^{-6} cm²/sec. Both types of impregnations were designed to fill all accessible pores with entrance diameters exceeding 0.25 μ m. The bismuth was more effective, as expected. Since gas permeability was measured at room temperature, the analog impregnation with bismuth, which expands on freezing, should have approximated the best sealing for a molten fluoride salt. The graphite that had a minimum of closed porosity and a narrow range of pore entrance diameters to its accessible porosity sealed more effectively than the other graphites. Additional tests are required to determine the practical limits toward the desired goal of below 10^{-8} cm²/sec and the effectiveness of salt impregnations for reducing fission gas penetration into the graphite. This work has been temporarily suspended pending results on the sealing of bulk graphite by pyrolytic carbon coating or impregnation.

GRAPHITIZATION OF A LAMPBLACK-PITCH CARBON

O. B. Cavin W. H. Cook J. L. Griffith

Samples from a near-isotropic lampblack-pitch stock were fired at 1500, 2000, 2200, 2400, 2600 and 2800°C in purified argon. These were characterized by bulk densities, electrical resistivities, and x-ray diffraction in a correlative investigation³¹ with their stability under fast neutron irradiation at 715°C.

This is part of a comprehensive investigation that was initiated when it was demonstrated that propylene-derived pyrocarbons with very small crystallites were quite stable in a neutron irradiation environment.³² Before this, polycrystalline lampblack materials had not been considered as potential materials for the MSBR graphites because of the extremely large neutron-induced crystalline growth rates reported by Bokros.³³

For this heat-treatment series the apparent crystallite sizes and the lattice parameters, a_0 and c_0 , were determined by x-ray diffraction. The a_0 values re-

mained relatively constant at 2.45 Å. The c_0 decreased from 6.98 to 6.796 Å, with little indication of saturation. The apparent average crystallite size increased from 10 to 240 Å. The bulk densities increased from 1.49 to 1.69 g/cm³ and appeared to be saturating, but the electrical resistivity decreased from 5150 to 3040 $\mu\Omega$ -cm without appreciable saturation.

The crystalline growth and bulk density changes were retarded until 1500°C was reached, after which the rates increased up to 2000°C. Above 2000°C the crystalline growth rate remained constant, but the bulk density changes tended to saturate. The electrical resistivities and c_0 showed step-wise decreases, between 2000 to 2400°C and 2300 to 2600°C, respectively.

The importance of these data in guiding the development of more irradiation-resistant grades of graphite will be presented with the irradiation data elsewhere in this chapter.

THERMAL CONDUCTIVITY OF GRAPHITE

J. P. Moore T. G. Kollie

Thermal conductivity, λ , and electrical resistivity, ρ , measurements from 300 to 980°K were completed on unirradiated AXF-5Q and H337 graphites in a guarded-longitudinal heat flow device.³⁴ Subsequently these six samples were irradiated in HFIR to various fluences from 800 to 1000°K. A series of further irradiations and subsequent remeasurements will allow the effects of irradiation on λ , ρ , and the coefficient of thermal expansion, α , to be determined.

The ρ values for the six unirradiated graphites, which are listed in Table 34.3, decrease with increasing temperature. For poor electrical conductors such as graphite, the phonon component dominates λ , and one expects $\lambda^{-1} = A + BT$. Above 500°K λ^{-1} of these graphites linearly increased with temperature with the coefficients listed in Table 34.4.

The components were obtained for a vitreous-silica push-rod dilatometer (see Chap. 8) for α measurements on these graphites from 80 to 1200°K.

31. O. B. Cavin, W. H. Cook, and J. L. Griffith, *MSR Program Semiannu. Progr. Rept. Feb. 28, 1971*, ORNL-4676, pp. 171-73.

32. D. M. Hewette II and C. R. Kennedy, *MSR Program Semiannu. Progr. Rept. Feb. 28, 1970*, ORNL-4548, pp. 215-18.

33. J. C. Bokros and R. J. Price, *Carbon* 5, 301 (1967).

34. J. P. Moore and D. L. McElroy, *Metals and Ceramics Div. Annu. Progr. Rept. June 30, 1970*, ORNL-4570, pp. 185-86. See also Chap. 8 of this report.

Table 34.3. Electrical resistivity of AXF-5Q and H337 graphites^a

Temperature (°K)	Resistivity ($\mu\Omega$ -cm) for various samples				
	H337	H337	AXF-5Q	AXF-5Q	H337
	22	13	72	43	32
300	775	784	1114	1124	761
400	699	702	973	990	683
500	648	655	879	891	640
600	626	633	816	824	614
700	613	619	777	782	599
800	606	610	753	758	593
900		604	740	744	593.5
1000			730	731	598.0

^aFor AXF-5Q (sample 62) at 295°K, $\rho = 1138.4 \mu\Omega$ -cm.

Table 34.4. Coefficients of thermal resistance of graphites

Specimen	Coefficient of $\lambda^{-1} = A + BT$	
	A	B
	[W cm ⁻¹ (°K) ⁻¹]	[W cm ⁻¹ (°K) ⁻²]
AXF-5Q - 43	0.459	890
AXF-5Q - 62 ^a	0.465	896
AXF-5Q - 72	0.435	903
H337 - 22, 13	0.311	883
H337 - 32	0.309	847

^aEstimated from ρ at 295°K.

35. Thorium Utilization

A. L. Lotts

The objective of the Thorium Utilization Program currently in progress in the Chemical Technology and Metals and Ceramics Divisions is to provide the necessary development for the Th-²³³U fuel cycle for the High-Temperature Gas-Cooled Reactor. The ultimate aim of the program is to demonstrate economic fuel recycle techniques for this reactor in a pilot-scale facility, the Thorium-Uranium Recycle Facility at ORNL. The program in the Metals and Ceramics Division consists of refabrication process development on an engineering scale, development of remote pilot-scale equipment that can be used in the TURF, and irradiation of fuels produced in engineering-scale equipment. The program utilizes extensively technology developed in the Gas-Cooled Reactor Program, the progress for which is reported in Chap. 31.

Equipment and processes are being developed to enable us to fabricate 25 kg/day of oxide fuel into the prismatic graphite fuel blocks used in the HTGR. The work involves development of engineering-scale processes for refabrication of HTGR fuel, irradiation testing of fuel, and, at present, maintenance of TURF for future use for the recycle processes. We have been instrumental in writing the National HTGR Fuel Recycle Program Plan,¹ which is a comprehensive plan for demonstration of HTGR fuel recycle. The demonstration with ²³³U is to start in TURF in 1976.

THORIUM-URANIUM RECYCLE FACILITY

J. M. Chandler²

The Thorium-Uranium Recycle Facility was constructed to enable processing of thorium fuels containing, as an impurity, high quantities of ²³²U, a material necessitating heavy shielding. The facility is of sufficient size that a number of processes can be developed and evaluated simultaneously at pilot-scale level.

1. *National HTGR Fuel Recycle Program Plan*, ORNL-4702 (in press).

2. On loan from Chemical Technology Division.

Work was conducted to maintain the TURF equipment in operational readiness in support of the heavily shielded process cell bank designed for the remote maintenance and operation of the in-cell process equipment. To do this we replaced some faulty electrical motors, replaced damaged off-gas filters, replaced a leaking waste line, relocated some off-gas fan bearings, and repaired some defects in the in-cell crane and manipulator system.

The final acceptance for select risk coverage was received from Factory Mutual Fire Insurance Company for the TURF in-cell CO₂ fire protection system. Work began in 1967 on the checkout, modification, and retest of this system. The system is ready for use if the occasion arises.

The hot waste line (ILW), through which TURF and TRU waste solutions are discharged to the Melton Valley waste tankage, developed several leaks at the rubber-gasketed joints and was replaced by a 2-in. sched 40 type 304 stainless steel line.

The large volume required to store, dispose of, and bury contaminated plastic bottles from radiochemical work has prompted us to test volume reduction by melting down the plastic; heating at 400°F softened the polyethylene bottles to the desired fluidity. In this type of volume reduction, glass, residues, and the like that are contained in the melt remain contained upon solidification. An inert atmosphere was not necessary to prevent ignition of the plastic, but we recommend it for in-cell safety. A 30-gal container filled with plastic bottles yielded 1.4 gal solid plastic for a 21.4-fold reduction.

The fuel storage basin was filled with water for the first time, and no leaks were found. It was drained to preserve the coatings and also to allow us to replace some carbon steel bolts with stainless steel.

Work continued on the checkout and maintenance of the in-cell crane and manipulator systems in Cells A, B, C, and D. All five lift rail clutches were modified to eliminate an interference between the pressure plate and a bearing.

We studied the "Materials Handling Requirements at TURF," for conducting the work prescribed in the National HTGR Fuel Recycle Program Plan. This program will produce 150 recycle fuel elements from ^{233}U and Th at a rate of 1.76/day. Inadequate facilities and equipment exist for spent fuel receiving, storage, and burner charging at the feed end of the process and for storage and shipping of the product recycle element. The Fort St. Vrain shipping cask, as designed, will not be accommodated in the TURF receiving area. The shipping arrangement (cask plus container plus truck) is 13 ft tall, and the receiving area can accommodate arrangements up to $11\frac{1}{2}$ ft tall.

After considering various facilities we concluded that no suitable place was available at a cost advantage over providing the desired facilities at TURF. A suitable facility should provide spent fuel receiving, storage, and handling area for 1000 elements plus shipping cask and fuel shipping container decontamination area; provide equipment to transfer elements from storage to the head-end cell; provide space and equipment for collecting and repackaging loose particles and fragments from damaged elements; and provide for receipt, storage, packaging, and shipment of product recycle elements. The preliminary estimate for this new facility is approximately \$2.5 million plus an additional \$800,000 for engineering services if we use actual TURF construction cost as basis.

To meet the July 1976 start of hot operations in TURF, the new facility must be operational for spent fuel storage in October 1973. The existing TURF receiving area will be used 95% of the time for handling reagents, for fuel element components other than ^{233}U , and for intraplant deliveries of ^{233}U between the Acid Thorex Pilot Plant and TURF.

REFABRICATION DEVELOPMENT

J. D. Sease W. H. Pechin
F. J. Furman J. G. Stradley
C. F. Sanders

The objective of the HTGR refabrication development program is to develop the technology necessary for the design and operation of a pilot-scale remote fueled graphite line in the Thorium Uranium Recycle Facility (TURF). This pilot line, scheduled for operation in 1976-1977, will be $\frac{1}{2}_0$ the scale of a commercial recycle facility and will produce two fuel blocks per day containing approximately 25 kg of heavy metal. The major process operations in the TURF Refabrication Pilot Plant are shown in Fig. 35.1. The major development areas in the Metals and Ceramics

Table 35.1. High-Temperature Gas-Cooled Reactor recycle fuel particles

	Fissile Particle	Fertile Particle
Kernel composition	(Th-20% U)O ₂	ThO ₂
Kernel diameter, μm	350	400
Buffer carbon thickness, μm	80	50
Outer pyrolytic carbon thickness, μm	120	70
Total particle diameter, μm	750	640

Division are associated with coating of fuel particles, stick fabrication, and element assembly.

Coating

The fuel particles proposed for the HTGR recycle element are described in Table 35.1. We have produced particles of this type in 1- to 2-kg batches on a semiproduction scale in a 5-in.-diam coater.³ We have continued the operation of this coater this year. A number of equipment modifications were completed, including the installation of equipment to permit the application of SiC coatings. We are now performing a series of statistically designed coating experiments to better delineate the influence of coating variables and their interactions.

Remote particle-handling devices have been developed for size and shape classification, valving, storing, and transferring. Laboratory devices for performing these operations have been assembled and tested, and are being used in coating development.

We are developing an automatic particle size analyzer to accurately measure the particle size distribution and mean particle weight after each coating operation. With this instrument we expect to obtain sufficient information to calculate coating thickness and density from a 1- to 2-g sample in about 5 min. The data indicate that we will be able to measure particle diameters to within $\pm 1\%$.

Stick Fabrication

The fuel sticks will be made by blending or feeding the desired proportions of coated fissile and fertile particles into a metal mold, then penetrating the voids with a matrix material. The reference matrix is a dispersion of graphite flour in coal tar pitch. This

3. R. B. Pratt, J. D. Sease, W. H. Pechin, and A. L. Lotts, "Pyrolytic Carbon Coating in an Engineering-Scale System," *Nucl. Appl.* 6, 241-55 (1969).

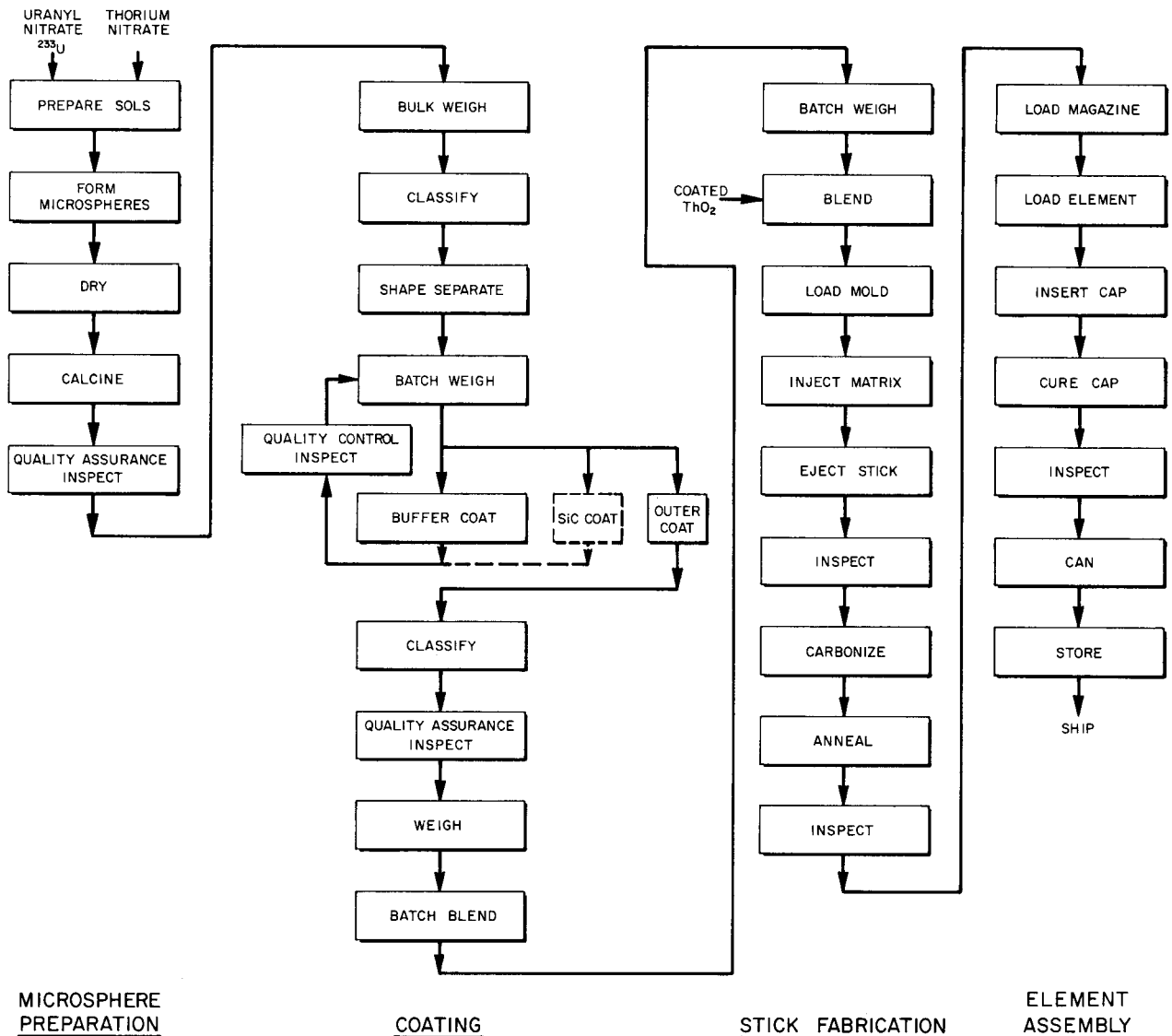


Fig. 35.1. Major process operations in TURF refabrication development line.

matrix must be heated to allow intrusion into the particle bed. The pitch-bonded stick is then carbonized and annealed before being loaded into the graphite fuel element. The finished sticks must have a uniform distribution of fissile and fertile particles, a uniform distribution of graphite flour to ensure uniform thermal conductivity, and an absolute minimum of particles with broken coatings to ensure minimum fission product release.

The processes currently in use for making 2-in.-long fuel sticks need to be more automated and simplified for use in TURF. Blending by simultaneous feeding of the fertile and fissile particles at controlled rates appears to be necessary to ensure proper loading of the

two different microsphere types. Preliminary experiments with a feeder blender in which the rate was adjusted by variation of the orifice size do not look encouraging; however, a newly developed roll feeder is capable of 1 to 2% accuracy. We have found that the graphite flour will segregate from the coal tar pitch if the matrix mixture is held in the liquid state without agitation. To avoid cracking particle coatings, the pressure at which the matrix is injected into the particle bed and that at which the stick is ejected from the mold must be held below 1500 psi, preferably around 500 psi. Although ejection pressures appear to depend on the metal used for the molds and the mold release agent, the injection pressure can be minimized by

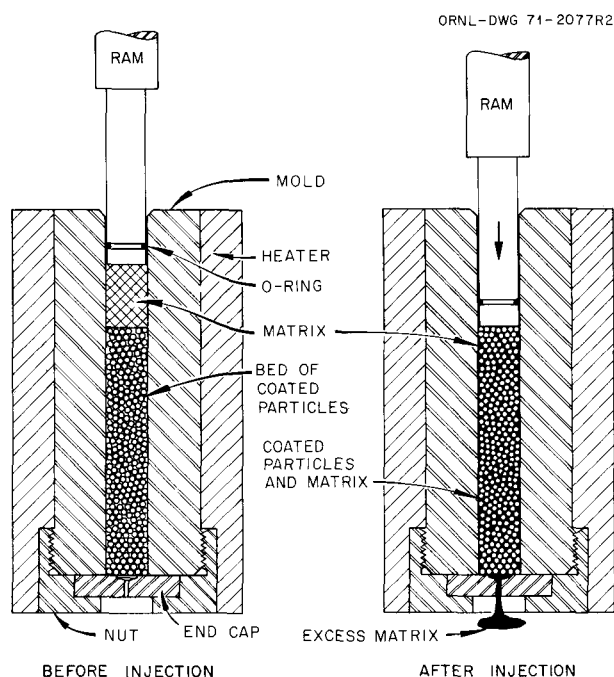


Fig. 35.2. Slug technique for making bonded bed fuel sticks.

injecting over the entire cross section of the stick. This approach is utilized in a new process termed "slug injection," which appears to have significant advantages for remote application. In slug injection a prepared slug of matrix material is warm pressed through the bed of particles (see Fig. 35.2).

Element Assembly

Element assembly involves loading and capping 210 fuel holes and inserting locating dowels. A technique for gravity loading all 210 fuel holes simultaneously from a magazine has been shown to be feasible. Current contact means of wet cementing the caps in the fuel elements do not appear suitable for remote assembly. Alternate techniques using thermoplastic cements are being studied.

HTGR RECYCLE FUELS IRRADIATION

T. N. Washburn R. B. Fitts A. R. Olsen

The irradiation tests on the HTGR recycle program have two main objectives: (1) to provide irradiated fuel for head-end process studies, and (2) to provide irradiation proof tests of the products of coated-particle process development. The test conditions of interest

include fuel temperatures between 600 and 1300°C, burnup to 20% FIMA in the (Th,U)O₂ particles, and fast fluence exposures up to 8×10^{21} neutrons/cm².

The first two stages in this program were implemented this year. They are: (1) accelerated-burnup capsule irradiations, and (2) irradiation of seven test fuel elements in the Peach Bottom Reactor.

Capsule Irradiations

A. R. Olsen

The irradiation of capsules H-1 and H-2 began in May with the start of ETR cycle 112. The design of these capsules, which contain thermal neutron filter shrouds to more nearly simulate the thermal-to-fast-flux ratio of operating high temperature gas-cooled reactors, was described previously.⁴ These two capsules contain primarily bonded beds (sticks) of the particle combinations listed in Table 35.2, plus loose particle beds of combination a and g. Each combination is being irradiated at all four test temperatures — 750, 950, 1050, and 1300°C — to fast fluence levels between 6 and 8×10^{21} neutrons/cm². The capsules should complete their planned irradiation in approximately seven months.

Table 35.2. Fuel combinations irradiated in HTGR capsules H-1 and H-2

Combination identity	Particle types
a	(4.2 Th,U)O ₂ BISO ^a + ThO ₂ BISO
c	(2 Th,U)O ₂ BISO + ThO ₂ BISO
f	UC ₂ TRISO ^a + ThC ₂ BISO
g	UO ₂ BISO + ThO ₂ BISO
x	UOS (resin particle) BISO + ThO ₂ BISO

^aA BISO coating comprises two layers of pyrolytic carbon, a porous inner layer and a dense outer layer. A TRISO coating also includes a silicon carbide layer.

Large-Scale Irradiations

R. B. Fitts

This cooperative irradiation program with Gulf General Atomic has three main objectives: (1) to provide gram quantities of unirradiated HTGR fuel for head-end reprocessing studies, (2) to provide irradiated fuel blocks for testing engineering-scale reprocessing equipment, and (3) to proof test recycle fuel particles

4. A. R. Olsen, *Metals and Ceramics Div. Annu. Progr. Rept. June 30, 1970*, ORNL-4570, pp. 198-99.

prepared in prototype equipment using the processes to be used in the Thorium-Uranium Recycle Facility. To achieve these objectives a set of Recycle Test Elements (RTE's) is being operated in the Peach Bottom Reactor. The fuels tested include all of those presently known to be of prime interest for larger HTGR systems. The test conditions cover the range from 540 to 1250°C, burnups to 20% FIMA⁵ in the (Th,U)O₂ particles, and fast fluences (>0.18 MeV) up to 4.2×10^{21} neutrons/cm².

The design of the RTE's and the particle types to be tested have been reported.⁶ The first six RTE's were irradiated without incident from July 14, 1970 to April 24, 1971, when the reactor was shut down on schedule.

5. Fission per initial metal atom.

6. R. B. Fitts, *Metals and Ceramics Div. Annu. Progr. Rept. June 30, 1970*, ORNL-4570, pp. 199-200.

The elements had accumulated about 265 full power days of operation and a peak fast fluence of about 1.4×10^{21} neutrons/cm². One RTE was removed and stored for subsequent shipment to ORNL for reprocessing studies and fuel examination.

The seventh RTE was inserted in April, and the eighth was deleted from the program. The fuel loading in the seventh RTE was modified to delete four 12-in.-long stacks of bonded UC₂ (BISO) + ThC₂ (BISO) fuel and replace it with UO₂ (TRISO) + ThO₂ (BISO) fuel, a mixture which has recently become of interest for possible use in larger HTGR's.

The two of the remaining six RTE's, which contain loose (unbonded) fuel in three of the six 15-in.-long bodies of each element, will be discharged about June 1972. The remaining four elements are scheduled for discharge in June 1973.

36. Transuranium Program

A. L. Lotts

The Transuranium Project is producing quantities of the heavier transuranium elements for research by successive neutron captures in ^{239}Pu . The program at ORNL started with primarily ^{242}Pu , ^{243}Am , and ^{244}Cm . Target elements containing principally these three isotopes are fabricated at ORNL and irradiated in the High Flux Isotope Reactor at a flux of approximately 3×10^{15} neutrons $\text{cm}^{-2} \text{sec}^{-1}$. In addition, special target elements of higher isotopes are fabricated occasionally and irradiated in HFIR. The target elements are removed periodically from the HFIR and reprocessed in the Transuranium Processing Facility (TRU). At TRU the product actinides are separated and the target actinides are recovered and fabricated into recycle target elements. In addition, special targets for irradiation in the HFIR Hydraulic Rabbit Facility are fabricated and special encapsulations are made of the product actinides.

The program at TRU is carried out jointly by the Chemical Technology, Metals and Ceramics, and Analytical Chemistry Divisions. Our present tasks in the program include the fabrication of targets in TRU for HFIR, the fabrication of HFIR rabbits, the fabrication of special encapsulations for neutron and gamma sources, the evaluation of the performance of the target elements, the improvement of the target element design, and the improvement of the processing equipment in TRU.

TARGET FABRICATION

L. C. Williams J. E. Van Cleve, Jr.

The production line used to fabricate target rods containing $(\text{Am,Cm})\text{O}_2$ as the starting material has operated with minimum trouble as feed was available. The difficulty in making the final closure weld on the targets¹ was corrected by a complete overhaul of the

1. L. C. Williams and J. E. Van Cleve, *Metals and Ceramics Div. Annu. Progr. Rept. June 30, 1970, ORNL-4570*, pp. 201-2.

remote portion of the equipment and the installation of a new welding power supply. During this reporting period we fabricated 17 targets, containing on the average 5.80 g Cm as oxide microspheres.

Small amounts of isotopes of special interest are most efficiently produced by exposing the starting material in the HFIR hydraulic rabbit facility. The rabbits are returned to the TRU by a newly installed transfer system, and the irradiated sample is recovered and shipped to the requester. Five rabbits fabricated during this year contained 0.5 mg ^{252}Cf , 1.1 mg ^{241}Am , 1.1 mg ^{240}Am , 0.5 mg ^{244}Pu , and 1.0 μg ^{253}Es .

We assembled 20 neutron sources containing 5 to 5000 μg Cf, one gamma source containing 10 mg ^{241}Am , and one containing 0.5 g ^{242}Pu . One source was encapsulated in hardware obtained from the Savannah River Laboratory to demonstrate our capabilities using their hardware design.

HFIR TARGET PERFORMANCE

J. E. Van Cleve, Jr.

Status of the Targets Exposed in HFIR

Table 36.1 lists the targets exposed in HFIR during the past year. These are the original HFIR loading, which contained 8 g $^{242}\text{PuO}_2$ per target with the pellets containing 10% void volume; targets that contain 11 g $^{242}\text{PuO}_2$ per target with the pellets containing 20% void volume; and the recycle targets, which contain 11 g mixed $(^{243}\text{Am}, ^{244}\text{Cm})\text{O}_2$, with the pellets containing 20% void volume. The second and third type targets were fabricated remotely in the TRU.

Analysis of Target Performance

Several different types of targets were removed from the HFIR and chemically processed to recover the contained transplutonium elements. One type consisted of three "virgin" plutonium targets that had been irradiated in HFIR only. Two of these had developed

Table 36.1. HFIR target element performance as of June 30, 1971

Actinide oxide loading (g)	Pellet void volume (%)	Number of targets	Present status	Range of burnup (% FIMA)	Range of fluence (neutrons/cm ²)	
					<0.41 eV	>0.81 MeV
					$\times 10^{22}$	$\times 10^{22}$
11	20	8	Scheduled removal	42.0–71.0	8.79–15.03	2.35–4.56
8	10	2	Failed	62.6–72.8	12.97–15.81	4.13–4.90
11	20	2	Failed	49.7–66.7	10.22–13.93	3.16–4.23
11	20	5	Scheduled removal	67.6–74.0	10.32–12.31	3.22–4.15
8	10	1	Scheduled removal	70.3	15.24	4.82
10–11	20	26	In HFIR	74–9.5	12.3–0.57	4.15–0.15

cladding cracks of the same type as previously shown.^{2,3} These three targets were in the area of exposure where failure was to be expected.

The second type consisted of targets remotely fabricated in TRU and containing 11 g of PuO₂ pressed into pellets with 20% void volume. These targets all operated without failure and were removed on schedule. Again the successful exposure of these targets confirms the validity of the target performance model, which is presented later in this chapter.

A third type is the recycle target fabricated in the TRU plant. These targets are loaded with a mixture of americium and curium oxides, and the pellets were pressed to contain 20% void volume. These targets were removed on schedule.

The last group of targets removed were loaded with 11 g of PuO₂ in pellets pressed to 20% void volume. These targets developed cracks in the target cladding before the predicted point of failure. A detailed examination of the assembly and loading data indicated that in both cases a pellet of considerably lower void volume than 20% was inadvertently placed near the center of the target length. These pellets would expand because of fission product accumulation and stress the cladding, as predicted in the target performance model. When these stresses equaled the ultimate strength of the target cladding, a crack would develop. Details of the model and this particular type failure are also summarized later in this chapter.

Although these two targets failed prematurely, the target performance model adequately explains the early

failures. The successful exposure of the 13 targets removed on schedule supports the need for a minimum of 20% void volume to obtain burnups of 70 to 80% FIMA. Twenty-six targets of this type are presently in the HFIR.

THERMAL CONDUCTIVITY STUDIES

R. S. Graves R. M. Steele

High thermal conductivity (λ) HFIR target pellets result in moderate operating temperatures, so determination of λ for every pellet would be a useful quality control step. The cold-pressed pellets, which are nominally aluminum with 20 vol % each of transuranium oxide and voids, should possess good thermal conductivity λ and electrical conductivity σ , if the aluminum matrix is continuous. Development of a hot-cell eddy-current test to measure σ of every pellet and establishment of the correlation function for λ and σ could yield λ for every pellet as a quality control inspection measure.

Modifications to a comparative heat flow apparatus were completed to obtain λ data needed for the λ : σ correlation on available cermet samples and on specific stand-in pellets. Table 36.2 presents typical data at 300°K on two sets of cermet strips, Al-U₃O₈ and Al-Al₂O₃, fabricated from HFIR fuel-plate cores, as described in Chap. 27 of this report. These λ values were measured with a guarded longitudinal heat flow apparatus.⁴ All of the determinations of σ using a four-probe dc technique and an eddy-current probe agree to better than $\pm 2\%$, thus validating the eddy-current technique. If one assumes neither voids nor U₃O₈ conduct electrically or thermally, the aluminum-U₃O₈ results are within $\pm 3.5\%$ of a simplified Eucken

2. J. E. Van Cleve and E. J. Manthos, *Metals and Ceramics Div. Annu. Progr. Rept. June 30, 1968*, ORNL-4370, pp. 194–97.

3. A. L. Lotts, E. J. Manthos, J. E. Van Cleve, Jr., E. L. Long, Jr., R. T. King, J. R. Weir, and R. E. Adams, *Metals and Ceramics Div. Annu. Progr. Rept. June 30, 1967*, ORNL-4170, pp. 187–91.

4. J. P. Moore, D. L. McElroy, and R. S. Graves, *Can. J. Phys.* 45, 3849–65 (1967).

Table 36.2. Thermal conductivity and electrical conductivity for aluminum cermet at 300°K

Specimen	Thermal conductivity [W cm ⁻¹ (°K)]	Electrical conductivity [(Ω-cm) ⁻¹]	
		4-Probe dc	Eddy-current
		× 10 ⁶	× 10 ⁶
Al-U ₃ O ₈			
13.5% Burned	1.73	0.265	0.270
19.5% Burned	1.47	0.227	0.225
12.5% High fired	1.77	0.276	0.274
18.0% High fired	1.59	0.245	0.244
Al-Al ₂ O ₃			
0% Al ₂ O ₃	2.23	0.341	
12% Al ₂ O ₃	1.86	0.275	0.278
19% Al ₂ O ₃	1.72	0.248	0.251
10% Al ₂ O ₃	1.93	0.294	0.293
20% Al ₂ O ₃	1.67	0.242	0.242
30% Al ₂ O ₃	1.43	0.198	0.197
40% Al ₂ O ₃	1.17	0.153	0.150

two-phase conductivity equation

$$\lambda_{\text{cermet}} = \frac{\lambda_{\text{Al}}}{\sigma_{\text{Al}}} \cdot \sigma_{\text{cermet}} = 6.5 \times 10^{-6} \sigma_{\text{cermet}},$$

where λ is in W cm⁻¹ (°K)⁻¹ and σ is in (Ω-cm)⁻¹. Since $\lambda(\text{Al}_2\text{O}_3) \approx 0.16\lambda(\text{Al})$, the more complex Eucken relation is required to describe the aluminum-Al₂O₃ results. The HFIR target pellets are expected to be similar to the aluminum-U₃O₈ case.

NONDESTRUCTIVE TEST DEVELOPMENT

C. V. Dodd W. A. Simpson, Jr.

The development of an eddy-current test to measure the electrical conductivity (which, as shown above, measures the thermal conductivity) of the aluminum-transuranium oxide core in the HFIR target pellet is proceeding on an analytical and experimental basis.

Calculations were made for a reflection-type coil (as used with the phase-sensitive eddy-current instrument) above two flat planar conductors, as shown in Fig. 36.1. This is not the exact case for the HFIR target pellets, but it is presently the best model available and does approach the HFIR case for the coil being small compared to the curvature of the pellet. Figure 36.1 shows how the phase shift for a 10% conductivity variation and the error due to lift-off (coil-to-pellet spacing) vary with test variables. The phase-sensitive eddy-current instrument can measure phase shifts of about 2×10^{-4} radians, which correspond to a 0.2%

change in the conductivity of the core material. The error due to a 0.006-in. lift-off is comparable. The phase of the eddy currents induced in machined sample pellets with cores of different electrical resistivity was measured with the phase-sensitive eddy-current instrument. The sensitivity to changes in the measured resistivity with a 0.150-in.-diam coil was approximately one-half the calculated value. The difference was probably due to the curvature. The measured values for a 0.100-in.-diam coil were 1.75 times the calculated values, but the sensitivity was slightly lower and the lift-off errors were slightly higher than for the larger coil. Measurements and calculations will be made for a 0.208-in.-diam coil to seek improvement.

The measurements and calculations performed thus far show that the 0.150-in.-diam coil will easily measure the conductivity to the desired accuracy if other variables can be controlled. Calculations have shown that a change in conductivity of the core material can be completely obscured by variations in the conductivity of the pellet outer shell and variations in the wall thickness of the outer shell. However, a two-frequency technique can substantially reduce the error. The same combination of the conductivity and thickness variations can be measured at a higher frequency, and the results can be used to make a correction in the measurement of the conductivity of the core material at a lower frequency. The maximum error caused by any combination of variations of wall thickness and conductivity ranging from 0 to ±10% is ±3% and for most combinations is less than ±1%. A three- or four-frequency measurement theoretically would reduce the error to zero, but in its present version the modular phase-sensitive instrument can only measure at two frequencies simultaneously. Samples with various conductivities and wall thicknesses are being machined to study the effects on actual measurements and to use as calibration standards for two-frequency measurements.

Another possible source of difficulty is a void or insulating layer between the pellet container wall and the core material. While the calculations show the addition of this void layer would cause a relatively small error in the measurement of the core conductivity, it would affect the heat transfer properties and be very desirable to detect. Again a multiple-frequency approach will be necessary.

ALUMINUM IRRADIATION DAMAGE

R. T. King K. Farrell

We are continuing to investigate the in-reactor failure of the HFIR target rod cladding. The cladding operates

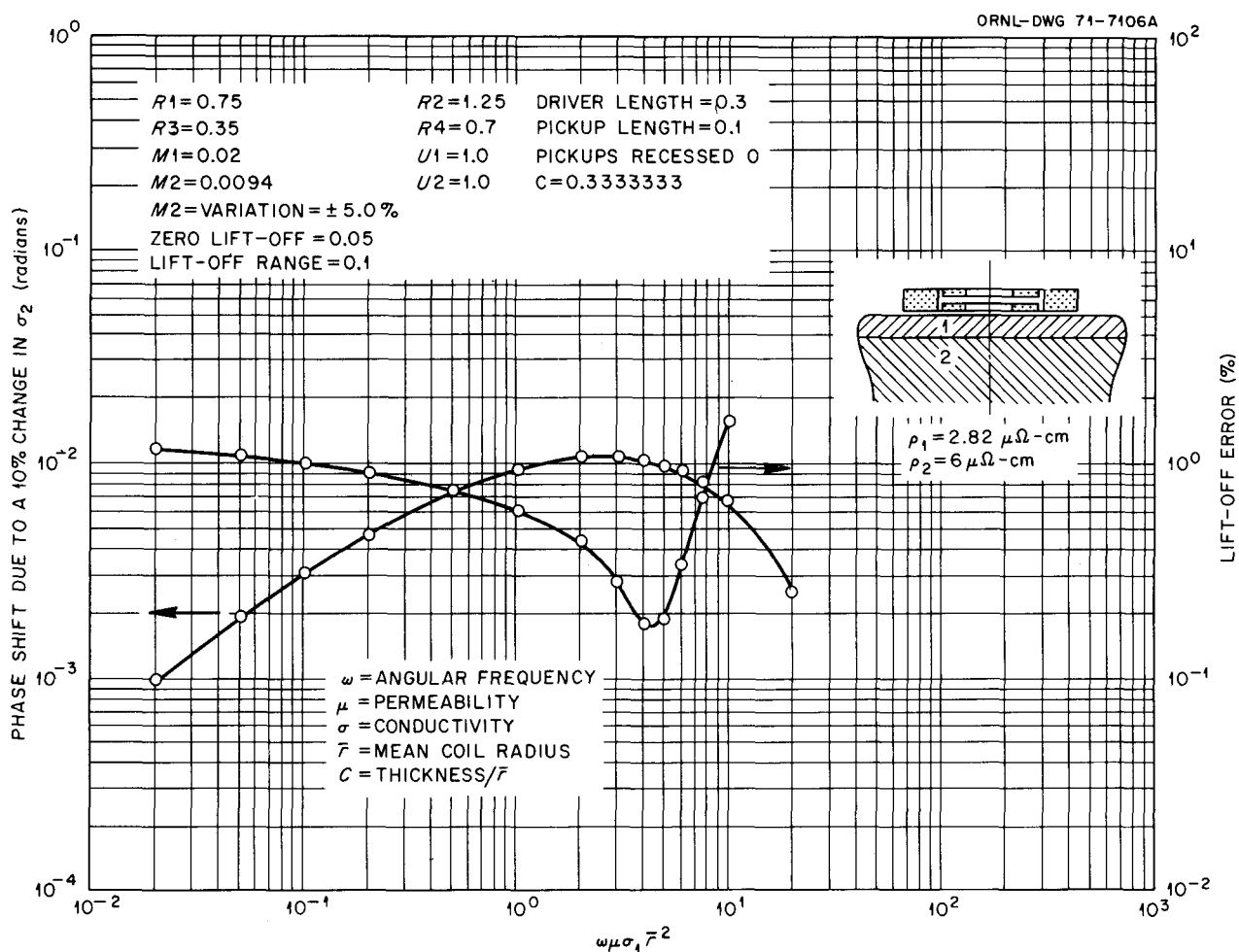


Fig. 36.1. Variation in phase shift due to a 10% change in the base material conductivity and percent error due to a 0.006-in. lift-off variation for 0.150-in.-diam reflection coil above two flat conductors.

at about 125°C and does not strain measurably before fracturing. An electron microscopic examination of the 8001 alloy cladding stripped from one failed target rod has revealed the presence of radiation voids and much transmutation-induced silicon precipitate. The voids tended to be locally concentrated in bands and patches near certain large precipitate particles and grain boundaries. The exact nature of the boundary or interface is probably important in determining the heterogeneous distribution of the voids. These voids may play a role in the failure of the rods. However, stringers of precipitate have been found in the regions where failure occurs and may weaken the tube locally through several proposed mechanisms.

Experiments intended to irradiate creep-rupture specimens near the cladding temperature were unfortunately operated somewhat above 125°C, and very few specimens contained voids even after irradiation to 1.6

$\times 10^{22}$ neutrons/cm² (>0.8 MeV). Dispersion strengthening by transmutation-produced silicon caused the greatest changes in mechanical properties; with increasing irradiation temperature, the dispersion became coarser and the postirradiation strength decreased correspondingly, but ductility was increased. Strength increases in the 8001 and 1100 alloys agree well with Orowan's dislocation pinning model. Arguments favoring the use of the 6061 precipitation-hardened alloy for cladding and other work on these alloys are summarized in Chaps. 5 and 29 of this report.

HFIR TARGET PERFORMANCE MODEL

R. E. Adams

The performance of HFIR target rods has been of concern since failures developed in service at 21 to 32%

FIMA, even though prototype rods in the ETR had shown no failures at up to 60% FIMA. Differences in behavior were attributed to cladding embrittlement by the much higher fast neutron fluence in HFIR, which did not allow cladding expansion to accommodate the increasing volume of fission products.

A mathematical model was developed to evaluate the complex interactions between the fabrication and irradiation variables that affect the fuel rod lifetime.^{5,6} The failure model was based on the premise that fission gases are confined within the individual pellets and stresses from the accumulating pressure eventually exceed the cladding yield strength.

On the basis of the model, swelling and cladding strain are calculated from known or estimated values for several variables that control target rod performance. The estimated burnup limit, if failure is presumed to occur at zero plastic strain, occurs when the cladding stress reaches the yield point. For targets of nominally 10% porosity and containing the equivalent of 10 g Pu per 35 pellet target, the predicted pellet swelling and cladding strain are shown in Fig. 36.2. Plotted points are data measured metallographically on the prototype ETR pellets.

The accuracy with which the model can predict burnup limits for any specified values of void volume and target loading for irradiation in the HFIR depends on the uncertainties in assigning values for the different variables. The uncertainties associated with achieving specified values of initial void volume and volume of oxide fuel in a fabricated pellet are considerable, as discussed in detail elsewhere^{6,7} and briefly considered below. Uncertainties involved in estimating values of the irradiation variables, such as fuel temperature and volumetric swelling from fission products, are also considered.

The fission gas pressure and cladding yield strength depend on temperature. The operating temperature of the target rod depends on its heat rate (which varies with oxide loading and burnup level) and on the probable development of a thermally insulating oxide film at the target surface. The yield stress probably increases with fast neutron fluence, and the increase probably depends on temperature during the irradi-

5. R. E. Adams, "Failure Model for HFIR Target Rods," *Trans. Amer. Nucl. Soc.* **12**, 560-61 (1969).

6. A. L. Lotts, R. E. Adams, J. E. Bigelow, R. T. King, E. L. Long, Jr., E. J. Manthos, and J. E. Van Cleve, Jr., *Analysis of Failure of HFIR Target Elements Irradiated in SRL and HFIR*, ORNL-TM-2236 (in preparation).

7. J. D. Sease, *Fabrication of Target Elements for the High Flux Isotope Reactor*, ORNL-TM-1712 (March 1967).

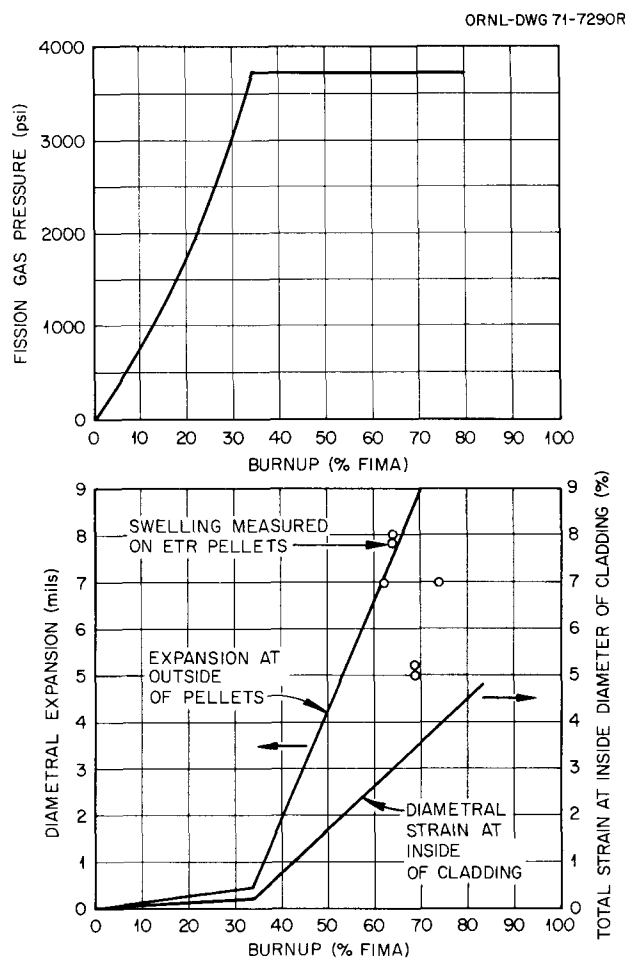


Fig. 36.2. Fission gas pressure, pellet swelling, and maximum calculated strain for ETR pellets on basis of model.

ation. We have used a value of 14,000 psi for the yield stress, a value of 1.21×10^{-4} mole of gas generated per cm^3 per % FIMA, and 1% solid fission product swelling per % FIMA. Any of these variables may be in error by perhaps 100%. However, the combination of these three variables to yield an overall irradiation variable has been established on the basis of the SRL-HFIR and ETR prototype irradiation test data.⁶ The validity of these values under differing irradiation conditions must be established as additional experimental data become available.

The extent to which the calculated burnup limit of pellets operating in HFIR is affected by the pellet porosity is estimated in Fig. 36.3. The curves are based on operating temperatures estimated by the GENGTC code, the appropriate heat rate being calculated (at a specific burnup level) from data based on a 10-g Pu loading, with a linear correction applied for 8- or 12-g

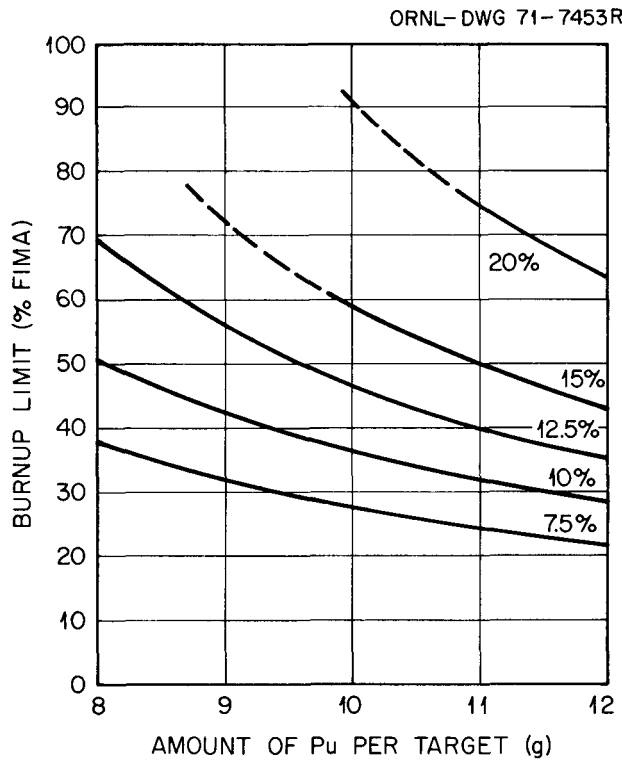


Fig. 36.3. Effect of pellet porosity and plutonium loading on calculated burnup limit for target rods exposed in HFIR.

loadings. A linear variation of cladding yield stress with temperature was assumed between the extreme values of 16,750 psi at 177°F (at the 4kW/ft power level at 75% FIMA for the 8-g-Pu rods) and 12,500 psi at 253°F (the maximum cladding temperature calculated at 11.3 kW/ft for the 12-g-Pu rods at 30% FIMA).

Some additional data on target performance have become available. During the past two years nine targets failed. Seven rods fabricated to contain 8 g Pu and 10% porosity failed at burnups ranging between 57 and 76% FIMA, 11 similar rods showed no failures when removed after 60 to 75% FIMA nor did 13 at 40 to 50% FIMA. The failure model predicts no failure on these rods below 50% FIMA if they are of nominal composition.

Rods fabricated to contain 20% porosity and 10 g Pu or Am-Cm have now achieved high burnups. No failures are predicted, but two failures at 49.7 and 66.7% FIMA have occurred with plutonium rods; two others did not fail at 49 and 71% FIMA. Of 18 rods containing 10 g Cm, no failures developed at between 67 and 74% FIMA.

From fabrication records of pellets used in target rod K-23 (which failed at 49.7% FIMA), data on weight, length, and location of individual pellets were available.

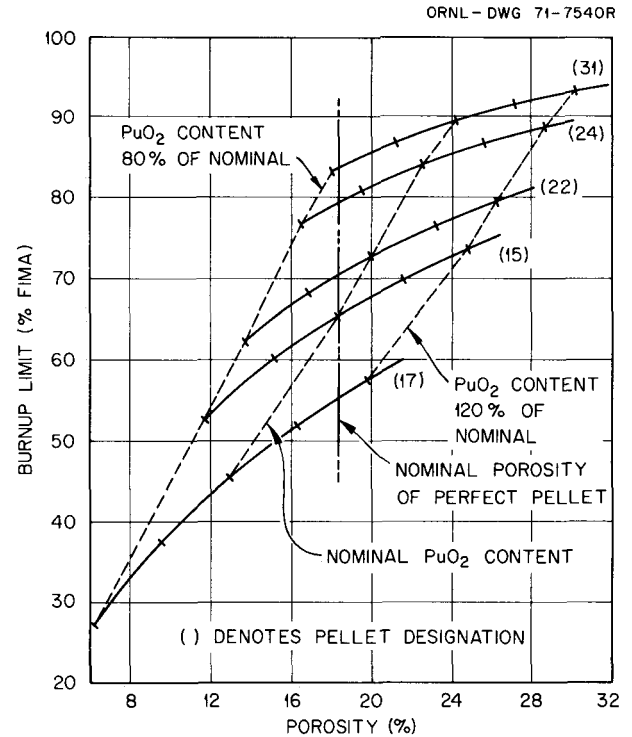


Fig. 36.4. Range of burnup limits calculated for pellets irradiated in target K-23.

Pellets differ slightly in porosity and plutonium content, and these differences are reflected but not identified by differences in pellet weight and length. For instance, a short or a heavy pellet may contain less than nominal porosity or more than nominal PuO_2 .

From weight and length data, the porosity of pellets used in K-23 was calculated, assuming the PuO_2 content to be at some specific value between 80 and 120% of its intended value. For each hypothetical value of porosity and PuO_2 content, the burnup limit was calculated on the basis of the failure model. The results for several selected pellets are shown in Fig. 36.4. Since exact PuO_2 loadings are not known, burnup limits are calculated for a constant heat rating of 9.46 kW/ft and a yield stress of 14,000 psi and thus differ from results shown in Fig. 36.3, in which heat rates were adjusted for PuO_2 content and burnup level.

Pellet 17 was one of the two pellets with lowest predicted burnup at failure. Pellet 22 was typical of the desired 20% porosity and 10 g Pu per target. We conclude that significant differences in burnup to failure can be expected from pellets fabricated in the same batch. These differences can be identified by weight and length data and can be utilized to select pellets for location along the flux profile of the rod to achieve optimum burnup from a batch of pellets.

37. Water Reactor Safety

P. L. Rittenhouse

Perhaps the most serious accident considered "credible" in light-water reactors (LWR's) is the double-ended rupture of one of the large pipes in the primary system. This accident is one of a spectrum of loss-of-coolant accidents (LOCA's) that would result in loss of system pressure and coolant and a subsequent increase in the temperature of the Zircaloy fuel cladding. Heatup of the cladding is, at first, primarily the result of redistribution of the heat stored in the UO_2 fuel. At later times the decay heat of fission products is the dominant heat source, and, if the temperature is high enough, heat will be generated by reaction between cladding and steam.

Although the probability of any LOCA is considered to be small and that of the maximum LOCA extremely small, their consequences could be severe. Therefore, engineered safety features such as emergency core cooling systems (ECCS's) are provided to ensure that the accident temperature transient can be terminated safely. Because it is vital that the ECCS's be effective, it is important to understand or investigate thoroughly factors that may influence their performance. Such factors include the effects of damage, blockage, and displacement of portions of the reactor core caused by failure of fuel rods. Many such failures would occur during a large LOCA because the temperatures reached by many of the fuel rods before transient turnaround and termination would be high enough to cause swelling and rupture of the cladding. This would reduce the cross-sectional area for coolant passage (coolant channel area) and perhaps restrict coolant entirely from local areas on some rods. At some relatively high degree of coolant channel blockage, termination of the temperature transient could be delayed sufficiently to significantly increase the probability of cladding embrittlement by reaction with steam.

Because of the possibilities mentioned above, work has been underway to (1) examine the modes of failure of the Zircaloy cladding of the fuel rods in terms of accident conditions and reactor operating history, and (2) determine to what extent fuel rod failures may

affect emergency cooling capability. In such experimental programs it is desirable to assess the safety margin associated with any limiting conditions. Hence, conditions exceeding the maximum calculated accident transients are also explored.

PROGRAM COORDINATION

P. L. Rittenhouse

The research and testing necessary to assess failure modes and their effect on emergency cooling are coordinated by us for the United States Atomic Energy Commission (USAEC). In addition to the several studies we are conducting on the high-temperature deformation and embrittlement of Zircaloy cladding, other USAEC-sponsored research on fuel rod failure and its effects is being performed at Idaho Nuclear Corporation (Idaho Falls, Idaho), Battelle Memorial Institute (Columbus, Ohio), and in the Reactor and Reactor Chemistry Divisions at ORNL. Related activities conducted by LWR manufacturers are factored into the direction and scope of the USAEC studies to ensure that all problem areas are investigated thoroughly and that just enough overlap of programs is permitted to provide confirmation of important results.

We also have the responsibility for preparing program documents covering these areas of work. The most recent of these is a review of fiscal year 1970 progress in failure modes research.¹ This report describes needed continuing work and additional areas where effort is justified.

MULTIROD TRANSIENT BURST EXPERIMENTS

P. L. Rittenhouse

The maximum coolant channel blockage that could occur in LWR fuel assemblies can be calculated from

1. P. L. Rittenhouse, *Review of Recent Progress in Zircaloy-Cladding Failure Modes Research*, ORNL-TM-3188 (December 1970).

the results of burst tests of single Zircaloy tubes. For example, if uniform expansion of fuel tubes at identical axial positions reaches just over 30% (enough to cause contact between adjacent tubes), the coolant channel cross-sectional area will be reduced to 40% of its original value. At less than 60% uniform cladding expansion, complete channel blockage is theoretically possible. However, the calculations that give these results cannot account fully for the interaction and interference of simultaneously deforming tubes and the axial spread of deformation and rupture locations. Therefore, multirod transient burst experiments are needed to provide realistic and meaningful channel blockage data. The primary variables in these experiments are internal pressure (selected to simulate fission-gas pressures in the fuel rods after various periods of reaction operation) and heating rate (chosen to cover the calculated range of rates expected for LOCA's). Details of testing and examination have been reported.²

The blockage results of the multirod transient burst experiments are summarized in Fig. 37.1. The datum point for each test is the blockage measured on the "worst" cross section. Expansion results from single-tube experiments were used to calculate the "predicted" curve. This curve, although not exact because the effect of heating rate is averaged, permits comparison of the theoretical maximum and measured values of coolant channel blockage. As might be expected, the experimentally determined values are consistently lower than those predicted. One reason for this is randomness of failure (i.e., points of maximum deformation on individual tubes generally are distributed over a 2- to 3-in. span rather than occurring at identical elevations). Another factor contributing to the observed result involves bundle size and geometry. For example, in Fig. 37.2 the variation of channel blockage along the bundle of test 7 is shown for two groups of channels. (An individual channel is the open area between any four adjacent tubes centered on a square array.) Channels 1 through 5 are those in the center of the bundle; 14 through 21 constitute the outer row of channels. At the position of maximum blockage the results for the two groups of channels differ by a factor of 2. To enable us to rationalize such results and to extrapolate and apply the data obtained to particular reactor accident cases, we have developed a method of analysis that characterizes each channel in a test bundle or fuel assembly by a channel coefficient.² A typical result, channel blockage as a function of channel coefficient, is shown in Fig.

2. P. L. Rittenhouse et al., *Nuclear Safety Program Annu. Progr. Rept. Dec. 31, 1970*, ORNL-4647, pp. 9-14.

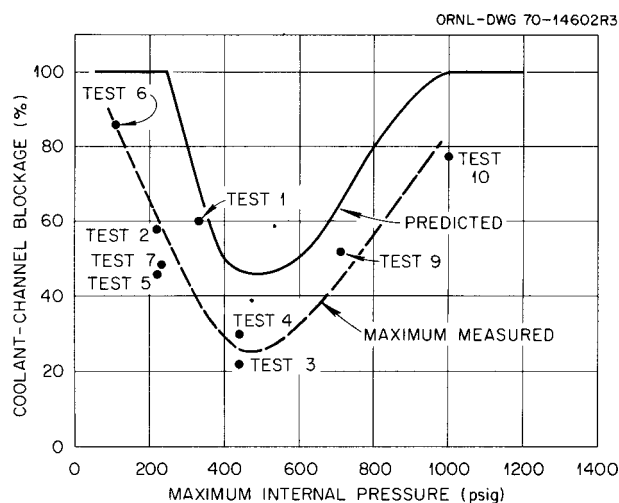


Fig. 37.1. Summary of multirod experiment channel blockage results. Coolant channel blockages measured in multirod experiments are shown as a function of maximum internal pressure in the simulated fuel rods during the transient burst test. Tests 1-6 were 13-rod experiments; 7, 9, and 10 were run with 32 rods. Heating rates were 10° F/sec (tests 7 and 9), 25° F/sec (tests 4, 5, and 10), 50° F/sec (test 6), and 100° F/sec (tests 1-3).

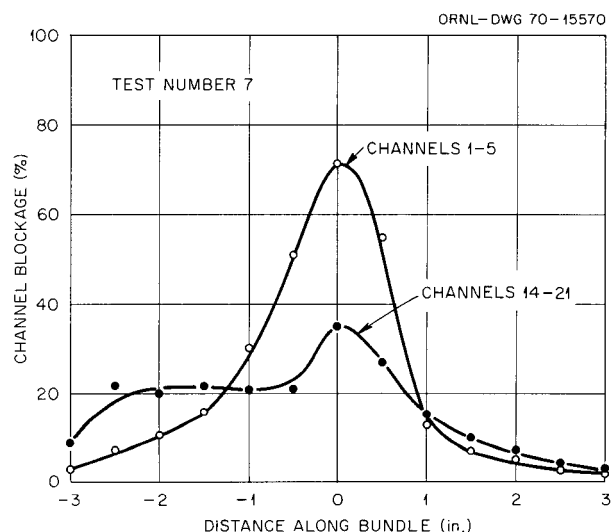


Fig. 37.2. Variation in channel blockage with position in test bundle. Channel blockages in test 7 (32 rods, 225 psig, 10° F/sec) are shown as a function of distance along and position within the test bundle.

37.3. This type of correlation has been found valid at about $\pm 1/2$ in. from the cross section of maximum blockage.

In summary, the multirod tests have shown that the most important factor in determining channel blockage is internal pressure. The rate of heating of the test has a

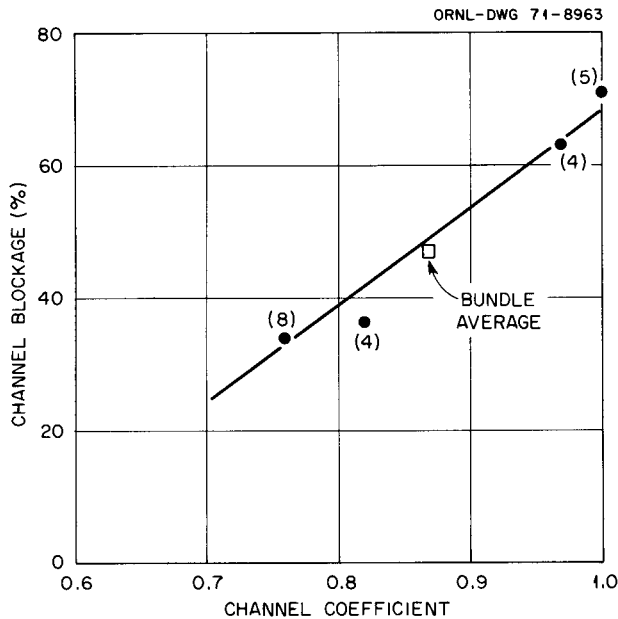


Fig. 37.3. Channel blockage in test 7 (32 rods, 225 psig, $10^{\circ}\text{F}/\text{sec}$) as a function of channel coefficient. The five channels with coefficients of 1.0 are at the center of the bundle; the eight channels of lowest coefficient (0.76) are on the outer row of the bundle. Two other groups of channels (four channels each) are at intermediate positions across the bundle. The "bundle average" is the average blockage in the 21 channels of the cross section plotted at the value of average coefficient.

smaller effect, and its magnitude varies with the internal pressure level. Blockages measured in the test are lower than those predicted. This discrepancy can be attributed to some degree of randomness of failure position along the bundle, interference between deforming tubes, and the geometry and size of the test bundle.

EMBRITTLMENT OF LIGHT-WATER REACTOR FUEL CLADDING

D. O. Hobson

The objective of this study has been to determine the behavior of Zircaloy cladding exposed to steam at elevated temperatures. We have examined the effects of high-temperature exposure of Zircaloy to steam under isothermal conditions and have integrated the data to estimate the effect of the transient (LOCA) condition. Sections of cladding were exposed to steam under 19 different combinations of time and temperature ranging from 10 to 60 min at 1700°F to 2 to 4 min at 2500°F . Ring compression specimens were cut from the cladding sections and were deformed by impact at temperatures to 1900°F in an inert gas atmosphere. The most

important result of these tests was that they provided a definite relationship between steam exposure conditions and the zero-ductility temperature (ZDT) of the material.

Exposure of a Zircaloy surface to steam at elevated temperatures produces a characteristic microstructure across the tube wall: ZrO_2 on the outer surface, a region of oxygen-stabilized α -phase (stable at the elevated temperatures in question) immediately below the oxide, and, below this, α -phase that transformed from the β -phase upon cooling. The α transformed from the β -phase is the only material in the tube wall that exhibits any ductility. Our specimens were exposed to steam on both the inner and outer surfaces, producing a symmetrical arrangement of the above phases about the midwall of the tube. We believe this is justified by the fact that, for a pressurized-water reactor, temperatures above about 1700°F will cause cladding rupture no matter at what time in reactor life the accident (LOCA) is assumed to take place. After rupture both surfaces are exposed to steam.

Our specimens are characterized by a parameter, ξ , which represents the combined thicknesses of ZrO_2 and oxygen-stabilized α on one surface. A plot of ξ vs the square root of exposure time yielded a set of straight lines, each corresponding to a different exposure temperature. The slopes of these lines were fitted to an equation with temperature ($^{\circ}\text{F}$) as the variable:

$$\frac{d\xi}{d\sqrt{t}} = 1.08 \times 10^{-5} T + 5.15$$

$$\times 10^{-5} e^{0.0168(T-2200)} - 1.7 \times 10^{-2}$$

This empirical equation allows ξ to be calculated directly from any given temperature-vs-time curve for a LOCA. Any postulated LOCA transient curve can be fitted by n th-order regression analysis, the resulting equation for temperature as a function of time substituted into the equation above, and that expression integrated by Simpson's rule or its equivalent over the appropriate time interval. Therefore, for any given LOCA transient curve, we can obtain a value for ξ . This value can then be used to find the ZDT.

One finding of this study that needs continuing emphasis is the rapidity with which the rate of the Zircaloy-steam reaction changes with temperature, with a parallel increase in the rate of oxygen penetration into the cladding. For instance, our experimental data show that isothermal exposures for 4 min at 2100, 2300, and 2500°F produce cladding with zero ductility below room temperature, 300, and 1900°F , respectively.

Notice the large increase in the ZDT on increasing the exposure temperature from 2300 to 2500°F. Extrapolation of our data to 2700°F indicates that a 12-sec isothermal exposure to steam at that temperature would produce a ZDT of 2000°F.

METALLURGICAL SUPPORT

D. O. Hobson

Study of specimens produced outside the Division in various experiments connected with the fuel rod failure program has continued. We have been concerned

principally with metallographic examination and microhardness measurements on various sections of fuel cladding from the TREAT tests.³ Our results have been consistent with the history of the specimens and with their post-test behavior. All metallurgical support findings have been integrated into our other experimental work to help produce a clearer understanding of the consequences of a LOCA.

3. R. A. Lorenz et al., *Final Report on the First Fuel Rod Failure Transient Test of a Zircaloy-Clad Fuel Rod Cluster in TREAT*, ORNL-4635 (March 1971).

Part VI. Other Program Activities

38. Metallography

R. J. Gray

Technical services are provided by three metallography groups. Nonradioactive and alpha radioactive materials are prepared by the General Metallography Group. Radioactive materials requiring mild or heavy shielding facilities are prepared by the Radiation Metallography Group, and examinations of specimens from both these groups requiring microprobe analysis and scanning electron microscopy are the responsibility of the Electron Metallography Group. Each of these groups has technicians who provide special talents for the required investigations. Each also has technical personnel who take special problems for study as well as improve and extend our capabilities.

ELECTRON MICROPROBE ANALYSIS

R. S. Crouse H. V. Mateer
T. J. Henson J. L. Miller, Jr.

While performing service analyses over the past year, we explored the limits of analytical capabilities of the electron beam microprobe analyzer. We used both the MAC model 400S in the cold laboratory and the MAC model 450 shielded microprobe in the HRLEL.

A request that tested the detectability limit of the model 400S required the analysis of La_2O_3 evaporated onto the surface of a crystal of NaCl. The La_2O_3 had been evaporated on only part of the surface, and part of the crystal was assumed to be bare. The average thickness of the film was known to be about 150 Å. An accelerating voltage of 11 kV was used so as to excite as little of the substrate NaCl as possible. We assumed that the x-ray intensity of lanthanum would be proportional to the thickness of the film. Because of the very small amount present, long counting times (100 sec) were used, and much of the work was done after working hours to minimize variations in line current, stray

magnetic fields, and interruptions by visitors. A step scan from well within the film across the edge onto the bare NaCl formed a profile of the La_2O_3 . The minimum thickness we could detect was 10 ± 4 Å, or two or three monolayers.

Several years ago an empirical method of correcting x-ray intensity ratios for absorption, secondary fluorescence, and atomic number was developed by Ziebold and Oglivie.¹ Using a programmable calculator, we can routinely correct our raw data. Since most of our analyses do not generate masses of numbers, this procedure is sufficiently accurate and less time-consuming than other available computer services.

The beam scanning capability of the microprobe enabled us to characterize features in an oxide layer on a U-Nb-Zr alloy at magnifications above our optical capability. Optically one could see suggestions of columnar crystallites in the oxide. Using the beam scanning system of the microprobe in the backscattered electron and x-ray modes resolved the crystallites at 2000X and showed them to be enriched in niobium. Figure 38.1 illustrates this analysis.

The beam scanning system of the microprobe is the same in principle as that on a scanning electron microscope and is used in the same manner, although it is not nearly as flexible. Figure 38.2 shows the fractured surface of a nickel fusion weld. Microspheres of almost pure iron, 50 to 300 μm in diameter, were found, displayed in the secondary electron mode, and qualitatively analyzed at essentially the same time. The brittle behavior of the weld was attributed to sulfur detected on the surface.

The most accurate microprobe analyses use homogeneous standards in the composition range of the

1. T. O. Ziebold and R. E. Oglivie, *Anal. Chem.* 36, 322-27 (1964).

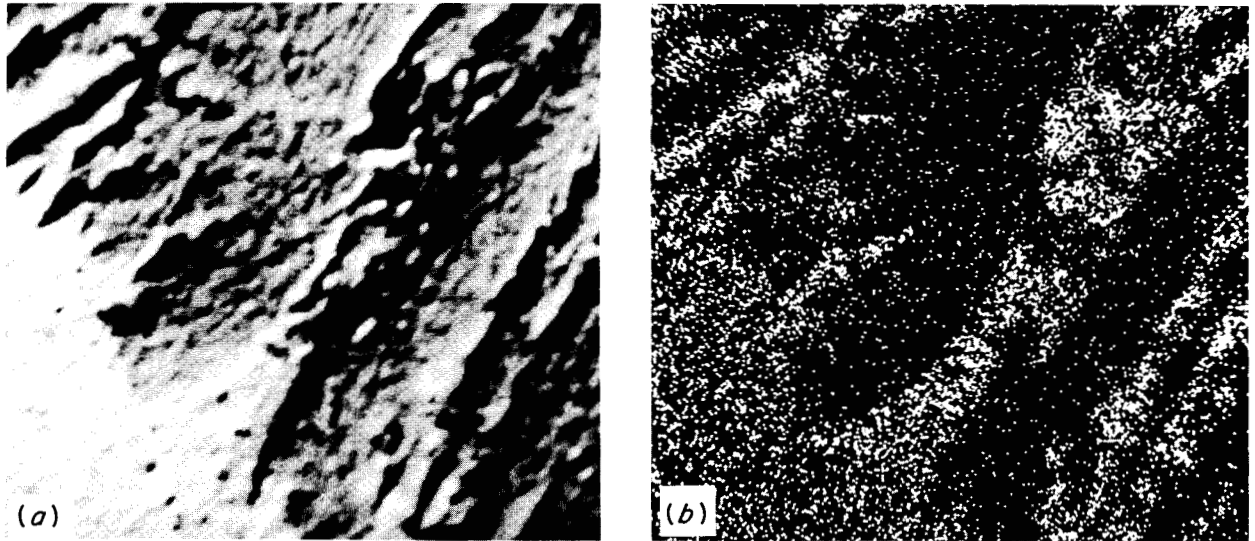


Fig. 38.1. Niobium distribution in oxide layer on a uranium alloy. 2000X. (a) Image shown by backscattered electrons. The metal is the light phase in the lower left, and the darker ridged phase is the oxide. (b) Display of Nb L α x rays from the same area.

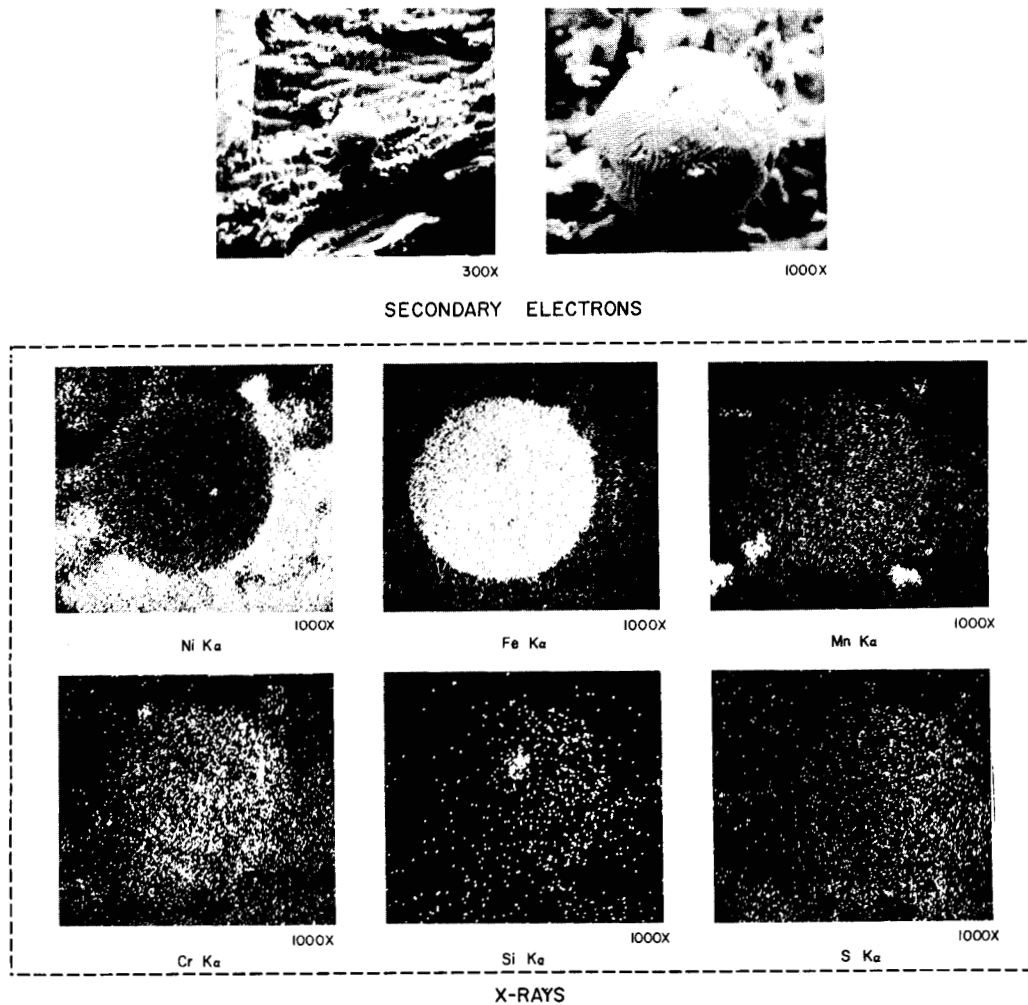


Fig. 38.2. Elemental characteristics of an iron microsphere found on the surface of a fracture of a nickel weld. Reduced 22%.

unknown. Such standards are seldom available. We were supplied with standard niobium-molybdenum alloys by the Solid State Division for an analysis related to loss of molybdenum on annealing such alloys. We determined the radial distribution of molybdenum in two alloy rods, one as zone leveled and one annealed 2.5 hr. Comparing intensities with the standards (Fig. 38.3) showed no loss of molybdenum in the former rod but a drop from 4.5% Mo in the center to 2.6% Mo at the edge of the annealed rod.

Some very excellent correlation of elemental segregation with microstructure was done on some niobium-stabilized steel. Niobium segregated in grain boundaries in the heat-affected zone of a weld. Figure 38.4

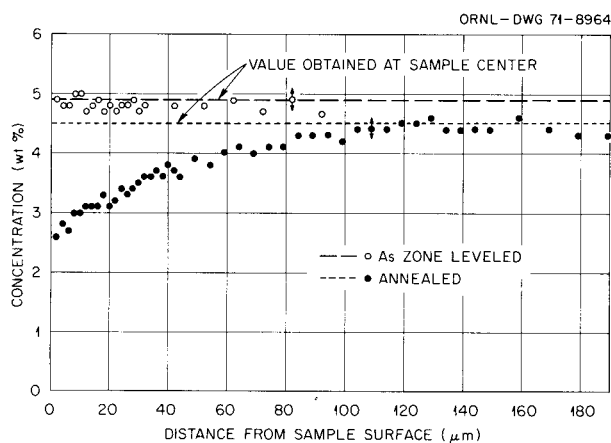
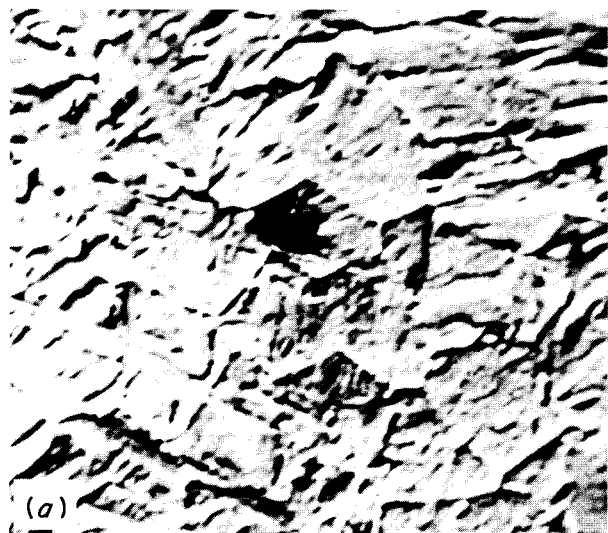


Fig. 38.3. Molybdenum distribution in niobium-molybdenum rods, showing loss on annealing.



illustrates this visual correlation as performed with the microprobe. A backscattered electron display produced a photomicrograph not unlike an optical phase contrast display, and a display of Nb $L\alpha$ x rays shows exactly where the niobium was enriched.

Data obtained with the shielded microprobe is reported elsewhere. However, the types of analyses may be summarized as follows:

1. identification of unknown metallic phases in irradiated materials,
2. detection of elements apparently causing degradation in fuel microspheres,
3. determination of uranium and plutonium to obtain redistribution of plutonium in mixed oxide fuel pins,
4. qualitative determination of fission product distribution in irradiated fuel pins,
5. measurement of elemental gradients in MSRE surveillance samples and in heat exchanger and sample cage rod sections.

With the present shielded microprobe we cannot locate areas to be probed and accurately position the electron beam. An improved electron beam scanning system will be installed to rectify this.

We are obtaining a scanning electron microscope and glove box to examine contaminated and radioactive samples. We hope to be able to develop a system and operating techniques that will permit us to examine radioactive and nonradioactive samples interchangeably.

Y-104905

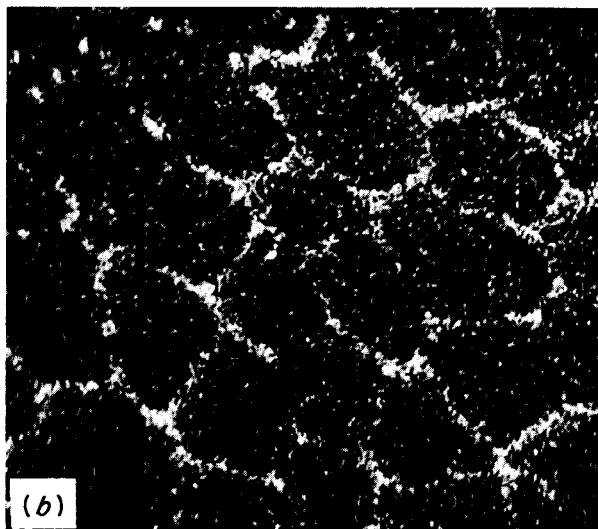


Fig. 38.4. Grain boundary segregation in niobium-stabilized steel. (a) Image shown by backscattered electrons. (b) Display of Nb $L\alpha$ x rays.

ALPHA METALLOGRAPHY FACILITY

R. J. Gray B. C. Leslie
H. R. Gaddis

The alpha metallography facility² was moved from Building 3019 to Building 4508. As shown in Fig. 38.5, the move was completed and preparation of alpha-emitting samples began in the new laboratory on February 26, 1971.

Advantage was taken of the downtime during the move to evaluate and upgrade the glove box suite and its equipment. A T-box with an evacuation transfer chamber was added to the line to isolate the etching box from the remainder of the boxes. Acid fumes and water vapor generated in the etching process can be contained within this one box to protect the moisture-free argon in the remainder of the line. New covers were designed and installed on the syntron polishing units to eliminate vaporization of the polishing vehicle during extended periods of operation. New sample holders for these units, fabricated from nylon and epoxy resin with lead inserts, were added to prevent microscopic fragments of metal from being removed from the stainless steel holders during polishing and embedded within the pores of ceramic samples. A xenon lamp and cooling chamber replaced the carbon arc lamp with the metallograph. The xenon lamp³ provides much better light-

ing and aids greatly in all phases of photography. A combustible gas detector with four monitoring stations was installed in the box line for use with an air atmosphere.

ETCHING OF TYPE 308 STAINLESS STEEL WELD METAL

T. M. Kegley

Etching procedures for identifying and differentiating the constituent phases in austenitic stainless steel have been reported,⁴⁻⁶ but none has been applied to

2. R. J. Gray, B. C. Leslie, H. R. Gaddis, and J. W. Chumley, *Metals and Ceramics Div. Annu. Progr. Rept. June 30, 1970*, ORNL-4570, pp. 220-21.

3. R. J. Gray and B. C. Leslie, *Metals and Ceramics Div. Annu. Progr. Rept. June 30, 1970*, ORNL-4570, p. 222.

4. G. N. Emanuel, "Metallographic Examination of Sigma in 25-20 Austenitic Alloy," *Metal Progr.* 52, 78 (1947).

5. E. J. Dulis and G. V. Smith, "Identification and Mode of Formation and Resolution of Sigma Phase in Austenitic Chromium-Nickel Steels," pp. 3-29 in *Symposium on the Nature, Occurrence and Effects of Sigma Phase*, ASTM STP-110, American Society for Testing Materials, Philadelphia, 1951.

6. John J. Gilman, "Electrolytic Etching - The Sigma Phase Steels," *Trans. Amer. Soc. Metals* 44, 566 (1952).

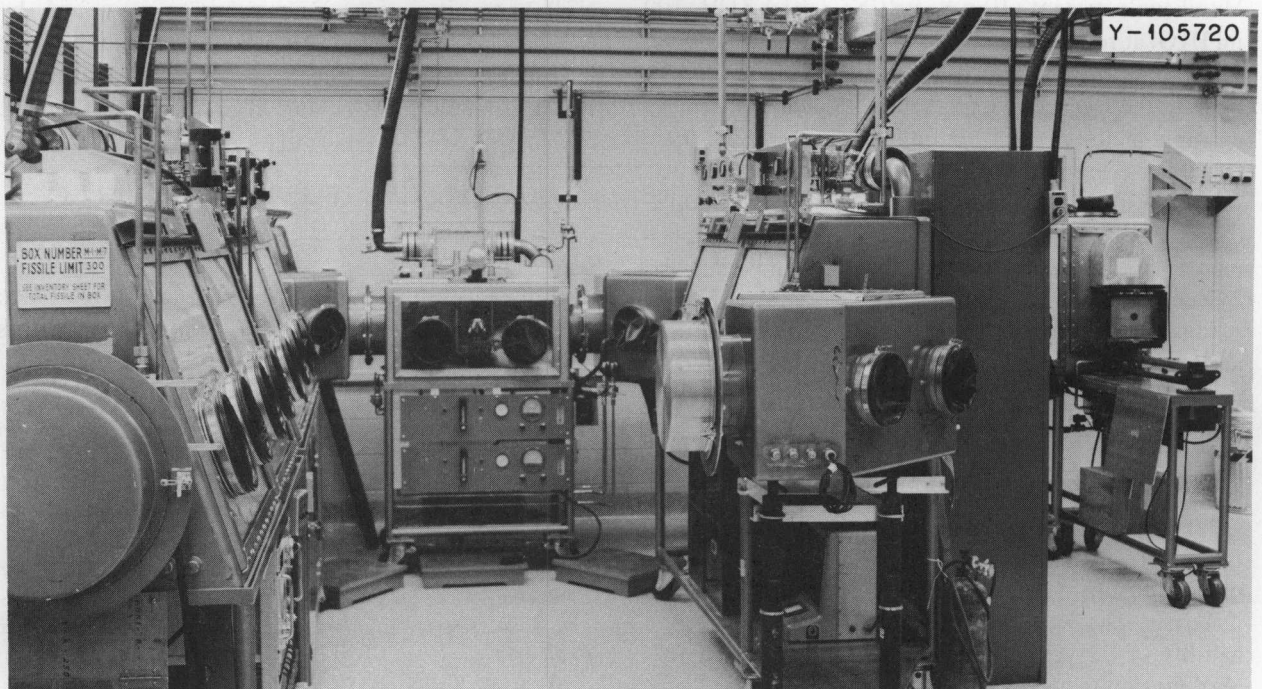


Fig. 38.5. Alpha metallography facility in new location. Numerous small but highly important improvements have been incorporated in the reinstallation.

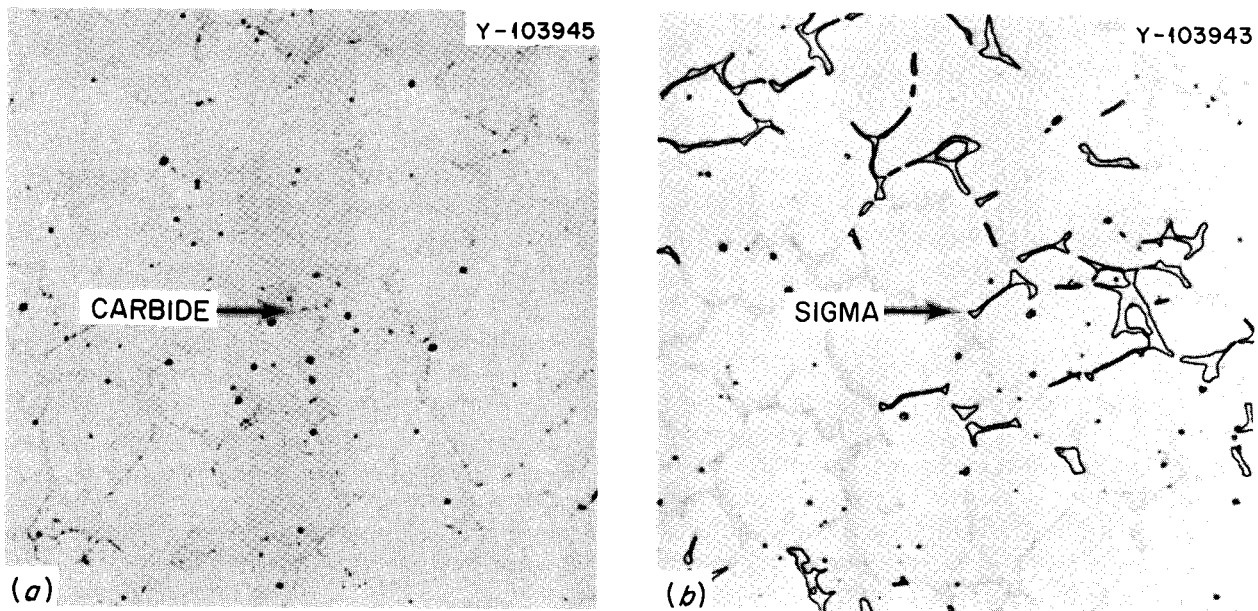


Fig. 38.6. Type 308 stainless steel weld metal heated 10 hr at 800°C. (a) Etched 1 min at room temperature in Murakami's reagent. (b) Etched 4 sec at room temperature in modified Murakami's reagent.

identify the constituents of stainless steel weld metal. Although the electrolytic etching method proposed by Gilman⁶ was quite effective, the chemical method proposed by Emmanuel⁴ proved equally effective and yet needed no electrical contacts. Emmanuel employed Murakami's reagent (10 g $K_3Fe(CN)_6$, 10 g KOH, 100 ml H_2O) at room temperature to etch carbide and modified Murakami's reagent (30 g $K_3Fe(CN)_6$, 30 g KOH, 60 ml H_2O) at room temperature to etch σ -phase. An example of the microstructure obtained by using these reagents is given in Fig. 38.6, which shows type 308 stainless steel weld metal after 10 hr at 800°C (1492°F). Carbide was etched by immersing the specimen 15 to 60 sec in Murakami's reagent, and sigma was etched by immersing the specimen 3 to 5 sec in modified Murakami's reagent. Both reagents were used at room temperature.

BETA AUTORADIOGRAPHY

T. M. Kegley, Jr.

Beta autoradiography was used to show the distribution of nickel in welds made using Inconel 82 filler metal to join Incoloy 800 and Inconel 625 base materials. The weld wire contained ^{63}Ni , which has a half-life of 92 years and emits beta particles of 0.067 MeV maximum energy.

A contact autoradiograph was obtained by exposing Kodak Royal Pan sheet film for 20 hr to radiation from a metallographic section taken from a multipass weld.

The macrograph of the contact autoradiograph presented in Fig. 38.7(a) shows the nonhomogeneous distribution of nickel, particularly in the root pass of the weld. A microautoradiograph of the same weld was prepared by placing Kodak nuclear track emulsion NTB-2 on the polished surface, as described by Gehlbach et al.,⁷ exposing 48 hr, and developing. The microautoradiograph, which shows the interface between the weld and Incoloy 800, is presented in Fig. 38.7(b).

QUANTITATIVE TELEVISION MICROSCOPY

T. M. Kegley, Jr.

Although evaluation of the Quantimet Image Analyzing Computer⁸⁻¹⁰ continues, greater emphasis has

7. R. E. Gehlbach, M. D. Allen, and J. D. Braun, "Autoradiographic Study of Carbon-14 in Hastelloy N," pp. 113-18 in *Proceedings, First Annual Technical Meeting, International Metallographic Society, Inc., November 11, 12, and 13, 1968 - Denver, Colorado, U.S.A.*, ed. by K. A. Johnson and J. H. Bender, International Metallographic Society, Inc., Los Alamos, N.M., 1969.

8. T. M. Kegley, Jr., *Metals and Ceramics Div. Annu. Progr. Rept. June 30, 1970*, ORNL-4570, pp. 222-23.

9. T. M. Kegley, Jr., *Metals and Ceramics Div. Annu. Progr. Rept. June 30, 1969*, ORNL-4470, pp. 216-17.

10. T. M. Kegley, Jr., "Quantimet Area Measurement Problems," pp. 163-69 in *Proceedings of Second Annual Technical Meeting, International Metallographic Society, Sept. 8-10, 1969, San Francisco, Calif.*, International Metallographic Society, Los Alamos, N.M., 1970.

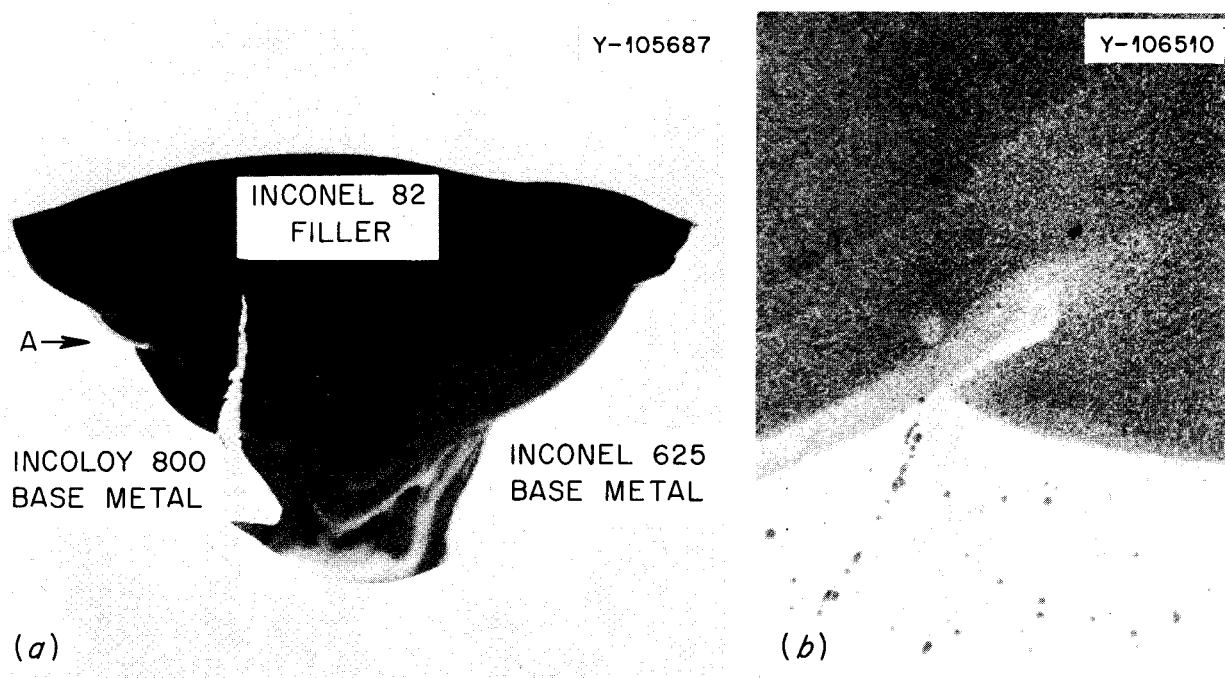


Fig. 38.7. Autoradiograph of metallographic section through multipass weld made with filler metal containing ^{63}Ni . (a) Contact autoradiograph. 6X. (b) Microautoradiograph of region about A. Base metal is Incoloy 800 and filler metal is Inconel 82. 50X.

been directed toward service work. This involves the analysis of both metallographic specimens, which require use of the microscope, and photomicrographs, which require the epidiascope. Previously, to attach the epidiascope, we had to remove the microscope from the control unit where the television camera was located. This required about one hour and usually required optical alignment. To avoid this problem, we obtained a second television camera and constructed a stand for the epidiascope, so the second camera could be mounted permanently to it. The microscope was then mounted permanently to the control unit. Plugs were installed on the control unit so cables from either camera could be connected, so a change from the microscope to the epidiascope required only switching camera cables. The new arrangement should expedite the flow of service work by ending the natural reluctance to switch from one setup to the other.

REVEALING FERROMAGNETIC PHASES WITH FERROFLUIDS

R. J. Gray

Magnetic domain patterns on ferromagnetic phases have been observed for many years with a suspension of

colloidal magnetite in a magnetic field. Bitters¹¹ and independently von Hamos and Thiessen¹² first observed these patterns with relatively macroscopic results using iron powder. In the interim, many improvements have been reported;^{13,14} however, a continuing major difficulty is to find a recipe for making a suitable stable colloid. We tried a commercial product¹⁵ not designed for the described purpose and found it to be highly satisfactory. It is extremely stable, has 100 to 300 Å particle size, and is quite simple to use. We observed stainless steel welds macroscopically and domain patterns in δ -ferrite in stainless steel welds and cast stainless (Fig. 38.8) at 1000X with very satisfactory results.

11. F. Bitter, *Phys. Rev.* **38**, 1903 (1931).

12. L. von Hamos and Thiessen, *Z. Phys.* **71**, 442 (1931).

13. R. Cary and E. D. Isaac, *Magnetic Domains and Techniques for Their Observation*, Academic Press, New York, 1966.

14. M. F. Bowman and A. D. Booth, *Metallography* **4**, 103–31 (1971).

15. Ferrofluid (water base), Ferrofluids Corp., Burlington, Mass.

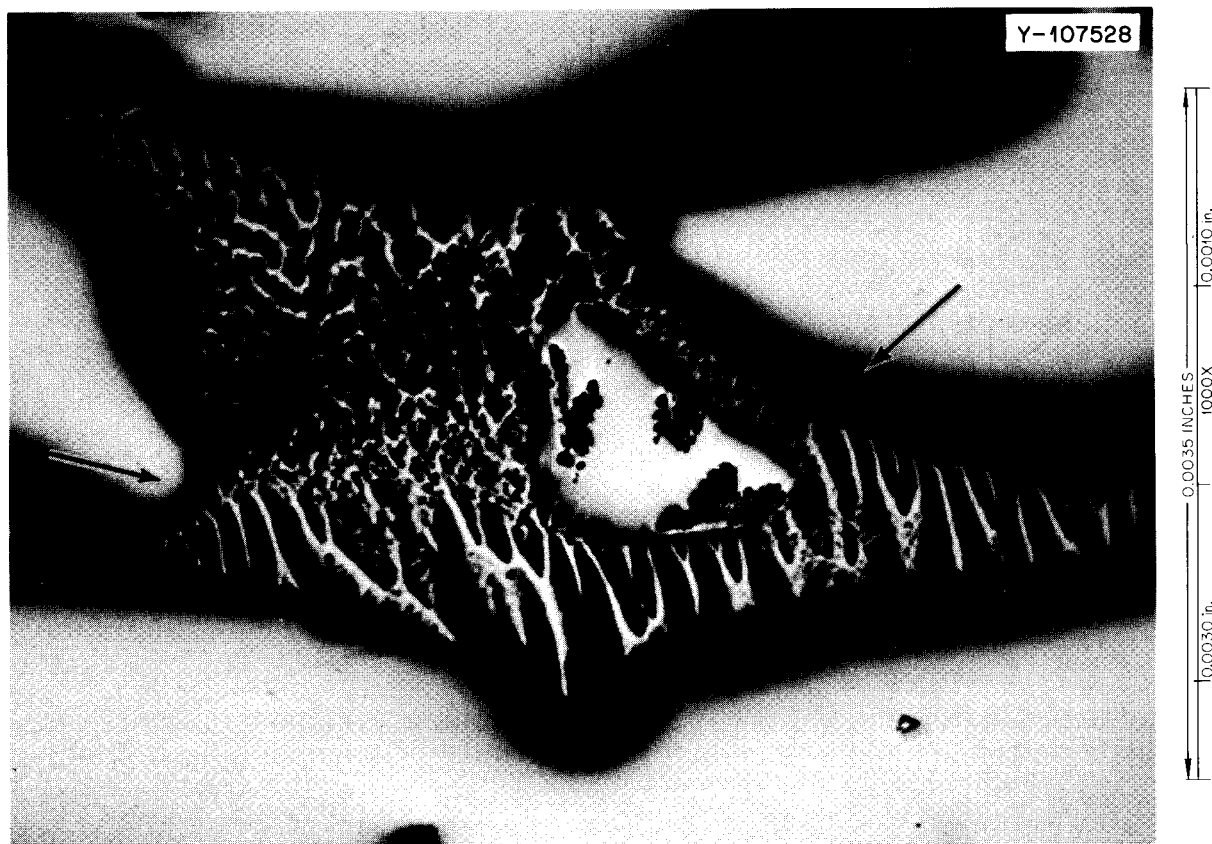


Fig. 38.8. Magnetic domain patterns in δ -ferrite. Note the change in the pattern (arrows) indicating a possible subgrain boundary. 1000X.

IMPROVED METALLOGRAPH ILLUMINATION SYSTEM

R. J. Gray B. C. Leslie

Earlier developments and application¹⁶ of a retrofit xenon lamp system for older metallographs were extended.¹⁷ Light beam temperatures of carbon arc and 450-W xenon illumination systems were compared. The alignment procedure — an important step for a safe, long operation of the lamp — for the 450-W retrofit system was described.

16. R. J. Gray and B. C. Leslie, *Metals and Ceramics Div. Annu. Progr. Rept. June 30, 1970*, ORNL-4570, p. 222.

17. R. J. Gray and B. C. Leslie, "More on the Metallographic Applications of Xenon Lamp Systems," pp. 65-73 in *Proceedings, Third Annual Technical Meeting, International Metallographic Society, Nov. 16-18, 1970, Cleveland, Ohio*. International Metallographic Society, Los Alamos, N.M. 1971.

EXAMINATION OF THE ALCO/BLH STEAM GENERATOR

Photography

B. C. Leslie E. P. Griggs
W. E. Denny J. W. Nave

We are using both still photography (color and black and white) and video tape recordings (Fig. 38.9) to show the disassembly operations in the dissecting of the steam generator. To date, we have made over 90 still photographs and have taped three reels (90 min) showing the dissecting operation. When the examination is completed, the video tape will be edited to delete repetitious operations and add narration.

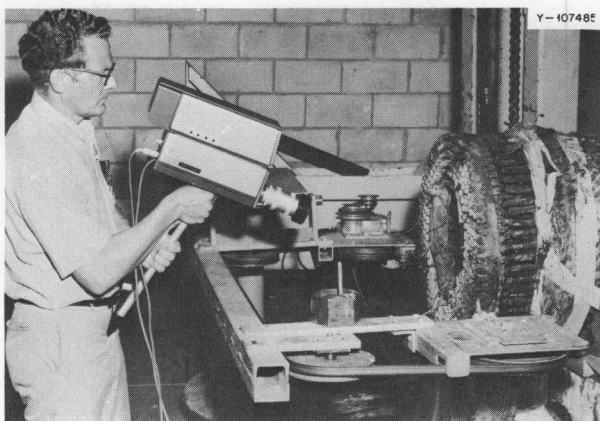


Fig. 38.9. Audio-video taping of the cutting of tube bundles near the top tube sheet of steam generator.

Metallography

B. C. Leslie C. P. Haltom
H. V. Mateer T. J. Henson
H. R. Gaddis C. E. Zachary

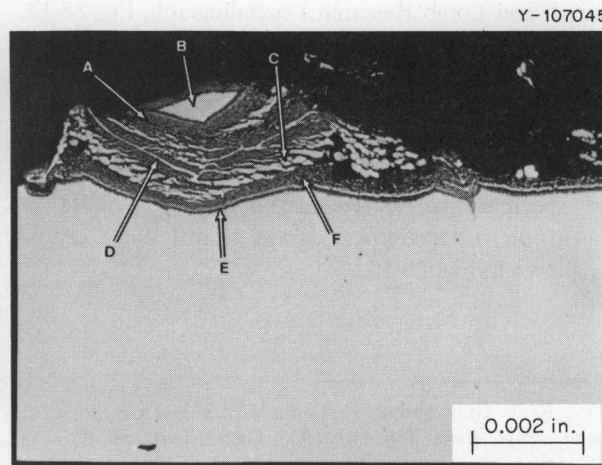
Metallographic examination of areas of interest has started. We have examined a few tubing samples from the lower tube sheet and shell samples from both the sodium and gas blanket regions. Figure 38.10 shows the microstructure and the electron beam microprobe analysis of a reaction product from a shell sample located about 5 in. from the top tube sheet in the gas blanket region of the steam generator. We are examining samples from the lower tube sheet, including tube ends, tube welds, header and shell welds, and other samples necessary to determine the cause of failure.

OPTICAL ANISOTROPY FACTOR STUDIES

R. J. Gray D. M. Hewette II

Microscopic equipment was designed for measuring reflectance intensities of coatings on fuel microspheres. Reflectance characteristics of areas 5 to 15 μm in diameter are measured with a plane-polarized light source and a microphotometer. Optical anisotropy factor (OPTAF¹⁸) values near 1.0 indicate a low optical

18. $\text{OPTAF} = I_{\text{max}}/I_{\text{min}}$, where I_{max} and I_{min} are the maximum and minimum intensity of the same microscopic field during 360° rotation.



	Ni	Fe	Cr
Area A	10.6	41.9	14.9
B	11.9	67.0	20.9
C	4.9	77.7	6.9
D	5.9	83.3	10.7
E	17.5	49.2	14.4
F	12.5	44.5	17.5
Base Metal	12.2	64.1	21.3

Fig. 38.10. Microstructure and electron beam microprobe analysis (wt %) of a reaction product from a shell sample of the steam generator.

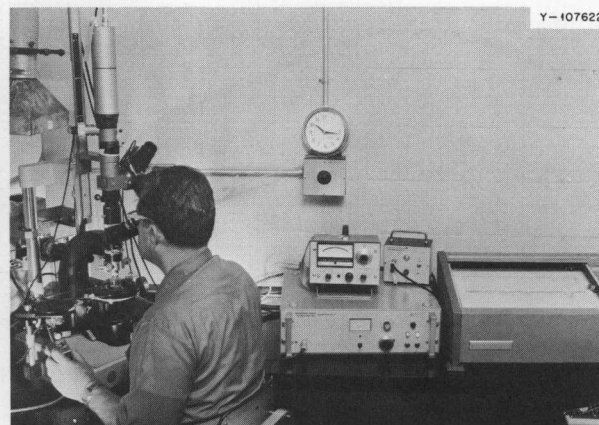


Fig. 38.11. Leitz microscope adapted for examination of nonradioactive materials in OPTAF studies.

anisotropy, a desirable characteristic for stability during exposure to radiation. A Leitz microscope, Fig. 38.11, has been adapted for the examination of nonradioactive materials, and a Reichert microphotometer and a

Bausch and Lomb Research I metallograph, Fig. 38.12, have been adapted for our glove box metallograph^{19,20} for the evaluation of coatings on alpha-radioactive fuels.

For standardization, a single crystal of graphite was measured normal to the *c* axis and normal to the *a* axis. The *c* axis should display an isotropic characteristic as the specimen is rotated and the *a* axis should be anisotropic. Characteristic curves of this single crystal are shown in Fig. 38.13.

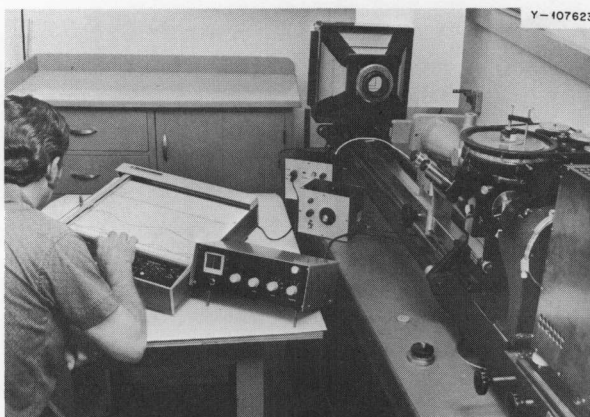


Fig. 38.12. Reichert microphotometer and Bausch and Lomb research I metallograph adapted for glove box evaluation of coatings on alpha-radioactive fuels.

19. R. J. Gray and B. C. Leslie, *Metals and Ceramics Div. Annu. Progr. Rept. June 30, 1968*, ORNL-4370, pp. 230-31.

20. R. J. Gray, B. C. Leslie, H. R. Gaddis, and J. W. Chumley, *Metals and Ceramics Div. Annu. Progr. Rept. June 30, 1969*, ORNL-4470, pp. 213-15.

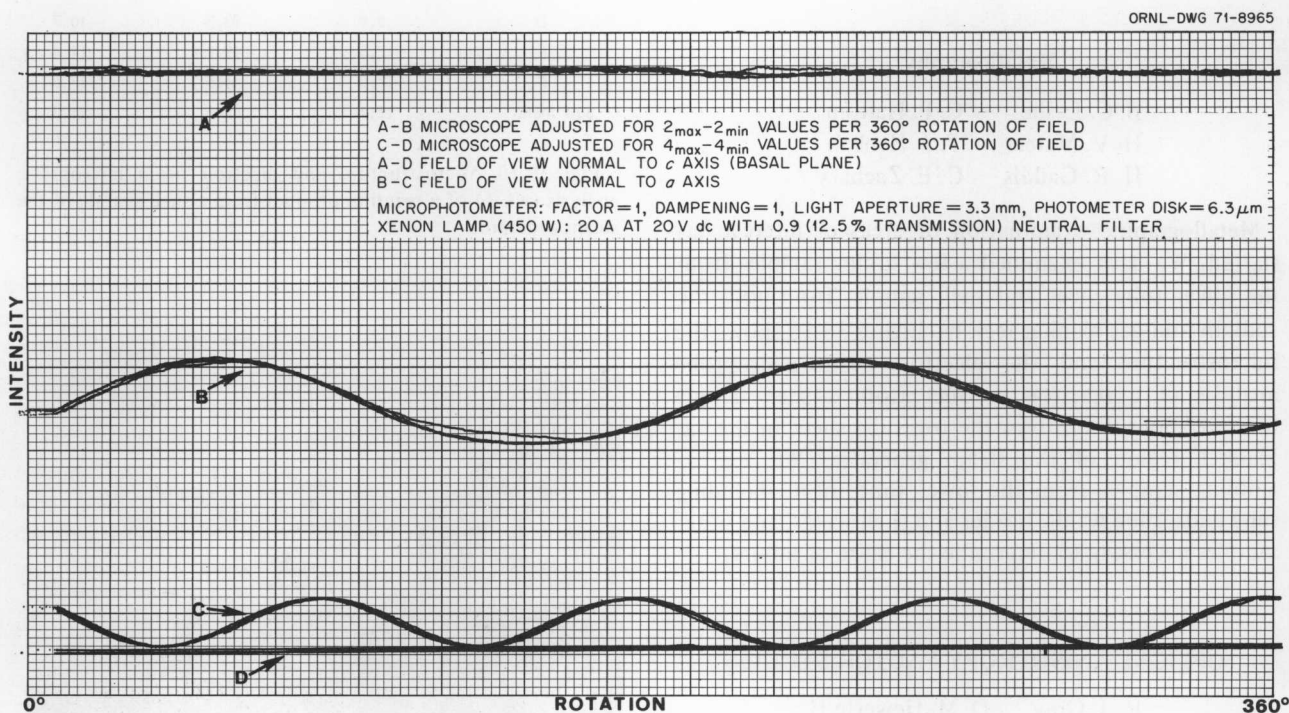


Fig. 38.13. Characteristic reflection curves of graphite single crystals.

39. NERVA Program Metallurgical Support

R. E. Clausing

We continue to provide support for the Materials and Structures Branch of the AEC-NASA Space Nuclear Systems Office on the NERVA Program.¹⁻³ We provide technical consultation for NASA and its contractors and also perform experimental work including studying (1) outgassing characteristics of NERVA fuel elements, (2) adhesion and friction of NERVA materials and components in simulated space environments, and (3) selected physical properties of NERVA materials.

EFFECTS OF SPACE ENVIRONMENT ON NERVA MATERIALS

R. E. Clausing

Exposure of the NERVA engine to the environment of space may produce materials problems not encountered in ground tests. The tendency of atomically clean surfaces to adhere and for friction and wear to increase are important space-related phenomena. Adhesion and friction of clean surfaces are not well understood, but the presence or absence of adsorbed gases on otherwise atomically clean surfaces is known to alter adhesional and frictional properties of both pure materials and engineering alloys. To assess the importance of these effects on the materials in the NERVA system we need to know (1) the specific environment at the location of particular components in the engine and (2) how this environment will influence adhesion and friction. We are providing information on both of these subjects through the two experimental studies described below.

1. R. E. Clausing et al., *Metals and Ceramics Div. Annu. Progr. Rept. June 30, 1968*, ORNL-4370, pp. 235-37.

2. R. E. Clausing et al., *Metals and Ceramics Div. Annu. Progr. Rept. June 30, 1969*, ORNL-4470, pp. 218-21.

3. R. E. Clausing et al., *Metals and Ceramics Div. Annu. Progr. Rept. June 30, 1970*, ORNL-4570, pp. 224-27.

Outgassing of NERVA Fuel Elements

R. E. Clausing D. S. Easton

The gaseous atmosphere at any point in the NERVA engine will depend upon the temperature and history of the entire engine system; in the present design it will be determined primarily by the outgassing of the fuel elements and graphite reactor components. This outgassing cannot be accurately estimated because of the special nature of the core material, its configuration, and its coating. Experimental data has been obtained for the prototype core elements at temperatures and pressures similar to those expected in space operation.

The facility to provide outgassing data was previously designed, built, tested, and put into operation.¹⁻³ Several reports describe the apparatus, the data processing, and the results obtained for the outgassing of graphite fuel elements of the XE II type.⁴⁻⁷ The outgassing of each gaseous species can be described by the equation $q = A(t/t_0)^B$, where q is the outgassing rate in torr liters per second, t is the time in hours, and A and B are empirical constants. The desorption constants A and B have been tabulated⁴ for 13 gases at seven temperatures from 50 to 870°C. The data are for XE II fuel elements pretreated to simulate conditions before and after the first rocket firing. These data have been used to predict the gaseous environment in a NERVA engine during operation in space. Figure 39.1

4. D. S. Easton and R. E. Clausing, "Outgassing of Nuclear Rocket Fuel Elements," *J. Vacuum Sci. Technol.* 7, S116-23 (1970).

5. D. S. Easton, S. H. Merriman, C. L. Armstrong, and R. E. Clausing, *A Computer Program for Calculating, Tabulating, and Plotting Outgassing Rates of Selected Gases*, ORNL-TM-3220 (February 1971).

6. D. S. Easton and R. E. Clausing, "A Computer Program for Calculating, Tabulating, and Plotting Outgassing Rates of Selected Gases," *Scripta Met.* 5, 181-84 (1971).

7. D. S. Easton, C. L. Armstrong, S. H. Merriman, and R. E. Clausing, *A Program for Computing Partial Pressures from Residual Gas Analyzer Data*, ORNL-TM-3455 (in preparation).

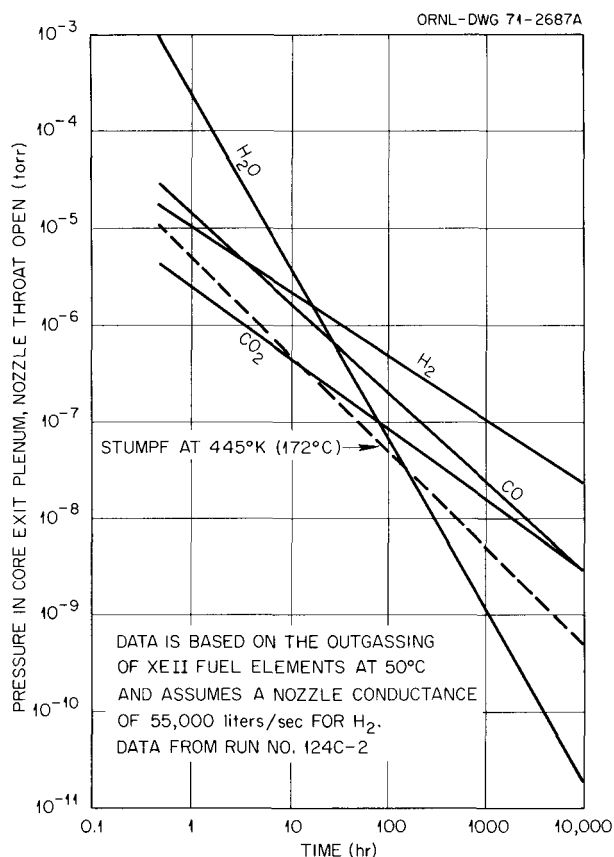


Fig. 39.1. Partial pressures in the NERVA engine reactor core exit plenum predicted from ORNL data for the outgassing of XE II fuel elements.

shows the predicted partial pressures for hydrogen, water vapor, carbon monoxide, and carbon dioxide in the reactor core exit plenum chamber as a function of time after initial exposure to the vacuum of space. Predictions of this same type are available for core temperatures from 50 up to 870°C after initial exposure to vacuum and over the same temperature range and for the period after the first firing of the engine.⁸

Adhesion and Friction of NERVA Materials

R. E. Clausing D. S. Easton

This program began with an adhesion study conducted at the Syracuse University Research Corporation under subcontract to ORNL.⁹⁻¹¹ Special emphasis was placed on determining the roles of surface contamination and shear motion in the adhesion of engineering materials of interest to NERVA. These studies combined a simple crossed wire sample configuration with contact resistance and force measure-

ments¹² to provide a preliminary evaluation of possible adhesion problems and to provide a guide for additional materials and component testing. Adhesion was obtained for engineering materials only after severe cleaning and high normal-force loading or after surface shearing motions. In all cases rubbing increased the tendency for adhesion, either by the growth of true contact area or by a disruption of contaminant films.¹¹ These results indicated the need for studying the frictional behavior of NERVA materials. The adhesion testing has been completed. The results of this program are reported elsewhere in detail.^{3,9-11}

With the above study as a guide we decided to conduct friction studies using materials, test geometries, and operating parameters as near to those expected in service as is practical and to measure the coefficient of friction or the component operating forces in the worst cases and the most critical cases. Apparatus has been designed and built for these tests. Three basic test configurations are available, (1) an angle of repose friction test (flat on flat) for measuring the static coefficient of friction, (2) a sinusoidal reciprocating motion (flat on flat) test for both static and dynamic friction, and (3) a components test module that provides instrumented motion of up to 2 in. in two dimensions with forces available up to 100 lb. All tests are operable from room temperature to 400°C in either ultrahigh vacuum or hydrogen at pressures up to 1 atm. Test temperatures up to about 870°C are possible under vacuum and down to 77°K in hydrogen.

The angle of repose test is being used to explore the frictional behavior of graphite. Figure 39.2 shows the result of one of the first tests on this apparatus. The material was P-03 graphite sliding on P-03 graphite tested at room temperature. The samples were not degassed before the test and were very lightly loaded.

The highest friction coefficient obtained was about 0.3 and occurred only after more than 800 hr in vacuum and more than 10⁵ cycles. This is to be

8. R. E. Clausing and D. S. Easton, *A Prediction of the Gaseous Environment inside a NERVA Reactor During Space Operations*, ORNL report in preparation.

9. R. G. Aldrich, *Ultra High Vacuum Adhesion Testing of NERVA Engine Materials*, TID-25088 (July 1968).

10. R. G. Aldrich and D. V. Keller, Jr., "Application of Static Metallic Adhesion Data to Friction," *J. Vac. Sci. Technol.* 7, S82-89 (1970).

11. R. G. Aldrich, *Ultra High Vacuum Adhesion Testing of NERVA Engine Materials, Final Report*, ORNL subcontract 3245.

12. K. I. Johnson and D. V. Keller, *J. Appl. Phys.* 38, 1896-1904 (1967).

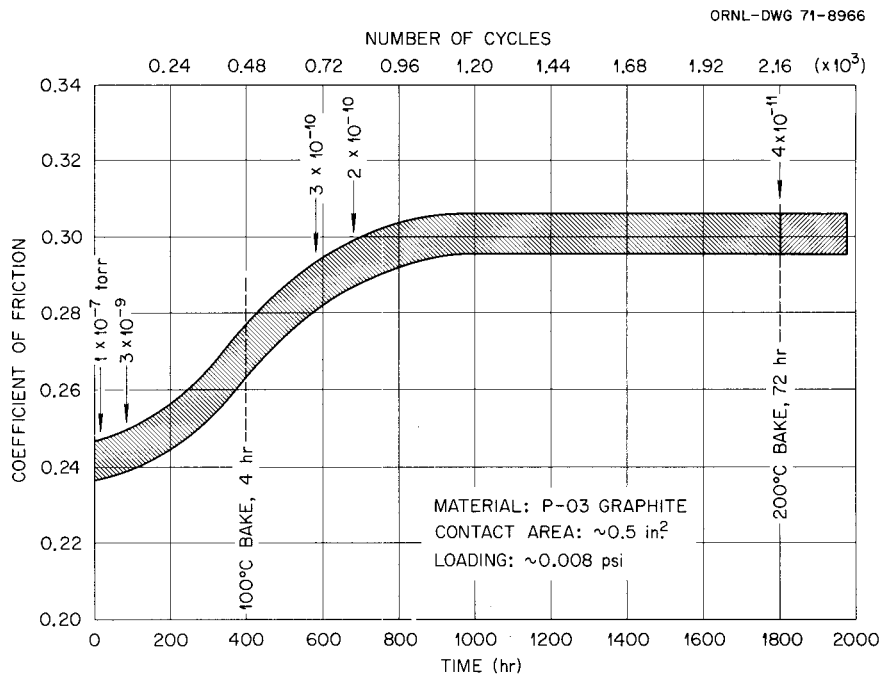


Fig. 39.2. Coefficient of friction for P-03 graphite on P-03 graphite in vacuum for a very light load (0.008 psi).

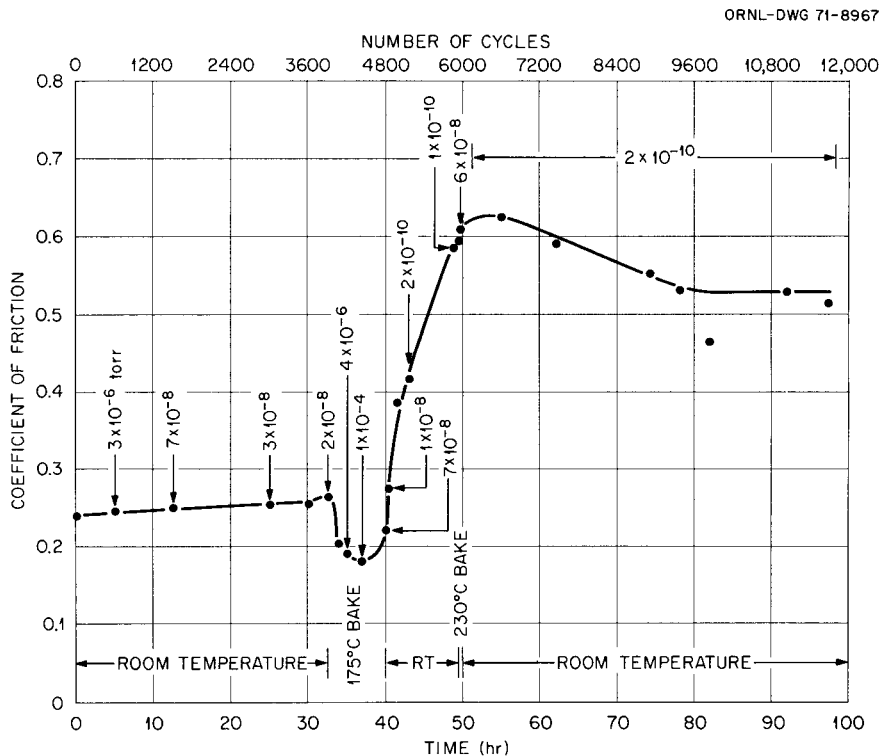


Fig. 39.3. Coefficient of friction for P-03 graphite on P-03 graphite in vacuum for a heavier load (20.6 psi).

contrasted with values above 0.6 found in the literature for graphite on graphite under heavy loading. This result suggests that for graphite in vacuum wear is important in the development of high coefficients of friction. Baked graphite and ultrahigh vacuum per se are not sufficient. Wear occurs rapidly under high loads, so additional tests were conducted under similar conditions except for increased normal force loading. A normal force load of 20.6 psi produced coefficients of friction above 0.6, but only after the sample was baked in situ 7.5 hr at 175°C. Operation in vacuum for 32 hr and 3600 cycles before the bake gave coefficients of 0.24 to 0.25. Figure 39.3 shows these results. The test temperature is room temperature except when indicated otherwise. Both wear and freedom from surface contamination appear necessary for graphite to develop high coefficients of friction in vacuum. The bakeout removes the sources available to contaminate the surface as it wears.

Regular operation of the second test method is just beginning, and components are not ready for testing by the third method.

THERMAL CONDUCTIVITY OF P-03 GRAPHITE

J. P. Moore R. S. Graves D. L. McElroy

Thermal conductivity (λ) measurements were completed from 300 to 1000°K in the radial heat flow

apparatus on isostatic molded grade P-03 graphite. We measured λ with heat flow perpendicular to and parallel to the molding axis of two blocks. For all four samples λ decreases with increasing temperature. The thermal resistivity, λ^{-1} , depends linearly on temperature from 475 to 1000°K with the coefficients shown in Table 39.1. The raw λ data are described to about $\pm 0.5\%$ by these equations. Thermal conductivity values near 375°K deviate about 4% from the equation, reflecting a maximum in λ as a function of T . Previous low-temperature λ measurements¹³ on another P-03 sample are 9% lower than the B \parallel results at 400°K. The electrical resistivity, ρ , of rods machined from these blocks depended upon orientation and varied as much as 6% over the 7-cm rod length. Heat treatments to 1500°C did not remove this variation. Radiographs revealed the presence of a denser but unidentified phase distributed nonuniformly along the rod. The particle density appeared to correlate with ρ^{-1} .

13. J. P. Moore, R. S. Graves, D. L. McElroy, and W. P. Murray, *Metals and Ceramics Div. Annu. Progr. Rept. June 30, 1970*, ORNL-4570, pp. 226-27.

Table 39.1. Coefficients of thermal resistance of isostatic molded P-03 graphite

Block, direction	Density (g/cm ³)	A^a (W cm ⁻¹ deg ⁻¹)	B^a (W cm ⁻¹ deg ⁻²)	Electrical resistivity ($\mu\Omega$ -cm)
A \parallel	1.846	0.73736	0.989×10^{-3}	1423
A \perp		0.69435	1.014×10^{-3}	1460
B \parallel	1.852	0.79398	0.971×10^{-3}	1510
B \perp		0.71260	1.022×10^{-3}	1404

^aCoefficients of $\lambda^{-1} = A + BT$, (T in °K).

40. Powder Process Development for LWBR

J. D. Sease J. M. Leitnaker

The Light Water Breeder Reactor (LWBR) is being developed to demonstrate breeding with a thermal neutron spectrum in an existing light water reactor. This program is being principally carried out by the Bettis Atomic Power Laboratory (BAPL). Participation by ORNL involves the receipt and storage of about 750 kg of ^{233}U , its purification to remove ^{232}U daughters, conversion of uranyl nitrate to $^{233}\text{UO}_2$ powder at a rate of about 20 kg/week, packaging and shipping it to BAPL, and the recovery of ^{233}U scrap generated at ORNL and BAPL. Metals and Ceramics participation in this program is in conjunction with the Chemical Technology Division and is the development of processes and specifications for producing the uranium dioxide powder.

The UO_2 powder produced at ORNL will be blended (up to about 6%) with a thoria powder and pelletized. The UO_2 powder process developed uses gaseous ammonia to precipitate ammonium diuranate (ADU) from the nitrate solution, centrifugation to remove the ADU from its supernate, microwave heat for drying the ADU cake, and hydrogen reduction of the ADU at 600 to 700°C, followed by stabilization of the reduced powder. This process differs from usual UO_2 production processes in the centrifugation step and the use of microwave drying. Microwave drying appears to be attractive for commercial preparation of UO_2 , PuO_2 , and $(\text{U,Pu})\text{O}_2$ powders. Limited parametric studies were carried out in precipitation, centrifugation, drying, reduction, and stabilization. In addition to developing the $^{233}\text{UO}_2$ process specifications, we produced approximately 18 kg of fully enriched UO_2 powder by the developed processes for evaluation by BAPL.

PRECIPITATION

J. M. Leitnaker

The precipitation step involves the introduction of gaseous ammonia to a circulating solution stream to precipitate ADU. Gaseous ammonia was selected over aqueous because the additions could be controlled more

precisely. A factorial experiment was performed to determine the effects of free HNO_3 concentration in the uranyl nitrate solution, temperature of precipitation, time of digestion, and final pH on the surface area of the final powder. These variables caused the surface area of the UO_2 to vary from 5.8 to 10.4 m^2/g . The major effect (1.6 m^2/g) was caused by an interaction of temperature and free HNO_3 .

CENTRIFUGATION AND MICROWAVE DRYING

J. M. Leitnaker J. D. Sease

Centrifugation and microwave drying were chosen over the more conventional techniques of filtering and thermal drying to eliminate handling the moist ADU and reduce the in-process inventory. This is particularly important in handling powder with high fissile content (i.e., ^{235}U or ^{233}U) because of criticality consideration and material losses. The same Teflon container is used for both centrifugation and drying. In microwave heating, the precipitate cake can be dried in $1/4$ to $1/10$ the time required for conventional thermal drying. A study on the effect of drying temperature below 115°C and time showed little effect on surface area on the final reduced powder.

REDUCTION AND STABILIZATION

J. M. Leitnaker M. L. Smith¹

The dried ADU cake is reduced in two steps, the thermal decomposition of the ADU to UO_3 and then the reduction to UO_2 . In BAPL process, the ADU cake is first heated in argon and then at a predetermined temperature the argon is replaced by hydrogen. The temperature of reduction has an extremely important

1. Co-op student from Virginia Polytechnic Institute and State University.

effect on the surface area of the powder. For example, the surface area of a powder reduced at 400°C was 20 m²/g, compared to 7 m²/g at 600°C.

Stabilized UO₂ powder will not ignite on exposure to air and will not change appreciably upon storage. Ignition is caused by the heat released during the almost instantaneous surface reaction of the powder with air. Customary stabilization methods have been the use of dry ice, water, or various organic substances to protect the surface. The stabilization method developed for the BAPL process uses a thin bed of powder on a conducting surface to allow heat dissipation. In addition, we learned that if the surface area is kept below about 9 m²/g, not enough heat is released to ignite the powder in beds about 3/4 in. thick. Since each O₂ molecule occupies about 14 Å², a 9-m²/g powder would absorb approximately 0.028 mole O₂. A heat of absorption of 30 kcal/mole of O₂ leads to a computed heat of 860 cal/mole of UO₂, and hence a temperature rise of about 53°C. This rise, verified experimentally, is insufficient to cause ignition in our sample geometry. Reduced powders with a mean surface area below 9 m²/g may still require stabilization because of inhomogeneities in the powder.

We studied² room-temperature contamination of UO₂ powder during storage in air of varying moisture contents for several hundred hours. An initial rapid

chemisorption of oxygen was followed by a slow and independent sorption of water and oxygen. Both the slow sorption rates are nonlinear in the logarithm of time.

PRODUCTION OF ENRICHED POWDER

J. M. Leitnaker

We prepared 18 kg of fully-enriched uranium oxide powder in 500-g batches for testing at BAPL. Powder with surface areas from 19 to 4 m²/g were produced to test the effects of the powder preparation parameters on BAPL's pellet production. All powders produced satisfactory pellets. The target for the ²³³UO₂ powder production will be a 6 to 7 m²/g surface area. The general parameters for producing a powder of this characteristic are:

1. precipitate at pH 8 at 50°C,
2. centrifuge and microwave dry at 115°C,
3. reduce at 600°C with H₂ for 5.5 hr,
4. mechanically stabilize.

2. M. L. Smith and J. M. Leitnaker, *Atmospheric Contamination of Uranium Dioxide Powder*, ORNL 4704 (June 1971).

41. Reactor Evaluation

A. L. Lotts

Our purposes are to derive and maintain up-to-date methods for predicting the performance, capabilities, and cost of fuel fabrication for fuel elements of various designs and to evaluate reactor concepts of current interest. The fuel element performance and cost are significant factors in the economic production of power by nuclear reactors and must be examined in detail to assess the potential of any reactor concept. Thus, we contribute to reactor evaluation by assessing fuel cycle costs and determining the performance limits of the fuels that are envisioned by the reactor designer. The engineer is able to incorporate the assessment into his overall evaluation. Our level of activity in this program has decreased significantly because of funding limitation.

This year, we continued efforts to improve the methods of cost analysis for High-Temperature Gas-Cooled Reactor fuel. We assisted the USAEC in fuel cycle analysis and continued our information indexing activities.

FUEL FABRICATION COST ANALYSIS

A. L. Lotts

As a part of the overall approach to reducing power costs, we evaluate fuel fabrication costs as they relate to the fuel cycle component of total power costs. Fabrication procedures and flowsheets are selected and analyzed for capital and operating increments at each point in the processes, and the results are stored in the computer program along with estimated hardware costs for a wide range of production rates.

The computer code for rod-bundle fuel elements¹ was instrumental in providing basic data for a Geneva IV

1. For a description of the basic code, see A. L. Lotts, T. N. Washburn, and F. J. Homan, *FABCØST 9, A Computer Code for Estimating Fabrication Costs for Rod-Bundle Fuel Elements*, ORNL-4287 (August 1968).

paper on the economics of thermal reactor fuel manufacture in the United States.²

FUEL RECYCLE TASK FORCE

A. L. Lotts

We continued to participate in the AEC FRTF activities by serving as the working group to obtain a final document for reactor fuel cycle costs. This document,³ which contains fuel cycle data for approximately 40 reactor concepts, is now being circulated to task force members and the nuclear community for comment. A Geneva IV paper⁴ was based on work done in preparation of the report.

HTGR FUEL COST ANALYSIS

W. H. Pechin

We are conducting an economic study of fabrication costs for HTGR fuels. The major objectives are to provide a basis for economic comparison of the thorium-uranium cycle with other fuel cycles and to provide the means of comparing various fuel designs and fabrication methods for HTGR fuels.

The major portion of this study consists of the preparation of a computer code to calculate the cost of fabricating HTGR fuel, starting with uranyl nitrate solution and finishing with a fuel block ready for

2. A. L. Lotts, T. N. Washburn, L. Geller, H. H. Klepfer, and W. H. Layman, "The Status of Thermal Reactor Fuel Manufacture in the United States," paper to be published in the Proceedings of the Fourth International Conference on the Peaceful Uses of Atomic Energy, Geneva, Sept. 6-16, 1971.

3. *Reactor Fuel Cycle Costs for Nuclear Power Evaluation*, WASH-1099 (in press).

4. R. Salmon, J. T. Roberts, A. L. Lotts, T. N. Washburn, and W. H. McVey, "Price Forecasting and Resource Utilization for the Fuel Cycle Industry of the United States," paper to be published in the Proceedings of the Fourth International Conference on the Peaceful Uses of Atomic Energy, Geneva, Sept. 6-16, 1971.

shipping. The major parameters to be included in the code are plant size, fuel design, fabrication flowsheet, and degree of shielding required for the process. This code is approximately 75% complete.

METALS AND CERAMICS DIVISION INFORMATION ACTIVITIES

Meredith R. Hill

The subject indexing for the Division literature through June 30, 1971, has been completed and can be searched by computer in the Computing Technology Center (CTC). This will bring the number of entries to

over 2000. The Division's bibliography for the calendar year 1969 was issued,⁵ and the publication of the bibliography for the year 1970 and the first half of 1971 is tentatively planned for the early part of 1972.

Externally originated bibliographic information computer tapes from the American Society for Metals,⁶ purchased by the Division, have been received by CTC.

5. M. R. Hill, *Bibliography of the Technical Literature of the Metals and Ceramics Division for 1969*, ORNL-4270, vol. 2 (October 1970).

6. W. H. Bridges and M. R. Hill, *Metals and Ceramics Div. Annu. Progr. Rept. June 30, 1970*, ORNL-4570, p. 194.

42. Examination of Nickel Heat Pipes Containing Potassium¹

J. H. DeVan D. H. Jansen

Three pure nickel heat pipes that contained potassium as a working fluid were examined after operation at 600°C for 6000 to 10,000 hr. These heat pipes had been designed and operated by the Electronic Components Division of the Radio Corporation of America and were shipped intact to ORNL for metallurgical analyses.

No deterioration of the pipes had been indicated during operation, and visual examination confirmed that no serious corrosion occurred under the test conditions. Metallographic examination did reveal local areas of the evaporator in which the capillary wick and adjacent pipe wall had been attacked and the attendant

formation of a black oxide scale, which appeared to be a double oxide of the type $Ni_xO_yK_z$. Metallographic examination of the condenser area revealed no changes other than grain growth.

After test, the potassium contained 50 to 120 ppm O and less than 50 ppm metal impurities.

We suggest that the evaporation process, which is indigenous to the operation of heat pipes, may promote reactions induced by impurities in potassium. Local imbalances between the rates of vaporization and liquid replenishment can lead to enrichment of impurities with low volatility. Such a process could explain why nickel suffered local attack in these pipes, even though the bulk oxygen concentration of the potassium was below a level where oxidation would be expected.

1. Abstracted from ORNL-TM-3077 (December 1970).

Presentations at Technical Meetings

Compiled by Frances A. Scarboro

1970 International Powder Metallurgy Conference, New York, July 12–16, 1970

C. S. Morgan,* “Mechanistic Interpretation of Non-Steady State Sintering”

2nd International Conference on Small-Angle X-Ray Scattering, Graz, Austria, August 26–29, 1970

John W. Anderegg* and Robert W. Hendricks, “A Small-Angle X-Ray Investigation of Ribonuclease”

Robert W. Hendricks,* “Absolute Intensity Measurements in Small-Angle X-Ray Scattering. I. Theory”

Robert W. Hendricks,* “Two Modifications of the Kratky Small-Angle X-Ray Camera”

Robert W. Hendricks,* C. C. Koch, and G. R. Love, “On the Mechanism and Kinetics of the Omega Transformation in a Ti–25 at. % Nb Alloy”

Second Inter-American Conference on Materials, Mexico City, August 24–27, 1970

Carl D. Lundin,* “Welding Defects, Their Origin and Effect”

International Conference on Transport Properties of Solids, Sydney, Australia, August 27–29, 1970

R. K. Williams, J. P. Moore, and D. L. McElroy, “Transport Properties of Ta and Ta-W Alloys,” (presented by P. G. Klemens, consultant not under contract – Head, Physics Department, University of Connecticut)

Second International Conference on the Strength of Metals and Alloys, Pacific Grove, Calif., Aug. 30–Sept. 4, 1970

E. E. Bloom* and J. O. Stiegler, “Effects of Fast Neutron Irradiation on the Tensile Properties of Austenitic Stainless Steels”

R. W. Carpenter* and C. T. Liu, “Strengthening of Nb-Hf Alloys by α Precipitation”

D. G. Harman,* “Effects of Thermal Aging and Neutron Irradiation on Incoloy 800”

C. T. Liu* and H. Inouye, “The Influence of Various Ordered States on the Mechanical Properties of Vanadium-Cobalt-Nickel Ternary Alloys”

H. E. McCoy, R. E. Gehlbach, and C. E. Sessions,* “Influence of Composition on the Postirradiation Mechanical Properties of Hastelloy N”

C. E. Sessions,* R. E. Gehlbach, E. E. Stansbury, and H. E. McCoy, Jr., “Influence of Titanium on the Strengthening of a Ni-Mo-Cr Alloy”

A. Wolfenden,* “An Analysis of Some Theories of Work Hardening in Terms of Stored Energy Data on FCC Single Crystals”

Conference on Structure of Molten Salts, Aberdeen, Scotland, Sept. 11–12, 1970

G. Pedro Smith,* “Electronic Optical Spectroscopy of Molten Salts – Past and Future”

1970 Fall Meeting of the American Ceramic Society, Bedford, Pa., Sept. 13–16, 1970

J. L. Scott* and J. H. Coobs, “Status of High-Temperature Gas-Cooled Reactor Fuel-Element Development at the Oak Ridge National Laboratory”

*Speaker.

- Space Simulation Conference, National Bureau of Standards, Gaithersburg, Md., Sept. 14–16, 1970
 R. W. McClung,* “Nondestructive Examination Methods to Monitor Service Testing”
- Symposium on Technology of Pressure-Retaining Steel Components, Vail Village, Colo., Sept. 21–23, 1970
 D. A. Canonico* and R. G. Berggren, “Tensile and Impact Properties of Thick-Section Plate and Weldments”
- Tenth Conference on Thermal Conductivity, Boston, Mass., Sept. 28–30, 1970
 M. J. Laubitz and D. L. McElroy,* “Precise Measurement of Thermal Conductivity at High Temperatures”
 J. P. Moore* and D. L. McElroy, “The Thermal Conductivity of Near Stoichiometric Single Crystal and Polycrystal UO_2 ”
 R. K. Williams, J. P. Moore,* and D. L. McElroy, “Transport Properties of Ta and Ta-W Alloys”
- International Meeting on Fast Reactor Fuel and Fuel Elements, Karlsruhe, Germany, Sept. 28–30, 1970
 R. H. Simon, J. R. Lindgren, J. N. Siltanen,* and R. B. Fitts, “Gas-Cooled Fast Reactor Fuel Element Development – Fuel Rod Irradiation Tests”
- 1970 Fall Meeting of the Electrochemical Society (Corrosion Division Commemorative Symposium on the Oxidation of Metals), Atlantic City, N.J., Oct. 4–9, 1970
 R. E. Pawel* and J. V. Cathcart, “Flexure Measurements on a U-Nb-Zr Alloy During Oxidation”
- American Welding Society National Fall Meeting, Baltimore, Md., Oct. 5–8, 1970
 N. C. Binkley,* G. M. Goodwin, and D. G. Harman, “Effects of Electrode Coatings on Austenitic Stainless Steel Weld Metal”
 D. A. Canonico* and W. J. Werner, “Effect of Sulfur, Phosphorus, and Manganese on the Hot Ductility of Inconel 600”
 W. J. Werner and G. M. Slaughter,* “Development of Filler Metals and Procedures for Vacuum Brazing Aluminum”
- Fourth International Conference on Plutonium and Other Actinides, Santa Fe, N.M., Oct. 5–9, 1970
 W. Fulkerson, T. G. Kollie, S. C. Weaver,* J. P. Moore, and R. K. Williams, “Electrical and Thermal Properties of the NaCl Structured Metallic Actinide Compounds”
- Eleventh General Meeting of Irradiation Effects on Reactor Structural Materials Program, WADCO, Oct. 13–15, 1970
 J. R. Weir, N. H. Packan, K. Farrell, A. Wolfenden, R. T. King, J. O. Stiegler,* E. E. Bloom,* and F. W. Wiffen,* “Metals and Ceramics Division Contribution to General Meeting of Irradiation Effects on Reactor Structural Materials Program”
- 1970 American Society for Metals Precongress Seminar on the Oxidation of Metals, Cleveland, Ohio, Oct. 17–18, 1970
 John V. Cathcart,* “The Structure and Properties of Thin Oxide Films”
- 1970 Fall Meeting of the Metallurgical Society of AIME, Cleveland, Ohio, Oct. 18–22, 1970 (Special Session on “The Relationship Between Theory and Practice in Metal Forming”)
 D. O. Hobson,* “Analyses of Deformation and Texture as Functions of Fabrication in Mandrel-Drawn Tubing”
- 1970 Fall Meeting of the Metallurgical Society of AIME, Cleveland, Ohio, Oct. 18–22, 1970
 R. L. Klueh,* “The Effect of Oxygen on the Compatibility of Tantalum and Sodium”
 C. C. Koch* and R. W. Carpenter, “The Influence of Metallurgical Variables on Superconductivity in Hf-Nb Alloys”
 T. S. Lundy,* “Cation Self-Diffusion in Rutile”

- A. J. Moorhead* and T. R. Housley, "Welding of a Molybdenum System for Chemical Processing"
- C. E. Sessions* and R. E. Gehlbach, "Effect of Heat Treatment and Straining on Formation of Stacking Fault Precipitates in Hastelloy N"
- R. L. Stephenson* and R. W. Gunkel, "Creep Rupture Properties of Welds in Tantalum Alloys"
- J. O. Stiegler* and E. E. Bloom, "A Comparison of Void Formation in Nickel and Stainless Steel"
- R. A. Vandermeer,* "Solid Solution Impurities and Grain Growth in Metals"
- R. K. Williams, J. P. Moore,* and D. L. McElroy, "Transport Properties of Ta and Ta-W Alloys"
- A. Wolfenden,* "Damage in Aluminum by 200 kV Electrons"
- M. H. Yoo* and B. T. M. Loh, "Dissociation of Nonbasal Dislocations in Hexagonal Close-Packed Metals"
- C. S. Yust,* "Deformation of UO₂-W Composites"

25th Annual Calorimetry Conference, Gaithersburg, Md., Oct. 19–22, 1970

- T. G. Kollie,* "Pulse Calorimetry Using a Small Digital Computer for Data Acquisition and Experiment Control"

American Society for Metals Fall Meeting, (Special Session on "Bubbles and Voids in Solids"), Cleveland, Ohio, Oct. 19–22, 1970

- K. Farrell,* "Nonrandomly Dispersed Irradiation Voids in Aluminum and Iron"

American Society for Metals Fall Meeting, Cleveland, Ohio, Oct. 19–22, 1970

- C. S. Yust* and C. J. McHargue, "Thermochemical Generation of Voids in UO₂"

American Society for Metals Fall Meeting – Metallographic Exhibit, Cleveland, Ohio, Oct. 19–22, 1970

- Jack C. Ogle* and William H. Farmer, "Thermal Etching of Uranium Alloy"

30th Annual Fall Conference of the American Society for Nondestructive Testing, Cleveland, Ohio, Oct. 19–22, 1970

- C. V. Dodd* and W. A. Simpson, "Measurement of Small Magnetic Permeability Changes by Eddy-Current Techniques"

- H. L. Whaley* and Laszlo Adler, "Flaw Characterization by Ultrasonic Frequency Analysis"

Thermionic Conversion Specialist Conference, Miami, Fla., Oct. 26–29, 1970

- J. R. DiStefano,* "Compatibility of ²⁴⁴Cm₂O₃ with Refractory Metals at Thermionic Temperatures"

- J. I. Federer* and A. C. Schaffhauser, "Chemical Vapor Deposition and Characterization of Tungsten-Rhenium Alloys"

- R. L. Stephenson* and J. I. Federer, "Creep Rupture Properties of CVD-Tungsten"

1970 Pacific Coast Regional American Ceramic Society Meeting, San Francisco, Calif., Oct. 27–30, 1970

- J. H. Coobs,* J. M. Robbins, and J. L. Scott, "Development of Bonding Materials for High-Temperature Gas-Cooled Reactor Fuel Elements"

- C. B. Pollock* and R. L. Beatty, "The Effect of Fast Neutrons on Carbon-Impregnated Graphite at 700°C"

Fall Meeting of the Nuclear Division Basic Science Division of the American Ceramic Society, Gatlinburg, Tenn., Nov. 3–6, 1970

- W. J. Lackey,* "Electronic and Ionic Conductivity in Sapphire"

- K. H. McCorkle and C. S. Morgan,* "Desintering of Thoria"

- C. S. Yust* and C. J. McHargue, "Deformation of Hyperstoichiometric UO₂ Single Crystals"

28th Pittsburgh Diffraction Conference, Pittsburgh, Pa., Nov. 4–6, 1970

- Cullie J. Sparks, Jr.,* "Highly Oriented Graphite as an Incident and Diffracted Beam Monochromator"

- Cullie J. Sparks, Jr.,* and Wen Lin, "X-Ray Diffraction from Stacking Disorder in Hexagonal Graphite Caused by Neutron Irradiation"
- Continuum Aspects of Graphite Design Conference, Gatlinburg, Tenn., Nov. 9–12, 1970
- John W. Prados* and Hall C. Roland, "Analysis of Spherical Coatings on Nuclear Fuel Particles"
- 75th Anniversary Symposium of the Discovery of X-Ray, Milwaukee, Wis., Nov. 13–14, 1970
- R. W. McClung,* "The Use of X Rays for Nondestructive Testing in the Nuclear Industry"
- 1970 Winter Meeting of the American Nuclear Society, Washington, D.C., Nov. 15–19, 1970
- L. L. Bennett,* W. E. Thomas, and F. J. Homan, "Nuclear and Economic Performance of Niobium and Molybdenum in LMFBR Cores"
- C. M. Cox,* E. J. Manthos, and D. R. Cuneo, "Transient Performance of Sol-Gel (U,Pu)O₂ Sphere-Pac and Pellet Fuels"
- R. B. Fitts,* V. A. DeCarlo, E. L. Long, Jr., and A. R. Olsen, "Thermal Performance and Restructuring of Pellet and Sphere-Pac Fuels"
- F. J. Homan,* Fuel-Cladding Mechanical Interaction During Startup"
- J. P. Jarvis,* W. B. Burch, and J. M. Chandler, "Transfer of Californium Sources by Pneumatic Rabbit"
- T. M. Kegley, Jr.,* "Use of Cellulose Nitrate for Alpha Autoradiography in Metallography"
- A. W. Longest, N. Baldwin, J. A. Conlin, R. B. Fitts,* and J. R. Lindgren, "Fission Gas Release Measurements from Fast Breeder (U,Pu)O₂ Fuel"
- J. L. Scott,* J. H. Coobs, J. M. Robbins, and J. A. Conlin, "Irradiation Performance of Loose and Bonded Beds of Coated Fuel Particles"
- Third Annual Technical Meeting of the International Metallographic Society, Cleveland, Ohio, Nov. 16–18, 1970
- C. K. H. DuBose,* G. L. Copeland, and D. N. Braski, "Transmission Electron Microscopy of Boron Carbide"
- R. J. Gray* and B. C. Leslie, "More on the Metallographic Applications of Xenon Lamp Systems"
- 1970 Fall Meeting of The American Physical Society, New Orleans, La., Nov. 23–25, 1970
- J. O. Betterton, Jr.,* D. S. Easton, and J. O. Scarbrough, "Effects of Heat Treatment and Impurities on Critical Current Densities of Nb-Ti, Nb-Zr, Nb-Hf, Ta-Ti, and Ta-Zr Superconductors"
- American Chemical Society Meeting, New Orleans, La., Dec. 1–5, 1970
- Jorulf Brynestad* and G. Pedro Smith, "Titanium Chemistry in Aluminum Chloride and in Chloroaluminate Systems"
- C. R. Boston,* "Electrical Conductivities of Molten AlBr₃-NaBr Mixtures"
- Conference on Ceramics in Severe Environments, Raleigh, N.C., Dec. 7–9, 1970
- W. J. Lackey,* "Effect of Temperature on Electrical Conductivity and Transport Mechanisms in Sapphire"
- V. J. Tennery,* T. N. Washburn, and J. L. Scott, "Fabrication and Irradiation Behavior of Uranium Mononitride"
- 31st Meeting of the High Temperature Fuels Committee, Argonne, Ill., Dec. 8–10, 1970
- C. M. Cox* and J. L. Scott (compilers), "Summaries of Recent ORNL Work on Fuels and Cladding Materials"
- International Symposium on Atomic, Molecular, and Solid-State Theory and Quantum Biology, Sanibel Island, Fla., Jan 18–23, 1971
- J. S. Faulkner,* "Electronic States in Disordered Alloys: Comparison of Methods"
- G. S. Painter,* "Application of the Discrete Variational Method to the Electronic Structure of LiF"
- G. M. Stocks,* "Electronic States in Some Disordered Noble Metal-Transition Metal Alloys"

- 1971 Western Metal and Tool Exposition and Conference (WESTEC), Los Angeles, Calif., Mar. 8–11, 1971
 G. M. Slaughter,* D. A. Canonico, N. C. Cole, and W. J. Werner, “Brazing of Ceramics, Graphite, and Aluminum”
- American Society for Nondestructive Testing Annual Spring Conference, Los Angeles, Calif., Mar. 8–12, 1971
 C. V. Dodd* and C. C. Lu, “Nondestructive Test for Measuring the State of Heat Treatment in Closure Welds”
- Preferential Corrosion of Alloys Session of the National Association of Corrosion Engineers, 1971 Corrosion Research Conference, Chicago, Ill., Mar. 22–26, 1971
 J. W. Koger* and J. H. DeVan, “Selective Attack of Alloys by Molten Fluoride Salts”
- The British Nuclear Energy Society, European Conference on Voids, University of Reading, England, Mar. 24–25, 1971
 N. H. Packan,* “The Effect of Neutron Dose on Void Formation in High Purity Aluminum”
- The American Physical Society Meeting, Cleveland, Ohio, Mar. 29–Apr. 1, 1971
 L. A. Boatner,* M. M. Abraham, C. B. Finch, and R. W. Reynolds, “EPR of $5f^5$ Configuration Ions: Pu(3+) and Am(4+) in Thorium Dioxide and Pu(3+) in Strontium Chloride”
 J. S. Faulkner,* “A Simple Method for Symmetrizing KKR Band Theory Calculations”
 D. M. Kroeger* and C. C. Koch, “The Influence of Surface Current on Bean Method Critical Current Density Measurements”
 P. L. Land,* E. T. Rodine, and C. B. Finch, “Thermoluminescence of CeO₂”
- American Nuclear Society Conference on Fast Reactor Fuel Element Technology, New Orleans, La., Apr. 13–15, 1971
 C. M. Cox,* D. R. Cuneo, and E. J. Manthos, “Performance of Sphere-Pac and Pelletized (U,Pu)O₂ During Severe Overpower Transients”
 R. B. Fitts,* E. L. Long, Jr., and J. M. Leitnaker, “Observations of Fuel-Cladding Chemical Interactions as Applied to GCBR Fuel Rods”
 F. J. Homan,* C. M. Cox, and W. J. Lackey, “Comparisons Between Predicted and Measured Fuel Pin Performance”
 A. R. Olsen,* R. B. Fitts, and W. J. Lackey, “In-Reactor Restructuring Temperatures and Kinetics for (U,Pu)O₂”
 T. N. Washburn* and J. L. Scott, “Performance Capability of Advanced Fuels for Fast Breeder Reactors”
- The Seventh Annual Symposium of the New Mexico Section, American Vacuum Society, Albuquerque, N.M., Apr. 21–23, 1971
 H. Inouye,* “Interstitials in Refractory Metals and Alloys”
- 73rd Annual Meeting of the American Ceramic Society, Chicago, Ill., Apr. 24–29, 1971
 R. A. Bradley,* W. J. Lackey, and J. D. Sease, “Fabrication and Characterization of Sol-Gel (U,Pu)O₂ Pellets”
 G. L. Copeland,* R. G. Donnelly, and W. R. Martin, “Irradiation Performance of Boron Carbide Powders”
 W. J. Lackey,* R. A. Bradley, and W. H. Pechin, “Use of Statistical Designs to Solve (U,Pu)O₂ Fabrication and Characterization Problems”
 T. B. Lindemer* and R. A. Bradley, “Kinetic Models for the Synthesis of (U,Pu)O_{2-y} by Hydrogen-Reduction and Carbothermic Techniques”
 W. H. Pechin,* R. A. Bradley, and J. D. Sease, “Gas Release by (U,Pu)O₂ Fuels”
 J. D. Sease* and F. E. Harrington, “U-Fine – A New Concept in Microsphere Fuels”
 V. J. Tennery* and E. S. Bomar, “The Lattice Parameter of (U,Pu)N Solid Solutions”

- T. N. Washburn,* D. R. Cuneo, and E. L. Long, Jr., "Irradiation Performance of Uranium Nitride at 1500°C"
American Welding Society 52nd Annual Meeting, San Francisco, Calif., Apr. 26–30, 1971
- N. C. Binkley, D. G. Harman, G. M. Goodwin,* and G. M. Slaughter, "Effects of Slight Compositional Variation on Type E308 Electrode Deposits"
- D. A. Canonico* and G. M. Slaughter, "Brazing and the Phenomenon of Remelt Temperature"
- N. C. Cole,* R. W. Gunkel, and J. W. Koger, "Development of Corrosion-Resistant Filler Metals for Brazing Molybdenum"
- G. M. Goodwin,* N. C. Cole, and G. M. Slaughter, "The Effect of Heat Treatment on Austenitic Stainless Steel Weld Metal"
- J. P. Hammond, P. Patriarca, G. M. Slaughter, and W. A. Maxwell, "Recent Corrosion Studies on High-Nickel Alloy Weldments in Superheated Steam" (presented by D. A. Canonico)
- J. W. Hendricks and G. M. Slaughter, "Compatibility of Brazed Joints with Alkali Metals and Vacuum" (presented by N. C. Cole)
- A. J. Moorhead* and D. A. Canonico, "Effect of Ferrite and Martensite on the Weldability of Stainless Steels"
- A. J. Moorhead,* T. R. Housley, and G. M. Slaughter, "Welding a Large Molybdenum Chemical Processing Loop"
- 32nd Meeting of the High Temperature Fuels Committee, Bettis Atomic Power Laboratory, Pittsburgh, Pa., May 11–13, 1971
- T. N. Washburn* and J. L. Scott,* "Summaries of Recent ORNL Work on Fuels and Cladding Materials"
- 32nd Meeting of the High Temperature Fuels Committee, Bettis Atomic Power Laboratory, Pittsburgh, Pa., May 12, 1971 (special session on Boron Carbide)
- W. R. Martin* and G. L. Copeland, "Review of Oak Ridge National Laboratory's Neutron Absorber Program"
- Spring Meeting of The Metallurgical Society of AIME, Atlanta, Ga., May 17–20, 1971
- K. H. G. Ashbee,* "Plasticity of Hot Glass-Ceramics"
- E. E. Bloom, "Effect of Titanium Additions on the Creep-Rupture Properties of Types 304 and 316 Stainless Steels" (presented by F. W. Wiffen)
- R. W. Carpenter,* "Morphological Forms of the α -Phase During Precipitation from a bcc Matrix in Nb-Hf Alloys"
- W. A. Coghlan,* "Partial Correlation Functions for Vacancy Diffusion in Body-Centered Tetragonal Lattices"
- N. C. Cole,* G. M. Goodwin, and G. M. Slaughter, "Effect of Heat Treatments on the Microstructure of Stainless Steel Weld Metal"
- D. S. Easton* and J. O. Betterton, "The Zirconium-Rich Region of the Zirconium-Cadmium Phase Diagram"
- R. E. Gehlbach,* S. W. Cook, and H. E. McCoy, "The Effects of Composition and Aging on the Microstructure of Ti-Hf-Nb Modified Hastelloy N"
- H. Inouye,* "Effect of Low-Pressure Oxygen on the Creep Properties of Tungsten–25% Rhenium"
- R. T. King,* K. Farrell, and A. Jostsons, "Effect of High Fast Neutron Fluence on the 6061 Aluminum Alloys"
- R. T. King,* G. A. Reimann, and K. V. Cook, "Biaxial Stress-Rupture Properties of Stainless Steel Tubing and the Effects of Artificially Induced Defects"
- C. C. Koch* and D. M. Kroeger, "The Influence of Grain Size and Dislocation Distribution on Superconducting Critical Current Density in a Nb–10 at. % Ti Alloy"
- John W. Koger,* "Compatibility of Molybdenum-Base Alloy TZM with the Molten Salt $\text{LiF-BeF}_2\text{-ThF}_4\text{-UF}_4$ (68–20–11.7–0.3 mole %)"

H. E. McCoy* and R. E. Gehlbach, "Influence of Zirconium Additions on the Mechanical Properties of a Ni-Mo-Cr Alloy in the Irradiated and Unirradiated Conditions"

F. W. Wiffen,* "The Effect of Neutron Irradiation on the Strength Properties and Failure Mode of Molybdenum Alloys"

F. W. Wiffen,* "Voids and the Microstructure of Neutron Irradiated Niobium"

A. Wolfenden,* "Effects of Long-Range Order on the Energy Stored in Cu_3Au "

M. H. Yoo* and B. T. M. Loh, "Displacement Fields of Straight Dislocations in Anisotropic Crystals"

1971 International Conference on Radiation-Induced Voids in Metals, State University of New York at Albany, N.Y., June 9–11, 1971

E. E. Bloom,* "Nucleation and Growth of Voids in Stainless Steels During Fast Neutron Irradiation"

K. Farrell,* J. T. Houston, A. Wolfenden, R. T. King, and A. Jostsons, "Effects of Structural Imperfections on Voids in Aluminum"

A. Jostsons,* E. L. Long, J. O. Stiegler, K. Farrell, and D. N. Braski, "Annealing of Voids in Aluminum"

J. O. Stiegler,* "Void Formation in Neutron Irradiated Metals"

F. W. Wiffen,* "The Effect of Alloying and Purity on the Formation and Ordering of Voids in bcc Metals"

1971 Annual Meeting of the American Nuclear Society, Boston, Mass., June 13–17, 1971

G. L. Copeland,* C. K. H. DuBose, and D. N. Braski, "Transmission Electron Microscopy of Irradiated Boron Carbide"

C. M. Cox,* A. R. Olsen, R. B. Fitts, and E. L. Long, Jr., "Fuel-Cladding Chemical Interactions in Low-Density (U,Pu) O_2 Fuel Pins"

D. O. Hobson and P. L. Rittenhouse,* "Effects of Test Configurations on the Validity of Fuel Rod Failure Results"

R. T. King,* A. Jostsons, and K. Farrell, "Creep-Rupture Properties of Neutron-Irradiated Aluminum Alloys"

R. T. King,* G. A. Reimann, and K. V. Cook, "Creep Rupture of Type 316 Stainless Steel Tubing with Artificial Defects"

R. L. Klueh* and J. H. DeVan, "The Effect of Chromium in Vanadium on the Interaction with Oxygen in Sodium"

W. J. Lackey,* A. R. Olsen, J. L. Miller, Jr., and D. K. Bates, "Actinide Redistribution in Irradiated (U,Pu) O_2 "

J. M. Leitnaker,* J. P. De Luca, and R. B. Fitts, "Influence of Burnup on Reactivity of Oxide Fuel with Cladding"

C. B. Pollock,* J. L. Scott, and J. M. Leitnaker, "Recent Developments in Pyrolytic-Carbon-Coated Fuels"

L. E. Poteat,* R. W. Knight, R. G. Donnelly and J. I. Federer, "Evaluation of Fabrication Techniques for Cermet Isotope Fuel Simulants"

P. L. Rittenhouse,* D. O. Hobson, and R. D. Waddell, Jr., "Interpretation of Fuel Rod Failure Test Results Based on Test Configurations"

T. N. Washburn,* R. B. Fitts, A. W. Longest, J. A. Conlin, R. Campana, J. R. Lindgren, and N. L. Baldwin, "Fuel Element Development for the Gas-Cooled Breeder Reactor"

Fifth Symposium on Temperature, Its Measurement and Control in Science and Industry, Washington, D.C., June 21–24, 1971

R. K. Adams,* J. T. Hutton, R. F. Hyland, J. M. Jansen, T. G. Kollie, C. D. Martin, C. A. Mossman, J. L. Redford, R. L. Simpson, and V. A. Voelker, "Applications of Small Computers as Thermometry Research Tools"

R. B. Fitts, J L Miller, and E. L. Long, Jr., "Observations on Tungsten-Rhenium Thermocouples Used In-Reactor in (U,Pu)O₂ Fuel Pins" (presented by D. L. McElroy)

T. G. Kollie,* D. L. McElroy, R. K. Adams, and J. M. Jansen, "Measurement Accuracy of a Computer Operated Data Acquisition System"

7th Plansee Seminar, Reutte, Tyrol, Austria, June 21–25, 1971

C. S. Morgan,* "Material Transport by Dislocation Motion in Sintering"

Tenth Biennial Conference on Carbon, Lehigh University, Bethlehem, Pa., June 27–July 2, 1971

M. D. Allen, W. H. Cook,* B. C. Leslie, and R. J. Gray, "High Resolution Microscopy of Carbon and Graphite"

O. B. Cavin,* W. H. Cook, and C. R. Kennedy, "A Study of the Graphitization of Lampblack Graphite"

R. L. Hamner,* J M Robbins, J. H. Coobs, and J. L. Scott, "Fuel Elements for High-Temperature Gas Cooled Reactors"

C. R. Kennedy,* "The Irradiation Behavior of Graphite at 715°C"

C. B. Pollock and R. L. Beatty, "The Fabrication and Irradiation Behavior of Pyrolytic-Carbon Impregnated Graphite" (presented by W. P. Eatherly)

American Society for Testing and Materials Symposium on Testing for Prediction of Material Performance and Structures and Components, Atlantic City, N.J., June 29–July 1, 1971

R. W. McClung,* "Nondestructive Monitoring for Optimization of Performance Tests"

Publications

Compiled by Meredith R. Hill

- Abraham, M. M., L. A. Boatner, C. B. Finch, and R. W. Reynolds, "Electron-Paramagnetic-Resonance Investigations of $5f^5$ Configuration Ions in Cubic Single Crystals: Pu^{3+} in the ThO_2 and SrCl_2 , and Am^{4+} in ThO_2 ," *Phys. Rev. B* **3**(9), 2864–68 (May 1971).
- Abraham, M. M., C. B. Finch, J. L. Kolopus, and J. T. Lewis, "Electron Paramagnetic Resonance of Several Rare-Earth Impurities in the Cubic Perovskite KMgF_3 ," *Phys. Rev. B* **3**(9), 2855–64 (May 1971).
- Begun, G. M., C. R. Boston, G. Torsi, and G. Mamantov, "The Raman Spectra of Molten Aluminum Trihalide-Alkali Halide Systems," *Inorg. Chem.* **10**(5), 886–89 (May 1971).
- Bennett, L. L., W. E. Thomas, and F. J. Homan, "Nuclear and Economic Performance of Niobium and Molybdenum in LMFBR Cores," (Summary) *Trans. Amer. Nucl. Soc.* **13**(2), 469–70 (November 1970).
- Bennett, L. L., W. E. Thomas, and F. J. Homan, *Calculated Nuclear and Economic Performance of Niobium and Molybdenum in LMFBR Cores*, ORNL-TM-3271 (February 1971).
- Bloom, E. E., and J. O. Stiegler, *Effect of Fast Neutron Irradiation on the Creep-Rupture Properties of Type 304 Stainless Steel at 600°C*, ORNL-TM-3169 (January 1971).
- Bloom, Everett E., *An Investigation of Fast Neutron Radiation Damage in an Austenitic Stainless Steel*, ORNL-4580 (August 1970). Ph.D. Thesis, the University of Tennessee, June 1970.
- Bloom, E. E., and J. O. Stiegler, "Letters to the Editors – The Effect of Helium on Void Formation in Irradiated Stainless Steel," *J. Nucl. Mater.* **36**(3), 331–34 (September 1970).
- Bloom, E. E., J. W. Woods, and A. F. Zulliger, *Description of EBR-II Subassembly X-100*, ORNL-TM-3389 (June 1971).
- Bloom, E. E., and J. O. Stiegler, "Effects of Fast Neutron Irradiation on the Tensile Properties of Austenitic Stainless Steels," pp. 768–72 in *Second International Conference on the Strength of Metals and Alloys, Conf. Proc.*, vol. II, The American Society for Metals, Metals Park, Ohio, 1970.
- Bloom, E. E., and J. O. Stiegler, "Effect of Fast Neutron Irradiation on the Creep Rupture Properties of Type 304 Stainless Steel at 600°C," pp. 451–67 in *Irradiation Effects on Structural Alloys for Nuclear Reactor Applications, Spec. Tech. Publ. 484*, American Society for Testing and Materials, Philadelphia, March 1971.
- Borie, Bernard, "An Interpretation of Temperature Diffuse Scattering," *Acta Cryst.* **A26**(Part 5), 533–35 (September 1970).
- Boston, C. R., and W. M. Ewing, "Densities of Molten NaBr-AlBr_3 Mixtures," *J. Chem. Eng. Data* **16**(1), 65–66 (January 1971).
- Boston, C. R., "Electrical Conductivities of Molten $\text{AlBr}_3\text{-NaBr}$ Mixtures," *J. Electrochem. Soc.* **118**(3), 425–28 (March 1971).
- Boston, C. R., "Molten Salt Chemistry of the Haloaluminates," pp. 129–63 in *Advances in Molten Salt Chemistry*, vol. 1, ed. by J. Braunstein, Gleb Mamantov, and G. P. Smith, Plenum Press, New York, 1971.
- Bourgette, D. T. (ed.), "Proceedings of the Second International Vacuum Metallurgy Conference, 15–19 June 1970, Anaheim, California," *J. Vac. Sci. Technol.* **7**(6), S1–S168 (November/December 1970).
- Braunstein, J., Gleb Mamantov, and G. P. Smith (eds.), *Advances in Molten Salt Chemistry*, vol. 1, Plenum Press, New York, 1971.

- Brynestad, J., S. Von Winbush, H. L. Yakel, and G. P. Smith, "Titanium(II) Tetrachloroaluminate, Titanium Aluminum Pentachloride, and Solutions of Titanium(II) in Liquid Aluminum Chloride," *Inorg. Nucl. Chem. Letters* **6**(12), 889–93 (December 1970).
- Buchanan, Mary G., and Robert W. Hendricks, *Program WEIGHT: A FORTRAN IV Program for Evaluation of Weighting Functions Used in Small-Angle X-Ray Scattering*, ORNL-TM-1950 (Rev. 1) (November 1970).
- Canonico, D. A., *Transition Temperature Considerations for Thick-Wall Nuclear Pressure Vessels*, ORNL-TM-3114 (October 1970).
- Canonico, D. A., and R. G. Berggren, *Tensile and Impact Properties of Thick-Section Plate and Weldments*, ORNL-TM-3211 (January 1971).
- Cardwell, R. G., B. E. Foster, and J. C. Gower, *An Integrated System of Nuclear Materials Control at Oak Ridge National Laboratory*, ORNL-4607 (April 1971).
- Carpenter, R. W., and C. T. Liu, "Strengthening Nb-Hf Alloys by α Precipitation," pp. 674–78 in *Second International Conference on the Strength of Metals and Alloys, Conf. Proc.*, vol. II, The American Society for Metals, Metals Park, Ohio, 1970.
- Carpenter, R. W., C. T. Liu, and P. G. Mardon, "Phase Relations in Concentrated Ta-Hf and Nb-Hf Alloys," *Met. Trans.* **2**(1), 125–31 (January 1971).
- Carpenter, R. W., and H. L. Yakel, "Observations of $\text{CuK}\bar{\alpha}_{3,4}$ Reflections in X-Ray Diffraction Experiments," *J. Appl. Phys.* **42**(2), 887–88 (February 1971).
- Carpenter, R. W., and C. T. Liu, "Transition Morphology During HCP Precipitation from Beta-Isomorphous Alloys," *Scripta Met.* **5**(4), 255–57 (April 1971).
- Cepolina, A. G., and D. A. Canonico, *The Measurement of Residual Stresses*, ORNL-TM-3113 (October 1970).
- Cepolina, A. G., and D. A. Canonico, "The Measurement of Residual Stresses," *Welding J. (N.Y.)* **50**(1), 31-s–38-s (January 1971).
- Chakraborty, A. K., R. S. Crouse, and W. R. Martin, "Factors Affecting the Swelling During Degassing of Compacts Containing Uranium-Aluminum Intermetallics Dispersed in Aluminum," *J. Nucl. Mater.* **38**(1), 93–104 (January 1971).
- Chakraborty, A. K., C. K. H. DuBose, and W. R. Martin, *Effect of Boron on the Ductility and Strength of Inconel 600 and Types 304 and 316 Stainless Steel at Hot Metalworking Temperatures*, ORNL-TM-3316 (May 1971).
- Chandler, J. M., and S. E. Bolt, "Uranium-233-Bearing Salt Preparation for the Molten Salt Reactor Experiment," *Nucl. Appl. Technol.* **9**(6), 807–13 (December 1970).
- Clousing, R. E., "Application of Auger Electron Spectroscopy to Reactor Materials Research," (Summary) *J. Vac. Sci. Technol.* **76**(6), S124 (November/December 1970).
- Copeland, G. L., C. K. H. DuBose, and D. N. Braski, "Transmission Electron Microscopy of Irradiated Boron Carbide," (Summary) *Trans. Amer. Nucl. Soc.* **14**(1), 171–72 (June 1971).
- Couch, T. W., and G. P. Smith, "Polarized Electronic Absorption Spectrum of Tetragonal $\text{NiCl}_4^{2-}\text{Cs}_3(\text{MgCl}_4)\text{Cl}$," *J. Chem. Phys.* **53**(4), 1336–47 (August 1970).
- Cox, C. M., and F. J. Homan, "Performance Analysis of a Mixed-Oxide LMFBR Fuel Pin," *Nucl. Appl. Technol.* **9**(3), 317–25 (September 1970).
- Cox, C. M., E. J. Manthos, and D. R. Cuneo, "Transient Performance of Sol-Gel $(\text{U,Pu})\text{O}_2$ Sphere-Pac and Pellet Fuels," (Summary) *Trans. Amer. Nucl. Soc.* **13**(2), 653–54 (November 1970).
- Cox, C. M., D. R. Cuneo, and E. J. Manthos, "Performance of Sphere-Pac and Pelletized $(\text{U,Pu})\text{O}_2$ During Severe Overpower Transients," (Summary) *Trans. Amer. Nucl. Soc.* **14**, suppl. 1, 31–33 (April 1971).
- Cox, C. M., A. R. Olsen, R. B. Fitts, and E. L. Long, Jr., "Fuel-Cladding Chemical Interactions in Low-Density $(\text{U,Pu})\text{O}_2$ Fuel Pins," (Summary) *Trans. Amer. Nucl. Soc.* **14**(1), 173–75 (June 1971).
- DeVan, J. H., and D. H. Jansen, *Examination of Nickel Heat Pipes Containing Potassium*, ORNL-TM-3077 (December 1970).

- Dewey, B. R., *Discrete Element Analysis of the Creep of Stainless Steel Tubing for LMFBR Application*, ORNL-TM-3294 (March 1971).
- DiStefano, J. R., "Compatibility of $^{244}\text{Cm}_2\text{O}_3$ with Refractory Metals at Thermionic Temperatures," pp. 26–33 in *IEEE Conference Record of 1970 Thermionic Conversion Specialist Conference, October 26–29, 1970*, The Institute of Electrical and Electronics Engineers, New York, 1970. (70 C 53-ED).
- Dodd, C. V., and C. C. Lu, *Nondestructive Test for Measuring the State of Heat Treatment in Closure Welds*, ORNL-TM-3024 (July 1970).
- Dodd, C. V., W. E. Deeds, and W. G. Spoeri, "Optimizing Defect Detection in Eddy Current Testing," *Mater. Evaluation* 29(3), 59–63 (March 1971).
- Easton, D. S., and R. E. Clausing, "Outgassing of Nuclear Rocket Fuel Elements," *J. Vac. Sci. Technol.* 7(6), S116–S123 (November/December 1970).
- Easton, D. S., and J. O. Betterton, Jr., "The Eutectoid Region of the Zr-Ga System," *Met. Trans.* 1(12), 3295–99 (December 1970).
- Easton, D. S., S. H. Merriman, C. L. Armstrong, and R. E. Clausing, *A Computer Program for Calculating, Tabulating, and Plotting Outgassing Rates of Selected Gases*, ORNL-TM-3220 (February 1971).
- Easton, D. S., and R. E. Clausing, "A Computer Program for Calculating, Tabulating, and Plotting Outgassing Rates of Selected Gases," *Scripta Met.* 5(3), 181–84 (March 1971).
- Easton, D. S., J. O. Scarbrough, and J. O. Betterton, Jr., *The Effect of Heat Treatment and Impurities on the Current Density of Transition Metal Superconductors*, ORNL-4703 (June 1971).
- Eatherly, W. P., and C. R. Kennedy, "Reactor Graphite," pp. 22–26 in *Conceptual Design Study of a Single-Fluid Molten-Salt Breeder Reactor*, ORNL-4541, compiled by R. C. Robertson (June 1971).
- Ellis, D. E., and G. S. Painter, "Discrete Variational Method for the Energy Band Problem," pp. 271–75 in *Computational Methods in Band Theory*, ed by P. M. Marcus, J. F. Janak, and A. R. Williams, Plenum Press, New York, 1971.
- Evans, R. B., III, J. O. Stiegler, and G. M. Watson, "Diffusion of Actinides in Pyrocarbons: Thin-Layer Experiments," *J. Appl. Phys.* 41(12), 4808–19 (November 1970).
- Evans, R. B., III, and J. O. Stiegler, *Uranium and Thorium Diffusion in Columnar Pyrocarbons as Influenced by Actinide Concentration*, ORNL-TM-2989 (January 1971).
- Evans, R. B., III, and P. Nelson, Jr., *Corrosion in Polythermal Loop Systems. I. Mass Transfer Limited by Surface and Interface Resistances as Compared with Sodium-Inconel Behavior*, ORNL-4575, vol. 1 (March 1971).
- Evans, R. B., III, J. W. Koger, and J. H. DeVan, *Corrosion in Polythermal Loop Systems. II. A Solid-State Diffusion Mechanism With and Without Liquid Film Effects*, ORNL-4575, vol. 2 (June 1971).
- Farrell, K., and J. T. Houston, "Thermal Rejection and Growth of Gas Bubbles in Electrodeposited Nickel," *Met. Trans.* 1(7), 1979–86 (July 1970).
- Farrell, K., J. O. Stiegler, and R. E. Gehlbach, "Transmutation-Produced Silicon Precipitates in Irradiated Aluminum," *Metallography* 3(3), 275–84 (September 1970).
- Farrell, K., A. C. Schaffhauser, and J. T. Houston, "Effect of Gas Bubbles on Recrystallization of Tungsten," *Met. Trans.* 1(10), 2899–2905 (October 1970).
- Farrell, K., J. I. Federer, A. C. Schaffhauser, and W. C. Robinson, Jr., "Gas Bubble Formation in Metal Deposits," pp. 263–67 in *Chemical Vapor Deposition 2nd Intern. Conf.*, ed. by J. M. Blocher, Jr., and J. C. Withers, The Electrochemical Society, New York, 1970.
- Farrell, K., and R. T. King, "Supervoids in Irradiated Aluminum," *Phys. Status Solidi (a)* 2, K-5–K-7 (1970).
- Farrell, K., A. Wolfenden, and R. T. King, "The Effects of Irradiation Temperature and Preinjected Gases on Voids in Aluminum," *Radiat. Eff.* 8(1-2), 107–14 (March 1971).
- Farrell, K., and J. T. Houston, "Planar Interfaces and the Hardness of Polycrystalline α -Brass," *Scripta Met.* 5(6), 463–66 (June 1971).

- Federer, J. I., and A. C. Schaffhauser, "Chemical Vapor Deposition and Characterization of Tungsten-Rhenium Alloys," pp. 74–81 in *IEEE Conference Record of 1970 Thermionic Conversion Specialist Conference, October 26–29, 1970*, The Institute of Electrical and Electronics Engineers, New York, 1970. (70 C 53-ED)
- Finch, C. B., and G. W. Clark, "Czochralski Growth of Single-Crystal Mg_2SiO_4 (Forsterite)," *J. Cryst. Growth* **8**(3), 307–8 (March 1971).
- Fitts, R. B., V. A. DeCarlo, E. L. Long, Jr., and A. R. Olsen, "Thermal Performance and Restructuring of Pellet and Sphere-Pac Fuels," (Summary) *Trans. Amer. Nucl. Soc.* **13**(2), 549–51 (November 1970).
- Fitts, R. B., E. L. Long, Jr., and J. M. Leitnaker, "Observations of Fuel Cladding/Chemical Interactions as Applied to GCBR Fuel Rods," (Summary) *Trans. Amer. Nucl. Soc.* **14**, suppl. 1, 18–19 (April 1971).
- Flynn, P. W., R. F. Hinz, S. Langer, J. R. Lindgren, R. J. Price, T. N. Washburn, and A. F. Weinberg, *High-Temperature Fast-Flux Irradiation Experiment for Mixed-Oxide Fuel Rods*, GA-10264 (Oct. 15, 1970).
- Folzer, Cynthia, R. W. Hendricks, and A. H. Narten, *X-Ray Diffraction Data on Liquid Trimethylamine Decahydrate at 5°C*, ORNL-4571 (August 1970).
- Folzer, Cynthia, R. W. Hendricks, and A. H. Narten, "Diffraction Pattern and Structure of Liquid Trimethylamine Decahydrate at 5°C," *J. Chem. Phys.* **54**(2), 799–805 (January 1971).
- Frye, J. H., Jr., J. E. Cunningham, and staff, *Metals and Ceramics Div. Annu. Progr. Rept. June 30, 1970*, ORNL-4570.
- Fulkerson, W., T. G. Kollie, S. C. Weaver, J. P. Moore, and R. K. Williams, "Electrical and Thermal Properties of the NaCl Structured Metallic Actinide Compounds," pp. 374–85 in *Plutonium 1970 and Other Actinides*, *Nucl. Met.* **17**(Part 1), ed. by W. N. Miner, The Metallurgical Society of American Institute of Mining, Metallurgical, and Petroleum Engineers, New York, 1970.
- Gehlbach, R. E., J. O. Stiegler, and K. Farrell, "Direct Observation and Identification of Transmutation-Produced Silicon in a Neutron-Irradiated Aluminum Alloy," pp. 148–59 in *Technical Papers of the 23rd Metallographic Group Meeting held September 11–12, 1969, San Francisco, California*, CONF. 690954.
- Godfrey, T. G., W. S. Ernst, V. J. Tennery, and L. A. Harris, *Characterization and Behavior of Alkalized Alumina During the Sulfur Dioxide Sorption-Regeneration Process – A Summary Report*, ORNL-TM-3210 (January 1971).
- Gray, R. J., and B. C. Leslie, "High-Intensity Xenon Arc Lamp for Older Research Metallographs," pp. 121–38 in *Proc. 2nd Ann. Tech. Meet. Int. Metallographic Soc., Sept. 8–10, 1969*, International Metallographic Society, Los Alamos, New Mexico, 1970.
- Gray, R. J., E. L. Long, Jr., and A. E. Richt, "Metallography of Radioactive Materials at Oak Ridge National Laboratory," pp. 67–96 in *Modern Metallographic Techniques, Spec. Tech. Publ. 480*, American Society for Testing and Materials, Philadelphia, 1970.
- Gray, R. J., "Metallographic Reagents: Hastelloy N," *Microstructures* **2**(2), 26 (February/March 1971).
- Gurtner, F. B., P. K. Shutt, Jr., F. T. Kirk, Jr., C. F. Burrows, Robert O'Keefe, W. J. Werner, G. M. Slaughter, and J. L. McCall, *Vacuum Brazing – Gas Quenching History, Development, and Overall Program*, Edgewood Arsenal Technical Report EATR 4482 (January 1971).
- Guthrie, Paul Vincent, Jr., *Recovery Characteristics of Columbium and the Alloy Columbium-40 Vanadium*, Ph.D. Thesis, University of Cincinnati, June 1970.
- Hall, L. L., and C. S. Morgan, "Observation of Dislocations Occurring During Sintering," *J. Amer. Ceram. Soc.* **54**(1), 55 (January 1971).
- Hammond, J. P., and G. M. Slaughter, "Bonding Graphite to Metals with Transition Pieces," *Welding J. (N.Y.)* **50**(1), 33–40 (January 1971).
- Harman, D. G., "Incoloy 800: Enhanced Resistance to Radiation Damage," *Nucl. Appl. Technol.* **9**(4), 561–71 (October 1970).

- Harris, L. A., W. Ernst, and V. J. Tennery, "A High-Temperature X-Ray and Thermal Analysis Study of Synthetic Dawsonite," *Amer. Mineral.* **56**(5-6), 1111 (May-June 1971).
- Haynes, V. O., and A. E. Richt, *Postirradiation Examination of Fuel Element S-83 from Core II of the Army SM-I Stationary Medium Power Reactor*, ORNL-TM-3081 (October 1970).
- Hendricks, R. W., "Two Modifications of the Kratky Small-Angle X-Ray Camera," *J. Appl. Cryst.* **3**(Part 5), 348-53 (October 1970).
- Hill, Meredith R., compiler, *Bibliography of the Technical Literature of the Metals and Ceramics Division for 1969*, ORNL-4270, vol. 2 (October 1970).
- Homan, F. J., "Fuel-Cladding Mechanical Interaction During Startup," (Summary) *Trans. Amer. Nucl. Soc.* **13**(2), 576-77 (November 1970).
- Homan, F. J., W. H. Bridges, W. J. Lackey, and C. M. Cox, "Comparison of FMØDEL Predictions with EBR-II Irradiation Data," (Summary) *Trans. Amer. Nucl. Soc.* **14**, suppl. 1, 8-10 (April 1971).
- Homan, F. J., W. J. Lackey, and C. M. Cox, *Comparison Between Predicted and Measured Fuel Pin Performance*, ORNL-TM-3386 (May 1971).
- Houston, J. T., and K. Farrell, "Swelling of Carbonyl Nickel," *Metallography* **4**(2), 157-64 (April 1971).
- Jarvis, J. P., W. D. Burch, and J. M. Chandler, "Transfer of Californium Sources by Pneumatic Rabbit," (Summary) *Trans. Amer. Nucl. Soc.* **13**(2), 844 (November 1970).
- Jostsons, A., and K. Farrell, "Radiation Induced Voids in High-Purity Magnesium," *Radiat. Eff.* **8**(3-4), 287-88 (April 1971).
- Kegley, T. M., Jr., "Use of Cellulose Nitrate for Alpha Autoradiography in Metallography," (Summary) *Trans. Amer. Nucl. Soc.* **13**(2), 528 (November 1970).
- Kegley, T. M., Jr., "Quantimet Area Measurement Problems," pp. 163-69 in *Proc. 2nd Ann. Tech. Meet. Int. Metallographic Soc., Sept. 8-10, 1969*, International Metallographic Society, Los Alamos, New Mexico, 1970.
- King, R. T., *Production of Displacement Damage by Light Ions*, ORNL-TM-3013 (July 1970).
- King, R. T., Cyclotron simulation of neutron-transmutation produced gases in reactor cladding and structural materials," pp. 294-315 in *The Uses of Cyclotrons in Chemistry, Metallurgy and Biology* (Proceedings of a Conference held at St. Catherine's College, Oxford, 22-23 September 1969) ed. by C. B. Amphlett, Butterworths, London, 1970.
- King, R. T., *Cyclotron Simulation of Neutron-Transmutation Produced Gases in Reactor Cladding and Structural Materials*, ORNL-TM-3299 (April 1971).
- King, R. T., A. Jostsons, and K. Farrell, "Creep-Rupture Properties of Neutron-Irradiated Aluminum Alloys," (Summary) *Trans. Amer. Nucl. Soc.* **14**(1), 170-71 (June 1971).
- Klueh, R. L., and J. H. DeVan, "Effect of Oxygen in Sodium on Vanadium and Vanadium Alloys," *J. Less-Common Metals* **22**(4), 389-98 (December 1970).
- Klueh, R. L., "Penetration of Refractory Metals by Alkali Metals," pp. 177-96 in *Corrosion by Liquid Metals*, ed. by J. E. Draley and J. R. Weeks, Plenum Press, New York, 1970. (Proceedings of a Conference on Corrosion by Liquid Metals, Fall Meeting AIME, Philadelphia, Oct. 13-16, 1969.)
- Klueh, R. L., and J. H. DeVan, "The Effect of Chromium in Vanadium on the Interaction with Oxygen in Sodium," (Summary) *Trans. Amer. Nucl. Soc.* **14**(1), 188-89 (June 1971).
- Koch, C. C., P. Mardon, and C. J. McHargue, "An Elevated Temperature X-Ray Diffraction and an Electron Microscopy Study of the Transformations to the Samarium-Type Structure in Gadolinium-Cerium Alloys," pp. 664-72 in *Proc. Conf. Rare Earth Res., 8th, Reno, Nev., 1970*, vol. II, ed. by T. A. Henrie and R. E. Lindstrom, Bureau of Mines, U.S. Department of the Interior, Washington, D.C., 1970.
- Koch, C. C., "Solid Solution Intra-Rare-Earth Alloys: A Review of Alloying Behavior and Structure," *J. Less-Common Metals* **22**(2), 149-73 (October 1970).

- Koch, C. C., and J. O. Scarbrough, "Superconductivity in Mo-Re and Nb-Ir σ Phases," *Phys. Rev. B* 3(3), 742–48 (February 1971).
- Koch, C. C., P. G. Mardon, and C. J. McHargue, "A Study of the Transformation to the Samarium-Type Structure in Gd-Ce Alloys," *Met. Trans.* 2(4), 1095–1100 (April 1971).
- Kollie, T. G., J. O. Scarbrough, and D. L. McElroy, "Effects of Configurational Order on the Specific-Heat Capacity of Ni₃Fe Between 1.2 and 4.4 K," *Phys. Rev. B 3rd Ser.* 2(8), 2831–39 (October 1970).
- Kolopus, J. L., C. B. Finch, and M. M. Abraham, "ESR of Pb³⁺ Centers in ThO₂," *Phys. Rev. B* 2(6), 2040–45 (September 1970).
- Kopp, O. C., and P. A. Staats, "Characterization of RbOH-Grown Quartz by Infrared and Mass Spectroscopy," *J. Phys. Chem. Solids* 31(11), 2469–76 (November 1970).
- Kopp, O. C., and G. W. Clark, "Lamellar Dendritic Growth in Lead Sulfide," *J. Cryst. Growth* 8(1), 135–36 (January 1971).
- Lackey, W. J., R. A. Bradley, W. H. Pechin, and T. L. Hebble, *Statistical Technique for Determining Sources of Variation in (U,Pu)O₂ Oxygen-to-Metal Ratio*, ORNL-TM-3362 (June 1971).
- Lackey, W. J., A. R. Olsen, J. L. Miller, Jr., and D. K. Bates, "Actinide Redistribution in Irradiated (U,Pu)O₂," (Summary) *Trans. Amer. Nucl. Soc.* 14(1), 180–82 (June 1971).
- Laubitz, M. J., and D. L. McElroy, "Precise Measurement of Thermal Conductivity at High Temperatures (100–1200 K)," *Metrologia* 7(1), 1–15 (January 1971).
- Leitnaker, J. M., T. B. Lindemer, and C. M. Fitzpatrick, "Reaction of UC with Nitrogen from 1475° to 1700°C," *J. Amer. Ceram. Soc.* 53(9), 479–81 (September 1970).
- Leitnaker, J. M., J. P. De Luca, and R. B. Fitts, "Influence of Burnup on Reactivity of Oxide Fuel with Cladding," (Summary) *Trans. Amer. Nucl. Soc.* 14(1), 177 (June 1971).
- Lin, Wen, J. E. Spruiell, and R. O. Williams, "Short-Range Order in a Gold–40.0 Atomic Percent Palladium Alloy," *J. Appl. Cryst.* 3(Part 5), 297–305 (October 1970).
- Lindemer, T. B., J. M. Leitnaker, and M. D. Allen, "Kinetics of the Reaction of UC₂ and Nitrogen from 1500° to 1700°C," *J. Amer. Ceram. Soc.* 53(8), 451–56 (August 1970).
- Lindemer, T. B., M. D. Allen, and J. M. Leitnaker, "Reply to 'Discussion of Kinetics of the Graphite-Uranium Dioxide Reaction from 1400° to 1765°C,'" *J. Amer. Ceram. Soc.* 53(10), 581 (October 1970).
- Lindemer, T. B., "Rate Controlling Factors in the Carbothermic Synthesis of Advanced Fuels," *Nucl. Appl. Technol.* 9(5), 711–15 (November 1970).
- Lindemer, T. B., J. M. Leitnaker, and K. E. Spear, "The Role of Carbon in Reactions in the U-C-O-N System," pp. 351–68 in *Heterogeneous Kinetics at Elevated Temperatures* (Proceedings of an International Conference in Metallurgy and Materials Science held at the University of Pennsylvania, September 8–10, 1969) ed. by G. R. Belton and W. L. Worrell, Plenum Press, New York, 1970.
- Lindemer, T. B., and R. A. Bradley, *Kinetic Models for the Synthesis of (U,Pu)O_{2-y} by Hydrogen-Reduction and Carbothermic Techniques*, ORNL-TM-3358 (April 1971).
- Lindgren, J. R., P. W. Flynn, N. L. Baldwin, R. B. Fitts, and A. W. Longest, "Irradiation Testing of Fast Breeder Reactor (U-Pu)O₂ Fuels," (Summary) *Trans. Amer. Nucl. Soc.* 14, Suppl. 1, 33–34 (April 1971).
- Liu, C. T., and H. Inouye, "The Influence of Various Ordered States on the Mechanical Properties of Vanadium-Cobalt-Nickel Ternary Alloys," pp. 283–87 in *Second International Conference on the Strength of Metals and Alloys, Conf. Proc.*, vol. I, The American Society for Metals, Metals Park, Ohio, 1970.
- Liu, C. T., R. W. Armstrong, and J. Gurland, "Determination of the Frictional Stress for Polycrystalline Iron and Carbon Steels from their Stress-Strain Behaviour and Its Grain-Size Dependence," *J. Iron Steel Inst. (London)* 209(2), 142–46 (February 1971).
- Liu, C. T., H. Inouye, and R. W. Carpenter, *A Simple Method to Determine the Interstitial Distribution and Solubility Limit in Substitutional Solid Solutions*, ORNL-4697 (June 1971).

- Loh, B. T. M., and K. Farrell, "Comments on 'Stability of the Gas Bubbles in Solids,'" *J. Nucl. Sci. Technol.* **7**(5), 274–75 (May 1970).
- Loh, B. T. M., "Reply to Comments on 'Stress Concentration and Cavity Growth,'" *Scripta Met.* **4**(9), 665–66 (September 1970).
- Longest, A. W., N. Baldwin, J. A. Conlin, R. B. Fitts, and J. R. Lindgren, "Fission Gas Release Measurements from Fast Breeder (U,Pu)O₂ Fuel," (Summary) *Trans. Amer. Nucl. Soc.* **13**(2), 604 (November 1970).
- Lorenz, R. A., D. O. Hobson, and G. W. Parker, *Final Report on the First Fuel Rod Failure Transient Test of a Zircaloy-Clad Fuel Rod Cluster in TREAT*, ORNL-4635 (March 1971).
- Lotts, A. L., "Preface: Symposium on Theoretical Models for Predicting In-Reactor Performance of Fuel and Cladding Material," *Nucl. Appl. Technol.* **9**(1), 7–8 (July 1970).
- Lotts, A. L., "Introduction, Fuels I – Special Session on Fuel Cladding Models," *Nucl. Appl. Technol.* **9**(1), 9 (July 1970).
- Love, G. R., and D. M. Kroeger, "Losses Due to Moving Fluxoids in Superconductors," *Phil. Mag.* **22**(177), 583–99 (September 1970).
- Lundin, C. D., and K. Farrell, "Distribution and Effects of Porosity in Welds in CVD Tungsten," *Welding J. (N.Y.)* **49**(10), 461-s–470-s (October 1970).
- Luquire, J. W., W. E. Deeds, and C. V. Dodd, "Axially Symmetric Eddy Currents in a Spherical Conductor," *J. Appl. Phys.* **41**(10), 3976–82 (September 1970).
- Luquire, J. W., W. E. Deeds, and C. V. Dodd, "Alternating Current Distribution Between Planar Conductors," *J. Appl. Phys.* **41**(10), 3983–91 (September 1970).
- Martin, M. M., and W. R. Martin, *Fabrication Voids in Aluminum-Base Fuel Dispersions*, ORNL-4611 (October 1970).
- McClung, R. W., "Nondestructive Testing of Nuclear Ceramic Materials," *Amer. Ceram. Soc. Bull.* **49**(9), 777–81 (September 1970).
- McCoy, H. E., *Influence of Titanium, Zirconium, and Hafnium Additions on the Resistance of Modified Hastelloy N to Irradiation Damage at High Temperature – Phase I*, ORNL-TM-3064 (January 1971).
- McCoy, H. E., R. W. Gunkel, and G. M. Slaughter, "Tensile Properties of Hastelloy N Welded After Irradiation," *Welding J. (N.Y.)* **50**(2), 71-s–76-s (February 1971).
- McCoy, H. E., Jr., *An Evaluation of the Molten-Salt Reactor Experiment Hastelloy N Surveillance Specimens – Fourth Group*, ORNL-TM-3063 (March 1971).
- McCoy, H. E., and R. E. Gehlbach, "Influence of Irradiation Temperature on the Creep-Rupture Properties of Hastelloy N," *Nucl. Technol.* **11**(1), 45–60 (May 1971).
- McCoy, H. E., "Hastelloy N," pp. 26–28 in *Conceptual Design Study of a Single-Fluid Molten-Salt Breeder Reactor*, ORNL-4541, compiled by R. C. Robertson (June 1971).
- Moore, J. P., and D. L. McElroy, "Thermal Conductivity of Nearly Stoichiometric Single-Crystal and Polycrystalline UO₂," *J. Amer. Ceram. Soc.* **54**(1), 40–46 (January 1971).
- Moore, W. L., M. K. Preston, and J. D. Sease, *Fabrication of ORNL Series I Irradiation Test Capsules for Experimental Breeder Reactor II*, ORNL-TM-2922 (July 1970).
- Moorhead, A. J., "Welding and Drilling Applications," *Welding J. (N.Y.)* **50**(2), 97–106 (February 1971).
- Olsen, A. R., R. B. Fitts, and W. J. Lackey, "In-Reactor Restructuring Temperatures and Kinetics for (U,Pu)O₂," (Summary) *Trans. Amer. Nucl. Soc.* **14**, Suppl. 1, 24–25 (April 1971).
- Packan, N. H., "Voids in Re-Irradiated Aluminum," *J. Nucl. Mater.* **37**(2), 251–54 (November 1970).
- Packan, N. H., *Voids in Neutron Irradiated Aluminum*, ORNL-TM-3109 (January 1971). Ph.D. Thesis, University of Missouri, Rolla, December 1970.

- Painter, G. S., and D. E. Ellis, "Discrete Variational Method for the Energy Band Problem with LCAO Basis and Non-Spherical Local Potential," pp. 276–83 in *Computational Methods in Band Theory*, ed. by P. M. Marcus, J. F. Janak, and A. R. Williams, Plenum Press, New York, 1971.
- Patriarca, P., *Fuels and Materials Development Program Quart. Progr. Rept. June 30, 1970*, ORNL-4600.
- Patriarca, P., *Fuels and Materials Development Program Quart. Progr. Rept. Sept. 30, 1970*, ORNL-4630.
- Patriarca, P., *Fuels and Materials Development Program Quart. Progr. Rept. Dec. 31, 1970*, ORNL-TM-3300.
- Patriarca, P., *Fuels and Materials Development Program Quart. Progr. Rept. Mar. 31, 1971*, ORNL-TM-3416.
- Peterson, Sigfred, and C. E. Curtis, *Thorium Ceramics Data Manual, Volume I – Oxides; Volume II – Nitrides*, ORNL-4503 (September 1970).
- Peterson, Sigfred, and C. E. Curtis, *Thorium Ceramics Data Manual, Volume III -- Carbides*, ORNL-4503 (April 1971).
- Pollock, C. B., J. L. Scott, and J. M. Leitnaker, "Recent Developments in Pyrolytic-Carbon-Coated Fuels," (Summary) *Trans. Amer. Nucl. Soc.* **14**(1), 139–40 (June 1971).
- Poteat, L. E., R. W. Knight, R. G. Donnelly, and J. I. Federer, "Evaluation of Fabrication Techniques for Cermet Isotope Fuel Simulants," (Summary) *Trans. Amer. Nucl. Soc.* **14**(1), 16 (June 1971).
- Reagan, P. E., J. G. Morgan, E. L. Long, Jr., and J. H. Coobs, *Performance of Bonded Beds of Coated Fuel Particles During Irradiation*, ORNL-TM-3361 (June 1971).
- Reimann, G. A., "Development of an Ultrafine Grain Size Type-316 Stainless-Steel Cladding," *Nucl. Technol.* **10**(1), 62–66 (January 1971).
- Reimann, D. K., D. M. Kroeger, and T. S. Lundy, "Cation Self-Diffusion in UN_{1+x} ," *J. Nucl. Mater.* **38**(2), 191–96 (February 1971).
- Richt, A. E., and V. O. Haynes, *Postirradiation Examination of Fuel Elements from Core I and Core II of the Army SM-1A Stationary Medium Power Reactor*, ORNL-TM-2967 (August 1970).
- Rittenhouse, P. L., *Progress in Zircaloy Cladding Failure Modes Research*, ORNL-TM-3188 (December 1970).
- Rittenhouse, P. L., D. O. Hobson, and R. D. Waddell, Jr., "Interpretation of Fuel Rod Failure Test Results Based on Test Configurations," (Summary) *Trans. Amer. Nucl. Soc.* **14**(1), 142 (June 1971).
- Scott, J. L., J. H. Coobs, J. M. Robbins, and J. A. Conlin, "Irradiation Performance of Loose and Bonded Beds of Coated Fuel Particles," (Summary) *Trans. Amer. Nucl. Soc.* **13**(2), 580–81 (November 1970).
- Sessions, Charles Edward, *Influence of Titanium on the High-Temperature Deformation and Fracture Behavior of Some Nickel Based Alloys*, ORNL-4561 (July 1970). Ph.D. Thesis, the University of Tennessee, March 1970.
- Sessions, C. E., and J. H. DeVan, "Thermal Convection Loop Tests of Nb–1% Zr Alloy in Lithium at 1200 and 1300°C," *Nucl. Appl. Technol.* **9**(2), 250–59 (August 1970).
- Sessions, C. E., "Influence of Titanium on the High-Temperature Deformation and Fracture Behavior of Some Nickel-Based Alloys," *Scripta Met.* **4**(10), 795–98 (October 1970).
- Sessions, C. E., E. E. Stansbury, R. E. Gehlbach, and H. E. McCoy, Jr., "Influence of Titanium on the Strengthening of a Ni-Mo-Cr Alloy," pp. 626–30 in *Second International Conference on the Strength of Metals and Alloys, Conf. Proc.*, vol. II, The American Society for Metals, Metals Park, Ohio, 1970.
- Sessions, C. E., and J. H. DeVan, *Effect of Oxygen, Heat Treatment, and Test Temperature on the Compatibility of Several Advanced Refractory Alloys with Lithium*, ORNL-4430 (April 1971).
- Simon, R. H., J. R. Lindgren, J. N. Siltanen, and R. B. Fitts, "Gas-Cooled Fast Reactor Fuel-Element Development – Fuel-Rod Irradiation Tests," pp. 834–57 in *Fast Reactor Fuel and Fuel Elements* (Proc. Intern. Meeting, Kernforschungszentrum, Karlsruhe, 28–30, Sept. 1970), American Nuclear Society, Local Section in Europe, 1970.
- Simpson, W. A., W. E. Deeds, C. C. Cheng, and C. V. Dodd, "An Infrared Microscope System for the Detection of Internal Flaws in Solids," *Mater. Evaluation* **28**(9), 205–11 (September 1970).

- Simpson, W. A., C. V. Dodd, J. W. Luquire, and W. G. Spoeri, *Computer Programs for Some Eddy-Current Problems – 1970*, ORNL-TM-3295 (June 1971).
- Slaughter, G. M., "Brazing," pp. 60.88–60.103 in *Welding Handbook*, 6th ed., Section 3B, ed. by Len Griffing, American Welding Society, New York, 1971.
- Smith, M. L., and J. M. Leitnaker, *Atmospheric Contamination of Uranium Dioxide Powder*, ORNL-4704 (June 1971).
- Spear, K. E., and J. M. Leitnaker, "Phase Investigations in the U-Cr-N System," *High Temp. Sci.* **3**(1), 26–28 (January 1971).
- Spear, K. E., and J. M. Leitnaker, "Phase Behavior of the U-V-N System and Properties of UVN₂," *High Temp. Sci.* **3**(1), 29–40 (January 1971).
- Spruiell, J. E., "Chemical Vapor Deposition of Silicon Carbide from Silicon Tetrachloride-Methane-Hydrogen Mixtures," pp. 279–95 in *Chemical Vapor Deposition, 2nd Intern. Conf.*, ed. by J. M. Blocher, Jr., and J. C. Withers, The Electrochemical Society, New York, 1970.
- Stephenson, R. L., "Effect of Heat Treatment on the Creep-Rupture Properties of T-111," *Met. Trans.* **1**(9), 2644–45 (September 1970).
- Stephenson, R. L., *The Analysis of Creep Data in the Selections of Materials for Thermionic Capsules*, ORNL-TM-3202 (November 1970).
- Stephenson, R. L., "Creep-Rupture Properties of C-129Y," *J. Vac. Sci. Technol.* **7**(6), S112–S115 (November/December 1970).
- Stephenson, R. L., and J. I. Federer, "Creep Rupture Properties of CVD-Tungsten," pp. 90–94 in *IEEE Conference Record of 1970 Thermionic Conversion Specialist Conference, October 26–29, 1970*, The Institute of Electrical and Electronics Engineers, New York, 1970. (70 C 53-ED)
- Stephenson, R. L., "Comparative Creep-Rupture Properties of Tungsten–25% Rhenium Consolidated by Arc-Melting and Powder-Metallurgy Techniques," *J. Less-Common Metals* **24**(2), 173–82 (June 1971).
- Stiegler, J. O., and E. E. Bloom, "Void Formation in Irradiated Nickel 270," *Radiat. Eff.* **8**(1-2), 33–41 (March 1971).
- Stillman, W. E., *TRANS – A One-Dimensional FØRTRAN IV Program for Computing the Time Response of Fuel Rods to a Loading-Unloading Environment*, ORNL-TM-3293 (May 1971).
- Stocks, G. M., R. W. Williams, and J. S. Faulkner, "Densities of States in Cu-Rich Ni-Cu Alloys by the Coherent-Potential Approximation: Comparisons with Rigid-Band and Virtual-Crystal Approximation," *Phys. Rev. Letters* **26**(5), 253–56 (February 1971).
- Swindeman, R. W., *Some Creep-Rupture Data for Newer Heats of Haynes Alloy No. 25 (L-605)*, ORNL-TM-3028 (August 1970).
- Tenckhoff, Erich, "Defocusing for the Schulz Technique of Determining Preferred Orientation," *J. Appl. Phys.* **41**(10), 3944–48 (September 1970).
- Tennery, V. J., T. G. Godfrey, and R. A. Potter, *Synthesis, Characterization, and Fabrication of UN*, ORNL-4608 (December 1970).
- Tennery, V. J., and E. S. Bomar, "Lattice Parameters of (U,Pu)N Solid Solutions," *J. Amer. Ceram. Soc.* **54**(5), 247–49 (May 1971).
- Waddell, R. D., Jr., and P. L. Rittenhouse, *High-Temperature Burst Strength and Ductility of Zircaloy Tubing*, ORNL-TM-3289 (March 1971).
- Wagner, R. L., "Nitrogen Diffusion and Solubility in Tungsten," *Met. Trans.* **1**(12), 3365–70 (December 1970).
- Washburn, T. N., and J. L. Scott, "Performance Capability of Advanced Fast Breeder Reactor Fuels," (Summary) *Trans. Amer. Nucl. Soc.* **14**, suppl. 1, 35 (April 1971).
- Washburn, T. N., and J. L. Scott, *Performance Capability of Advanced Fuels for Fast Breeder Reactors*, ORNL-TM-3388 (May 1971).

- Washburn, T. N., R. B. Fitts, and J. A. Conlin, *Fuel Element Development for the Gas-Cooled Fast Breeder Reactor. Part I. Sealed Fuel Rod Design*, ORNL-TM-3427 (June 1971).
- Washburn, T. N., R. B. Fitts, A. W. Longest, J. A. Conlin, R. Campana, J. R. Lindgren, and N. L. Baldwin, "Fuel Element Development for the Gas-Cooled Breeder Reactor," (Summary) *Trans. Amer. Nucl. Soc.* **14**(1), 275 (June 1971).
- Weaver, S. C., V. A. DeCarlo, R. B. Fitts, R. L. Senn, K. R. Thoms, and J. L. Scott, *Results from Irradiation Testing of UO_2 Fuel Pins Designed for the Medium Power Reactor Experiment*, ORNL-TM-2859 (August 1970).
- Whaley, H. L., and Laszlo Adler, *A New Technique for Ultrasonic Flaw Determination by Spectral Analysis*, ORNL-TM-3056 (September 1970).
- Williams, R. K., T. E. Banks, and D. L. McElroy, *Measurement and Correlation of Thermal Resistances of UN-Metal Interfaces*, ORNL-4660 (May 1971).
- Wolfenden, A., "Effects of Preinjected Helium on Void Formation in Quenched Aluminum," *J. Nucl. Mater.* **36**(2), 218–22 (August 1970).
- Wolfenden, A., "Erratum – The Ratio of Stored to Expended Energy During the Room-Temperature Deformation of Copper Single Crystals," *Scripta Met.* **4**(9), 747 (September 1970).
- Wolfenden, A., "Comments on 'Stored Energy and Workhardening Theories,'" *Scripta Met.* **4**(11), 899–903 (November 1970).
- Wolfenden, A., "An Analysis of Some Theories of Work Hardening in Terms of Stored Energy Data on FCC Single Crystals," pp. 489–93 in *Second International Conference on the Strength of Metals and Alloys, Conf. Proc.*, vol. II, The American Society for Metals, Metals Park, Ohio, 1970.
- Wolfenden, A., "Damage in Aluminum by 200 kV Electrons," *J. Nucl. Mater.* **38**(1), 114–15 (January 1971).
- Wolfenden, A., "The Energy Stored in Polycrystalline Cu_3Au : Effects of Long-Range Order," *Scripta Met.* **5**(5), 371–78 (May 1971).
- Wymer, R. G., and A. L. Lotts, *Status and Progress Report for Thorium Fuel Cycle Development for January 1, 1969 Through March 31, 1970*, ORNL-4629 (February 1971).
- Yoo, M. H., and B. T. M. Loh, "Structural and Elastic Properties of Zonal Twin Dislocations in Anisotropic Crystals," pp. 479–94 in *Fundamental Aspects of Dislocation Theory, Nat. Bur. Stand. (U.S.) Spec. Publ. 317*, vol. 1, U.S. National Bureau of Standards, Washington, D.C., 1970.
- Yust, C. S., C. S. Morgan, and H. R. Gaddis, "Transmission Electron Microscopy of Polycrystalline Graphite," *Carbon* **8**(4), 449–51 (August 1970).

Author Index

- Abraham, M. M., 3, 4
Adams, R. E., 179
Adamson, G. M., Jr., 124
Adler, Laszlo, 138
Ashbee, K. H. G., 14, 15
- Banus, M. D., 11
Bates, D. K., 54
Beaver, R. J., 156
Begun, G. M., 5
Berggren, R. G., 82, 149, 150
Binkley, N. C., 82, 85
Bloom, E. E., 69, 72, 131
Boatner, L. A., 3, 4
Bomar, E. S., 62, 64
Borie, Bernard, 34, 35
Boston, C. R., 5
Botts, J. L., 63
Bradley, R. A., 38, 39, 40, 42, 54
Braski, D. N., 103
Brynstad, J., 5, 18, 19
Buhl, R. A., 50
- Canonico, D. A., 85, 111, 128, 129, 149, 150
Carlson, P. T., 10
Carpenter, R. W., 8, 9, 27, 111
Cathcart, J. V., 28, 29, 30
Cavin, O. B., 164, 169
Chandler, J. M., 171
Chandler, T. L., 132
Chapman, A. T., 1
Cheng, C. C., 136
Clark, G. W., 1, 2, 4
Clausing, R. E., 21, 195, 196
Coghlan, W. A., 20, 21
Cole, N. C., 82, 117, 163
Conlin, J. A., 144, 146
Coobs, J. H., 140, 144, 146
Cook, K. V., 78, 80, 81, 100, 138
Cook, S. W., 17, 158
Cook, W. H., 168, 169
Copeland, G. L., 102, 103, 104, 157
Cox, C. M., 38, 45, 46, 52, 54
- Crouse, R. S., 186
Cuneo, D. R., 46, 47, 121
- Deeds, W. E., 136
DeLuca, J. P., 19, 42, 65, 66
Denny, W. E., 192
DeVan, J. H., 95, 97, 98, 113, 203
Dewey, B. R., 57
DiStefano, J. R., 106, 162
Dodd, C. V., 100, 136, 178
Donnelly, R. G., 104, 105, 107, 109
DuBose, C. K. H., 15, 104, 152
Dworkin, A. A., 5
Dyslin, D. A., 104, 118
- Early, B. F., 108
Easton, D. S., 195, 196
Eatherly, W. P., 140, 143, 157, 165, 166
Ellis, D. E., 32
Epperson, J. E., 37
Erwin, J. H., 40, 61, 137
Ewing, W. M., 144
- Fahr, D., 72
Farrell, K., 12, 13, 14, 15, 134, 178
Faulkner, J. S., 31, 32, 33
Federer, J. I., 106, 115, 164
Finch, C. B., 2, 3, 4
Fitts, R. B., 50, 51, 57, 146, 174
Fleischer, B., 51, 123
Foster, B. E., 126, 138
Furman, F. J., 172
- Gaddis, H. R., 189, 193
Gehlbach, R. E., 17, 72, 158
Gibbs, P., 33
Godfrey, T. G., 120
Goodwin, G. M., 82, 108
Graves, R. S., 126, 144, 177, 198
Gray, R. J., 186, 189, 191, 192, 193
Griffith, J. L., 169
Griggs, E. P., 192

- Haltom, C. P., 193
 Hamner, R. L., 143
 Hammond, J. P., 90
 Harms, W. O., 95, 97, 100, 136
 Harris, L. A., 34, 36, 42
 Heitkamp, D., 10
 Hendricks, R. W., 37
 Henson, T. J., 186, 193
 Hewette, D. M. II, 144, 146, 193
 Hill, Meredith R., 202, 212
 Hobson, D. O., 184, 185
 Homan, F. J., 52, 57
 Houston, J. T., 13, 14, 15
 Hudson, J. D., 150

 Inouye, H., 105, 109, 111, 118
 Isaacs, L., 27

 Jansen, D. H., 97, 203
 Jones, R. H., 97
 Jostsons, A., 13, 134

 Keilholtz, G. W., 104
 Kegley, T. M., Jr., 57, 189, 190
 Kennedy, C. R., 166
 King, R. T., 12, 81, 134, 178
 Klueh, R. L., 95, 113, 114
 Knight, R. W., 106, 124, 125
 Koch, C. C., 26, 27
 Koger, J. W., 160, 163, 165
 Kollie, T. G., 24, 25, 169
 Kolopos, J. L., 3
 Kopp, O. C., 4
 Kistorz, G., 27
 Kroeger, D. M., 26, 27

 Lackey, W. J., 38, 42, 52, 54, 57
 Leitnaker, J. M., 19, 41, 42, 66, 67, 199, 200
 Leonard, W. J., 40
 Leslie, B. C., 189, 192, 193
 Lewis, J. T., 3
 Lindemer, T. B., 40, 67
 Liu, C. T., 8, 14, 105, 106, 111
 Loh, B. T. M., 7, 14, 15, 111
 Long, E. L., Jr., 57
 Longest, A. W., 146
 Lotts, A. L., 38, 171, 176, 201
 Lubell, M. S., 27
 Lubinsky, A. R., 32
 Lundin, C. D., 111
 Lundy, T. S., 10, 11

 Mamantov, G., 5
 Manley, L. C., Jr., 10, 11
 Manthos, E. J., 46, 61, 121
 March, N. H., 33
 Martin, M. M., 107, 124
 Martin, W. R., 78, 102, 124
 Mateer, H. V., 186, 193
 McClung, R. W., 78, 80, 100, 136
 McCoy, H. E., Jr., 17, 69, 115, 118, 131, 157, 159, 160, 161
 McDonald, R. E., 162
 McElroy, D. L., 52, 118, 198
 McHargue, C. J., 18
 McNabb, B., Jr., 157, 159, 161
 Miller, J. L., Jr., 54, 127, 186
 Montgomery, B. H., 144, 146
 Moore, J. P., 23, 24, 112, 169, 198
 Moore, R. E., 104
 Moorhead, A. J., 111, 129, 162

 Nave, J. W., 192
 Nugent, L. J., 2

 Oetting, F. L., 67
 Ogle, J. C., 20
 Ohr, S. M., 8
 Oliver, B. F., 1, 2
 Olsen, A. R., 45, 47, 54, 57, 174

 Padgett, R. A., 10, 11
 Painter, G. S., 32
 Panosh, R. L., 27
 Parameswaran, T., 32
 Patriarca, P., 61, 97, 115, 120
 Pawel, R. E., 28, 29
 Pechin, W. H., 42, 172, 201
 Pemsler, J. P., 29
 Petersen, G. F., 28
 Pollock, C. B., 140, 165
 Poteat, L. E., 106, 164
 Potter, R. A., 120
 Preston, M. K., 40, 61, 123

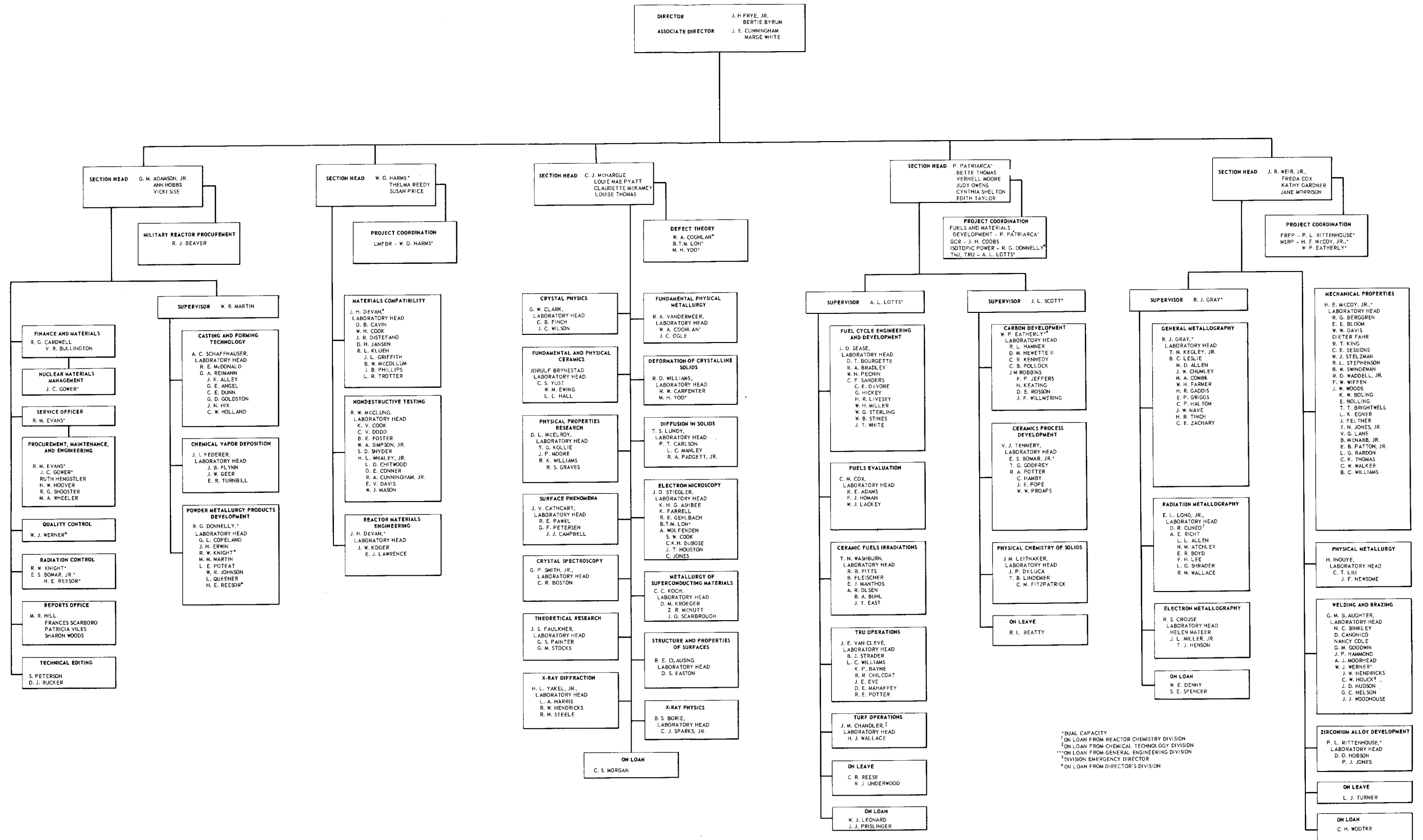
 Reimann, G. A., 78, 80, 81
 Reynolds, R. W., 3, 4
 Richt, A. E., 127
 Rittenhouse, P. L., 182
 Robbins, J. M., 143, 146

 Sanders, C. F., 172
 Scarboro, Frances A., 204
 Scarbrough, J. O., 25, 26

- Schaffhauser, A. C., 78, 115, 162
Scott, J. L., 61, 68, 140, 144, 146
Sease, J. D., 38, 41, 172, 199
Senn, R. L., 51, 146
Shaffer, L. B., 37
Simpson, W. A., Jr., 100, 136, 178
Slaughter, G. M., 82, 97, 111, 117, 128
Smith, G. P., 5
Smith, M. L., 199
Snyder, S. D., 126, 138
Sparks, Cullie J., Jr., 34, 35
Staats, P. A., 4
Steele, R. M., 34, 177
Stelzman, W. J., 149, 150
Stephenson, R. L., 113
Stiegler, J. O., 12, 69, 72, 119, 131
Stocks, G. M., 31, 32, 33
Stradley, J. G., 172
Swindeman, R. W., 57
- Tennery, V. J., 62, 63, 64, 102, 120
Thoms, K. R., 123
Torsi, G., 5
Trotter, L. R., 164
Tunali, Namik K., 10
- Van Cleve, J. E., 176
Vandermeer, R. A., 20
- Waddell, R. D., Jr., 57
Washburn, T. N., 45, 50, 61, 68, 121, 146, 174
Weaver, S. C., 24
Weir, J. R., Jr., 69, 131, 157
Werner, W. J., 128
Whaley, H. L., 100, 138
Wiffen, F. W., 118, 133
Williams, L. C., 176
Williams, R. K., 23, 112, 118
Williams, R. O., 7
Williams, R. W., 31
Wilson, J. C., 1, 2, 4
Wolfenden, A., 12, 13, 14, 16, 17
- Yakel, H. L., 9, 34, 36, 102
Yoo, M. H., 7
Yust, C. S., 18
- Zachary, C. E., 193
Zeldes, H., 4

METALS AND CERAMICS DIVISION

JUNE 30, 1971





INTERNAL DISTRIBUTION

- | | |
|--|--------------------------|
| 1–2. Central Research Library | 103. W. B. Cottrell |
| 3–4. ORNL – Y-12 Technical Library
Document Reference Section | 104. C. M. Cox, Jr. |
| 5–59. Laboratory Records Department | 105. J. A. Cox |
| 60. Laboratory Records, ORNL R. C. | 106. R. S. Crouse |
| 61. MIT Practice School | 107. F. L. Culler |
| 62. ORNL Patent Office | 108. J. E. Cunningham |
| 63. Laboratory Shift Supervisor | 109. W. W. Davis |
| 64. R. E. Adams | 110. J. P. DeLuca |
| 65. G. M. Adamson, Jr. | 111. J. H. DeVan |
| 66. H. I. Adler | 112. Rian Dippenaar |
| 67. K.H.G. Ashbee | 113. J. R. DiStefano |
| 68. S. I. Auerbach | 114. C. V. Dodd |
| 69. S. E. Beall | 115. R. G. Donnelly |
| 70. R. J. Beaver | 116. D. S. Easton |
| 71. M. Bender | 117. J. H. Erwin |
| 72. L. L. Bennett | 118. W. P. Eatherly |
| 73. R. G. Berggren | 119. D. Fahr |
| 74. D. S. Billington | 120. K. Farrell |
| 75. E. E. Bloom | 121. J. S. Faulkner |
| 76. E. S. Bomar | 122. J. I. Federer |
| 77. A. L. Boch | 123. D. E. Ferguson |
| 78. B. S. Borie | 124. C. B. Finch |
| 79. C. J. Borkowski | 125. R. B. Fitts |
| 80. C. R. Boston | 126. B. Fleischer |
| 81. G. E. Boyd | 127. B. E. Foster |
| 82. R. A. Bradley | 128. A. P. Fraas |
| 83. R. B. Briggs | 129. J. H. Frye, Jr. |
| 84. W. E. Browning, Jr. | 130. W. Fulkerson |
| 85. J. Brynstad | 131. R. E. Gehlbach |
| 86. F. R. Bruce | 132. J. H. Gillette |
| 87. D. A. Canonico | 133. T. G. Godfrey |
| 88. P. T. Carlson | 134. G. M. Goodwin |
| 89. R. W. Carpenter | 135. R. J. Gray |
| 90. J. M. Case (Y-12) | 136. Bill L. Greenstreet |
| 91. J. V. Cathcart | 137. W. R. Grimes |
| 92. O. B. Cavin | 138. J. P. Hammond |
| 93. J. M. Chandler | 139. R. L. Hamner |
| 94. G. W. Clark | 140. W. O. Harms |
| 95. R. E. Clausing | 141. C. S. Harrill |
| 96. W. A. Coghlan | 142. L. A. Harris |
| 97. N. C. Cole | 143. R. F. Hibbs |
| 98. W. C. Colwell | 144–158. M. R. Hill |
| 99. J. H. Coobs | 159. R. W. Hendricks |
| 100. K. V. Cook | 160. D. M. Hewette II |
| 101. W. H. Cook | 161. D. O. Hobson |
| 102. G. L. Copeland | 162. F. J. Homan |
| | 163. A. P. Huber (K-25) |

164. H. Inouye
165. R. G. Jordan (K-25)
166. W. H. Jordan
167. P. R. Kasten
168. S. I. Kaplan
169. T. M. Kegley, Jr.
170. M. T. Kelley
171. C. R. Kennedy
172. E. M. King
173. R. T. King
174. R. L. Klueh
175. R. W. Knight
176. C. C. Koch
177. J. W. Koger
178. T. G. Kollie
179. D. M. Kroeger
180. W. J. Lackey
181. J. M. Leitnaker
182. B. C. Leslie
183. T. B. Lindemer
184. C. Liu
185. J. L. Liverman
186. R. S. Livingston
187. B.T.M. Loh
188. E. L. Long, Jr.
189. A. L. Lotts
190. T. S. Lundy
191. E. J. Manthos
192. M. M. Martin
193. W. R. Martin
194. H. V. Mateer
195. R. W. McClung
196. H. E. McCoy
197. H. C. McCurdy
198. R. E. McDonald
199. H. F. McDuffie
200. D. L. McElroy
201. C. J. McHargue
202. J. P. Moore
203. A. J. Moorhead
204. C. S. Morgan
205. R. A. McNees
206. F. H. Neill
207. J. C. Ogle
208. A. R. Olsen
209. G. S. Painter
- 210-211. R. B. Parker
212. P. Patriarca
213. R. E. Pawel
214. W. H. Pechin
215. G. F. Petersen
216. S. Peterson
217. C. B. Pollock
218. H. Postma
219. R. A. Potter
220. J. J. Prisliger
221. G. A. Reimann
222. A. E. Richt
223. P. L. Rittenhouse
224. J M Robbins
225. M. W. Rosenthal
226. C. F. Sanders
227. A. C. Schaffhauser
228. J. L. Scott
229. H. E. Seagren
230. J. D. Sease
231. M. D. Silverman
232. W. A. Simpson, Jr.
233. G. M. Slaughter
234. G. P. Smith, Jr.
235. A. H. Snell
236. S. D. Snyder
237. C. J. Sparks, Jr.
238. R. M. Steele
239. D. Steiner
240. W. J. Stelzman
241. J. O. Stiegler
242. G. M. Stocks
243. D. A. Sundberg
244. R. W. Swindeman
245. V. J. Tennery
246. D. B. Trauger
247. J. E. VanCleve, Jr.
248. R. A. Vandermeer
249. P. R. Vanstrum (Y-12)
250. R. D. Waddell, Jr.
251. T. N. Washburn
252. A. M. Weinberg
253. J. R. Weir, Jr.
254. W. J. Werner
255. H. L. Whaley
256. G. D. Whitman
257. F. W. Wiffen
258. R. K. Williams
259. R. O. Williams
260. J. C. Wilson
261. C. H. Wodtke
262. A. Wolfenden
263. J. W. Woods
264. H. L. Yakel, Jr.
265. M. H. Yoo
266. F. W. Young, Jr.
267. C. S. Yust
268. C. M. Adams, Jr. (consultant)
269. Leo Brewer (consultant)
270. Walter Kohn (consultant)
271. Sidney Siegel (consultant)

EXTERNAL DISTRIBUTION

272. Lazlo Adler, 4206 Taliluna Ave., Knoxville, TN 37919
 273. Lida K. Barrett, 7100 Downing Drive, Knoxville, TN 37919
 274. R. L. Beatty, 317 Northeast 47th Street, Seattle, WA 98100
 275. R. T. Begley, Westinghouse, Astronuclear Laboratory, P.O. Box 10864, Pittsburgh, PA 15236
 276. C. R. Brooks, Department of Chemical and Metallurgical Engineering, University of Tennessee, Knoxville, TN 37916
- 277–278. E. G. Case, Director, Division of Reactor Standards, AEC, Washington, DC 20545
 279. W. T. Case, Mound Laboratory, P.O. Box 32, Miamisburg, OH 45342
 280. A. T. Chapman, School of Ceramic Engineering, Georgia Institute of Technology, Atlanta, GA 30332
 281. C. C. Cheng, Apartment 408, 1611 Laurel Ave., Knoxville, TN 37916
- 282–283. D. F. Cope, RDT, SSR, AEC, Oak Ridge National Laboratory
 284. E. C. Creutz, National Science Foundation, 1800 G Street, Washington, DC 20545
 285. W. E. Deeds, Department of Physics and Astronomy, University of Tennessee, Knoxville, TN 37916
 286. John DeMastey, Westinghouse, Astronuclear Laboratory, P.O. Box 10864, Pittsburgh, PA 15236
- Division of Isotope Development, AEC, Washington, DC 20545
 287. E. E. Fowler
- Division of Reactor Development and Technology, AEC, Washington, DC 20545
 288. M. Shaw, Director
 289. LTC H. L. Arnold
 290. W. G. Belter
 291. J. W. Crawford, Jr.
 292. G. W. Cunningham
 293. M. D. Dubrow
 294. A. P. D'Zmura
 295. P. A. Halpine
 296. J. R. Hunter
 297. E. E. Kintner
 298. R. E. Kosiba
 299. E. C. Kovacic
 300. W. H. Layman
 301. T. W. McIntosh
 302. W. H. McVey
 303. J. J. Morabito
 304. E. C. Norman
 305. R. E. Pahler
 306. A. J. Pressesky
 307. D. R. Riley
 308. M. A. Rosen
 309. F. A. Ross
- 310–313. J. M. Simmons
 314. E. E. Sinclair
 315. B. Singer
 316. A. N. Tardiff
 317. C. E. Weber
 318. M. J. Whitman
 319. W. A. Williams, Jr.
- Division of Research, AEC, Washington, DC 20545
 320. L. C. Ianniello
 321. R. W. Gould
 322. Dorothy Smith
 323. P. W. McDaniel
 324. D. K. Stevens

Division of Space Nuclear Systems, AEC, Washington, DC 20545

- 325. C. E. Johnson, Jr.
- 326. M. Klein
- 327. A. P. Litman
- 328. J. A. Powers
- 329. F. C. Schwenk

Division of Waste Management and Transportation, AEC, Washington, DC 20545

- 330. F. K. Pittman
- 331–335. Executive Secretary, Advisory Committee on Reactor Safeguards, AEC, Washington, DC 20545
- 336. W. W. Grigorieff, Assistant to the Executive Director, Oak Ridge Associated Universities
- 337. F. B. Gurtner, U.S. Army Edgewood Arsenal, Edgewood Arsenal, MD 21010
- 338. V. D. Frechette, Ceramics Department, Alfred University, Alfred, NY 14802
- 339. R. F. Hehemann, Department of Metallurgical Engineering, Case Western Reserve University, Union Circle, Cleveland, OH 44106
- 340. W. R. Holman, Lawrence Radiation Laboratory, P.O. Box 808, Livermore, CA 94505
- 341. G. M. Kavanagh, Asst. Gen. Mgr. for Reactors, AEC, Washington, DC 20545
- 342. O. C. Kopp, Department of Geology and Geography, University of Tennessee, Knoxville, TN 37916
- 343. Jan Korringa, Department of Physics, Ohio State University, 174 West 18th Ave., Columbus, OH 43210
- 344. J. J. Lombardo, NASA, Lewis Research Center, 21000 Brookpark Road, Cleveland, OH 44135
- 345. C. D. Lundin, Department of Chemical and Metallurgical Engineering, University of Tennessee, Knoxville, TN 37916
- 346. W. D. Manly, Stellite Division, Cabot Corp., 1020 Park Ave., Kokomo, IN 46901
- 347. R. S. Mateer, Department of Metallurgical Engineering, University of Kentucky, Lexington, KY 40506
- 348. C. L. Matthews, RDT, OSR, AEC, Oak Ridge National Laboratory
- 349–351. P. A. Morris, Director, Division of Reactor Licensing, AEC, Washington, DC 20545
- 352. R. R. Nash, NASA, Washington, DC 20546
- 353. B. F. Oliver, 4211 Holston Hills Road, Knoxville, TN 37914
- 354. H. W. Paxton, National Science Foundation, 1800 G Street, Washington, DC 20545
- 355. F. N. Rhines, Department of Metallurgical and Materials Engineering, University of Florida, Gainesville, FL 32601
- 356. Neal Saunders, NASA, Lewis Research Center, 21000 Brookpark Road, Cleveland, OH 44135
- 357. L. M. Slifkin, University of North Carolina, Chapel Hill, NC 27514
- 358. J. E. Spruiell, Department of Chemical and Metallurgical Engineering, University of Tennessee, Knoxville, TN 37916
- 359. E. E. Stansbury, Department of Chemical and Metallurgical Engineering, University of Tennessee, Knoxville, TN 37916
- 360. J. A. Swartout, Union Carbide Corp., 270 Park Ave., New York, NY 10017
- 361. J. K. Tunali, Department of Chemistry, Mid-East Technical University, Ankara, Turkey
- 362. C.H.T. Wilkins, Department of Metallurgical Engineering, University of Alabama, P.O. Box G, University, AL 35486
- 363. L. Young, Gulf General Atomic, Post Office Box 1111, San Diego, CA 92112
- 364. Laboratory and University Division, AEC, ORO
- 365. Patent Office, AEC, ORO
- 366–560. Given distribution as shown in TID-4500 under Metals, Ceramics, and Materials category (25 copies – NTIS)